

**On Long-Term Climate Studies Using a
Coupled General Circulation Model**

by

Steven John Phipps
B.A. (Hons.), M.A.

Submitted in fulfilment of the
requirements for the Degree of
Doctor of Philosophy

University of Tasmania

November 2006

Declarations

I hereby declare that this thesis contains no material which has been accepted for a degree or diploma by the University or any other institution, except by way of background information and duly acknowledged in the thesis; that, to the best of my knowledge and belief, this thesis contains no material previously published or written by another person, except where due acknowledgement is made in the text of the thesis; and that this thesis does not contain any material which infringes copyright.

Signed: _____

Steven John Phipps

This thesis may be made available for loan and limited copying in accordance with the *Copyright Act 1968*.

Signed: _____

Steven John Phipps

Abstract

Coupled atmosphere-ocean general circulation models are the simplest models which are capable of simulating both the variability which occurs within each component of the climate system, and the variability which arises from the interactions between them. Only recently has it become computationally feasible to use coupled general circulation models to study climate variability and change on timescales of $O(10^4)$ years and longer. Flux adjustments are often employed to maintain a control climate that is both stable and realistic; however, the magnitude of the adjustments represents a source of concern.

This study employs the CSIRO Mk3L climate system model, a low-resolution coupled atmosphere-sea ice-ocean general circulation model. The atmospheric and oceanic components are spun up independently; the resulting atmospheric simulation is realistic, while the deep ocean is too cold, too fresh and too buoyant. The spin-up runs provide the initial conditions for the coupled model, which is used to conduct a 1400-year control simulation for pre-industrial conditions. After some initial adjustment, the simulated climate experiences minimal drift. The dominant mode of internal variability is found to exhibit the same spatial structure and correlations as the observed El Niño-Southern Oscillation phenomenon.

The ability of Mk3L to simulate the climate of the mid-Holocene is evaluated. It correctly simulates increased summer temperatures at northern mid-latitudes, and cooling in the tropics. However, it is unable to capture some of the regional-scale features of the mid-Holocene climate, with the precipitation over northern Africa being deficient. The model simulates a $\sim 13\%$ reduction in the strength of El Niño, a much smaller decrease than that implied by the palaeoclimate record.

A 1400-year transient simulation is then conducted, in which the atmospheric CO_2 concentration is stabilised at three times the pre-industrial value. The transient simulation exhibits a reduction in the rate of North Atlantic Deep Water formation, followed by its gradual recovery, and a cessation of Antarctic Bottom Water formation. The global-mean surface air temperature warms 2.7°C upon a trebling of CO_2 , and 5.3°C by the end of the simulation.

A number of modifications to the spin-up procedure for the ocean model are evaluated. A phase shift in the prescribed sea surface temperatures and salinities is found to reduce the phase lag between the model and observations, and to lead to a reduction in the magnitude of the diagnosed flux adjustments. When this spin-up run is used to initialise the coupled model, the reduced flux adjustments are found to have negligible impact upon the nature of the internal variability. While the flux adjustments are not found to have any *direct* influence upon the response of the model to external forcing, they are found to have an *indirect* influence via their effect upon the rate of drift within the control simulation.

An iterative spin-up technique is also developed, whereby the response of the ocean model is used to derive a set of *effective* surface tracers. These result in a much more realistic vertical density profile within the ocean. The coupled model exhibits slightly increased internal variability, with reduced convection within the ocean. There is a slightly greater surface warming in response to an increase in the atmospheric CO_2 concentration, with the reduced convection resulting in slower penetration of the surface warming to depth.

Acknowledgements

I would like to thank Bill Budd, Nathan Bindoff, Jason Roberts, Scott Power, Xingren Wu and Tas van Ommen for their supervision and guidance throughout my PhD candidature. Jason deserves special mention for many fruitful discussions, without which many of the ideas presented herein would never have evolved. His tireless support as I was writing this document was also very much appreciated.

Thanks should go to CSIRO Marine and Atmospheric Research for allowing me to use their climate system model, and for their assistance throughout this project.

The simulations presented herein were conducted on facilities at the Australian Partnership for Advanced Computing in Canberra, and at the Interactive Virtual Environments Centre in Perth, Western Australia. This project would not have been possible without access to these facilities, and I would like to thank the staff at both centres for their support.

Two productive visits were made to the Climate Modelling Group at the University of Victoria in British Columbia, Canada, during the course of this project. My time there was of enormous benefit, and I would like to thank Andrew Weaver and the remainder of the group for their hospitality.

This project was supported through grants of computer time from the APAC Merit Allocation Committee (project e56), the Tasmanian Partnership for Advanced Computing (project e00) and the Interactive Virtual Environments Centre (project ivec0042). Financial support was also received from the Australian Government (an International Postgraduate Research Scholarship), the University of Tasmania (a Tasmania Research Scholarship), the Antarctic CRC (an Antarctic CRC Top-Up Scholarship) and the Trans-Antarctic Association (grant TAA/99/12).

I would like to acknowledge use of the Ferret program (www.ferret.noaa.gov) in the production of the figures presented herein, and the NOAA-CIRES Climate Diagnostics Center (www.cdc.noaa.gov) for making a range of datasets freely available.

I would also like to thank Jason Roberts and Vicki Randell for their diligence in proof-reading this document.

List of Acronyms

AABW	Antarctic Bottom Water
ACC	Antarctic Circumpolar Current
AGCM	Atmospheric General Circulation Model
AMIP	Atmospheric Model Intercomparison Project
APAC	Australian Partnership for Advanced Computing
BP	Before Present
CFL	Courant-Friedrichs-Lewy
CIRES	Cooperative Institute for Research in Environmental Sciences
CMIP	Coupled Model Intercomparison Project
CSIRO	Commonwealth Scientific and Industrial Research Organisation
DJF	December-January-February
DOE	Department of Energy
EMIC	Earth System Model of Intermediate Complexity
ENSO	El Niño-Southern Oscillation
GCM	General Circulation Model
IPCC	Intergovernmental Panel on Climate Change
iVEC	Interactive Virtual Environments Centre
JJA	June-July-August
MSLP	Mean Sea Level Pressure
NADW	North Atlantic Deep Water
NCAR	National Center for Atmospheric Research
NCEP	National Centers for Environmental Prediction
NH	Northern Hemisphere
NOAA	National Oceanic & Atmospheric Administration
OGCM	Ocean(ic) General Circulation Model
OI	Optimum Interpolation
PMIP	Paleoclimate Modelling Intercomparison Project
RMS	Root-Mean-Square
SAT	Surface Air Temperature
SH	Southern Hemisphere
SOI	Southern Oscillation Index
SSS	Sea Surface Salinity
SST	Sea Surface Temperature
WOCE	World Ocean Circulation Experiment

Run nomenclature

Each of the simulations presented herein is given a two-part name, which is constructed as follows:

type-experiment

type indicates the type of simulation being performed, and can have the following values:

A	Atmosphere model spin-up run
CON	Coupled model control run
O	Ocean model spin-up run
3CO2	Coupled model simulation for a $3\times\text{CO}_2$ stabilisation scenario
6ka	Coupled model simulation for the mid-Holocene [6ka BP]

experiment indicates the experiment, and can have the following values:

DEF	Default configuration of the model
EFF	Effective surface tracers used to spin up the ocean model
SHF	Phase-shifted surface tracers used to spin up the ocean model
<i>nd</i>	Relaxation timescale of <i>n</i> days used to spin up the ocean model
<i>Spsu</i>	Sub-ice surface tracers used to spin up the ocean model ($dS = S$ psu)

Contents

1	Introduction	1
1.1	Climate variability and change	1
1.2	Climate models and model evaluation	2
1.3	Coupled models and flux adjustments	4
1.4	Aims	6
1.5	Overview	6
2	The CSIRO Mk3L climate system model	9
2.1	Introduction	9
2.2	Model description	10
2.2.1	Atmosphere model	10
2.2.2	Ocean model	14
2.2.3	Coupled model	19
2.3	Spin-up procedure	19
2.3.1	Atmosphere model	19
2.3.2	Ocean model	20
2.4	Atmosphere model evaluation	21
2.4.1	Surface air temperature	21
2.4.2	Cloud	24
2.4.3	Precipitation	24
2.4.4	Sea ice	28
2.5	Ocean model evaluation	30
2.5.1	Water properties	30
2.5.2	Circulation	35
2.6	Flux adjustments	41
2.6.1	The need for flux adjustments	41
2.6.2	Deriving the flux adjustments	42
2.6.3	Fields passed to the ocean model	45
2.6.4	Fields passed to the atmosphere model	52
3	Ocean model spin-up procedures	57
3.1	Introduction	57
3.2	Surface boundary conditions	58
3.2.1	The relaxation boundary condition	58
3.2.2	Mixed boundary conditions	59
3.2.3	Bulk forcing	60

3.2.4	Summary	62
3.3	The default model response	62
3.3.1	Errors in the annual-mean climate	68
3.3.2	Errors in the amplitude of the annual cycle	68
3.3.3	Phase lags between the simulated and observed climate	71
3.4	Modifying the relaxation boundary condition	71
3.4.1	The relaxation timescale	71
3.4.2	Surface tracers	73
3.5	Varying the relaxation timescale	75
3.5.1	The response of a slab ocean model	75
3.5.2	The response of a mixed-layer ocean	82
3.5.3	Summary	83
3.6	The response of the Mk3L ocean model	85
3.6.1	Annual-mean errors	85
3.6.2	Relative amplitudes and time lags	86
3.6.3	Densities of high-latitude surface waters	89
3.6.4	Water properties	89
3.6.5	Circulation	89
3.6.6	Annual-mean surface fluxes	95
3.6.7	Amplitudes of surface fluxes	97
3.6.8	Summary	101
4	Modified surface tracers	103
4.1	Introduction	103
4.2	Sub-ice surface tracers	104
4.2.1	Sea ice concentrations	104
4.2.2	Sea surface temperatures	104
4.2.3	Sea surface salinities	105
4.2.4	Densities of high-latitude surface waters	106
4.2.5	The response of the Mk3L ocean model	106
4.2.6	Summary	113
4.3	Phase-shifted surface tracers	113
4.3.1	Introduction	113
4.3.2	Spinning up the model	115
4.3.3	Surface fluxes and flux adjustments	115
4.3.4	Summary	117
4.4	Effective surface tracers	121
4.4.1	Spinning up the model	122
4.4.2	Convergence towards a solution	124
4.4.3	The effective surface tracers	126
4.4.4	The model response	126
4.4.5	Densities of high-latitude surface waters	130
4.4.6	Water properties	134
4.4.7	Circulation	139
4.4.8	Transport	139
4.4.9	Surface fluxes	139

4.4.10	Summary	146
5	Control runs	151
5.1	Introduction	151
5.2	Climate drift	152
5.2.1	Atmosphere	152
5.2.2	Ocean	156
5.2.3	Summary	173
5.3	Climate variability	175
5.3.1	Interannual variability	175
5.3.2	El Niño-Southern Oscillation	179
5.3.3	Summary	182
5.4	The impact of the spin-up procedure	183
5.4.1	Climate drift: atmosphere	183
5.4.2	Climate drift: ocean	185
5.4.3	Climate variability	193
5.4.4	Summary	199
6	The climate of the mid-Holocene	201
6.1	Introduction	201
6.2	Mean climate	205
6.2.1	Summary	210
6.3	Climate variability	210
6.3.1	Interannual variability	210
6.3.2	El Niño-Southern Oscillation	214
6.3.3	Summary	216
6.4	The impact of the spin-up procedure	217
6.4.1	Mean climate	217
6.4.2	Climate variability	223
6.4.3	Summary	228
7	3×CO₂ stabilisation experiments	231
7.1	Introduction	231
7.2	The default model response	232
7.2.1	Atmosphere	232
7.2.2	Ocean	235
7.2.3	Summary	253
7.3	The impact of the spin-up procedure	256
7.3.1	Atmosphere	256
7.3.2	Ocean	259
7.3.3	Summary	274
8	Concluding remarks	279
8.1	Conclusions	279
8.1.1	A coupled atmosphere-ocean general circulation model	279
8.1.2	The ocean model spin-up procedure	281
8.1.3	The effect of flux adjustments	283

8.1.4	The effect of the control climate	283
8.1.5	Summary	283
8.2	Future work	284
A	Experimental design	287
A.1	Introduction	287
A.2	PMIP2 experimental design	287
A.3	Spin-up procedures	288
A.3.1	Ocean model	288
A.3.2	Atmosphere model	289
A.4	Coupled model	289
A.4.1	Control runs	289
A.4.2	Mid-Holocene experiments	290
A.4.3	3×CO ₂ stabilisation experiments	291
B	Details of simulations	293
	Bibliography	295

Chapter 1

Introduction

1.1 Climate variability and change

The climate system is composed of interacting components which include, but are not restricted to, the atmosphere, the oceans, the cryosphere and the biosphere. The physical processes which govern their evolution are non-linear, with each component exhibiting different response timescales and thermodynamic properties (e.g. *Bard*, 2002). The large heat capacity and thermal isolation of the deep ocean provides the climate system with a long-term “memory”, as a result of which the spectrum of internal variability extends to millennial timescales (e.g. *Bigg and Wadley*, 2001).

Natural climate variability arises both from variability within each of the components of the climate system, and also from the interactions between them. The non-linear nature of the system gives rise to modes of variability that include phenomena such as stochastic resonances and rapid transitions between regimes. A well-known example of the former is the El Niño-Southern Oscillation (e.g. *Philander*, 1990), which represents a mode of internal variability of the coupled atmosphere-ocean system. Examples of the latter include the Dansgaard-Oeschger and Heinrich events that characterise the glacial climate (e.g. *Bard*, 2002).

Climate variability can also have origins which are external to the climate system. Volcanic eruptions can result in cooling lasting several years, while changes in solar output cause decadal- to centennial-scale variability (e.g. *Ramaswamy et al.*, 2001; *Robertson et al.*, 2001). On timescales of $O(10^4-10^5)$ years, pseudo-cyclic variations in the Earth’s orbital parameters give rise to the glacial cycles (e.g. *Berger and Loutre*, 2004); on timescales of $O(10^6)$ years and longer, tectonic processes become significant, as do the sun’s evolution and orbital path through the galaxy (e.g. *Pavlov et al.*, 2005; *Sloan*, 2006).

Human activity is also having a discernible influence upon the global climate (e.g. *Mitchell et al.*, 2001). While this is generally attributed to the emission of carbon dioxide and other greenhouse gases during the industrial era, it has been suggested that land-use changes began to exert an influence upon global climate as long as 8,000 years ago (*Ruddiman*, 2003). There is therefore a two-way interaction between the climate system and human society: while it provides people with an environment within which to live, their activities also have a significant impact.

An understanding of the full spectrum of natural climate variability is necessary

not only if recent climatic changes (e.g. *Mann and Jones, 2003; Jones and Mann, 2004*) are to be attributed to human influence, but also in order to anticipate the full range of climate states that might be encountered in the future. Given the potential for significant anthropogenic climate change during the coming decades (e.g. *Cubasch et al., 2001*), the ability to anticipate future change, both natural and anthropogenic, is essential for informed decision making.

1.2 Climate models and model evaluation

Computer models of the climate system enable the numerical solution of the physical equations which govern the evolution of the climate. They therefore represent an invaluable tool in the study of the Earth's climate, enabling the degree of natural variability within the climate system to be studied, and enabling the responses to external forcing - such as an increase in the atmospheric carbon dioxide concentration - to be simulated. Different models are used to address different questions, with the models exhibiting varying degrees of complexity. The range of models which exists has variously been described as forming either a "heirarchy" (*McGuffie and Henderson-Sellers, 1997; McAvaney et al., 2001*) or a "spectrum" (*Claussen et al., 2002*).

The most complex models are coupled general circulation models (e.g. *Gordon et al., 2002; Collins et al., 2006; Delworth et al., 2006; Johns et al., 2006*), which include three-dimensional representations of the atmosphere and ocean. Various other sub-models are incorporated, representing components of the climate system such as sea ice, the land surface, vegetation, atmospheric chemistry and marine biogeochemistry. Earth system models of intermediate complexity (EMICs, e.g. *Weaver et al., 2001; Claussen et al., 2002; Goosse et al., 2003; Montoya et al., 2005; Wang et al., 2005*) lie towards the middle of the spectrum. EMICs simulate the interactions between the components of the climate system but, to enable longer simulations to be conducted, are simpler in nature than coupled general circulation models. A typical EMIC consists of an oceanic general circulation model, a sea ice model and an energy-moisture balance atmosphere model; they can also incorporate ice sheet models, vegetation models and ocean biogeochemistry models. The simplest models are zero-, one- or two-dimensional models (e.g. the one-dimensional box model of *Wigley and Raper, 1987*), which can be used to study the global response to external forcing over a wide range of parameter space. A comprehensive review of the history of climate modelling, and of the recent state of the field, is provided by *McGuffie and Henderson-Sellers (2001)*.

Despite their increasing sophistication, it is important to understand that numerical climate models have their limitations. They are only reliable to the extent that they correctly encapsulate the physical processes which they seek to represent, and to the extent that they are supplied with correct boundary and initial conditions. The physical realism of a model is restricted not only by understanding of the climate system, but also by computational limitations. The spatial resolution of a model, and the extent to which it incorporates representations of physical processes, are chosen in accordance with the questions which are to be addressed. They will be restricted, however, by the need to obtain answers to those questions within a

particular timeframe.

The results of numerical models must therefore be analysed within an appropriate context. This context includes not only an understanding of the physical limitations of the model (specifically, the spatial resolution, and the range of physical processes which it incorporates), but also an evaluation of its ability to answer a particular question. Such an evaluation might, therefore, consider its ability to simulate the mean climate state, its ability to simulate natural variability, or its ability to simulate the climatic changes arising from external forcing (such as an increase in the atmospheric carbon dioxide concentration, or a change in insolation). It should be emphasised that, within this context, *evaluation* is a more appropriate term than the commonly-used term *validation*. Validation implies an affirmation that a model is a complete and accurate representation of the system which is being simulated; however, this is impossible in practice, given that such an affirmation requires a complete and accurate understanding of that system (Oreskes *et al.*, 1994).

As a result of limited understanding of the climate system, and given that many physical processes occur on spatial scales much finer than the spatial resolution of numerical climate models, these processes are represented within climate models via *parameterisations* (e.g. McGuffie and Henderson-Sellers, 1997, 2001). These schemes aim to represent physical processes on the spatial scales of the model, rather than on the spatial scales at which they occur in the real world. Examples of such parameterisations are the cloud schemes which are employed within atmospheric general circulation models, and which simulate the *average* cloud cover within a gridbox (as a function, for example, of the relative humidity of the air), rather than seeking to simulate individual clouds. However, such schemes are governed by input parameters - in the case of a cloud scheme, such a parameter might be a critical relative humidity, above which clouds begin to form. These parameters often have no physical basis, and are generally only weakly constrained by observations.

A typical coupled general circulation model contains $O(10^2-10^3)$ such parameters, and there are therefore a very large number of degrees of freedom in the possible physical configurations of the model. While incomplete understanding of the climate system precludes the possibility that a climate model can be a perfect representation of the real world, observations can be used to determine optimal values for the input parameters, a process which is often referred to as “tuning”. However, to determine the optimal set of values (as determined by some pre-defined criterion), observations are required of a number of distinct climate states which equals, or exceeds, the number of degrees of freedom in the physical configuration of the model. This is essentially unachievable in practice, and the physical configuration of general circulation models can therefore contain considerable uncertainty.

Attempts to quantify the uncertainties inherent in the output of climate models have typically sought to compare and contrast the response of different models to a given scenario. The Coupled Model Intercomparison Project (e.g. Covey *et al.*, 2003; Meehl *et al.*, 2005) compared the ability of coupled general circulation models to simulate the present day climate, and the response of the models to a 1% per year increase in the atmospheric carbon dioxide concentration, while the Paleoclimate Modelling Intercomparison Project (e.g. Joussaume *et al.*, 1999; Harrison *et al.*, 2002; Crucifix *et al.*, 2005; *Paleoclimate Modelling Intercomparison Project*,

2005) aims to compare the ability of models to simulate palaeoclimate epochs. Ensembles of simulations have also been conducted, using the same model but with perturbations to the model physics; the largest example of such an ensemble is the ongoing “climateprediction.net” experiment (*Stainforth et al.*, 2005), which aims to systematically explore model parameter space.

1.3 Coupled models and flux adjustments

Coupled general circulation models aim to represent both the variability within the components of the climate system, and the variability which arises from the interactions between them. They are therefore the only type of climate model which is capable of simulating the full range of internal variability within the atmosphere-sea ice-ocean system.

Coupled general circulation models have been shown to be capable of simulating the present-day climate, both with regard to the mean state, and with regard to the internal variability (e.g. *McAvaney et al.*, 2001; *Lambert and Boer*, 2001; *AchutaRao and Sperber*, 2002; *Covey et al.*, 2003; *Alexander et al.*, 2006; *Collins et al.*, 2006; *Delworth et al.*, 2006; *Deser et al.*, 2006; *Gnanadesikan et al.*, 2006; *Johns et al.*, 2006; *Wittenberg et al.*, 2006). Confidence in the ability of these models to simulate climatic change is enhanced by their ability to reproduce the observed trend in the global-mean climate surface air temperature during the twentieth century (e.g. *Mitchell et al.*, 1995; *Haywood et al.*, 1997; *Boer et al.*, 2000; *Meehl et al.*, 2000; *Broccoli et al.*, 2003). Coupled general circulation models have been used to simulate both the short- and long-term response of the climate system to an increase in the atmospheric carbon dioxide concentration (e.g. *Manabe and Stouffer*, 1994; *Cubasch et al.*, 2001; *Covey et al.*, 2003; *Dixon et al.*, 2003; *Stouffer and Manabe*, 2003; *Gregory et al.*, 2005; *Bryan et al.*, 2006; *Kiehl et al.*, 2006; *Meehl et al.*, 2006; *Stouffer et al.*, 2006), and also to simulate past climate states (e.g. *Hewitt and Mitchell*, 1998; *Bush*, 1999; *Otto-Bliesner*, 1999; *Braconnot et al.*, 2000b; *Voss and Mikolajewicz*, 2001; *Liu et al.*, 2003a,b; *Mikolajewicz et al.*, 2003; *Otto-Bliesner et al.*, 2006).

However, the control climates of coupled general circulation models are generally not completely stable, and tend to exhibit ongoing drift in global statistics such as the global-mean surface air temperature (e.g. *Bell et al.*, 2000; *Lambert and Boer*, 2001). If systematic errors are present within the physics of either the atmosphere and ocean models, then drift *will* be encountered upon the coupling of the two models (*Moore and Gordon*, 1994; *Weaver and Hughes*, 1996). The errors will cause the boundary conditions on each model to change upon coupling; if the simulated sea surface temperature differs from observations, for example, then the bottom boundary condition on the atmosphere model will change when coupled. It will therefore evolve into a different state, and the coupled model will drift.

One method for reducing this drift is to apply flux adjustments (*Sausen et al.*, 1988). These adjustments are diagnosed from the differences between the surface fluxes simulated by the atmosphere and ocean models during independent spin-up, and are applied to the surface fluxes within the coupled model. Flux adjustments are intended to ensure that the coupled model operates at the equilibrium reference state for which the atmosphere and ocean models were designed, and it is therefore being

assumed that the climatologies of the stand-alone atmosphere and ocean models represent the best available climatologies, given the spatial resolutions, the model physics and the boundary conditions which are imposed (*Sausen et al.*, 1988; *Weaver and Hughes*, 1996).

The application of flux adjustments is undesirable, however. The adjustments have no physical justification, and can exhibit large spatial and temporal variability; indeed, they can exceed in magnitude the fluxes which occur naturally within the climate system. It has been shown that when an ocean model is forced with a specified freshwater flux, and with the sea surface temperature relaxed towards observed values, it is capable of exhibiting self-sustaining oscillations on decadal timescales (*Weaver et al.*, 1993). It is therefore possible that, when the flux adjustments are large in magnitude, they determine the structure of the internal variability within the ocean, with this mode being excited by stochastic variability in the surface fluxes (*Weaver and Hughes*, 1996). It should also be noted that drift may still occur within a coupled model, even when flux adjustments are applied. *Power* (1995) demonstrates that the response of an ocean model to perturbations about a mean surface flux is asymmetric. If the magnitude of the variability in the surface fluxes is increased, as will happen upon the coupling to an atmosphere model, the ocean model may therefore evolve into a different state, even if the time-mean of the surface fluxes remains unchanged.

The need for flux adjustments within the coupled model suggests significant deficiencies in the physics of at least one of the constituent models. Furthermore, given that the adjustments are derived for a particular climate state, a coupled model which employs flux adjustments can only be regarded as being suitable for simulating *small* perturbations about the reference state (*Cubasch et al.*, 1992). While there is no apparent definition as to what represents a small perturbation, the glacial climate, or a large increase in the atmospheric carbon dioxide concentration, would not seem to represent small perturbations relative to the climate of the present day.

Several studies have addressed the role of flux adjustments within coupled models. *Duffy et al.* (2000) assess the variability in surface air temperatures within 17 simulations which were submitted to the Coupled Model Intercomparison Project, and find no evidence that flux adjustments *directly* influence variability in coupled general circulation models; however, they note that models with lower global-mean surface air temperatures exhibit more high-latitude variability, and that, by influencing the global-mean surface air temperature, flux adjustments may have a weak *indirect* effect upon internal variability. For a scenario in which the atmospheric carbon dioxide concentration is increased at 1% per year, *Gregory and Mitchell* (1997) find that the Hadley Centre coupled model exhibits a $\sim 30\%$ reduction in the global-mean surface temperature response when flux adjustments are not applied, relative to an otherwise-identical configuration of the model in which flux adjustments *are* applied. The spatial patterns of the temperature changes are similar in the two runs, indicating that the flux adjustments are not causing any gross distortion. In contrast, *Fanning and Weaver* (1997), who study the response of an idealised coupled model with and without flux adjustments, find only regional differences in the model response as the atmospheric CO₂ concentration is increased; once the CO₂ concentration is stabilised, however, they find that the model which employs flux

adjustments exhibits greater warming, consistent with *Gregory and Mitchell (1997)*.

Based on these studies, and given uncertainty regarding the validity of using coupled general circulation models to simulate large perturbations around the control state, the role of flux adjustments within coupled GCMs appears to be worthy of further study. Both the effect of flux adjustments upon the simulated internal climate variability, and upon the response of the model to external forcing, merit investigation.

1.4 Aims

This project seeks to employ a computationally-efficient coupled atmosphere-ocean general circulation model to address some of the questions raised above. Such a model would enable multi-millennial climate simulations to be conducted, enabling the full spectrum of internal climate variability to be investigated. It would also enable the equilibrium response of the model to external forcing, such as an increase in the atmospheric carbon dioxide concentration or a change in insolation, to be determined.

The aims of this project are therefore to use such a model to address the following questions:

1. How does the spin-up procedure for the ocean model influence the degree of realism of the control climate, and the magnitude of the flux adjustments which are diagnosed for use within the coupled model?
2. Do the flux adjustments influence the nature of the internal variability within the model, and the response to external forcing?
3. Does the control climate of the ocean model influence the nature of the internal variability within the model, and the response to external forcing?

1.5 Overview

Chapter 2 describes the CSIRO Mk3L climate system model, which was developed as part of this project. The atmospheric and oceanic components are spun up for pre-industrial conditions, consistent with PMIP2 (*Paleoclimate Modelling Intercomparison Project*, 2005) experimental design, and the control climates of each model are evaluated against observations. The method used to diagnose flux adjustments is discussed, and flux adjustments are derived from the atmosphere and ocean model spin-up runs. The magnitude and spatial structure of the adjustments are then analysed.

In Chapter 3, the spin-up procedure for the ocean model is considered further, with the aim of obtaining a more realistic ocean climate. A number of spin-up procedures are considered, and it is concluded that the relaxation boundary condition is the most appropriate. The effectiveness of the relaxation boundary condition is assessed, first by studying the default response of the ocean model, and then using a simple theoretical model. The response of the ocean model to changes in the relaxation timescale is then investigated.

The spin-up procedure for the ocean model is further considered in Chapter 4, with a number of modifications to the surface boundary conditions being assessed. In the first of these, the prescribed sea surface temperatures (SSTs) and sea surface salinities (SSSs) are modified to allow for the presence of sea ice and, in particular, to allow for the effects of brine rejection. The second modification attempts to correct for the phase lag between the observed and simulated SSTs and SSSs by shifting the prescribed SSTs and SSSs forward in time by one month. Finally, an iterative technique is developed, whereby the response of the model is used to obtain a set of *effective* surface tracers. These are derived so as to minimise the errors in the simulated SSTs and SSSs.

The control climate of the Mk3L coupled model, with regard to both the drift in the mean climate, and the internal variability of the model, is presented in Chapter 5. Three configurations of the model are considered: the default configuration, and two new configurations in which the ocean model is spun up in accordance with the techniques developed in the previous chapter.

In Chapters 6 and 7, the response of each configuration of the model to changes in the external boundary conditions is studied. The ability of Mk3L to simulate the climate of the mid-Holocene (6,000 years BP) is evaluated in Chapter 6. The transient response of the model to an increase in the atmospheric carbon dioxide concentration is then studied in Chapter 7. A scenario is employed in which the CO₂ concentration is increased at 1% per year, and then stabilised at three times the pre-industrial level.

Concluding remarks, including suggestions for future work, are presented in Chapter 8.

Two appendices are also included. Appendix A provides information regarding the experimental design, while Appendix B provides some statistics for the simulations which are presented herein.

Chapter 2

The CSIRO Mk3L climate system model

2.1 Introduction

The CSIRO Mk3L climate system model comprises two components: an atmospheric general circulation model, which incorporates both a sea ice model and a land surface model, and an oceanic general circulation model. The atmospheric general circulation model is a low-resolution version of the atmospheric component of the CSIRO Mk3 coupled model (*Gordon et al.*, 2002), while the oceanic general circulation model is the oceanic component of the CSIRO Mk2 coupled model (*Gordon and O'Farrell*, 1997).

This combination takes advantage of the rapid execution times of the Mk2 coupled model, which result from the low horizontal resolution, while also taking advantage of the enhanced physics of the Mk3 atmosphere model. Relative to the Mk2 atmosphere model, enhancements to the physics include:

- an increase in the vertical resolution from 9 to 18 levels
- the incorporation of a prognostic scheme for stratiform cloud
- the incorporation of a new cumulus convection scheme
- an enhanced land surface model

The development of Mk3L from these components is described in detail by *Phipps* (2006). The resulting model is computationally efficient, portable across a wide range of computer architectures, and suitable for studying climate variability and change on millennial timescales.

The model physics is described in Section 2.2, while Section 2.3 outlines the spin-up procedure. The ability of the atmospheric and oceanic components to simulate the present-day climate is evaluated in Sections 2.4 and 2.5 respectively, and the flux adjustments required by the coupled model are derived in Section 2.6.

The material presented in Section 2.2 also appears in *Phipps* (2006), but is reproduced here in the interests of completeness.

2.2 Model description

2.2.1 Atmosphere model

The CSIRO Mk3 atmosphere model consists of three components: an atmospheric general circulation model, a multi-layer dynamic-thermodynamic sea ice model and a land surface model. As each of these components is documented in detail by *Gordon et al.* (2002), only a brief summary is provided here. This summary concentrates on those features which are unique to Mk3L, and on those which are particularly relevant to this project.

The standard configuration of the Mk3 atmosphere model employs a spectral resolution of T63. However, a spectral resolution of R21 is also supported for research purposes, and it is this resolution which is used within Mk3L. The zonal and meridional resolutions are therefore 5.625° and $\sim 3.18^\circ$ respectively.

Atmospheric general circulation model

The dynamical core of the atmosphere model is based upon the spectral method, and uses the flux form of the dynamical equations (*Gordon, 1981*). Physical parameterisations and non-linear dynamical flux terms are calculated on a latitude-longitude grid, with Fast Fourier Transforms used to transform fields between their spectral and gridded forms. Semi-Lagrangian transport is used to advect moisture (*McGregor, 1993*), and gravity wave drag is parameterised using the formulation of *Chouinard et al.* (1986).

A hybrid vertical coordinate is used, which is denoted as the η -coordinate. The Earth's surface forms the first coordinate surface, as in the σ -system, while the remaining coordinate surfaces gradually revert to isobaric levels with increasing altitude. The 18 vertical levels used in the Mk3L atmosphere model are listed in Table 2.1 (*Gordon et al., 2002, Table 1*).

The topography is derived by interpolating the $1^\circ \times 1^\circ$ dataset of *Gates and Nelson* (1975a) onto the model grid. Some modifications are then made, in order to avoid areas of significant negative elevation upon fitting to the (truncated) resolution of the spectral model (*Gordon et al., 2002*). The resulting topography is shown in Figure 2.1.

Time integration is via a semi-implicit leapfrog scheme, with a Robert-Asselin time filter (*Robert, 1966*) used to prevent decoupling of the time-integrated solutions at odd and even timesteps. The Mk3L atmosphere model uses a timestep of 20 minutes.

The radiation scheme treats solar (shortwave) and terrestrial (longwave) radiation independently. Full radiation calculations are conducted every two hours, allowing for both the annual and diurnal cycles. Clear-sky radiation calculations are also performed at each radiation timestep. This enables the cloud radiative forcings to be determined using Method II of *Cess and Potter* (1987), with the forcings being given by the differences between the radiative fluxes calculated with and without the effects of clouds.

The shortwave radiation scheme is based on the approach of *Lacis and Hansen* (1974), which divides the shortwave spectrum into 12 bands. Within each of these

Level (k)	η	Approximate height (m)
18	0.0045	36355
17	0.0216	27360
16	0.0542	20600
15	0.1001	16550
14	0.1574	13650
13	0.2239	11360
12	0.2977	9440
11	0.3765	7780
10	0.4585	6335
9	0.5415	5070
8	0.6235	3970
7	0.7023	3025
6	0.7761	2215
5	0.8426	1535
4	0.8999	990
3	0.9458	575
2	0.9784	300
1	0.9955	165

Table 2.1: The hybrid vertical levels used within the Mk3L atmosphere model: the value of the η -coordinate, and the approximate height (m).

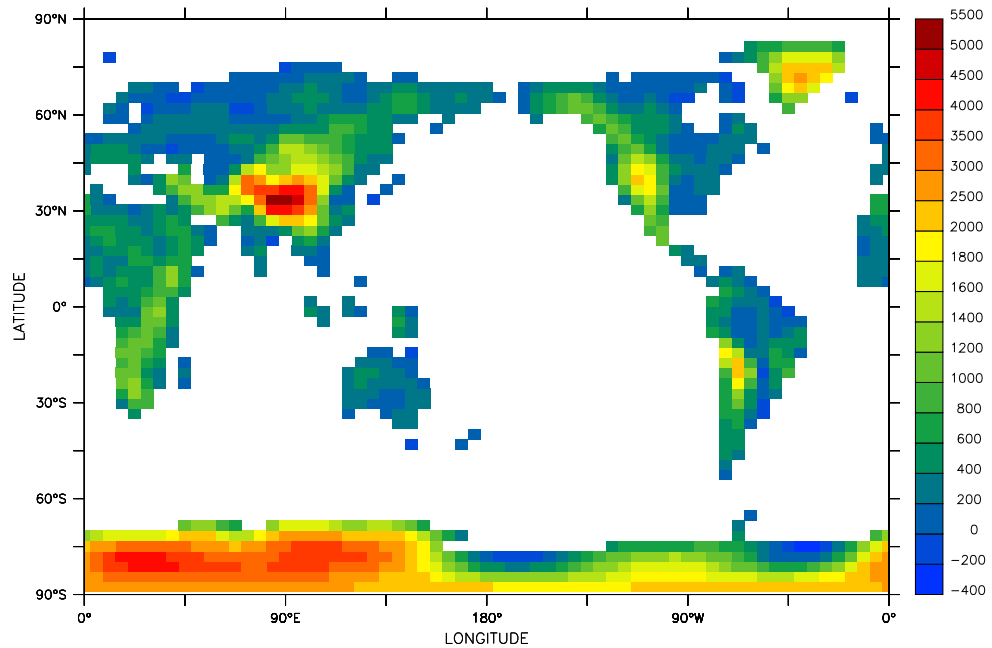


Figure 2.1: The topography of the Mk3L atmosphere model: the elevation of land gridpoints (m).

bands, the radiative properties are taken as being uniform. Ozone concentrations are taken from the AMIP II recommended dataset (*Wang et al.*, 1995). Additional code has been inserted into Mk3L, enabling both the solar constant and the epoch to be specified at runtime, with the Earth’s orbital parameters being calculated by the model (*Phipps*, 2006).

The longwave radiation scheme uses the parameterisation developed by Fels and Schwarzkopf (*Fels and Schwarzkopf*, 1975, 1981; *Schwarzkopf and Fels*, 1985, 1991), which divides the longwave spectrum (wavelengths longer than 5 μm) into seven bands. Values for the CO₂ transmission coefficients must be provided at runtime.

The cumulus convection scheme is based on the U.K. Meteorological Office scheme (*Gregory and Rowntree*, 1990), and generates both the amount and the liquid water content of convective clouds. This scheme is coupled to the prognostic cloud scheme of *Rotstayn* (1997, 1998, 2000), which calculates the amount of stratiform cloud, using the three prognostic variables of water vapour mixing ratio, cloud liquid water mixing ratio and cloud ice mixing ratio.

In the stand-alone atmosphere model, four types of surface gridpoint are employed: land, sea, mixed-layer ocean and sea ice. The temperatures of the sea gridpoints are determined from monthly observed sea surface temperatures, which must be provided at runtime. Linear interpolation in time is used to estimate values at each timestep, with no allowance for any diurnal variation. At high latitudes, sea gridpoints may be converted to mixed-layer ocean gridpoints, with self-computed temperatures; these can then evolve into sea ice gridpoints. This is discussed further in the following description of the sea ice model.

Sea ice model

The sea ice model includes both ice dynamics and ice thermodynamics, and is described by *O’Farrell* (1998). Internal resistance to deformation is parameterised using the cavitating fluid rheology of *Flato and Hibler* (1990, 1992). The thermodynamic component is based on the model of *Semtner* (1976), which splits the ice into three layers, one for snow and two for ice. Sea ice gridpoints are allowed to have fractional ice cover, representing the presence of leads and polynyas.

Ice advection arises from the forcing from above by atmospheric wind stresses, and from below by oceanic currents. The currents are obtained from the ocean model when running as part of the coupled model; in the stand-alone atmosphere model, climatological ocean currents must be provided.

The advance and retreat of the ice edge in the stand-alone atmosphere model is controlled by using a mixed-layer ocean to compute water temperatures for those sea gridpoints which lie adjacent to sea ice. The mixed-layer ocean has a fixed depth of 100 m, and the evolution of the water temperature T_s is calculated using the surface heat flux terms and a weak relaxation towards the prescribed sea surface temperature T_{SST} , as follows (*Gordon et al.*, 2002, Equation 19.6):

$$\gamma_0 \frac{dT_s}{dt} = (1 - \alpha_s)S_s^\downarrow + R_s^\downarrow - \epsilon_s \sigma T_s^4 - (H_s + E_s) + \lambda_c(T_{SST} - T_s) \quad (2.1)$$

Here, γ_0 represents the areal heat capacity of a 100 m-thick layer of water, t represents time, α_s represents the surface albedo, S_s^\downarrow and R_s^\downarrow represent the net

downward surface fluxes of shortwave and longwave radiation respectively, ϵ_s represents the surface emissivity, σ represents the Stefan-Boltzmann constant, H_s and E_s represent the net upward surface fluxes of sensible and latent heat respectively, and λ_c represents a relaxation constant. Mk3L uses a relaxation timescale of 23 days.

A mixed-layer ocean gridpoint can become a sea ice gridpoint either when its temperature falls below the freezing point of seawater, which is taken as being -1.85°C , or when ice is advected from an adjacent sea ice gridpoint. When a mixed-layer ocean gridpoint is converted to a sea ice gridpoint, the initial ice concentration is set at 4%. The neighbouring equatorward gridpoint, if it is a sea gridpoint, is then converted to a mixed-layer ocean gridpoint.

Within a gridpoint that has fractional sea ice cover, both in the stand-alone atmosphere model and the coupled model, the water temperature is calculated using a mixed-layer ocean with a fixed depth of 100 m. The surface heat flux is given by Equation 2.1, except that the final relaxation term is replaced with a basal heat flux F_i , which is calculated as follows (Gordon *et al.*, 2002, Equation 19.8):

$$F_i = \frac{k_{f_{rz}}\rho_w c_w dz (T_{SST} - T_f)}{(dz/2)^2} + F_{geog} \quad (2.2)$$

Here, $k_{f_{rz}} = 0.15 \times 10^{-4} \text{ s}^{-1}$ is the heat transfer coefficient, ρ_w and c_w are the density and specific heat capacity of seawater respectively, $dz = 25 \text{ m}$ is the thickness of the upper layer of the ocean model, and $T_f = -1.85^\circ\text{C}$ represents the freezing point of seawater. T_{SST} represents the prescribed sea surface temperature in the case of the stand-alone atmosphere model, and the temperature of the upper level of the ocean in the case of the coupled model. The additional fixed component F_{geog} allows for the effects of sub-gridscale mixing. Its value is resolution-dependent and, at the horizontal resolution of R21 used in Mk3L, is equal to 2 Wm^{-2} in the Northern Hemisphere, and 15 Wm^{-2} in the Southern Hemisphere.

If, within the coupled model, the temperature of the upper level of the ocean T_{OC} falls below -2°C , an additional term is added to the ice-ocean heat flux, as follows (Gordon *et al.*, 2002, Equation 19.9):

$$F_{f_{rz}} = \frac{k_{f_{rz}}\rho_w c_w dz (T_{OC} - T_f)}{(dz/2)^2} \quad (2.3)$$

In this case, $k_{f_{rz}}$ is increased to $6 \times 10^{-4} \text{ s}^{-1}$ in order to stimulate the formation of sea ice in sub-freezing waters.

Surface processes can lead to either a decrease in ice volume, as a result of either melting or sublimation, or an increase in ice volume; this can occur either when the depth of snow exceeds 2 m, in which case the excess is converted into an equivalent amount of ice, or when the weight of snow becomes so great that the floe becomes completely submerged. When the latter occurs, any submerged snow is converted into ‘‘white’’ ice.

Lateral and basal ice growth and melt are determined by the temperature of the mixed-layer ocean. Additional ice can grow when the water temperature falls below the freezing point of seawater, -1.85°C , subject to a maximum allowable thickness of 6 m. Once the water temperature rises above -1.5°C , half of any additional heating is used to melt ice; once it rises above -1.0°C , all of the additional heating is used

to melt ice. In the case of the stand-alone atmosphere model, a sea ice gridpoint is converted back to a mixed-layer ocean gridpoint once the sea ice has disappeared. The neighbouring equatorward gridpoint, if it is a mixed-layer ocean gridpoint, is then converted back to a sea gridpoint.

Land surface model

The land surface model is an enhanced version of the soil-canopy scheme of *Kowalczyk et al.* (1991, 1994). A new parameterisation of soil moisture and temperature has been implemented, a greater number of soil and vegetation types are available, and a multi-layer snow cover scheme has been incorporated.

The soil-canopy scheme allows for 13 land surface and/or vegetation types and nine soil types. The land surface properties are pre-determined, with seasonally-varying values being provided for the albedo and roughness length, and annual-mean values for the vegetation fraction. The stomatal resistance is calculated by the model, as are seasonally-varying vegetation fractions for some vegetation types. The soil model has six layers, each of which has a pre-set thickness. Soil temperature and the liquid water and ice contents are calculated as prognostic variables. Run-off occurs once the surface layer becomes saturated, and is assumed to travel instantaneously to the ocean via the path of steepest descent.

The snow model computes the temperature, snow density and thickness of three snowpack layers, and calculates the snow albedo. The maximum snow depth is set at 4 m (equivalent to 0.4 m of water).

2.2.2 Ocean model

The CSIRO Mk2 ocean model is a coarse-resolution, z -coordinate general circulation model, based on the implementation by *Cox* (1984) of the primitive equation numerical model of *Bryan* (1969). It is described by *Gordon and O'Farrell* (1997) and *Hirst et al.* (2000) and, with some slight modifications to the physics, by *Bi* (2002).

The prognostic variables used by the model are potential temperature, salinity, and the zonal and meridional components of the horizontal velocity. The Arakawa B-grid (*Arakawa and Lamb*, 1977) is used, in which the tracer gridpoints are located at the centres of the gridboxes, and the horizontal velocity gridpoints are located at the corners. The vertical velocity is diagnosed through application of the continuity equation.

The horizontal grid matches the Gaussian grid of the atmosphere model, such that the tracer gridpoints on the ocean model grid coincide with the gridpoints on the atmosphere model grid. The zonal and meridional resolutions are therefore 5.625° and $\sim 3.18^\circ$ respectively. There are 21 vertical levels, which are listed in Table 2.2.

The bottom topography is derived by interpolating the $1^\circ \times 1^\circ$ dataset of *Gates and Nelson* (1975b) onto the model grid, with some slight smoothing to ensure that a solution is achieved when calculating the barotropic streamfunction (*Cox*, 1984). The resulting bathymetry is shown in Figure 2.2.

Level (k)	Thickness (m)	Depth (m)		κ_e (m^2s^{-1})
		Centre	Base	
1	25	12.5	25	0*
2	25	37.5	50	70*
3	30	65	80	180*
4	37	98.5	117	290*
5	43	138.5	160	420*
6	50	185	210	580 [†]
7	60	240	270	770 [†]
8	80	310	350	1000 [‡]
9	120	410	470	1000 [‡]
10	150	545	620	1000 [‡]
11	180	710	800	1000 [‡]
12	210	905	1010	1000 [‡]
13	240	1130	1250	1000 [‡]
14	290	1395	1540	1000 [‡]
15	360	1720	1900	1000 [‡]
16	450	2125	2350	1000 [‡]
17	450	2575	2800	1000 [‡]
18	450	3025	3250	1000 [‡]
19	450	3475	3700	1000 [‡]
20	450	3925	4150	1000 [‡]
21	450	4375	4600	1000 [‡]

Table 2.2: The vertical levels used within the Mk3L ocean model: the thickness, the depth of the centre and base of each gridbox, and the value of the isopycnal thickness diffusivity. *These values are hard-coded into the model. [†]These values are the maximum allowable values, and are hard-coded into the model; lower values may be specified via the model control file. [‡]These values are specified via the model control file, and represent the values used for this project.

A number of changes are made to the land/sea mask, relative to the atmosphere model. The land gridpoints at the tips of South America and the Antarctic Peninsula are replaced with ocean gridpoints, ensuring that Drake Passage accommodates three horizontal velocity gridpoints. In order to ensure adequate resolution of the Greenland-Scotland sill, Iceland is removed; likewise, adequate resolution of the flows through the Indonesian archipelago is ensured through a number of modifications to the land/sea mask.

Europe, Africa, Asia, and North and South America are combined into a single landmass through the closure of Bering Strait. Greenland, Madagascar and Japan are joined to this landmass through closure of the Canadian archipelago, the Mozambique Channel and the Sea of Japan respectively. Tasmania, continental Australia and New Guinea are also combined into a single island. Svalbard, which lies to the north of Norway and which occupies a single isolated gridpoint on the model grid, is removed.

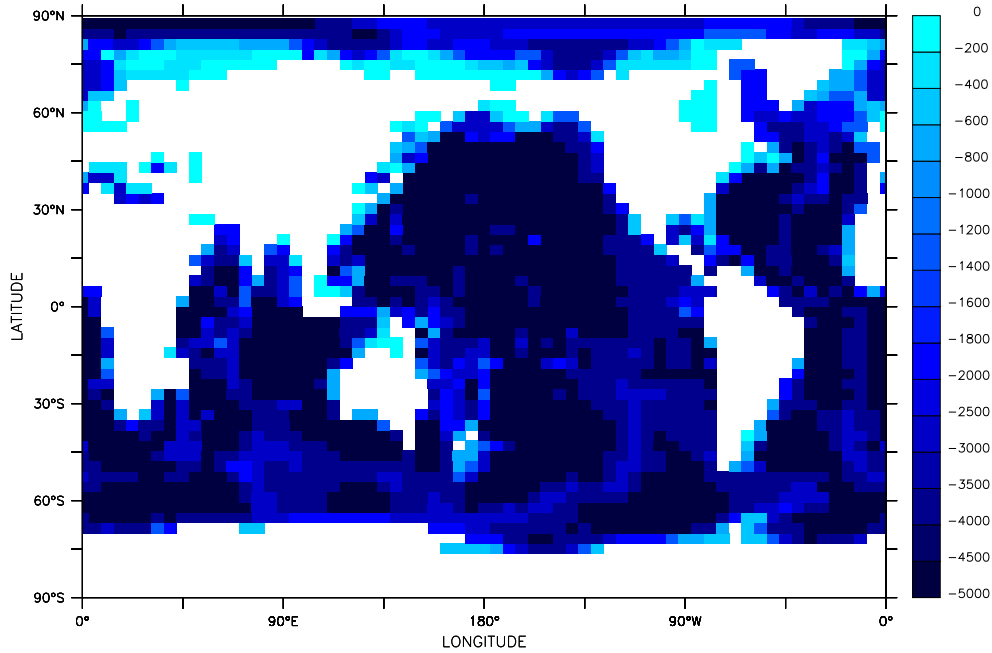


Figure 2.2: The bathymetry of the Mk3L ocean model: the depth of ocean gridpoints (m).

As a result of these changes, there are just four landmasses on the ocean model grid:

- Europe/Africa/Asia/North America/South America/Greenland
- Antarctica
- Australia/New Guinea
- New Zealand

The only other modifications to the land/sea mask are to the Hudson and Gibraltar Straits, which are too narrow on the model grid to contain any horizontal velocity gridpoints; these straits are therefore closed.

The consolidation of the Earth's land surface into four landmasses improves the computational performance of the ocean model. This is a consequence of the *rigid-lid* boundary condition (Cox, 1984), which is employed in order to remove the timestep limitation associated with high-speed external gravity waves. Under this boundary condition, the external mode of momentum is represented by a volume transport streamfunction, ψ :

$$\bar{u} = -\frac{1}{aH} \frac{\partial \psi}{\partial \phi} \quad (2.4)$$

$$\bar{v} = \frac{1}{aH \cos \phi} \frac{\partial \psi}{\partial \lambda} \quad (2.5)$$

Here, \bar{u} and \bar{v} represent the zonal and meridional components, respectively, of the vertically-averaged velocity, a represents the radius of the Earth, H represents the depth of the ocean, and ϕ and λ represent latitude and longitude respectively. At lateral walls, the boundary conditions on u and v are

$$u = v = 0 \quad (2.6)$$

The boundary condition on ψ at lateral walls is therefore

$$\frac{\partial\psi}{\partial\phi} = \frac{\partial\psi}{\partial\lambda} = 0 \quad (2.7)$$

This condition is satisfied by setting ψ constant along the boundary of each unconnected landmass. If islands are present, the constant value of ψ for each island indicates the net flow around that island, and hence must be predicted by the governing equations. The method used in the ocean model is *hole relaxation*, in which the line integral of the quantity $\nabla p_{surface}$, where $p_{surface}$ is the surface pressure, around each island is required to vanish.

By consolidating the Earth's land surface into four landmasses, and by setting the net flow around Europe-Africa-Asia-North America-South America-Greenland equal to zero, it is only necessary to calculate the line integrals around three relatively small islands (Antarctica, Australia-New Guinea and New Zealand).

The bathymetry of the Mk3L ocean model defines six basins which have no resolved connection with the world ocean: the Baltic, Black, Caspian and Mediterranean Seas, Hudson Bay and the Persian Gulf. It does not therefore adequately represent the physical connections which exist within the ocean; with the exception of the Caspian Sea, each of these basins exchanges water with the world ocean via straits which are not resolved on the model grid. The effects of these exchanges are parameterised within the model through an imposed mixing between the gridpoints which lie to either side of each unresolved strait. This mixing has been substantially improved in Mk3L (*Phipps, 2006*).

Time integration is via a leapfrog scheme, with mixing timesteps conducted once every 19 tracer timesteps in order to prevent decoupling of the time-integrated solutions at odd and even timesteps. Fourier filtering is used to reduce the timestep limitation arising from the CFL criterion (e.g. *Washington and Parkinson, 1986*) associated with the convergence of meridians at high latitudes, particularly in the Arctic Ocean (*Cox, 1984*). In the Mk3L ocean model, Fourier filtering is only applied northward of 79.6°N in the case of tracers, and northward of 81.2°N in the case of horizontal velocities (*Phipps, 2006*). The ocean bottom is assumed to be insulating, while no-slip and insulating boundary conditions are applied at lateral boundaries.

The stand-alone ocean model employs an asynchronous timestepping scheme, with a timestep of 1 day used to integrate the tracer equations and a timestep of 20 minutes used to integrate the momentum equations. Within the coupled model - and during the final stage of spin-up runs, prior to coupling to the atmosphere model - a synchronous timestepping scheme is employed, with a timestep of 1 hour used to integrate both the tracer and momentum equations.

The vertical diffusivity κ_v varies as the inverse of the Brunt-Väisälä frequency, following the scheme of *Gargett (1984)*. The minimum diffusivity is set

at $3 \times 10^{-5} \text{ m}^2\text{s}^{-1}$, except in the upper levels of the ocean, where it is increased in order to simulate the effects of mixing induced by surface winds. The minimum diffusivity between the upper two levels of the model is set at $2 \times 10^{-3} \text{ m}^2\text{s}^{-1}$, while that between the second and third levels is set at $1.5 \times 10^{-4} \text{ m}^2\text{s}^{-1}$. Whenever static instability arises, the vertical diffusivity is increased to $100 \text{ m}^2\text{s}^{-1}$, simulating convective mixing.

Two parameterisations are incorporated in order to represent the mixing along isopycnal surfaces (i.e. surfaces of constant density). The first of these parameterisations is the isopycnal diffusion scheme of *Cox* (1987), which allows for a more realistic representation of the tendency for tracers to be mixed along surfaces of constant density. For this project, the isopycnal diffusivity was set to the depth-independent value of $1000 \text{ m}^2\text{s}^{-1}$.

The second parameterisation is the scheme of *Gent and McWilliams* (1990) and *Gent et al.* (1995), which parameterises the adiabatic transport of tracers by mesoscale eddies. An eddy-induced horizontal transport velocity is diagnosed, which is added to the resolved large-scale horizontal velocity to give an effective horizontal transport velocity. The continuity equation can be used to derive the vertical component of either the eddy-induced transport velocity or the effective transport velocity. In Mk3L, Gent-McWilliams eddy diffusion is employed at all latitudes; previously there was a transition to horizontal diffusion within the Arctic Ocean (*Phipps*, 2006).

Previous studies (e.g. *Hirst and McDougall*, 1996; *England and Hirst*, 1997; *Hirst and McDougall*, 1998) have found significant improvements in the ocean climate, particularly in the Southern Ocean, upon incorporation of Gent-McWilliams eddy diffusion into their implementations of the Bryan-Cox ocean model. These improvements include: more realistic deep water properties; a substantial reduction in the amount of convective overturning in the Southern Ocean; a corresponding reduction in the magnitude of the implied surface fluxes in the Southern Ocean; and a more realistic meridional overturning circulation. Furthermore, it was found that it was possible to remove the non-physical horizontal diffusivity that had previously been required to suppress numerical noise, and yet which significantly distorted the ocean climate through the production of large and spurious horizontal diffusive fluxes. Further studies by *Hirst et al.* (1996, 2000) found that the incorporation of Gent-McWilliams eddy diffusion into the oceanic component of a coupled general circulation model reduced the magnitude of the flux adjustments required in the Southern Ocean, and virtually eliminated the drift that was previously found to occur.

The values for the isopycnal thickness diffusivity which were used for this project are shown in Table 2.2. Notewhich that the values for levels 1 to 5 are fixed, and are hard-coded into the model. The values for levels 6 and 7 are maximum values, and these upper limits are also hard-coded into the model. Smaller values may be specified via the model control file, but the diffusivity may not exceed 580 and $770 \text{ m}^2\text{s}^{-1}$ for levels 6 and 7 respectively. The values for the remaining levels are specified via the model control file. The decrease in the isopycnal thickness diffusivity in the upper layers, with a value of zero at the surface, is required by the continuity constraint imposed on the eddy-induced transport (*Bi*, 2002).

In the stand-alone ocean model, monthly values must be provided for the sea surface temperature (SST), sea surface salinity (SSS), and the zonal and meridional components of the surface wind stress. Linear interpolation in time is used to estimate values at each timestep. The temperature and salinity of the upper layer of the model are relaxed towards the prescribed SST and SSS, using a default relaxation timescale of 20 days. In Mk3L, it is possible for a different relaxation timescale to be specified via the model control file (*Phipps, 2006*).

2.2.3 Coupled model

The coupling between the atmosphere model (AGCM) and ocean model (OGCM) has been modified in Mk3L, in order to ensure that heat and freshwater are rigorously conserved (*Phipps, 2006*). Within the Mk3L coupled model, four fields are passed from the AGCM to the OGCM: the surface heat flux, surface salinity tendency, and the zonal and meridional components of the surface momentum flux. Four fields are also passed from the OGCM to the AGCM: the sea surface temperature (SST), sea surface salinity (SSS), and the zonal and meridional components of the surface velocity.

The Mk3L coupled model runs in a synchronous mode, with one OGCM timestep (1 hour) being followed by three AGCM timesteps (3×20 minutes). The surface fluxes calculated by the AGCM are averaged over the three consecutive AGCM timesteps, before being passed to the ocean model.

In the case of the surface fields passed from the OGCM to the AGCM, instantaneous values for the zonal and meridional components of the surface velocity are passed to the AGCM. These velocities act as the bottom boundary condition on the sea ice model for the following three AGCM timesteps. In the case of the SST and SSS, however, the OGCM passes two copies of each field: one containing the values at the current OGCM timestep, and one containing the values which have been predicted for the next OGCM timestep. The AGCM then uses linear interpolation in time to estimate the SST and SSS at each AGCM timestep.

Flux adjustments are applied to each of the fluxes passed from the AGCM to the OGCM, and also to the SST and SSS. The need to apply adjustments to the surface velocities is avoided by using climatological values, diagnosed from an OGCM spin-up run, to spin up the AGCM.

2.3 Spin-up procedure

2.3.1 Atmosphere model

The atmosphere model was spun up for pre-industrial conditions, consistent with PMIP2 experimental design (Section A.2). The atmospheric carbon dioxide was set equal to 280 ppm, the solar constant was set equal to 1365 Wm^{-2} , and modern (AD 1950) values were used for the Earth's orbital parameters.

World Ocean Atlas 1998 (*National Oceanographic Data Center, 2002*) sea surface temperatures and sea surface salinities were applied as the bottom boundary condition, while the ocean currents required by the sea ice model were diagnosed

Stage	Boundary conditions	Timesteps		Duration (years)
		T, S	ψ , u , v	
1	Annual means	1 day	20 minutes	1,000
2	Monthly means	1 day	20 minutes	3,000
3	Monthly means	1 hour	1 hour	500

Table 2.3: A summary of the spin-up procedure for the Mk3L ocean model.

from the final 100 years of the ocean model spin-up run (Section 2.3.2). Further information regarding the experimental design is provided in Appendix A.

The run was integrated for 50 years, and shall be referred to herein as A-DEF.

2.3.2 Ocean model

The spin-up procedure for the ocean model was essentially that of *Gordon and O'Farrell* (1997) and *Bi* (2002), and is summarised in Table 2.3.

The World Ocean Atlas 1998 dataset (*National Oceanographic Data Center*, 2002) was used to initialise the model, in accordance with PMIP2 experimental design (Section A.2). The model was forced with the NCEP-DOE Reanalysis 2 (*Kanamitsu et al.*, 2002) wind stresses, while the temperature and salinity of the upper layer of the model were relaxed towards the World Ocean Atlas 1998 values, using a relaxation timescale of 20 days. Further information regarding the experimental design is provided in Appendix A.

The model was initially integrated to equilibrium using asynchronous timestepping. This allows for a much longer tracer timestep than synchronous timestepping would impose (1 day, as opposed to 1 hour), thereby accelerating convergence towards an equilibrium solution. For the first 1,000 years, annual-mean surface boundary conditions were applied to the model, reducing the magnitude of the initial surface fluxes and allowing for longer timesteps than would otherwise be possible. Monthly-mean surface boundary conditions were applied thereafter.

The convergence criteria were those of *Bi* (2002), with the ocean model being regarded as having attained equilibrium once the rates of change in global-mean temperature and salinity, at each model level, were less than $0.005^{\circ}\text{C}/\text{century}$ and $0.001 \text{ psu}/\text{century}$ respectively. These criteria were found to be satisfied after 4,000 years of asynchronous timestepping.

The final stage of the spin-up employed synchronous timestepping, with a timestep of 1 hour used to integrate both the tracer and momentum equations. These are the same timesteps used within the coupled model, and this final stage therefore ensures no change in the ocean model configuration upon coupling to the atmosphere model. Although the aforementioned convergence criteria were satisfied after just 200 years, the model was integrated for a total of 500 years under synchronous timestepping. This created an extended period from which an ocean model climatology could be derived, while also ensuring that any residual drift was negligible.

Between the penultimate and final centuries of the run, the changes in global-mean temperature and salinity did not exceed $1.9 \times 10^{-3}^{\circ}\text{C}$ and $1.8 \times 10^{-4} \text{ psu}$ respectively at any ocean model level. Averaged over the final century of the run,

	NCEP-DOE Reanalysis 2	Mk3L atmosphere	Model discrepancy
Globe	14.41	13.78	-0.63
Land	8.59	8.31	-0.28
Ocean	16.73	16.05	-0.68

Table 2.4: Annual-mean surface air temperature ($^{\circ}\text{C}$): the NCEP-DOE Reanalysis 2 (1979–2003 average), the Mk3L atmosphere model (average for the final 40 years of run A-DEF), and the model discrepancy.

the mean heat flux into the ocean was $-4.0 \times 10^{-3} \text{ Wm}^{-2}$, while the mean surface salinity tendency was $-9.9 \times 10^{-5} \text{ psu/year}$, equivalent to a net freshwater flux into the ocean of $\sim 0.07 \text{ mm/year}$.

This run shall be referred to herein as O-DEF.

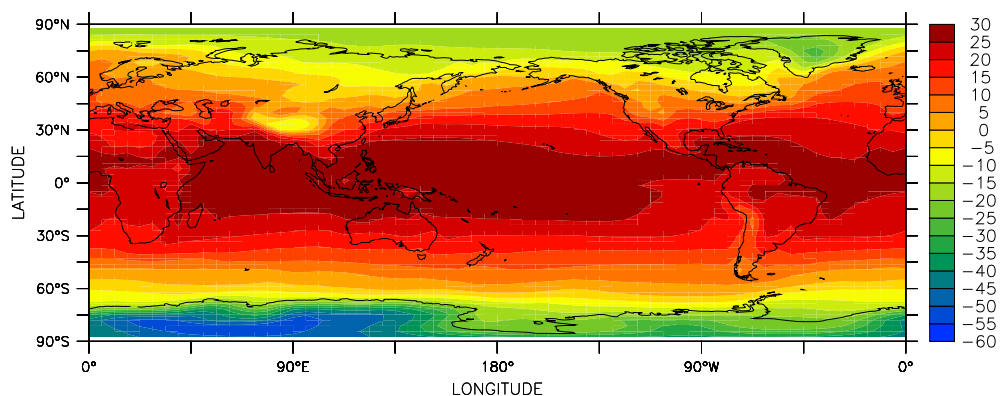
2.4 Atmosphere model evaluation

2.4.1 Surface air temperature

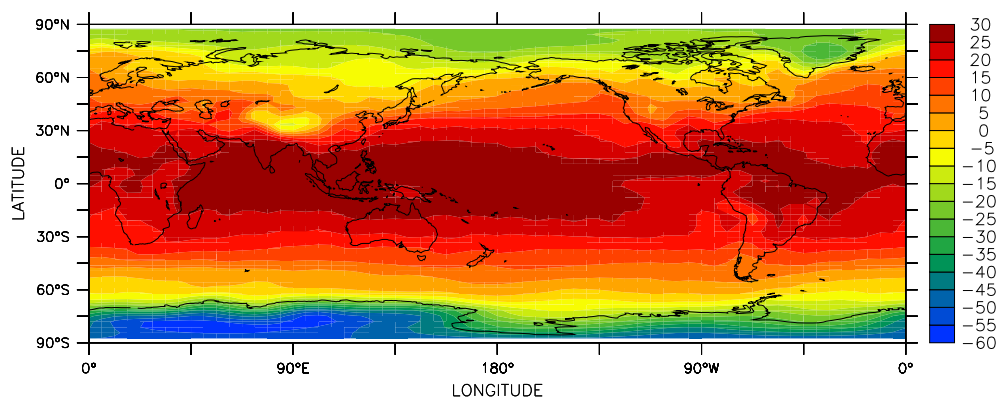
Figure 2.3 shows the simulated annual-mean surface air temperature, and compares it with the NCEP-DOE Reanalysis 2 (*Kanamitsu et al.*, 2002). The agreement is excellent, with the model agreeing with the reanalysis to within 1°C over 60% of the Earth’s surface, and to within 2°C over 85% of the Earth’s surface. The only large-scale discrepancies are over Hudson Bay, where the model is too warm, and over western Antarctica, where it is too cold.

Figure 2.4 shows the simulated mean surface air temperatures for December-January-February (DJF) and June-July-August (JJA), and the discrepancies relative to the NCEP-DOE Reanalysis 2. The large-scale discrepancies in the annual-mean surface air temperature over both Hudson Bay and western Antarctica can be seen to arise from the simulated winter temperatures. The excessively warm winter temperatures over Hudson Bay appear to arise from the failure by the model to form sea ice in this region, due to the World Ocean Atlas 1998 sea surface temperatures being too warm (Section 2.4.4).

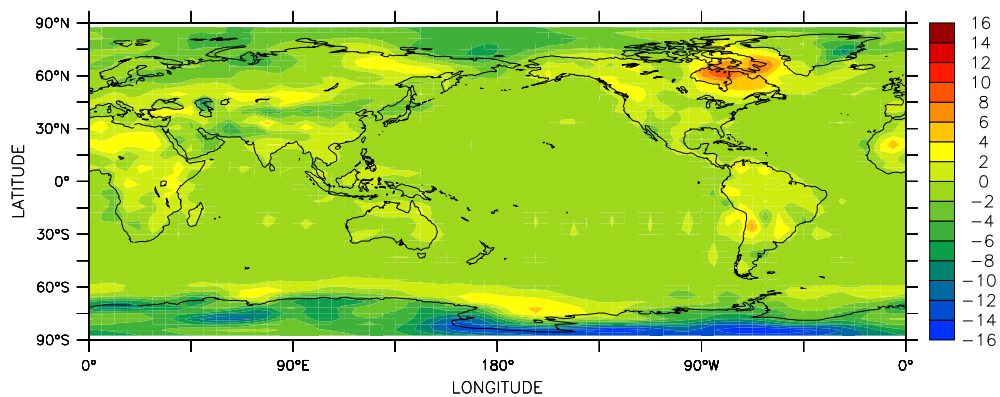
The global-mean temperatures, and the means over land and over the ocean, are shown in Table 2.4. Although Mk3L is slightly cooler than the NCEP-DOE Reanalysis 2, it should be emphasised that the Mk3L atmosphere model was spun-up for pre-industrial conditions, while the NCEP-DOE Reanalysis 2 values represent the 1979–2003 climatology. Indeed, the global-mean discrepancy of -0.63°C is entirely consistent with *Folland et al.* (2001), who estimate that the global-mean surface air temperature increased by $0.6 \pm 0.2^{\circ}\text{C}$ between the late 19th century and the year 2000; as they also indicate that there was no significant change in global-mean surface air temperature between 1750, being the nominal year for which the atmosphere model was spun-up, and the late 19th century, their estimate can also be interpreted as representing the estimated change in global-mean surface air temperature between 1750 and 2000.



(a) NCEP-DOE Reanalysis 2



(b) Mk3L



(c) Mk3L minus NCEP-DOE Reanalysis 2

Figure 2.3: Annual-mean surface air temperature ($^{\circ}\text{C}$): (a) the NCEP-DOE Reanalysis 2 (1979–2003 average), (b) the Mk3L atmosphere model (average for the final 40 years of run A-DEF), and (c) Mk3L minus NCEP-DOE Reanalysis 2. The NCEP-DOE Reanalysis 2 data has been area-averaged onto the Mk3L atmosphere model grid.

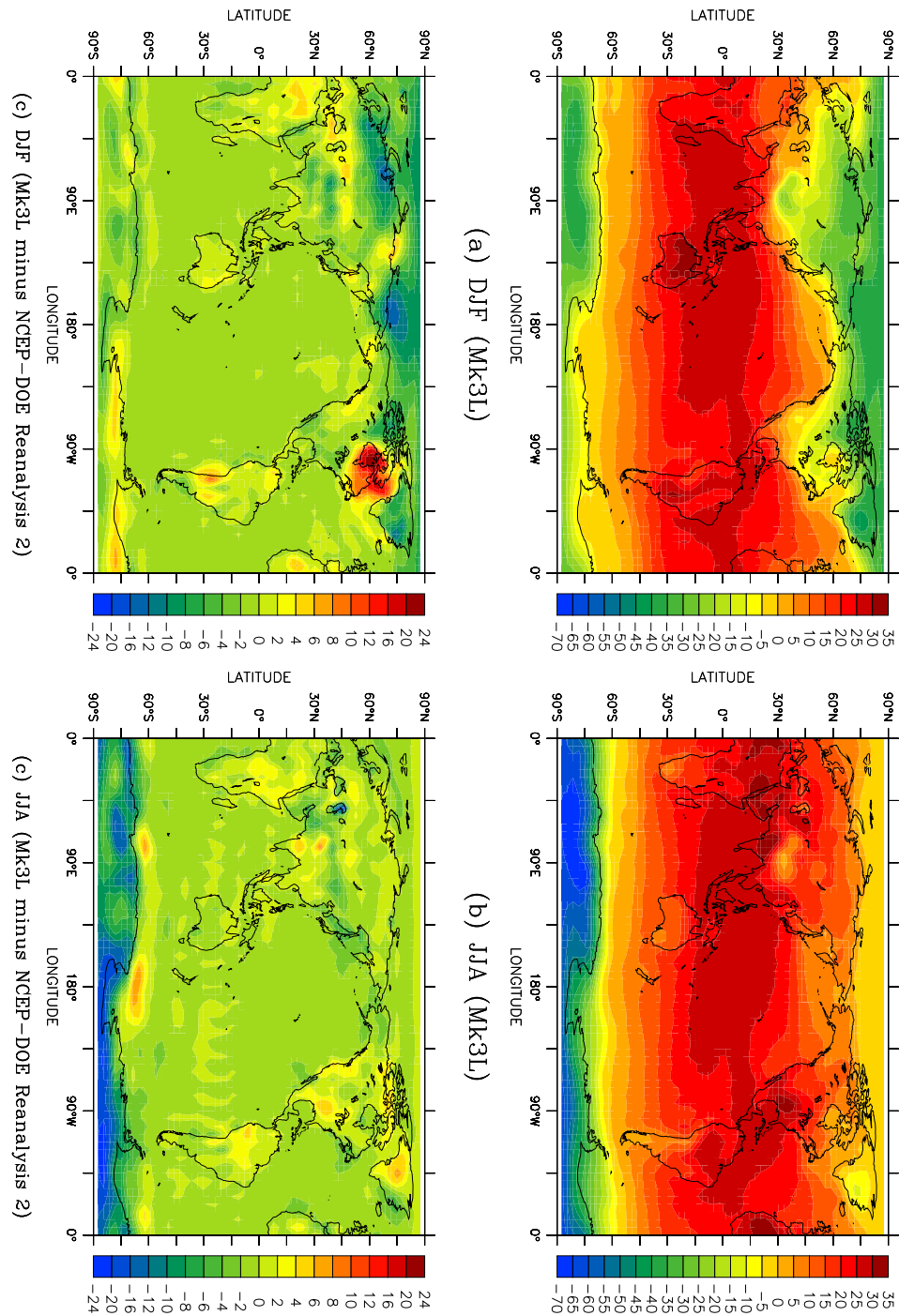


Figure 2.4: Average December-January-February (DJF) and June-July-August (JJA) surface air temperature ($^{\circ}\text{C}$), for the Mk3L atmosphere model (average for the final 40 years of run A-DEF) and the NCEP-DOE Reanalysis 2 (1979–2003 average): (a), (b) Mk3L, DJF and JJA respectively, and (c), (d) Mk3L minus NCEP-DOE Reanalysis 2, DJF and JJA respectively. The NCEP-DOE Reanalysis 2 data has been area-averaged onto the Mk3L atmosphere model grid.

	NCEP-DOE Reanalysis 2	Warren climatology*	Mk3L atmosphere
Globe	55.16	62.33	67.41
Land	44.59	56.41	55.47
Ocean	59.37	65.01	72.39

Table 2.5: Annual-mean total cloud cover (percent): the NCEP-DOE Reanalysis 2 (1979–2003 average), the Warren climatology, and the Mk3L atmosphere model (average for the final 40 years of run A-DEF). *The Warren climatology only covers 98.0% of the Earth’s surface.

2.4.2 Cloud

Figure 2.5 shows the annual-mean cloud cover according to the NCEP-DOE Reanalysis 2, the observed climatology of *Warren et al.* (1986, 1988) and *Hahn et al.* (1995), hereinafter referred to as the “Warren climatology”, and the Mk3L atmosphere model. The model can be seen to have excessive cloud cover over the tropical oceans, particularly in the western Pacific Ocean. The model also fails to reproduce the marine stratocumulus which is encountered in the north-eastern and south-eastern Pacific Ocean, and the south-eastern Atlantic Ocean. These clouds are often poorly simulated by climate models and yet, through reflection of sunlight, have a strong influence on the surface heat fluxes in these regions (*Terray, 1998; Bretherton et al., 2004*).

Figure 2.6 shows the zonal-, annual-mean cloud cover, while the global-mean cloud cover, and the means over land and over the ocean, are shown in Table 2.5. The model is generally in good agreement with the observed Warren climatology, although the excessive model cloud cover over the tropical oceans is apparent.

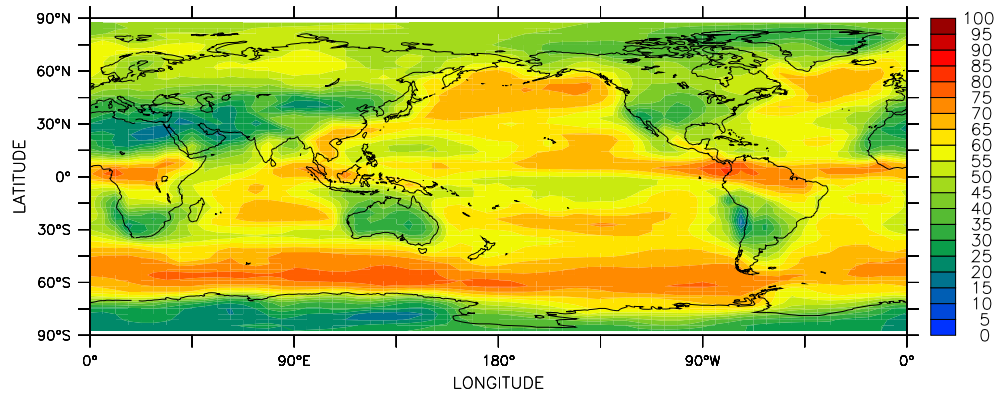
The simulated cloud radiative forcing is also in good agreement with observed values (*Phipps, 2006*).

2.4.3 Precipitation

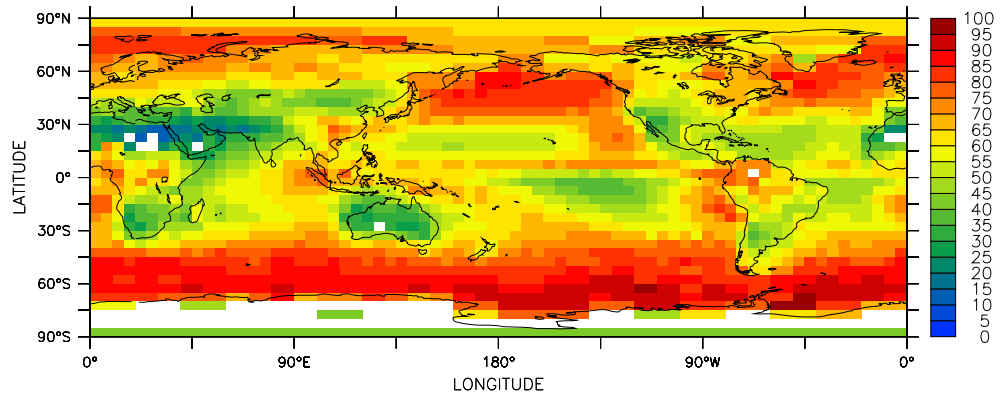
Annual-mean precipitation is shown in Figure 2.7 for the NCEP-DOE Reanalysis 2, version 2.01 of the observed climatology of *Legates and Willmott* (1990), and the Mk3L atmosphere model. While the model can be seen to reproduce the large-scale features of the global distribution of precipitation, it is only moderately successful at reproducing the positions of the monsoons.

Over the western tropical Pacific and Indian Oceans, where the simulated cloud cover is excessive (Section 2.4.2), the simulated precipitation is also excessive. Over the eastern tropical Pacific, Indian and Atlantic Oceans, however, the simulated precipitation is deficient.

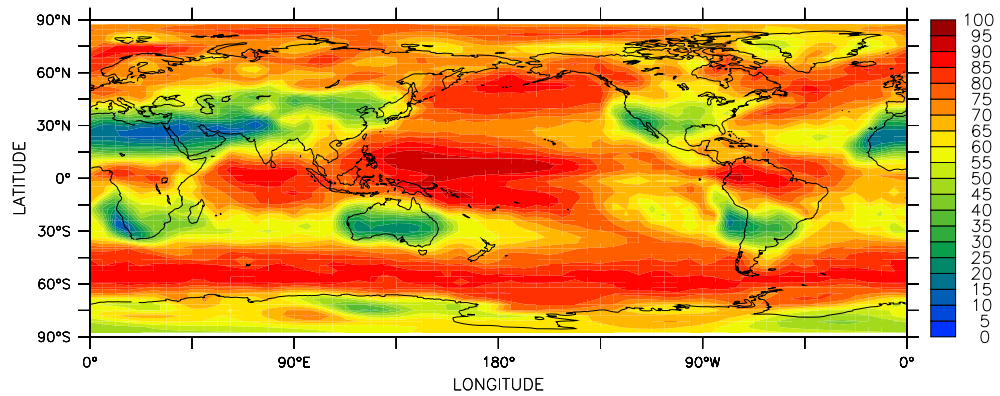
The global-mean precipitation, and the means over land and over the ocean, are shown in Table 2.6. Relative to both the analysed and observed datasets, the model exhibits a slight dry bias.



(a) NCEP-DOE Reanalysis 2



(b) Warren climatology



(c) Mk3L

Figure 2.5: Annual-mean total cloud cover (percent): (a) the NCEP-DOE Reanalysis 2 (1979–2003 average), (b) the Warren climatology, and (c) the Mk3L atmosphere model (average for the final 40 years of run A-DEF). The NCEP-DOE Reanalysis 2 data has been area-averaged onto the Mk3L atmosphere model grid.

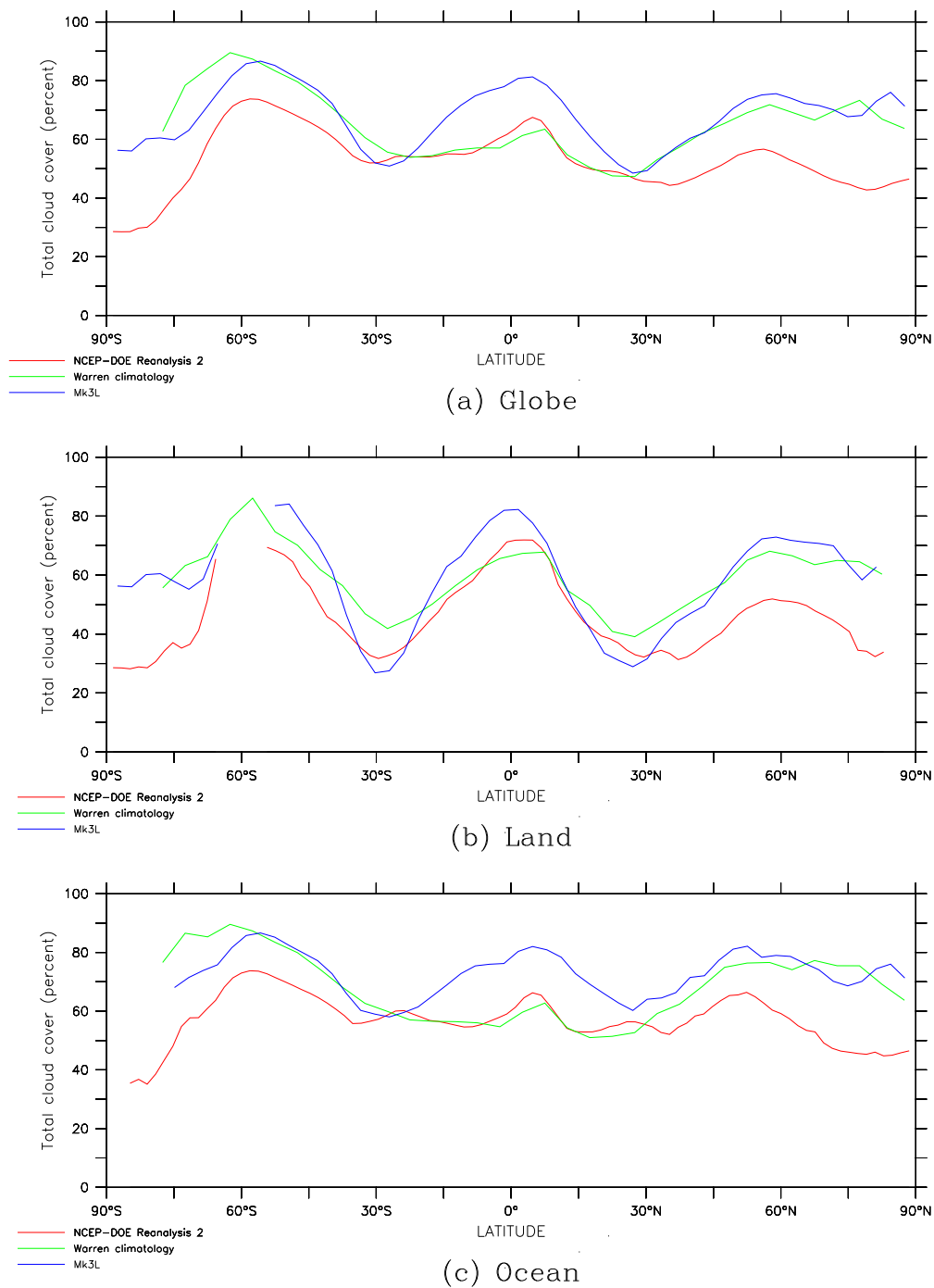
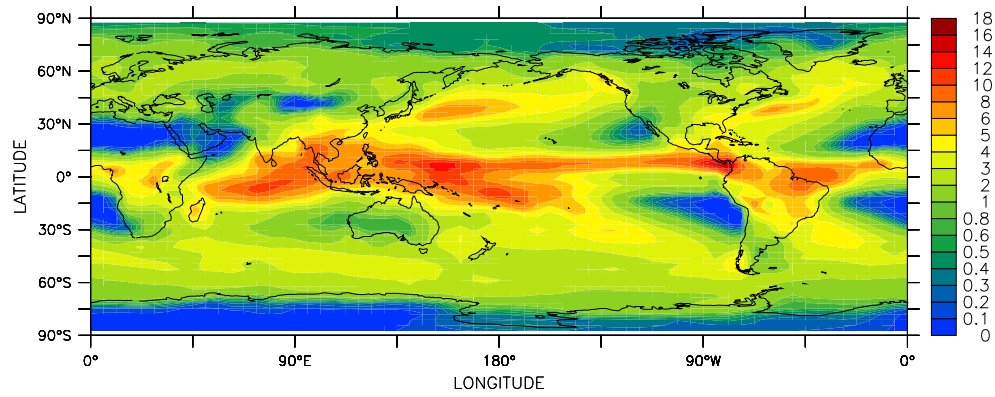
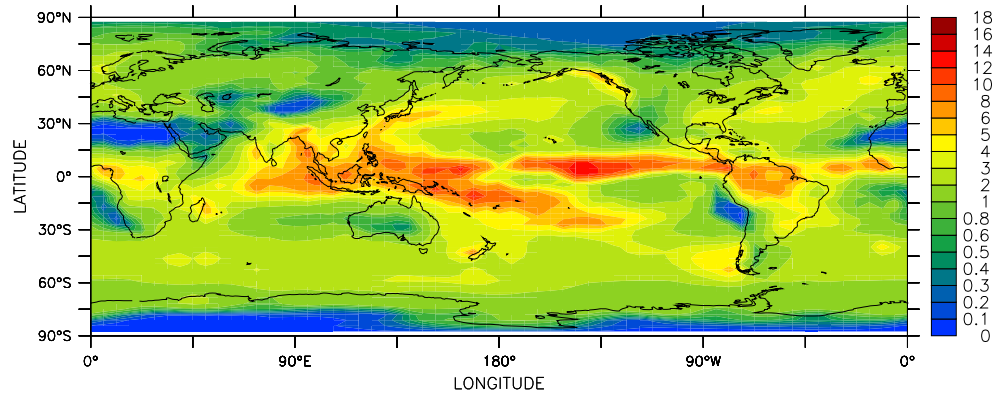


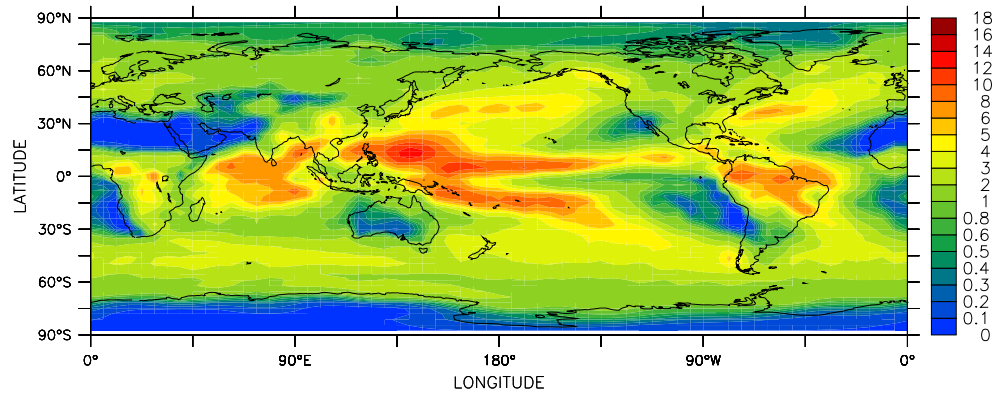
Figure 2.6: Zonal-, annual-mean total cloud cover (percent) for the NCEP-DOE Reanalysis 2 (red, 1979–2003 average), the Warren climatology (green) and the Mk3L atmosphere model (blue, average for the final 40 years of run A-DEF): (a) the globe, (b) land, and (c) the ocean.



(a) NCEP-DOE Reanalysis 2



(b) Legates and Willmott v2.01



(c) Mk3L

Figure 2.7: Annual-mean precipitation (mm/day): (a) the NCEP-DOE Reanalysis 2 (1979–2003 average), (b) the Legates and Willmott climatology v2.01, and (c) the Mk3L atmosphere model (average for the final 40 years of run A-DEF). The NCEP-DOE Reanalysis 2 and Legates and Willmott data have been area-averaged onto the Mk3L atmosphere model grid.

	NCEP-DOE Reanalysis 2	Legates and Willmott v2.01	Mk3L atmosphere
Globe	3.112	2.814	2.699
Land	2.282	-*	1.830
Ocean	3.441	-*	3.062

Table 2.6: Annual-mean precipitation (mm/day): the NCEP-DOE Reanalysis 2 (1979–2003 average), the Legates and Willmott climatology v2.01, and the Mk3L atmosphere model (average for the final 40 years of run A-DEF). *No land/sea mask provided.

		NOAA OI v2	Mk3L atmosphere
Extent (10^{12} m²)	NH	12.19	10.40
	SH	13.23	12.54
Volume (10^{12} m³)	NH	-	10.17
	SH	-	5.19

Table 2.7: Annual-mean sea ice extent and volume, for the Northern Hemisphere (NH) and Southern Hemisphere (SH): the NOAA OI v2 analysis (1982–2003 average), and the Mk3L atmosphere model (average for the final 40 years of run A-DEF). The sea ice extent is defined as the area over which the ice concentration is greater than or equal to 15%; the sea ice volume is the total volume for *all* gridpoints at which sea ice is present.

2.4.4 Sea ice

The simulated Northern and Southern Hemisphere sea ice extents and volumes are plotted in Figure 2.8. Sea ice extents derived from the NOAA Optimum Interpolation (OI) v2 sea surface temperature analysis (*Reynolds et al.*, 2002) are also shown; this analysis combines not only *in situ* observations from ships and buoys, but also satellite observations. The standard definition of sea ice extent (e.g. *Parkinson et al.*, 1999) is employed, which is that the sea ice extent is the area over which the ice concentration is greater than or equal to 15%.

The simulated ice extents can be seen to lag the observed values by around one month; this time lag can be attributed to the relaxation bottom boundary condition on the temperature of the mixed-layer ocean, which is employed by the stand-alone atmosphere model at high latitudes (Section 2.2.1). The simulated annual range in Southern Hemisphere ice extent is in excellent agreement with observations; in the Northern Hemisphere, the summer minimum is well reproduced by the model, but sea ice covers too small an area in winter.

Annual-mean sea ice extents and volumes are shown in Table 2.7. The area covered by ice within the model is 5% less than the observed area in the Southern Hemisphere, but 15% less in the Northern Hemisphere; this discrepancy can be attributed to the deficient winter ice cover.

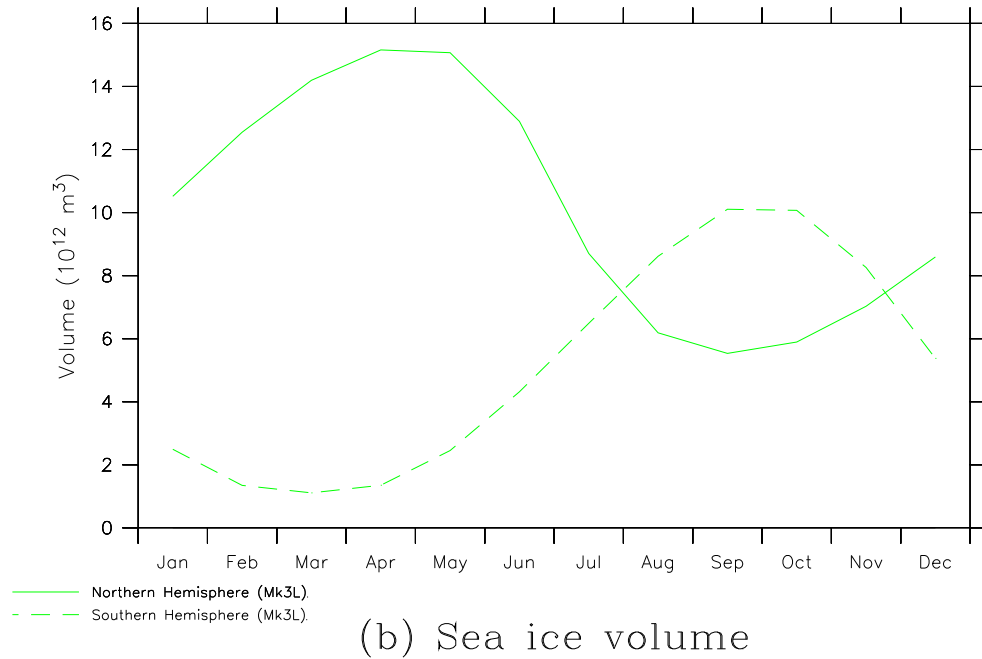
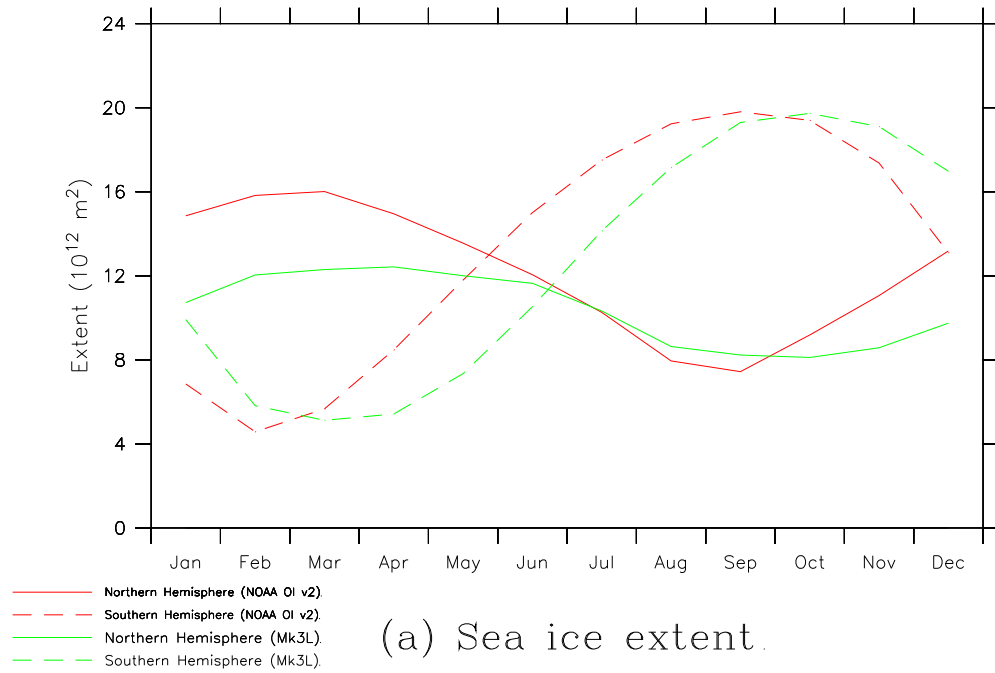


Figure 2.8: Sea ice extent (10^{12} m^2) and volume (10^{12} m^3): (a) sea ice extent for the NOAA OI v2 analysis (red, 1982–2003 average) and the Mk3L atmosphere model (green, average for the final 40 years of run A-DEF), (b) sea ice volume for the Mk3L atmosphere model (average for the final 40 years of run A-DEF). The sea ice extent is defined as the area over which the ice concentration is greater than or equal to 15%; the sea ice volume is the total volume for *all* gridpoints at which sea ice is present.

Figures 2.9 and 2.10 compare the simulated March and September ice concentrations, for the Northern and Southern Hemispheres respectively, with those derived from the NOAA OI v2 analysis. In the Northern Hemisphere, the deficiency in the winter sea ice extent can be seen to arise from the failure by the model to form sea ice in the Hudson Bay region. While the simulated extents in the Southern Hemisphere are in reasonable agreement with observations, the sea ice concentrations are much too low in both the Weddell and Ross Seas.

Figure 2.11 shows the monthly-mean sea surface temperature for the 11 sea gridpoints which constitute Hudson Bay on the Mk3L atmosphere model grid. The temperature of the mixed layer ocean does not attain the freezing point of seawater, which is taken as being -1.85°C , and the model does not therefore form sea ice. The World Ocean Atlas 1998 sea surface temperatures, which act as the bottom boundary condition to the mixed layer ocean, do not fall below -0.92°C ; the failure of the model to form sea ice can therefore be attributed to the fact that the World Ocean Atlas 1998 sea surface temperatures are insufficiently cold.

The simulated March and September sea ice thicknesses are shown in Figure 2.12. There are no comprehensive observational datasets against which to compare the simulated thicknesses. However, *Wadhams* (2000), summarising the available data, indicates that ice thicknesses in the Arctic range from ~ 1 m in the sub-polar regions (such as Baffin Bay and the southern Greenland Sea) to ~ 7 – 8 m along the northern coasts of Greenland and the Canadian archipelago. In the Antarctic, undeformed first-year ice has a mean thickness of ~ 0.6 m, while in the limited regions where multi-year ice is encountered, such as the Weddell Sea, the mean thickness is ~ 1.4 m. Compared to these estimates, the simulated Antarctic sea ice thicknesses are reasonable, while the Arctic sea ice is too thin.

2.5 Ocean model evaluation

2.5.1 Water properties

The global-mean potential temperature, salinity and potential density are shown in Table 2.8, for both the World Ocean Atlas 1998 and the Mk3L ocean model. The potential temperature and potential density represent the temperature and density, respectively, that a volume of seawater would have if raised adiabatically to the surface. While the model prognoses the potential temperature, the World Ocean Atlas 1998 dataset contains *in situ* temperatures. These are therefore converted to potential temperature, using the multivariant polynomial method of *Bryden* (1973). Densities are calculated using the International Equation of State of Seawater 1980 (*UNESCO*, 1981), as described by *Fofonoff* (1985). For convenience, the quantity σ_{θ} , which represents the potential density minus 1000 kgm^{-3} , is presented here.

In the same manner as *Bi* (2002), Table 2.8 divides the world ocean into three vertical layers: the upper ocean (model levels 1–11, spanning the depth range 0–800 m), the mid-ocean (model levels 12–16, spanning the depth range 800–2350 m), and the deep ocean (model levels 17–21, spanning the depth range 2350–4600 m). It can be seen that the model ocean is too cold, too fresh and too buoyant at depth, with the deep ocean being too cold by 1.01°C , too fresh by 0.28 psu, and too buoyant

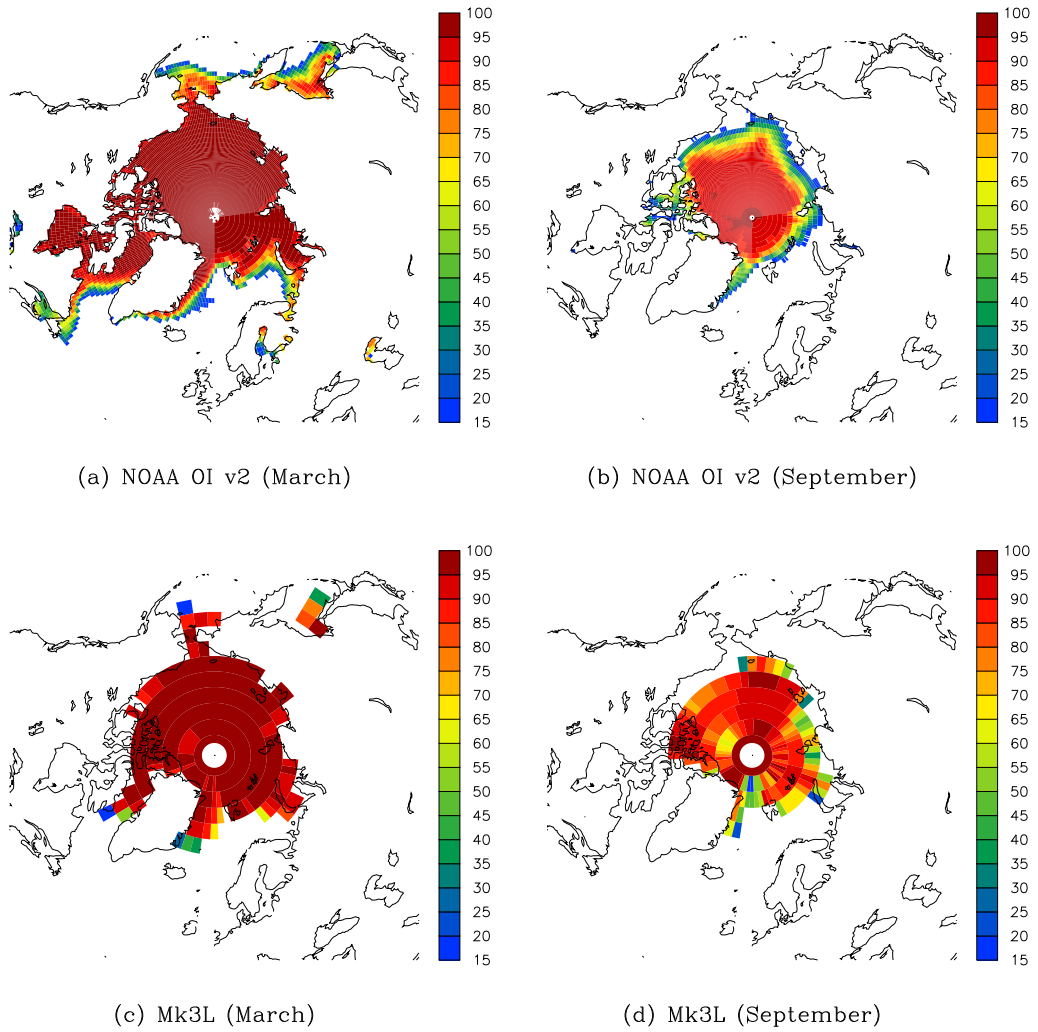


Figure 2.9: Northern Hemisphere sea ice concentration (percent): (a), (b) the NOAA OI v2 (1982–2003 average), March and September respectively, (c), (d) the Mk3L atmosphere model (average for the final 40 years of run A-DEF), March and September respectively. Values are only shown where the concentration is greater than or equal to 15%.

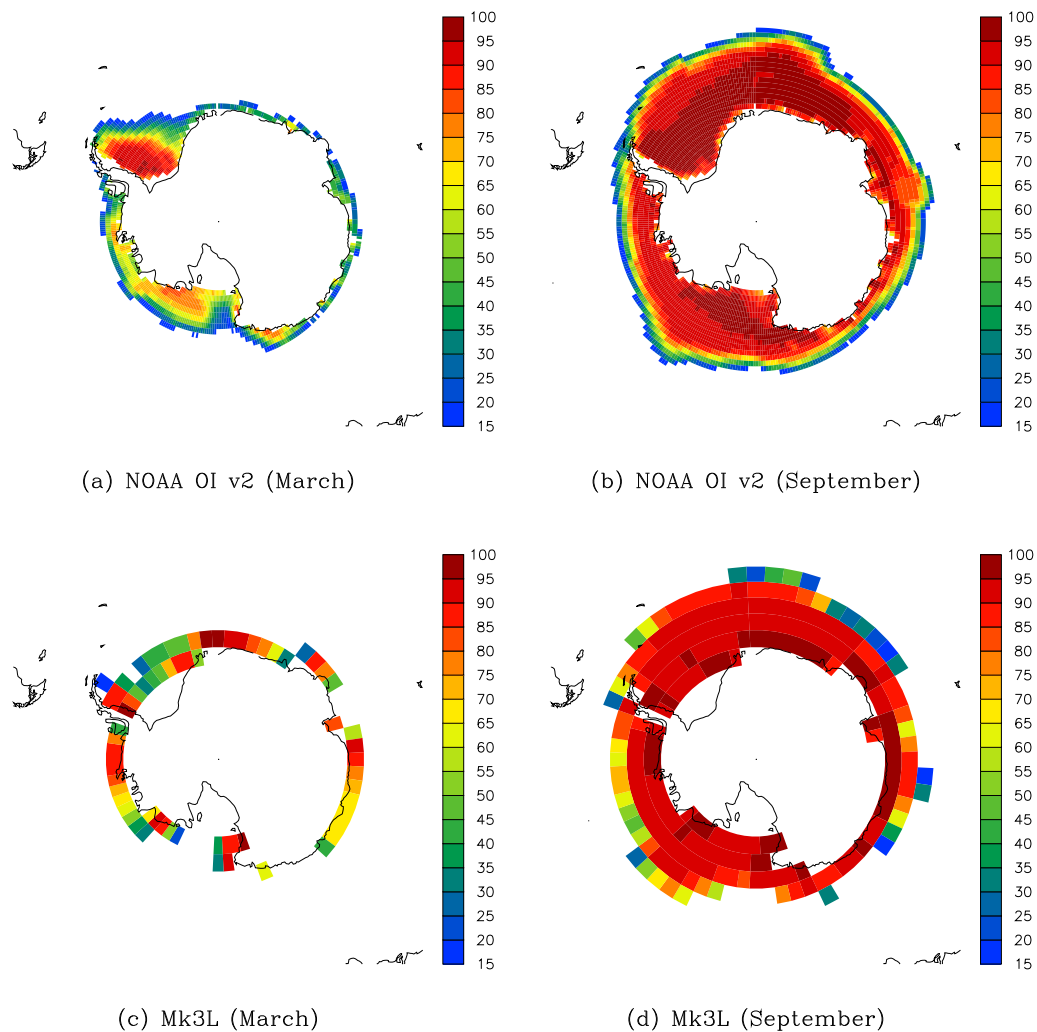


Figure 2.10: Southern Hemisphere sea ice concentration (percent): (a), (b) the NOAA OI v2 (1982–2003 average), March and September respectively, (c), (d) the Mk3L atmosphere model (average for the final 40 years of run A-DEF), March and September respectively. Values are only shown where the concentration is greater than or equal to 15%.

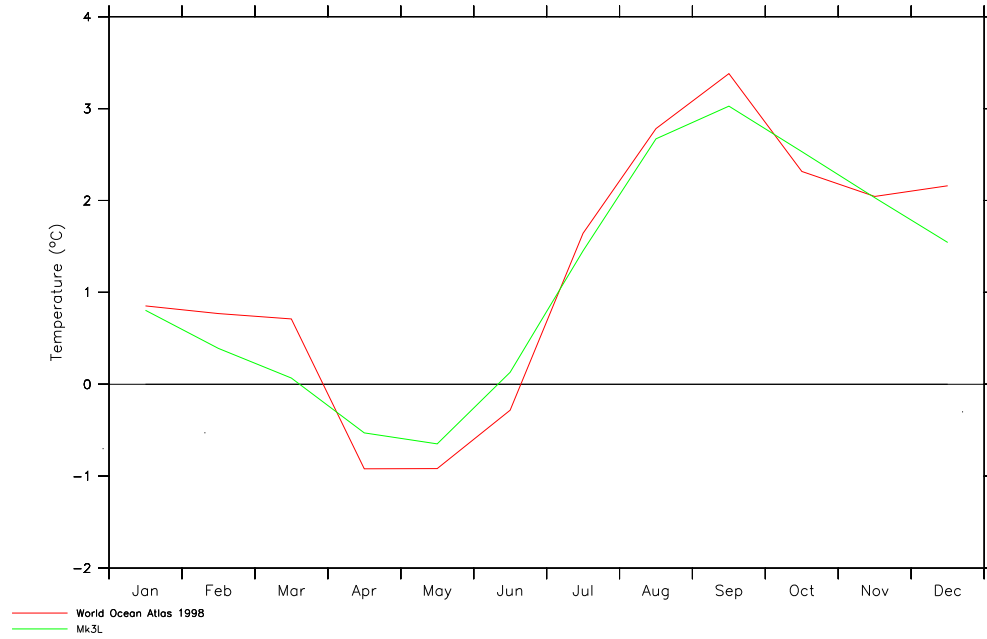


Figure 2.11: The mean sea surface temperature ($^{\circ}\text{C}$) for the 11 sea gridpoints which constitute Hudson Bay on the Mk3L atmosphere model grid: the World Ocean Atlas 1998 (red) and the Mk3L atmosphere model (green, average for the final 40 years of run A-DEF).

		World Ocean Atlas 1998	Mk3L ocean	Model discrepancy
Potential temperature ($^{\circ}\text{C}$)	0–800 m	9.61	10.88	+1.27
	800–2350 m	2.98	3.08	+0.10
	2350–4600 m	1.36	0.35	-1.01
Salinity (psu)	0–800 m	34.75	34.69	-0.06
	800–2350 m	34.68	34.50	-0.18
	2350–4600 m	34.74	34.46	-0.28
σ_{θ} (kgm^{-3})	0–800 m	26.60	26.32	-0.28
	800–2350 m	27.62	27.45	-0.17
	2350–4600 m	27.81	27.64	-0.17

Table 2.8: Global-mean potential temperature ($^{\circ}\text{C}$), salinity (psu), and σ_{θ} (kgm^{-3}): the World Ocean Atlas 1998, the Mk3L ocean model (average for the final 100 years of run O-DEF), and the model discrepancy. The World Ocean Atlas 1998 data has been volume-averaged onto the Mk3L ocean model grid.

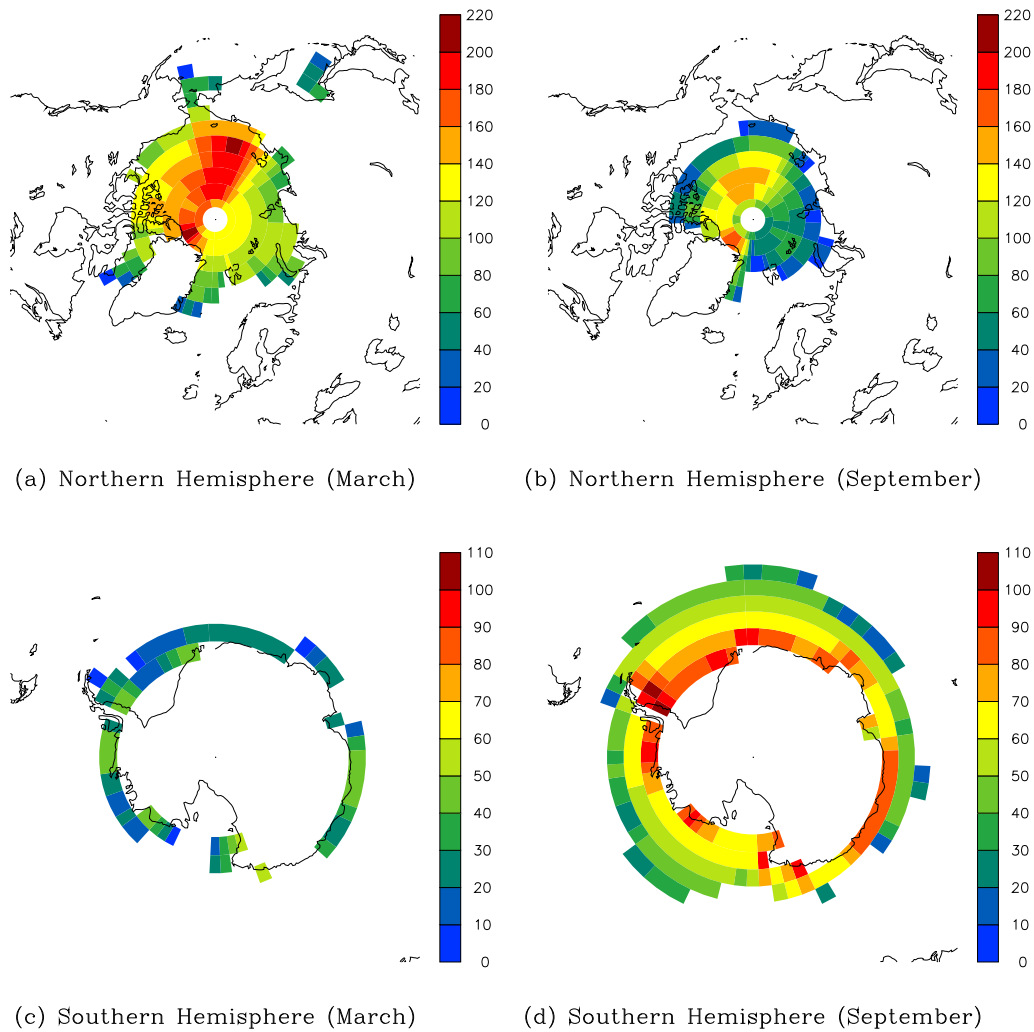


Figure 2.12: Sea ice thicknesses for the Mk3L atmosphere model (cm, average for the final 40 years of run A-DEF): (a), (b) Northern Hemisphere, March and September respectively, (c), (d) Southern Hemisphere, March and September respectively. Values are only shown where the concentration is greater than or equal to 15%.

by 0.17 kgm^{-3} .

These biases in the properties of the deep ocean are illustrated by Figure 2.13, which shows the vertical profiles of potential temperature, salinity and σ_θ , and by Figures 2.14, 2.15 and 2.16, which show the zonal-mean potential temperature, salinity and σ_θ respectively. Note that, in calculating the zonal means, the six inland seas which do not have a resolved connection with the world ocean (Section 2.2.2) are excluded.

The cold, fresh and buoyant bias of the deep ocean is consistent with other comparable studies (e.g. *Moore and Reason, 1993; England and Hirst, 1997; Hirst et al., 2000; Bi, 2002*). The reasons for these deficiencies in the model climate are discussed in Chapter 3.

2.5.2 Circulation

Meridional overturning streamfunctions for the world ocean, and for the Atlantic and Pacific/Indian Oceans are shown in Figure 2.17. The rates of formation of North Atlantic Deep Water (NADW) and Antarctic Bottom Water (AABW) are 13.6 Sv and 9.5 Sv respectively; these are comparable with the rates obtained in other studies using a coarse-resolution version of the Bryan-Cox ocean model which incorporates Gent-McWilliams eddy diffusion (e.g. *England and Hirst, 1997; Hirst et al., 2000; Bi, 2002*).

Estimated values for the rate of NADW formation lie within the range 15–20 Sv (*Gordon, 1986*), while those for the rate of AABW formation lie within the range 5–15 Sv (e.g. *Gill, 1973; Carmack, 1977*). More recent studies, based on the observed distribution of dissolved chlorofluorocarbons, estimate that the rates of NADW and AABW formation are ~ 17.2 Sv (*Smethie and Fine, 2001*) and ~ 8.1 – 9.4 Sv (*Orsi et al., 1999*) respectively. The simulated rate of AABW formation is therefore consistent with observational estimates, while the rate of NADW formation is too weak. As AABW is $\sim 2^\circ\text{C}$ colder than NADW (*Orsi et al., 2001*), this provides a possible explanation for the cold bias in the modelled deep ocean.

The annual-mean barotropic streamfunction is shown in Figure 2.18. The Antarctic Circumpolar Current is evident, as are the mid-latitude gyres in the Atlantic, Pacific and Indian Oceans.

The simulated rate of transport through Drake Passage is 145 Sv, which agrees well with observational estimates. *Cunningham et al. (2003)*, using the data from six hydrographic sections conducted across Drake Passage between 1993 and 2000 as part of the World Ocean Circulation Experiment (WOCE), estimate that the rate of transport is 136.7 ± 7.8 Sv. *Stammer et al. (2003)*, using an ocean global circulation model to assimilate WOCE data over the same period, estimate that the rate of transport through Drake Passage is 124 ± 5 Sv. The agreement between the Mk3L ocean model and observations is particularly good when it is considered that other global ocean models simulate rates of transport through Drake Passage which range from less than 100 Sv to more than 200 Sv (*Olbers et al., 2004*).

The simulated western boundary currents, however, are too weak and too diffuse. The maximum strength of the simulated Gulf Stream for example, is 23.9 Sv, whereas the observed strength is ~ 30.5 Sv (*Schott et al., 1988*). This is a feature of coarse-resolution ocean models which employ the no-slip boundary condi-

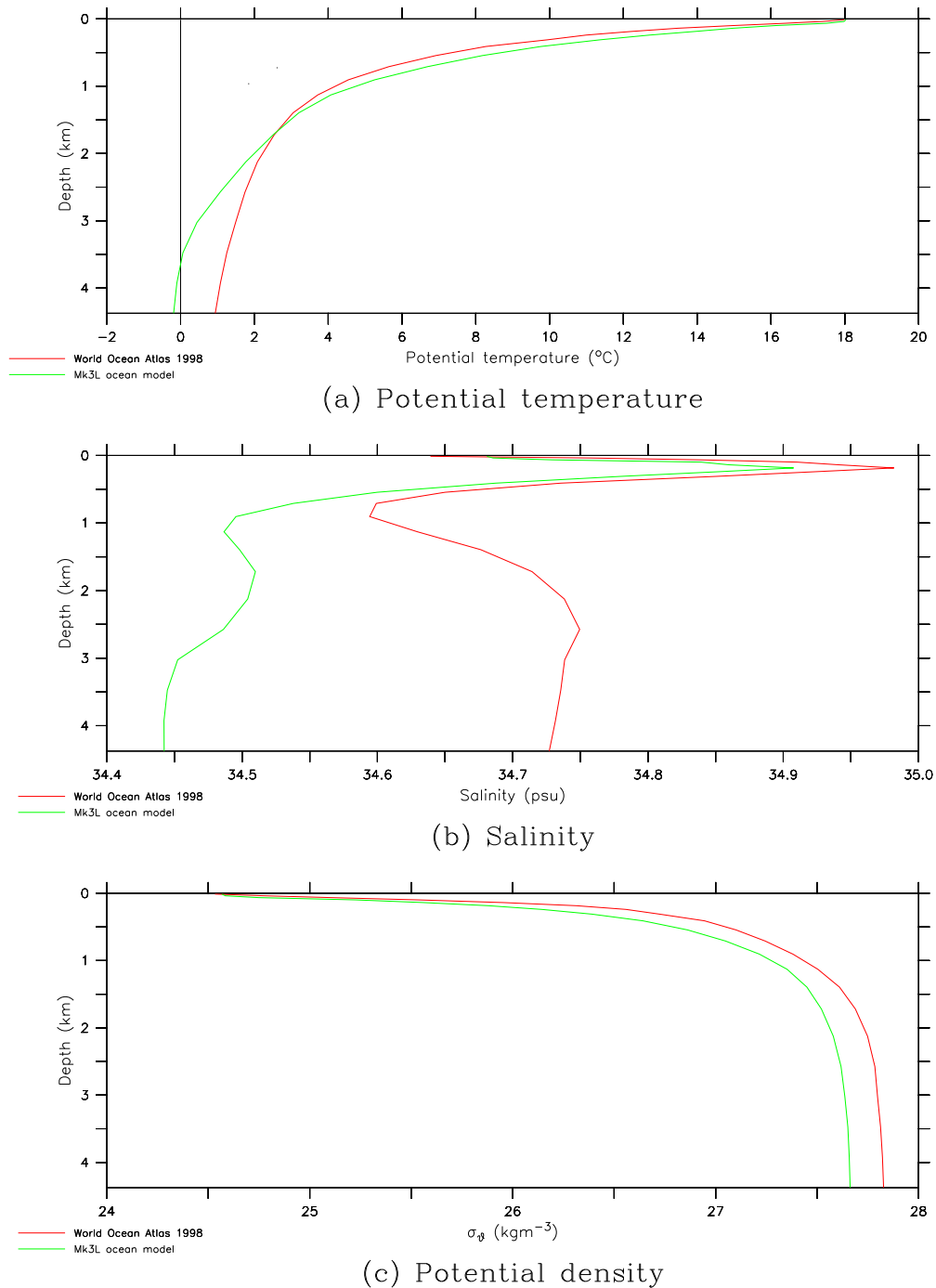
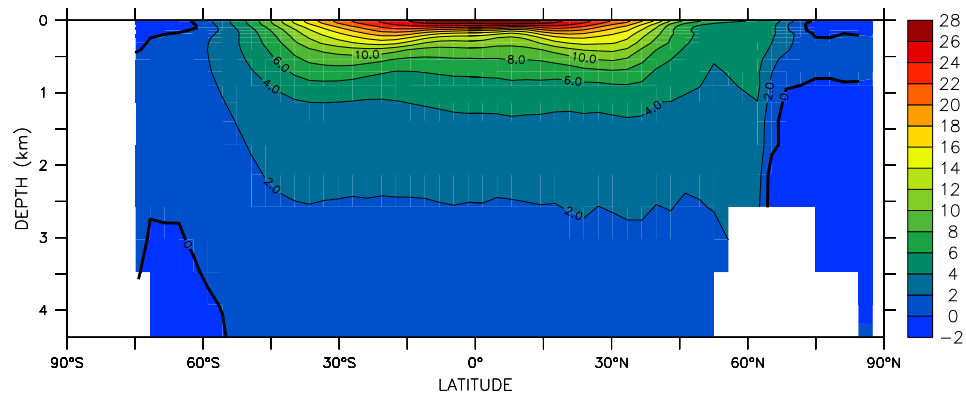
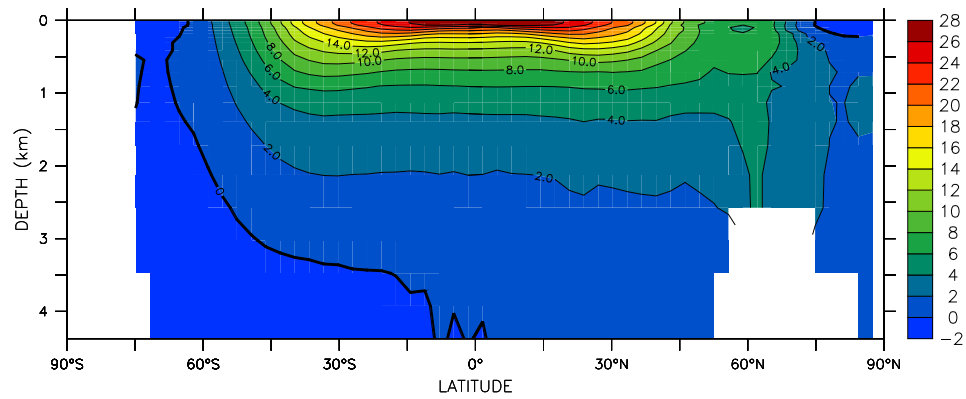


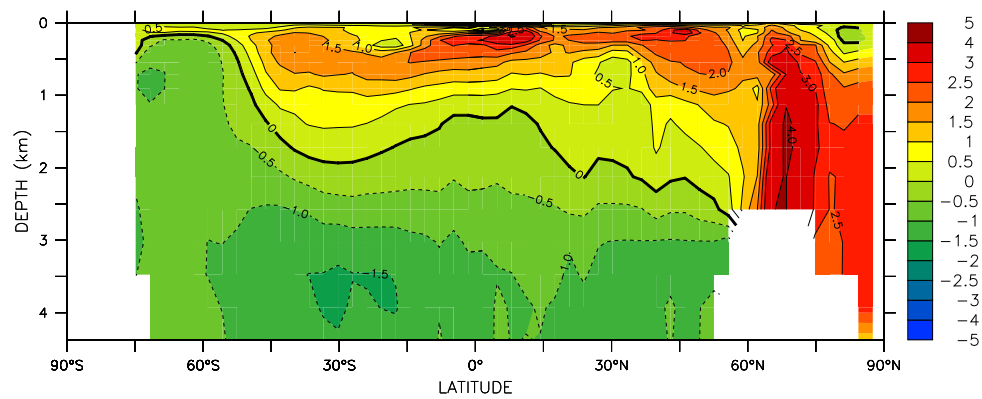
Figure 2.13: The global-mean potential temperature, salinity and σ_θ on each model level for the World Ocean Atlas 1998 (red), and for the Mk3L ocean model (green, average for the final 100 years of run O-DEF): (a) potential temperature ($^{\circ}\text{C}$), (b) salinity (psu), and (c) σ_θ (kgm^{-3}). The World Ocean Atlas 1998 data has been volume-averaged onto the Mk3L ocean model grid.



(a) World Ocean Atlas 1998

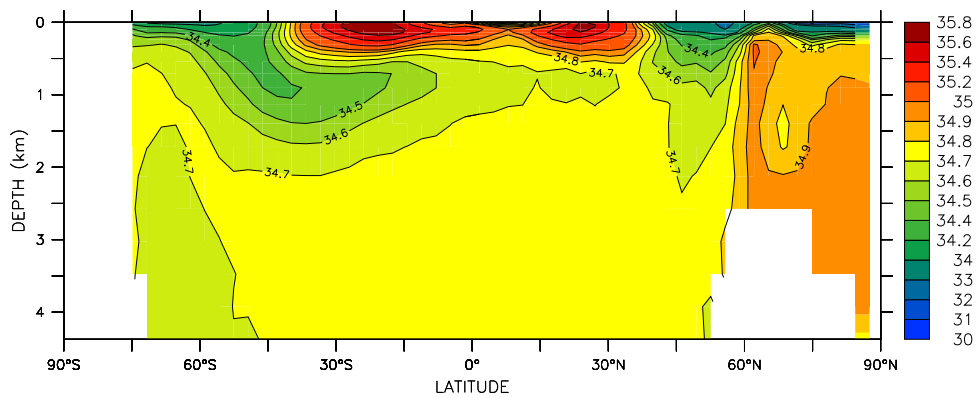


(b) Mk3L

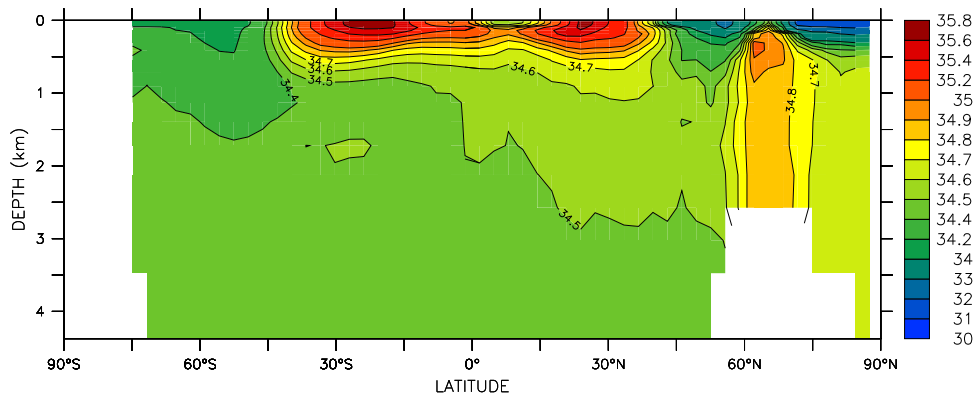


(c) Mk3L minus World Ocean Atlas 1998

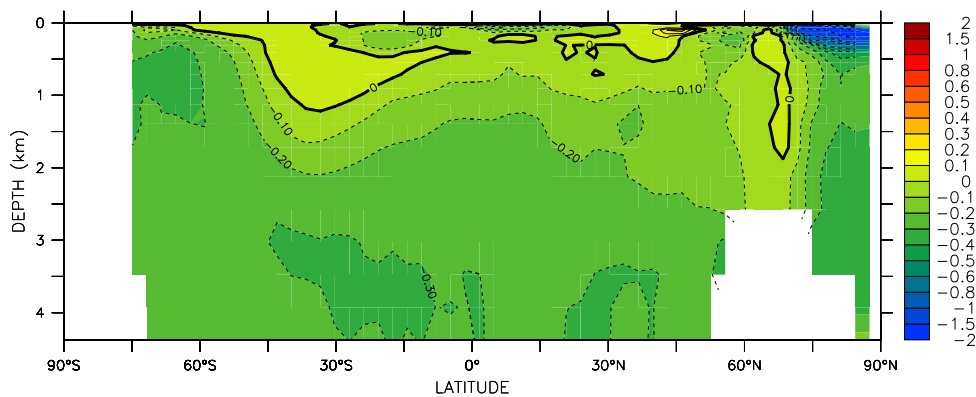
Figure 2.14: Zonal-mean potential temperature ($^{\circ}\text{C}$) for the world ocean (excluding inland seas): (a) the World Ocean Atlas 1998, (b) the Mk3L ocean model (average for the final 100 years of run O-DEF), and (c) the model discrepancy. The World Ocean Atlas 1998 data has been volume-averaged onto the Mk3L ocean model grid.



(a) World Ocean Atlas 1998

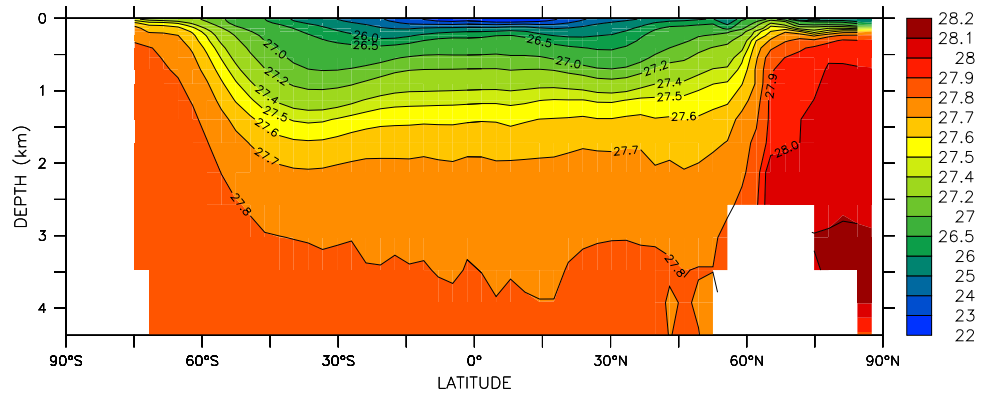


(b) Mk3L

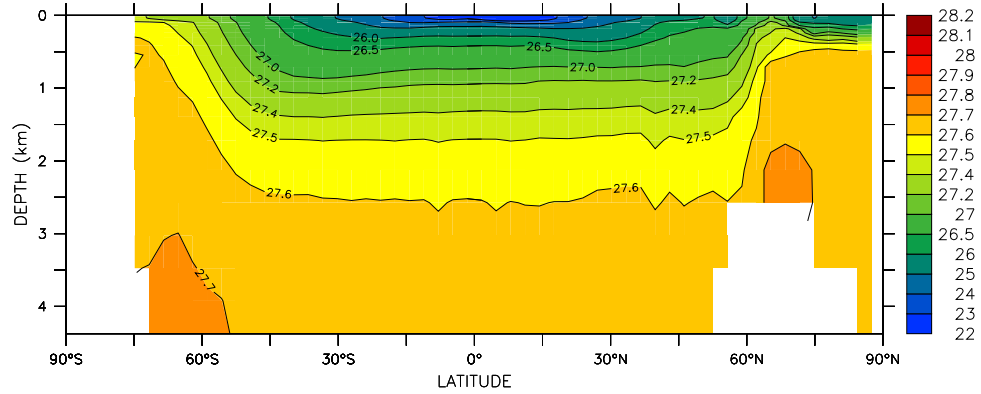


(c) Mk3L minus World Ocean Atlas 1998

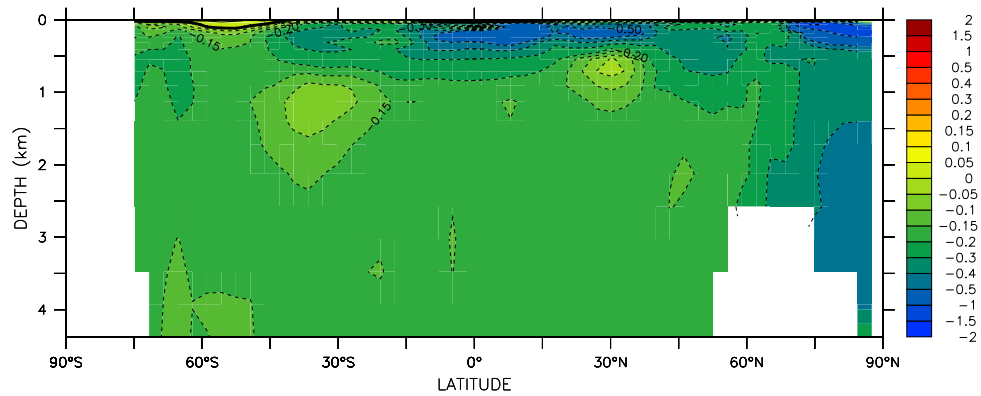
Figure 2.15: Zonal-mean salinity (psu) for the world ocean (excluding inland seas): (a) the World Ocean Atlas 1998, (b) the Mk3L ocean model (average for the final 100 years of run O-DEF), and (c) the model discrepancy. The World Ocean Atlas 1998 data has been volume-averaged onto the Mk3L ocean model grid.



(a) World Ocean Atlas 1998

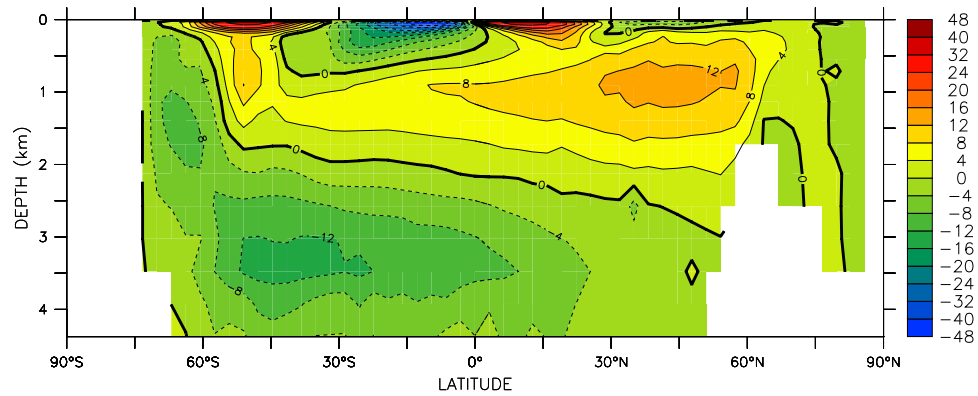


(b) Mk3L

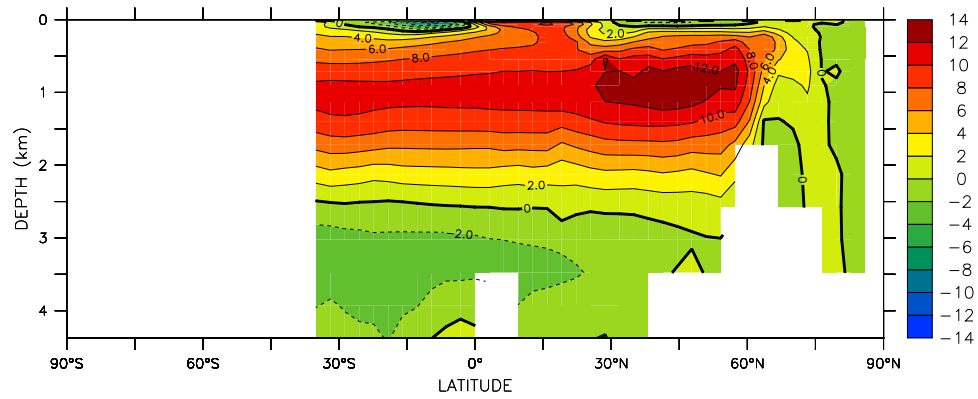


(c) Mk3L minus World Ocean Atlas 1998

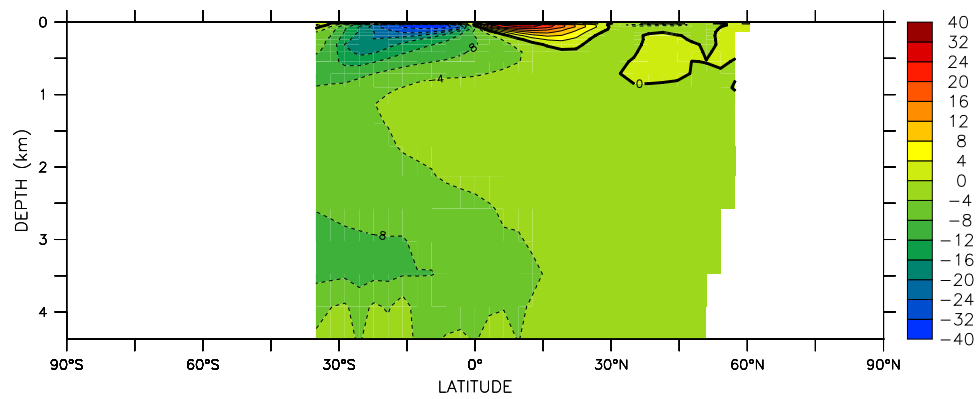
Figure 2.16: Zonal-mean σ_θ (kgm^{-3}) for the world ocean (excluding inland seas): (a) the World Ocean Atlas 1998, (b) the Mk3L ocean model (average for the final 100 years of run O-DEF), and (c) the model discrepancy. The World Ocean Atlas 1998 data has been volume-averaged onto the Mk3L ocean model grid.



(a) World Ocean



(b) Atlantic Ocean



(c) Pacific/Indian Oceans

Figure 2.17: Meridional overturning streamfunctions (S_v) for the Mk3L ocean model (averages for the final 100 years of run O-DEF): (a) the world ocean, (b) the Atlantic Ocean, and (c) the Pacific/Indian Oceans.

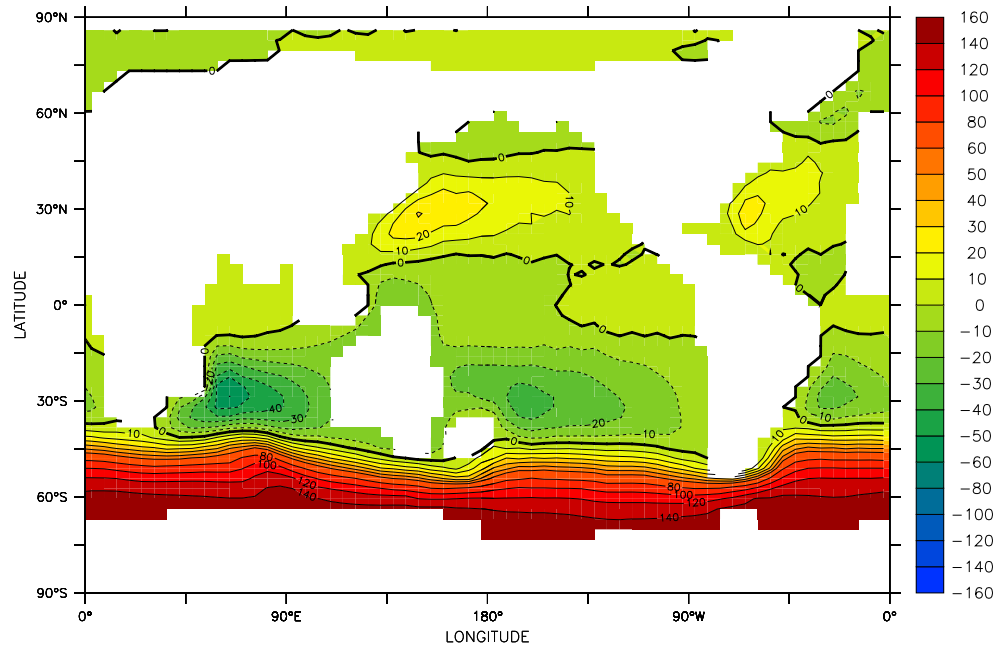


Figure 2.18: The annual-mean barotropic streamfunction (Sv) for the Mk3L ocean model (average for the final 100 years of run O-DEF).

tion at lateral walls (e.g. *Moore and Reason, 1993; Bi, 2002*), and arises not only from the coarse resolution, but also from the large horizontal viscosity which is required in order to resolve a viscous boundary layer at the lateral walls (*Bryan et al., 1975*). For the simulations analysed herein, the horizontal viscosity was set equal to $9 \times 10^5 \text{ m}^2 \text{ s}^{-1}$.

2.6 Flux adjustments

2.6.1 The need for flux adjustments

As discussed in Chapter 1, any change in the surface boundary conditions on either the atmosphere or ocean models, upon the coupling of the two models, will represent a potential source of drift within the coupled model. One method of minimising this drift is through the application of flux adjustments.

The incompatibility between the surface fluxes of heat and freshwater, as simulated by stand-alone atmosphere and ocean models, is studied by *Weaver and Hughes (1996)*. They compare the oceanic meridional transports of heat and salt, as simulated by an ocean model, and as implied by the surface fluxes calculated by an atmosphere model. They demonstrate that, in the absence of flux adjustments, drift can only be avoided within a coupled model if the transports simulated by the ocean model agree with those implied by the atmosphere model. Agreement between the simulated and implied transports is therefore a *necessary* condition for drift to be avoided within a coupled model, without the use of flux adjustments. It is not, however, a *sufficient* condition.

The oceanic meridional transports, both simulated and implied, can be derived by integrating the surface fluxes northwards from the South Pole. If the surface heat flux is F_{heat} , then the northward transport of heat Q_{heat} is given by

$$Q_{heat}(\phi) = \int_0^{2\pi} \int_{-\pi/2}^{\phi} F_{heat} a^2 \cos \phi' d\lambda d\phi' \quad (2.8)$$

where a is the radius of the Earth, and ϕ and λ are the latitude and longitude respectively.

The surface salinity tendency dS_O/dt can be converted into a surface salt flux, through multiplication by the thickness of the upper layer of the ocean model Δz . The northward transport of salt Q_{salt} is then given by

$$Q_{salt}(\phi) = \int_0^{2\pi} \int_{-\pi/2}^{\phi} \Delta z \frac{dS_O}{dt} a^2 \cos \phi' d\lambda d\phi' \quad (2.9)$$

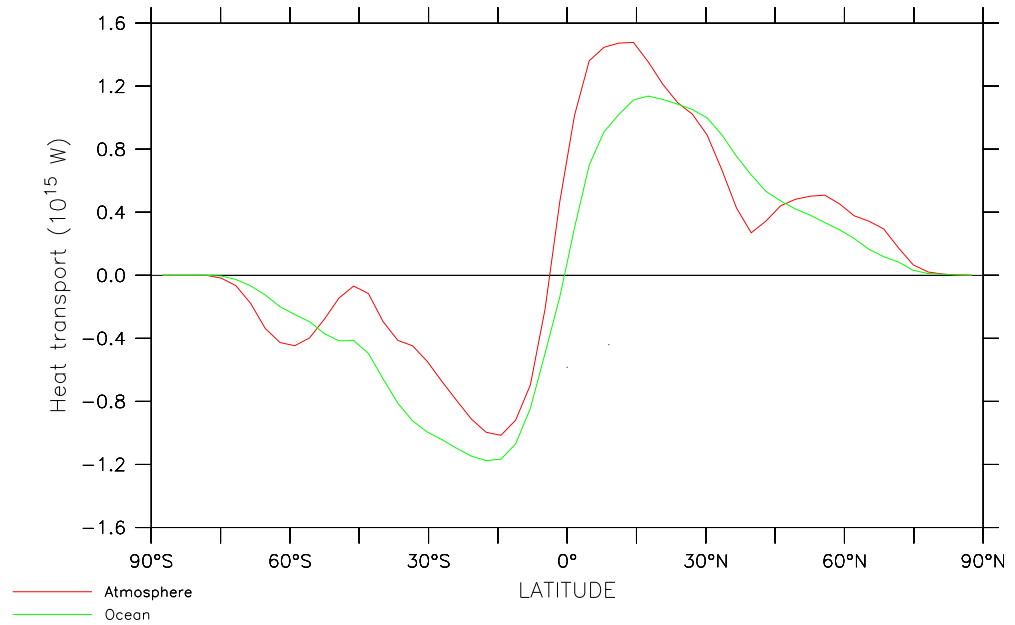
Figure 2.19 shows the northward transports of heat and salt, as simulated by the Mk3L ocean model, and as implied by the Mk3L atmosphere model surface fluxes. They can be seen to be in reasonable agreement, particularly in the case of the oceanic salt transport. This indicates that the zonal means of the flux adjustments diagnosed for the coupled model will be small.

The oceanic meridional heat transports can also be compared with observational estimates, although there are large discrepancies between the various observational datasets (*Gleckler et al.*, 1995). Estimated values for the peak poleward transport, in both the Northern and Southern Hemispheres, range from $\sim 1-3.5 \times 10^{15}$ W, with median values of $\sim 2 \times 10^{15}$ W in both hemispheres. The peak poleward transports simulated by the Mk3L atmosphere and ocean models are 1.02×10^{15} W and 1.18×10^{15} W respectively in the Southern Hemisphere, and 1.48×10^{15} W and 1.14×10^{15} W respectively in the Northern Hemisphere. These values are consistent with the observational estimates, although they lie towards the lower end of the observational range. The success of the atmosphere model in simulating the implied poleward heat transport in the Southern Hemisphere can be attributed to the realism of the simulated cloud radiative forcing (*Gleckler et al.*, 1995).

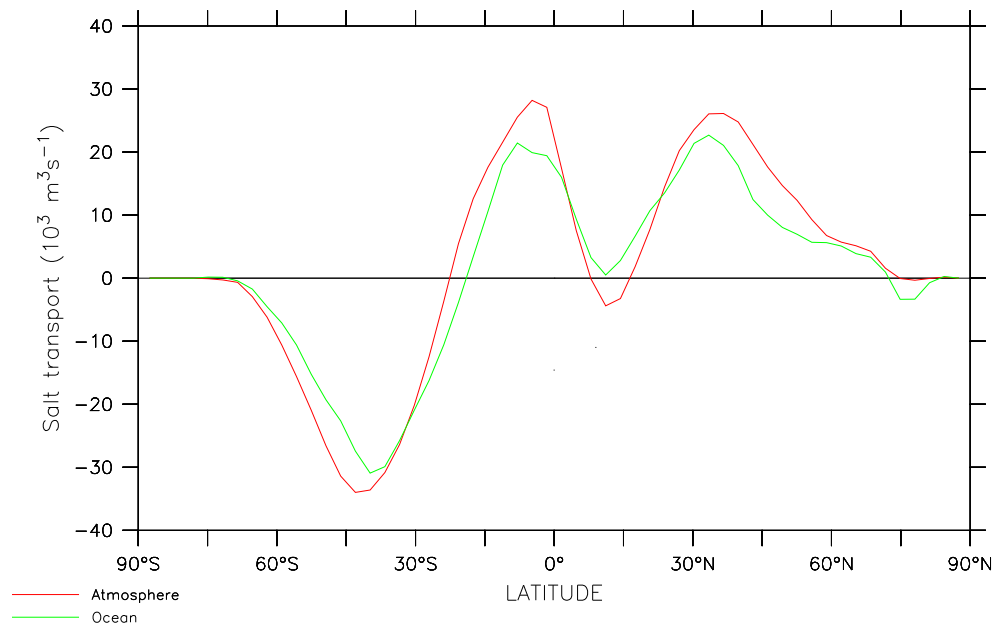
2.6.2 Deriving the flux adjustments

Within the Mk3L coupled model, four fields are passed from the atmosphere model (AGCM) to the ocean model (OGCM): the surface heat flux, the surface salinity tendency, and the zonal and meridional components of the surface momentum flux. Any differences between the surface fluxes calculated by the stand-alone AGCM, and those which are required to maintain the stand-alone OGCM in its equilibrium state, will represent a potential source of drift within the coupled model. Flux adjustments are therefore applied to each of these four fields.

The derivation of the flux adjustments is straightforward. If F_A is the surface flux diagnosed from an AGCM spin-up run, and F_O the surface flux diagnosed from an OGCM spin-up run (or, in the case of the components of the surface momentum flux, the flux applied to the stand-alone OGCM), then the flux adjustment ΔF is given by



(a) Heat



(b) Salt

Figure 2.19: The annual-mean oceanic northward transports implied by the Mk3L atmosphere model surface fluxes (red, average for the final 40 years of run A-DEF), and simulated by the Mk3L ocean model (green, average for the final 100 years of run O-DEF): (a) heat, and (b) salt. Any net global-mean fluxes were subtracted from the data prior to performing the integration, ensuring that the northward transport at the North Pole is equal to zero.

$$\Delta F(\lambda, \phi, t) = F_O(\lambda, \phi, t) - F_A(\lambda, \phi, t) \quad (2.10)$$

where λ, ϕ, t represent longitude, latitude and the time of year respectively. The flux adjustments therefore vary temporally, as well as spatially. Within the coupled model, if F represents the surface flux calculated by the AGCM, then the adjusted flux F' which is passed to the OGCM is given by

$$F'(\lambda, \phi, t) = F(\lambda, \phi, t) + \Delta F(\lambda, \phi, t) \quad (2.11)$$

[Note that within Mk3L, the flux adjustments are *subtracted* from the AGCM surface fluxes, and therefore have the opposite sign to the values given by Equation 2.10. However, Equation 2.10 is used to derive the values presented herein, in order to maintain the convention, followed throughout this document, that downward fluxes are positive.]

Four fields are also passed from the OGCM to the AGCM: the sea surface temperature (SST), the sea surface salinity (SSS), and the zonal and meridional components of the surface velocity. Any differences between the values of these fields, and the values which were imposed as the bottom boundary condition on the stand-alone AGCM, will also represent a potential source of drift within the coupled model. The need to apply “flux” adjustments to the components of the surface velocity is avoided through the use of climatological surface currents, diagnosed from an OGCM spin-up run, to spin up the AGCM. However, “flux” adjustments are applied to the SST and SSS within the Mk3L coupled model.

The derivation of the adjustments to the SSS is straightforward. If S_{obs} is the SSS which was imposed as the surface boundary condition on the stand-alone OGCM, and S_O is the SSS which was simulated by the model, then the SSS adjustment ΔS is given by

$$\Delta S(\lambda, \phi, t) = S_{obs}(\lambda, \phi, t) - S_O(\lambda, \phi, t) \quad (2.12)$$

Within the coupled model, if S represents the SSS calculated by the OGCM, then the adjusted sea surface salinity S' which is passed to the AGCM is given by

$$S'(\lambda, \phi, t) = S(\lambda, \phi, t) + \Delta S(\lambda, \phi, t) \quad (2.13)$$

The derivation of the adjustments to the SST is more complex. If T_A is the SST which was imposed as the surface boundary condition on the stand-alone AGCM, and T_O is the SST simulated by the stand-alone OGCM, then the SST adjustment ΔT is given by

$$\Delta T(\lambda, \phi, t) = T_A(\lambda, \phi, t) - T_O(\lambda, \phi, t) \quad (2.14)$$

However, the stand-alone OGCM uses a mixed-layer ocean to calculate the SST at high latitudes. If T_{obs} is the SST which was imposed as the surface boundary condition on the stand-alone AGCM, and ΔT_{mlo} is the temperature of the mixed-layer ocean (expressed as an anomaly, relative to the value of T_{obs}), then T_A is given by

$$T_A(\lambda, \phi, t) = T_{obs}(\lambda, \phi, t) + \Delta T_{mlo}(\lambda, \phi, t) \quad (2.15)$$

Substituting this value for T_A into Equation 2.14, the SST adjustment is given by

$$\Delta T(\lambda, \phi, t) = T_{obs}(\lambda, \phi, t) + \Delta T_{mlo}(\lambda, \phi, t) - T_O(\lambda, \phi, t) \quad (2.16)$$

The SST adjustments are applied on the atmosphere model grid. Prior to using Equation 2.16 to calculate the SST adjustments, it is therefore necessary to interpolate the ocean model SST T_O onto the atmosphere model grid, in exactly the same fashion as takes place within the model.

2.6.3 Fields passed to the ocean model

Zonal means

Figure 2.20 shows the zonal-mean surface fluxes diagnosed from Mk3L atmosphere and ocean model runs A-DEF and O-DEF, and the zonal-mean flux adjustments which are diagnosed for use in the coupled model. As anticipated from the agreement between the simulated and implied oceanic meridional heat and salt transports, the zonal-mean surface heat flux and surface salinity tendency adjustments are small, not exceeding 34.1 Wm^{-2} and 1.55 psu/year in magnitude.

The largest zonal-mean heat flux adjustments arise at the equator, where the atmosphere model simulates a larger net downward heat flux than the ocean model; at mid-latitudes in both hemispheres, where the atmosphere model simulates a net downward heat flux, while the ocean model simulates a net upward heat flux; and beneath sea ice, where the atmosphere model simulates a larger net upward heat flux than the ocean model.

The zonal-mean surface salinity tendencies agree well, with both the atmosphere and ocean model simulating positive salinity tendencies (corresponding to an excess of evaporation over precipitation) in the sub-tropics, and negative salinity tendencies elsewhere. Only in the Arctic Ocean, where the high spatial variability of the World Ocean Atlas 1998 sea surface tendencies gives rise to high spatial variability in the surface salinity tendency simulated by the ocean model, does the zonal-mean flux adjustment exceed 1 psu/year .

The zonal-mean zonal momentum flux simulated by the atmosphere model is in reasonable agreement with the NCEP-DOE Reanalysis 2, although the maxima in both hemispheres are slightly too weak, and too close to the equator. As a result, the zonal-mean flux adjustment is small, except for peaks of $\sim 0.10 \text{ Nm}^{-2}$ at $\sim 60^\circ\text{S}$, and $\sim 0.09 \text{ Nm}^{-2}$ at $\sim 60^\circ\text{N}$. The simulated zonal-mean meridional momentum flux is in good agreement with the NCEP-DOE Reanalysis 2, and as a result the zonal-mean flux adjustment does not exceed 0.033 Nm^{-2} in magnitude.

Spatial variability

The simulated annual-mean surface fluxes, and the annual-mean flux adjustments which are diagnosed for use within the coupled model, are shown in Figures 2.21, 2.22 and 2.23. In all cases, but particularly in the case of the surface heat flux and

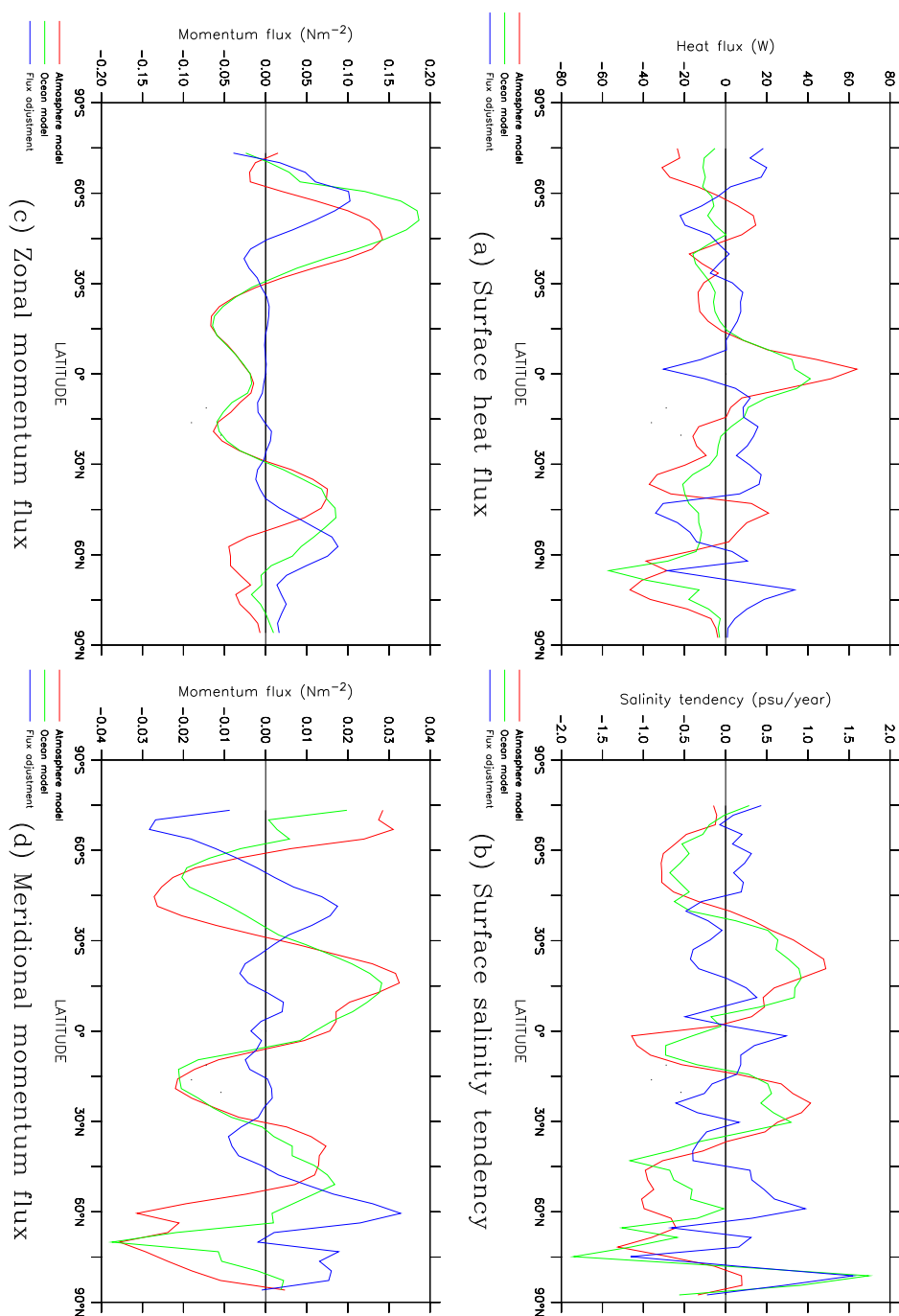


Figure 2.20: Zonal-, annual-mean surface fluxes, for the Mk3L atmosphere model (red, average for the final 40 years of run A-DEF) and the Mk3L ocean model (green, average for the final 100 years of run O-DEF), and the zonal-, annual-mean flux adjustments (blue): (a) the surface heat flux, (b) the surface salinity tendency, and (c), (d) the zonal and meridional components, respectively, of the surface momentum flux. The ocean model momentum fluxes represent the NCEP-DOE Reanalysis 2 (1979–2003 average).

surface salinity tendency, high spatial variability is encountered, with large contrasts occurring between the flux adjustments applied at adjacent gridpoints.

The large-scale spatial structure of the heat flux adjustments (Figure 2.21c) is dominated by variations in the zonal direction, rather than in the meridional direction. Positive adjustments (i.e. heat being added to the ocean) are required along the western boundaries of the ocean basins, while negative adjustments (i.e. heat being removed from the ocean) are required along the eastern boundaries. The positive heat flux adjustments can be attributed to the failure of the ocean model to adequately resolve the western boundary currents (Section 2.5.2); as a result of this failure to advect heat polewards from the tropics, this heat must instead be supplied in the form of flux adjustments. The negative heat flux adjustments can be attributed to the failure of the atmosphere model to simulate the marine stratocumulus which occurs along the eastern boundaries of the ocean basins (Section 2.4.2); the surface heat flux is therefore excessive, and must be adjusted accordingly.

Relatively large heat flux adjustments also occur within the Southern Ocean. These tend to take the form of dipoles, with adjacent positive and negative flux adjustments; it is therefore hypothesised that they arise from a failure by the ocean model to correctly simulate the finer-scale structure of the Antarctic Circumpolar Current.

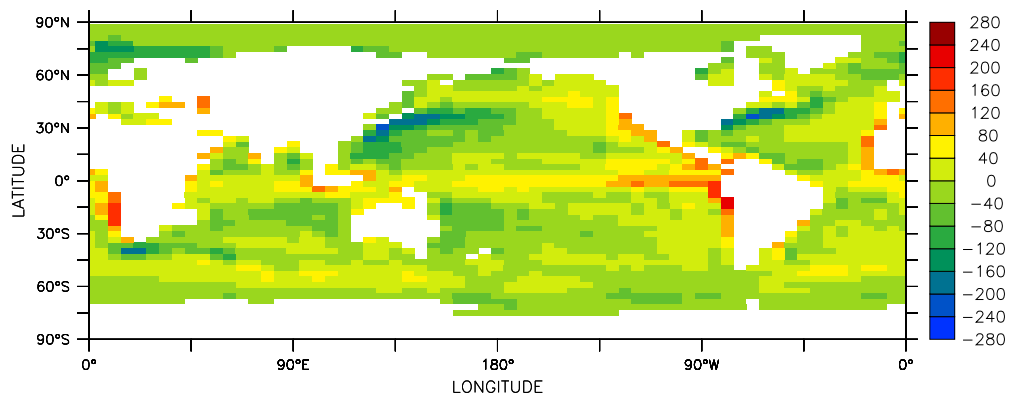
The surface salinity tendency adjustments (Figure 2.22c) are generally small, and exhibit no large-scale spatial structure. Large adjustments do occur, however, in the Arctic Ocean, and in the vicinity of the Amazon Delta. The large salinity tendency adjustments in the Arctic Ocean can be attributed to the high spatial variability in the surface salinity tendency simulated by the ocean model. The large adjustments in the vicinity of the Amazon Delta can be attributed to the large mismatch between the surface freshwater fluxes simulated by the stand-alone atmosphere and ocean models.

The relatively large adjustments to the zonal momentum flux at $\sim 60^\circ\text{S}$ and $\sim 60^\circ\text{N}$ are apparent (Figure 2.23c). Particularly large adjustments are applied in the North Atlantic, where the maximum in the atmosphere model momentum flux lies further south than in the NCEP-DOE Reanalysis 2, and across the Southern Ocean. The adjustments to the meridional momentum flux are small (Figure 2.23d).

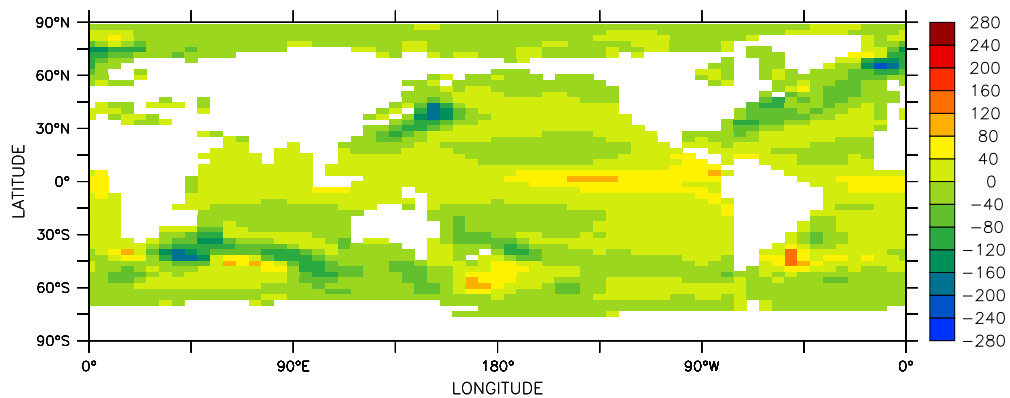
Temporal variability

In addition to the spatial variability exhibited by the flux adjustments, they also exhibit temporal variability in the form of an annual cycle. Figure 2.24 shows the root-mean-square amplitude of the annual cycle exhibited by the adjustments to each of the four surface fluxes. The amplitudes can be as large as 229 Wm^{-2} in the case of the surface heat flux adjustments, 21.4 psu/year in the case of the surface salinity tendency adjustments, and 0.104 Nm^{-2} in the case of the momentum flux adjustments.

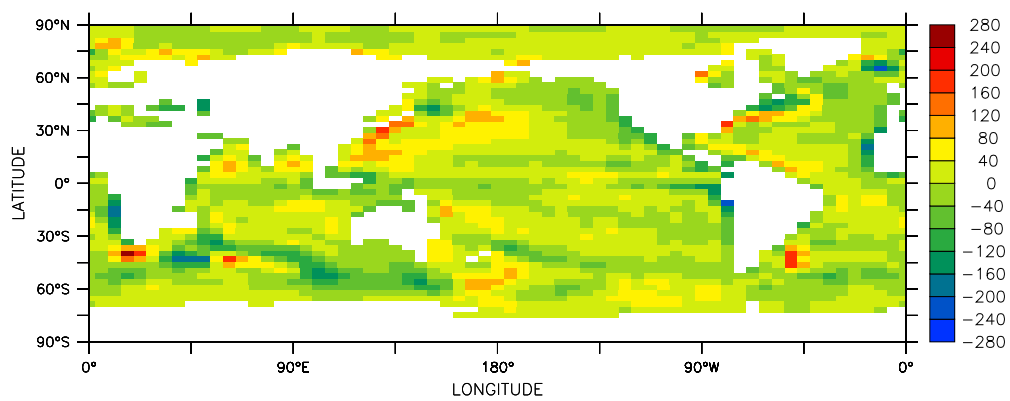
While the annual-mean flux adjustments can be large in magnitude, the monthly-mean adjustments, which represent the values which would actually be applied within the coupled model, are even larger. Table 2.9 shows some statistics for the adjustments diagnosed for each of the four surface fluxes. The surface heat flux adjustment can be as large in magnitude as 443.68 Wm^{-2} , while the surface salinity



(a) Atmosphere model

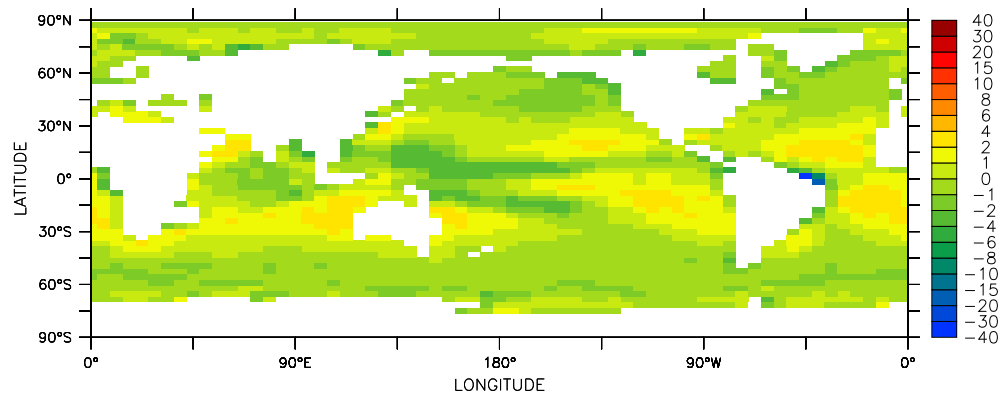


(b) Ocean model

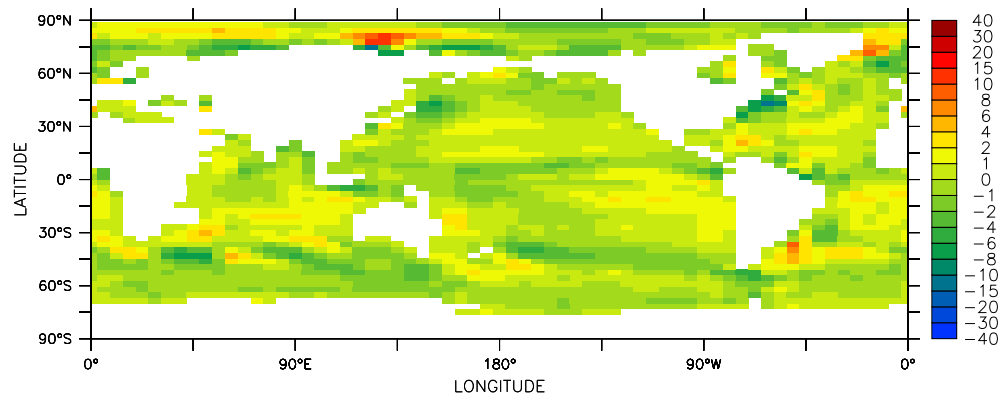


(c) Flux adjustment

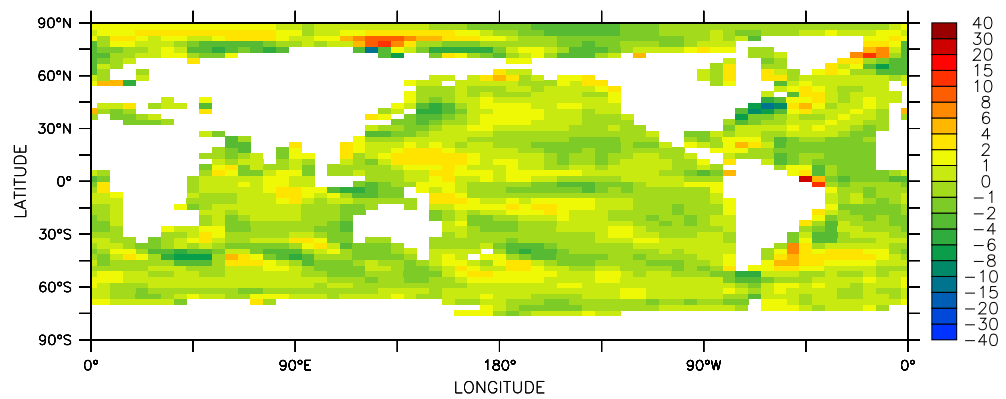
Figure 2.21: The annual-mean surface heat flux (Wm^{-2}): (a) the Mk3L atmosphere model (average for the final 40 years of run A-DEF), (b) the Mk3L ocean model (average for the final 100 years of run O-DEF), and (c) the annual-mean heat flux adjustment.



(a) Atmosphere model



(b) Ocean model



(c) Flux adjustment

Figure 2.22: The annual-mean surface salinity tendency (psu/year): (a) the Mk3L atmosphere model (average for the final 40 years of run A-DEF), (b) the Mk3L ocean model (average for the final 100 years of run O-DEF), and (c) the annual-mean salinity tendency adjustment.

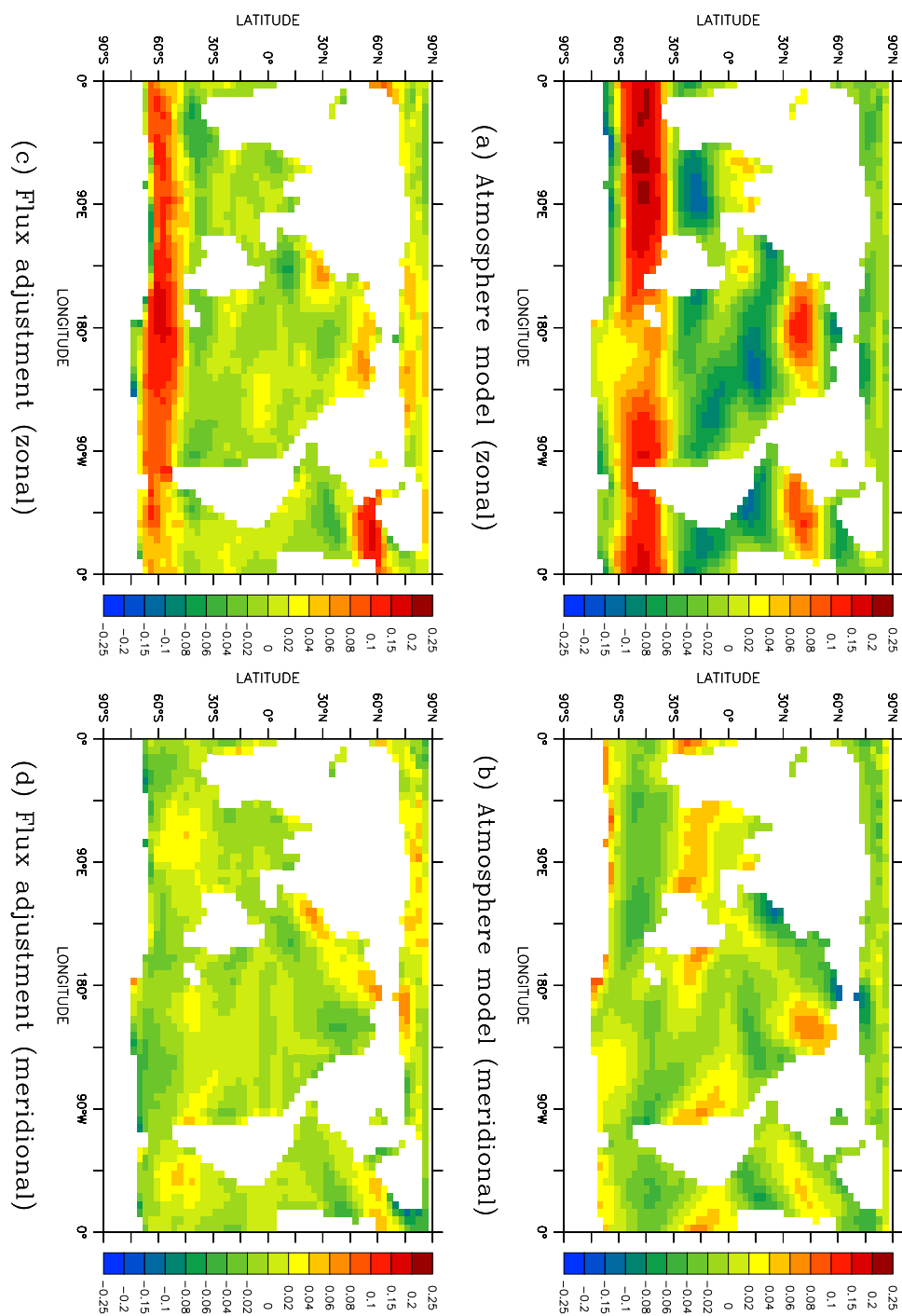


Figure 2.23: The annual-mean surface momentum flux (Nm^{-2}): (a), (b) the zonal and meridional components, respectively, for the Mk3L atmosphere model (average for the final 40 years of run A-DEF), and (c), (d) the zonal and meridional components, respectively, of the annual-mean momentum flux adjustment.

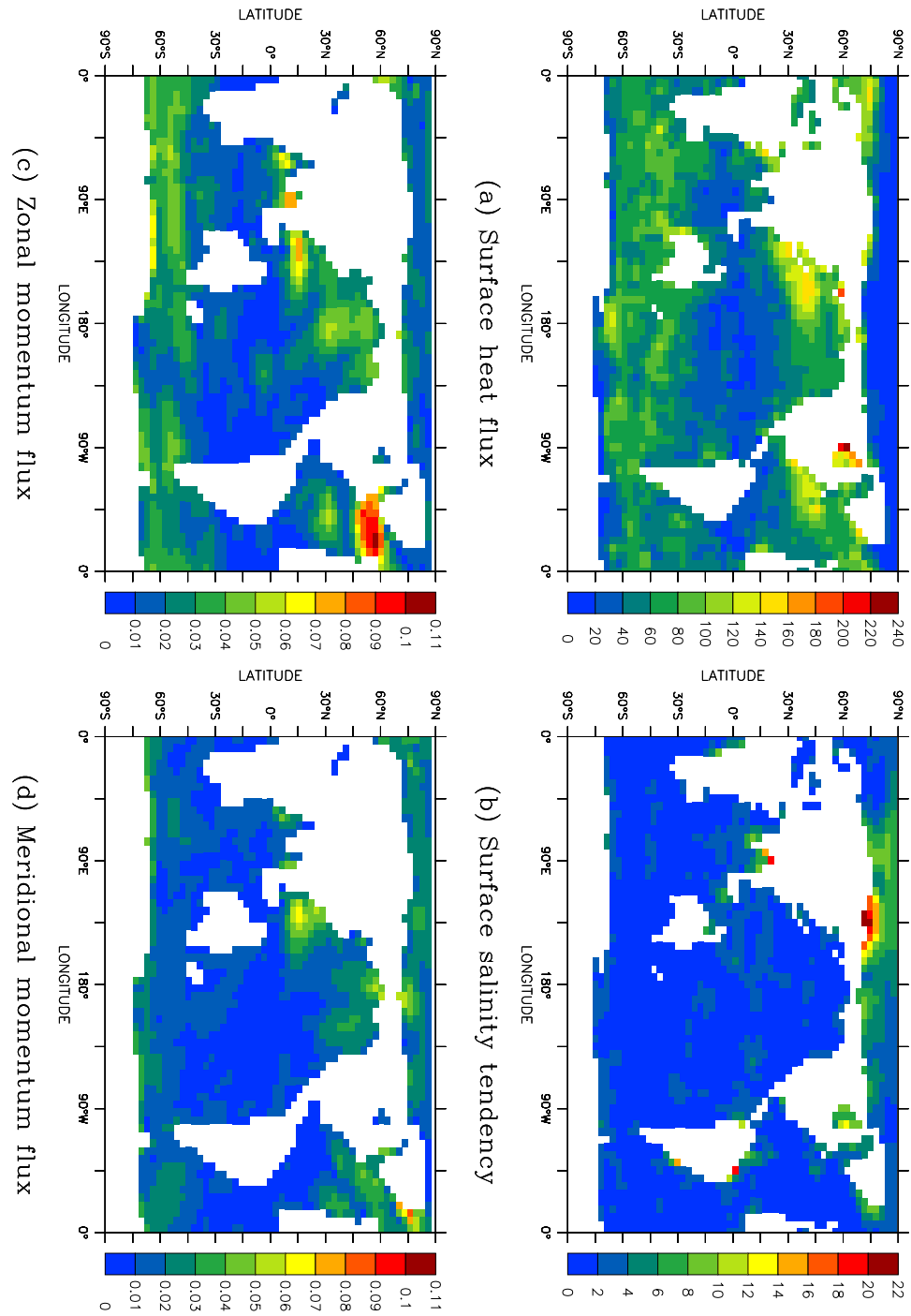


Figure 2.24: The root-mean-square amplitude of the annual cycle in the flux adjustments: (a) the surface heat flux (Wm^{-2}), (b) the surface salinity tendency (psu/year), and (c), (d) the zonal and meridional components, respectively, of the surface momentum flux (Nm^{-2}).

Field	Units	Annual means				Monthly means	
		Mean	RMS	Min	Max	Min	Max
Heat flux	Wm^{-2}	+0.20	45.21	-208.10	+247.90	-386.55	+443.68
Salinity tendency	psu/year	-0.00	1.69	-13.08	+27.83	-43.14	+51.55
τ_x	Nm^{-2}	+0.012	0.041	-0.110	+0.186	-0.187	+0.333
τ_y	Nm^{-2}	+0.001	0.019	-0.100	+0.076	-0.200	+0.192

Table 2.9: The flux adjustments diagnosed from the final 40 years of Mk3L atmosphere model run A-DEF, and the final 100 years of Mk3L ocean model run O-DEF, for the surface heat flux, the surface salinity tendency, and the zonal and meridional components of the surface momentum flux (τ_x , τ_y). For each field, the global-mean, root-mean-square, minimum and maximum values of the annual-mean flux adjustments are given, as are the minimum and maximum values of the monthly-mean flux adjustments.

tendency adjustment can be as large in magnitude as 51.55 psu/year, equivalent to a freshwater flux of ~ 37 m/year.

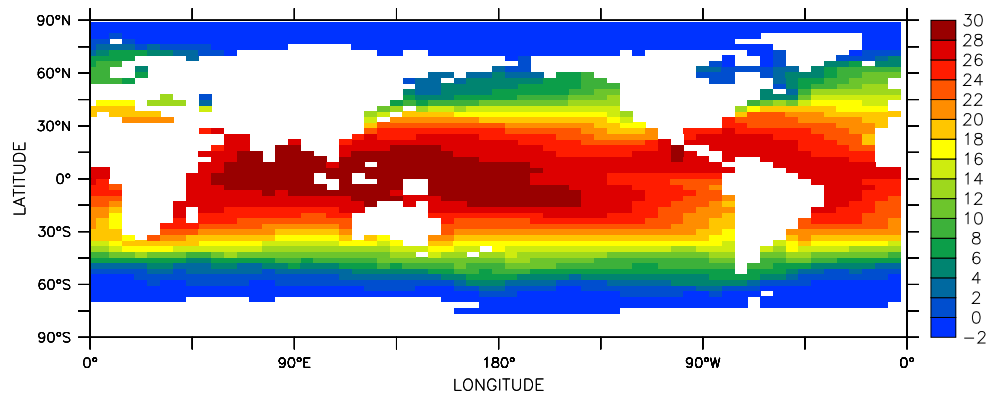
Such adjustments are comparable to, or even larger in magnitude than, the fluxes which are being simulated. The surface heat flux adjustment, for example, can be larger in magnitude than the incoming flux of solar radiation, which provides the only physical energy input to the climate system. Even under clear skies and at the equator, the daily-mean insolation cannot exceed $\sim 434 \text{ Wm}^{-2}$ (representing the value of the solar constant, divided by π). It is therefore the case at some locations, particularly at high latitudes, that the flux adjustments will represent the largest component of the surface fluxes which are applied to the ocean.

2.6.4 Fields passed to the atmosphere model

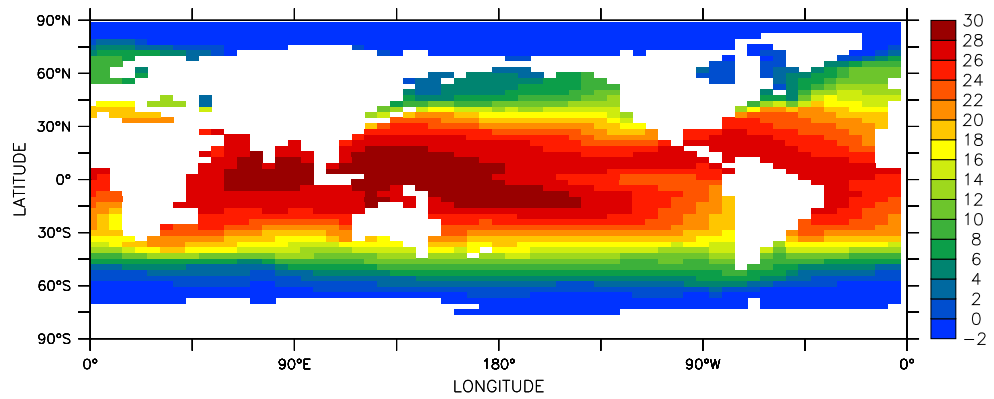
Figures 2.25 and 2.26 show the annual-mean adjustments to the sea surface temperatures and salinities. Unlike the adjustments applied to the surface fluxes, the adjustments to the sea surface temperature (SST) and sea surface salinity (SSS) are relatively small in magnitude. This is particularly true in the case of the annual-mean SSS adjustments, which do not exceed 0.75 psu in magnitude.

The adjustments to the SST reflect the deficiencies in the climate of the stand-alone ocean model. The adjustments are generally positive at low latitudes and negative at high latitudes, representing the tendency of coarse-resolution ocean general circulation models to simulate tropical SSTs that are too cold, and high-latitude SSTs that are too warm (e.g. *Gordon and O'Farrell, 1997*).

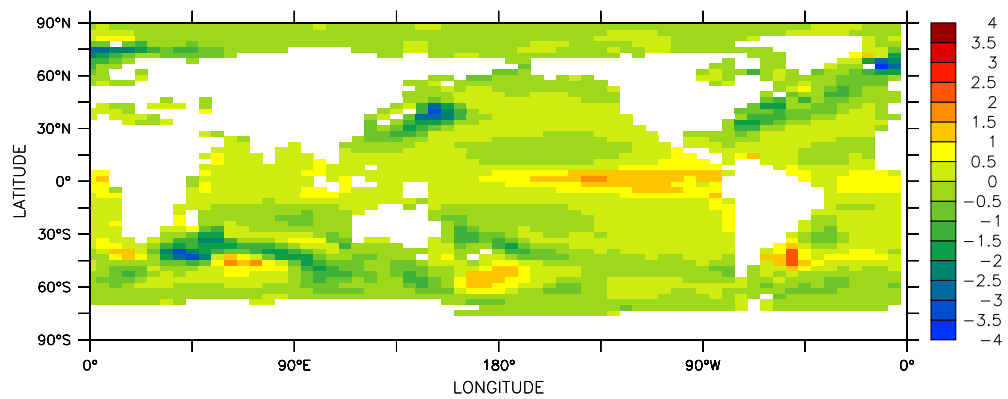
In addition to this meridional structure, negative adjustments are generally applied in the west of the ocean basins. This reflects the diffuse nature of the simulated western boundary currents, as a result of which the poleward advection of warm water occurs too far to the east, and the simulated SSTs in these regions are too warm. As with the surface heat flux adjustments, the positive/negative dipoles in the Southern Ocean are hypothesised to result from a failure to correctly simulate the finer-scale structure of the Antarctic Circumpolar Current.



(a) Atmosphere model



(b) Ocean model



(c) Flux adjustment

Figure 2.25: The annual-mean sea surface temperature ($^{\circ}\text{C}$): (a) the Mk3L atmosphere model (average for the final 40 years of run A-DEF), (b) the Mk3L ocean model (average for the final 100 years of run O-DEF), and (c) the annual-mean sea surface temperature adjustment.

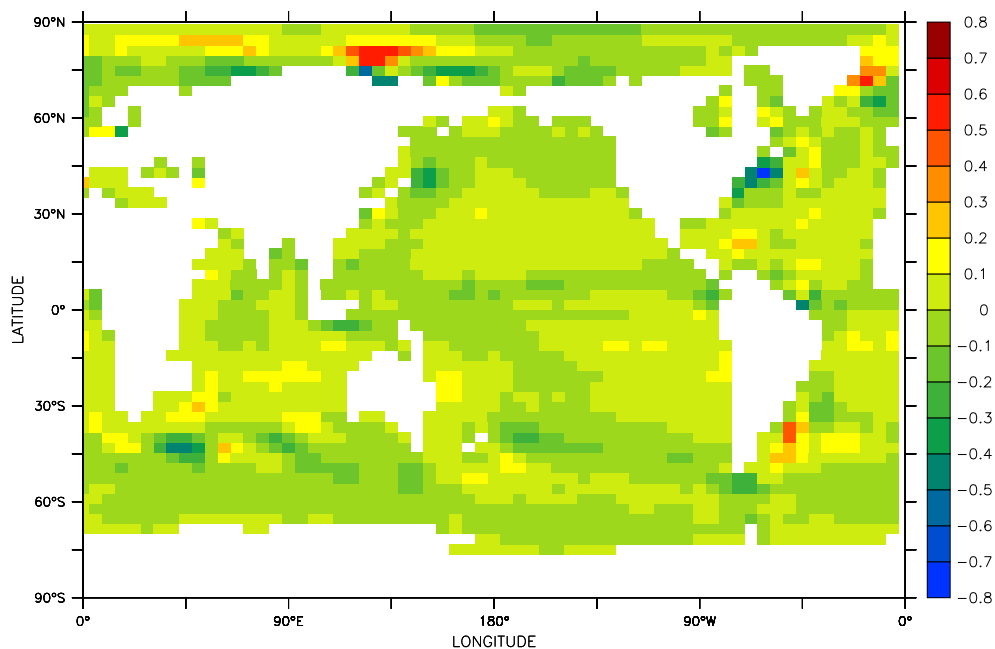
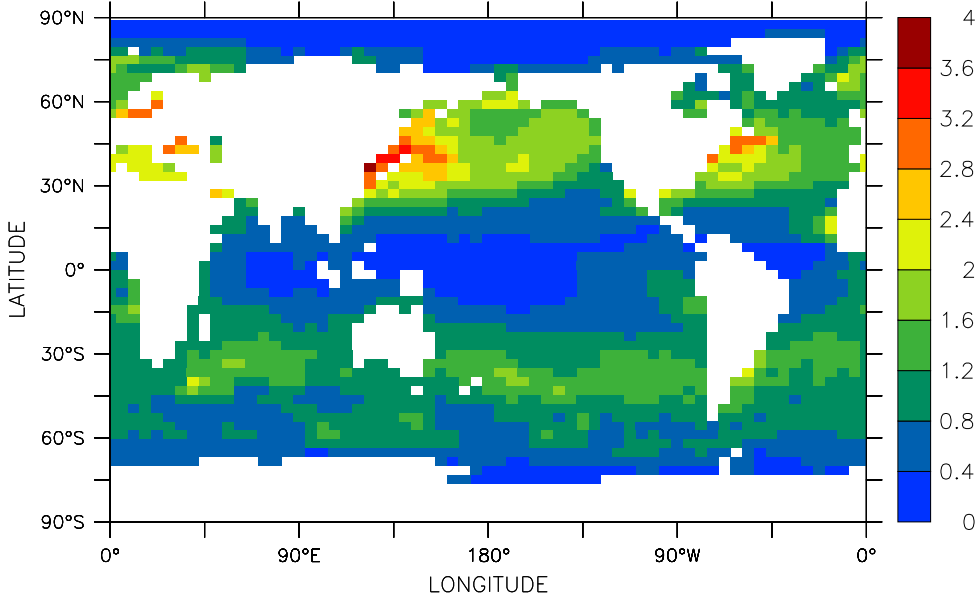


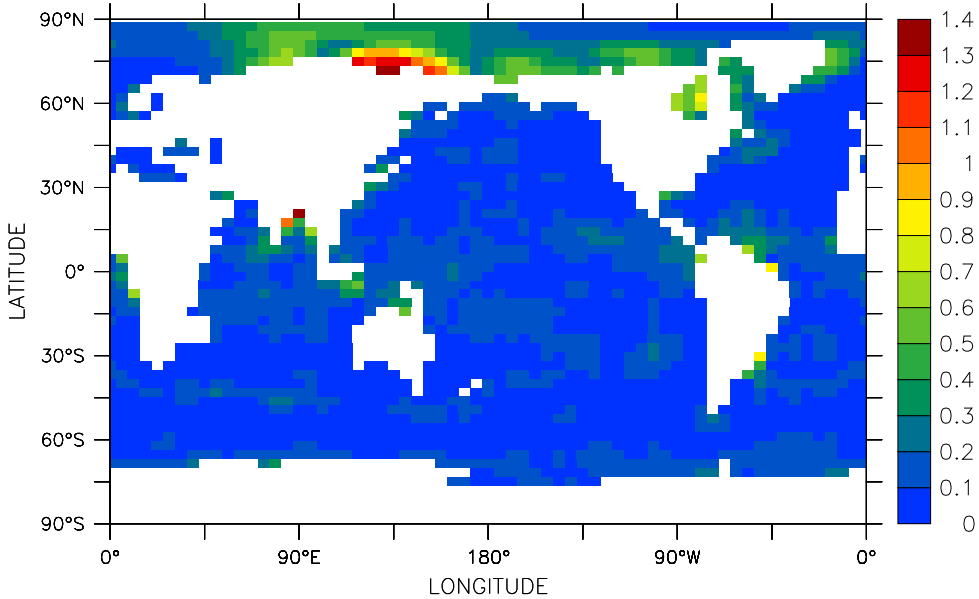
Figure 2.26: The annual-mean sea surface salinity adjustment (psu), diagnosed from the final 100 years of Mk3L ocean model run O-DEF.

Field	Units	Annual means				Monthly means	
		Mean	RMS	Min	Max	Min	Max
SST	°C	+0.003	0.566	-3.855	+2.362	-7.506	+5.468
SSS	psu	-0.000	0.082	-0.752	+0.579	-3.388	+2.990

Table 2.10: The sea surface temperature (SST) and sea surface salinity (SSS) adjustments diagnosed from the final 40 years of Mk3L atmosphere model run A-DEF, and the final 100 years of Mk3L ocean model run O-DEF. For each field, the global-mean, root-mean-square, minimum and maximum values of the annual-mean flux adjustments are given, as are the minimum and maximum values of the monthly-mean flux adjustments.



(a) Sea surface temperature



(b) Sea surface salinity

Figure 2.27: The root-mean-square amplitude of the annual cycle in the adjustments to (a) the sea surface temperature ($^{\circ}\text{C}$), and (b) the sea surface salinity (psu).

Figure 2.27 shows the amplitude of the annual cycle in the SST and SSS adjustments, while some statistics are shown in Table 2.10. As with the annual-mean adjustments, the monthly-mean adjustments are relatively small in magnitude. The largest annual cycle in the SST adjustments occurs in the vicinity of the western boundary currents in the Northern Hemisphere, while the largest annual cycle in the SSS adjustments occurs over the Arctic Ocean.

Chapter 3

Ocean model spin-up procedures

3.1 Introduction

The control climates of the Mk3L atmosphere and ocean models were evaluated in Chapter 2. A number of deficiencies were noted, including that:

- The climate of the ocean model is only moderately realistic. The deep ocean is too cold, too fresh and too buoyant, and the rate of North Atlantic Deep Water formation is too weak.
- There are significant mismatches between the surface fluxes diagnosed from the atmosphere and ocean model spin-up runs. In some regions, these mismatches are larger in magnitude than the fluxes themselves.

The deficiencies in the climate of the ocean model arise, in part, because the surface waters in the regions of deep water formation are insufficiently dense or saline (*England and Hirst, 1997; Bi, 2002*). While this may indicate deficiencies in the model physics, an alternative explanation is associated with the surface boundary conditions on the ocean model. These have two potential flaws:

- The relaxation boundary condition is physically unrealistic, and ensures that the peak winter density and salinity of the surface waters do not attain the maximum observed values (*England and Hirst, 1997; Bi, 2002*).
- The prescribed sea surface temperatures and salinities may be erroneous. In particular, a “fair weather” bias in observed sea surface temperatures and salinities at high latitudes, including a lack of observations beneath sea ice, has been noted (e.g. *Weaver and Hughes, 1996; Duffy and Caldeira, 1997*). As a result of this bias, the observed sea surface temperatures can be too high, and the sea surface salinities too low.

In Section 3.2, the surface boundary conditions which have been employed in other studies are examined. It is concluded that the relaxation boundary condition is

the most appropriate, as it gives rise to a stable ocean climate. The default response of the Mk3L ocean model to the relaxation boundary condition is therefore studied in further detail in Section 3.3.

Potential modifications to the relaxation boundary condition are considered in Section 3.4. The remainder of the chapter then studies the dependence of the simulated ocean climate upon the relaxation timescale. In Section 3.5, this relationship is investigated using a simple theoretical slab ocean model. In Section 3.6, a series of spin-up runs are then conducted using the Mk3L ocean model, with the relaxation timescale being varied from 5 to 80 days.

The dependence of the simulated ocean climate upon the prescribed sea surface temperatures and salinities is studied in Chapter 4.

3.2 Surface boundary conditions

3.2.1 The relaxation boundary condition

Under the relaxation boundary condition on the sea surface temperature (SST) and sea surface salinity (SSS), the temperature and salinity of the upper level of the ocean model are relaxed towards prescribed values. An exponential relaxation is employed, using a constant timescale.

The Mk3L ocean model uses the relaxation boundary condition to calculate the surface heat flux F and the surface salinity tendency dS_O/dt as follows:

$$F = c_v \Delta z \gamma (T_{obs} - T) \quad (3.1)$$

$$\frac{dS_O}{dt} = \gamma (S_{obs} - S) \quad (3.2)$$

Here, T and S are the temperature and salinity, respectively, of the upper level of the model, T_{obs} and S_{obs} are the prescribed SST and SSS respectively, c_v is the volumetric heat capacity of seawater, and Δz is the thickness of the upper layer of the ocean model. γ is the relaxation constant, and is equal to the inverse of the relaxation timescale. The model employs an insulating boundary condition at lateral walls and at the base; neither are there any internal sources of heat or salt. The evolution of the heat and salt contents of the ocean are therefore governed entirely by the respective surface fluxes, and by internal redistribution of these properties.

From Equations 3.1 and 3.2, it can be seen that the surface fluxes are linearly proportional to the difference between the prescribed and simulated values for the surface tracers. The constants of proportionality are $c_v \Delta z \gamma$ for the SST, and γ for the SSS; for a relaxation timescale of 20 days, these equate to $\sim 59 \text{ Wm}^{-2}\text{K}^{-1}$ and $\sim 5.8 \times 10^{-7} \text{ s}^{-1}$ respectively.

The prescribed SST and SSS for spin-up run O-DEF (Section 2.3.2) were taken from the World Ocean Atlas 1998 (*National Oceanographic Data Center, 2002*). However, the use of observational values for the prescribed SST and SSS precludes the possibility that the simulated SST and SSS can equal the observed values, *and* that there can be non-zero surface fluxes. As the surface fluxes of heat and freshwater are not, in general, equal to zero, the use of the relaxation boundary condition in

conjunction with observational values for the SST and SSS therefore ensures that there *must* be discrepancies in the ocean model climate. An alternative approach to the relaxation boundary condition on the SST is that of *Haney (1971)* and *Han (1984)*, in which T_{obs} in Equation 3.1 is set equal to a prescribed *apparent surface air temperature*. These temperatures are calculated such that, when the simulated SST is equal to an observed value, the surface heat flux will also be equal to an observed value.

The relaxation boundary condition on the SST simulates the strong feedback which exists between the temperature of the sea surface and that of the atmosphere, through the temperature-dependence of the surface fluxes of latent heat, sensible heat and longwave radiation. While there is therefore a physical justification for the use of the relaxation boundary condition in the case of the SST, there is no such justification in the case of the SSS, as no equivalent feedback mechanism operates. An alternative to the relaxation boundary condition on the SSS is therefore to prescribe the surface freshwater flux (Section 3.2.2).

The validity of the relaxation boundary condition is examined by *Pierce (1996)*, *Chu et al. (1998)* and *Killworth et al. (2000)*.

3.2.2 Mixed boundary conditions

Under mixed boundary conditions, the surface freshwater flux is prescribed, while the relaxation boundary condition (Equation 3.1) is used to calculate the surface heat flux. The prescribed freshwater flux can be derived from observations; alternatively, it can be derived from an ocean model simulation conducted under the relaxation boundary condition, with the intention that the equilibrium state under mixed boundary conditions will resemble that under relaxation boundary conditions. A further possibility is to diagnose the flux from an atmosphere model spin-up run, avoiding the need to apply adjustments to the freshwater flux within the coupled model.

The response of ocean general circulation models, of varying degrees of realism, to mixed boundary conditions has been widely studied (e.g. *Bryan, 1986*; *Weaver and Sarachik, 1991a,b*; *Weaver et al., 1993*; *Power and Kleeman, 1993*; *Zhang et al., 1993*; *Tziperman et al., 1994*; *Cai, 1995*). The response is found to be highly model-dependent, and also to depend upon the nature of the surface freshwater forcing. In some cases, the steady-state solution obtained under relaxation boundary conditions is found to be stable upon a switch to mixed boundary conditions (*Weaver et al., 1993*; *Tziperman et al., 1994*). However, other responses include a steady-state solution with an enhanced thermohaline circulation (*Power and Kleeman, 1993*), collapse of the thermohaline circulation (“the polar halocline catastrophe”, *Bryan, 1986*; *Weaver and Sarachik, 1991b*; *Weaver et al., 1993*; *Tziperman et al., 1994*; *Cai, 1995*), violent overturning events (“flushes”, *Weaver and Sarachik, 1991b*; *Weaver et al., 1993*), and oscillations on decadal timescales (*Weaver and Sarachik, 1991a,b*; *Weaver et al., 1993*; *Cai, 1995*).

One drawback with mixed boundary conditions is that the feedback mechanisms that exist between the SSS and the ocean circulation are free to operate, while those that exist between the SST and the ocean circulation are suppressed by the relaxation boundary condition. The relative importances of variations in the SST

and SSS in determining variations in density are therefore distorted. *Cai (1995)* finds that this is the cause of the unstable nature of the thermohaline circulation under mixed boundary conditions. A positive feedback mechanism exists, whereby any freshening of the surface waters at high latitudes leads to reduced convection, which in turn leads to a weakening of the poleward salt transport. This leads to further surface freshening, and ultimately results in the collapse of the thermohaline circulation. If the SST was also free to evolve, then the reduction in poleward transport would lead to a cooling of the surface waters at high latitudes, which would offset the effects of any freshening and hence tend to stabilise the meridional overturning.

By varying the prescribed surface fields, *Weaver et al. (1993)* also find that the stability behaviour of their model depends upon the relative importance of the freshwater and thermal forcing in determining the density of the surface waters. Under weak freshwater forcing, in which case the dominant influence on the surface water density is the relaxation boundary condition on the SST, the thermohaline circulation is stable upon the switch from relaxation boundary conditions to mixed boundary conditions. As the relative importance of the freshwater forcing is increased, however, the thermohaline circulation becomes increasingly unstable under mixed boundary conditions. Decadal oscillations are encountered and, under the strongest freshwater forcing, the thermohaline circulation remains in a predominantly collapsed state, experiencing occasional violent “flushes” on centennial timescales.

The importance of thermal forcing in stabilising the thermohaline circulation is further confirmed by *Zhang et al. (1993)*. They find that, under mixed boundary conditions, the reduction in the surface heat loss at high latitudes is essential for the development of a “polar halocline catastrophe”. When the relaxation boundary condition on the SST is replaced with a prescribed surface heat flux, the thermohaline circulation is found to become stable in nature. A polar halocline catastrophe cannot be induced, even when freshwater anomalies are applied at high latitudes.

Power and Kleeman (1993) find that the use of mixed boundary conditions can cause an ocean general circulation model to exhibit multiple equilibria. This arises because of the relaxation towards a (fixed) observed SST, which allows the surface heat flux (but not the SST) to evolve upon a change in the ocean circulation. Multiple equilibrium states can therefore exist, which are maintained by the same surface freshwater fluxes, but by very different surface heat fluxes. They encounter two equilibrium states in their model under mixed boundary conditions, one with deep water forming in the North Atlantic, and one with deep water forming in the North Pacific. However, only the state with deep water formation in the North Atlantic is stable under both relaxation boundary conditions, and the application of prescribed heat *and* freshwater fluxes.

3.2.3 Bulk forcing

Under bulk forcing, the surface fluxes are calculated interactively, allowing the SST and SSS to evolve, and hence allowing the associated feedback mechanisms with the ocean circulation to operate.

Hirst and Godfrey (1993) and *Oberhuber (1993)* employ bulk forcing to calculate the surface heat flux, while using the relaxation boundary condition on the SSS.

The net surface heat flux F_N is given by the sum of the sensible heat flux F_S , the latent heat flux F_L , and the net radiative heat flux F_R (*Hirst and Godfrey*, 1993, Equation 2):

$$F_N = F_S + F_L + F_R \quad (3.3)$$

F_S and F_L are given by (*Hirst and Godfrey*, 1993, Equation 3):

$$F_S = \rho_a C_{pa} C_H V_a (T_a - T_1) \quad (3.4)$$

$$F_L = \rho_a L C_E V_a [q_a - q_s(T_1)] \quad (3.5)$$

Here, ρ_a is the surface density of air, C_{pa} the specific heat capacity of air, C_H the transfer coefficient for sensible heat, V_a the surface wind speed, T_a the surface air temperature, T_1 the model SST, L the latent heat of vaporisation, C_E the transfer coefficient for latent heat, q_a the specific humidity, and $q_s(T_1)$ the saturated specific humidity. Constant values are used for ρ_a , C_{pa} , C_H , L and C_E , while $q_s(T_1)$ is calculated by the model. Annual-mean observational values are used for V_a , T_a , q_a and F_R . Beneath sea ice, the model SST is relaxed towards observational values, rather than using bulk forcing to calculate the surface heat flux.

Oberhuber (1993) also uses Equations 3.3–3.5 to calculate the surface heat flux. However, his model calculates C_H and C_E using the method of *Large and Pond* (1981, 1982), while F_R is calculated using expressions for the net surface fluxes of shortwave and longwave radiation. Observational values are then used for V_a , T_a and q_a . His model incorporates a sea ice model, which calculates the ice-ocean fluxes of heat and salt in ice-covered areas.

While the approach of *Hirst and Godfrey* (1993) and *Oberhuber* (1993) avoids the problems associated with the application of a prescribed freshwater flux, it also fails to represent the feedbacks between the heat and freshwater fluxes which arise as a result of evaporation.

Large et al. (1997) employ bulk forcing to calculate the surface fluxes of both heat and freshwater. The approach is similar to *Oberhuber* (1993), except that their model does not calculate the net surface flux of shortwave radiation, and that their expression for the net surface flux of longwave radiation requires observed values for the cloud cover. The observed precipitation rate is also required, in order to calculate the surface freshwater flux (Equation 3.5 provides the evaporation rate, which is given by F_L/L). Their model therefore requires that six observational quantities be supplied: the surface wind speed, the surface air temperature, the surface specific humidity, the cloud fraction, the net surface flux of shortwave radiation, and the precipitation rate. As with *Hirst and Godfrey* (1993), the SST and SSS are relaxed towards observed values beneath sea ice.

Large et al. (1997) compare a simulation conducted using bulk forcing with one conducted using the relaxation boundary condition on both SST and SSS. They find that bulk forcing gives a marked improvement in the ocean salinities, as well as slight improvements in the ocean temperatures and the oceanic transports. However, the use of bulk forcing also introduces complications: in order to ensure closure of the global budgets of heat and freshwater, the observed values for the net surface flux

of shortwave radiation, surface specific humidity and the precipitation rate are all modified. The shortwave radiation flux and specific humidity are multiplied by a temporally- and spatially-uniform factor, while the precipitation rate is multiplied by a factor which is spatially uniform, but which varies on an annual basis.

Despite these changes, a weak relaxation towards the observed SSS has to be used over the ice-free ocean in order to constrain salinity drift. They also acknowledge that the improvement in the ocean salinities arises, at least in part, from the annual adjustments to the precipitation field, and they find that the realism of the ocean climate is significantly dependent upon the strength of the relaxation employed beneath sea ice.

The method of *Haney* (1971) and *Han* (1984), in which the surface heat flux is calculated by relaxing the simulated SST towards a *prescribed apparent surface air temperature*, can be regarded as a simplified and linearised form of bulk forcing.

3.2.4 Summary

Given the unpredictable, and generally unstable, response of ocean models to mixed boundary conditions, it was considered that these were unsuitable for spinning up the ocean model. Bulk forcing was not considered to be suitable either. While *Large et al.* (1997) are able to obtain a more realistic ocean climate under bulk forcing than under relaxation boundary conditions, it is also an approach which appears to have significant flaws. It introduces dependence upon a considerable number of observational fields, and therefore introduces potential sources of error. Indeed, *Large et al.* (1997) are only able to obtain a realistic ocean climate after making significant and physically-unjustified modifications to a number of the observational fields.

It was therefore decided to retain the use of the relaxation boundary condition, and to seek to improve the ocean model climate through modifications to this technique.

3.3 The default model response

Prior to modifying the spin-up procedure for the ocean model, the response of the model to the default boundary conditions is now evaluated in further detail, with particular attention paid to the density of the surface waters at high latitudes. This will provide benchmarks against which modifications to the relaxation boundary condition can be assessed.

Figure 3.1 shows the annual-maximum surface σ_θ , according to the World Ocean Atlas 1998 and the Mk3L ocean model spin-up run O-DEF (Section 2.3.2). The peak values encountered in the key regions of deep water formation are also shown in Table 3.1; the excessively buoyant nature of the surface waters in the model is apparent.

In the Southern Ocean, the peak surface densities for both the World Ocean Atlas 1998 and the Mk3L ocean model, of 28.06 kgm^{-3} and 27.76 kgm^{-3} respectively, occur in the southwestern Ross Sea. The next highest surface densities occur in the Weddell Sea, with a simulated peak surface density of 27.73 kgm^{-3} in the western

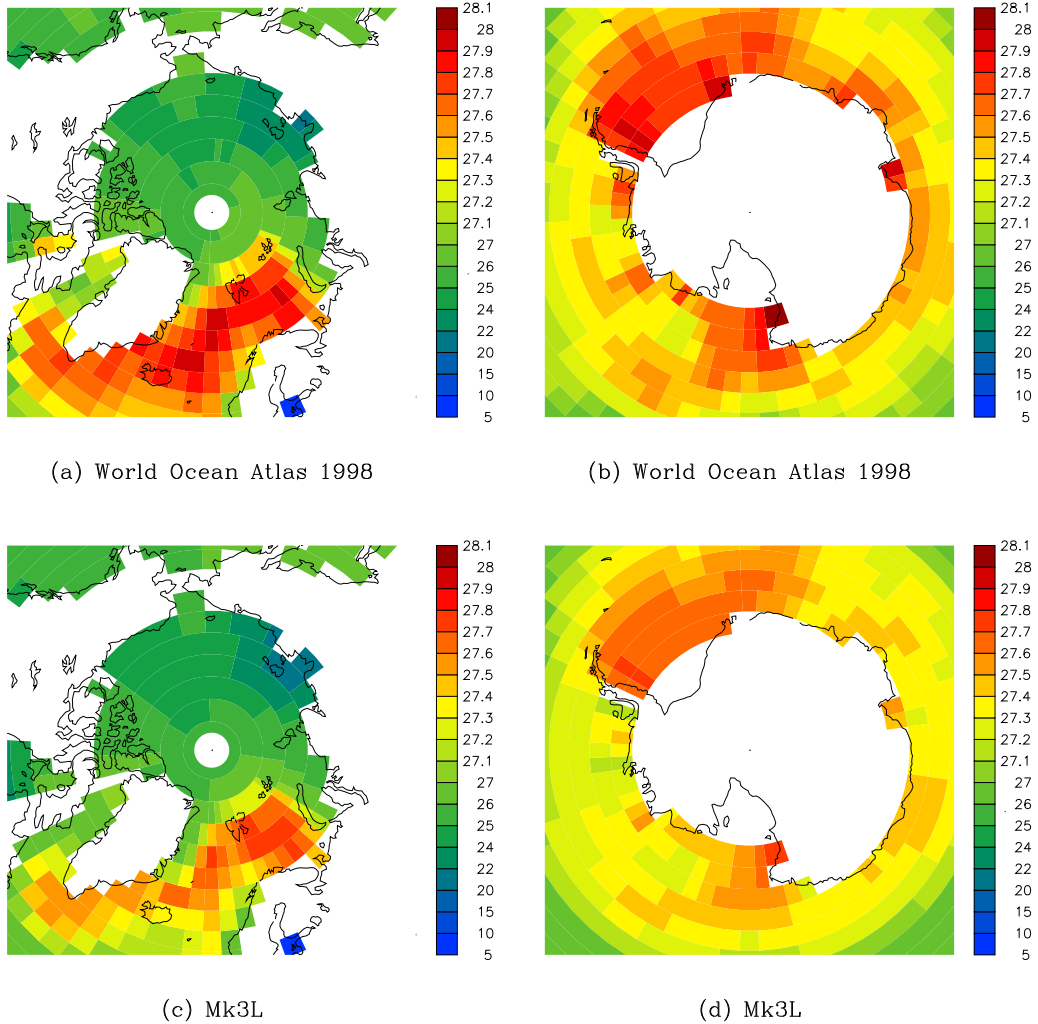


Figure 3.1: The annual-maximum surface σ_θ (kgm^{-3}): (a), (b) the World Ocean Atlas 1998, Northern and Southern Hemispheres respectively, and (c), (d) the Mk3L ocean model (average for the final 100 years of run O-DEF), Northern and Southern Hemispheres respectively. The value plotted at each gridpoint is the maximum monthly-mean density which occurs during the annual cycle. The World Ocean Atlas 1998 data has been area-averaged onto the Mk3L ocean model grid, prior to determining the annual maximum.

	World Ocean Atlas 1998	Mk3L ocean	Model discrepancy
Ross Sea	28.06	27.76	-0.30
Weddell Sea	27.98	27.73	-0.25
Nordic Seas	27.96	27.72	-0.24

Table 3.1: The peak surface σ_θ (kgm^{-3}) in regions of deep water formation: the World Ocean Atlas 1998, the Mk3L ocean model (average for the final 100 years of run O-DEF), and the model discrepancy. The World Ocean Atlas 1998 data has been area-averaged onto the Mk3L ocean model grid.

Weddell Sea. The peak surface density in this region, according to the World Ocean Atlas 1998, is 27.96 kgm^{-3} , although a slightly higher density of 27.98 kgm^{-3} occurs in the southeastern Weddell Sea. A peak surface density of 27.98 kgm^{-3} also occurs in Prydz Bay, at 73°E , 69°S ; the simulated surface density at this point is just 27.53 kgm^{-3} .

In the Arctic, the World Ocean Atlas 1998 features a peak surface density of 27.96 kgm^{-3} , which occurs in the Nordic (Greenland-Iceland-Norwegian) Seas. The peak surface density simulated by the model in this region is just 27.72 kgm^{-3} . (The maximum simulated surface density in the Arctic is 27.80 kgm^{-3} , but this occurs in the Barents Sea, at 45°E , 75°N , and is therefore located outside the regions of deep water formation.)

In the regions of Antarctic Bottom Water and North Atlantic Deep Water formation, the peak densities of the simulated surface waters are therefore too buoyant by $\sim 0.25\text{--}0.3 \text{ kgm}^{-3}$. This offers a potential explanation for the buoyant nature of the simulated deep ocean (Section 2.5.1), and shall therefore now be studied further.

The simulated and observed annual cycles in sea surface temperature, salinity and density in the three regions of deep water formation are shown in Figures 3.2, 3.3 and 3.4. The discrepancies in the simulated annual-mean surface density are small (being -0.01 , -0.04 and -0.12 kgm^{-3} for the Ross, Weddell and Nordic Seas respectively), with the failure to simulate the peak surface densities arising from the failure by the model to correctly simulate the magnitude of the annual cycle.

Figures 3.2, 3.3 and 3.4 reveal three distinct errors in the simulated sea surface temperature and salinity:

- an error in the annual mean
- an error in the amplitude of the annual cycle
- a phase lag between the simulated and observed fields

Each of these errors can be diagnosed independently of the others, and are investigated in the following sections. While they indicate potential deficiencies in the model physics, they can also be attributed, at least in part, to the relaxation boundary condition (*Pierce, 1996; Killworth et al., 2000*).

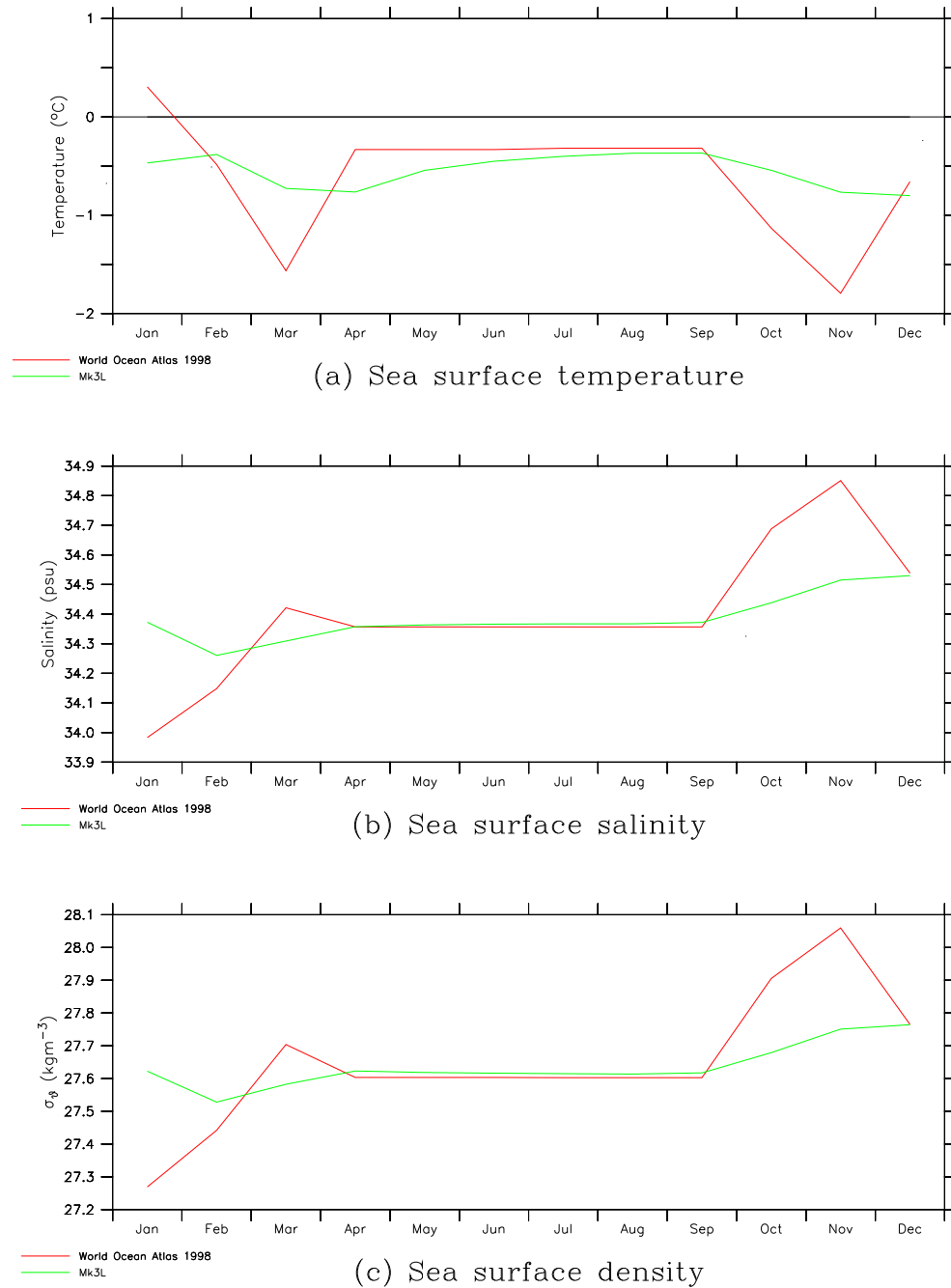


Figure 3.2: The monthly-mean sea surface temperature, salinity and σ_θ in the southwestern Ross Sea, for the World Ocean Atlas 1998 (red) and the Mk3L ocean model (green, average for the final 100 years of run O-DEF): (a) sea surface temperature, (b) sea surface salinity, and (c) sea surface σ_θ . The values plotted are for the gridpoint located at 163°E , 75°S . The World Ocean Atlas 1998 data has been area-averaged onto the Mk3L ocean model grid; the values for April appear to have been propagated throughout the winter months of May to August, indicating a lack of observational data.

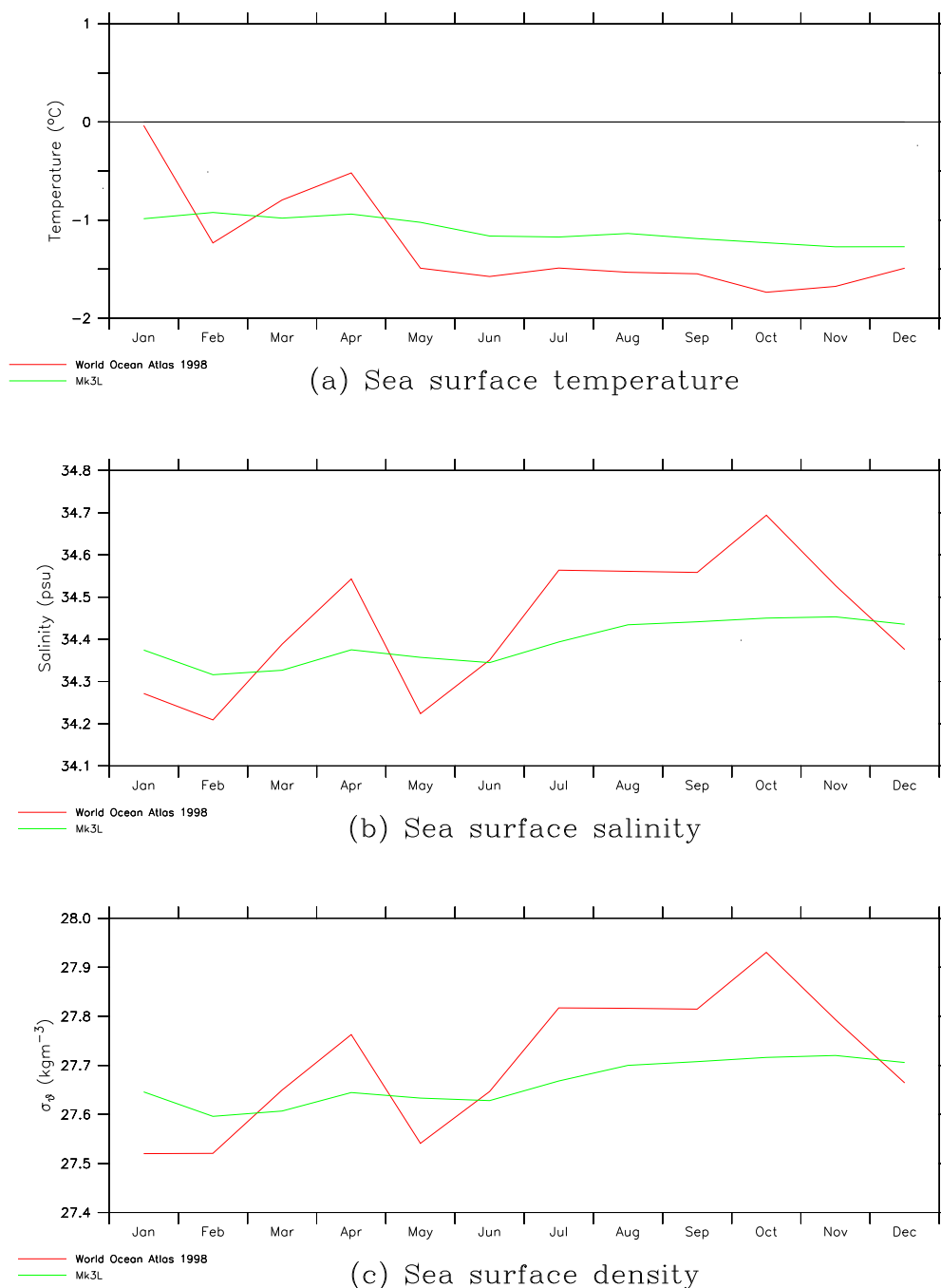


Figure 3.3: The monthly-mean sea surface temperature, salinity and σ_θ in the western Weddell Sea, for the World Ocean Atlas 1998 (red) and the Mk3L ocean model (green, average for the final 100 years of run O-DEF): (a) sea surface temperature, (b) sea surface salinity, and (c) sea surface σ_θ . The values plotted are averages for the two gridpoints located at 56°W , 72°S , and 56°W , 68°S . The World Ocean Atlas 1998 data has been area-averaged onto the Mk3L ocean model grid.

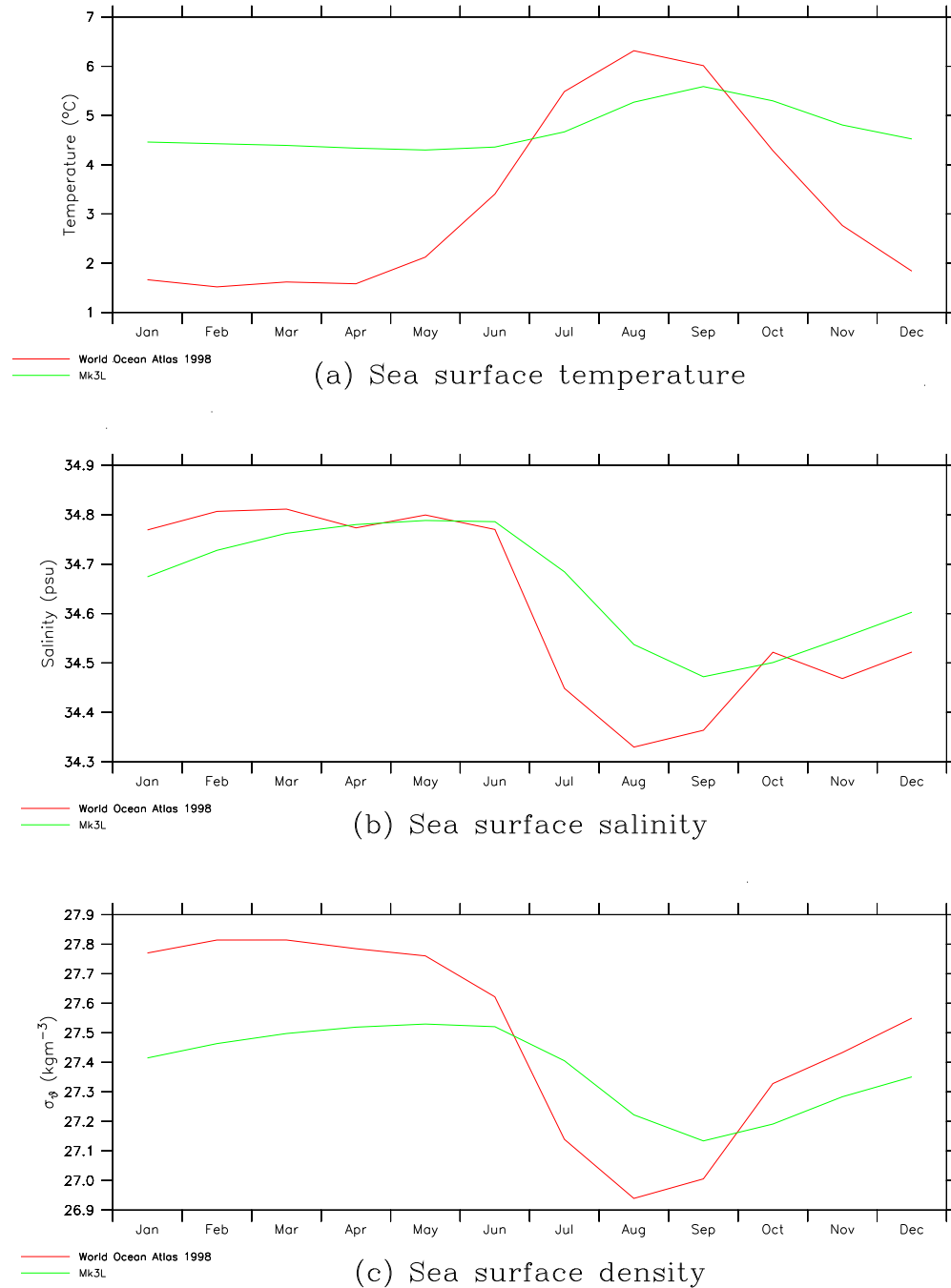


Figure 3.4: The monthly-mean sea surface temperature, salinity and σ_θ in the Nordic (Greenland-Iceland-Norwegian) Seas, for the World Ocean Atlas 1998 (red) and the Mk3L ocean model (green, average for the final 100 years of run O-DEF): (a) sea surface temperature, (b) sea surface salinity, and (c) sea surface σ_θ . The values plotted are averages for the 12 gridpoints which cover the region 14°W – 8°E , 67° – 76°N . The World Ocean Atlas 1998 data has been area-averaged onto the Mk3L ocean model grid.

These errors must be rectified if realistic high-latitude sea surface temperature and salinity fields, and hence realistic high-latitude surface densities, are to be obtained within the model.

3.3.1 Errors in the annual-mean climate

Figure 3.5 shows the annual-mean errors in the simulated SST and SSS, relative to the World Ocean Atlas 1998 values which were imposed as the surface boundary condition; the errors are as large in magnitude as 3.86°C and 0.752 psu respectively.

A consequence of the relaxation boundary condition (Equations 3.1 and 3.2) is that there *must* be errors in the annual-mean SST and SSS, wherever advection and diffusion give rise to non-zero annual-mean surface fluxes. Comparing Figure 3.5 with Figures 2.21b and 2.22b, the linear relationship between the annual-mean SST (or SSS) error, and the annual-mean surface heat flux (or surface salinity tendency), is apparent. The maximum annual-mean SST error of 3.86°C corresponds to an annual-mean surface heat flux of 229 W m^{-2} (utilising Equation 3.1), while the maximum annual-mean SSS error of 0.752 psu corresponds to an annual-mean surface salinity tendency of 13.7 psu/year (via Equation 3.2).

3.3.2 Errors in the amplitude of the annual cycle

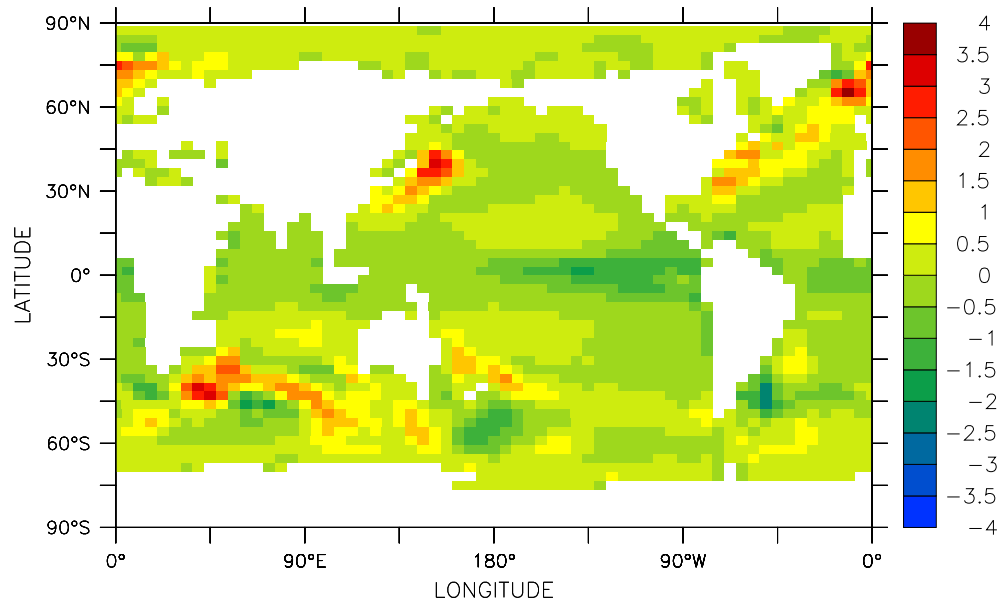
Figure 3.6 shows the amplitude of the annual cycle in the simulated SST and SSS, expressed as a fraction of the amplitude in the annual cycle of the World Ocean Atlas 1998 SST and SSS. If T_n and \bar{T} are the monthly-mean and annual-mean SST (or SSS) respectively, then the root-mean-square amplitude of the annual cycle is given by

$$a = \left[\frac{1}{12} \sum_{n=1}^{12} (T_n - \bar{T})^2 \right]^{1/2} \quad (3.6)$$

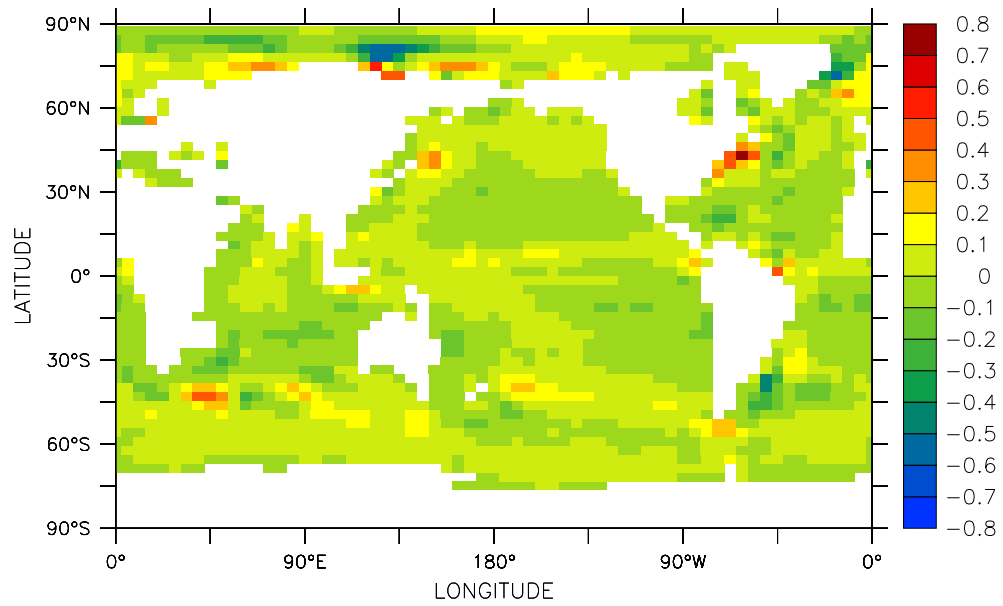
Let a_{obs} be the root-mean-square amplitude of the observed annual cycle, according to the World Ocean Atlas 1998, and let a_{mod} be the root-mean-square amplitude of the simulated annual cycle, according to the Mk3L ocean model. The response of the model can be studied by expressing the simulated amplitude as a fraction of the observed amplitude, as follows:

$$r = \frac{a_{mod}}{a_{obs}} \quad (3.7)$$

It is this ratio, which shall be referred to herein as the *relative amplitude*, which is shown in Figure 3.6. The simulated amplitudes of the annual cycle in SST and SSS are generally much smaller than the observational values. In the case of the SST, the relative amplitude varies from 0.066 to 1.093, with an area-weighted global-mean value of 0.559, while in the case of the SSS, it varies from 0.094 to 1.575, with an area-weighted global-mean value of 0.544.

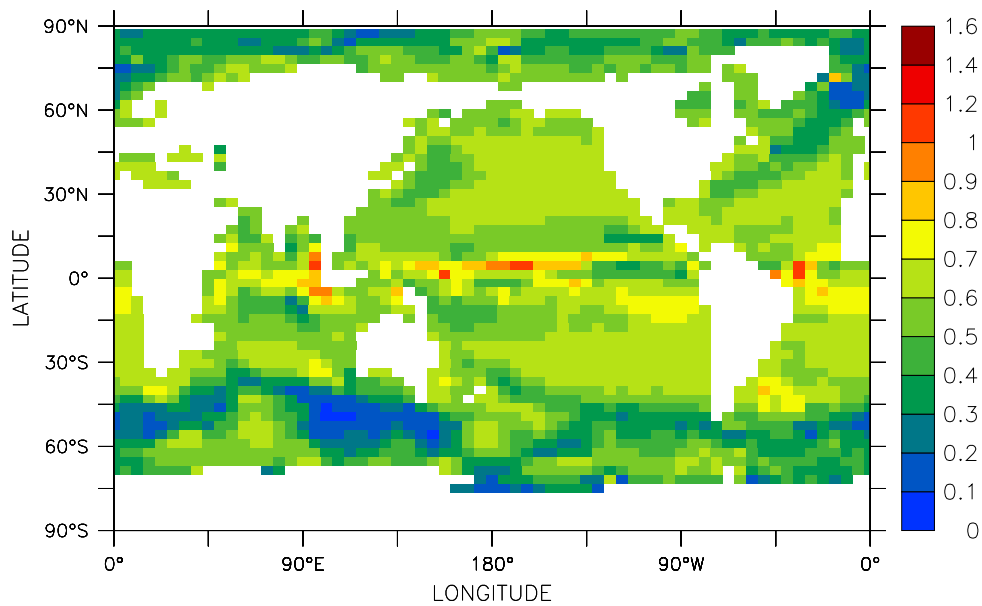


(a) Sea surface temperature

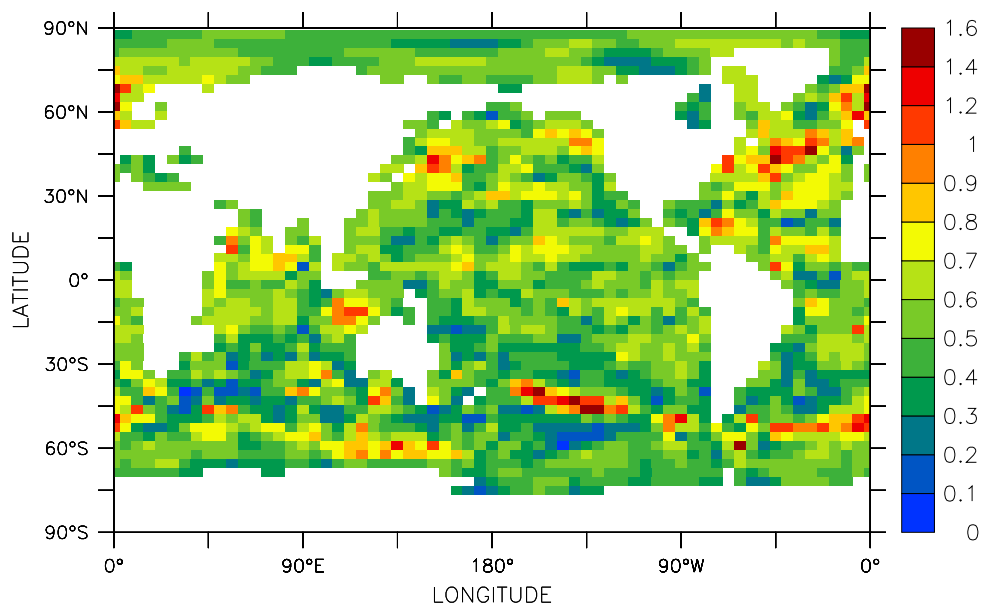


(b) Sea surface salinity

Figure 3.5: The annual-mean sea surface temperature and salinity for the Mk3L ocean model (average for the final 100 years of run O-DEF), expressed as anomalies relative to the World Ocean Atlas 1998: (a) sea surface temperature ($^{\circ}\text{C}$), and (b) sea surface salinity (psu). The World Ocean Atlas 1998 data has been area-averaged onto the Mk3L ocean model grid.



(a) Sea surface temperature



(b) Sea surface salinity

Figure 3.6: The root-mean-square amplitude of the annual cycle in sea surface temperature and salinity for the Mk3L ocean model (average for the final 100 years of run O-DEF), expressed as a fraction of the root-mean-square amplitude of the annual cycle in the World Ocean Atlas 1998 data: (a) sea surface temperature, and (b) sea surface salinity. The World Ocean Atlas 1998 data has been area-averaged onto the Mk3L ocean model grid.

3.3.3 Phase lags between the simulated and observed climate

Figure 3.7 shows the lag of maximum correlation between the Mk3L ocean model SST and SSS, and the World Ocean Atlas 1998 data. This lag is calculated from the monthly-mean values as follows:

1. Linear interpolation in time is used to estimate daily values, for both the Mk3L ocean model and the World Ocean Atlas 1998.
2. For each integer value of n from -182 to +182:
 - (a) the ocean model values are shifted forward in time by n days
 - (b) the correlation coefficient is calculated between the phase-shifted ocean model values, and the World Ocean Atlas 1998 values
3. The value of n which maximises the correlation coefficient is called the *lag of maximum correlation*.

The area-weighted global-mean lags are 31.7 and 22.1 days in the case of the SST and SSS respectively, with unimodal distributions which are tightly clustered around the means. At some gridpoints, particularly in the case of the SSS, the above technique does not produce a meaningful value for the lag; this can occur when either the simulated or observed values do not exhibit a distinct annual cycle.

3.4 Modifying the relaxation boundary condition

Equations 3.1 and 3.2 indicate two ways in which the relaxation boundary condition can be modified:

1. the relaxation constant γ can be varied
2. the prescribed sea surface temperature T_{obs} and sea surface salinity S_{obs} can be modified

Each of these modifications shall now be considered in turn.

3.4.1 The relaxation timescale

The relaxation timescales used in some of the modelling studies referred to herein are shown in Table 3.2, and are typically of order one month. *Hirst and Cai* (1994) and subsequent studies, however, choose to use a much shorter timescale of 4 days, as they find that it improves the realism of the water mass properties within their model.

This raises the question as to why longer relaxation timescales have generally been employed in other studies. Of the three errors in the simulated surface water properties which were identified in Section 3.3, and which can be attributed at least in part to the relaxation boundary condition, each would be reduced through the use of a shorter relaxation timescale.

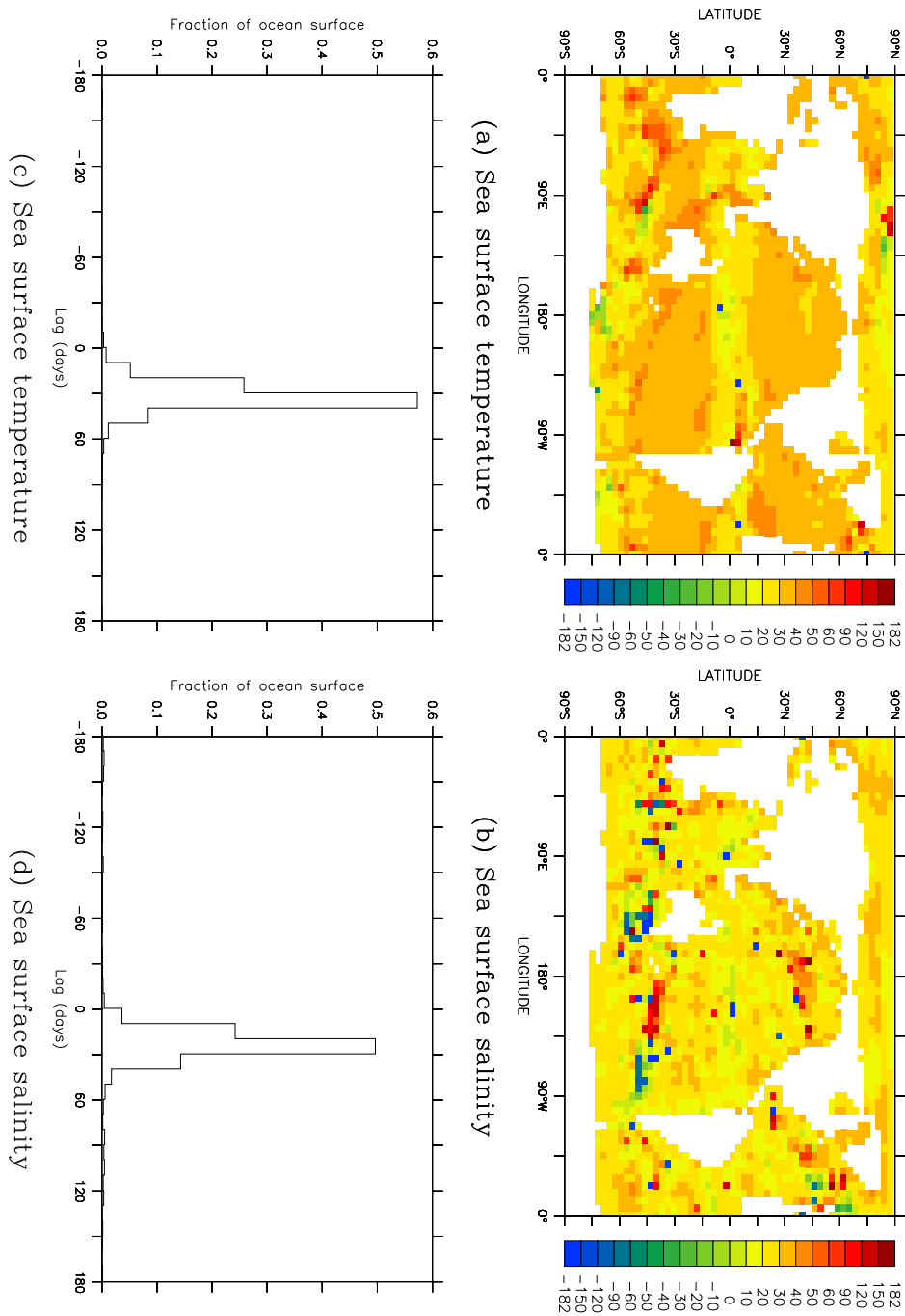


Figure 3.7: The lag of maximum correlation (days) between the Mk3L ocean model (average for the final 100 years of run O-DEF) and the World Ocean Atlas 1998: (a), (b) the lag at each gridpoint, sea surface temperature and sea surface salinity respectively, and (c), (d) the fraction of the surface area of the ocean over which the lags lie within the ranges shown, sea surface temperature and sea surface salinity respectively. The World Ocean Atlas 1998 data has been area-averaged onto the Mk3L ocean model grid.

	Relaxation timescale (days)	
	Temperature	Salinity
<i>Hirst and Cai</i> (1994) <i>Hirst and McDougall</i> (1996) <i>Hirst and McDougall</i> (1998)	4	4
<i>England and Hirst</i> (1997)	10	10
<i>Hirst and McDougall</i> (1998)	15	15
<i>Power and Kleeman</i> (1993) <i>Cai</i> (1995) <i>Gordon and O'Farrell</i> (1997) <i>Bi</i> (2002)	20	20
<i>Tziperman et al.</i> (1994) <i>Hirst and McDougall</i> (1996)	30	30
<i>England</i> (1993) <i>England and Hirst</i> (1997)	30	50
<i>Tziperman et al.</i> (1994)	30	120
<i>Weaver and Hughes</i> (1996)	50	50

Table 3.2: The relaxation timescales used in some of the studies referred to herein.

Timescales such as that employed by *Hirst and Cai* (1994), however, improve the simulated SST and SSS at the expense of poorer simulated surface fluxes and internal transport (*Pierce*, 1996), with the surface fluxes exhibiting unrealistically large spatial and temporal variability (e.g. *Hirst and McDougall*, 1996; *Bi*, 2002). This tends to increase the mismatch with the atmosphere model surface fluxes, and leads to an undesirable increase in the magnitude of the flux adjustments diagnosed for use within the coupled model.

The use of very short relaxation timescales also degrades other aspects of the simulated ocean climate. *Pierce* (1996) notes that the stability characteristics of the thermohaline circulation are distorted, while *Killworth et al.* (2000) note that the western boundary currents are severely degraded, and that features such as eddies and planetary waves are suppressed.

3.4.2 Surface tracers

A number of studies have modified the prescribed surface tracers in order to improve the realism of the model climate. A common technique has been to modify the prescribed SST and SSS at high latitudes; there are two motivations for these modifications:

- in the absence of a sea ice model, to allow for the effects of brine rejection (e.g. *Toggweiler and Samuels*, 1995; *Weaver and Hughes*, 1996)
- to correct for perceived deficiencies in the observed SST and SSS, particularly with regard to a “fair weather” bias at high latitudes (e.g. *England*, 1993; *Hirst and Cai*, 1994; *Weaver and Hughes*, 1996; *Hirst and McDougall*, 1996, 1998; *Bi*, 2002)

In some of these studies, the modifications are used in conjunction with the application of perpetual winter surface tracers in both hemispheres (e.g. *Hirst and Cai*, 1994; *Hirst and McDougall*, 1996, 1998).

“Fair weather” biases in observational climatologies are noted by *Weaver and Hughes* (1996) and *Duffy and Caldeira* (1997). These biases arise from a lack of observations beneath sea ice in both the Arctic and Antarctic, and from a tendency for observations of sea surface temperature and salinity to be made only under fair weather conditions. The observed SSTs therefore tend to be too warm, and the observed SSSs too fresh. To compensate for these biases, *Weaver and Hughes* (1996) modify the observational climatology of *Levitus* (1982) at high latitudes. Over the Arctic Ocean, they replace the observed SSTs and SSSs with the average temperatures and salinities, respectively, of the upper 50 m of the water column. In the Ross and Weddell Seas, the observed SSTs are replaced with values of -1.85°C , and the observed SSSs are replaced with values of 35.1 psu.

Weaver and Hughes (1996) find that these modifications lead to the diagnosis of very large flux adjustments in the Southern Ocean. *Bi* (2002), however, does not encounter this problem. One possible explanation for this discrepancy is that the model employed by *Bi* (2002) incorporates Gent-McWilliams eddy diffusion (*Gent and McWilliams*, 1990), while that employed by *Weaver and Hughes* (1996) does not. Models which do not incorporate Gent-McWilliams eddy diffusion are prone to excessive convection in the high-latitude Southern Ocean, and can experience very unrealistic surface fluxes as a result (e.g. *Hirst et al.*, 2000).

Bi (2002) experiments with a more systematic approach towards modifying the surface tracers, also with the aim of improving the peak densities of the surface waters in the regions of deep water formation. He employs an iterative approach, as follows:

1. The ocean model is spun up using relaxation boundary conditions, with observed values for the SST and SSS being prescribed.
2. The anomaly in the simulated SST, $\Delta T = T_{mod} - T_{obs}$, is diagnosed at each gridpoint and for each month of the year.
3. These anomalies are subtracted from the observed SST, obtaining a timeseries of modified SSTs.
4. The ocean model spin-up run is continued, with the modified SSTs being prescribed.
5. SST anomalies are diagnosed from the new run, and are used to further modify the prescribed SSTs.

This process is repeated several times. However, numerical problems force him to confine the modifications to latitudes north of 40°N and south of 60°S , and to abandon attempts to apply the same technique to the SSS. His approach therefore has a relatively restricted application.

The approach of *Haney* (1971) and *Han* (1984), in which an *apparent surface air temperature* is prescribed instead of an observed SST, also represents a modification

to the prescribed surface tracers. However, this method is dependent upon an observational climatology for the surface heat flux, and therefore introduces a potentially significant source of error. An alternative would be to employ this approach to derive apparent surface tracers such that, when the simulated SST is equal to the prescribed value, the surface heat flux would be equal to the value derived from an atmosphere model spin-up run. This would avoid the need to apply adjustments to the heat flux within the coupled model. However, this approach would also introduce a potential source of error, as the surface fluxes calculated by the atmosphere model will reflect any errors in the model physics, and in the boundary conditions on the stand-alone atmosphere model.

A further alternative is the approach of *Pierce* (1996). Using Fourier analysis, he estimates the errors in the simulated SST that will arise when an ocean model is spun up using the relaxation boundary condition. He then uses these errors to calculate a timeseries of apparent surface air temperatures. This method avoids the dependence of the method of *Haney* (1971) and *Han* (1984) upon an observational climatology for the surface heat flux. While it is successful at reducing the differences between the observed and simulated SST, it is hampered by the assumption that there is no internal transport of heat within the ocean.

3.5 Varying the relaxation timescale

Having considered the ways in which the relaxation boundary condition might be modified, the remainder of this chapter studies the dependence of the simulated ocean climate upon the relaxation timescale. In this section, a simple theoretical model is used to investigate this relationship; in Section 3.6, the response of the Mk3L ocean model is studied.

The dependence of the simulated ocean climate upon the prescribed sea surface temperatures and salinities is studied in Chapter 4.

3.5.1 The response of a slab ocean model

Consider a slab ocean model, being one in which the evolution of the temperature and salinity at each gridpoint is determined solely by the relevant surface flux. Let the prescribed sea surface temperature be $T_{obs}(t)$, where t represents time in days, and let the response of the model be $T_{mod}(t)$. If τ represents the relaxation timescale in days, then the evolution of T_{mod} is determined by the equation

$$\frac{dT_{mod}}{dt} = \frac{1}{\tau}(T_{obs} - T_{mod}) \quad (3.8)$$

Let the model be forced with a sine wave of amplitude s_{obs} , and frequency ω :

$$T_{obs} = a_{obs} \sin \omega t \quad (3.9)$$

Let the equilibrium response of the model also be a sine wave, which exhibits both a phase lag ϕ and an amplification r relative to the forcing:

$$T_{mod} = r a_{obs} \sin(\omega t - \phi) \quad (3.10)$$

Substituting Equations 3.9 and 3.10 into Equation 3.8:

$$ra_{obs}\omega \cos(\omega t - \phi) = \frac{1}{\tau} [a_{obs} \sin \omega t - ra_{obs} \sin(\omega t - \phi)] \quad (3.11)$$

Substituting $\omega t = 0$ into Equation 3.11, and dividing through by $ra_{obs} \cos \phi$:

$$\omega = \frac{1}{\tau} \tan \phi \quad (3.12)$$

A solution is therefore obtained for ϕ :

$$\phi = \tan^{-1} \omega \tau \quad (3.13)$$

Substituting $\omega t = \phi$ into Equation 3.11, and dividing through by $a_{obs}\omega$, a solution is also obtained for r :

$$r = \frac{1}{\omega \tau} \sin \phi \quad (3.14)$$

Let the relaxation timescale be $\tau = 20$ days, being the default timescale employed by the Mk3L ocean model, and let the period of the sine wave be 365 days, corresponding to the annual cycle. Thus $\omega = 2\pi/(365 \text{ days})$, and Equations 3.13 and 3.14 give $\phi \approx 19.0^\circ$ and $r \approx 0.946$ respectively. The response of this simple model is therefore only slightly attenuated relative to the forcing signal, and it experiences a time lag of just 19.3 days (i.e. $19.0^\circ/360^\circ \times 365 \text{ days}$).

The observed annual cycle in the sea surface temperature or salinity will not, in general, be a perfect sine wave. The observed timeseries at any point on the Earth's surface can, however, be expressed as a truncated Fourier series, thus:

$$T_{obs}(t) = a_0 + \sum_{n=1}^N a_n \sin(n\omega t + \phi_n) \quad (3.15)$$

The truncation arises from the finite temporal resolution of any observational timeseries. For a dataset such as the World Ocean Atlas 1998, which contains monthly-mean data, the sampling interval is one month. The Nyquist frequency (e.g. *Wilks*, 1995) is therefore equal to $0.5 \text{ months}^{-1} = 6 \text{ years}^{-1}$, and the upper bound N in Equation 3.15 will be equal to 6.

Equation 3.8 is a linear differential equation, and can therefore be solved separately for each component of the Fourier series. The solutions are found to be

$$\phi_n = \tan^{-1} n\omega \tau \quad (3.16)$$

$$r_n = \frac{1}{n\omega \tau} \sin \phi_n \quad (3.17)$$

These solutions are plotted in Figure 3.8, for values of n from 1 to 6, and for relaxation timescales varying from 5 to 80 days. It can be seen that, as the frequency of the applied signal increases, the response of the model becomes increasingly attenuated, although the time lag also decreases. For a relaxation timescale of 20 days, r decreases from 0.946 to 0.436 as the period of the applied signal is decreased from one year to two months, while the time lag also decreases from 19.3 days to 10.8 days.

A reduction in the relaxation timescale can be seen to improve the response of the model, increasing the amplitude and reducing the time lag.

The World Ocean Atlas 1998 sea surface temperatures and salinities can be analysed within this context. Figure 3.8 shows that the amplitude of the simulated annual cycle is greatest for a sine wave of period one year, but that the same is also true for the phase lag. Hence, as the annual cycle in the observed SST or SSS becomes increasingly dominated by higher-frequency harmonics, the amplitude of the simulated annual cycle will decrease, but so will the phase lag. To investigate this further, a quantity is defined which shall be referred to herein as the *sinusoidality*. This represents the fraction of the total variance which is associated with a period of one year and, in terms of the coefficients defined in Equation 3.15, is given by

$$s = \frac{a_1^2}{\sum_{n=1}^N a_n^2} \quad (3.18)$$

If the annual cycle in the observed sea surface temperature or salinity is a perfect sine wave, then the sinusoidality will be equal to 1. However, as increasing variance becomes associated with higher-frequency harmonics, the sinusoidality will decrease.

Figure 3.9 shows the sinusoidality for the World Ocean Atlas 1998 sea surface temperature and salinity, after interpolation onto the Mk3L ocean model grid. Throughout the sub-tropics and mid-latitudes, the SST has a sinusoidality which exceeds 0.9, indicating that at least 90% of the variance is associated with a sine wave of period one year; only in the tropics and at high latitudes do the higher-frequency harmonics begin to dominate. The area-weighted global-mean sinusoidality is equal to 0.85.

The sea surface salinity, however, exhibits a distinct annual cycle in only very limited regions, mostly in the Northern Hemisphere. The sinusoidality exceeds 0.9 over just 4% of the surface of the ocean, in sharp contrast to the figure of 61% in the case of the SST. The area-weighted global-mean sinusoidality is just 0.47, indicating that the SSS generally exhibits a very indistinct annual cycle.

The equilibrium response of the slab ocean model, when forced with the same World Ocean Atlas 1998 sea surface temperatures and salinities that were used to spin up the Mk3L ocean model, is now investigated. Figure 3.10 shows the values for the relative amplitude and the time lag. The generally sinusoidal nature of the annual cycle in the SST in the sub-tropics, and at mid-latitudes, is reflected in values for the relative amplitude and the time lag which approach the theoretical maximum values, derived above, of 0.946 and 19.3 days respectively. In contrast, the less sinusoidal nature of the annual cycle in the SSS is reflected in much smaller relative amplitudes, and in shorter time lags.

This simple demonstration provides a partial explanation for the response of the Mk3L ocean model to the World Ocean Atlas 1998 sea surface temperatures and salinities (Figures 3.6 and 3.7). Mk3L generally exhibits smaller relative amplitudes, and longer time lags, than the slab ocean model. However, the Mk3L sea surface temperatures exhibit a consistently strong response, and relatively long time lag, throughout the sub-tropics and mid-latitudes. This response can be seen to weaken at high latitudes, while the time lag also decreases. The sea surface salinities exhibit

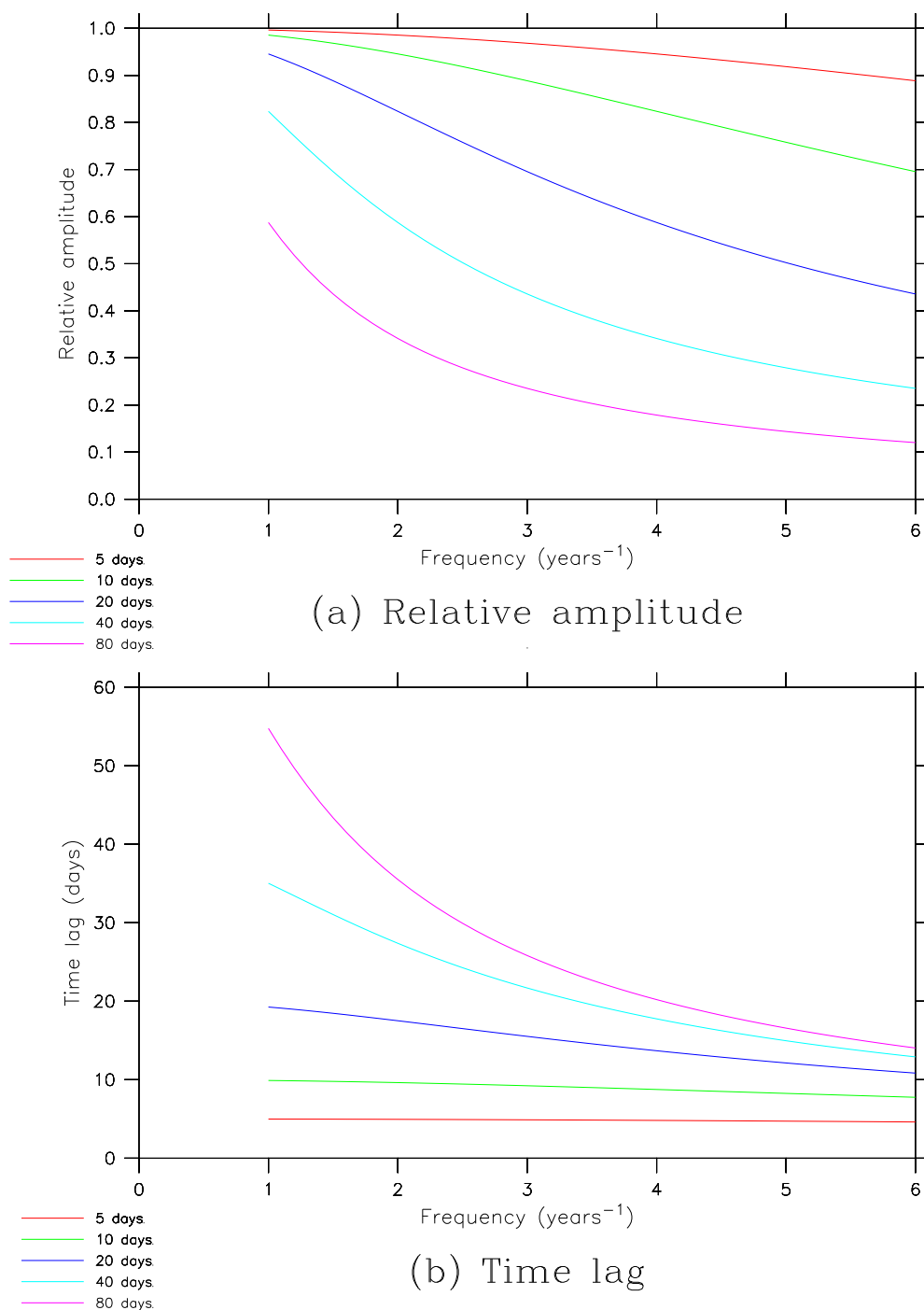
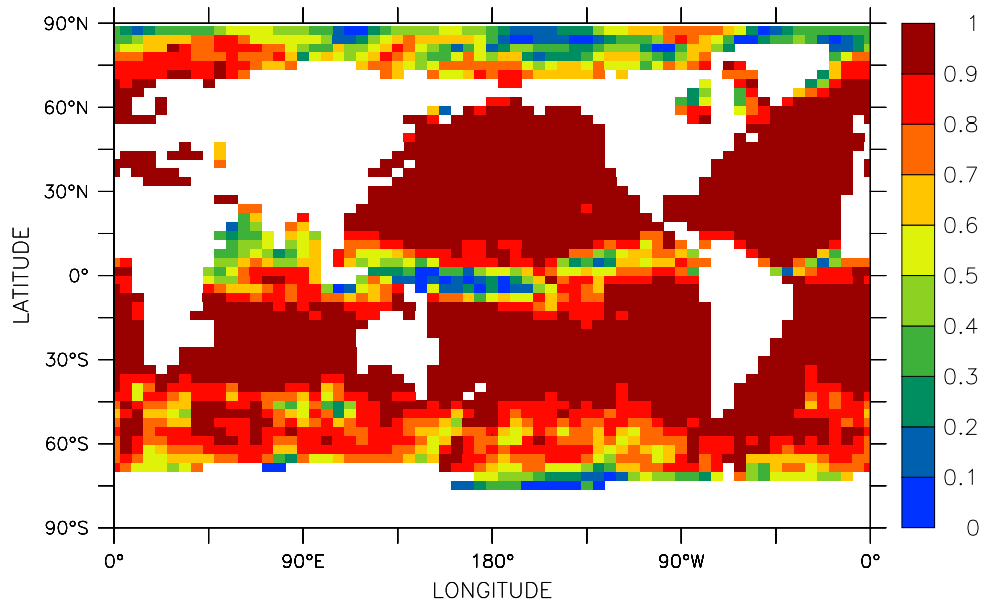
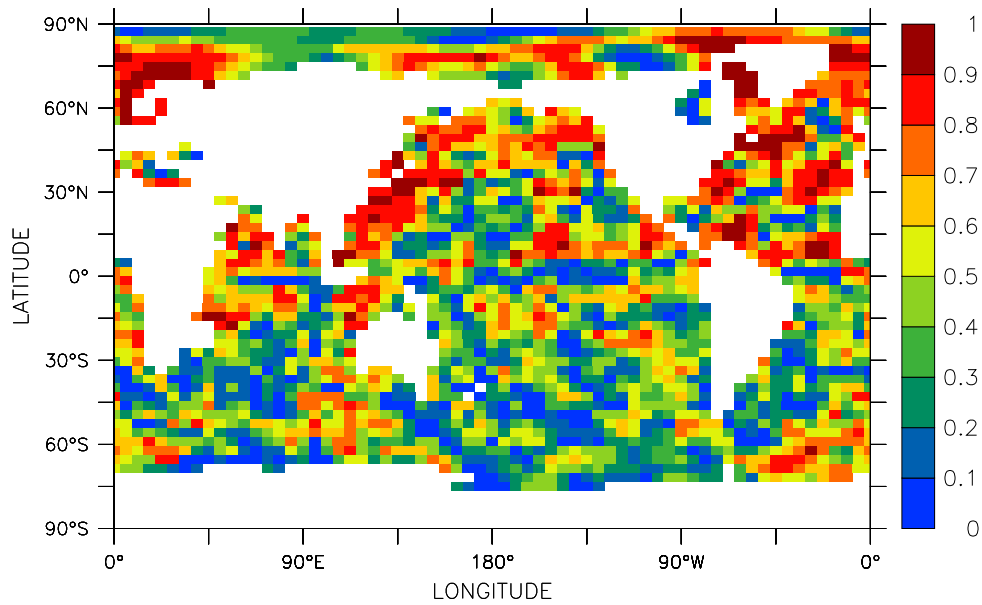


Figure 3.8: The equilibrium response of a slab ocean model to sinusoidal forcing, under the relaxation boundary condition and using relaxation timescales of 5 days (red), 10 days (green), 20 days (dark blue), 40 days (light blue) and 80 days (purple): (a) the relative amplitude, and (b) the time lag.



(a) Sea surface temperature



(b) Sea surface salinity

Figure 3.9: The sinusoidality for the World Ocean Atlas 1998 sea surface temperature and salinity: (a) sea surface temperature, and (b) sea surface salinity. The World Ocean Atlas 1998 data has been area-averaged onto the Mk3L ocean model grid.

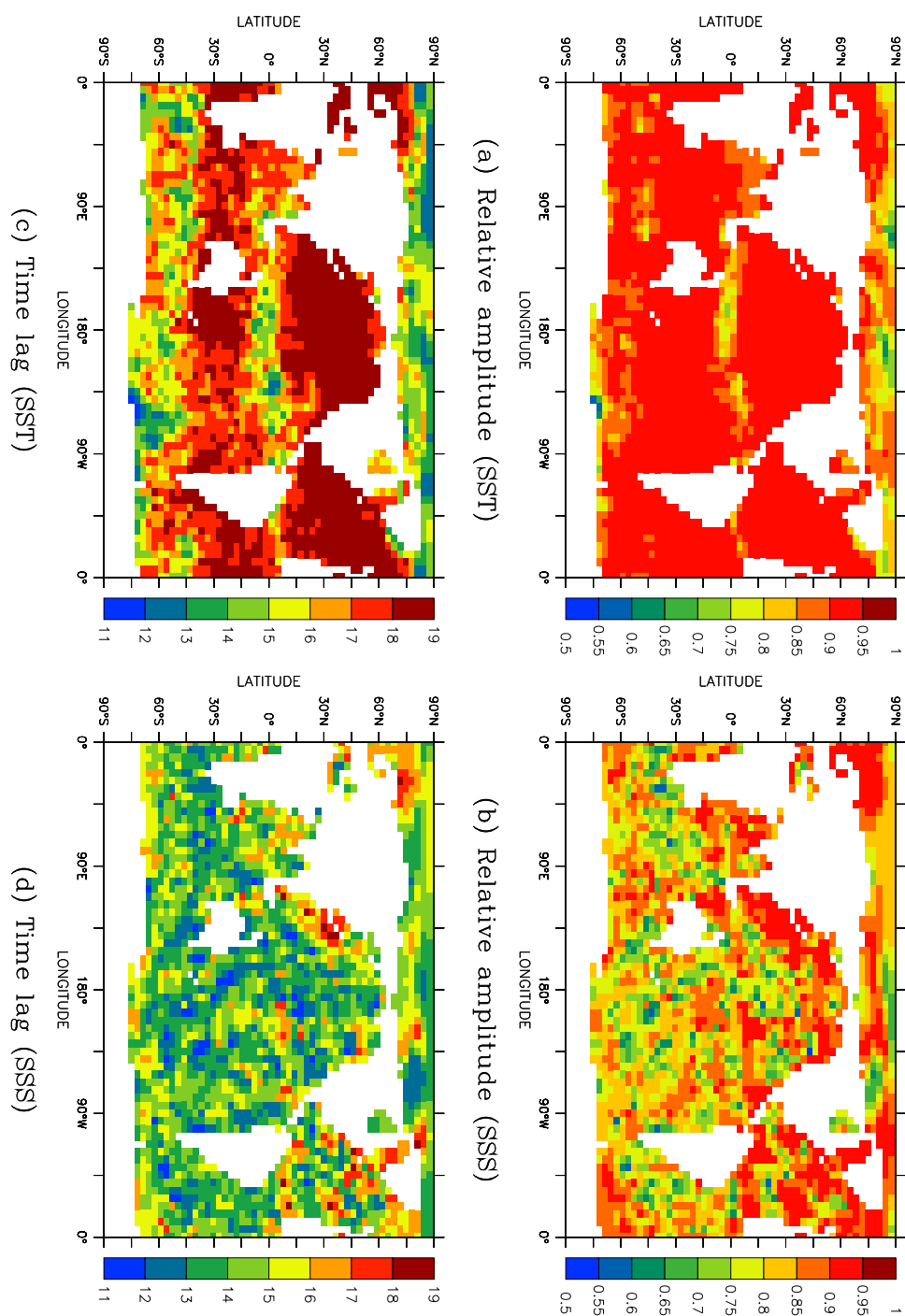


Figure 3.10: The response of a slab ocean model, when forced with the World Ocean Atlas 1998 sea surface temperature (SST) and sea surface salinity (SSS): (a), (b) the relative amplitude, SST and SSS respectively, and (c), (d) the time lag (days), SST and SSS respectively. The World Ocean Atlas 1998 data has been area-averaged onto the Mk3L ocean model grid.

relative amplitudes and time lags that are highly spatially variable, and the lags are generally shorter than for the sea surface temperature.

All these features are consistent with the behaviour of the slab ocean model. Indeed, the only large-scale features of the Mk3L ocean model that are not consistent with the slab ocean model are the strong sea surface temperature response in the tropics, and the fact that the relative amplitudes can exceed 1. Both these discrepancies can be attributed to either lateral or vertical fluxes within the ocean, which the slab ocean model cannot represent.

Surface fluxes

The slab ocean model can also be used to investigate the effect of a change in the relaxation timescale on the magnitude of the surface fluxes. If c_v is the volumetric heat capacity of seawater and Δz the thickness of the slab ocean, then the surface heat flux F is given by

$$F = \frac{d}{dt} (c_v \Delta z T_{mod}) \quad (3.19)$$

Let the model be forced by a prescribed sea surface temperature of amplitude a_{obs} and frequency $n\omega$, and let the equilibrium response of the model be

$$T_{mod} = r_n a_{obs} \sin(n\omega t - \phi_n) \quad (3.20)$$

Substituting Equation 3.20 into Equation 3.19:

$$F = \frac{d}{dt} [c_v \Delta z r_n a_{obs} \sin(n\omega t - \phi_n)] \quad (3.21)$$

$$= c_v \Delta z r_n a_{obs} n \omega \cos(n\omega t - \phi_n) \quad (3.22)$$

Expressing the surface heat flux as

$$F = F_0 \cos(n\omega t - \phi_n) \quad (3.23)$$

the ratio between the amplitude of the surface heat flux, and the amplitude of the prescribed SST, is therefore given by

$$\frac{F_0}{a_{obs}} = c_v \Delta z r_n n \omega \quad (3.24)$$

Let $c_v = 4.1 \times 10^6 \text{ Jm}^{-3}\text{K}^{-1}$ and $\Delta z = 25 \text{ m}$, being the values used within the Mk3L ocean model. Using the values of r_n given by Equation 3.17, the resulting solutions are plotted in Figure 3.11.

For a sine wave of period one year, the amplitude of the surface heat flux is only weakly dependent upon the relaxation timescale, increasing from $12.0 \text{ Wm}^{-2}\text{K}^{-1}$ to $20.3 \text{ Wm}^{-2}\text{K}^{-1}$ as the relaxation timescale is reduced from 80 to 5 days. r_n tends towards 1 as the relaxation timescale is reduced towards zero, and the limiting surface heat flux is therefore given by

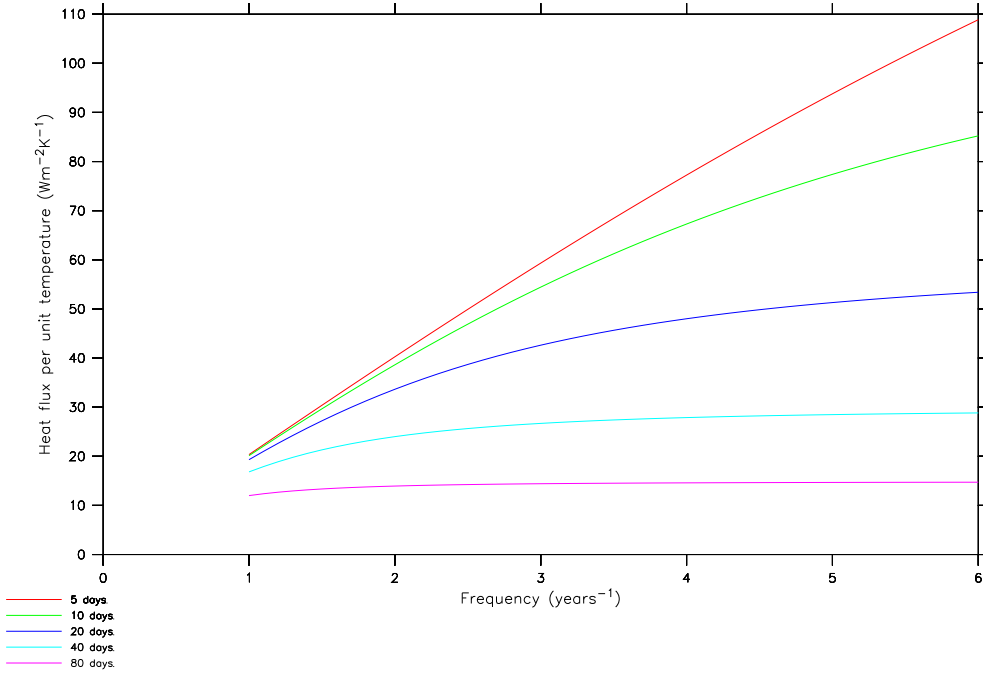


Figure 3.11: The amplitude of the surface heat flux, per unit amplitude of the applied sea surface temperature, for the equilibrium response of a slab ocean model to sinusoidal forcing. The relaxation boundary condition is employed, using relaxation timescales of 5 days (red), 10 days (green), 20 days (dark blue), 40 days (light blue) and 80 days (purple).

$$\lim_{\tau \rightarrow 0} \left(\frac{F_0}{A_{obs}} \right) = c_v \Delta z n \omega \quad (3.25)$$

The limiting flux is equal to $20.4 \text{ Wm}^{-2}\text{K}^{-1}$ for a sine wave of period one year, and $123 \text{ Wm}^{-2}\text{K}^{-1}$ for a sine wave of period two months.

Figure 3.11 suggests that, when an ocean model is forced with observed sea surface temperatures and salinities, the surface freshwater fluxes will be more sensitive to a reduction in the relaxation timescale than the surface heat fluxes. The annual cycle in the observed SST is generally dominated by a sine wave of period one year, in which case the amplitude of the surface heat flux is only weakly dependent upon the relaxation timescale. The annual cycle in the observed SSS is generally dominated by higher-frequency harmonics, however, in which case the dependence upon the relaxation timescale is stronger in the case of the surface freshwater flux.

3.5.2 The response of a mixed-layer ocean

The theoretical model studied in the previous section is very simple. It makes no allowance for fluxes through the lateral walls or base of each gridbox; these fluxes, arising from both diffusion and transport, would also contribute towards

the evolution of the SST and SSS within an ocean general circulation model. In particular, the existence of a homogeneous mixed layer would tend to attenuate the response of the model to external forcing.

However, the theoretical model can readily be extended to make a crude allowance for the presence of a mixed layer within the ocean. If a homogeneous mixed layer exists within the ocean, then it can be assumed that any flux of heat (or freshwater) into the ocean will be instantaneously and uniformly distributed, in the vertical direction, throughout the mixed layer. If the thickness of the mixed layer is $\alpha\Delta z$, where Δz is the thickness of the upper layer of the model and α is greater than or equal to 1, then Equation 3.8 becomes

$$\frac{dT_{mod}}{dt} = \frac{1}{\alpha\tau}(T_{obs} - T_{mod}) \quad (3.26)$$

The only difference between Equations 3.8 and 3.26 is that the relaxation timescale τ has been replaced with $\alpha\tau$. The solutions to Equation 3.26 are therefore given by the solutions to Equation 3.8, with the relaxation timescale replaced with an *effective* relaxation timescale $\tau^* = \alpha\tau$. The surface heat flux is also larger by a factor α , reflecting the increased heat capacity of the mixed-layer ocean relative to that of the upper layer of the model. The solutions to Equation 3.26 are therefore:

$$\phi = \tan^{-1} \alpha\omega\tau \quad (3.27)$$

$$r = \frac{1}{\alpha\omega\tau} \sin \phi \quad (3.28)$$

$$\frac{F_0}{a_{obs}} = c_v \Delta z r \alpha \omega \quad (3.29)$$

The solutions for forcing by a sine wave of period one year are plotted in Figure 3.12, for values of α from 1 to 100, and for relaxation timescales ranging from 5 to 80 days. As the depth of the mixed-layer ocean is increased, the amplitude of the model response decreases, while the time lag and surface heat flux increase. The limiting solutions as α tends towards infinity are as follows:

$$\lim_{\alpha \rightarrow \infty} \phi = 90^\circ (= 91.25 \text{ days}) \quad (3.30)$$

$$\lim_{\alpha \rightarrow \infty} r = 0 \quad (3.31)$$

$$\lim_{\alpha \rightarrow \infty} \left(\frac{F_0}{a_{obs}} \right) = \frac{c_v \Delta z}{\tau} \quad (3.32)$$

3.5.3 Summary

These investigations into the response of a simple theoretical model provide insight into the response that might be expected from an ocean general circulation model:

- Decreasing the relaxation timescale *increases* the amplitude of the model response, *reduces* the time lag, and *increases* the magnitude of the surface fluxes.

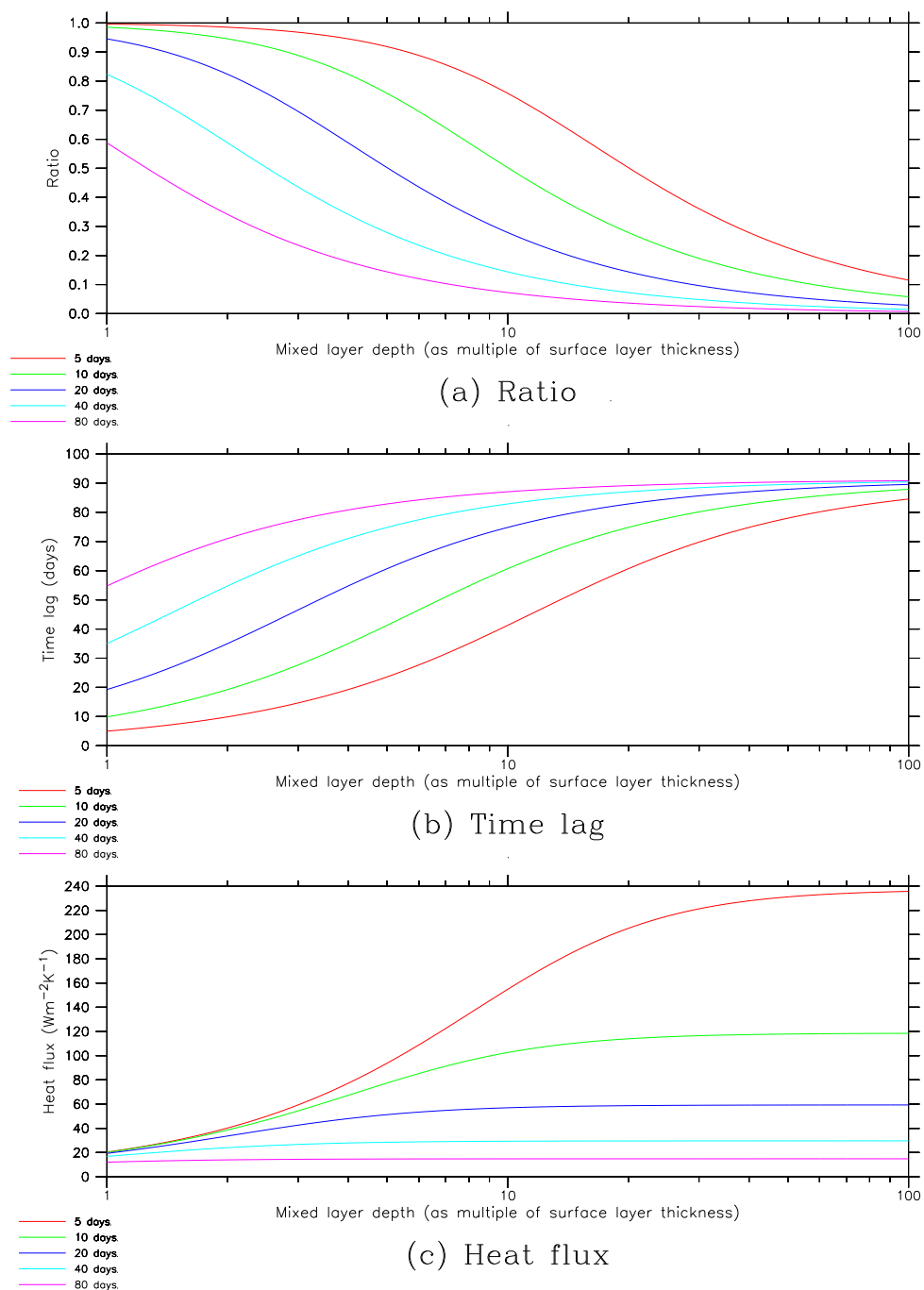


Figure 3.12: The equilibrium response of a mixed-layer ocean model to forcing by a sine wave of period one year, as a function of the relaxation timescale and of the depth of the mixed layer. The relaxation timescales are 5 days (red), 10 days (green), 20 days (dark blue), 40 days (light blue) and 80 days (purple). (a) The ratio between the amplitude of the model response and the amplitude of the forcing, (b) the time lag between the forcing and the model response, and (c) the amplitude of the surface heat flux, per unit amplitude of the forcing.

Run	Relaxation timescale (days)	Duration (years)	
		Asynchronous timestepping	Synchronous timestepping
O-5d	5	4000	500
O-7.5d	7.5	3000	500
O-10d	10	3000	500
O-15d	15	4000	500
O-DEF	20	4000	500
O-30d	30	5000	500
O-40d	40	5000	500
O-60d	60	5000	500
O-80d	80	6000	500

Table 3.3: A summary of the Mk3L ocean model spin-up runs in which the relaxation timescale was varied.

- Increasing the frequency of the forcing signal *reduces* the amplitude of the model response, *reduces* the time lag, and *increases* the magnitude of the surface fluxes.
- An increase in the depth of the mixed layer *reduces* the amplitude of the model response, *increases* the time lag, and *increases* the magnitude of the surface fluxes.

3.6 The response of the Mk3L ocean model

A series of spin-up runs was conducted using the Mk3L ocean model. These runs are summarised in Table 3.3; they are identical to run O-DEF (Section 2.3.2), with the exception that the relaxation timescale was varied from 5 to 80 days. Each run was integrated under asynchronous timestepping until the convergence criteria were satisfied (i.e. that the rates of change in global-mean potential temperature and salinity, on each model level, were less than $0.005^{\circ}\text{C}/\text{century}$ and $0.001\text{ psu}/\text{century}$ respectively). A further 500 years of integration was then conducted under synchronous timestepping, by which time the convergence criteria were once again satisfied.

The dependence of the simulated ocean climate upon the relaxation timescale is assessed in the following sections.

3.6.1 Annual-mean errors

The root-mean-square (RMS) errors in the annual-mean sea surface temperature and salinity, relative to the World Ocean Atlas 1998, are plotted in Figure 3.13 as a function of the relaxation timescale. Let the error in the sea surface temperature (or salinity) be defined as $\Delta T = T_{mod} - T_{obs}$, where T_{mod} and T_{obs} are the simulated and observed sea surface temperature (or salinity) respectively. If the error at each gridpoint is $\Delta T_{i,j}$, and the area of the gridbox centred on that gridpoint is $A_{i,j}$, then the RMS error ΔT_{rms} is given by

$$\Delta T_{rms} = \frac{\left[\sum_i \sum_j A_{i,j}^2 \Delta T_{i,j}^2 \right]^{1/2}}{\sum_i \sum_j A_{i,j}} \quad (3.33)$$

The errors can be seen to be very sensitive to the relaxation timescale. The RMS error in the annual-mean SST increases from 0.17°C to 1.53°C as the relaxation timescale is increased from 5 to 80 days, while that in the annual-mean SSS increases from 0.024 psu to 0.224 psu.

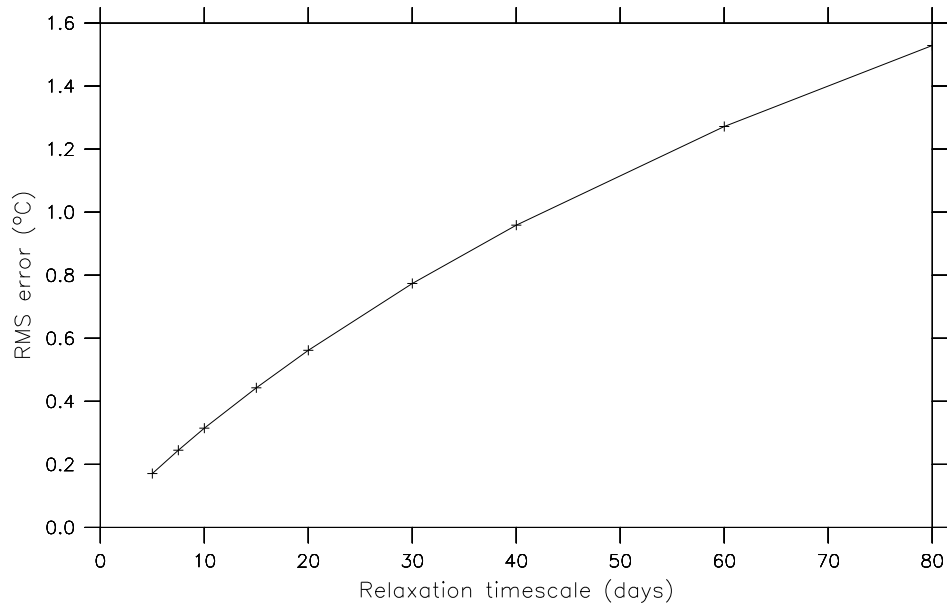
3.6.2 Relative amplitudes and time lags

The global-mean relative amplitude and time lag, for both the sea surface temperature and salinity, are plotted in Figure 3.14 as a function of the relaxation timescale. The area-weighted global means are shown; if the relative amplitude (or time lag) at each gridpoint is $r_{i,j}$, and if the area of the gridbox centred on that gridpoint is $A_{i,j}$, then the area-weighted global-mean relative amplitude (or time lag) \bar{r} is given by

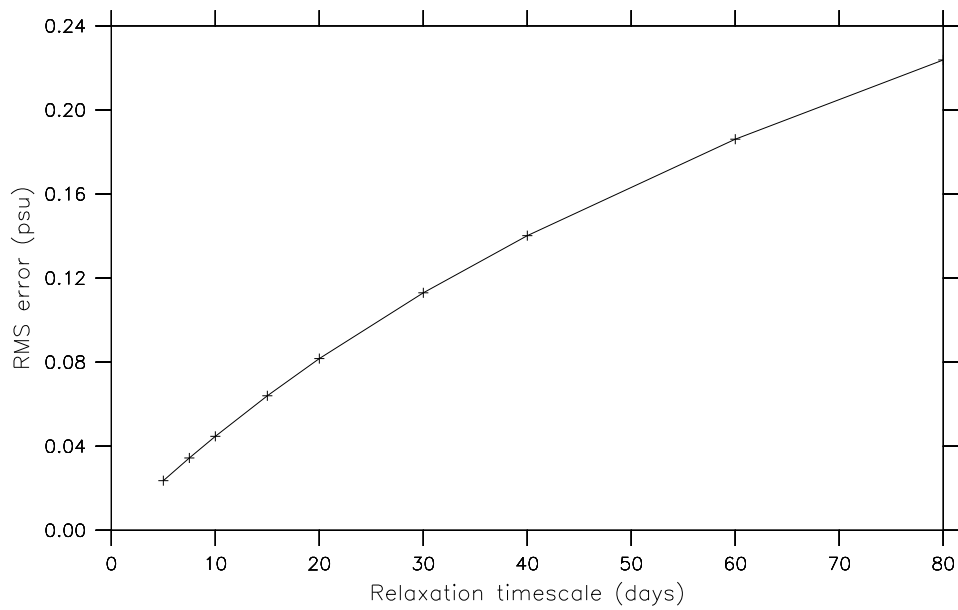
$$\bar{r} = \frac{\sum_i \sum_j A_{i,j} r_{i,j}}{\sum_i \sum_j A_{i,j}} \quad (3.34)$$

Consistent with the response of the simple theoretical model (Sections 3.5.1 and 3.5.2), the amplitude of the model response decreases as the relaxation timescale is increased, while the time lag decreases. In the case of the SST, the global-mean relative amplitude decreases from 0.836 to 0.239 as the relaxation timescale is increased from 5 to 80 days, while the global-mean time lag increases from 10.7 to 49.1 days. Similar behaviour is exhibited in the case of the SSS, with a decrease in the global-mean relative amplitude from 0.746 to 0.258, and an increase in the global-mean time lag from 6.4 to 37.3 days.

The response of the Mk3L ocean model is weaker than that of the slab ocean model to the same forcing, while the time lags are longer. This can be attributed, in part, to the presence of a mixed layer within the ocean; the response of the theoretical model was reduced, and the time lags were increased, when this was taken into account. The amplitude of the simulated SST is slightly more sensitive to the relaxation timescale than that of the simulated SSS; this may indicate the presence of feedback mechanisms within the model, whereby changes in the oceanic circulation, arising from changes in the surface forcing, affect the response of the model. The time lags are greater in the case of the SST than the SSS; this is consistent with the response of the slab ocean model, and can be attributed to the more sinusoidal nature of the observed annual cycle in the SST.

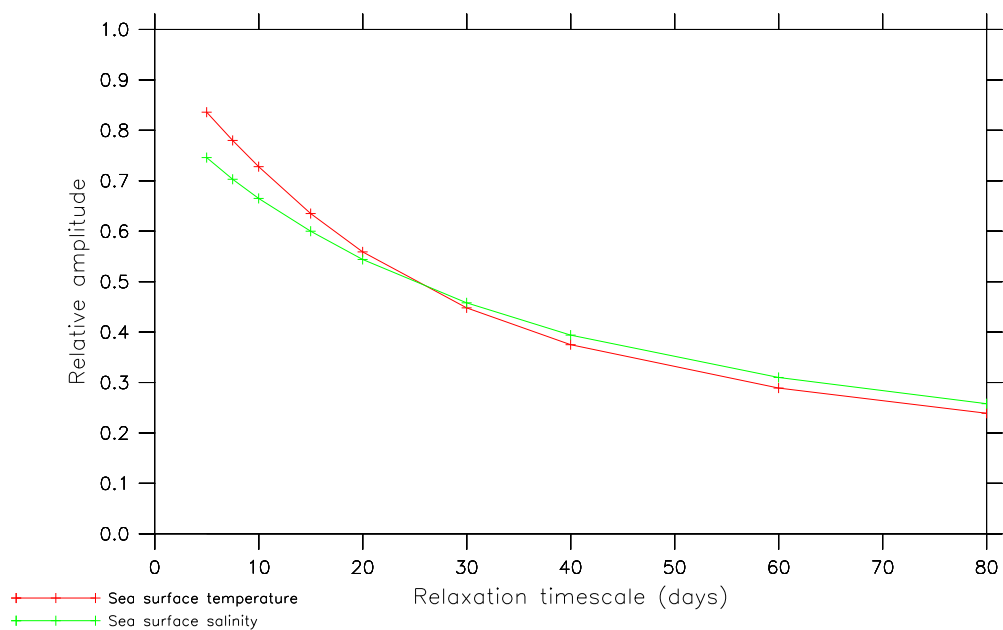


(a) Sea surface temperature

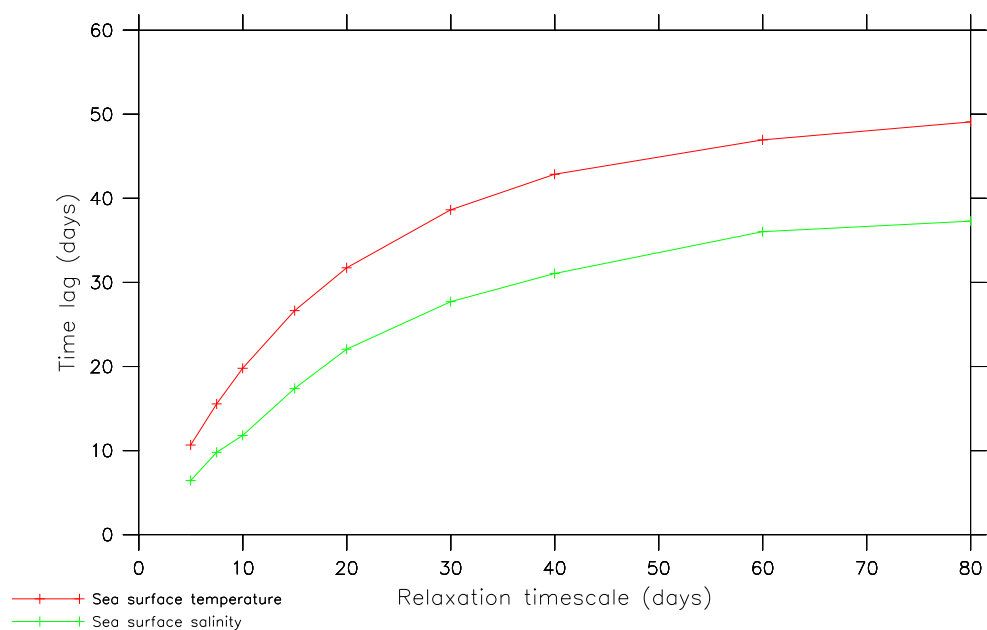


(b) Sea surface salinity

Figure 3.13: The root-mean-square error in the annual-mean sea surface temperature and salinity for the Mk3L ocean model (averages for the final 100 years of runs O-5d, O-7.5d, O-10d, O-15d, O-DEF, O-30d, O-40d, O-60d and O-80d), relative to the World Ocean Atlas 1998: (a) sea surface temperature, and (b) sea surface salinity.



(a) Relative amplitude



(b) Time lag

Figure 3.14: The annual cycle in sea surface temperature (red) and sea surface salinity (green) for the Mk3L ocean model (averages for the final 100 years of runs O-5d, O-7.5d, O-10d, O-15d, O-DEF, O-30d, O-40d, O-60d and O-80d), relative to the World Ocean Atlas 1998: (a) the area-weighted global-mean relative amplitude, and (b) the area-weighted global-mean time lag.

3.6.3 Densities of high-latitude surface waters

Figure 3.15 shows the peak surface water density, as a function of the relaxation timescale, for each of the three deep water formation regions which were studied in Section 3.3. The peak densities at each gridpoint, for runs O-5d, O-10d, O-40d and O-80d, are also shown in Figures 3.16 and 3.17, for the Antarctic and Arctic respectively. (Values for run O-DEF are shown in Figure 3.1.)

The peak densities are highly sensitive to the relaxation timescale. However, even when the timescale is reduced to 5 days, the surface waters remain too buoyant. The peak surface densities in this case are 27.90, 27.81 and 27.88 kgm^{-3} , for the southwestern Ross Sea, western Weddell Sea and Nordic Seas respectively. These densities represent light biases, relative to the World Ocean Atlas 1998, of 0.16, 0.15 and 0.08 kgm^{-3} respectively. While these figures represent a considerable improvement on the biases of $\sim 0.25\text{--}0.3 \text{ kgm}^{-3}$ encountered in the case of run O-DEF (Section 3.3), the peak high-latitude surface water densities remain inadequate.

3.6.4 Water properties

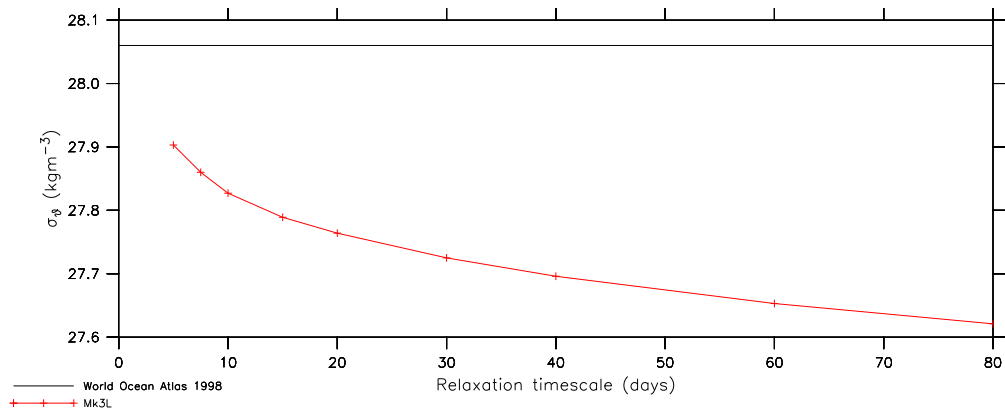
Vertical profiles of potential temperature, salinity and potential density are shown in Figure 3.18, for the World Ocean Atlas 1998 and for Mk3L ocean model runs O-5d, O-10d, O-DEF, O-40d and O-80d. As a result of the increased peak densities of the high-latitude surface waters, the density of the deep ocean increases as the relaxation timescale is reduced. This is achieved through an increase in the salinity of the deep ocean, with the relaxation timescale having little impact upon the temperature profile.

These trends are confirmed by Figure 3.19, which shows the mean potential temperature, salinity and potential density for the deep ocean (2350–4600 m, as defined in Chapter 2), as a function of the relaxation timescale. While the most realistic deep ocean salinity and density are achieved when the relaxation timescale is reduced to 5 days, it remains too fresh by 0.13 psu, and too buoyant by 0.04 kgm^{-3} . The deep ocean temperature is only weakly dependent upon the relaxation timescale, being consistently too cold by $\sim 1^\circ\text{C}$.

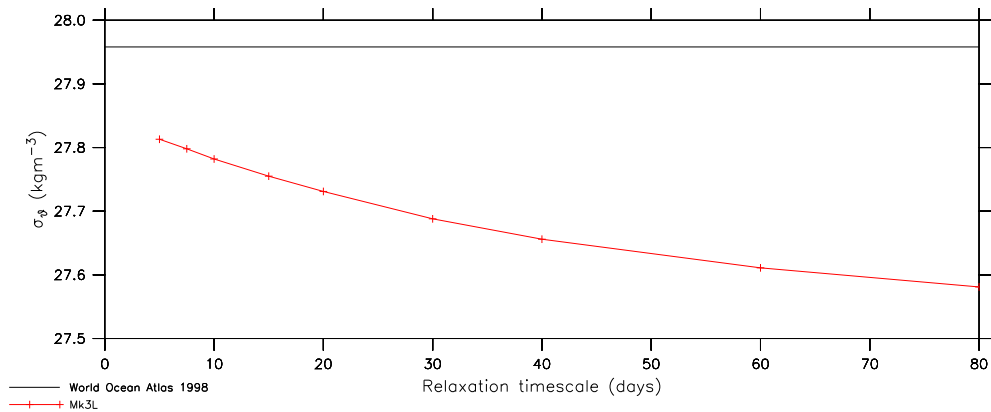
3.6.5 Circulation

The rates of North Atlantic Deep Water (NADW) and Antarctic Bottom Water (AABW) formation are plotted in Figure 3.20 as a function of the relaxation timescale.

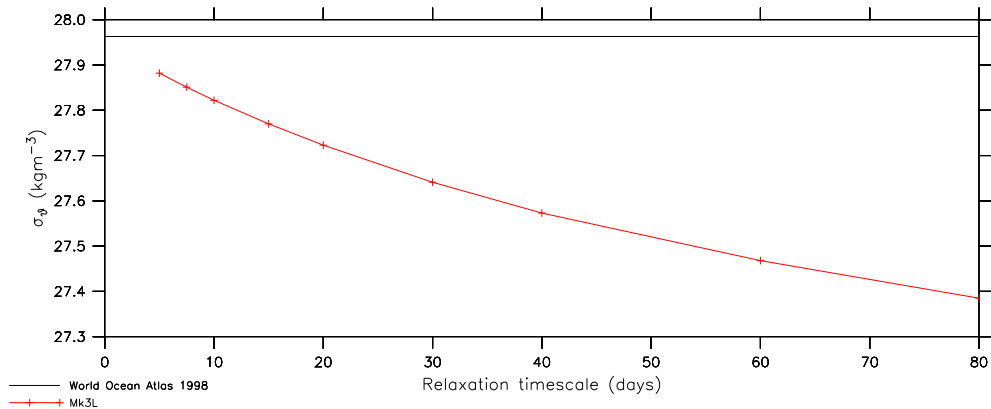
The rate of NADW formation declines as the relaxation timescale is increased, decreasing from 16.1 to 10.5 Sv as the timescale is increased from 5 to 80 days. This behaviour can be attributed to the strong dependence of the peak surface water density in the Nordic Seas upon the relaxation timescale (Figure 3.15); the peak density decreases by 0.49 kgm^{-3} , from 27.88 to 27.39 kgm^{-3} , as the timescale is increased from 5 to 80 days. In contrast, the density of the deep ocean decreases by just 0.29 kgm^{-3} , from 27.76 to 27.47 kgm^{-3} . The water column in the North Atlantic therefore becomes increasingly stratified, and the rate of NADW formation declines.



(a) Ross Sea



(b) Weddell Sea



(c) Nordic Seas

Figure 3.15: The annual-maximum surface σ_θ (kgm^{-3}) for the World Ocean Atlas 1998 (black), and the Mk3L ocean model (red, averages for the final 100 years of runs O-5d, O-7.5d, O-10d, O-15d, O-DEF, O-30d, O-40d, O-60d and O-80d): (a) the southwestern Ross Sea, (b) the western Weddell Sea, and (c) the Nordic (Greenland-Iceland-Norwegian) Seas. The World Ocean Atlas 1998 data has been area-averaged onto the Mk3L ocean model grid.

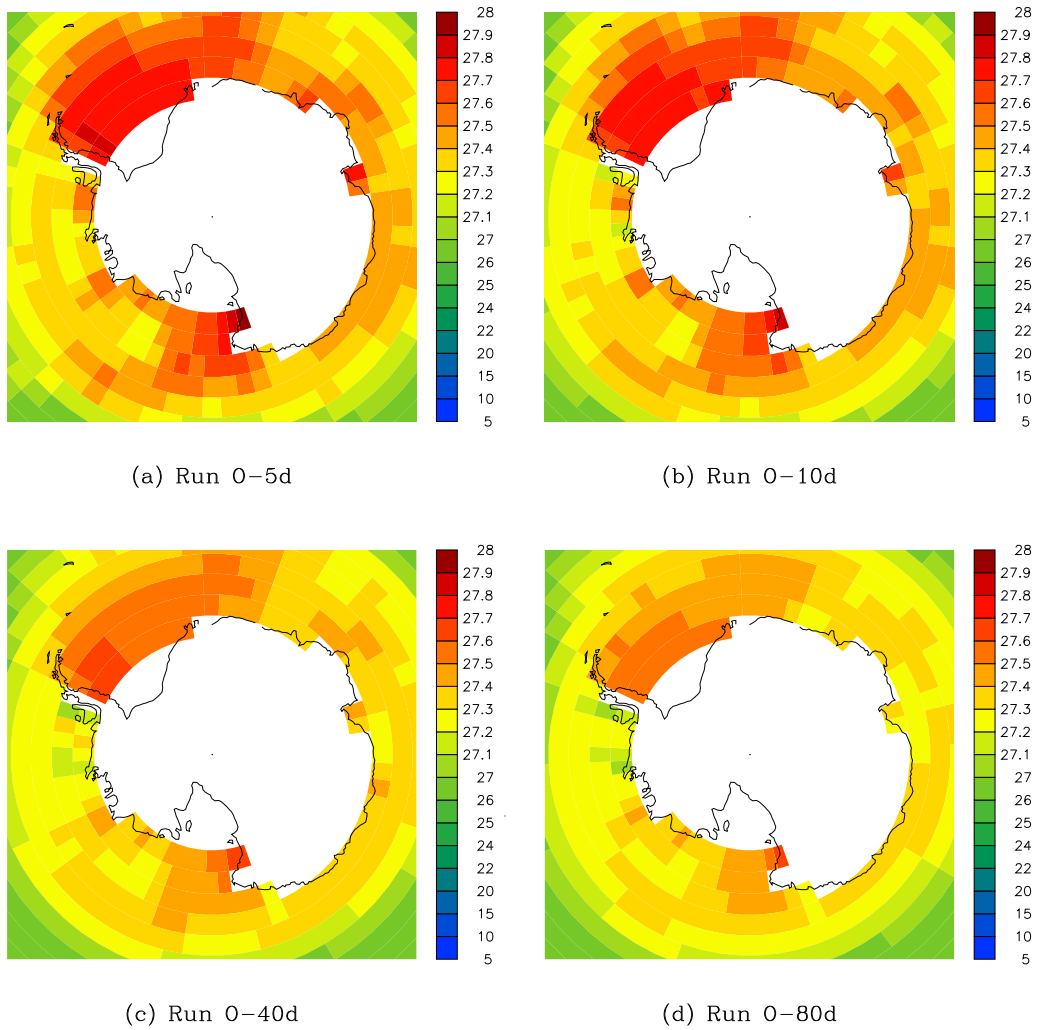


Figure 3.16: The annual-maximum surface σ_θ (kgm^{-3}) for the Mk3L ocean model (averages for the final 100 years of each run): (a) run O-5d, (b) run O-10d, (c) run O-40d, and (d) run O-80d.

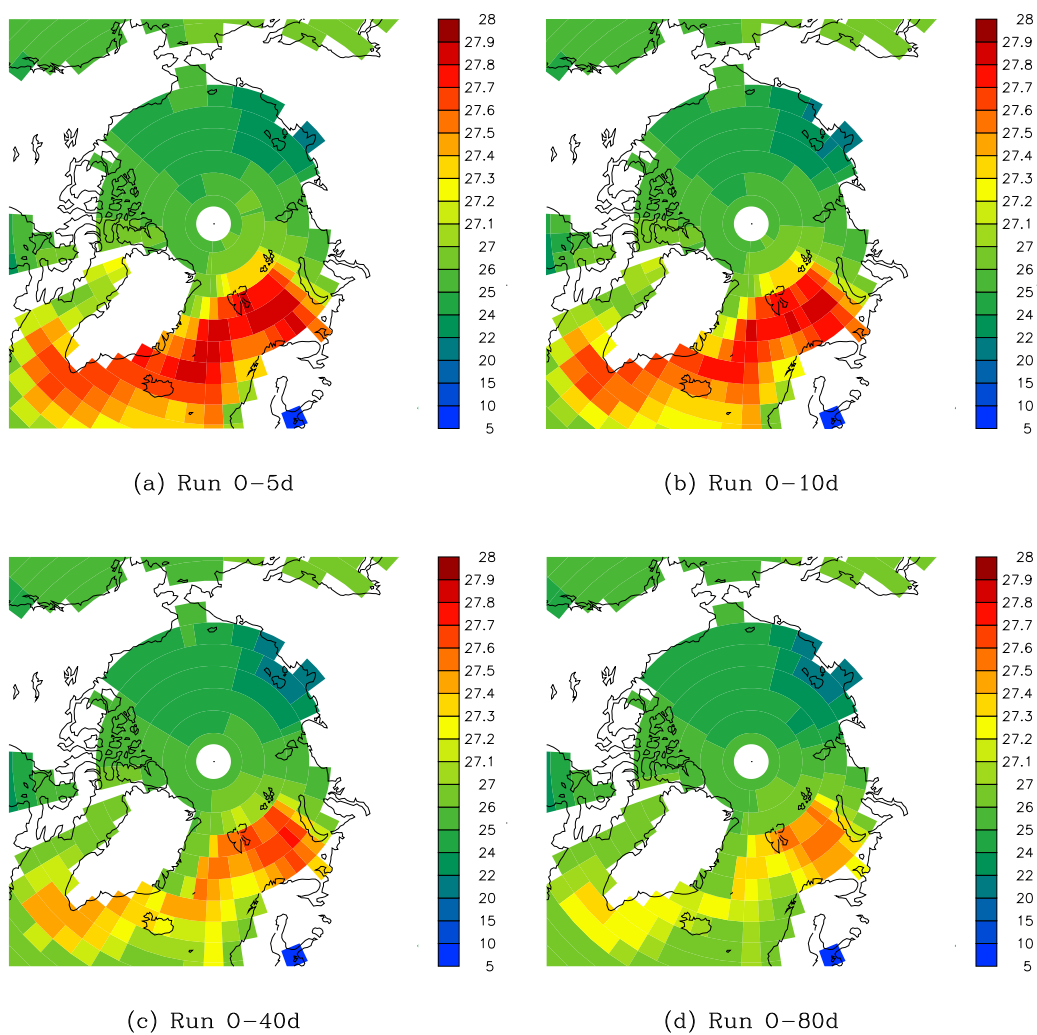


Figure 3.17: The annual-maximum surface σ_θ (kgm^{-3}) for the Mk3L ocean model (averages for the final 100 years of each run): (a) run O-5d, (b) run O-10d, (c) run O-40d, and (d) run O-80d.

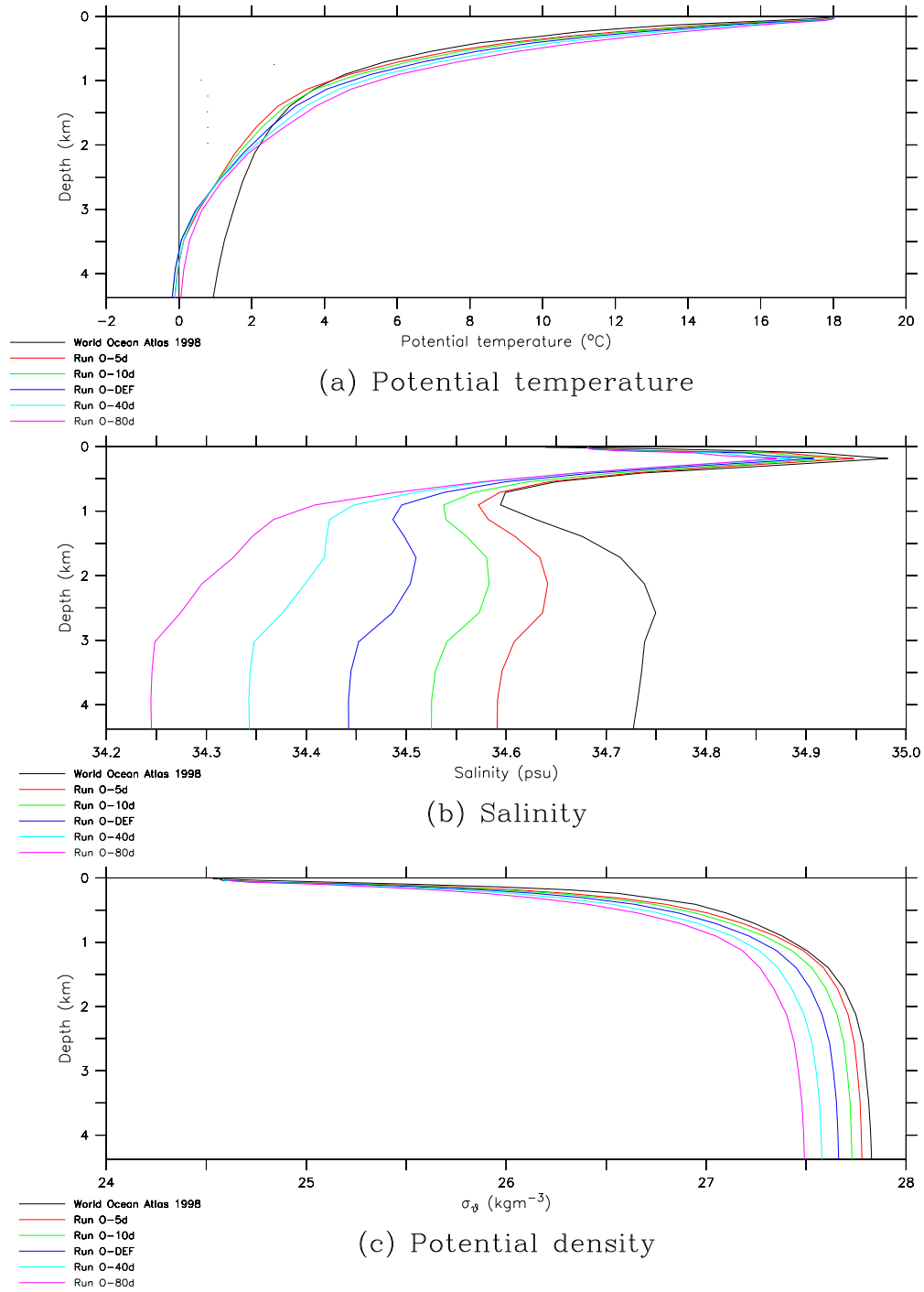
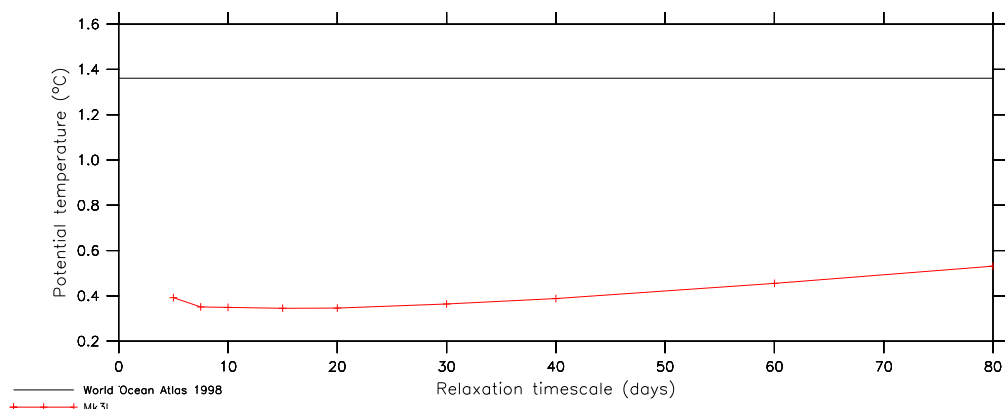
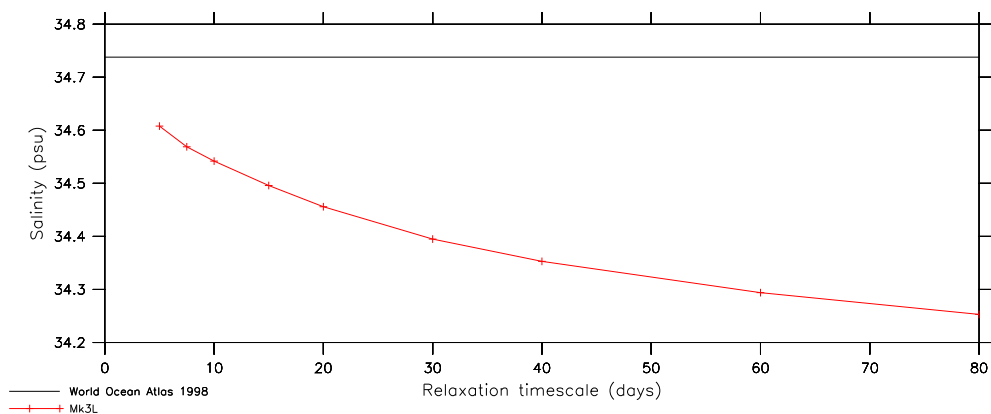


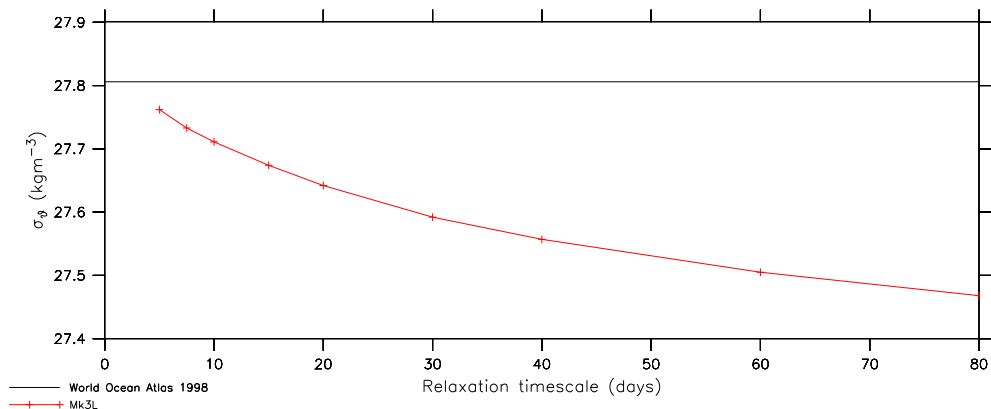
Figure 3.18: The global-mean potential temperature, salinity and σ_θ on each model level for the World Ocean Atlas 1998 (black), and for Mk3L ocean model runs O-5d (red), O-10d (green), O-DEF (dark blue), O-40d (light blue) and O-80d (purple): (a) potential temperature, (b) salinity, and (c) σ_θ . The World Ocean Atlas 1998 data has been volume-averaged onto the Mk3L ocean model grid. All values for Mk3L are averages for the final 100 years of each run.



(a) Potential temperature



(b) Salinity



(c) Potential density

Figure 3.19: The mean potential temperature, salinity and σ_θ for the deep ocean (2350–4600 m), for the World Ocean Atlas 1998 (black), and for the Mk3L ocean model (red, averages for the final 100 years of runs O-5d, O-7.5d, O-10d, O-15d, O-DEF, O-30d, O-40d, O-60d and O-80d): (a) potential temperature, (b) salinity, and (c) σ_θ . The World Ocean Atlas 1998 data has been volume-averaged onto the Mk3L ocean model grid.

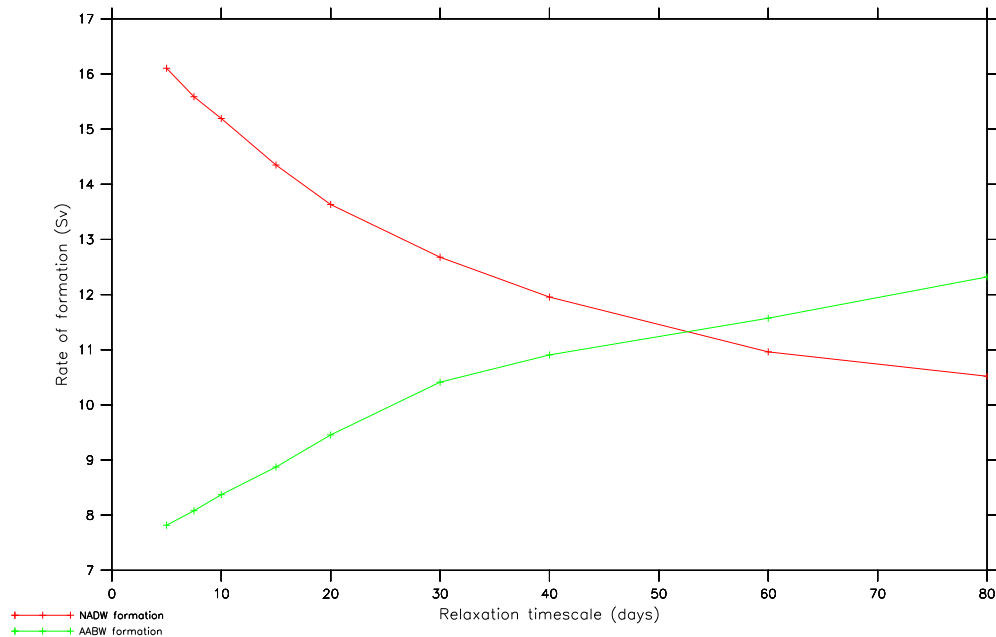
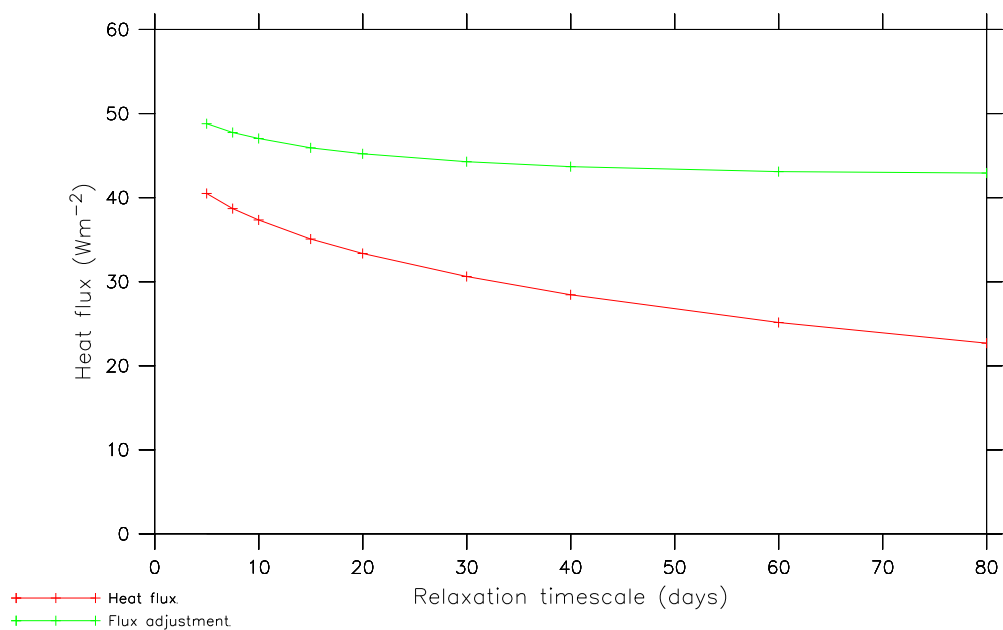


Figure 3.20: The rates of North Atlantic Deep Water formation (red) and Antarctic Bottom Water formation (green) for the Mk3L ocean model (averages for the final 100 years of runs O-5d, O-7.5d, O-10d, O-15d, O-DEF, O-30d, O-40d, O-60d and O-80d).

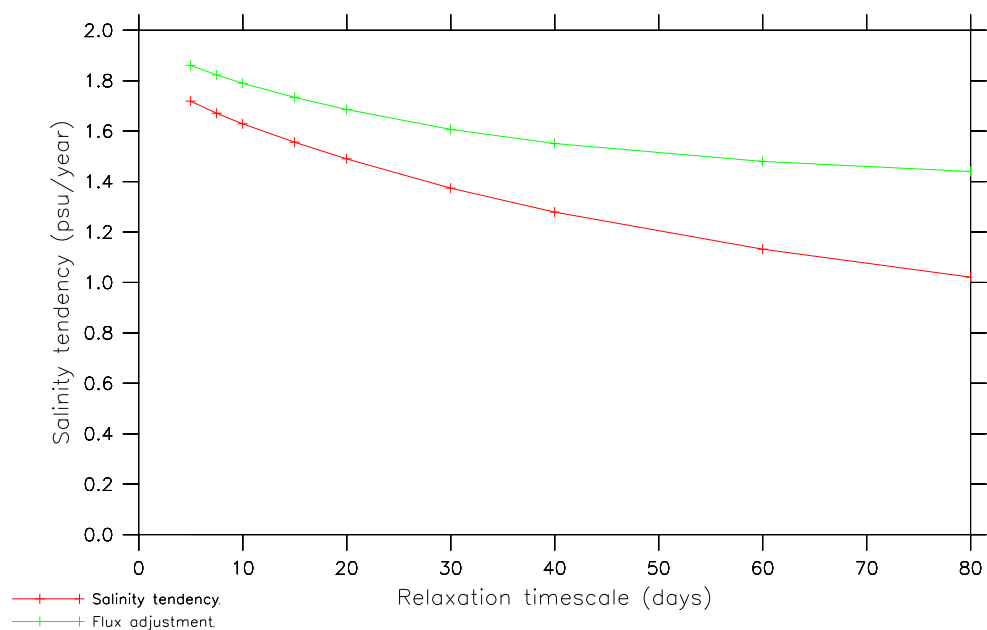
The rate of AABW formation *increases*, however, from 7.8 to 12.3 Sv; this can also be attributed to changes in the stratification of the water column. The peak surface water densities in the Ross and Weddell Seas decrease by 0.28 and 0.23 kgm^{-3} , respectively, as the timescale is increased from 5 to 80 days. These decreases are smaller than the reduction of 0.29 kgm^{-3} in the density of the deep ocean, and the water column in the Southern Ocean therefore becomes decreasingly stratified. As a result, the rate of AABW formation increases.

3.6.6 Annual-mean surface fluxes

The root-mean-square annual-mean surface fluxes for the Mk3L ocean model are plotted in Figure 3.21, along with the root-mean-square annual-mean flux adjustments diagnosed for use within the coupled model. The flux adjustments are derived by subtracting the surface fluxes diagnosed from atmosphere model spin-up run A-DEF (Section 2.3.1) from the surface fluxes diagnosed from each ocean model spin-up run. Theoretically, a separate atmosphere model spin-up run should be conducted for each ocean model spin-up run, because of the dependence of the sea ice component of the atmosphere model upon the ocean model surface currents. However, for the purposes of the present comparison, it is considered sufficient to use the surface fluxes diagnosed from atmosphere model run A-DEF.



(a) Surface heat flux



(b) Surface salinity tendency

Figure 3.21: The root-mean-square annual-mean surface fluxes for the Mk3L ocean model (red, averages for the final 100 years of runs O-5d, O-7.5d, O-10d, O-15d, O-DEF, O-30d, O-40d, O-60d and O-80d), and the root-mean-square annual-mean flux adjustments diagnosed for the coupled model (green): (a) the surface heat flux, and (b) the surface salinity tendency.

The annual-mean surface fluxes exhibit only a limited dependence upon the relaxation timescale. While this might seem surprising, it should be borne in mind that non-zero annual-mean surface fluxes only arise as a result of the ocean circulation, and as a result of diffusive processes within the ocean. Without these processes, there would be no net fluxes of heat or salt through either the lateral walls or the bases of the surface gridboxes, and the annual-mean surface fluxes would be equal to zero. In the previous section, the ocean circulation was shown to exhibit only a limited dependence upon the relaxation timescale; the dependence of the annual-mean surface fluxes upon the relaxation timescale is therefore similarly limited.

The annual-mean flux adjustments are even more weakly dependent upon the relaxation timescale. This arises because the flux adjustments depend upon the surface fluxes simulated by *both* the ocean model *and* the atmosphere model. As the relaxation timescale is increased, the magnitude of the ocean model fluxes decreases, and the atmosphere model surface fluxes become increasingly dominant in determining the magnitude of the flux adjustments. The flux adjustments therefore become increasingly independent of the relaxation timescale.

The annual-mean surface heat flux and salinity tendency adjustments, diagnosed from runs O-5d, O-10d, O-40d and O-80d, are shown in Figures 3.22 and 3.23 respectively; those diagnosed from run O-DEF are shown in Figures 2.21 and 2.22. While the magnitude of the annual-mean flux adjustments exhibits a weak dependence upon the relaxation timescale, the spatial structure remains unchanged. This indicates that the need for flux adjustments arises from inconsistencies between the oceanic transports of heat and salt, as simulated by the ocean model and as implied by the atmosphere model. The flux adjustments therefore represent deficiencies in the model physics, rather than arising as a result of stochastic variability in the simulated surface fluxes.

3.6.7 Amplitudes of surface fluxes

The area-weighted global-mean amplitudes of the annual cycles in the simulated surface fluxes are plotted in Figure 3.24, along with the area-weighted global-mean amplitudes of the annual cycles in the flux adjustments diagnosed for the coupled model. If F_n and \bar{F} are the monthly-mean and annual-mean surface flux (or flux adjustment) respectively, then the amplitude of the annual cycle is given by Equation 3.6, i.e.

$$a = \left[\frac{1}{12} \sum_{n=1}^{12} (F_n - \bar{F})^2 \right]^{1/2} \quad (3.35)$$

If the amplitude of the annual cycle at each gridpoint is $a_{i,j}$, and the area of the gridbox centred on that gridpoint is $A_{i,j}$, then the area-weighted global-mean amplitude is given by Equation 3.34, i.e.

$$\bar{a} = \frac{\sum_i \sum_j A_{i,j} a_{i,j}}{\sum_i \sum_j A_{i,j}} \quad (3.36)$$

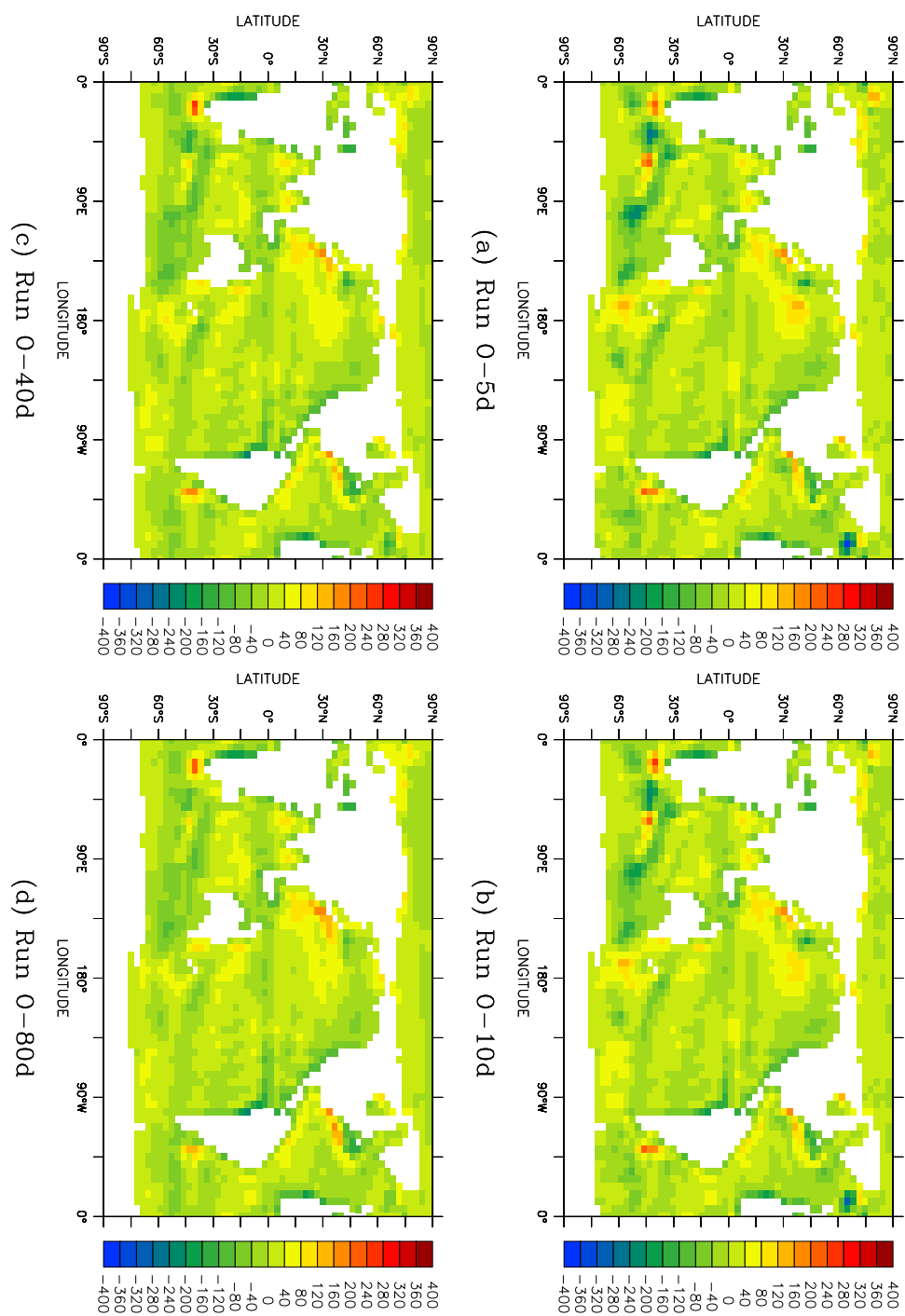


Figure 3.22: The annual-mean surface heat flux adjustment (Wm^{-2}) diagnosed from the Mk3L ocean model (averages for the final 100 years of each run): (a) run O-5d, (b) run O-10d, (c) run O-40d, and (d) run O-80d. The atmosphere model surface fluxes are derived from the final 40 years of run A-DEF.

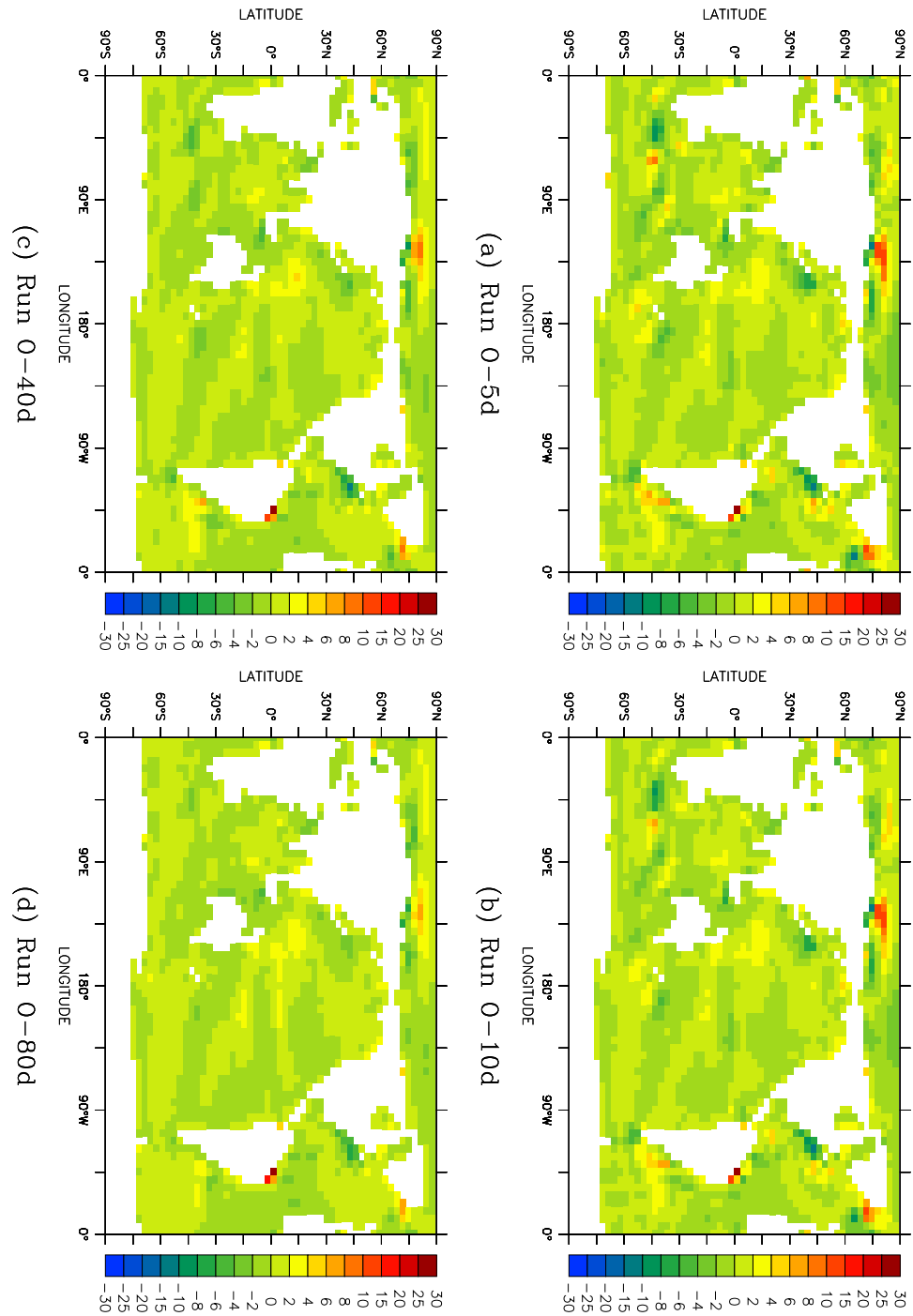
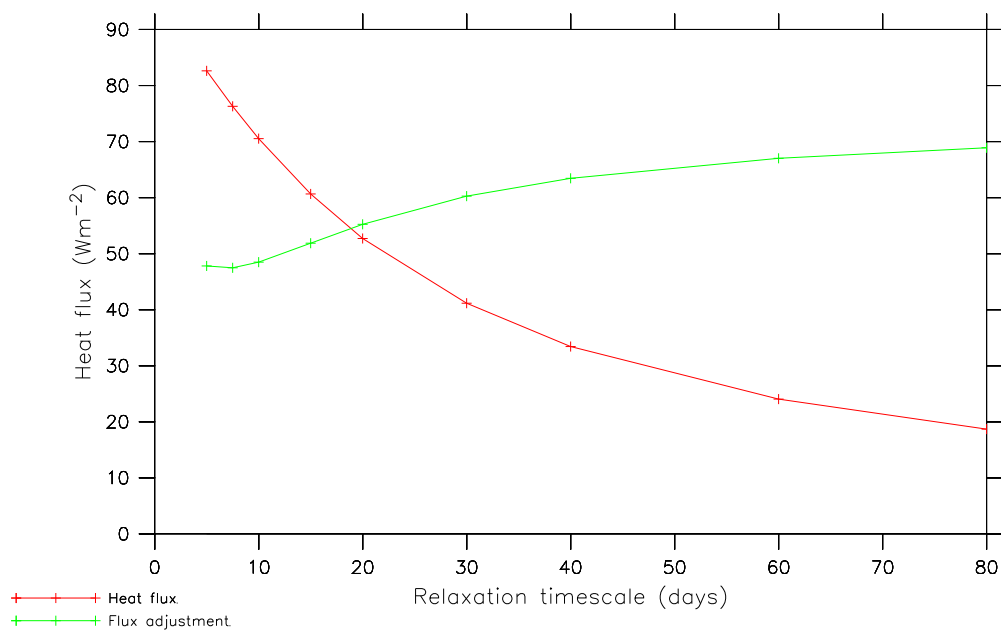
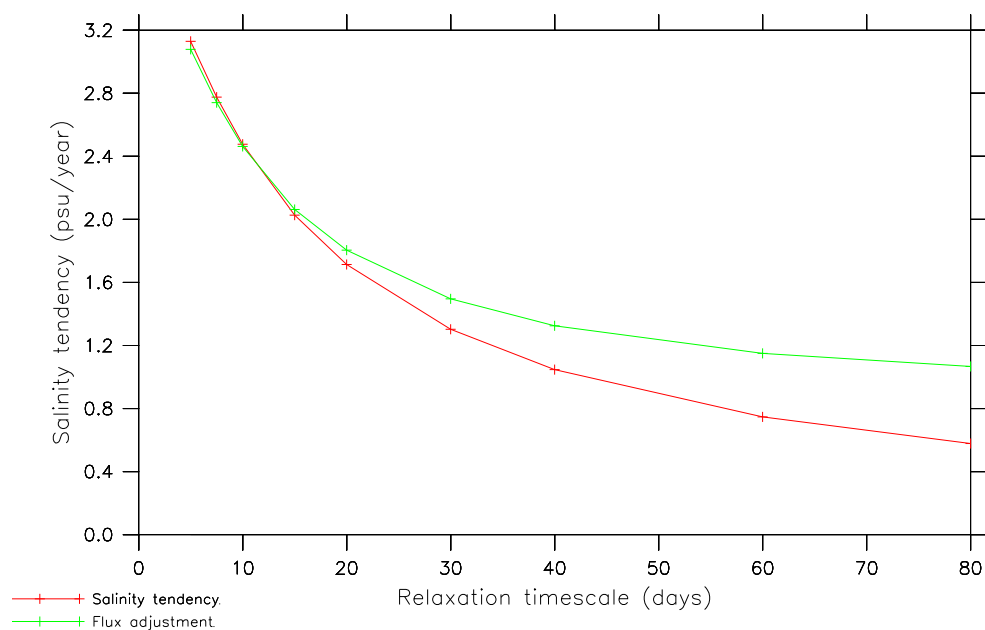


Figure 3.23: The annual-mean surface salinity tendency adjustment (psu/year) diagnosed from the Mk3L ocean model (averages for the final 100 years of each run): (a) run O-5d, (b) run O-10d, (c) run O-40d, and (d) run O-80d. The atmosphere model surface fluxes are derived from the final 40 years of run A-DEF.



(a) Surface heat flux



(b) Surface salinity tendency

Figure 3.24: The area-weighted global-mean amplitudes of the annual cycle in the surface fluxes for the Mk3L ocean model (red, averages for the final 100 years of runs O-5d, O-7.5d, O-10d, O-15d, O-DEF, O-30d, O-40d, O-60d and O-80d), and of the annual cycles in the flux adjustments diagnosed for the coupled model (green): (a) the surface heat flux, and (b) the surface salinity tendency.

Consistent with the response of the simple theoretical model (Sections 3.5.1 and 3.5.2), the amplitudes of the surface fluxes decrease as the relaxation timescale is increased. The global-mean amplitude of the surface heat flux decreases from 82.6 to 18.7 Wm^{-2} as the relaxation timescale is increased from 5 to 80 days. Similarly, the global-mean amplitude of the surface salinity tendency decreases from 3.13 to 0.58 psu/year .

It should be noted that, as the relaxation timescale is increased, the global-mean amplitudes decrease by factors of 4.42 and 5.42, in the case of the surface heat flux and surface salinity tendency respectively. This confirms the prediction made in Section 3.5.1, that the less sinusoidal nature of the annual cycle in the observed sea surface salinity would make the surface salinity tendency more sensitive to changes in the relaxation timescale.

The global-mean amplitude of the surface heat flux adjustment reaches a minimum of 47.5 Wm^{-2} at a relaxation timescale of 7.5 days. As the timescale is either increased or decreased, the surface heat fluxes simulated by the stand-alone ocean model become increasingly incompatible with those simulated by the stand-alone atmosphere model, and the amplitude of the heat flux adjustments increases. In contrast, the lack of spatial correlation between the surface salinity tendencies simulated by the stand-alone atmosphere and ocean models (Figure 2.22) is such that there is no optimal relaxation timescale. As the timescale is increased, the magnitude of the surface salinity tendencies simulated by the ocean model decreases, and the magnitude of the surface salinity tendency adjustments therefore also decreases.

3.6.8 Summary

Reducing the relaxation timescale from its default value of 20 days leads to some improvements in the ocean climate. Consistent with the response of a slab ocean model, the simulated sea surface temperatures and salinities exhibit a more realistic annual cycle, and the phase lags relative to observations are reduced. The resulting improvement in the properties of the high-latitude surface waters leads to increases in the salinity and density of the deep ocean, and enhanced North Atlantic Deep Water formation.

However, the deep ocean remains too cold, too fresh and too buoyant. Furthermore, although there is a slight reduction in the magnitude of the surface heat flux adjustments, the magnitude of the surface salinity tendency adjustments increases. It was therefore decided to leave the relaxation timescale unchanged at 20 days and to attempt, instead, to improve the realism of the simulated ocean climate through modifications to the prescribed sea surface temperatures and salinities.

Chapter 4

Modified surface tracers

4.1 Introduction

The response of a simple theoretical model, and of the Mk3L ocean model, to the relaxation surface boundary condition was studied in Chapter 3. This was determined to be the most suitable boundary condition for spinning up the ocean model, as it results in a stable climate state. However, it also gives rise to a number of deficiencies in the simulated ocean climate. A reduction in the relaxation timescale leads to some improvements in the properties of the deep ocean, but it remains too cold, too fresh and too buoyant. Furthermore, it leads to increased surface salinity tendency adjustments within the coupled model.

This chapter continues to study modifications to the relaxation boundary condition, but investigates the dependence of the simulated ocean climate upon the prescribed sea surface temperatures and salinities. As in Chapter 3, the aim is to obtain high-latitude surface waters which have a realistic peak winter density. In assessing each of the modifications, attention is paid both to the realism of the simulated ocean climate, and to the magnitude of the flux adjustments which are diagnosed for use within the coupled model.

In Section 4.2, the prescribed sea surface temperatures and salinities are modified to reflect the presence of sea ice. By making a crude representation of the effects of brine rejection, it is hypothesised that the peak winter density and salinity of the high-latitude surface waters will be enhanced, and that there will be a corresponding improvement in the properties of the deep ocean.

In Section 4.3, the prescribed sea surface temperatures and salinities are shifted forward in time by one month. It is hypothesised that this will reduce the time lag between the simulated and observed surface tracers which arises, at least in part, from the use of the relaxation boundary condition.

Finally, in Section 4.4, an iterative technique is developed, whereby the response of the ocean model is used to repeatedly modify the prescribed surface tracers. This process converges rapidly towards a solution, producing a set of *effective* surface tracers. When imposed as the boundary condition on the model, these tracers minimise the errors in the simulated sea surface temperatures and salinities.

4.2 Sub-ice surface tracers

The sea ice component of the Mk3L coupled model is incorporated into the *atmosphere* model, rather than the *ocean* model. This has two important consequences:

- the stand-alone ocean model does not incorporate a sea ice model, and cannot therefore directly simulate the effects of brine rejection arising from the formation of sea ice
- within the coupled model, the interface between the atmospheric and oceanic components is located at the ice-ocean interface, and *not* the atmosphere-ice interface

The prescribed surface tracers which form the upper boundary condition on the stand-alone ocean model should therefore, in ice-covered regions, reflect the temperature and salinity at the ice-ocean interface, rather than the atmosphere-ice interface. This can be achieved by increasing the prescribed sea surface salinity whenever sea ice is present, to simulate the effects of brine rejection, and by setting the prescribed sea surface temperature equal to the freezing point of seawater.

An attempt was made to modify the prescribed sea surface temperatures and salinities accordingly. The approach employed here can be regarded as a highly simplified version of that of *Duffy and Caldeira (1997)*. They use a simple sea ice model to explicitly calculate the rate of brine rejection, with the salt released during sea ice formation being uniformly mixed throughout the upper 160 m of the water column. Such an approach represents a modification to the model physics, and was not therefore considered to be appropriate here. Instead, observed sea ice concentrations are used to modify the prescribed sea surface temperatures and salinities to reflect the presence of sea ice.

4.2.1 Sea ice concentrations

Climatological monthly-mean sea ice concentrations for the period 1982–2003 were derived from the NOAA Optimum Interpolation v2 analysis (*Reynolds et al., 2002*). This dataset incorporates not only *in situ* observations from ships and buoys, but also satellite observations. Analysed values for the sea surface temperature and sea ice concentration are provided on a $1^\circ \times 1^\circ$ latitude-longitude grid.

4.2.2 Sea surface temperatures

Beneath sea ice, the water temperature was taken as being equal to $T_{ice} = -1.85^\circ\text{C}$, being the value used by Mk3L for the freezing point of seawater. The World Ocean Atlas 1998 sea surface temperature T_{obs} was therefore replaced with a modified value given by

$$T'_{obs} = \begin{cases} (1 - f)T_{obs} + fT_{ice} & f \geq 0.15 \\ T_{obs} & \text{otherwise} \end{cases} \quad (4.1)$$

where f is the sea ice concentration. A minimum ice concentration of 15% represents a conventional definition of sea ice extent (e.g. *Parkinson et al., 1999*), and

hence the World Ocean Atlas 1998 data was only replaced where the concentration was greater than or equal to this threshold.

4.2.3 Sea surface salinities

Modifying the sea surface salinities was less straightforward than modifying the sea surface temperatures, as there was no single value which could be taken as representing the salinity beneath sea ice. Instead, a more suitable approach was to apply an increment to the sea surface salinity in the presence of sea ice, representing the effects of brine rejection.

Estimates of the contribution of brine rejection to the salinity of Antarctic Bottom Water range from ~ 0.15 – 0.2 psu (*Toggweiler and Samuels*, 1995) to ~ 0.9 psu (*Broecker*, 1986). Given the uncertainty in these estimates, and the fact that they do not provide a value for the salinity enhancement at the ice-ocean interface, it was sought to develop an approach whereby the magnitude of the salinity increment could be estimated. Let the salinity of the ocean be S_{oce} (psu), and let ice of thickness H (m) and mean salinity S_{ice} (psu) form. The equivalent depth of salt rejected H_{salt} (m) is then given by

$$H_{salt} = \left(\frac{S_{oce} - S_{ice}}{1000} \right) H \quad (4.2)$$

If this salt is distributed uniformly throughout a mixed layer of depth dz (m), the increase in the sea surface salinity dS (psu) is given by

$$dS = 1000 \left(\frac{H_{salt}}{dz} \right) \quad (4.3)$$

$$= \frac{(S_{oce} - S_{ice})H}{dz} \quad (4.4)$$

S_{oce} can be taken as being ~ 35 psu, and Mk3L uses a value for S_{ice} of 10 psu. Thus, given values for H and dz , dS can be estimated using Equation 4.4.

An indicative value of H for each hemisphere can be obtained by dividing the magnitude of the annual cycle in sea ice volume by the mean sea ice extent; this will give an average value for the depth of ice which forms each year. While there do not appear to be any observational estimates of the magnitude of the annual cycle in sea ice volume (*Heil*, pers. comm.; *Massom*, pers. comm.), the values simulated by the Mk3L atmosphere model for each of the Northern and Southern Hemispheres is $\sim 10 \times 10^{12}$ m³ (Section 2.4.4). These magnitudes are consistent with those simulated by the CSIRO Mk2 and Mk3 climate system models (*Gordon and O'Farrell*, 1997; *Gordon et al.*, 2002), and the NCAR climate system model (*Boville and Gent*, 1998). The Hadley Centre coupled model simulates annual cycles of magnitude $\sim 25 \times 10^{12}$ m³ and $\sim 20 \times 10^{12}$ m³ in the Northern and Southern Hemispheres respectively, but suffers from excessive winter ice cover (*Gordon et al.*, 2000).

The annual-mean sea ice extent according to the NOAA OI v2 analysis for the period 1982–2003, neglecting monthly-mean ice concentrations less than 15% and weighting the extent by the ice concentration, is 9.4×10^{12} m² for the Northern

	World Ocean Atlas 1998	Modified surface tracers		
		0.25 psu	0.5 psu	1 psu
Ross Sea	28.06	28.21	28.37	28.71
Weddell Sea	27.98	28.16	28.35	28.74
Nordic Seas	27.96	27.97	28.00	28.06

Table 4.1: The peak surface σ_θ (kgm^{-3}) in regions of deep water formation, for the World Ocean Atlas 1998 data and the modified surface tracers, for salinity increments of 0.25, 0.5 and 1 psu. The data has been area-averaged onto the Mk3L ocean model grid.

Hemisphere, and 10.0×10^{12} m² for the Southern Hemisphere. Thus it is estimated that H is equal to ~ 1 m for both hemispheres.

A typical value for the mixed-layer depth is ~ 50 m (e.g. *Washington and Parkinson*, 1986). Substituting $H = 1$ m and $dz = 50$ m into Equation 4.4, a value is obtained for the salinity increment of $dS = 0.5$ psu. However, given the uncertainty regarding a suitable value for dS , three sets of modified sea surface salinities were produced, using increments of 0.25, 0.5 and 1 psu. The World Ocean Atlas 1998 sea surface salinity S_{obs} was therefore replaced with a modified value given by

$$S'_{obs} = \begin{cases} S_{obs} + fdS & f \geq 0.15 \\ S_{obs} & \text{otherwise} \end{cases} \quad (4.5)$$

4.2.4 Densities of high-latitude surface waters

Figure 4.1 shows the peak high-latitude surface water densities which are implied by the modified sea surface temperatures and salinities; values for the World Ocean Atlas 1998 data are shown in Figure 3.1. The peak densities in the three key regions of deep water formation are also shown in Table 4.1.

The modifications to the sea surface temperatures and salinities lead to significant increases in the implied peak surface water densities in the Ross and Weddell Seas, with increases of up to 0.65 and 0.76 kgm^{-3} respectively. However, the peak density in the Nordic Seas is almost unaffected; there is little sea ice cover in this region, and hence the modifications to the sea surface temperatures and salinities are small. Although there are large increases in the implied peak surface densities in the Barents Sea, to the north of Russia, this is not a region of deep water formation.

4.2.5 The response of the Mk3L ocean model

Three Mk3L ocean model spin-up runs were conducted; the spin-up procedure was identical to run O-DEF (Section 2.3.2), except that the temperature and salinity of the upper layer of the model were relaxed towards the modified sea surface temperatures and salinities. The runs which employed sub-ice salinity increments of 0.25, 0.5 and 1 psu shall herein be designated O-0.25psu, O-0.5psu and O-1psu respectively. Each run was integrated first under asynchronous timestepping, and then synchronous timestepping, until the convergence criteria were satisfied (i.e. that the

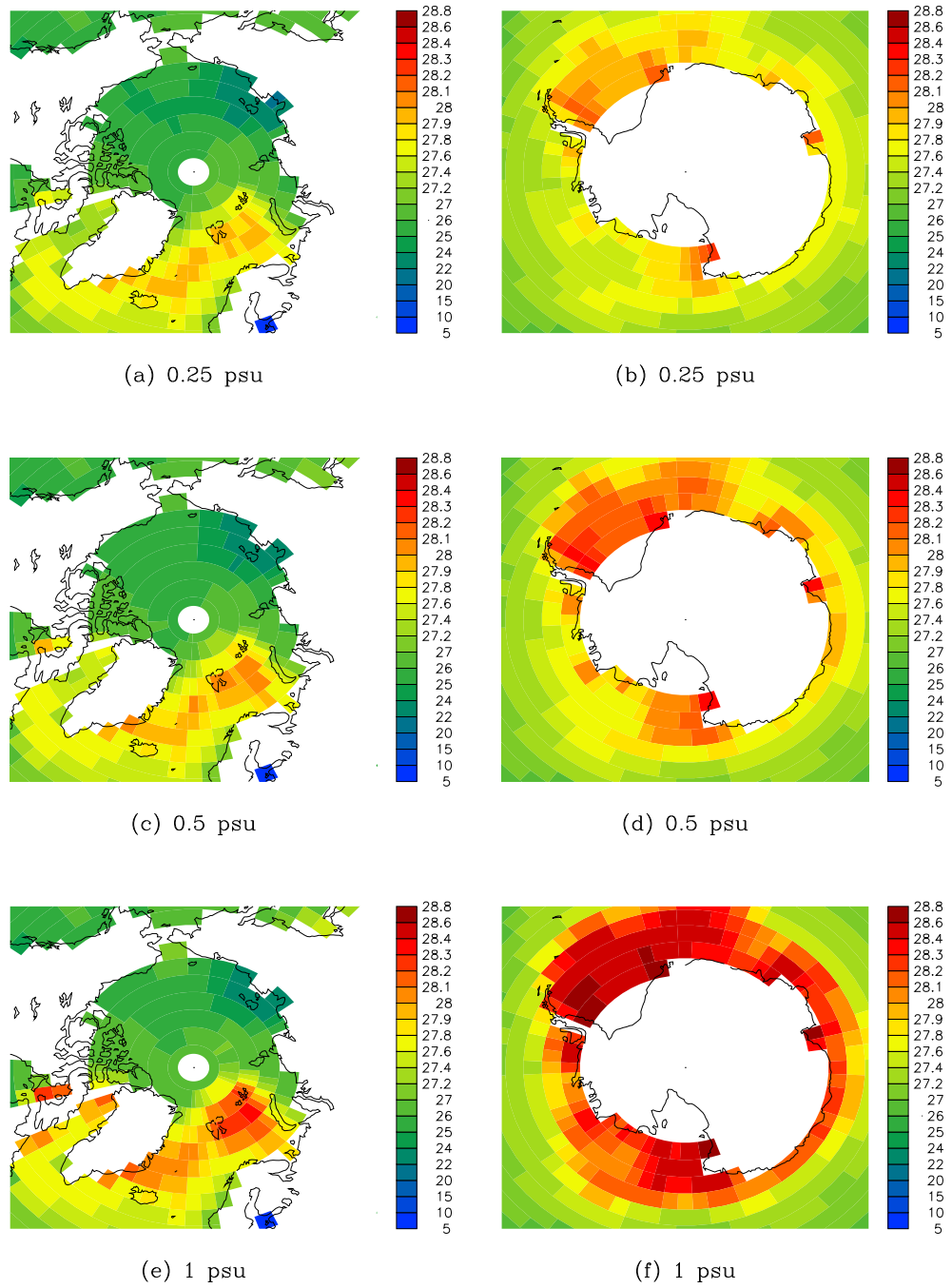


Figure 4.1: The annual-maximum σ_θ (kgm^{-3}) implied by the modified sea surface temperatures and salinities: (a), (b) a salinity increment of 0.25 psu, (c), (d) a salinity increment of 0.5 psu, and (e), (f) a salinity increment of 1 psu. The modified data has been area-averaged onto the Mk3L ocean model grid.

rates of change in global-mean potential temperature and salinity, on each model level, were less than $0.005^{\circ}\text{C}/\text{century}$ and $0.001 \text{ psu}/\text{century}$ respectively). As with run O-DEF, the durations of the asynchronous and synchronous stages were 4,000 and 500 years respectively.

Water properties

The vertical profiles of potential temperature, salinity and potential density are shown in Figure 4.2. The modifications to the sea surface temperatures and salinities lead to large increases in the salinity and density of the deep ocean, with run O-0.5psu having the most realistic deep ocean salinities, and run O-0.25psu having the most realistic deep ocean densities. However, the modifications also increase the cold bias of the deep ocean, accounting for that fact that the deep ocean of run O-0.25psu has the most realistic densities, even though it is too fresh.

The zonal-mean potential temperature, salinity and potential density are shown in Figures 4.3, 4.4 and 4.5 respectively, as anomalies relative to the World Ocean Atlas 1998; values for run O-DEF are shown in Figures 2.14c, 2.15c and 2.16c. The increased cold bias of the deep ocean is apparent, as is the realistic nature of the deep ocean salinities in run O-0.5psu, and the realistic nature of the deep ocean densities in run O-0.25psu.

The response of the deep Arctic Ocean differs from that of the remainder of the world ocean, however. While it is significantly too warm in run O-DEF, it cools as the salinity increment is increased, and has realistic temperatures in run O-1psu. Likewise, the deep Arctic Ocean was too fresh and too buoyant in run O-DEF, but has realistic salinities and densities in run O-1psu. This suggests, as has been indicated in other studies, that there is a “fair weather” bias in the observed sea surface temperatures and salinities over the Arctic Ocean (Section 3.4.2). Only when they are modified to reflect the presence of sea ice do they become consistent with the observed temperatures and salinities at depth.

Circulation

The rates of North Atlantic Deep Water (NADW) and Antarctic Bottom Water (AABW) formation are shown in Table 4.2. As the salinity increment is increased, the peak densities of the surface waters in the Ross and Weddell Seas increase, and the production of AABW intensifies. However, the resulting increase in the density of the deep ocean, and hence in the stratification of the water column, causes the production of NADW to diminish. Given that the rate of NADW formation in run O-DEF is too weak (Section 2.5.2), this represents a decrease in the realism of the simulated ocean climate.

The increased dominance of AABW formation over NADW formation provides an explanation for the increased cold bias of the deep ocean.

Surface fluxes

Figure 4.6 shows the effect of the modifications to the prescribed high-latitude surface tracers upon the diagnosed surface fluxes. In accordance with other studies

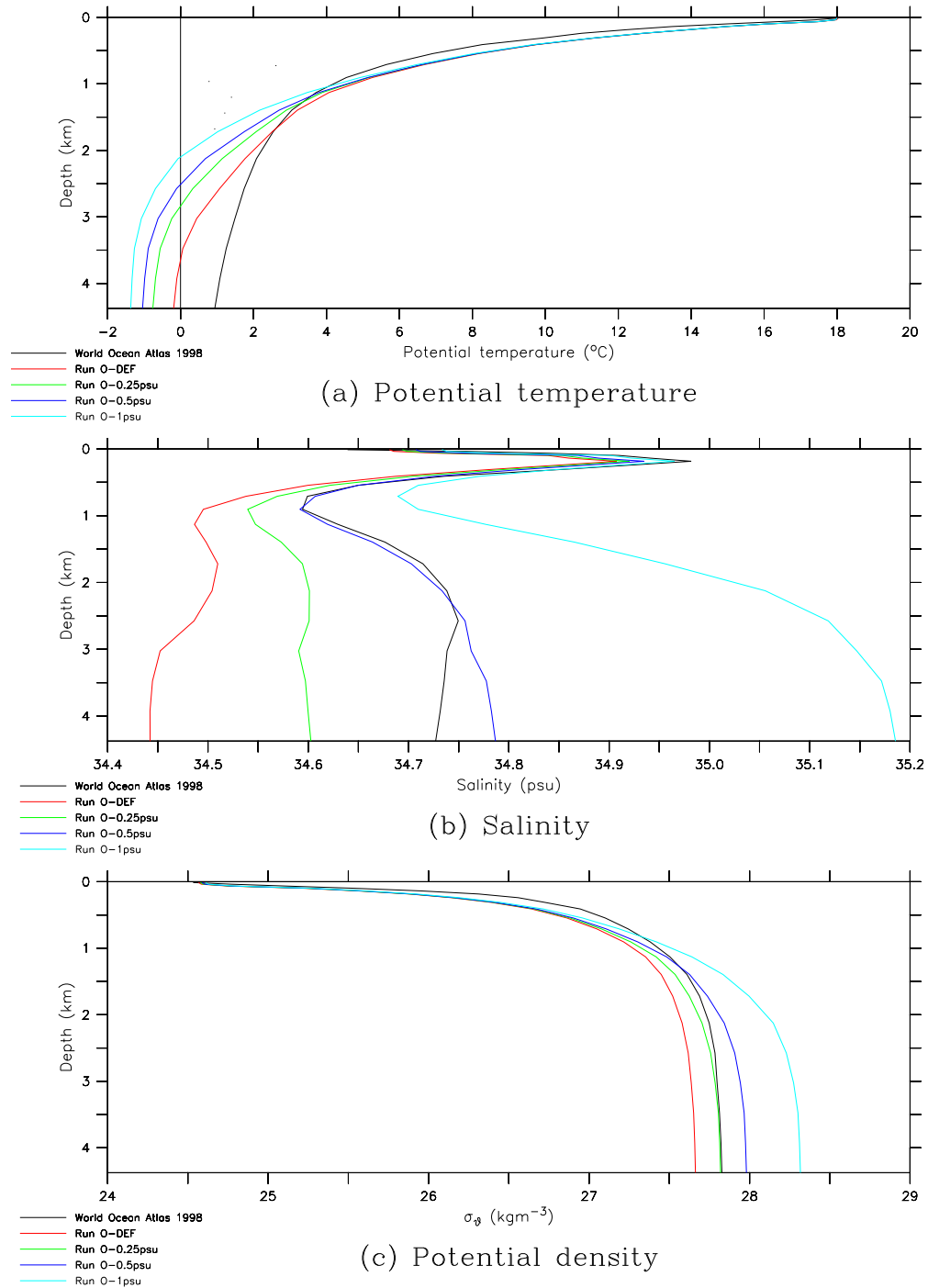
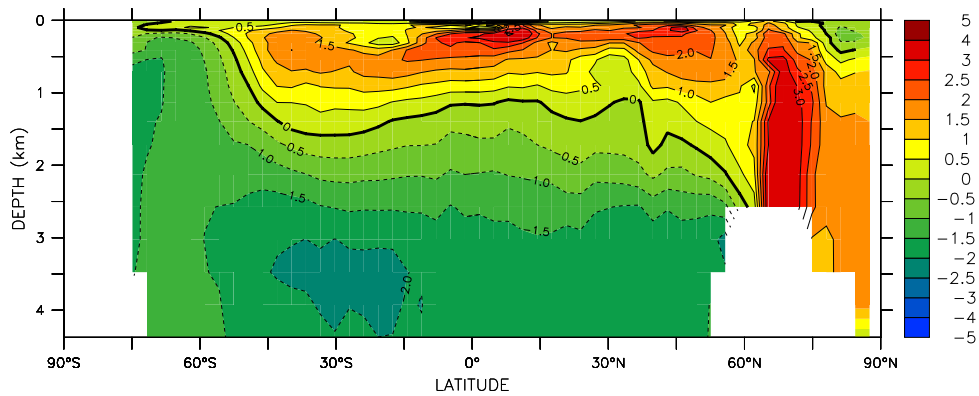
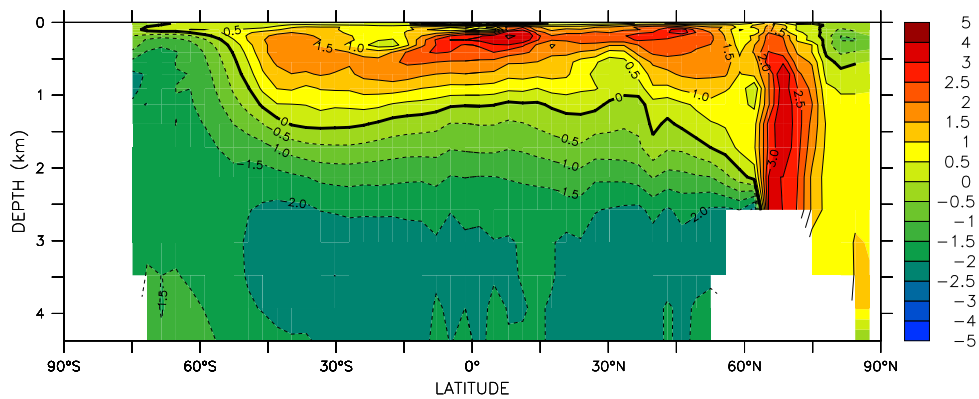


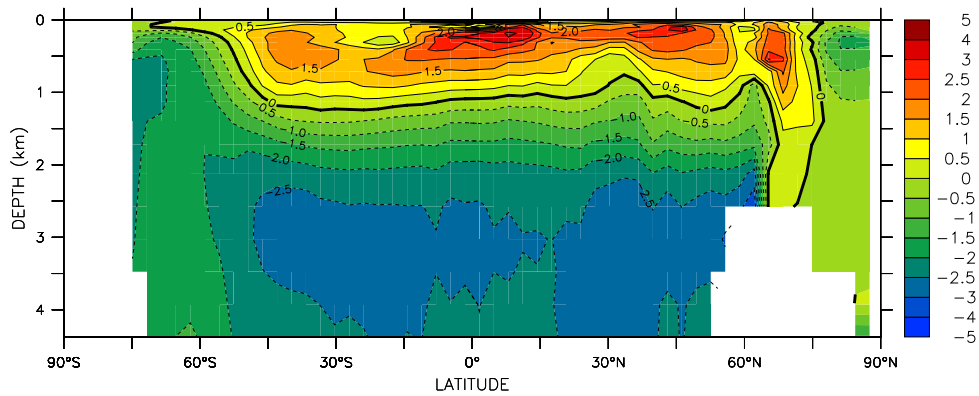
Figure 4.2: The global-mean potential temperature, salinity and σ_θ on each model level for the World Ocean Atlas 1998 (black), and for Mk3L ocean model runs O-DEF (red), O-0.25psu (green), O-0.5psu (dark blue) and O-1psu (light blue): (a) potential temperature, (b) salinity, and (c) σ_θ . All values for Mk3L are averages for the final 100 years of each run.



(a) Run 0-0.25psu

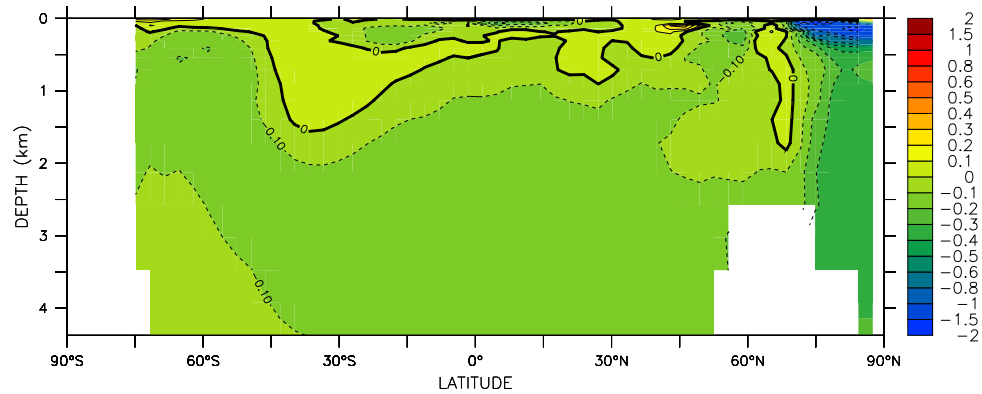


(b) Run 0-0.5psu

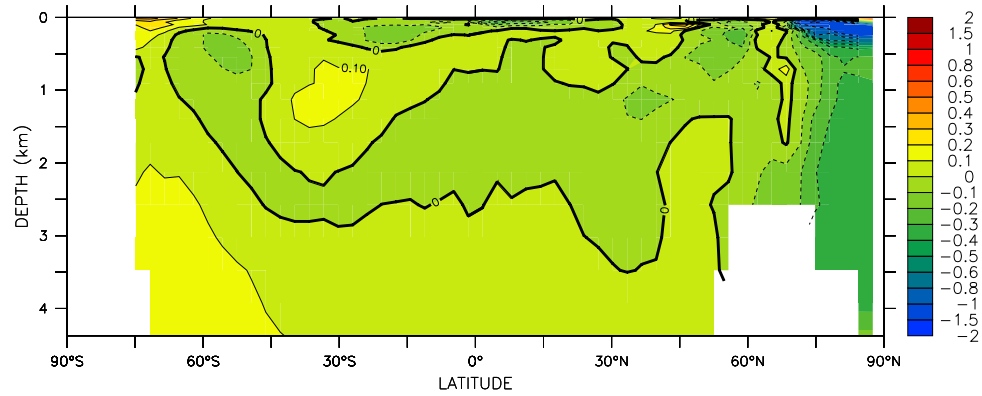


(c) Run 0-1psu

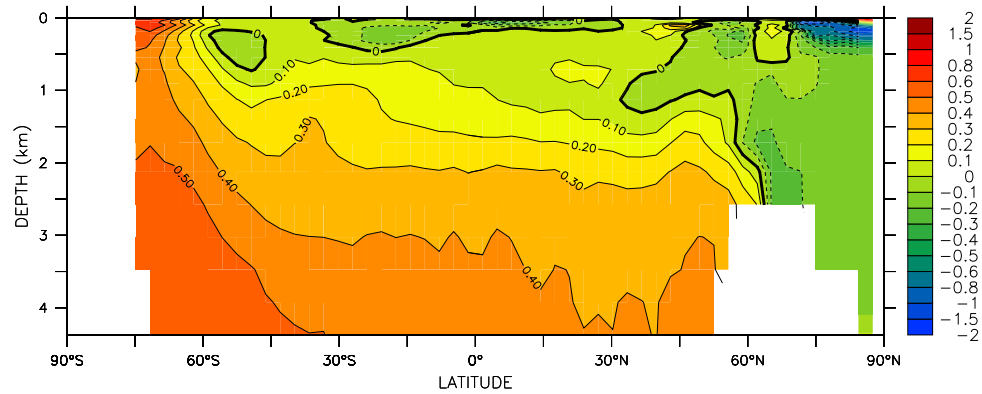
Figure 4.3: The zonal-mean potential temperature ($^{\circ}\text{C}$) for the world ocean (excluding inland seas) for the Mk3L ocean model (averages for the final 100 years of each run), expressed as an anomaly relative to the World Ocean Atlas 1998: (a) run O-0.25psu, (b) run O-0.5psu, and (c) run O-1psu. The World Ocean Atlas 1998 data has been volume-averaged onto the Mk3L ocean model grid.



(a) Run 0-0.25psu

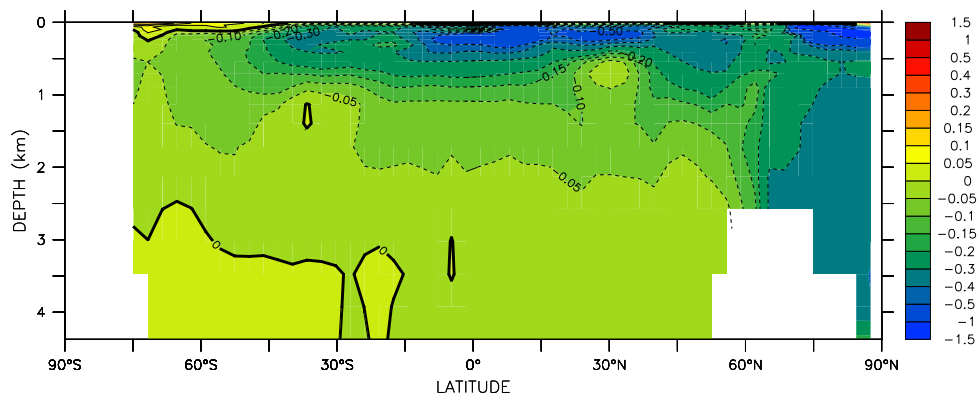


(b) Run 0-0.5psu

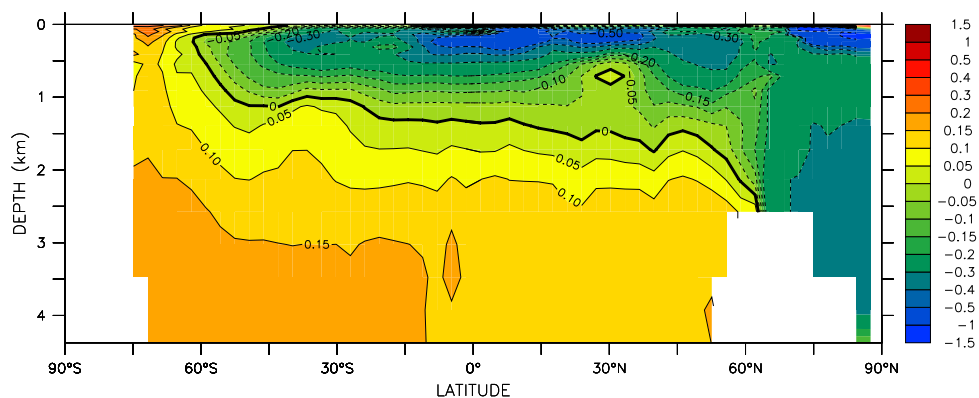


(c) Run 0-1psu

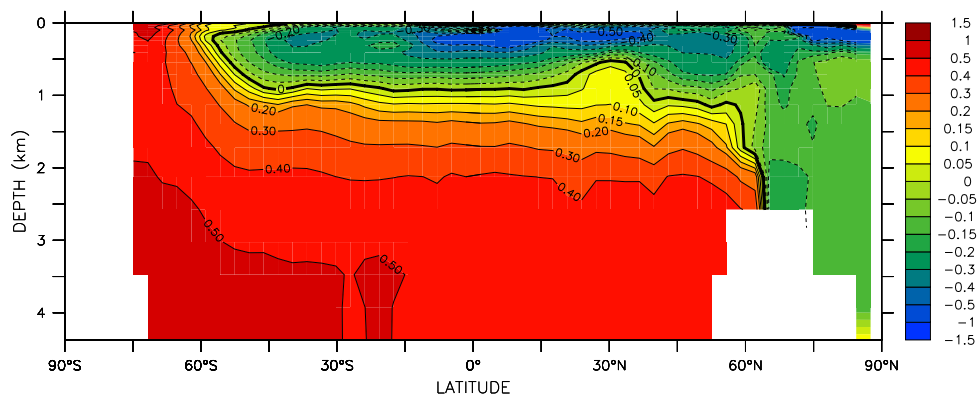
Figure 4.4: The zonal-mean salinity (psu) for the world ocean (excluding inland seas) for the Mk3L ocean model (averages for the final 100 years of each run), expressed as an anomaly relative to the World Ocean Atlas 1998: (a) run 0-0.25psu, (b) run 0-0.5psu, and (c) run 0-1psu. The World Ocean Atlas 1998 data has been volume-averaged onto the Mk3L ocean model grid.



(a) Run 0–0.25psu



(b) Run 0–0.5 psu



(c) Run 0–1psu

Figure 4.5: The zonal-mean σ_θ (kgm^{-3}) for the world ocean (excluding inland seas) for the Mk3L ocean model (averages for the final 100 years of each run), expressed as an anomaly relative to the World Ocean Atlas 1998: (a) run O-0.25psu, (b) run O-0.5psu, and (c) run O-1psu. The World Ocean Atlas 1998 data has been volume-averaged onto the Mk3L ocean model grid.

Run	Rate of formation (Sv)	
	NADW	AABW
O-DEF	13.6	9.5
O-0.25psu	13.0	11.2
O-0.5psu	12.3	11.8
O-1psu	11.8	12.6

Table 4.2: The rates of deep water formation (Sv) for Mk3L ocean model runs O-DEF, O-0.25psu, O-0.5psu and O-1psu (averages for the final 100 years of each run): North Atlantic Deep Water (NADW), and Antarctic Bottom Water (AABW).

which employ an ocean model incorporating Gent-McWilliams eddy diffusion (e.g. *Bi*, 2002), and contrary to studies which do not (e.g. *Weaver and Hughes*, 1996), the impact upon the surface fluxes is negligible.

4.2.6 Summary

The prescribed sea surface temperatures and salinities have been modified at high latitudes, in an attempt to reflect the presence of sea ice. Some aspects of the simulated ocean climate are improved, but others are diminished. While it is possible to obtain realistic deep ocean salinities and densities, an increase in the rate of Antarctic Bottom Water formation, combined with a decrease in the rate of North Atlantic Deep Water formation, increases the cold bias of the deep ocean.

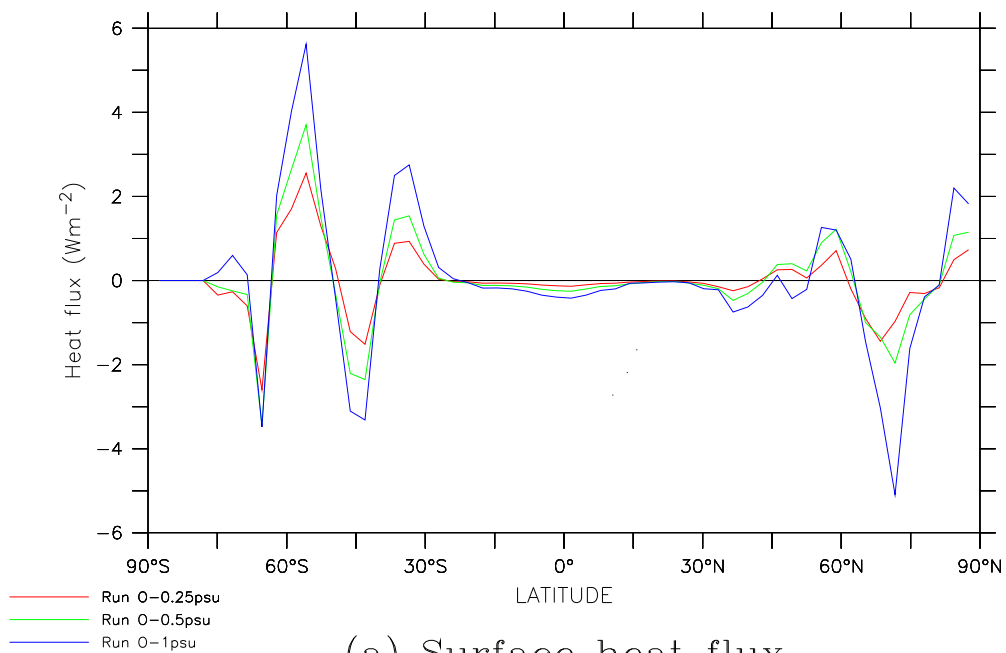
This experiment was not, therefore, considered to be a success. However, it has been shown that, by correcting for an apparent “fair weather” bias in the observed sea surface temperatures and salinities in the Arctic, it is possible to improve the properties of the simulated deep Arctic Ocean.

4.3 Phase-shifted surface tracers

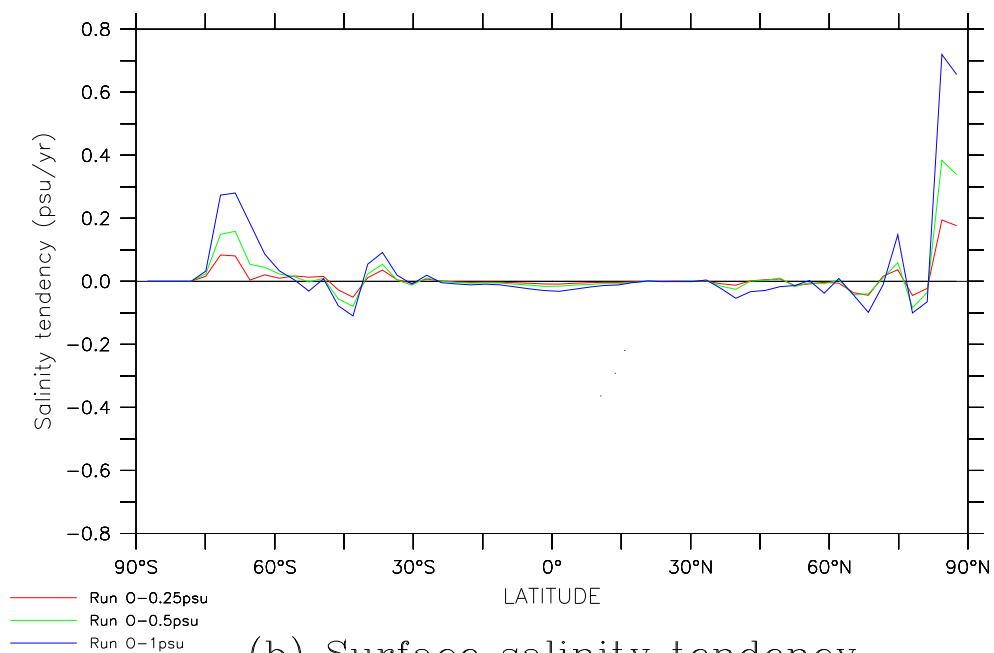
4.3.1 Introduction

The flux adjustments employed within the coupled model are diagnosed from the mismatch between the surface fluxes simulated by the stand-alone atmosphere and ocean models (Section 2.6). This methodology assumes that the climates of the stand-alone atmosphere and ocean models are the best that can be obtained, given the spatial resolutions, physical parameterisations and boundary conditions employed (*Weaver and Hughes*, 1996).

However, three distinct errors in the climate of the stand-alone ocean model were identified in Section 3.3, each of which can be attributed, at least in part, to the relaxation boundary condition. One of these errors is the phase lag between the observed and simulated annual cycles in the sea surface temperature (SST) and sea surface salinity (SSS). Given that the intention of the flux adjustments is to minimise any drift in the ocean model climate upon coupling to the atmosphere model, it follows that one of the roles of the flux adjustments within the coupled



(a) Surface heat flux



(b) Surface salinity tendency

Figure 4.6: The zonal-mean surface heat flux and surface salinity tendency for Mk3L ocean model runs O-0.25psu (red), O-0.5psu (green) and O-1psu (dark blue), expressed as anomalies relative to run O-DEF: (a) the surface heat flux, and (b) the surface salinity tendency. All values are averages for the final 100 years of each run.

model is to maintain the ocean in its phase-lagged state. *The flux adjustments are therefore maintaining an error in the simulated ocean climate.*

It is hypothesised that, if the phase lag in the climate of the stand-alone ocean model could be reduced, then the magnitude of the annual cycle in the flux adjustments would be reduced. Thus the realism of the simulated ocean climate could be *improved*, while the magnitude of the flux adjustments within the coupled model would be *reduced*.

In Section 3.3, the global-mean time lags for run O-DEF were diagnosed as being 31.7 days for the SST, and 22.1 days for the SSS. These mean lags, particularly in the case of the SST, are approximately equal to one month. This suggests a very straightforward modification to the prescribed surface tracers: to shift them forward in time by one month.

4.3.2 Spinning up the model

Run O-DEF (Section 2.3.2) was continued under synchronous timestepping, with the prescribed sea surface temperatures and salinities being shifted forward in time by one month. No change was made to the surface wind stresses, as these represent a flux boundary condition and hence do not generate a phase lag. The convergence criteria (i.e. that the rates of change in global-mean potential temperature and salinity, on each model level, were less than 0.005°C/century and 0.001 psu/century respectively) were satisfied after 500 years. This run shall be referred to herein as O-SHF.

In order to diagnose surface fluxes for the stand-alone atmosphere model, a 50-year atmosphere model spin-up run was also conducted. This run was identical to run A-DEF (Section 2.3.1), with the exception that the ocean currents were diagnosed from the final 100 years of run O-SHF. This run shall be referred to herein as A-SHF.

4.3.3 Surface fluxes and flux adjustments

The only difference between runs O-DEF and run O-SHF is that, relative to run O-DEF, the boundary conditions on the model during run O-SHF exhibited a one-month shift in the phase relationship between the prescribed surface tracers and the prescribed surface wind stresses. The differences between the annual-mean climates of the two runs are therefore negligible, and are not presented here.

Figure 4.7 shows the lags of maximum correlation between the sea surface temperatures and salinities diagnosed from run O-SHF, and the World Ocean Atlas 1998 values (*not* the phase-shifted values which were used to spin-up the model); it can be compared with the lags of maximum correlation diagnosed from run O-DEF (Figure 3.7). The phase shift in the prescribed sea surface temperatures and salinities has been successful in reducing the lags, with area-weighted global-mean time lags of +2.4 and -5.2 days for the SST and SSS respectively, as opposed to +31.7 and +22.1 days for run O-DEF.

Figures 4.8a and 4.8b show the amplitudes of the annual cycles in the surface heat fluxes, for runs O-DEF and O-SHF. They are negligibly different, indicating that the only significant difference between the two runs is in the *timing* of the

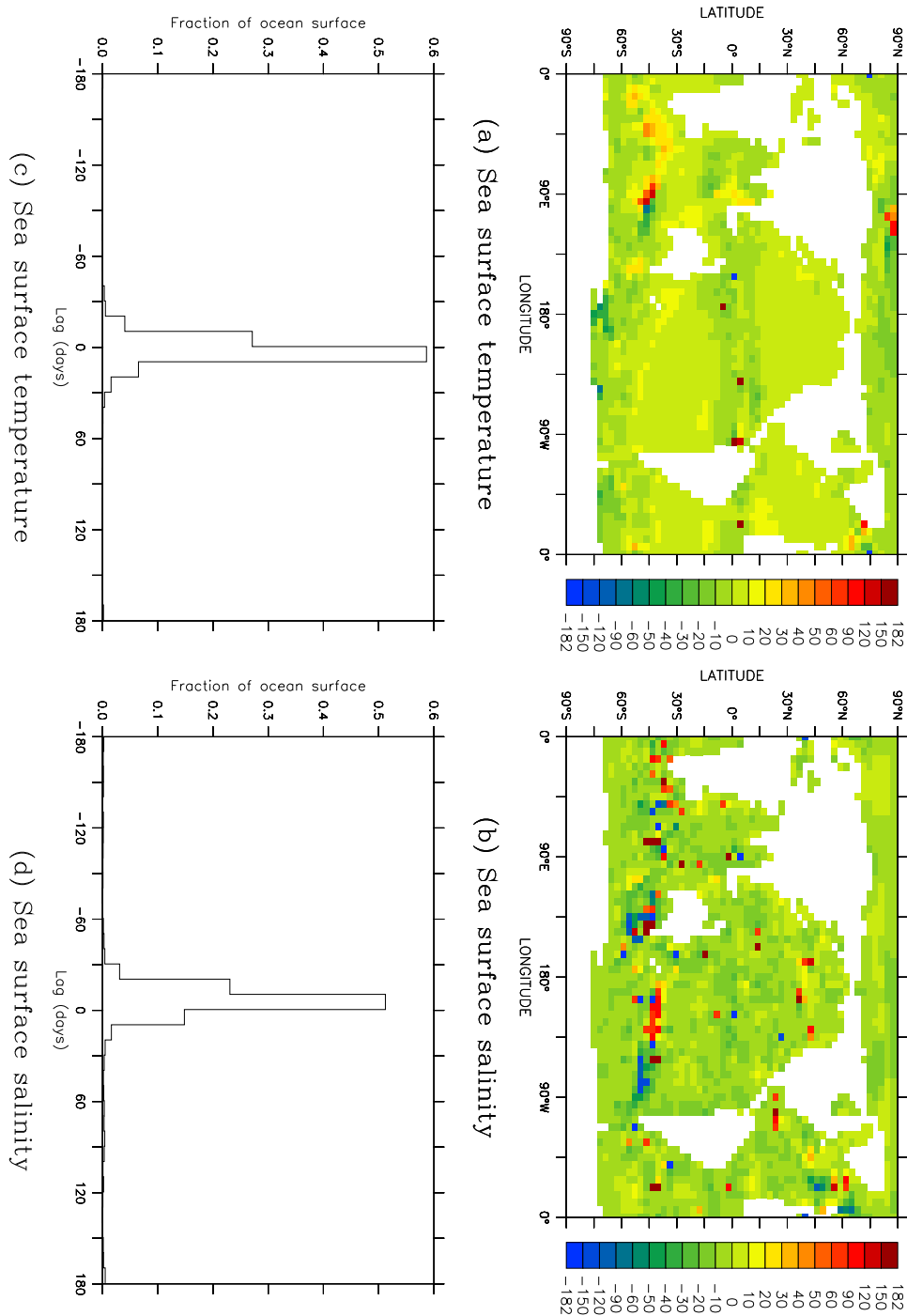


Figure 4.7: The lag of maximum correlation (days) between the Mk3L ocean model (average for the final 100 years of run O-SHF) and the World Ocean Atlas 1998: (a), (b) the lag at each gridpoint, sea surface temperature and sea surface salinity respectively, and (c), (d) the fraction of the surface area of the ocean over which the lags lie within the ranges shown, sea surface temperature and sea surface salinity respectively.

Quantity	Units	O-DEF/ A-DEF	O-SHF/ A-SHF
Sea surface temperature lag	days	+31.7	+2.4
Sea surface salinity lag	days	+22.1	-5.2
Amplitude of heat flux adjustment	Wm^{-2}	55.2	38.2
Amplitude of salinity tendency adjustment	psu/year	1.80	1.77
Amplitude of SST adjustment	$^{\circ}\text{C}$	0.955	0.685
Amplitude of SSS adjustment	psu	0.118	0.100

Table 4.3: Some area-weighted global-mean statistics for Mk3L ocean and atmosphere model runs O-DEF/A-DEF and O-SHF/A-SHF. Surface fields are diagnosed from the final 100 years of runs O-DEF and O-SHF, and from the final 40 years of runs A-DEF and A-SHF.

annual cycles. Figures 4.8c and 4.8d show the amplitudes of the annual cycles in the heat flux adjustments. They are generally much smaller in the case of runs O-SHF/A-SHF, confirming the hypothesis that the magnitude of the flux adjustments can be reduced by reducing the time lag between the ocean model climate and observations.

Figure 4.9 shows the amplitudes of the annual cycles in the surface salinity tendencies, and in the salinity tendency adjustments. The amplitudes of the surface fluxes can be seen to be negligibly different between the two ocean model runs. However, the reduction in the amplitudes of the flux adjustments is much smaller than in the case of the surface heat flux. This can be attributed to the lack of spatial correlation between the surface salinity tendencies simulated by the stand-alone atmosphere and ocean models, in which case a phase shift in the ocean model salinity tendencies will have little impact upon the magnitude of the flux adjustments.

The amplitudes of the annual cycles in the sea surface temperature (SST) and sea surface salinity (SSS) adjustments are shown in Figure 4.10. By reducing the phase lag between the observed and simulated SST, the magnitude of the SST adjustments is reduced over much of the surface of the ocean. In contrast, there is a much smaller reduction in the magnitude of the SSS adjustments. This can be attributed to the generally indistinct nature of the annual cycle exhibited by the observed SSS (Section 3.5.1), and to the correspondingly poor response of the model (Section 3.3). As a result of these, a phase shift in the simulated annual cycle will have little impact upon the magnitude of the SSS adjustments.

Some global-mean statistics are shown in Table 4.3. The amplitudes of the heat flux and sea surface temperature adjustments diagnosed from runs O-SHF/A-SHF are $\sim 30\%$ smaller than those diagnosed from runs O-DEF/A-DEF. The reductions in the amplitudes of the salinity tendency and sea surface salinity adjustments, however, are just 2% and 15% respectively.

4.3.4 Summary

The original hypothesis has been shown to be correct. By shifting the prescribed surface tracers forward in time by one month, the lag between the ocean model and

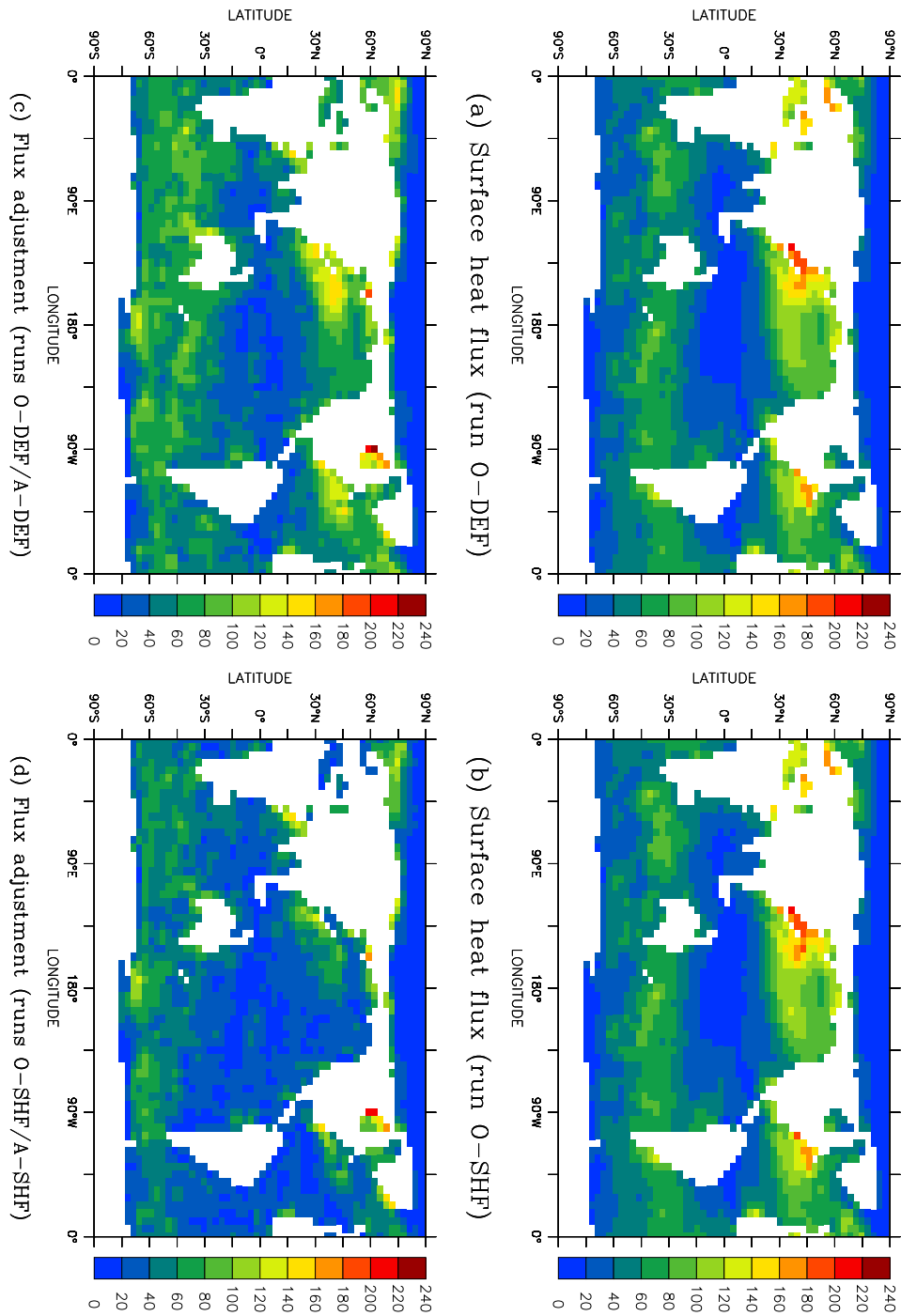


Figure 4.8: The amplitude of the annual cycle in the surface heat flux (Wm^{-2}) and the heat flux adjustment (Wm^{-2}): (a), (b) the surface heat flux, diagnosed from runs O-DEF and O-SHF respectively, and (c), (d) the heat flux adjustment, diagnosed from runs O-DEF/A-DEF and O-SHF/A-SHF respectively. Fluxes are diagnosed from the final 100 years of runs O-DEF and O-SHF, and from the final 40 years of runs A-DEF and A-SHF.

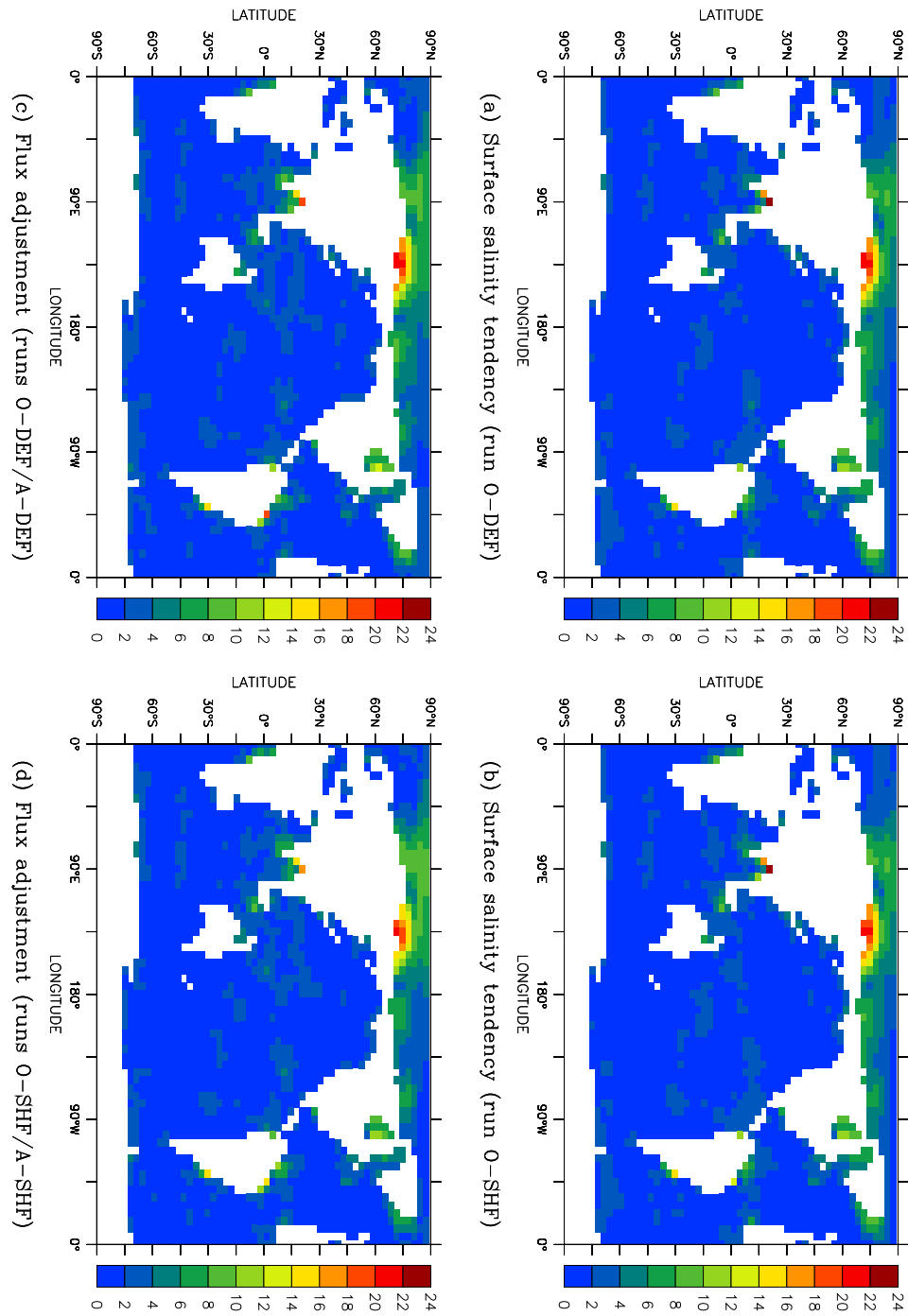


Figure 4.9: The amplitude of the annual cycle in the surface salinity tendency (psu/year) and the salinity tendency adjustment (psu/year): (a), (b) the surface salinity tendency, diagnosed from runs O-DEF and O-SHF respectively, and (c), (d) the salinity tendency adjustment, diagnosed from runs O-DEF/A-DEF and O-SHF/A-SHF respectively. Salinity tendencies are diagnosed from the final 100 years of runs O-DEF and O-SHF, and from the final 40 years of runs A-DEF and A-SHF.

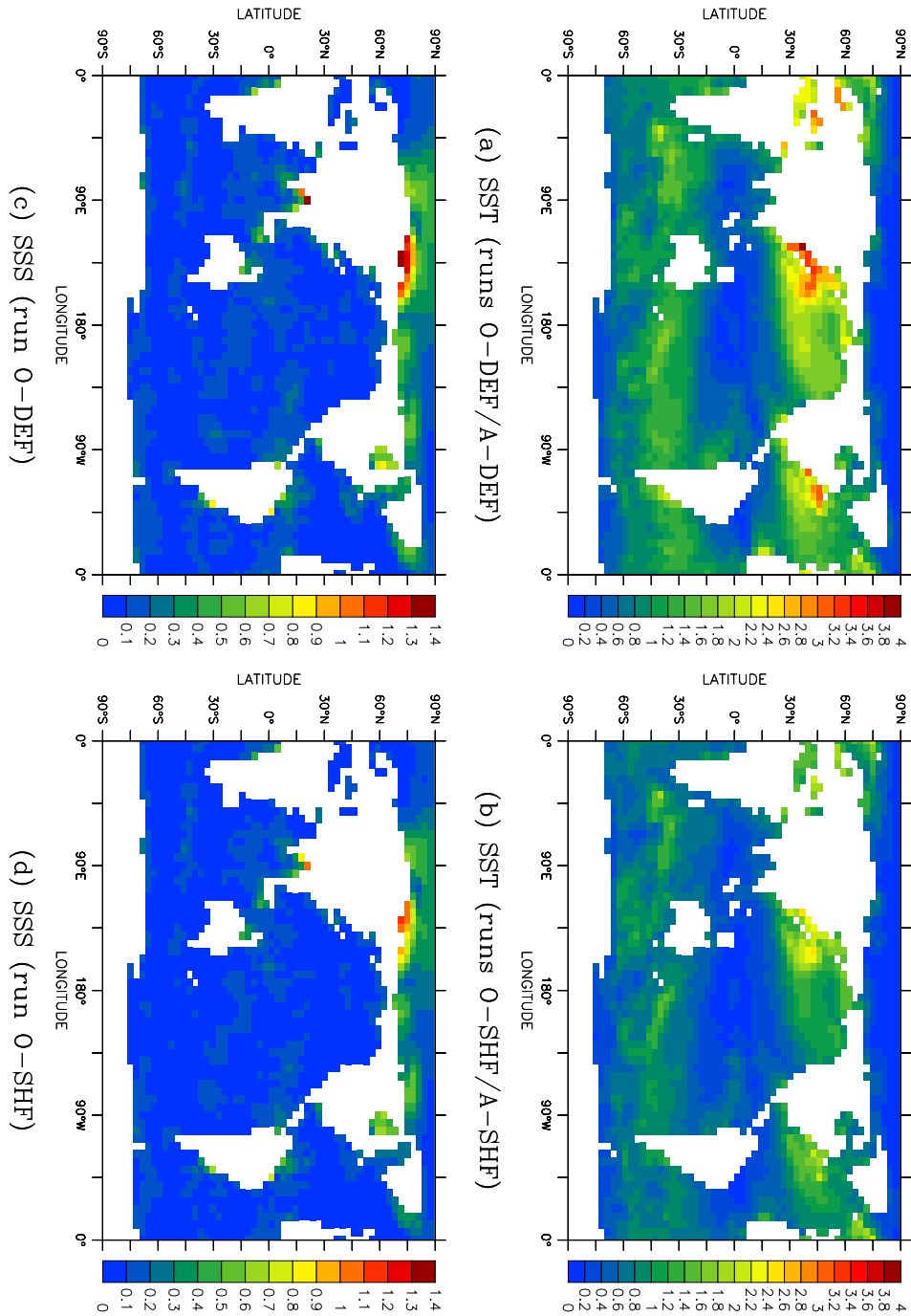


Figure 4.10: The amplitude of the annual cycle in the sea surface temperature (SST) adjustment ($^{\circ}\text{C}$) and the sea surface salinity (SSS) adjustment (psu): (a), (b) the SST adjustment, diagnosed from runs O-DEF/A-DEF and O-SHF/A-SHF respectively, and (c), (d) the SSS adjustment, diagnosed from runs O-DEF and O-SHF respectively. SSTs and SSSs are diagnosed from the final 100 years of runs O-DEF and O-SHF, and SSTs are diagnosed from the final 40 years of runs A-DEF and A-SHF.

observations has been reduced. As a result, there has also been a reduction in the magnitude of the flux adjustments diagnosed for use within the coupled model.

4.4 Effective surface tracers

In Section 3.3, three distinct errors in the simulated sea surface temperature (SST) and sea surface salinity (SSS) were identified:

- an error in the annual mean
- an error in the amplitude of the annual cycle
- a phase lag between the simulated and observed fields

In the previous section, it was shown that the phase lag could be addressed by simply shifting the prescribed SST and SSS forward in time relative to observations. It was therefore attempted to extend this approach, to address the errors in the annual means and in the amplitudes of the annual cycle.

Consider the equilibrium response of the model. Let the observed SST (or SSS) have the annual-mean value \bar{T}_{obs} , and let the amplitude of the annual cycle be a_{obs} . Let the SST (or SSS) which was prescribed as the boundary condition on the model, and which may not necessarily be equal to the observed values, have the annual-mean value \bar{T}_{pre} , and an annual cycle of amplitude a_{pre} . Let the equilibrium response of the model have annual-mean value \bar{T}_{mod} , and an annual cycle of amplitude a_{mod} . The errors in the simulated annual-mean SST (or SSS), and in the simulated amplitude of the annual cycle, can therefore be expressed as

$$\Delta T = \bar{T}_{mod} - \bar{T}_{obs} \quad (4.6)$$

$$r = \frac{a_{mod}}{a_{obs}} \quad (4.7)$$

Not only can these two errors be diagnosed independently of the phase lag, but they can also be diagnosed independently of each other. Having diagnosed the errors, they can be used to modify the prescribed SST (or SSS) accordingly. The modified climatology will have an annual-mean value \bar{T}'_{pre} and an annual cycle of amplitude a'_{pre} , where these values are given by

$$\bar{T}'_{pre} = \bar{T}_{pre} - \Delta T \quad (4.8)$$

$$a'_{pre} = \frac{1}{r} a_{pre} \quad (4.9)$$

If the prescribed SST (or SSS) for month n is expressed as the sum of the annual mean \bar{T} , and an anomaly \mathcal{T}_n , thus:

$$T_n = \bar{T} + \mathcal{T}_n \quad (4.10)$$

then the modified SST (or SSS) for month n will be given by

$$T'_n = \bar{T} - \Delta T + \frac{1}{r} \mathcal{T}_n \quad (4.11)$$

An iterative approach can therefore be developed, as follows:

1. Integrate the ocean model to equilibrium, with the prescribed SST (or SSS) at gridpoint (i, j) having annual-mean value $\bar{T}_{pre}(i, j)$, and with the amplitude of the annual cycle being $a_{pre}(i, j)$.
2. From the simulated SST (or SSS), diagnose the values for the annual mean $\bar{T}_{mod}(i, j)$, and for the amplitude of the annual cycle $a_{mod}(i, j)$.
3. Diagnose the errors in the simulated SST and SSS, using Equations 4.6 and 4.7.
4. Derive modified values for the prescribed SST and SSS, using Equation 4.11.
5. Repeat Steps 1–4, until a pre-defined convergence criterion is satisfied.

The final values which are obtained for the prescribed SST and SSS can be termed *effective* surface tracers. They will have been derived such that the simulated annual-mean SST and SSS at each gridpoint, and the simulated amplitudes of the annual cycles, will agree with observations to the greatest extent possible, given the spatial resolution of the model and the model physics.

This approach can be contrasted with that of *Bi* (2002), and with the limiting case of reducing the relaxation timescale to zero. Both these approaches seek to reduce the errors in the simulated SST and SSS, at each gridpoint *and* for each month of the year, to zero. However, the approach developed here only seeks to minimise the errors in the simulated annual-mean SST and SSS, and in the simulated amplitude of the annual cycle. It therefore avoids both the numerical instabilities which were encountered by *Bi* (2002), and the excessive surface fluxes which result when the relaxation timescale is reduced towards zero.

A comparison can also be made with the approach of *Pierce* (1996). By using the response of an ocean model to determine the amplitude and phase changes which arise as a result of the relaxation boundary condition, the internal transport of heat within the ocean is taken into account. The errors in both the simulated SST and SSS are also addressed, while *Pierce* (1996) only considers the SST.

4.4.1 Spinning up the model

The above approach was employed to spin up the Mk3L ocean model. The spin-up procedure is summarised in Table 4.4, and consisted of the following steps:

1. The model was initialised from the end of the asynchronous stage of the default spin-up run O-DEF (Section 2.3.2).
2. Model errors were diagnosed from the final 100 years of the asynchronous stage of run O-DEF (i.e. model years 3901–4000), and were used to derive the first set of effective surface tracers.

Iterations	Duration (years)	Timestepping	Phase shift?
1–5	1000	Asynchronous	No
6–8	500	Asynchronous	No
9–11	500	Asynchronous	Yes
12–14	200	Synchronous	Yes

Table 4.4: A summary of the spin-up procedure for Mk3L ocean model run O-EFF.

3. The model was repeatedly integrated to equilibrium under asynchronous timestepping. The effective surface tracers were employed as the boundary condition on the sea surface temperature and salinity, while the model was forced with the same NCEP-DOE Reanalysis 2 (*Kanamitsu et al.*, 2002) wind stresses that were used for run O-DEF. Model errors were diagnosed from the final 100 years of each iteration, and were used to derive the effective surface tracers to be used for the following iteration. The observed values for the sea surface temperature and salinity, which were used to calculate the model errors, were the same World Ocean Atlas 1998 values which were prescribed during the default spin-up run O-DEF.
4. During the iterative process, the convergence criterion for each iteration was that the rates of change in the global-mean sea surface temperature and salinity must be less than $0.005^{\circ}\text{C}/\text{century}$ and $0.001 \text{ psu}/\text{century}$ respectively. It was not necessary to apply these criteria to any levels other than the surface, as it was only the sea surface temperature and salinity which were required in order to calculate the model errors.
5. Five iterations of duration 1000 years were conducted, followed by three iterations of duration 500 years. An equilibrium solution had then been obtained, with the convergence criterion being that the differences in the global-mean potential temperature and salinity on each model level, between the final centuries of consecutive iterations, must be less than 0.005°C and 0.001 psu respectively. Note that *all* model levels were considered here, as it was desired that the final solution should represent an equilibrium solution for the ocean as a whole.
6. The final set of effective surface tracers were shifted forward in time by one month, to address the phase lag between the model and observations. The iterative process was then continued. A further three iterations, each of duration 500 years, were conducted, after which a fresh solution had been reached.
7. Synchronous timestepping was then employed, and the iterative process was continued, using iterations of duration 200 years. An equilibrium solution was reached after a further three iterations, representing a total of 14 iterations and 8,600 model years.

While Equations 4.6, 4.7 and 4.11 were used to modify the effective surface tracers, a number of constraints were imposed:

- The factor $\frac{1}{r}$, by which the amplitudes of the annual cycle in the prescribed surface tracers are multiplied from one iteration to the next, was constrained to lie within the range $[0.5, 2]$. This constraint was found to improve the stability of the iterative process by reducing “overshoot”, and hence to reduce the number of iterations required to reach a solution.
- To prevent the simulated sea surface temperatures from falling below the freezing point of seawater, the effective sea surface temperatures were constrained such that they must always be greater than or equal to -2.1°C ; this value represents the minimum sea surface temperature encountered within the World Ocean Atlas 1998 dataset. This constraint was implemented by reducing the amplitude of the annual cycle, such that the annual-minimum value of the effective sea surface temperature was equal to -2.1°C . By reducing the amplitude of the annual cycle, rather than simply modifying the effective sea surface temperatures for individual months, it could be ensured that there was no change to the annual-mean sea surface temperature. This constraint was found to improve the stability of the iterative process, and to reduce the number of iterations required to reach a solution.
- No modifications were made to the prescribed surface tracers for the northernmost three latitude rows on the Mk3L ocean model grid, representing the region north of 79.6°N . Within this region, the model applies a spatial Fourier filter to the simulated tracers (*Phipps, 2006*), and it does not therefore respond on a gridpoint-by-gridpoint basis to external forcing. It is not therefore meaningful to use the gridpoint response of the model to modify the prescribed surface tracers.
- No modifications were made to the amplitude of the annual cycle in the prescribed sea surface salinities over the Caspian Sea, as the World Ocean Atlas 1998 sea surface salinities exhibit no annual cycle in this region.

This run shall be referred to herein as O-EFF.

In order to diagnose surface fluxes for the stand-alone atmosphere model, a 50-year atmosphere model spin-up run was also conducted. This run was identical to run A-DEF (Section 2.3.1), with the exception that the ocean currents were diagnosed from the final 100 years of run O-EFF. This run shall be referred to herein as A-EFF.

4.4.2 Convergence towards a solution

The convergence of the ocean model towards a solution is shown in Figure 4.11. Most apparent is the rapid reduction in the root-mean-square (RMS) errors in the annual-mean SST and SSS. Excluding the region north of 79.6°N , over which the only modification to the prescribed SST and SSS was a one-month phase shift, the RMS error in the annual-mean SST is reduced from 0.562°C to 0.184°C after just one iteration. Ultimately, it is reduced to 0.007°C , just 1.3% of the initial error. Likewise, the RMS error in the annual-mean SSS is reduced from 0.081 psu to

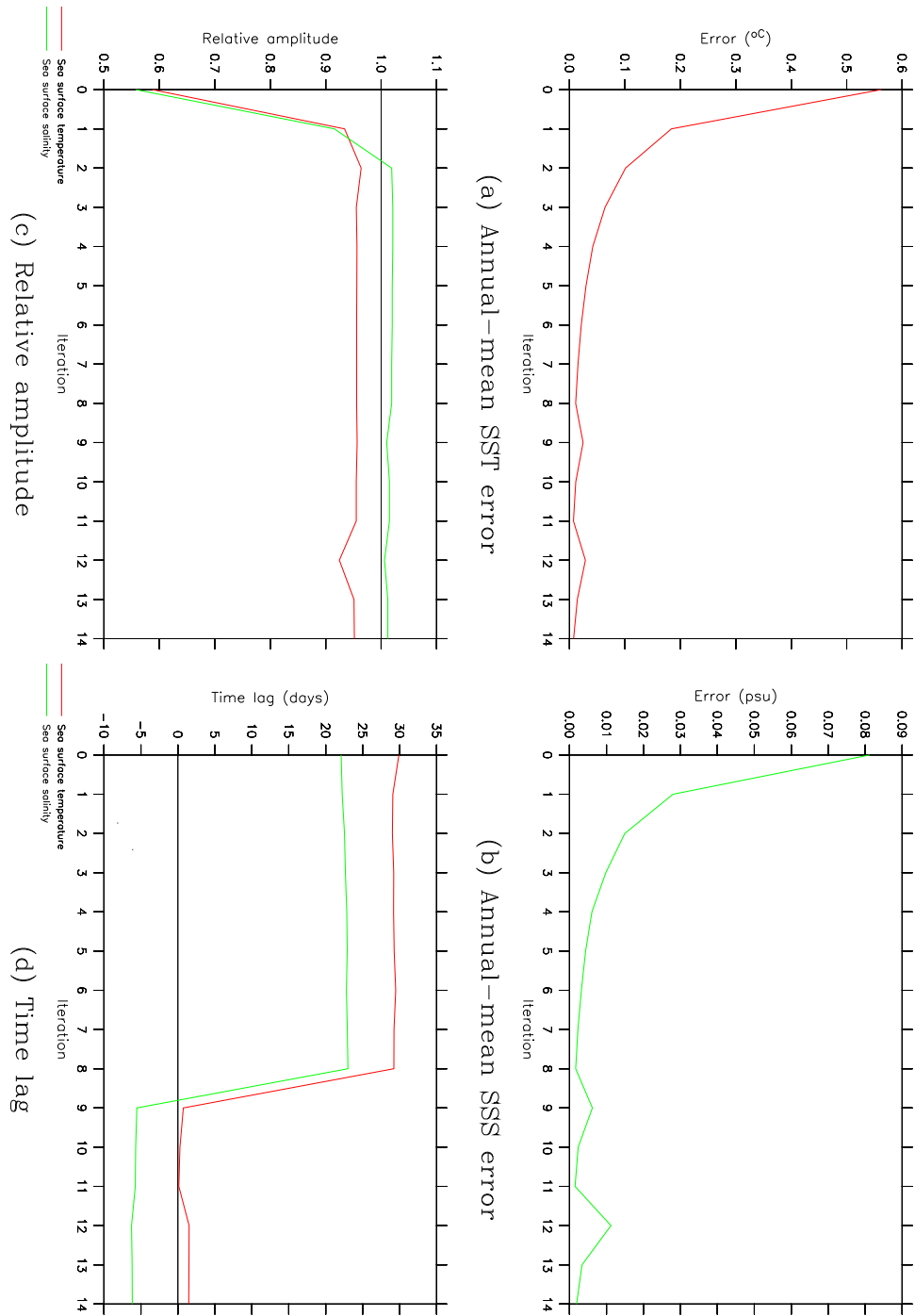


Figure 4.11: Global-mean statistics diagnosed from the final 100 years of each iteration of Mk3L ocean model run O-EFF: (a), (b) the root-mean-square error in the annual-mean sea surface temperature and sea surface salinity respectively, (c) the area-weighted global-mean relative amplitudes, and (d) the area-weighted global-mean time lags. Values north of 79.6°N are excluded; the values plotted for Iteration 0 represent those diagnosed from years 3901–4000 of run O-DEF.

0.028 psu after just one iteration, before ultimately being reduced to 0.002 psu, just 2.4% of the initial error.

The global-mean relative amplitudes increase from 0.587 to 0.952 in the case of the SST, and from 0.558 to 1.012 in the case of the SSS. The one-month phase shift in the effective surface tracers is successful in reducing the global-mean time lags to +1.5 days and -6.2 days, in the case of SST and SSS respectively.

The fact that most of the improvement in the simulated climate is achieved after just one iteration suggests that this approach could be applied to the output of other ocean models, *without* the need to conduct any iterative process. The effective surface tracers diagnosed from the output of an existing spin-up run would be sufficient, when used as the boundary conditions on a further run, to significantly reduce the errors in the simulated annual-mean SST and SSS, and to considerably improve the amplitudes of the simulated annual cycles.

4.4.3 The effective surface tracers

Figure 4.12 shows the annual-mean effective surface tracers diagnosed from run O-EFF. As would clearly be expected, the modifications to the World Ocean Atlas 1998 dataset are opposite in sign to the initial errors in the simulated annual-mean SST and SSS (Figure 3.5); however, they are also comparable in magnitude, not exceeding 4.89°C and 0.835 psu in the case of SST and SSS respectively.

Figure 4.13 shows the amplitudes of the annual cycle in the effective surface tracers, and compares them to the amplitudes of the annual cycle in the World Ocean Atlas 1998 dataset. The modifications to the amplitude of the World Ocean Atlas 1998 SST are generally small, but increase in the regions where the initial response of the model was weakest (Figure 3.6a). The amplitude is reduced at some high-latitude locations, particularly in the Southern Ocean, as a result of the constraint that the effective SST cannot be less than -2.1°C. The modifications to the amplitude of the World Ocean Atlas 1998 SSS are highly spatially variable, consistent with the initial response of the model (Figure 3.6b).

4.4.4 The model response

The errors in the simulated annual-mean SST and SSS, diagnosed from the final 100 years of run O-EFF, are shown in Figure 4.14. (Values for the region north of 79.6°N, over which the only modification to the prescribed SST and SSS was a one-month phase shift, are excluded; however the errors in the annual-mean SST and SSS do not exceed 0.87°C and 0.48 psu respectively.) The errors can be seen to be very small, being smaller in magnitude than 0.01°C and 0.004 psu over 92% and 97% of the surface of the ocean respectively.

The relative amplitudes are shown in Figure 4.15. North of 79.6°N, where no modifications were made to the annual cycles of the prescribed surface tracers, the response of the model is weak. The simulated amplitude of the annual cycle in the SST is also poor at other high-latitude locations; this arises from the suppression of the annual cycle in the effective SST, as a result of the constraint that the effective SST may not be less than -2.1°C. Otherwise the response of the model is excellent; over the region south of 79.6°N, the relative amplitudes lie between 0.9 and 1.1 over

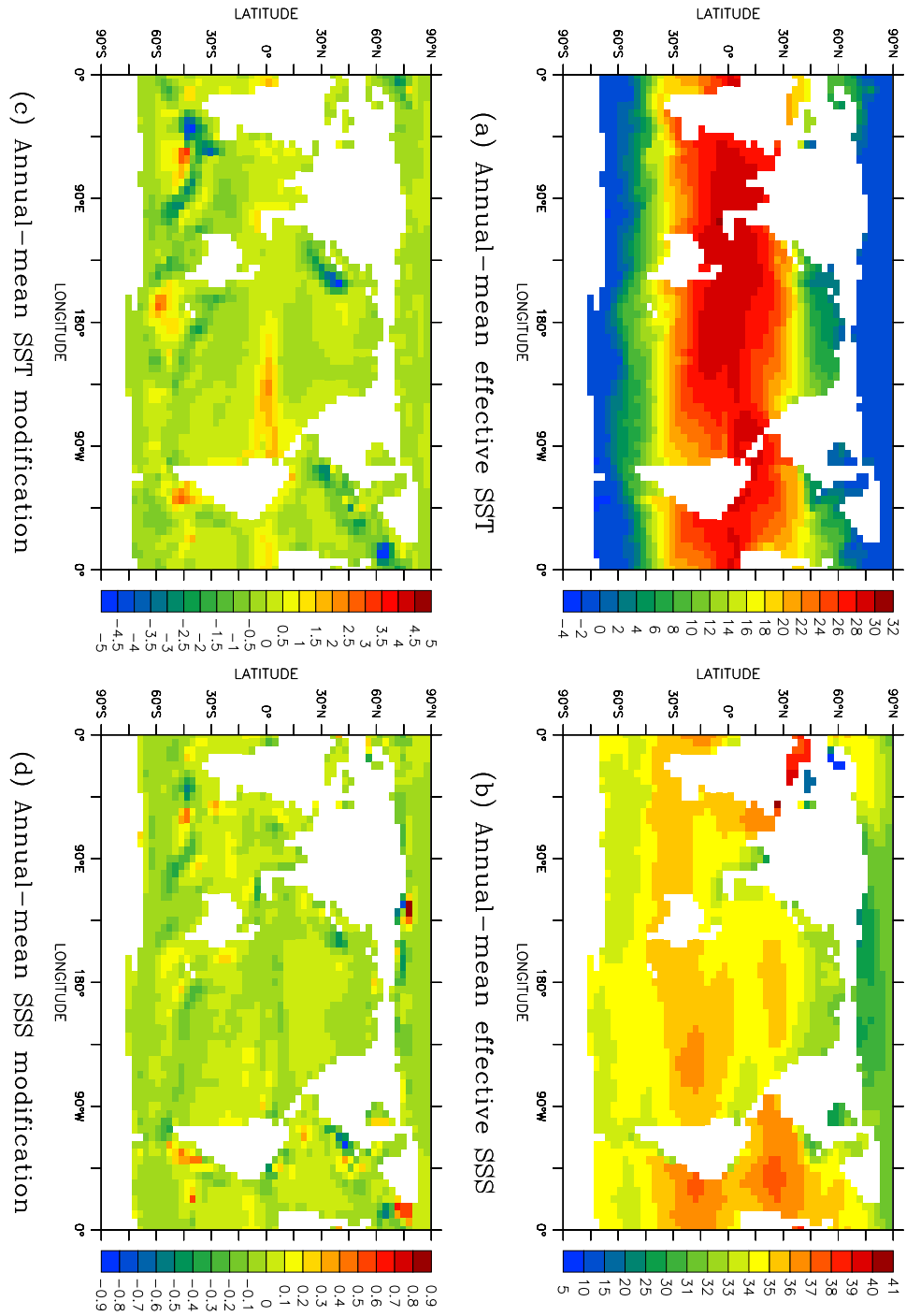


Figure 4.12: The annual-mean effective sea surface temperature (SST, °C) and sea surface salinity (SSS, psu) diagnosed from Mk3L ocean model run O-EFF: (a), (b) the annual-mean effective SST and SSS respectively, and (c), (d) the annual-mean modification to the World Ocean Atlas 1998 SST and SSS respectively.

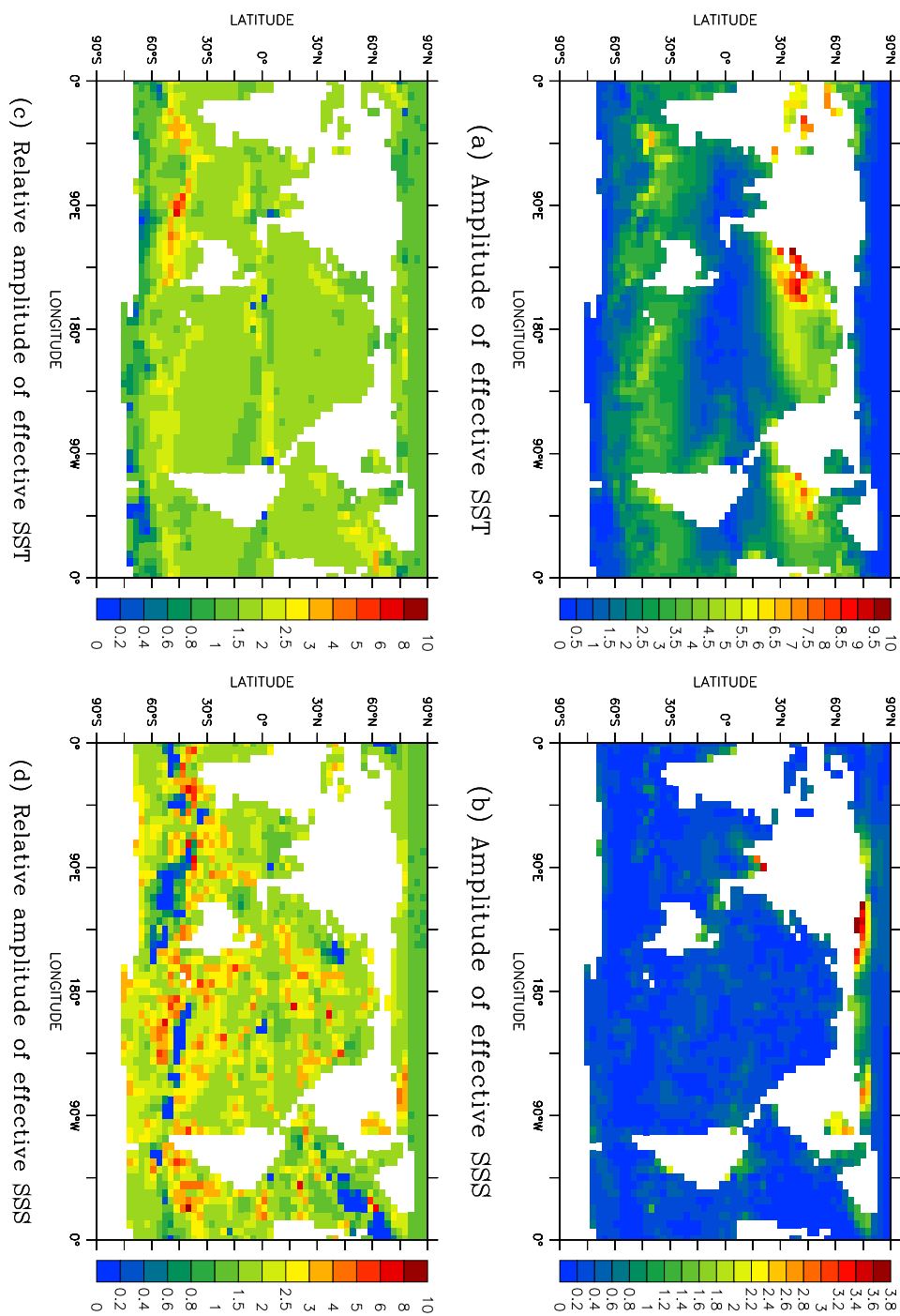
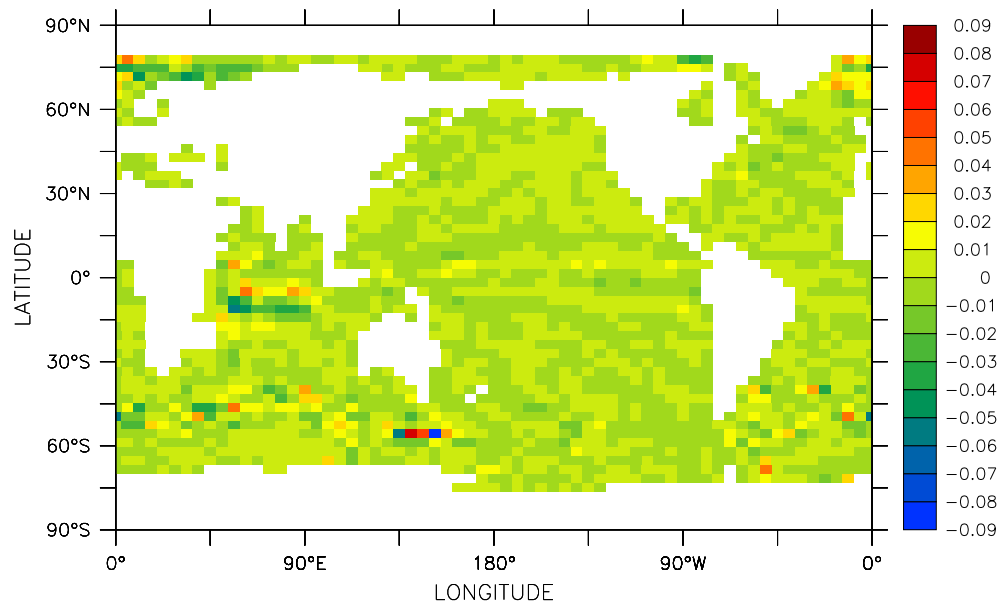
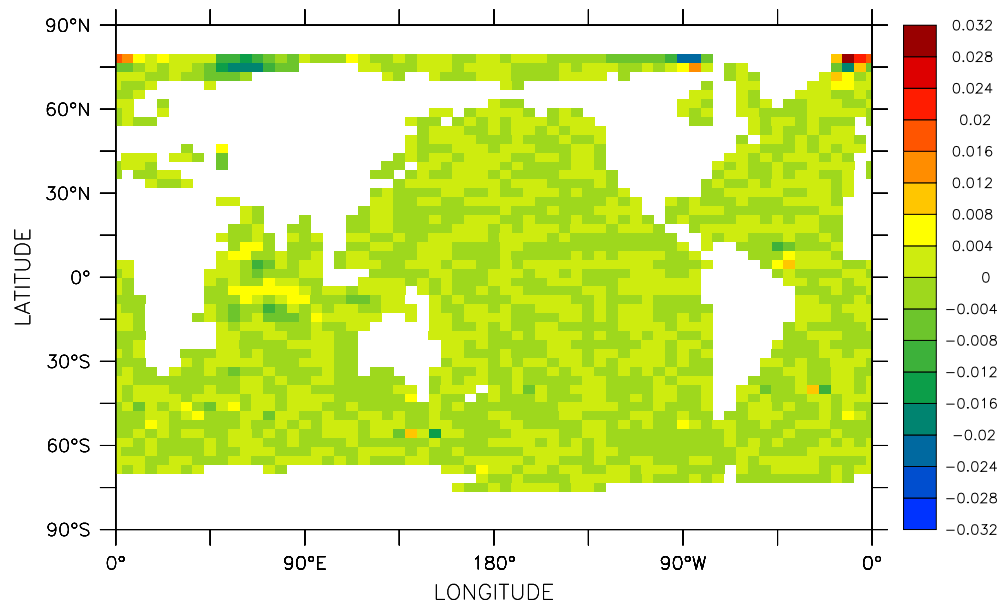


Figure 4.13: The amplitudes of the annual cycle in the effective sea surface temperature (SST, °C) and sea surface salinity (SSS, psu) diagnosed from Mk3L ocean model run O-EFF: (a), (b) the amplitudes of the annual cycle in the effective SST and SSS respectively, and (c), (d) the amplitudes relative to the World Ocean Atlas 1998 SST and SSS respectively.



(a) Sea surface temperature



(b) Sea surface salinity

Figure 4.14: The annual-mean sea surface temperature and salinity for Mk3L ocean model run O-EFF (averages for the final 100 years), expressed as anomalies relative to the World Ocean Atlas 1998: (a) sea surface temperature ($^{\circ}\text{C}$), and (b) sea surface salinity (psu).

	World Ocean Atlas 1998	Mk3L ocean model	
		Run O-DEF	Run O-EFF
Ross Sea	28.06	27.76	28.01
Weddell Sea	27.98	27.73	27.87
Nordic Seas	27.96	27.72	27.88

Table 4.5: The peak surface σ_θ (kgm^{-3}) in regions of deep water formation: the World Ocean Atlas 1998, and Mk3L ocean model runs O-DEF and O-EFF (averages for the final 100 years of each run). The World Ocean Atlas 1998 data has been area-averaged onto the Mk3L ocean model grid.

89% of the surface of the ocean in the case of the SST, and 96% in the case of the SSS.

The response of the model is weak at some locations in the tropics. This can be attributed, in part, to the relatively small number of iterations which were conducted, and particularly the fact that only three iterations were conducted under synchronous timestepping. The switch from asynchronous to synchronous timestepping led to some changes in the tropical climate, and three iterations appears to have been insufficient to have allowed the effective surface tracers to adapt accordingly. It is also possible that, at these locations, diffusive and advective processes are sufficiently strong that the surface boundary conditions have little effect upon the amplitude of the simulated annual cycle.

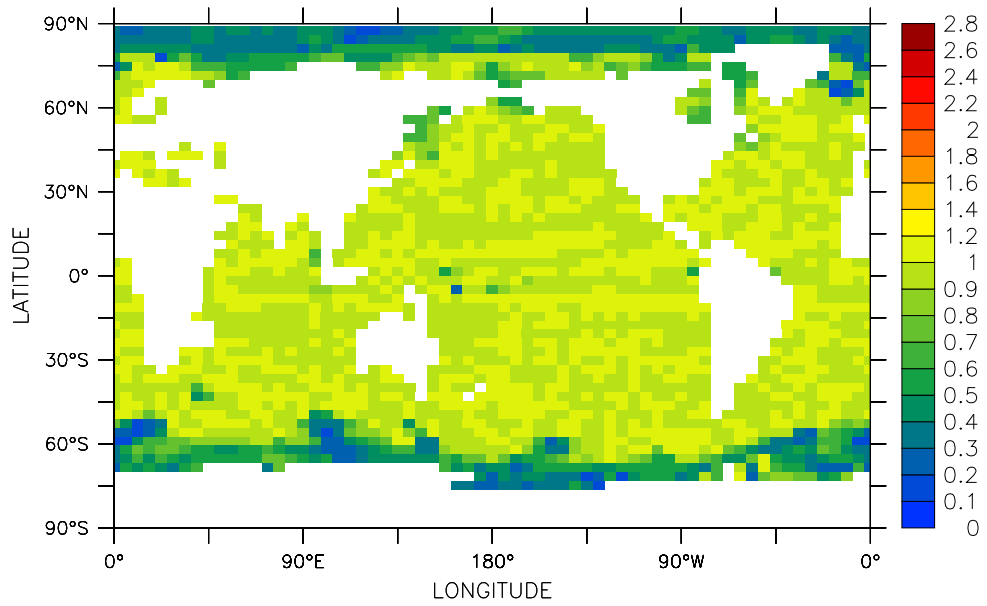
At other locations, the amplitude of the annual cycle in the simulated SSS is too strong, exceeding the observed amplitude even when the amplitude of the annual cycle in the effective SSS is reduced to zero. This can be attributed to an annual cycle in the fluxes of salt through the lateral walls and base of these gridboxes, in which case modification of the prescribed surface tracers is not sufficient to cause the amplitude of the simulated annual cycle to match observations.

The lags between the simulated and World Ocean Atlas 1998 SST and SSS are shown in Figure 4.16. Apart from a few locations at which the lags do not appear to have meaningful values, they are tightly clustered around zero, lying between -10 and +10 days over 95% of the surface of the ocean in the case of the SST, and 71% in the case of the SSS.

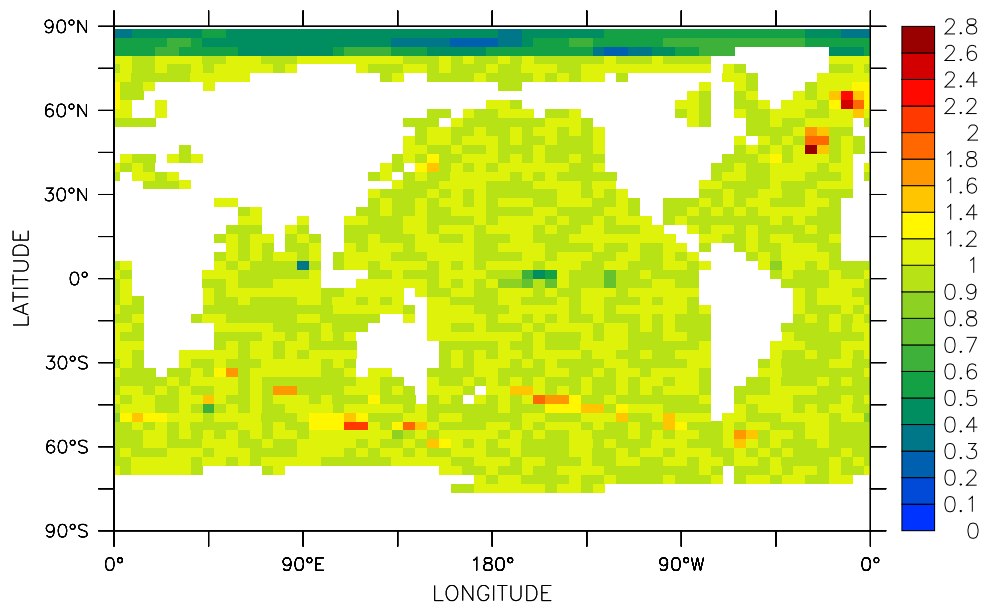
4.4.5 Densities of high-latitude surface waters

Figure 4.17 shows the peak surface water densities, as implied by the effective surface tracers, and as simulated by the Mk3L ocean model; the peak values encountered in the key regions of deep water formation are also shown in Table 4.5. The values implied by the effective surface tracers exhibit considerably greater spatial variability than those implied by the World Ocean Atlas 1998 dataset (Figure 3.1). In the Southern Hemisphere, the highest value of 29.55 kgm^{-3} occurs in Prydz Bay, with maximum values of 28.78 and 28.57 kgm^{-3} in the Ross and Weddell Seas respectively. In the Northern Hemisphere, the highest value of 32.63 kgm^{-3} occurs in Hudson Bay; the maximum value in the Nordic Seas is 28.82 kgm^{-3} .

The simulated high-latitude surface waters have peak densities in the Southern



(a) Sea surface temperature



(b) Sea surface salinity

Figure 4.15: The relative amplitudes for Mk3L ocean model run O-EFF (averages for the final 100 years): (a) sea surface temperature, and (b) sea surface salinity.

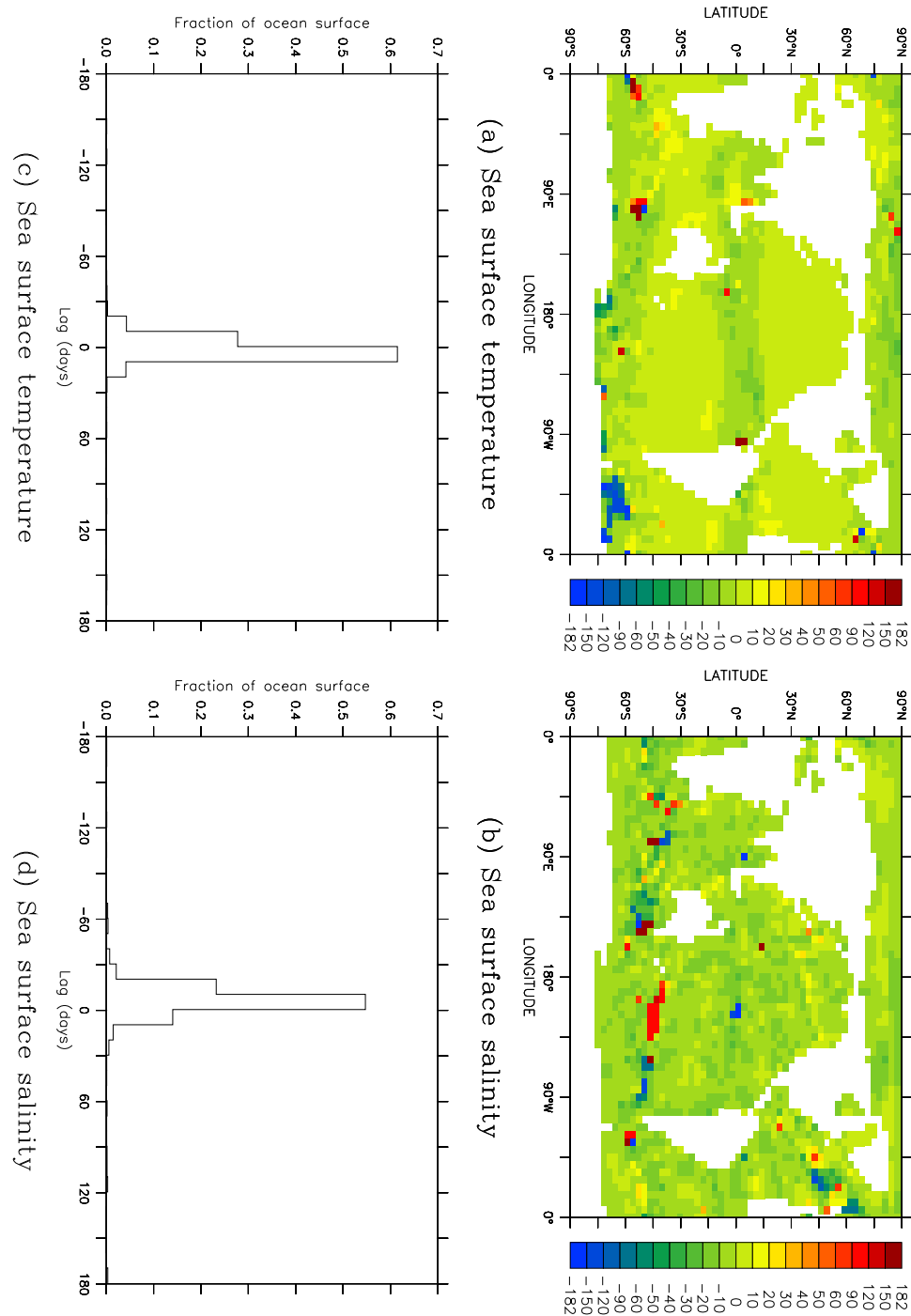


Figure 4.16: The lag of maximum correlation (days) between Mk3L ocean model run O-EFF (average for the final 100 years) and the World Ocean Atlas 1998: (a), (b) the lag at each gridpoint, sea surface temperature and sea surface salinity respectively, and (c), (d) the fraction of the surface area of the ocean over which the lags lie within the ranges shown, sea surface temperature and sea surface salinity respectively.

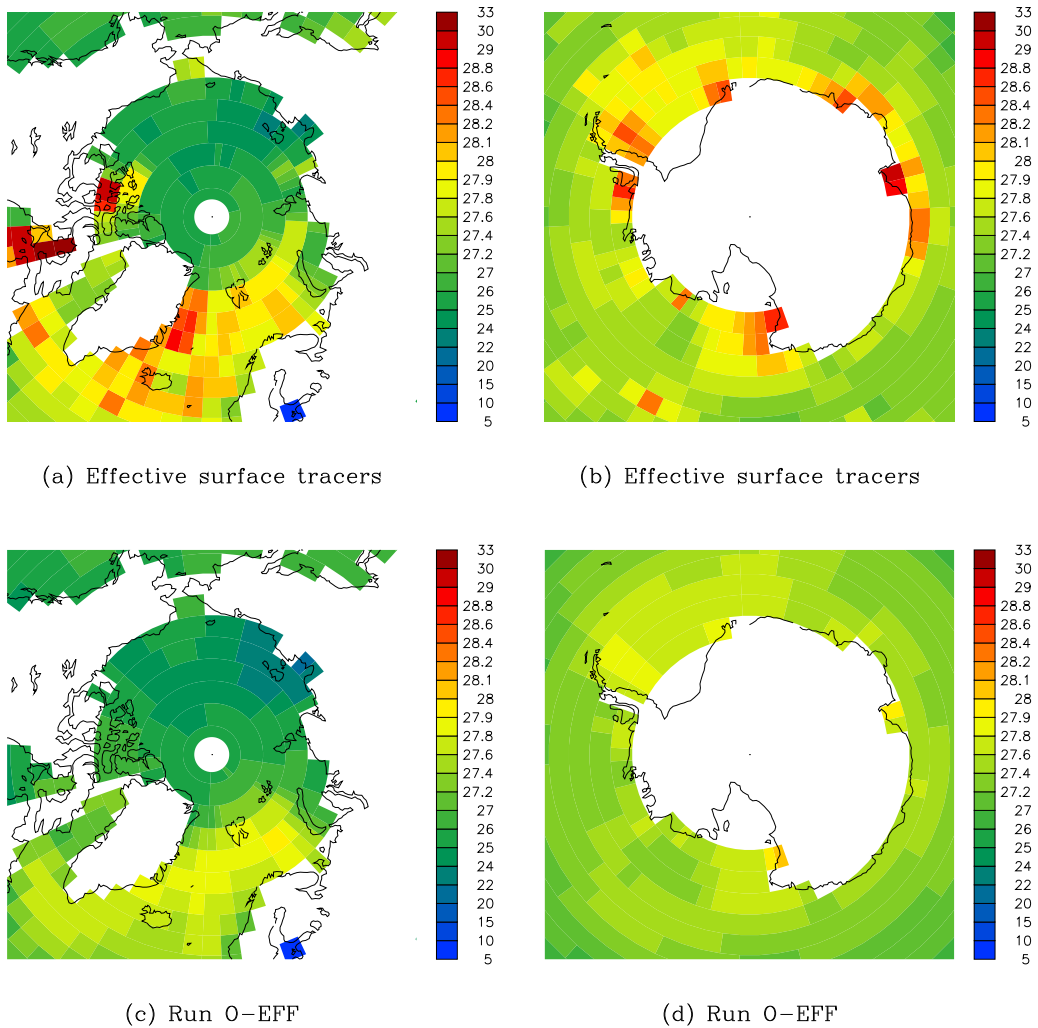


Figure 4.17: The annual-maximum σ_θ (kgm^{-3}): (a), (b) implied by the effective surface tracers diagnosed from Mk3L ocean model run O-EFF, and (c), (d) for Mk3L ocean model run O-EFF (average for the final 100 years).

		World Ocean Atlas 1998	Mk3L ocean model	
			O-DEF	O-EFF
Potential temperature (°C)	0–800 m	9.61	10.88	10.15
	800–2350 m	2.98	3.08	2.85
	2350–4600 m	1.36	0.35	0.73
Salinity (psu)	0–800 m	34.75	34.69	34.78
	800–2350 m	34.68	34.50	34.68
	2350–4600 m	34.74	34.46	34.69
σ_θ (kgm^{-3})	0–800 m	26.60	26.32	26.52
	800–2350 m	27.62	27.45	27.63
	2350–4600 m	27.81	27.64	27.81

Table 4.6: Global-mean potential temperature (°C), salinity (psu), and σ_θ (kgm^{-3}): the World Ocean Atlas 1998, and Mk3L ocean model runs O-DEF and O-EFF (averages for the final 100 years of each run). The World Ocean Atlas 1998 has been volume-averaged onto the Mk3L ocean model grid.

Hemisphere of 28.01 kgm^{-3} in the southwestern Ross Sea, 27.95 kgm^{-3} in Prydz Bay and 27.87 kgm^{-3} in the Weddell Sea. In the Northern Hemisphere, the highest density of 27.91 kgm^{-3} occurs in the Barents Sea, with a maximum density of 27.88 kgm^{-3} in the Nordic Seas. Relative to the World Ocean Atlas 1998, the peak surface water densities in the key regions of deep water formation are too buoyant by $\sim 0.05\text{--}0.11 \text{ kgm}^{-3}$. While this bias can be attributed to the constraint imposed on the effective sea surface temperatures, it represents a considerable improvement on the bias of $\sim 0.25\text{--}0.3 \text{ kgm}^{-3}$ exhibited by run O-DEF (Section 3.3).

Figures 4.18, 4.19 and 4.20 show the annual cycle in sea surface temperature, salinity and density, for the deep water formation regions of the southwestern Ross Sea, western Weddell Sea and the Nordic Seas. Values are plotted for the World Ocean Atlas 1998, the effective surface tracers, and Mk3L ocean model runs O-DEF and O-EFF.

Relative to the World Ocean Atlas 1998, the amplification of the annual cycle in the effective surface tracers is apparent, as is the one-month phase shift. It is also apparent that the effective surface tracers are successful at bringing the simulated surface water properties into much better agreement with the observational values.

4.4.6 Water properties

Figure 4.21 shows the vertical profiles of potential temperature, salinity and potential density, for the World Ocean Atlas 1998 and for Mk3L ocean model runs O-DEF and O-EFF. Mean values for the upper, mid- and deep ocean, as defined in Chapter 2, are also shown in Table 4.6. The effective surface tracers lead to significantly improved deep water properties, with the density of the deep ocean agreeing with the World Ocean Atlas 1998 to better than 0.01 kgm^{-3} .

Zonal-mean values for the potential temperature, salinity and potential density are shown in Figures 4.22, 4.23 and 4.24. They can be compared with the equivalent values for run O-DEF, which are shown in Figures 2.14, 2.15 and 2.16. While a slight

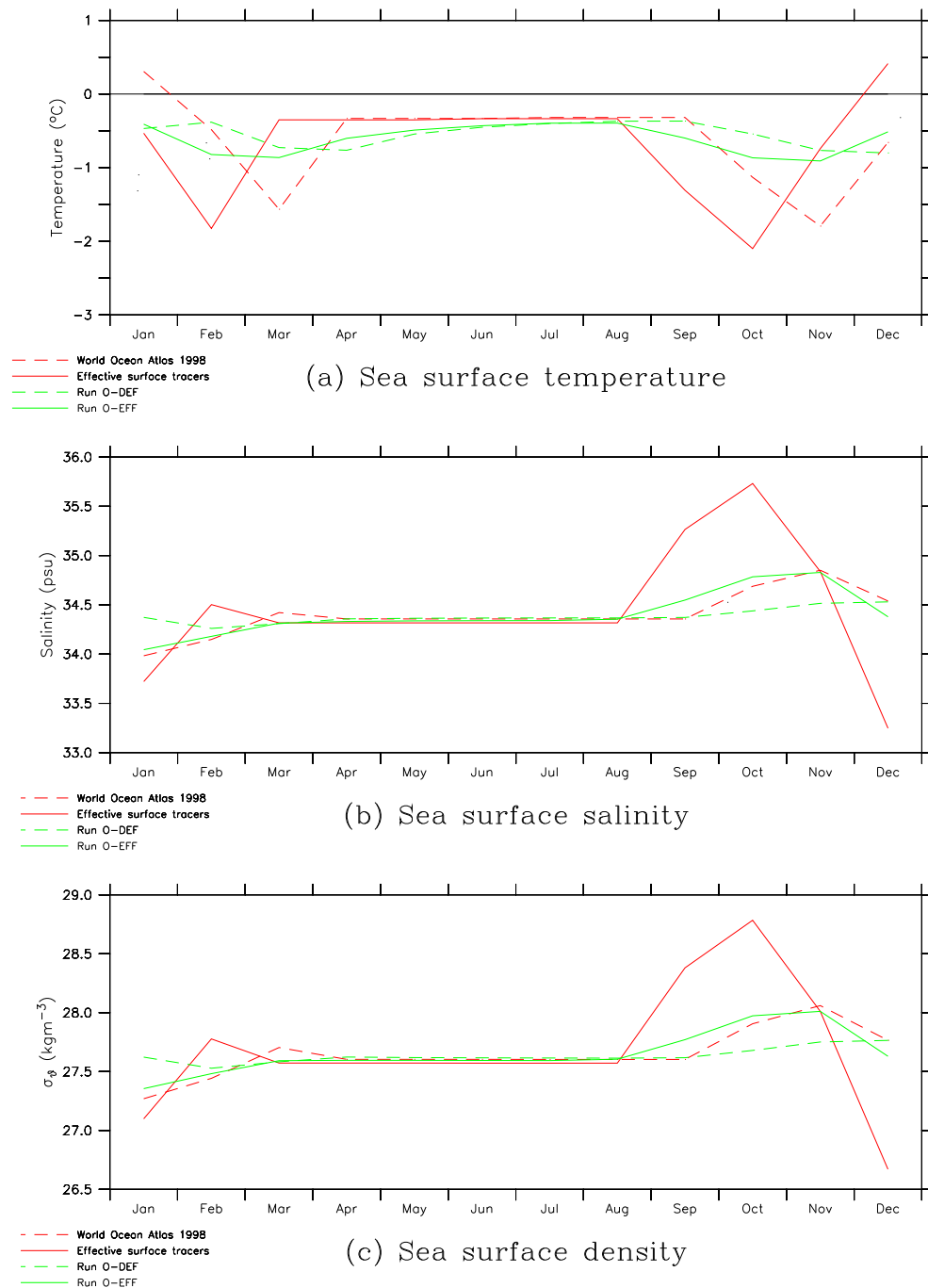


Figure 4.18: The monthly-mean sea surface temperature, salinity and σ_θ in the southwestern Ross Sea, for the World Ocean Atlas 1998 (dashed red), the effective surface tracers (red), and Mk3L ocean model runs O-DEF (dashed green) and O-EFF (green): (a) sea surface temperature, (b) sea surface salinity, and (c) sea surface σ_θ . The values plotted are for the gridpoint located at 163°E, 75°S. The World Ocean Atlas 1998 data has been area-averaged onto the Mk3L ocean model grid; the values for Mk3L are averages for the final 100 years of each run.

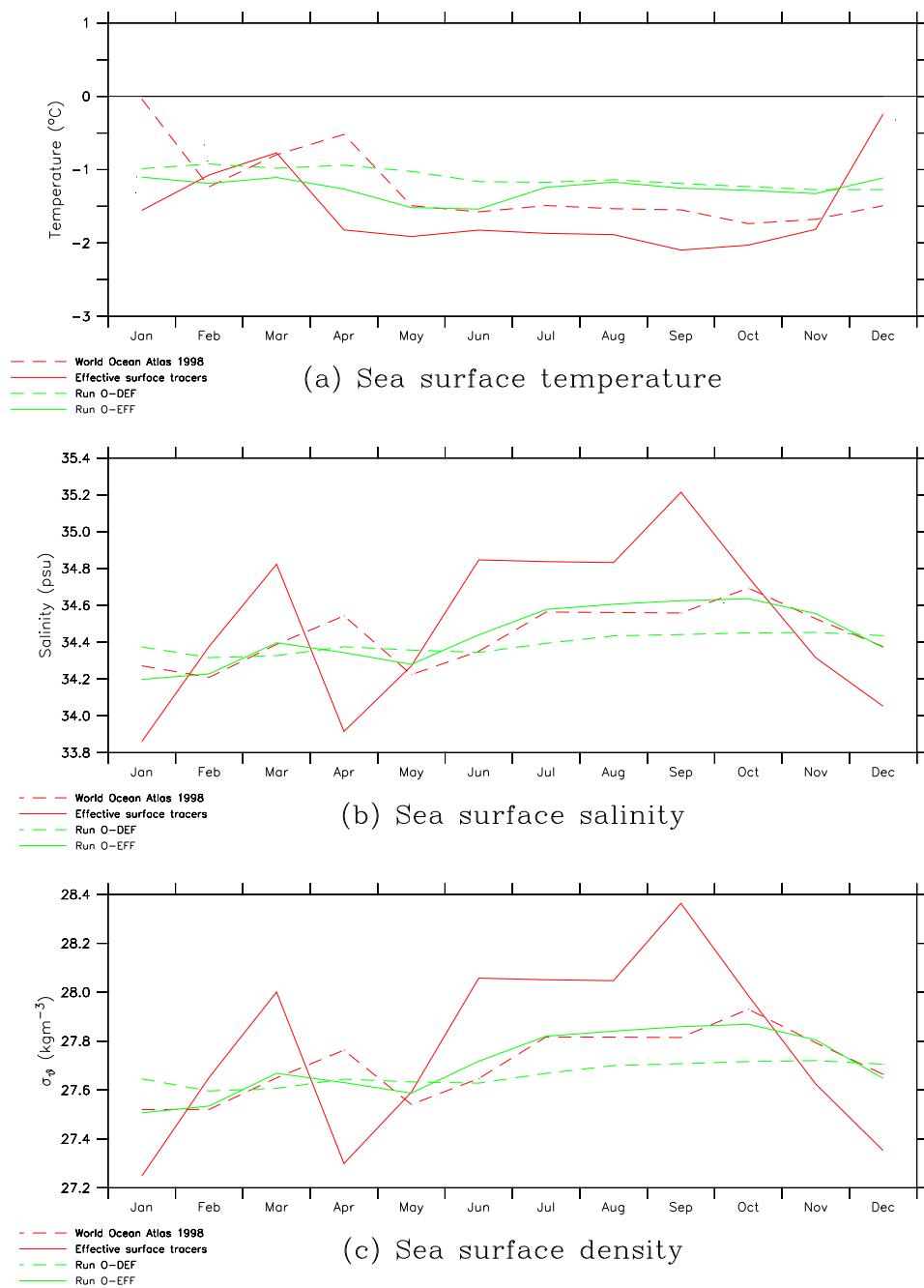


Figure 4.19: The monthly-mean sea surface temperature, salinity and σ_θ in the western Weddell Sea, for the World Ocean Atlas 1998 (dashed red), the effective surface tracers (red), and Mk3L ocean model runs O-DEF (dashed green) and O-EFF (green): (a) sea surface temperature, (b) sea surface salinity, and (c) sea surface σ_θ . The values plotted are the averages for the two gridpoints located at 56°W , 72°S , and 56°W , 68°S . The World Ocean Atlas 1998 data has been area-averaged onto the Mk3L ocean model grid; the values for Mk3L are averages for the final 100 years of each run.

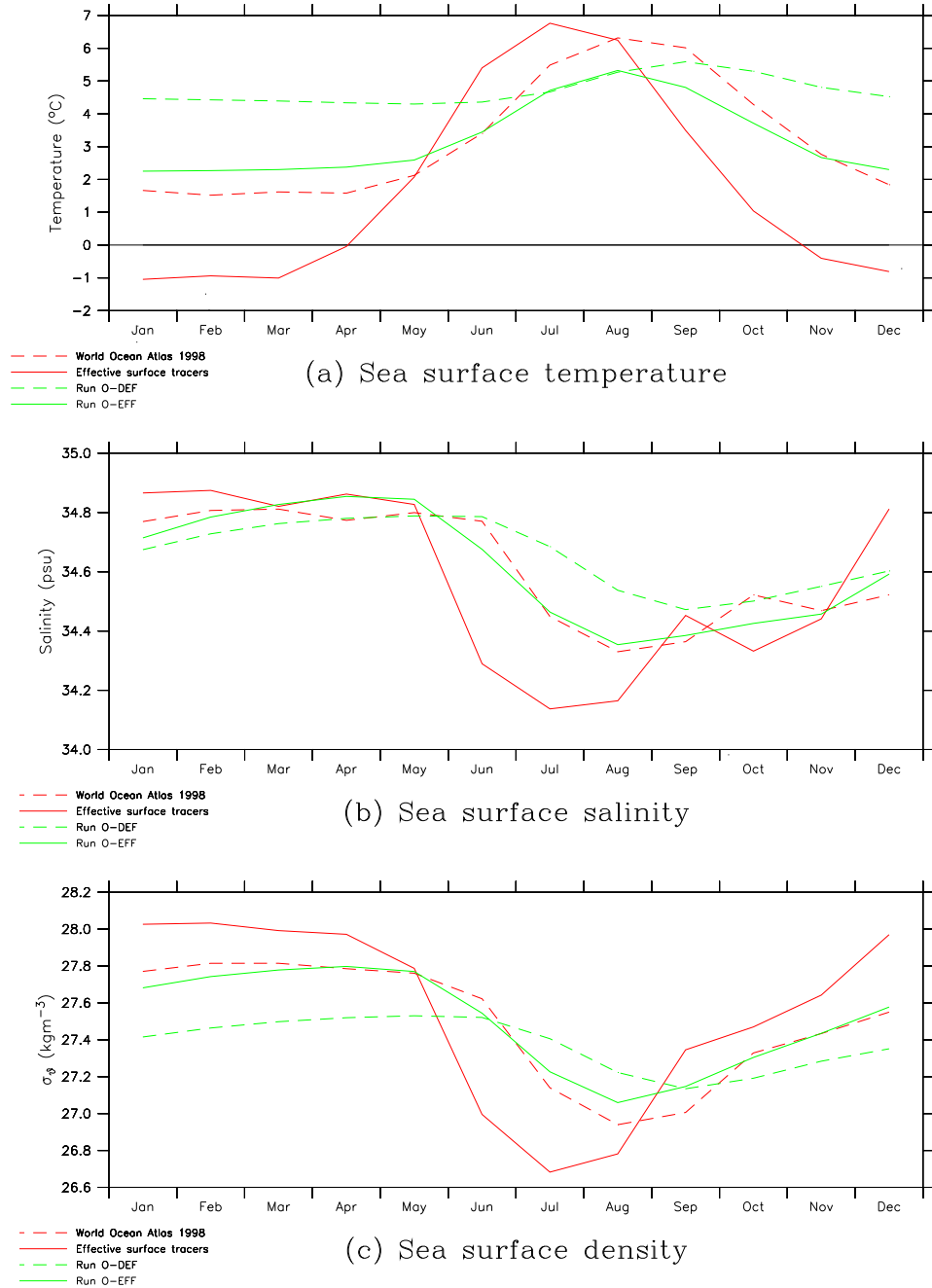


Figure 4.20: The monthly-mean sea surface temperature, salinity and σ_θ in the Nordic (Greenland-Iceland-Norwegian) Seas, for the World Ocean Atlas 1998 (dashed red), the effective surface tracers (red), and Mk3L ocean model runs O-DEF (dashed green) and O-EFF (green): (a) sea surface temperature, (b) sea surface salinity, and (c) sea surface σ_θ . The values plotted are averages for the 12 gridpoints which cover the region 14°W – 8°E , 67° – 76°N . The World Ocean Atlas 1998 data has been area-averaged onto the Mk3L ocean model grid; the values for Mk3L are averages for the final 100 years of each run.

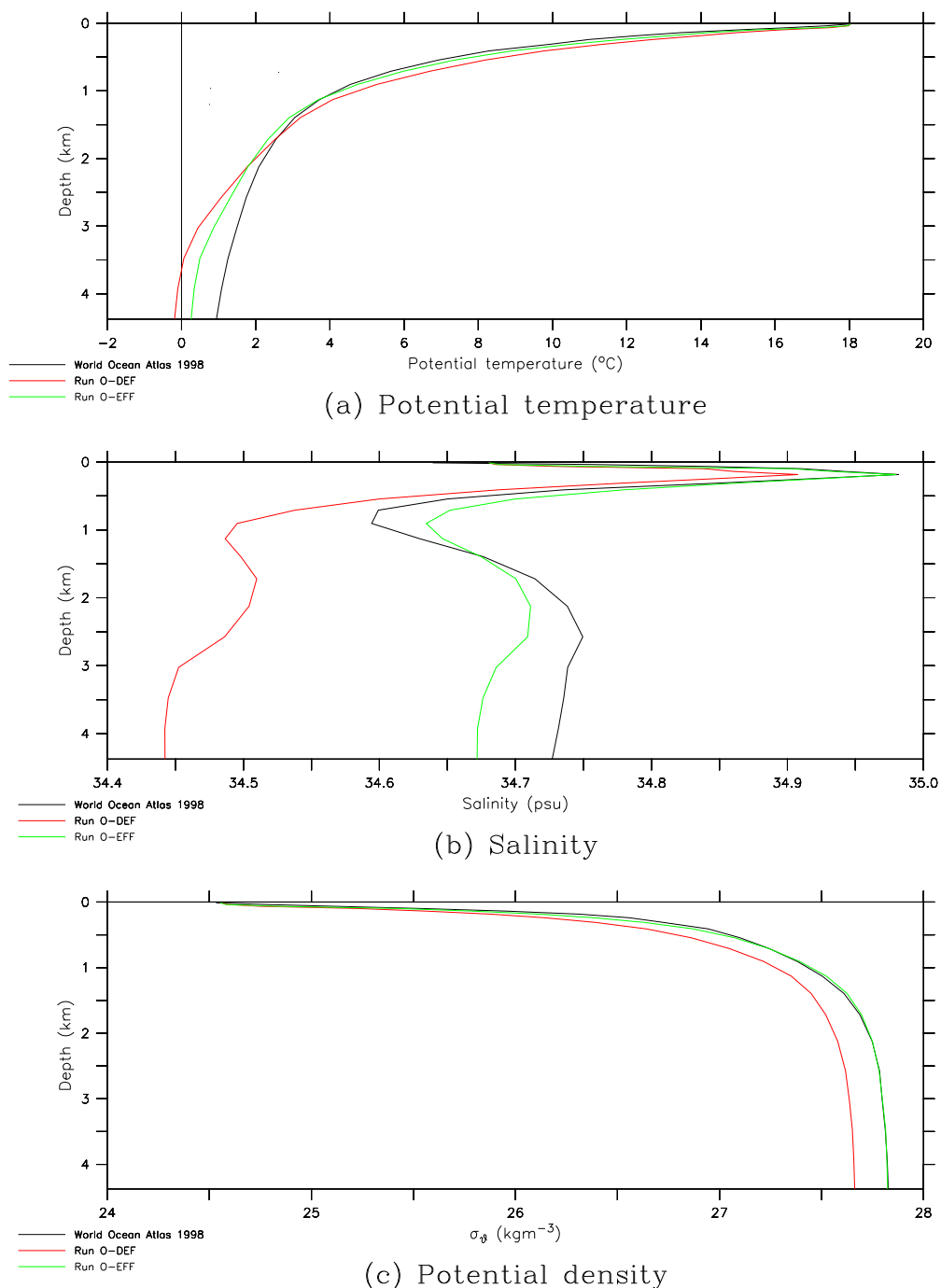


Figure 4.21: The global-mean potential temperature, salinity and σ_θ on each model level for the World Ocean Atlas 1998 (black), and for Mk3L ocean model runs O-DEF (red) and O-EFF (green): (a) potential temperature, (b) salinity, and (c) σ_θ . The World Ocean Atlas 1998 data has been volume-averaged onto the Mk3L ocean model grid. All values for Mk3L are averages for the final 100 years of each run.

cold bias remains in the simulated deep ocean, the deep ocean salinities and densities are in excellent agreement with the World Ocean Atlas 1998.

The Arctic Ocean is an exception, however, remaining too warm, too fresh and too buoyant at depth. It was shown in Section 4.2 that an enhancement of ~ 1 psu to the World Ocean Atlas 1998 sea surface salinities, in the presence of sea ice, led to much more realistic deep water properties in the Arctic Ocean. The failure of run O-EFF to correctly simulate the temperature and salinity of the deep Arctic Ocean, when it successfully simulates the deep water properties of the remainder of the world ocean, may further suggest that there is a “fair weather” bias in the World Ocean Atlas 1998 sea surface temperatures and salinities over the Arctic Ocean. However, this failure may also arise from the fact that, with the exception of a phase shift, no modifications were made to the prescribed surface tracers over the region north of 79.6°N .

4.4.7 Circulation

The meridional overturning streamfunctions for the world ocean, and for the Atlantic and Pacific/Indian Oceans, are shown in Figure 4.25; they can be compared with the streamfunctions diagnosed from run O-DEF, which are shown in Figure 2.17. The increased peak surface water density in the Nordic Seas leads to an increase in the rate of North Atlantic Deep Water (NADW) formation, from 13.6 Sv for run O-DEF to 16.4 Sv for run O-EFF. As a result of the increased stratification of the water column, however, the rate of Antarctic Bottom Water (AABW) formation weakens from 9.5 to 8.5 Sv.

The rates of formation of both NADW and AABW are therefore consistent with observational estimates (Section 2.5.2).

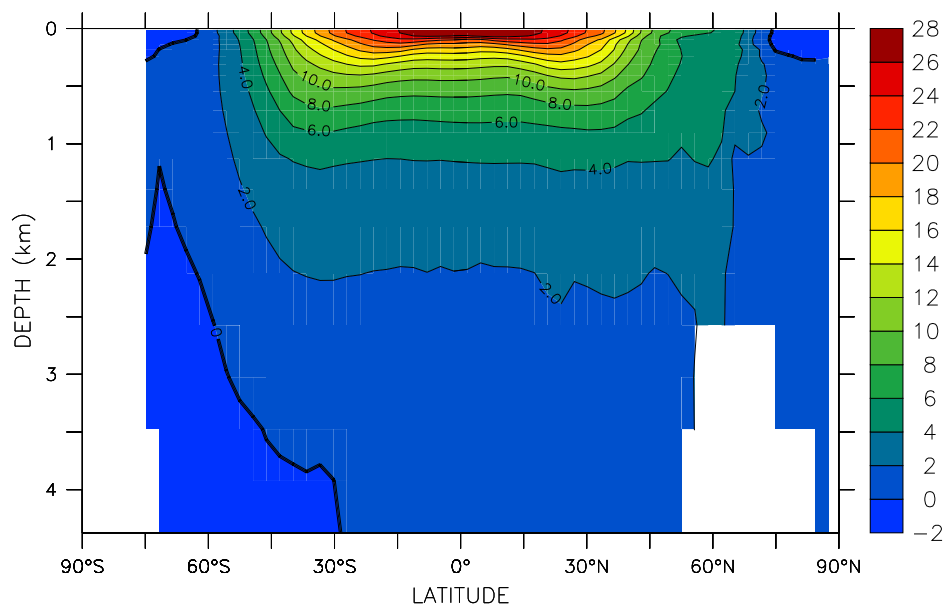
4.4.8 Transport

The oceanic meridional transports of heat and salt, as simulated by the ocean model and as implied by the atmosphere model, are shown in Figure 4.26. The values diagnosed from runs O-EFF and A-EFF are compared with those diagnosed from runs O-DEF and A-DEF. The increased meridional overturning in the North Atlantic leads to increased northward heat transport, bringing the simulated heat transports into better agreement with the values implied by the atmosphere model; this indicates a reduction in the magnitude of the zonal-mean heat flux adjustments.

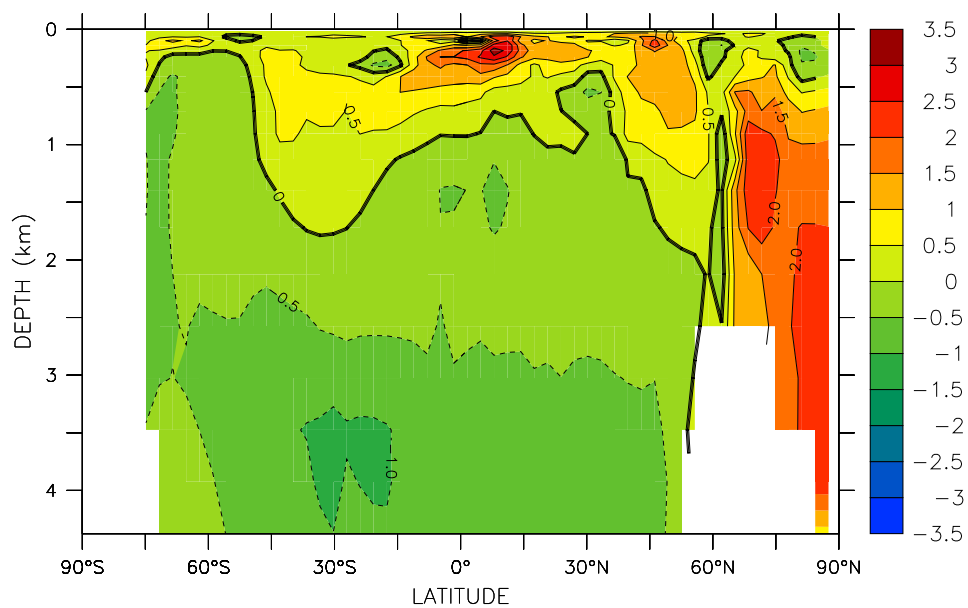
There is little change to the simulated oceanic salt transport, although there is better agreement with the values implied by the atmosphere model at high latitudes in the Southern Hemisphere.

4.4.9 Surface fluxes

Figure 4.27 shows the annual-mean surface fluxes, and the amplitudes of the annual cycles, diagnosed from run O-EFF. Reflecting the relatively small changes in the ocean circulation, the annual-mean surface fluxes are very similar to those diagnosed from run O-DEF (Figures 2.21b and 2.22b).

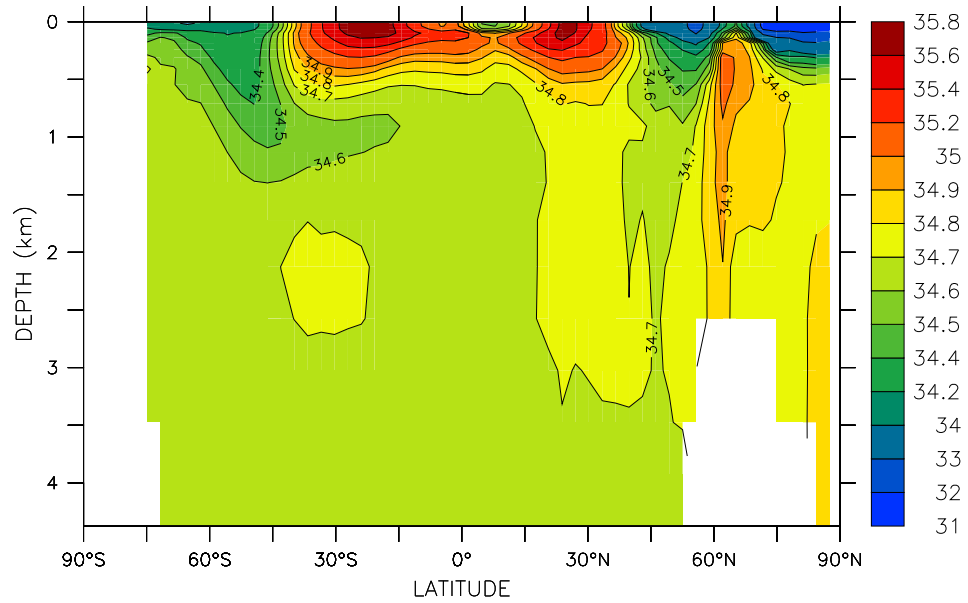


(a) Run O-EFF

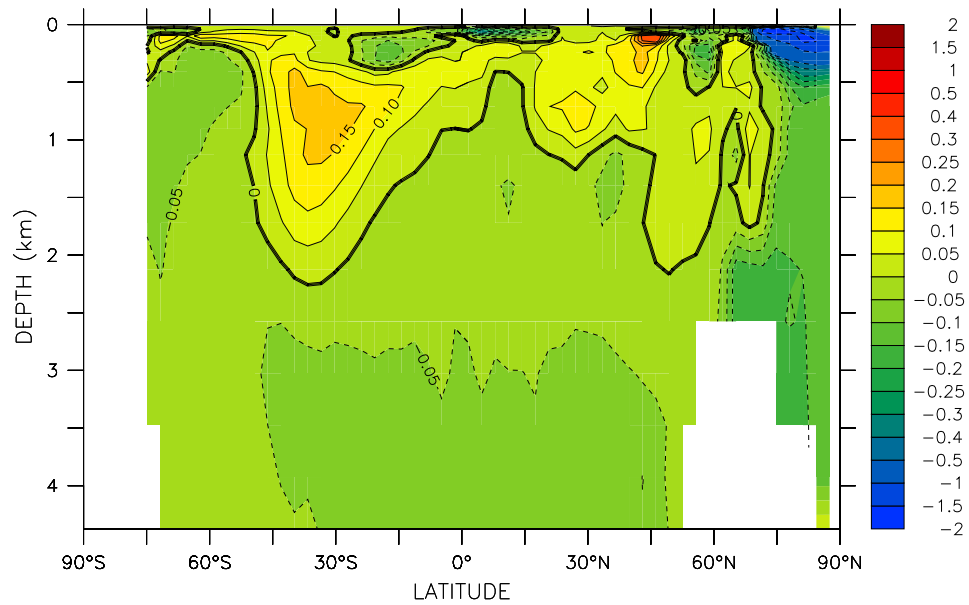


(b) Run O-EFF minus World Ocean Atlas 1998

Figure 4.22: The zonal-mean potential temperature ($^{\circ}\text{C}$) for the world ocean (excluding inland seas): (a) the Mk3L ocean model (average for the final 100 years of run O-EFF), and (b) the model discrepancy, relative to the World Ocean Atlas 1998. The World Ocean Atlas 1998 data has been volume-averaged onto the Mk3L ocean model grid.

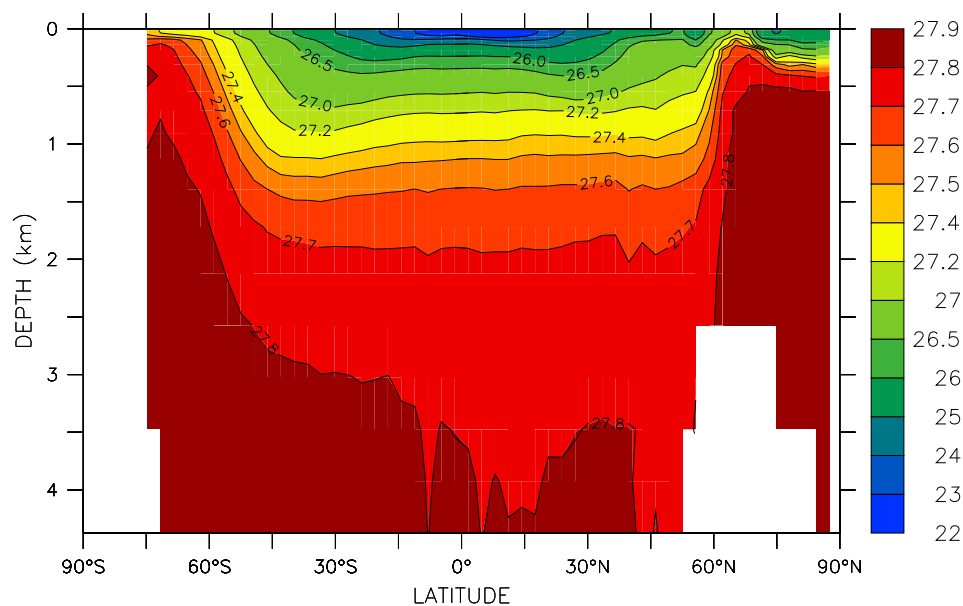


(a) Run O-EFF

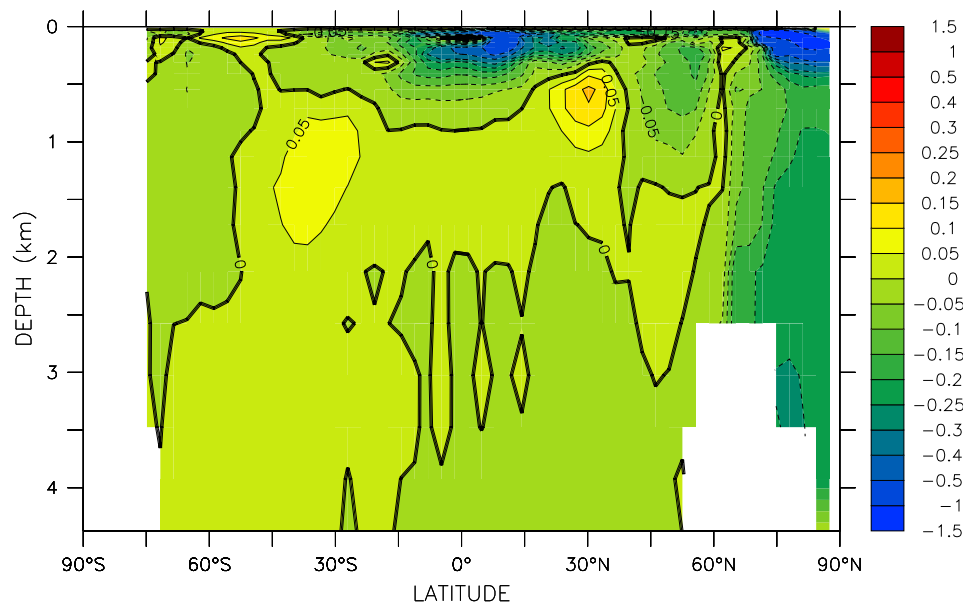


(b) Run O-EFF minus World Ocean Atlas 1998

Figure 4.23: The zonal-mean salinity (psu) for the world ocean (excluding inland seas): (a) the Mk3L ocean model (average for the final 100 years of run O-EFF), and (b) the model discrepancy, relative to the World Ocean Atlas 1998. The World Ocean Atlas 1998 data has been volume-averaged onto the Mk3L ocean model grid.

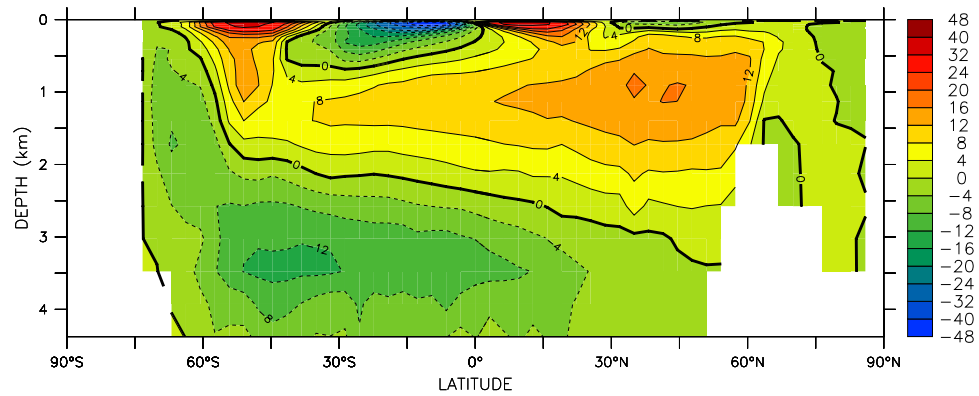


(a) Run O-EFF

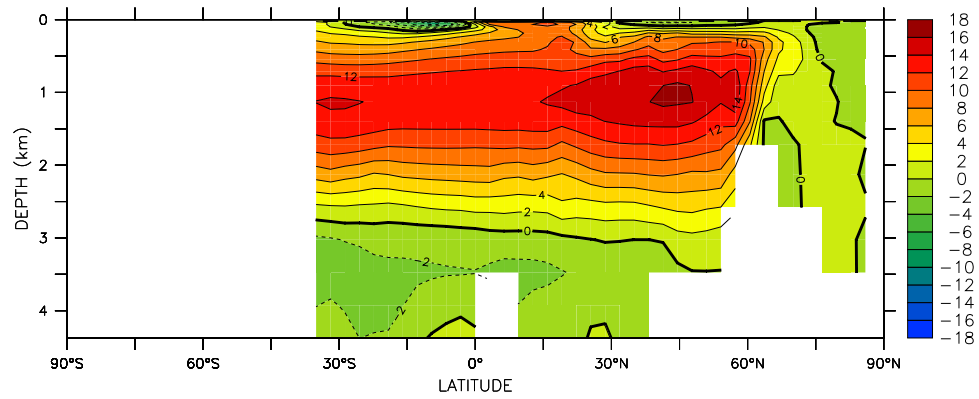


(b) Run O-EFF minus World Ocean Atlas 1998

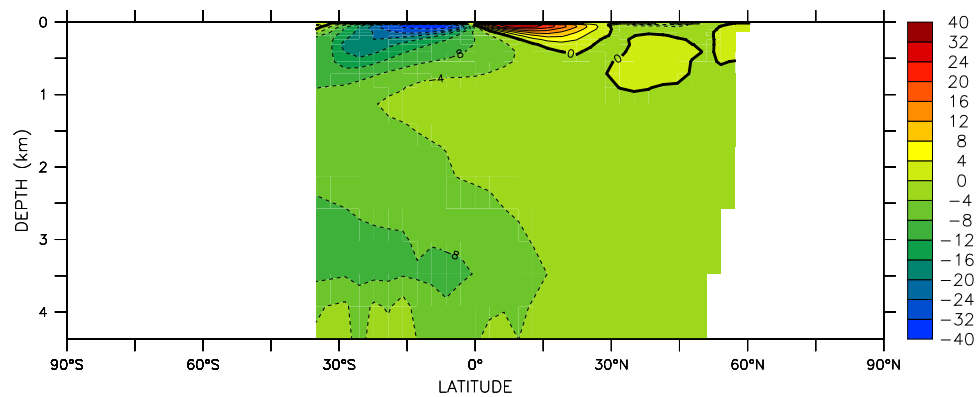
Figure 4.24: The zonal-mean σ_θ (kgm^{-3}) for the world ocean (excluding inland seas): (a) the Mk3L ocean model (average for the final 100 years of run O-EFF), and (b) the model discrepancy, relative to the World Ocean Atlas 1998. The World Ocean Atlas 1998 data has been volume-averaged onto the Mk3L ocean model grid.



(a) World Ocean



(b) Atlantic Ocean



(c) Pacific/Indian Oceans

Figure 4.25: Meridional overturning streamfunctions (S_v) for the Mk3L ocean model (averages for the final 100 years of run O-EFF): (a) the world ocean, (b) the Atlantic Ocean, and (c) the Pacific/Indian Oceans.

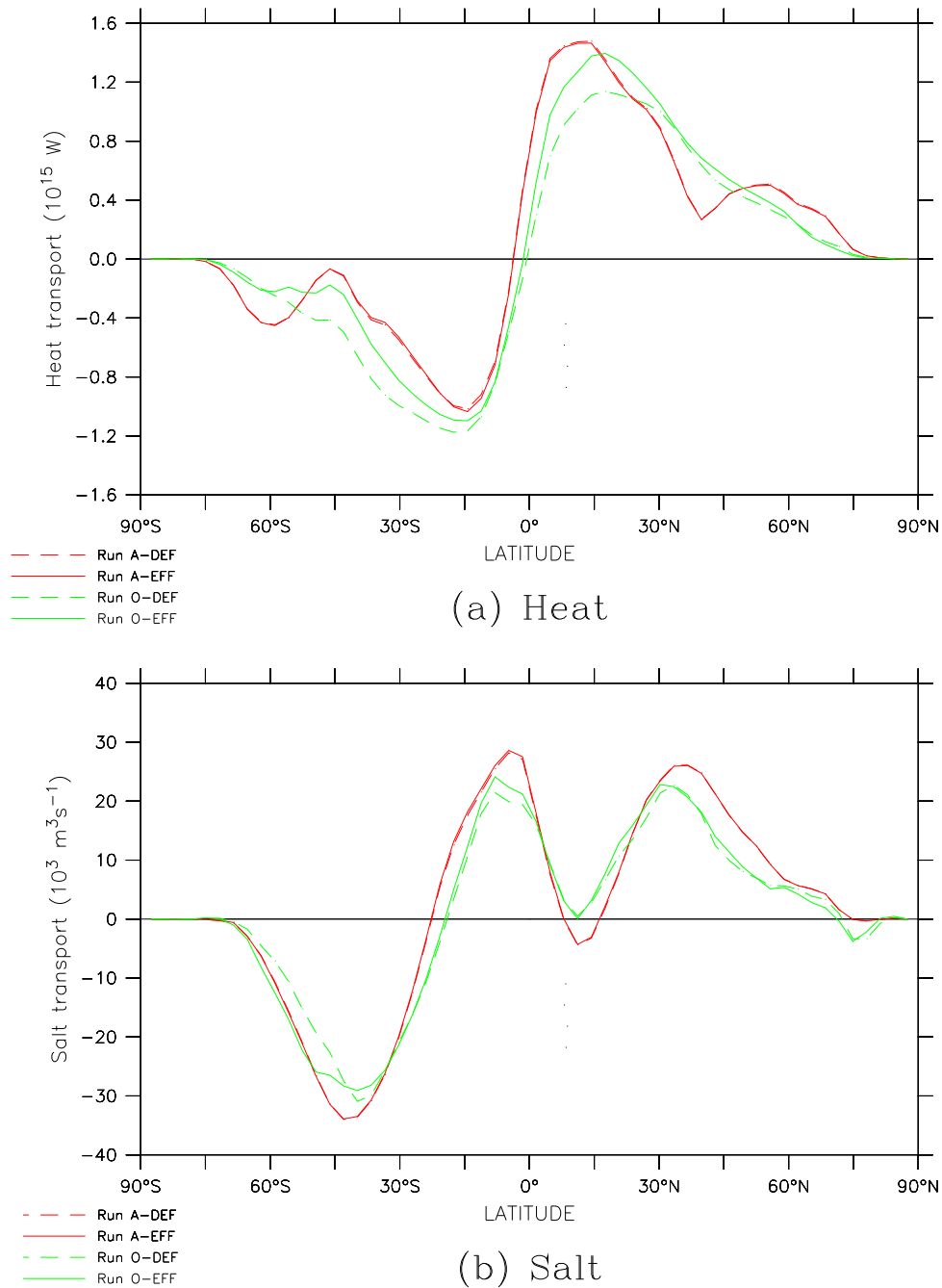


Figure 4.26: The annual-mean oceanic northward transports implied by the surface fluxes diagnosed from Mk3L atmosphere model runs A-DEF (dashed red) and A-EFF (red), and simulated by Mk3L ocean model runs O-DEF (dashed green) and O-EFF (green): (a) heat, and (b) salt. The surface fluxes were diagnosed from the final 40 years of the atmosphere model runs, and from the final 100 years of the ocean model runs; any net global-mean fluxes were subtracted from the data prior to performing the integration, ensuring that the northward transport at the North Pole is equal to zero.

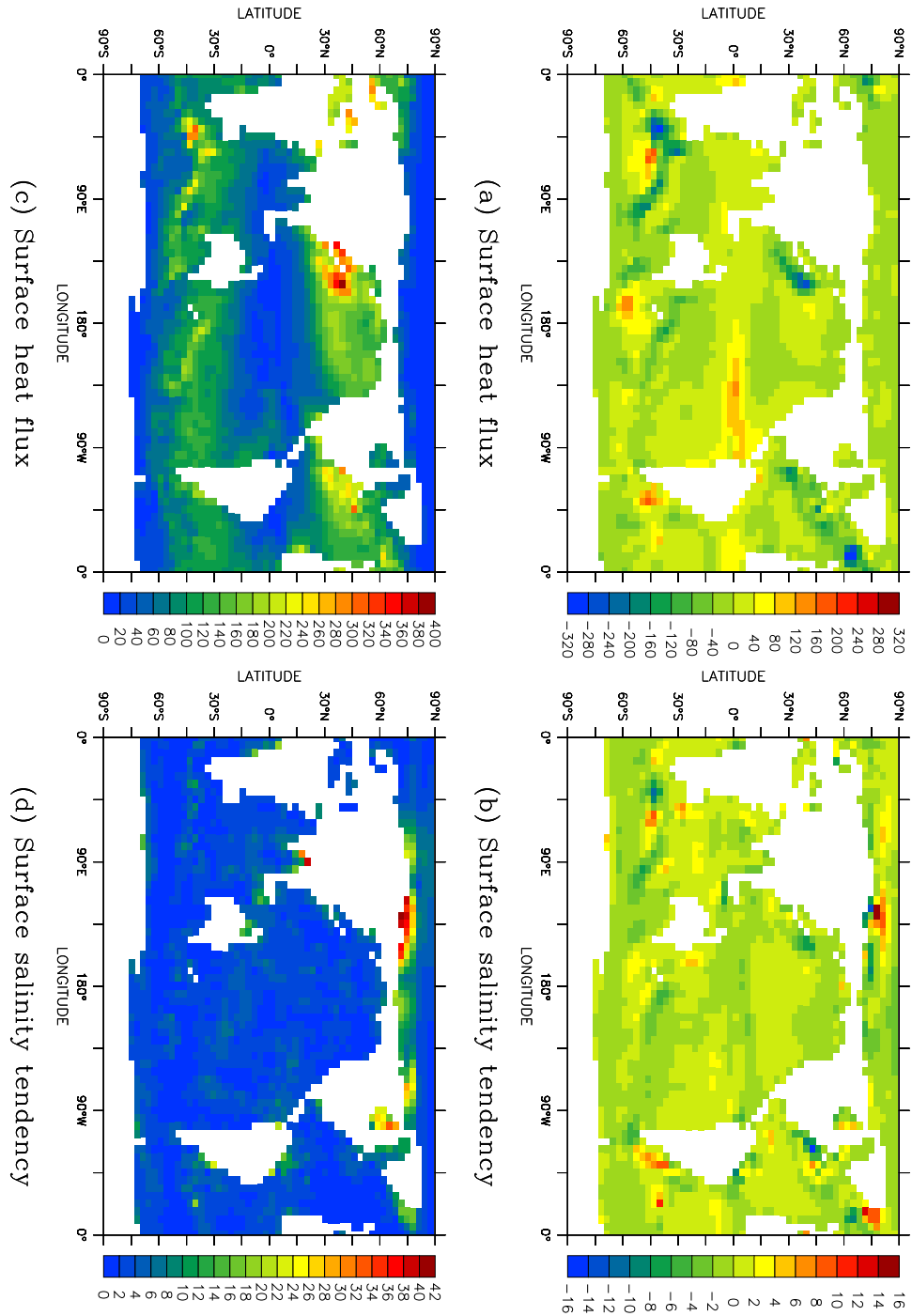


Figure 4.27: The surface heat flux (Wm^{-2}) and surface salinity tendency (psu/year) for the Mk3L ocean model (averages for the final 100 years of run O-EFF): (a), (b) the annual mean, surface heat flux and surface salinity tendency respectively, and (c), (d) the amplitude of the annual cycle, surface heat flux and surface salinity tendency respectively.

Field	Units	Annual-mean		Amplitude	
		O-DEF/ A-DEF	O-EFF/ A-EFF	O-DEF/ A-DEF	O-EFF/ A-EFF
Heat flux	Wm^{-2}	45.2	49.4	55.2	44.4
Salinity tendency	psu/ year	1.69	1.93	1.80	3.37
SST	$^{\circ}\text{C}$	0.566	0.061	0.955	0.347
SSS	psu	0.082	0.014	0.118	0.089

Table 4.7: The flux adjustments diagnosed from Mk3L atmosphere and ocean model runs O-DEF/A-DEF and O-EFF/A-EFF, for the surface heat flux, surface salinity tendency, sea surface temperature (SST), and sea surface salinity (SSS): the root-mean-square annual-mean flux adjustments, and the area-weighted global-mean amplitudes of the annual cycle in the flux adjustments. The surface fluxes are diagnosed from the final 100 years of ocean model runs O-DEF and O-EFF, and from the final 40 years of atmosphere model runs A-DEF and O-DEF.

Figure 4.28 shows the heat flux and salinity tendency adjustments diagnosed from runs O-EFF and A-EFF; these values can be compared with those diagnosed from runs O-DEF and A-DEF (Figures 2.21c and 2.22c). While there is little change to the annual-mean heat flux and salinity tendency adjustments, the amplitude of the heat flux adjustments is *reduced* across much of the world ocean. This was also found to occur in Section 4.3 when the phase lag between the observed and simulated sea surface temperatures was addressed. However, there is an *increase* in the amplitude of the salinity tendency adjustments; this can be attributed to the effective sea surface salinities having a larger amplitude than observations across much of the world ocean (Figure 4.13d).

Figure 4.29 shows the adjustments to the sea surface temperature (SST) and sea surface salinity (SSS); these values can be compared with those diagnosed from runs O-DEF and A-DEF (Figures 2.25 and 2.26). Reflecting the reductions which have been achieved in the annual-mean SST and SSS errors through the use of the effective surface tracers, the annual-mean adjustments are negligibly small across most of the world ocean. Also reflecting the improvements which have been achieved in the simulated annual cycles, both with regard to the amplitudes and the phase lags, the amplitudes of the adjustments are considerably smaller than those diagnosed from runs O-DEF and A-DEF, particularly in the case of the SST.

The root-mean-square annual-mean flux adjustments, and the global-mean amplitudes of the annual cycles, are shown in Table 4.7, for runs O-DEF/A-DEF and O-EFF/A-EFF. The reduction in the magnitude of the SST and SSS adjustments is apparent, as is the *reduction* in the amplitude of the heat flux adjustments, and the *increase* in the amplitude of the salinity tendency adjustments.

4.4.10 Summary

A simple iterative technique has been developed whereby *effective* surface tracers are derived, such that the simulated annual-mean sea surface temperatures and

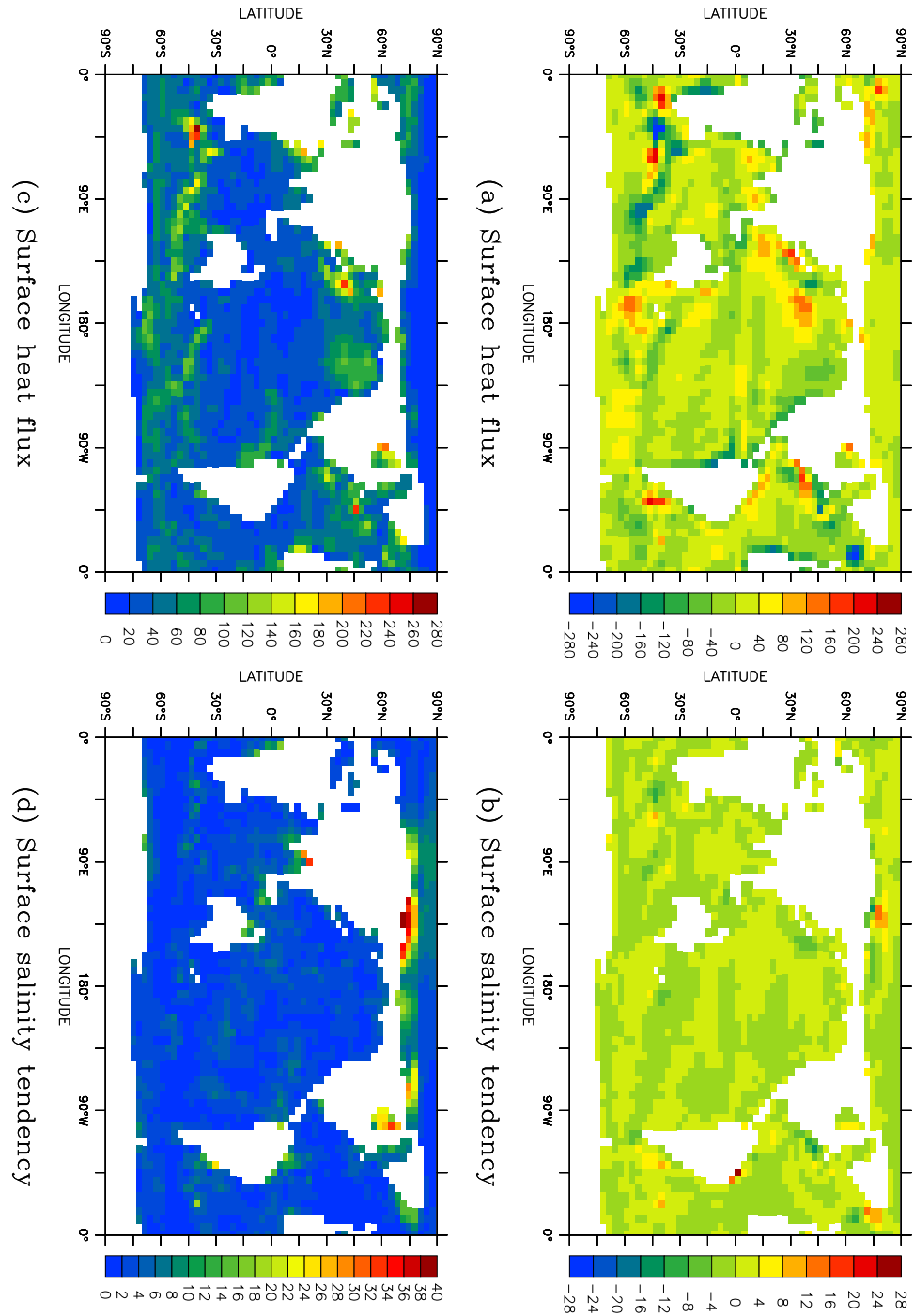


Figure 4.28: The heat flux adjustment (Wm^{-2}) and salinity tendency adjustment (psu/year) diagnosed from Mk3L ocean model run O-EFF and Mk3L atmosphere model run A-EFF: (a), (b) the annual mean, heat flux and salinity tendency respectively, and (c), (d) the amplitude of the annual cycle, heat flux and salinity tendency respectively. The surface fluxes have been diagnosed from the final 100 years of run O-EFF, and from the final 40 years of run A-EFF.

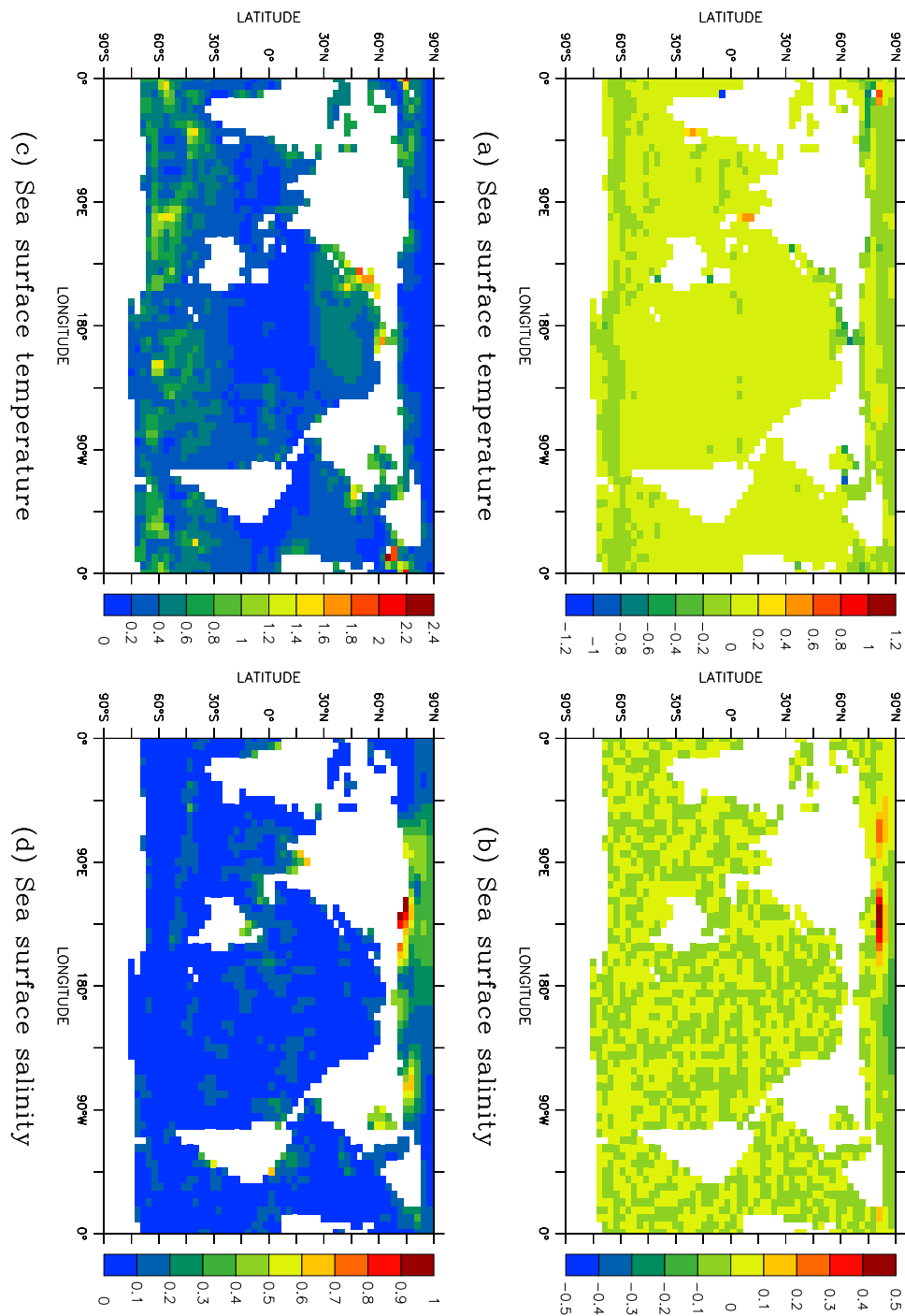


Figure 4.29: The sea surface temperature adjustment ($^{\circ}\text{C}$) and sea surface salinity adjustment (psu) diagnosed from Mk3L ocean model run O-EFF and Mk3L atmosphere model run A-EFF: (a), (b) the annual mean, sea surface temperature and salinity respectively, and (c), (d) the amplitude of the annual cycle, sea surface temperature and salinity respectively. The surface fluxes have been diagnosed from the final 100 years of run O-EFF, and from the final 40 years of run A-EFF.

salinities, and the simulated amplitudes of the annual cycles, agree with observations to the greatest extent possible. A considerable improvement in the simulated ocean climate is obtained, with a realistic vertical density profile and rates of deep water formation that are consistent with observational estimates.

By attempting to match the *amplitudes* of the simulated annual cycles with observations, rather than the *shapes*, this approach avoids the numerical problems which were encountered by *Bi* (2002), and the excessive surface fluxes which would result from a reduction in the relaxation timescale towards zero. Indeed, the improvements in the simulated ocean climate are achieved in conjunction with a *reduction* in the magnitudes of many of the flux adjustments which are diagnosed for use within the coupled model.

Chapter 5

Control runs

5.1 Introduction

Three coupled model control runs are presented in this chapter; these are summarised in Table 5.1. They differ from each another only in the initial states of the ocean and atmosphere models, and in the spatial and temporal distribution of the flux adjustments which are applied. Each run represents a control simulation for pre-industrial conditions, consistent with PMIP2 (*Paleoclimate Modelling Inter-comparison Project*, 2005) experimental design. The atmospheric carbon dioxide concentration is held constant at 280 ppm, while present-day values are used for the Earth’s orbital parameters. Further details regarding the experimental design are provided in Appendix A.

Run CON-DEF represents the default coupled model simulation. The initial states of the atmosphere and ocean models are provided by the final states of spin-up runs A-DEF (Section 2.3.1) and O-DEF (Section 2.3.2) respectively. The model is integrated for 1400 years, with flux adjustments (Section 2.6) being applied. The drift in the mean climate state is examined in Section 5.2, and the nature of the internal variability is examined in Section 5.3.

Run CON-SHF was initialised from the final state of ocean model run O-SHF, for which the prescribed surface tracers were shifted forward in time by one month relative to observations (Section 4.3), while run CON-EFF was initialised from the final state of ocean model run O-EFF, for which effective surface tracers were employed (Section 4.4). Each run is integrated for 1100 years. The climates of these

Name	Spin-up runs		Flux adjustments
	Ocean	Atmosphere	
CON-DEF	O-DEF	A-DEF	O-DEF/A-DEF
CON-SHF	O-SHF	A-SHF	O-SHF/A-SHF
CON-EFF	O-EFF	A-EFF	O-EFF/A-EFF

Table 5.1: Control runs conducted using the Mk3L coupled model: the name used herein, the names of the ocean and atmosphere model spin-up runs, and the spin-up runs from which the flux adjustments were derived.

two runs are contrasted with that of run CON-DEF in Section 5.4.

5.2 Climate drift

5.2.1 Atmosphere

Surface air temperature

The evolution of the simulated global-mean and zonal-mean surface air temperature (SAT) during run CON-DEF is shown in Figure 5.1. The global-mean SAT is very stable, cooling just 0.23°C by the final century of the run. The mean changes over land and the ocean are similar, with cooling of 0.28°C and 0.21°C respectively by the final century. The zonal-mean SAT exhibits negligible drift at most latitudes. Cooling at $\sim 60^{\circ}\text{N}$, and warming at $\sim 80^{\circ}\text{N}$, occur during the first century of the run, but the temperatures at these latitudes stabilise thereafter. Only at high latitudes in the Southern Hemisphere is there an ongoing trend, with the zonal-mean SAT warming slightly at first, but then cooling as the run progresses.

Figure 5.2 shows the change in SAT, between the atmosphere model spin-up run and the final century of run CON-DEF. The stability of the simulated surface air temperature is apparent, with the annual-mean SAT drifting by less than 1°C over 97% of the Earth's surface. The root-mean-square difference in the annual-mean surface air temperature, between the atmosphere model spin-up run and the final century of run CON-DEF, is just 0.53°C . The drift in the zonal-mean SAT at high latitudes in the Northern Hemisphere can be seen to arise from a reduction in winter temperatures in the Barents Sea, the Sea of Okhotsk and Hudson Bay, and from a warming in the Greenland Sea.

Sea ice

Figure 5.3 shows the evolution of the sea ice extent and volume in each hemisphere during run CON-DEF. After some initial adjustment, the Northern Hemisphere sea ice extent is highly stable; the mean extent for the final century of the run is $12.1 \times 10^{12} \text{ m}^2$, 16% greater than for the atmosphere model spin-up run. Consistent with the cooling trend at high southern latitudes, the sea ice extent in the Southern Hemisphere exhibits a slight upwards trend. The mean extent for the final century is $13.4 \times 10^{12} \text{ m}^2$, 7% greater than for the atmosphere model spin-up run.

The sea ice volumes in each hemisphere exhibit similar behaviour to the sea ice extent. The Northern Hemisphere ice volume exhibits some initial adjustment, but is then stable; the mean volume for the final century of the run is $13.1 \times 10^{12} \text{ m}^3$, 29% greater than for the atmosphere model spin-up run. The Southern Hemisphere sea ice volume exhibits a slight upwards trend; the mean volume for the final century is $5.6 \times 10^{12} \text{ m}^3$, 8% greater than for the spin-up run.

Figure 5.4 show the average sea ice concentrations for the final century of the run; this can be compared with Figures 2.9 and 2.10, which show the observed ice concentrations, and those for the stand-alone atmosphere model, for the Northern and Southern Hemispheres respectively. The changes in sea extent within the coupled model, relative to the atmosphere model spin-up run, correspond to the regions

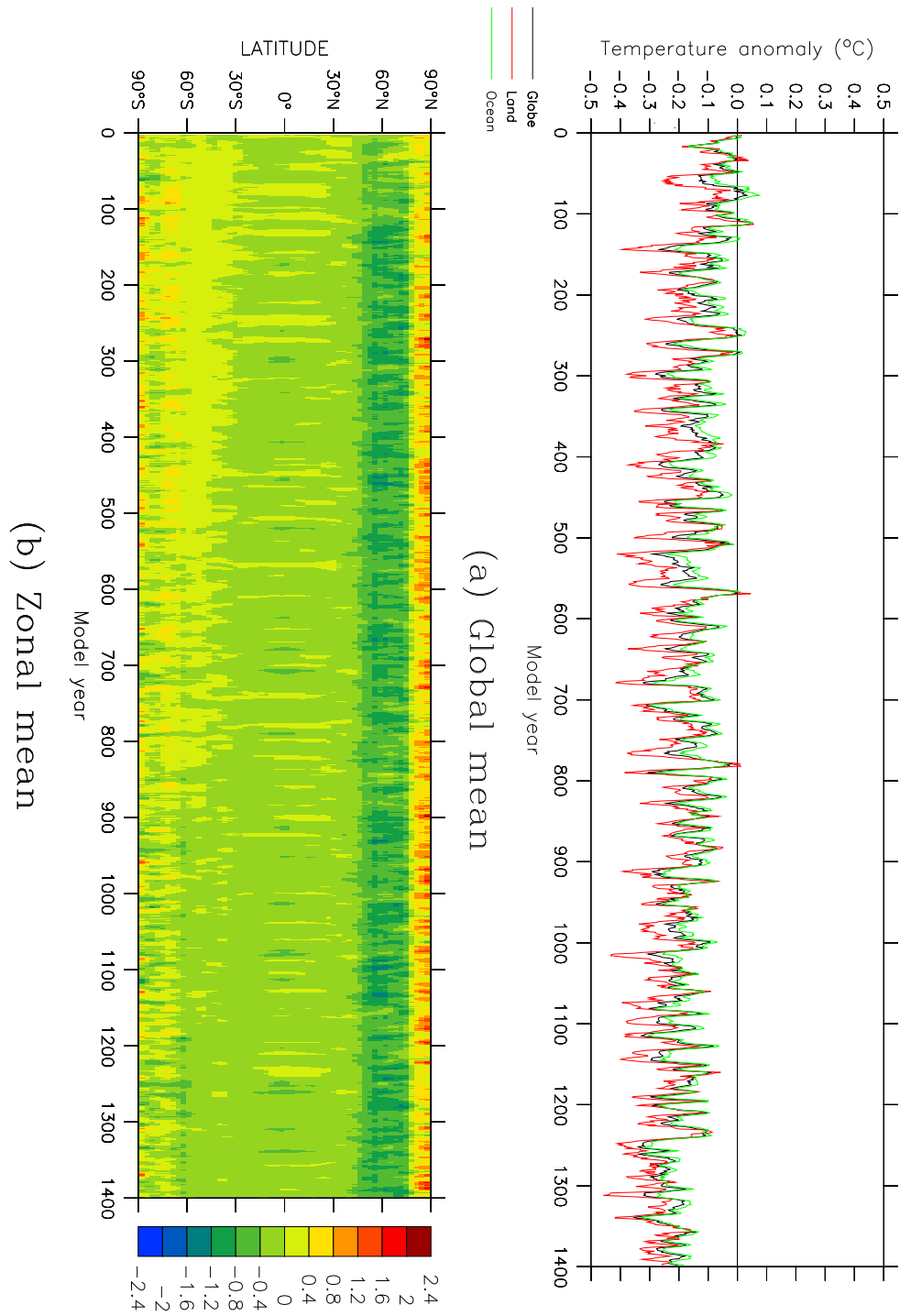
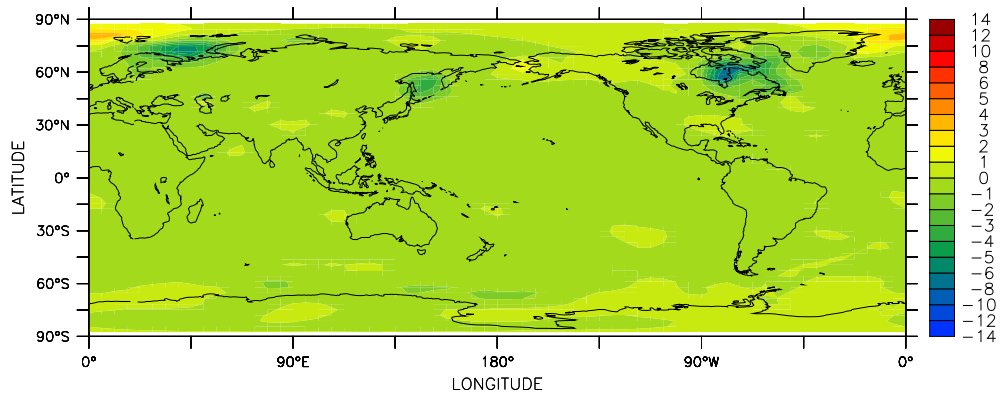
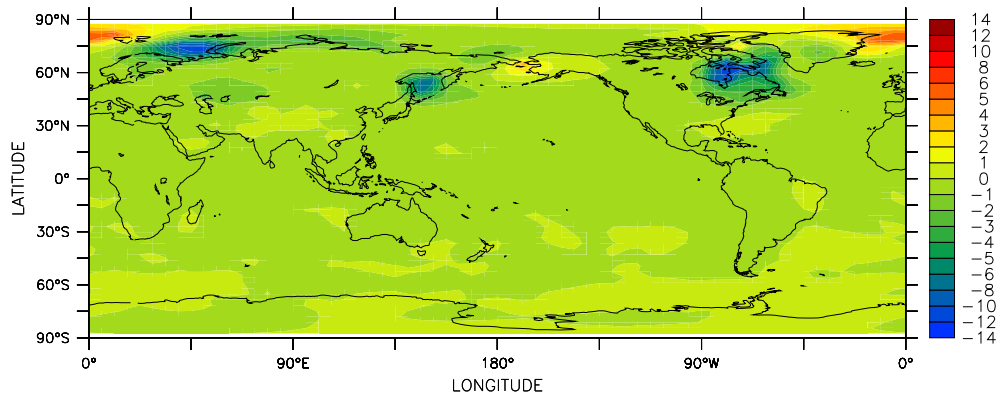


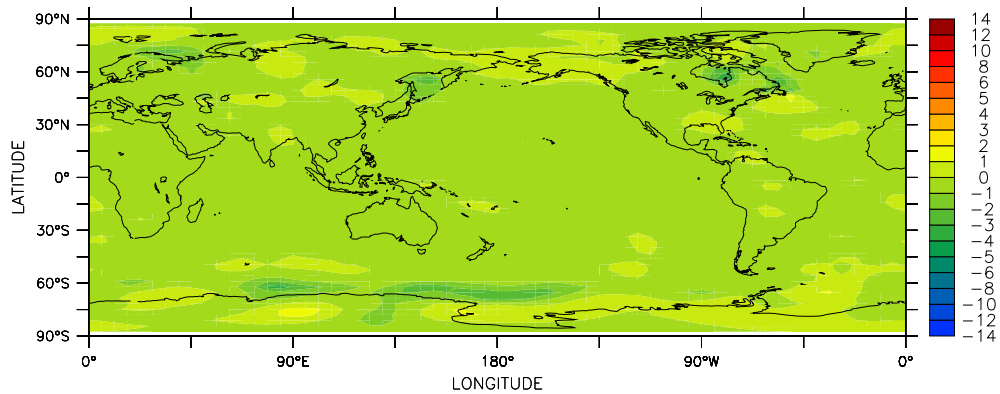
Figure 5.1: The drift in annual-mean surface air temperature ($^{\circ}\text{C}$) during coupled model run CON-DEF: (a) the global mean (black), and the means over land (red) and the ocean (green); (b) the zonal mean. The values shown are five-year running means, and are expressed as anomalies relative to the average surface air temperature for the final 40 years of run A-DEF.



(a) Annual mean



(b) DJF average



(c) JJA average

Figure 5.2: The average surface air temperature ($^{\circ}\text{C}$) for years 1301–1400 of coupled model run CON-DEF, expressed as an anomaly relative to the average surface air temperature for the final 40 years of atmosphere model spin-up run A-DEF: (a) the annual mean, (b) the December-January-February (DJF) average, and (c) the June-July-August (JJA) average.

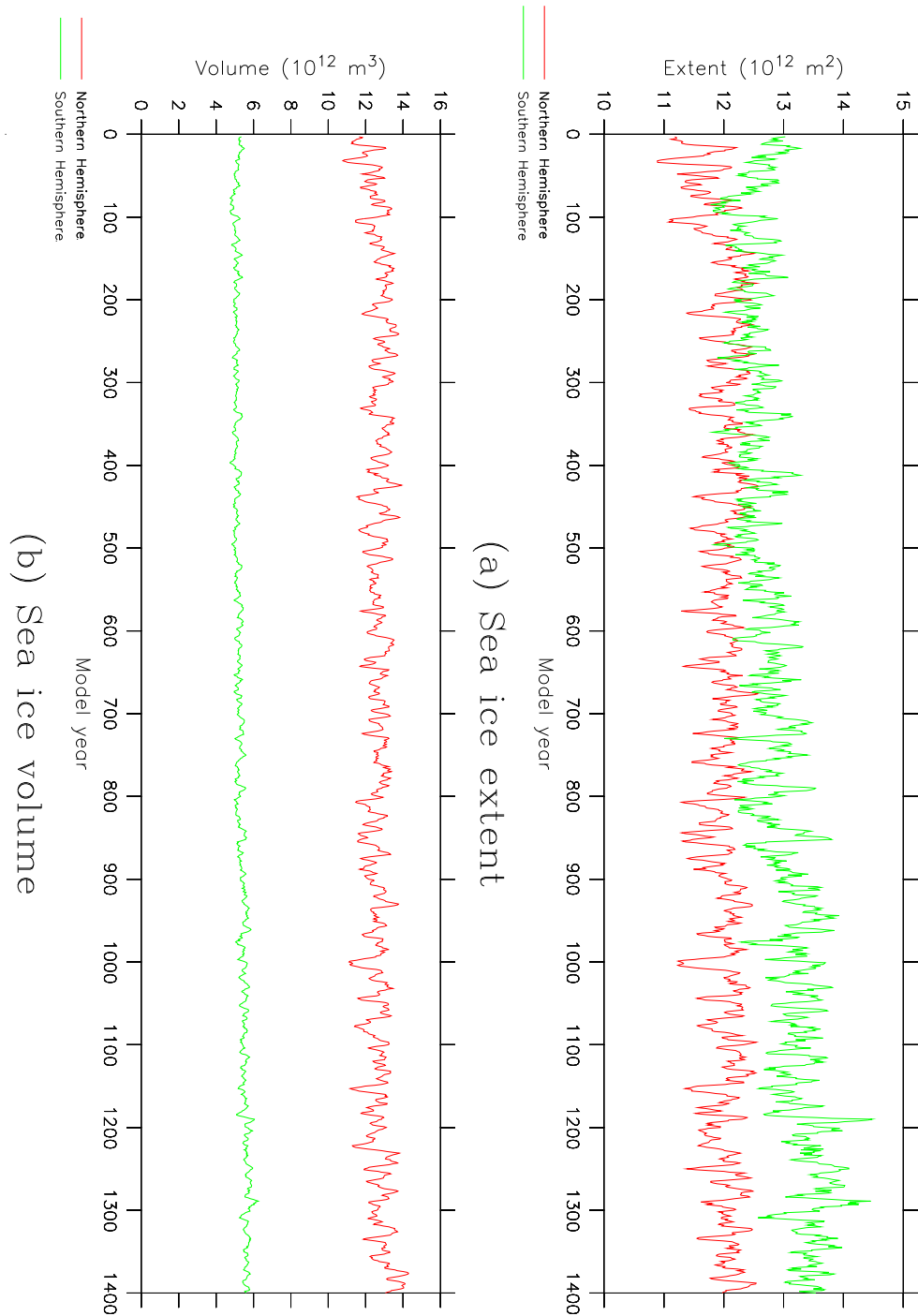


Figure 5.3: The annual-mean sea ice extent and volume for coupled model run CONDEF, for the Northern Hemisphere (red) and Southern Hemisphere (green): (a) sea ice extent, and (b) sea ice volume. The values shown are five-year running means.

where there has been a change in the surface air temperature.

In the Northern Hemisphere, these changes consist of an expansion in the ice cover in the Barents Sea and the Sea of Okhotsk, with the sea ice also now extending into Hudson Bay and the Labrador Sea. This accounts for the increase in sea ice extent relative to the atmosphere model spin-up run, and brings the model into significantly better agreement with observations. Sea ice formation is also simulated in the northern Caspian Sea, again in agreement with observations; however, this ice persists throughout the summer, which the observed cover does not. In contrast to these increases in ice extent, there is also a reduction in the sea ice cover in the Greenland Sea. In the Southern Hemisphere, there is an increase in the simulated winter ice extent, combined with a slight reduction in the summer ice cover.

Figure 5.5 shows the average sea ice thicknesses for the final century of the run. Comparison with Figure 2.12, which shows the climatology of the atmosphere model spin-up run, indicates that the ice thicknesses are very consistent between the stand-alone atmosphere model and the coupled model. The sea ice which forms in Hudson Bay is significantly thicker than that which forms elsewhere, however, and reaches the model's upper limit of 6 m (Section 2.2.1) during winter.

5.2.2 Ocean

Sea surface temperature and salinity

The evolution of the simulated global-mean and zonal-mean sea surface temperature (SST) and sea surface salinity (SSS) during run CON-DEF are shown in Figures 5.6 and 5.7 respectively. The drift in the simulated SST is similar to that in the simulated surface air temperature. The global-mean SST is very stable, cooling just 0.15°C by the final century of the run, while the zonal-mean SST exhibits an initial cooling at $\sim 60^{\circ}\text{N}$, and a warming at $\sim 80^{\circ}\text{N}$, but with little subsequent drift at these latitudes thereafter. As with the surface air temperature, there is also an initial warming in the Southern Ocean, followed by a slight cooling trend. The simulated SSS is very stable, with the global mean freshening just 0.053 psu by the final century of the run. The zonal-mean SSS exhibits an initial freshening at $\sim 75^{\circ}\text{N}$, and a slight upward trend at $\sim 45^{\circ}\text{N}$, but otherwise experiences little drift.

Figure 5.8 shows the change in SST between the ocean model spin-up run, and the final century of run CON-DEF. The stability of the simulated sea surface temperature is apparent, with the annual-mean SST drifting by less than 0.5°C over 95% of the surface of the ocean. The root-mean-square difference, between the ocean model spin-up run and the final century of run CON-DEF, is just 0.30°C . As with the surface air temperature, the largest drift occurs at high latitudes, particularly in the Northern Hemisphere; it therefore appears to be related to the changes in sea ice extent. The strongest cooling occurs in Hudson Bay, the Sea of Okhotsk, the Barents Sea, and along the Atlantic coast of Canada; these are the regions where the sea ice cover has expanded relative to the atmosphere model spin-up run. Slight warming is apparent at isolated locations in the North Atlantic, Arctic and Southern Oceans.

Figure 5.9 shows the change in the annual-mean SSS, between the ocean model spin-up run and the final century of run CON-DEF. The stability of the simulated

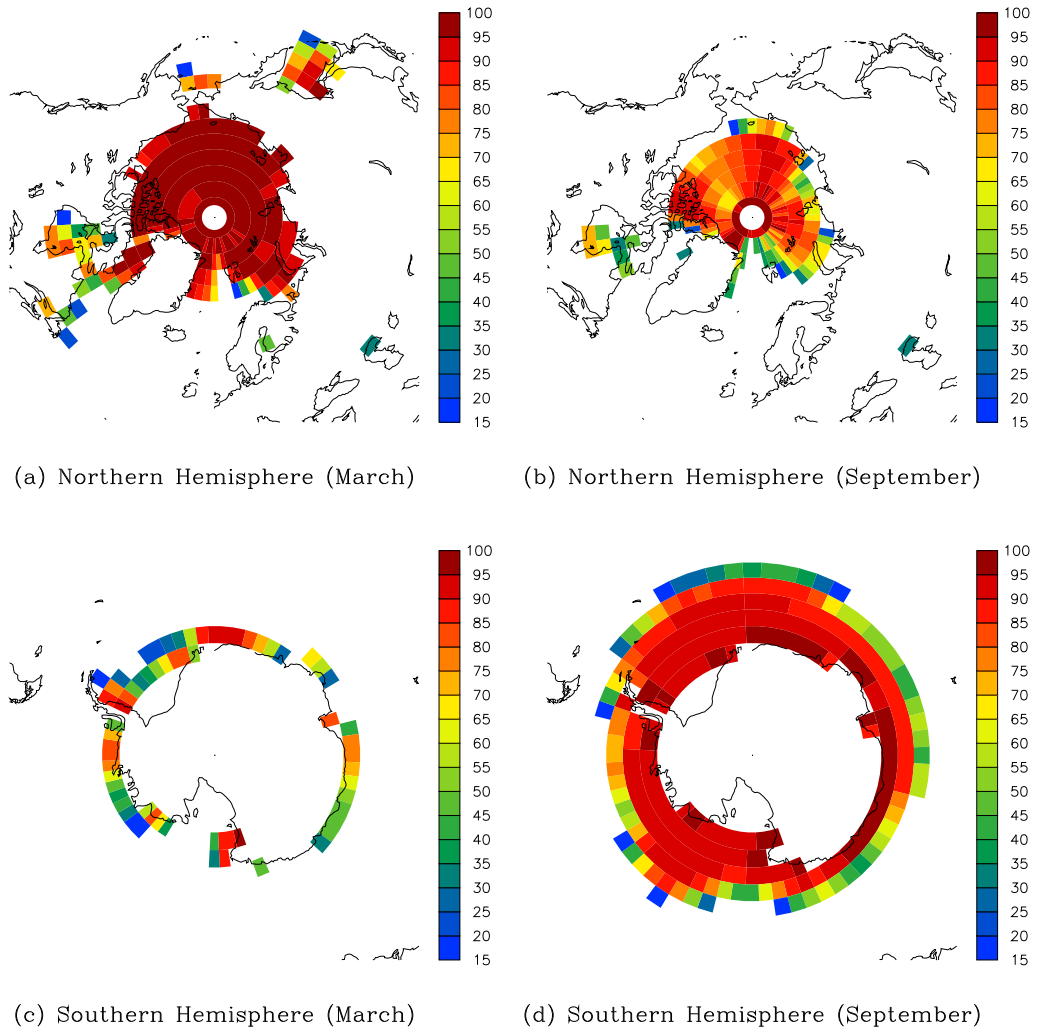


Figure 5.4: The average sea ice concentration (percent) for years 1301–1400 of coupled model run CON-DEF: (a), (b) Northern Hemisphere, March and September respectively, and (c), (d) Southern Hemisphere, March and September respectively. Values are only shown where the concentration is greater than or equal to 15%.

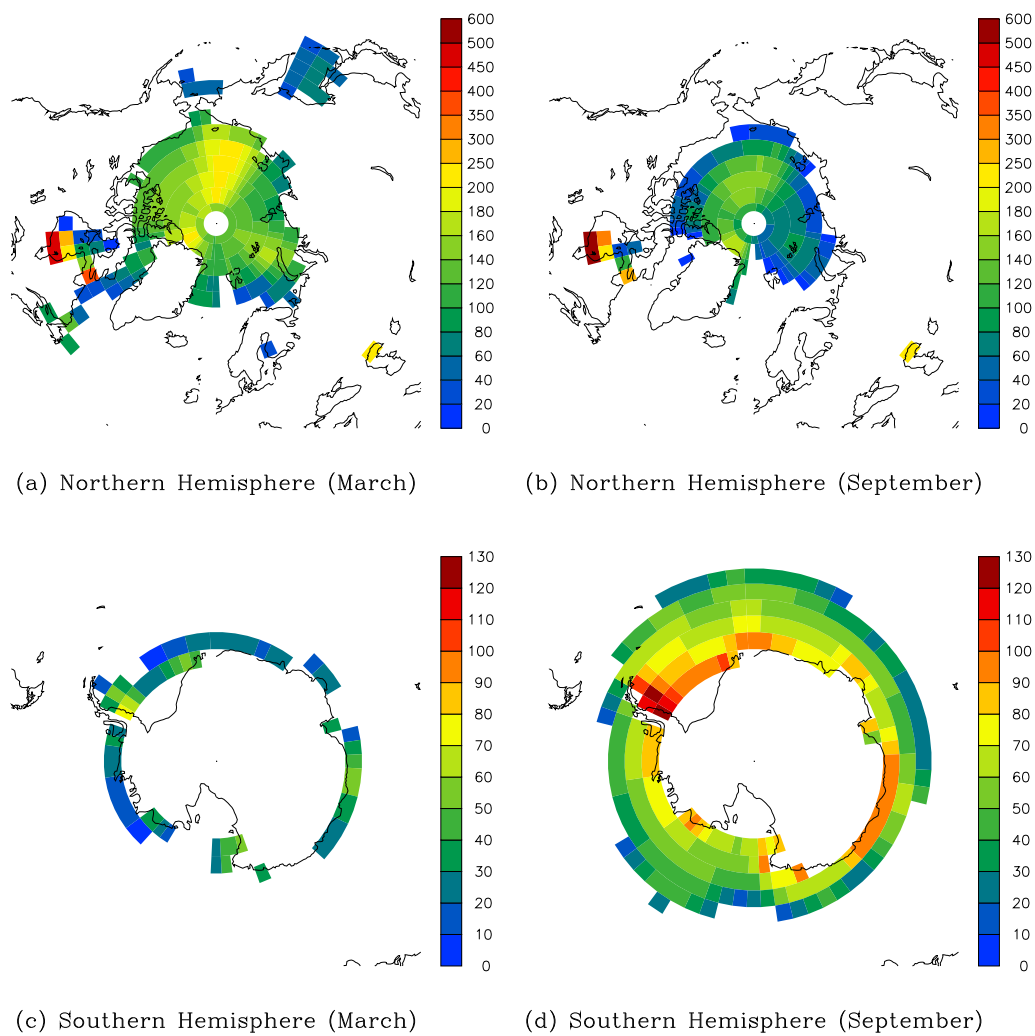


Figure 5.5: The average sea ice thickness (cm) for years 1301–1400 of coupled model run CON-DEF: (a), (b) Northern Hemisphere, March and September respectively, and (c), (d) Southern Hemisphere, March and September respectively. Values are only shown where the concentration is greater than or equal to 15%.

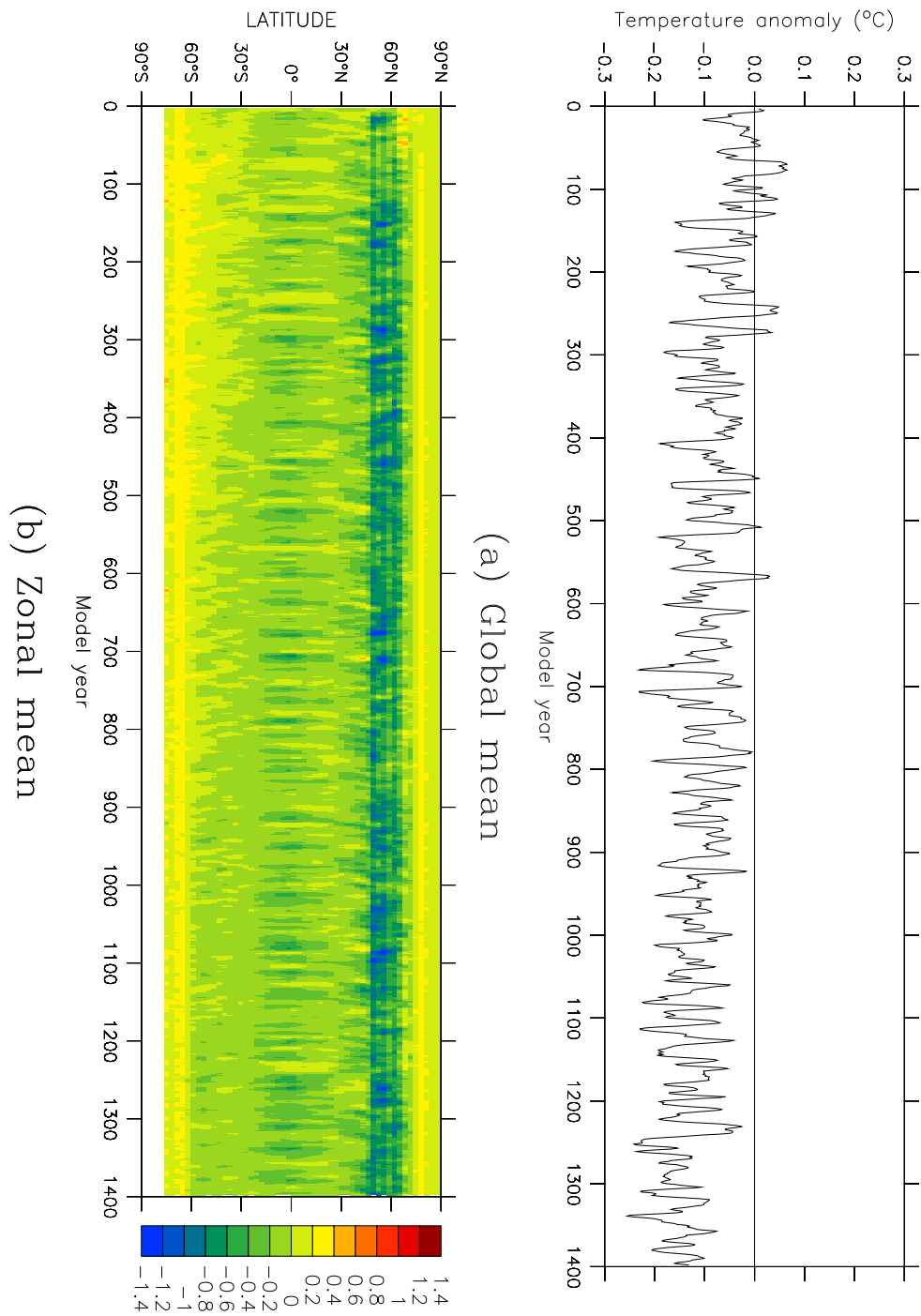


Figure 5.6: The drift in annual-mean sea surface temperature (°C) during coupled model run CON-DEF: (a) the global mean, and (b) the zonal mean. The values shown are five-year running means, and are expressed as anomalies relative to the average sea surface temperature for the final 100 years of run O-DEF.

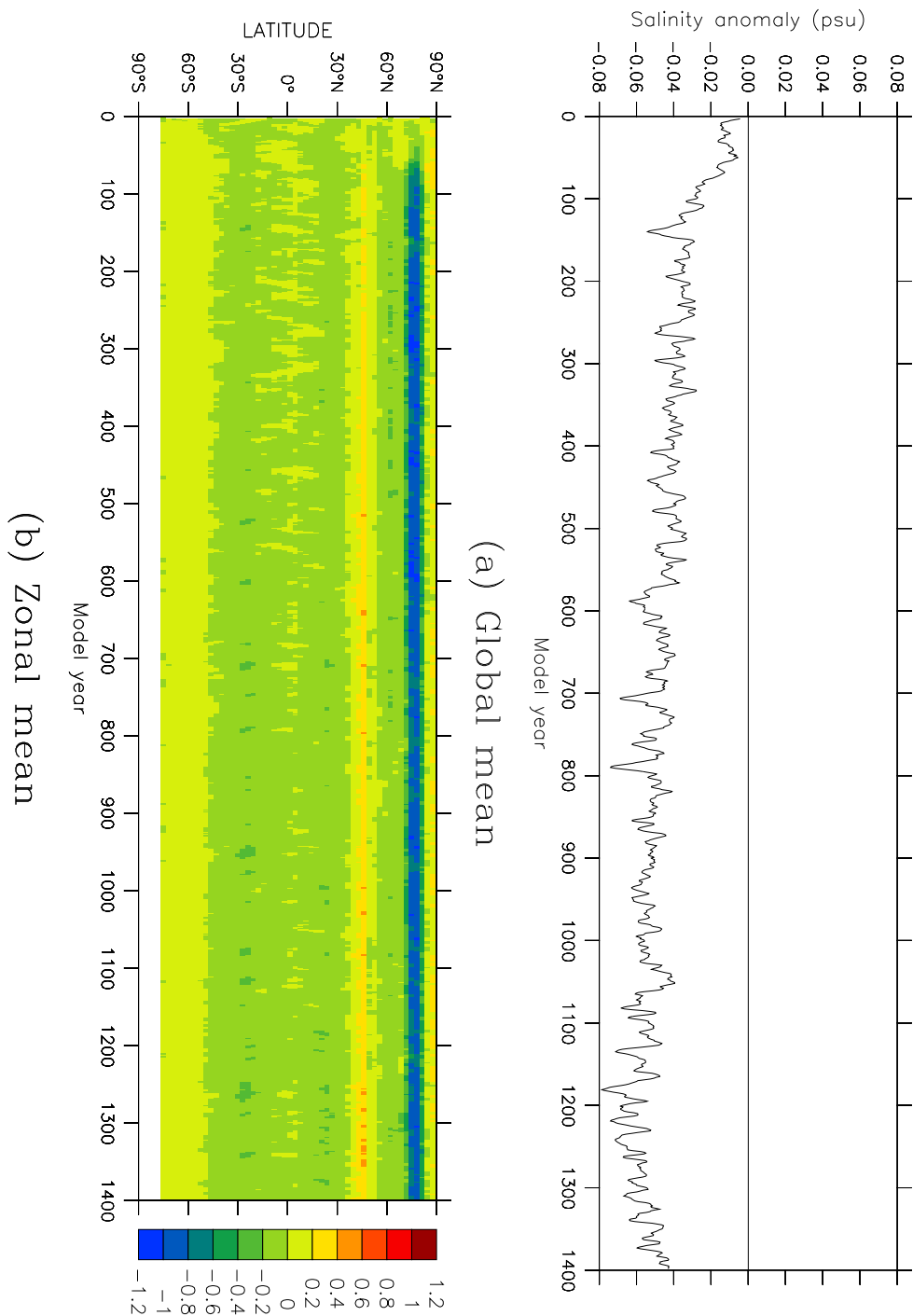
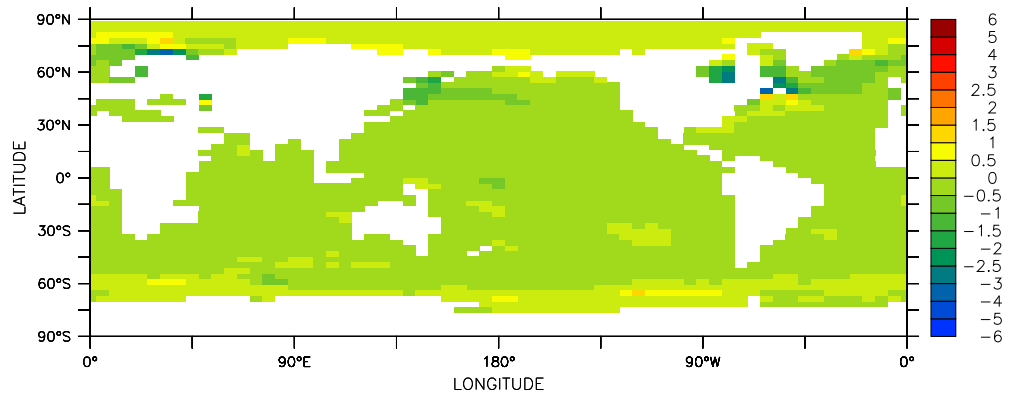
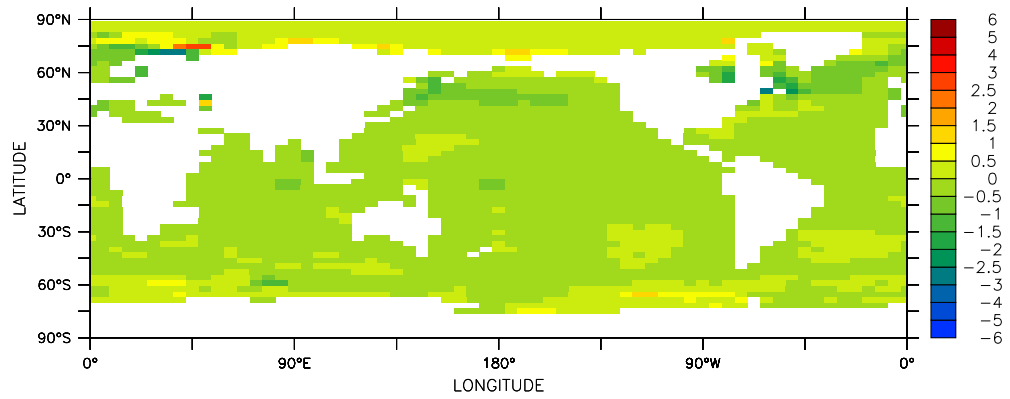


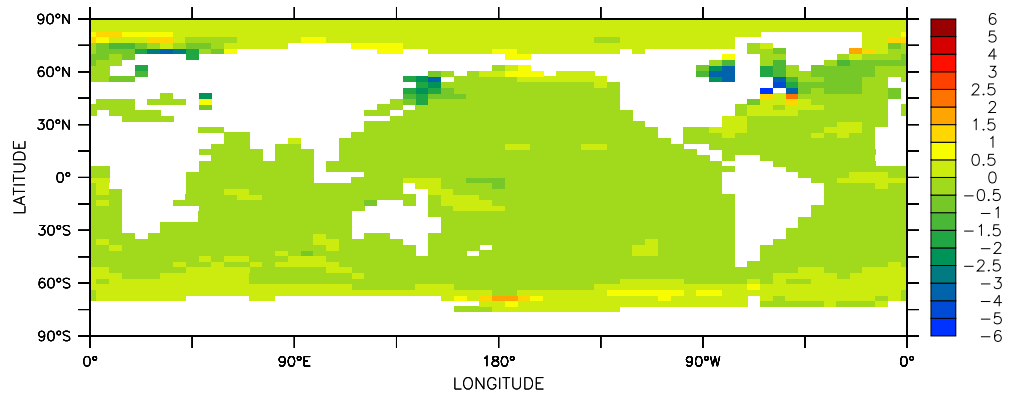
Figure 5.7: The drift in annual-mean sea surface salinity (psu) during coupled model run CON-DEF: (a) the global mean, and (b) the zonal mean. The values shown are five-year running means, and are expressed as anomalies relative to the average sea surface salinity for the final 100 years of run O-DEF.



(a) Annual mean



(b) DJF average



(c) JJA average

Figure 5.8: The average sea surface temperature ($^{\circ}\text{C}$) for years 1301–1400 of coupled model run CON-DEF, expressed as an anomaly relative to the average sea surface temperature for the final 100 years of ocean model spin-up run O-DEF: (a) the annual mean, (b) the December-January-February (DJF) average, and (c) the June-July-August (JJA) average.

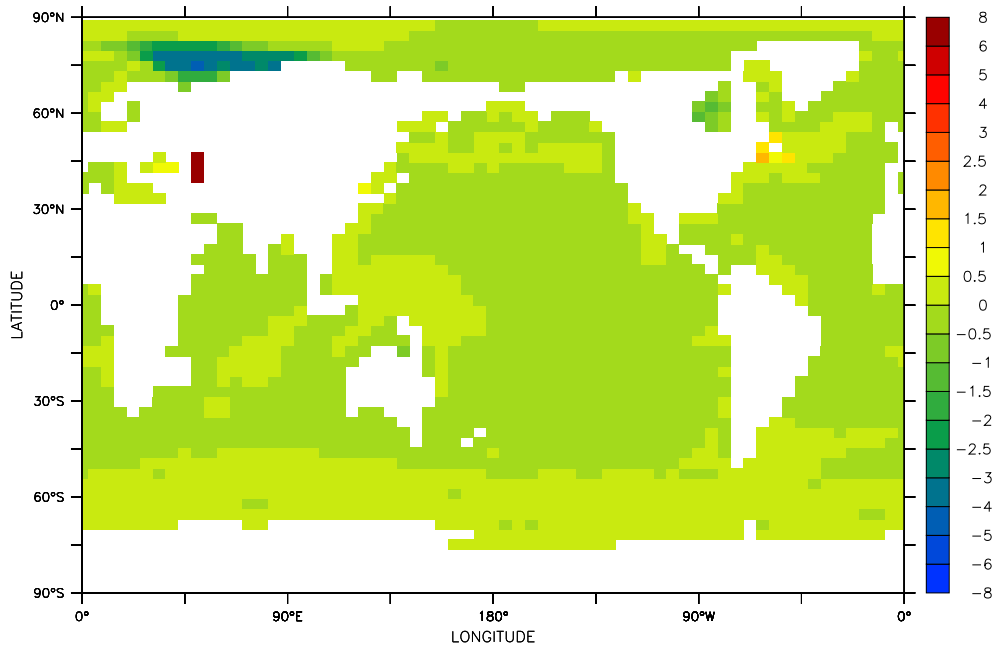


Figure 5.9: The annual-mean sea surface salinity (psu) for years 1301–1400 of coupled model run CON-DEF, expressed as an anomaly relative to the annual-mean sea surface salinity for the final 100 years of ocean model spin-up run O-DEF.

sea surface salinity is apparent, with the annual-mean SSS drifting by less than 0.5 psu over 99% of the surface of the ocean, and with the root-mean square change being just 0.35 psu. Excluding the inland seas, the only significant changes are a freshening in the Barents Sea and a slight increase in the SSS along the Atlantic coast of Canada, where there has been an increase in the simulated sea ice cover.

The largest salinity drift occurs in the Caspian Sea, where the mean SSS has increased by 6.7 psu by the final century of the run. This is the only ocean basin which is not connected to the world ocean within the Mk3L ocean model (*Phipps, 2006*). The flux adjustments which are applied within the coupled model are time-invariant, and any changes in the fluxes of freshwater into the Caspian Sea relative to the atmosphere model spin-up run, be they changes in the fluxes of precipitation, evaporation or run-off, will therefore result in a drift in the mean salinity.

The other inland seas do not exhibit a drift of the magnitude of that exhibited by the Caspian Sea; this suggests that the parameterised mixing across unresolved straits within the Mk3L ocean model (*Phipps, 2006*) is successful at representing the effects of the exchange of water between these bodies and the world ocean.

Water properties

The evolution of the simulated global-mean potential temperature, salinity and potential density of the world ocean, and of the simulated global-mean vertical profiles, during run CON-DEF are shown in Figures 5.10, 5.11 and 5.12 respectively.

Drift in the mean temperature of the ocean is small, with a decrease of just

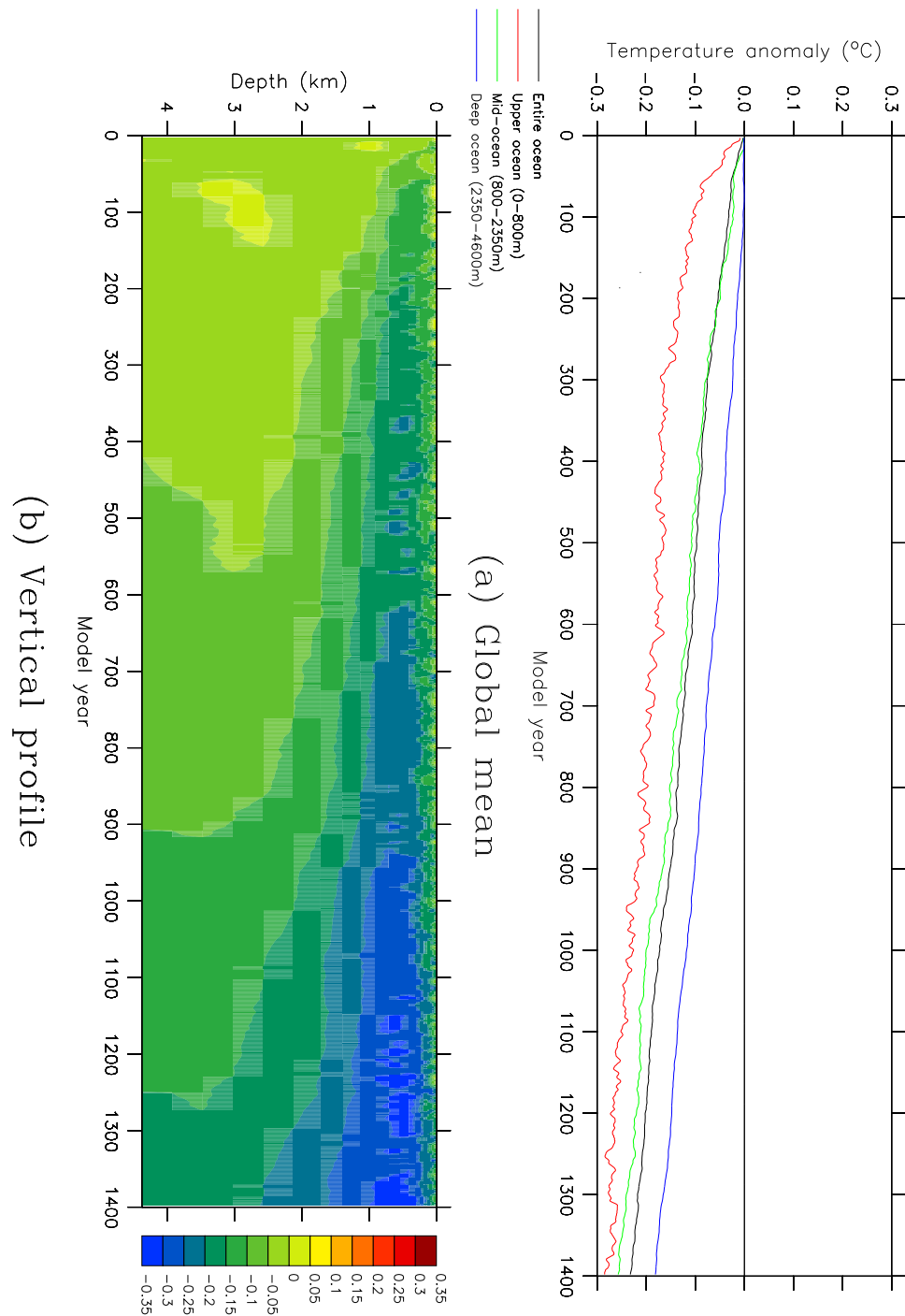


Figure 5.10: The drift in annual-mean potential temperature ($^{\circ}\text{C}$) during coupled model run CON-DEF: (a) the global means for the entire ocean (black), upper ocean (red, 0–800 m), mid-ocean (green, 800–2350 m) and deep ocean (dark blue, 2350–4600 m), and (b) the global-mean vertical profile. The values shown are five-year running means, and are expressed as anomalies relative to the annual-mean potential temperature for the final 100 years of run O-DEF.

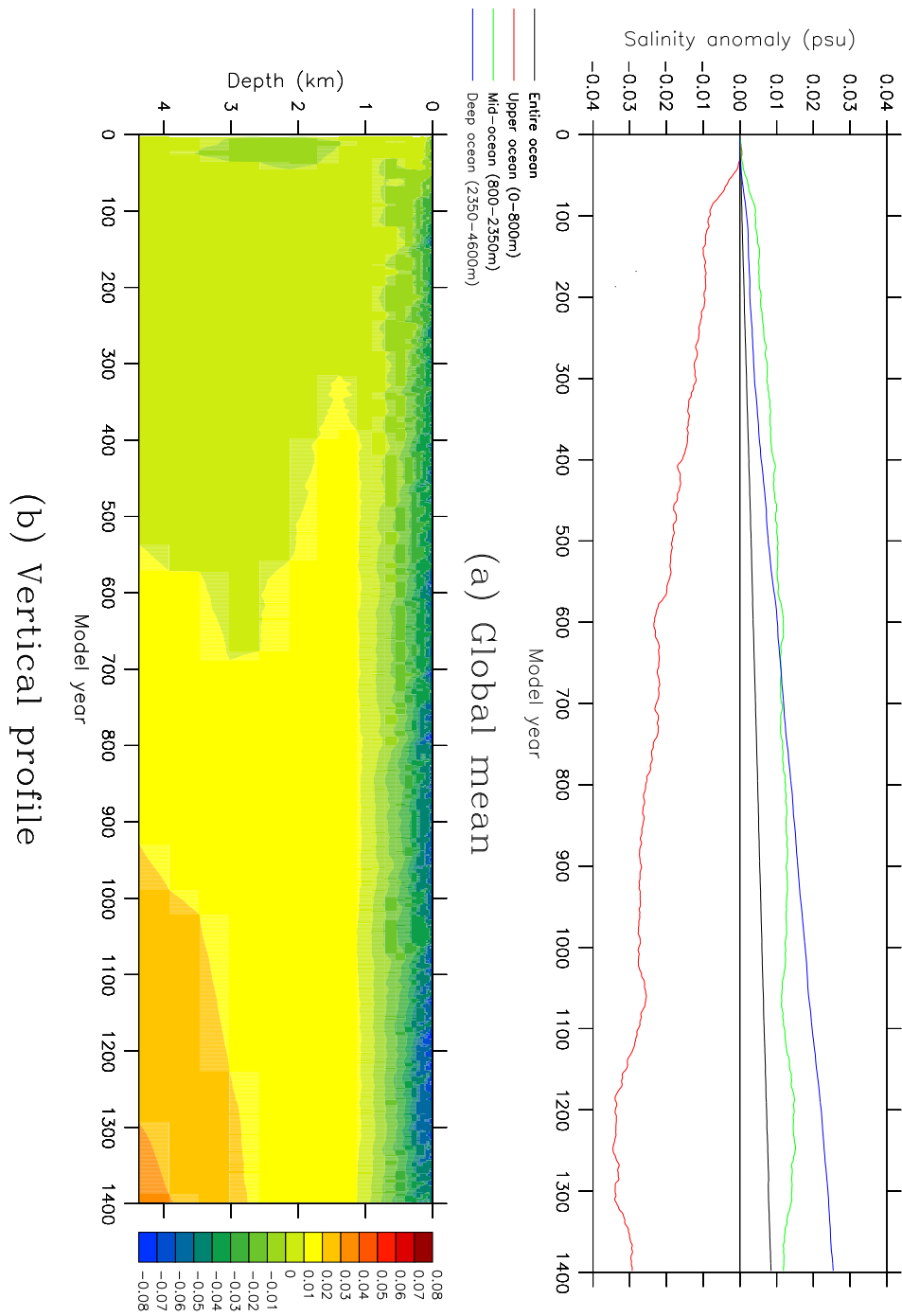


Figure 5.11: The drift in annual-mean salinity (psu) during coupled model run CON-DEF: (a) the global means for the entire ocean (black), upper ocean (red, 0–800 m), mid-ocean (green, 800–2350 m) and deep ocean (dark blue, 2350–4600 m), and (b) the global-mean vertical profile. The values shown are five-year running means, and are expressed as anomalies relative to the annual-mean salinity for the final 100 years of run O-DEF.

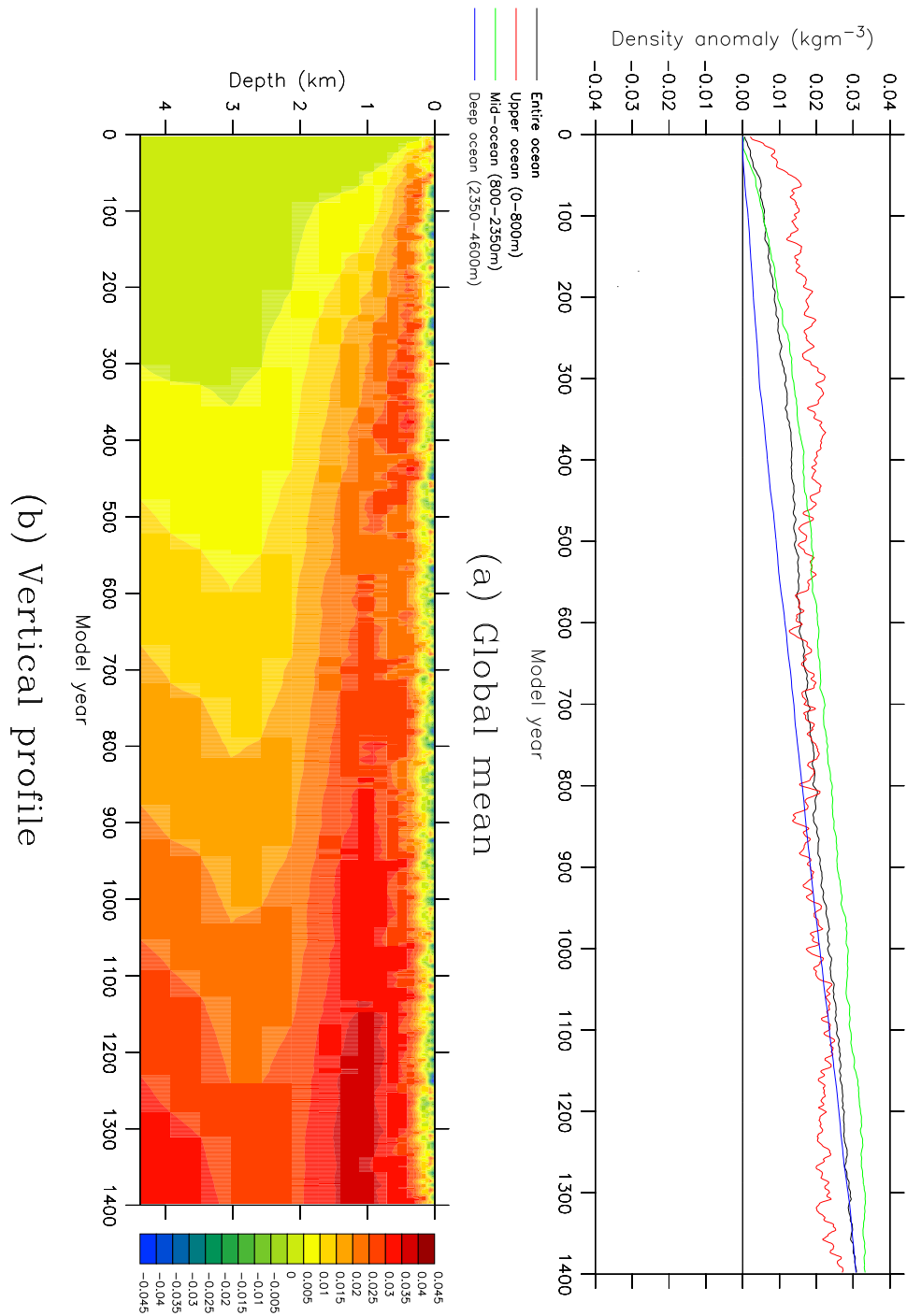


Figure 5.12: The drift in annual-mean σ_θ (kgm^{-3}) during coupled model run CON-DEF: (a) the global means for the entire ocean (black), upper ocean (red, 0–800 m), mid-ocean (green, 800–2350 m) and deep ocean (dark blue, 2350–4600 m), and (b) the global-mean vertical profile. The values shown are five-year running means, and are expressed as anomalies relative to the annual-mean σ_θ for the final 100 years of run O-DEF.

0.23°C by year 1400. The temperature of the upper ocean exhibits greater inter-annual variability than either the mid- or deep ocean, reflecting the attenuation of variability on interannual timescales with depth. There is an ongoing cooling trend at all depths, with the strongest cooling of 0.33°C occurring at a depth of 410 m. The evolution of the zonal-mean potential temperature during run CON-DEF is shown in Figure 5.13; the cooling can be seen to propagate outwards from a region located in the upper ocean at $\sim 50^\circ\text{N}$. This can be attributed to a decrease in the temperature of North Atlantic Deep Water, arising from a cooling of the surface waters in the North Atlantic (Figure 5.8). Although there is also a warming of the Arctic Ocean at depth, this appears to have stabilised by year 1000.

Drift in the mean salinity of the ocean is also small, with an increase of just 0.008 psu during the 1400 years of run CON-DEF. However, this increase cannot be accounted for by the increase in sea ice volume relative to the atmosphere model spin-up run. The increase of $3.4 \times 10^{12} \text{ m}^3$ in the ice volume represents an input of salt to the world ocean of $\sim 8.4 \times 10^{10} \text{ m}^3$, which is equivalent to an increase in the mean salinity of just $\sim 6.6 \times 10^{-5}$ psu.

Neither can the drift be attributed to changes in any of the reservoirs of freshwater within the climate system. The increase in the mean salinity is equivalent to a net freshwater flux of $\sim 3.2 \times 10^{14} \text{ m}^3$ out of the ocean; normalised by the surface area of the Earth, this flux is equivalent to a depth of freshwater of $\sim 0.6 \text{ m}$. Figure 5.14 shows the temporal integrals of the changes in the fluxes of precipitation, evaporation and run-off into the world ocean, relative to the atmosphere model spin-up run A-DEF. By year 1400, the changes amount to a net freshwater flux *into* the ocean of just $7 \times 10^{11} \text{ m}^3$. The salinity drift therefore appears to represent a conservation error within the model, and requires further investigation.

Figure 5.15 shows the evolution of the zonal-mean salinity during run CON-DEF. There is a vertical redistribution of salt, with freshening of the surface layers and an increase in the salinity of the deep ocean. The salinity of the deep Arctic Ocean appears to have stabilised by year 1000, with the ongoing increase in the salinity of the deep ocean appearing to arise instead from a slight increase in the salinity of the deep Southern Ocean.

As a result of the minimal drift in the potential temperature and salinity of the world ocean, the potential density is also very temporally stable. The increase in the mean density by year 1400 is just 0.031 kgm^{-3} ; apart from a slight increase in the buoyancy of the surface layers, arising from the freshening of the upper ocean, the increase in density is relatively uniformly distributed throughout the water column. Figure 5.16 shows the evolution of the zonal-mean potential density during run CON-DEF. There is a slight increase in the density of the deep Arctic Ocean, but otherwise the zonal-mean potential density is stable to within 0.05 kgm^{-3} throughout the mid- and deep ocean.

Circulation

Figure 5.17 shows the evolution in the rates of North Atlantic Deep Water (NADW) and Antarctic Bottom Water (AABW) formation, and in the rate of volume transport through Drake Passage, during run CON-DEF. After some adjustment during the first century of the run, the rates of deep water formation are stable thereafter;

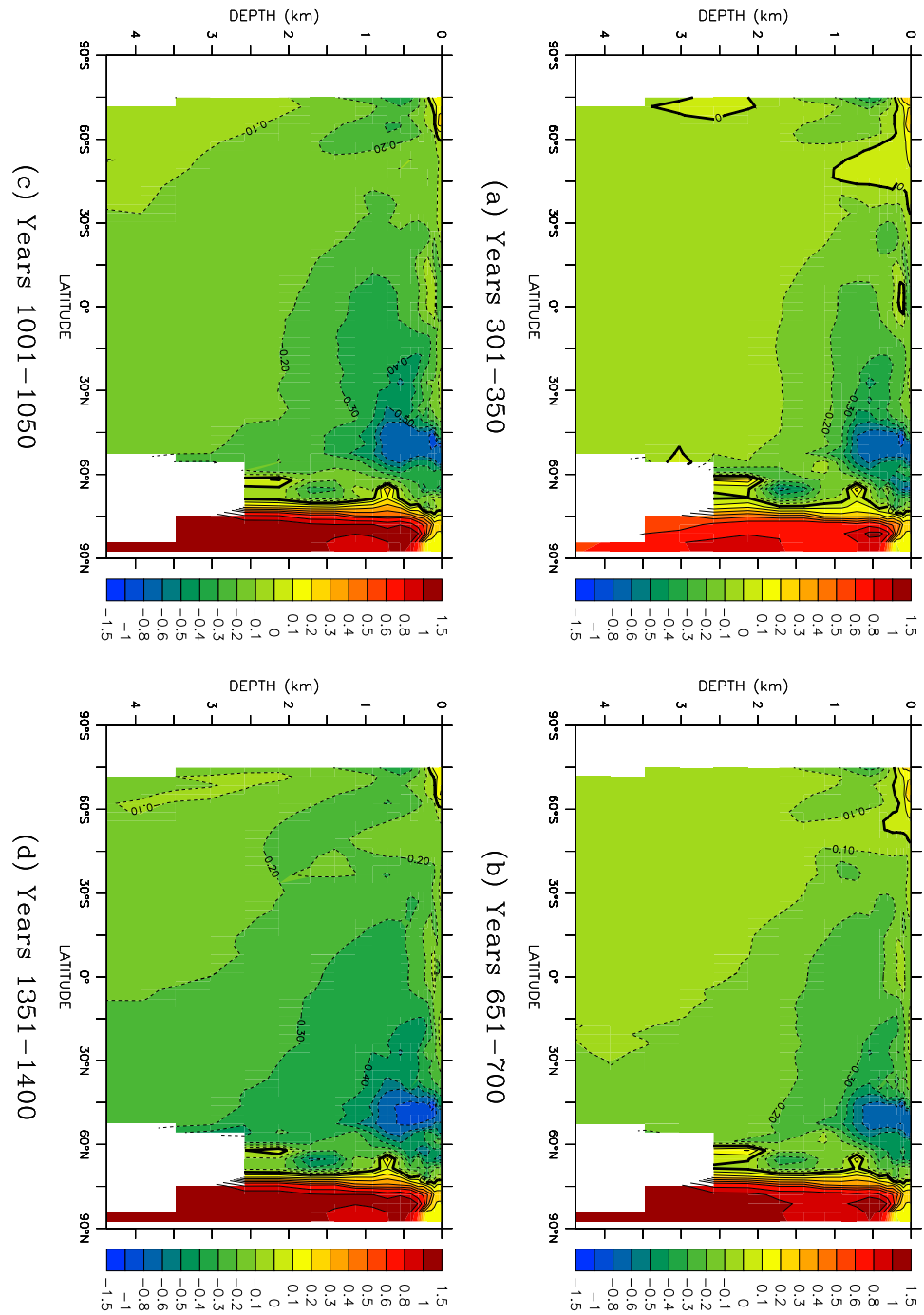


Figure 5.13: The zonal-mean potential temperature ($^{\circ}\text{C}$) for coupled model run CON-DEF, expressed as an anomaly relative to the average potential temperature for the final 100 years of ocean model spin-up run O-DEF: (a) years 301–350, (b) years 651–700, (c) years 1001–1050, and (d) years 1351–1400. The inland seas are excluded when calculating the zonal means.

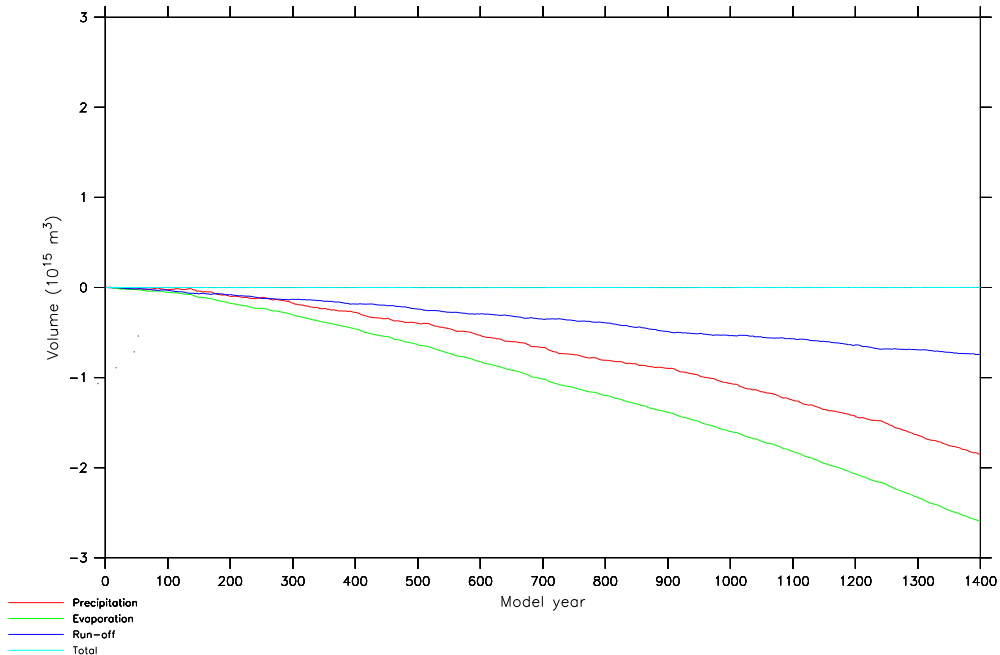


Figure 5.14: The changes in the freshwater fluxes into the world ocean during run CON-DEF: the temporal integrals of the changes in the fluxes of precipitation (red), evaporation (green), run-off (dark blue), and the total freshwater flux (light blue). Changes are expressed relative to the final 40 years of the atmosphere model spin-up run A-DEF.

the mean rates of NADW and AABW formation for the final century of the run are 13.8 and 11.2 Sv respectively. These figures represent slight increases on the rates of 13.6 and 9.5 Sv, respectively, for the final century of ocean model spin-up run O-DEF. The strength of the Antarctic Circumpolar Current exhibits only a very slight upward trend during the course of the run. The mean strength for the final century is 148.1 Sv, only slightly stronger than the mean strength of 145.3 Sv for the final century of ocean model spin-up run O-DEF.

The mean meridional overturning streamfunctions for the final century of the run are shown in Figure 5.18; they can be compared with those diagnosed from the final century of ocean model spin-up run O-DEF (Figure 2.17). The intensification in the rate of Antarctic Bottom Water formation within the coupled model is apparent.

Mean sea level

The Mk3L ocean model employs the rigid-lid approximation (Section 2.2.2), and hence cannot directly simulate any change in sea level. However, it is possible to infer the *steric* sea level change, being that which arises from changes in the density of the ocean. By assuming that the mass of water within each gridbox remains constant, then a volume change can be inferred from any change in the density of its contents. Let the gridbox (i, j, k) have mass $M_{i,j,k}$, and let the density and volume at time t be $\rho_{i,j,k}(t)$ and $V_{i,j,k}(t)$ respectively. Conservation of mass yields

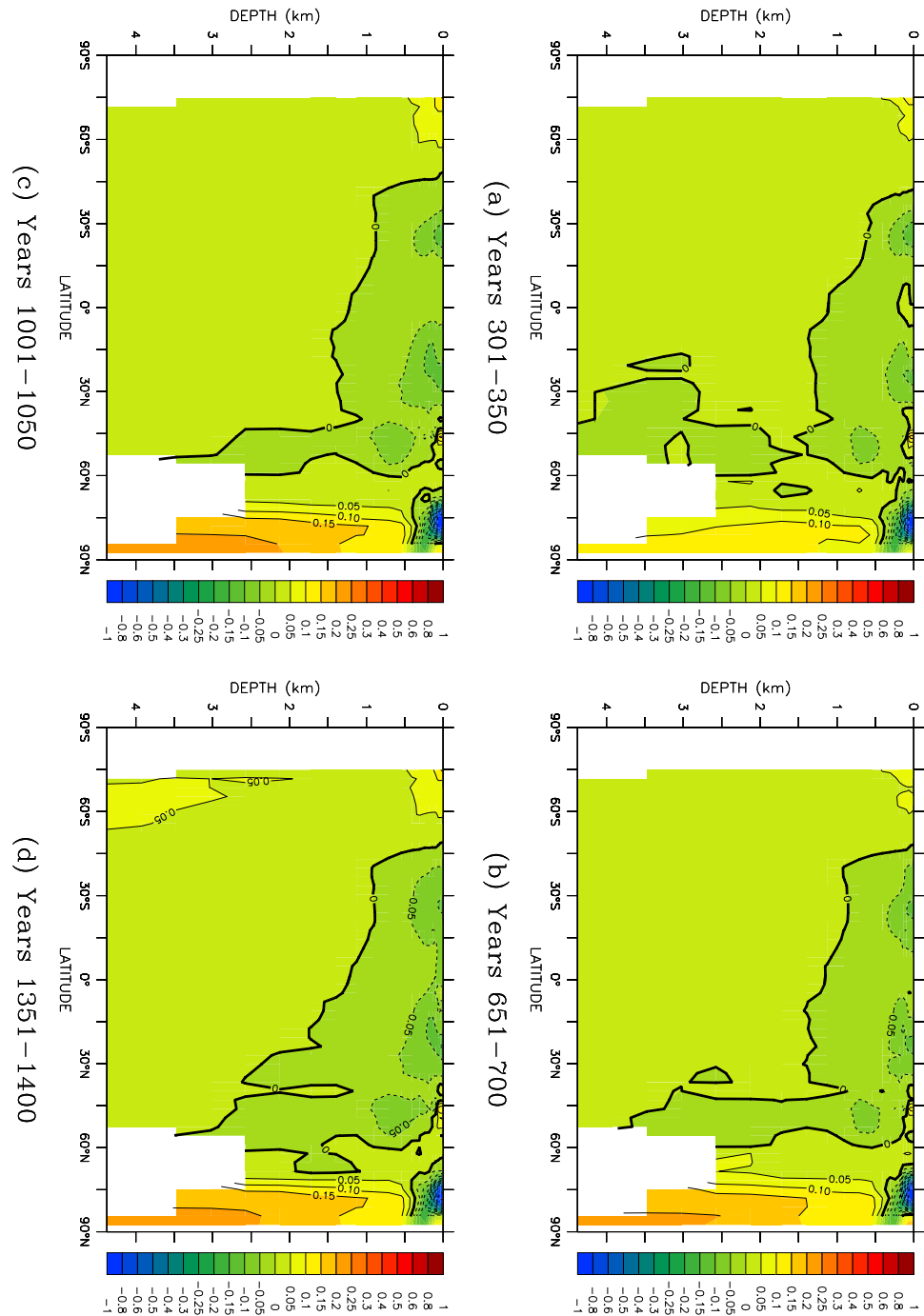


Figure 5.15: The zonal-mean salinity (psu) for coupled model run CON-DEF, expressed as an anomaly relative to the average salinity for the final 100 years of ocean model spin-up run O-DEF: (a) years 301–350, (b) years 651–700, (c) years 1001–1050, and (d) years 1351–1400. The inland seas are excluded when calculating the zonal means.

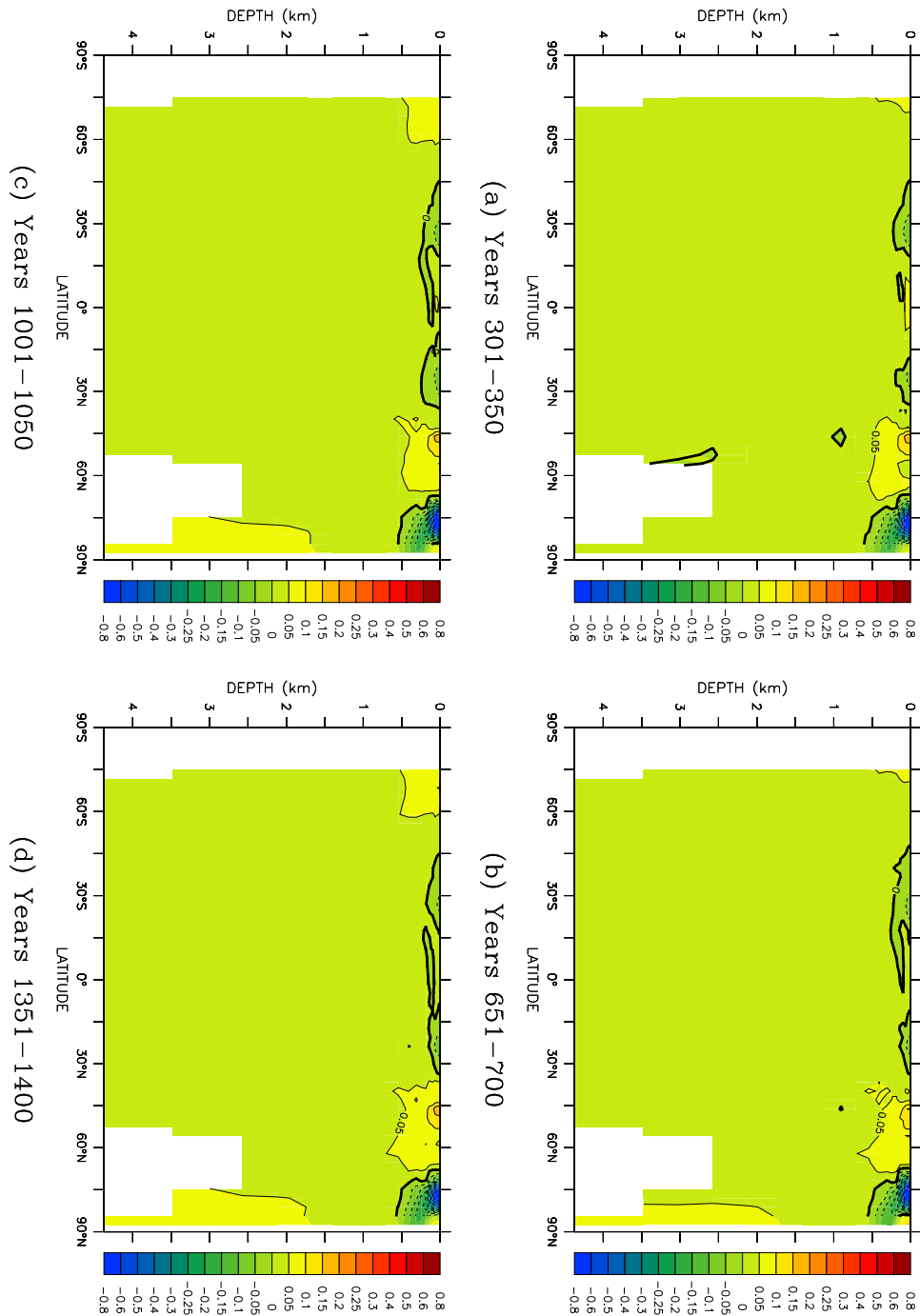


Figure 5.16: The zonal-mean σ_θ (kgm^{-3}) for coupled model run CON-DEF, expressed as an anomaly relative to the average σ_θ for the final 100 years of ocean model spin-up run O-DEF: (a) years 301–350, (b) years 651–700, (c) years 1001–1050, and (d) years 1351–1400. The inland seas are excluded when calculating the zonal means.

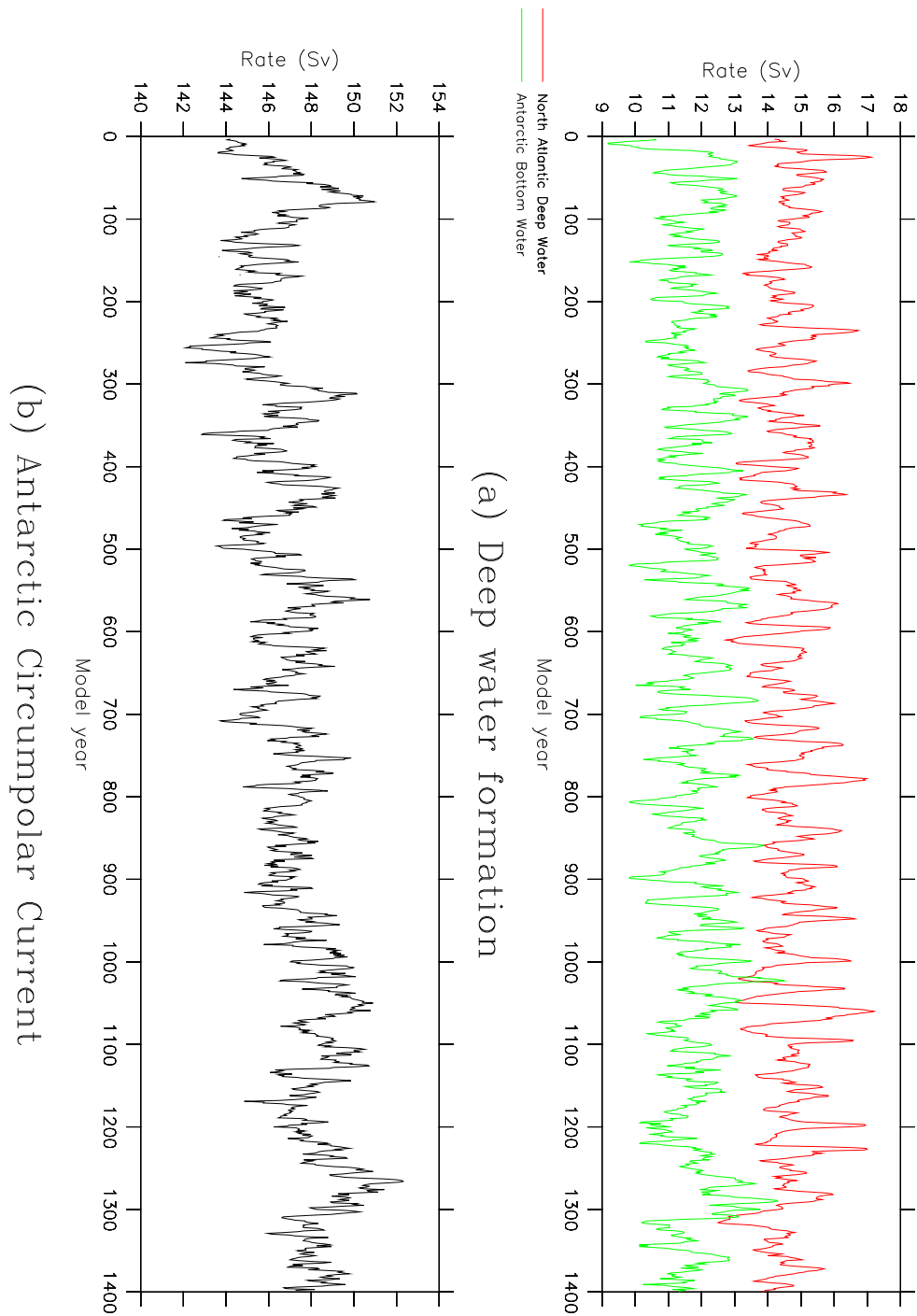
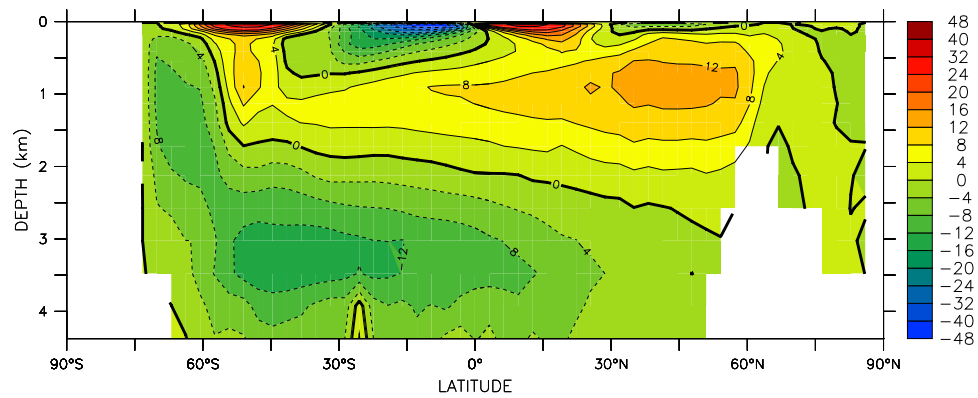
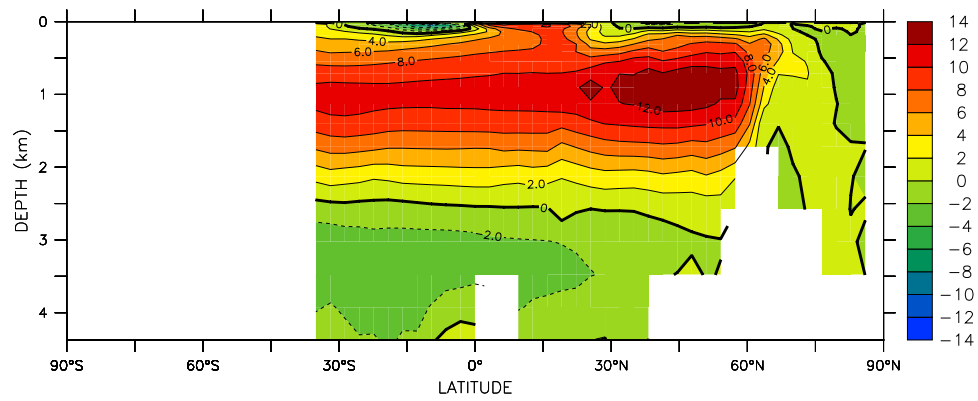


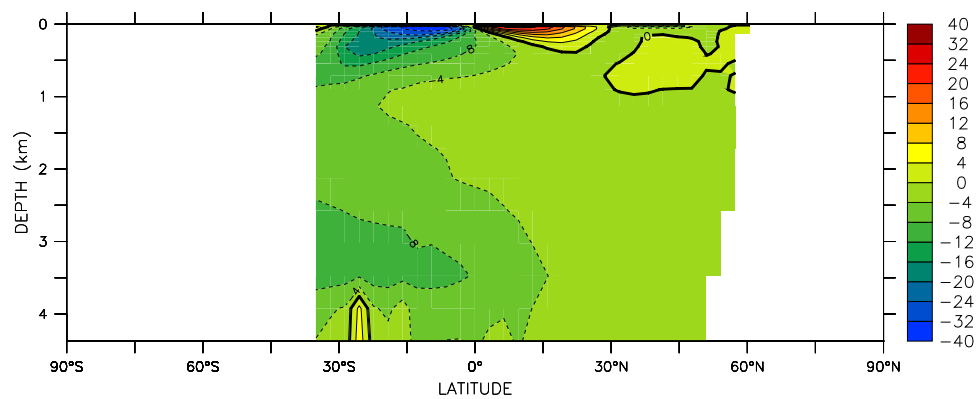
Figure 5.17: The rates of deep water formation, and the strength of the Antarctic Circumpolar Current, for coupled model run CON-DEF: (a) the rates of formation of North Atlantic Deep Water (red) and Antarctic Bottom Water (green), and (b) the rate of volume transport through Drake Passage. The values shown are five-year running means.



(a) World Ocean



(b) Atlantic Ocean



(c) Pacific/Indian Oceans

Figure 5.18: The average meridional overturning streamfunctions (S_v) for years 1301–1400 of coupled model run CON-DEF: (a) the world ocean, (b) the Atlantic Ocean, and (c) the Pacific/Indian Oceans.

the relation

$$\rho_{i,j,k}(0)V_{i,j,k}(0) = \rho_{i,j,k}(t)V_{i,j,k}(t) = M_{i,j,k} \quad (5.1)$$

which, upon re-arrangement, gives

$$V_{i,j,k}(t) = \frac{M_{i,j,k}}{\rho_{i,j,k}(t)} \quad (5.2)$$

$$= \frac{\rho_{i,j,k}(0)}{\rho_{i,j,k}(t)} V_{i,j,k}(0) \quad (5.3)$$

The change in the volume of the gridbox, $\Delta V_{i,j,k}(t)$, is therefore given by

$$\Delta V_{i,j,k}(t) = V_{i,j,k}(t) - V_{i,j,k}(0) \quad (5.4)$$

$$= \left(\frac{\rho_{i,j,k}(0)}{\rho_{i,j,k}(t)} - 1 \right) V_{i,j,k}(0) \quad (5.5)$$

The change in mean sea level $H(t)$ is obtained by summing these volume changes over all the ocean gridboxes, and then dividing the total change in the volume of the ocean by the surface area A , thus:

$$H(t) = \frac{1}{A} \sum_i \sum_j \sum_k \left(\frac{\rho_{i,j,k}(0)}{\rho_{i,j,k}(t)} - 1 \right) V_{i,j,k}(0) \quad (5.6)$$

Equation 5.6 can be used to infer the evolution of the mean sea level during a coupled model simulation. Using the International Equation of State of Seawater 1980 (*UNESCO*, 1981), as described by *Fofonoff* (1985), to calculate density, and using the final century of ocean model spin-up run O-DEF as the reference state, Figure 5.19 shows the changes in the mean sea level inferred from run CON-DEF. The cooling of the world ocean causes it to contract slightly, with a drop of 14.2 cm in the mean sea level by year 1400.

5.2.3 Summary

The control climate of the Mk3L coupled model exhibits a very high degree of stability. Over the course of a 1400-year control simulation, the global-mean surface air temperature cools 0.23°C, representing an average rate of change of just -0.016°C/century. Some initial adjustment occurs during the first century of the run, during which there is an expansion in the Northern Hemisphere sea ice cover. The resulting cooling in the North Atlantic results in a decrease in the temperature of North Atlantic Deep Water, which leads to a slow but ongoing cooling of the ocean. The thermohaline circulation strengthens slightly during the first century of the run, but is stable thereafter.

The decline in the temperature of the ocean, being slow but consistent, represents a source of concern. It is possible that this trend could be reduced by improving the spin-up procedure for the atmosphere model. It was noted in Section 2.4.4 that

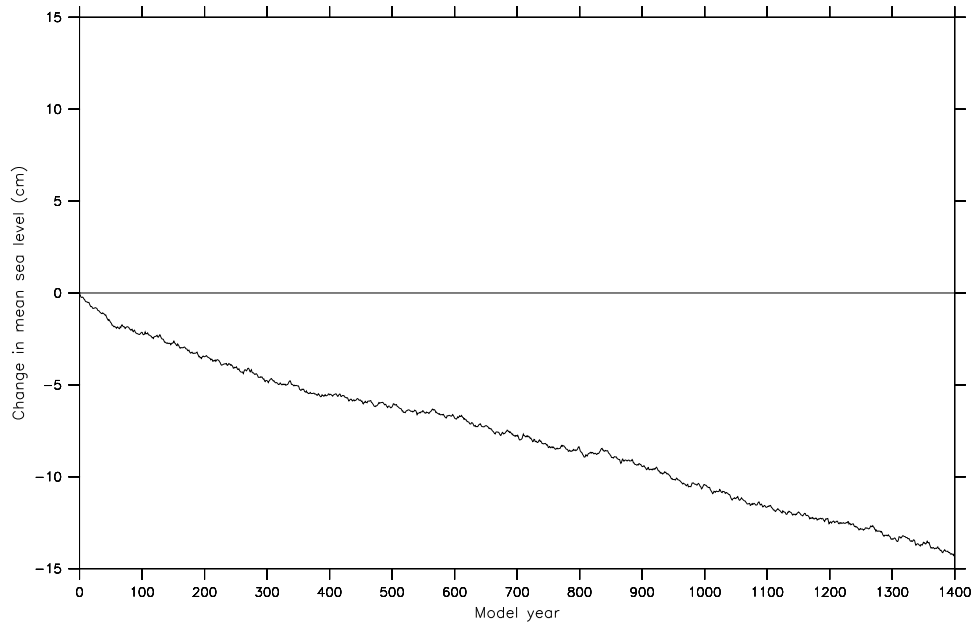


Figure 5.19: The steric change in mean sea level diagnosed from coupled model run CON-DEF.

the sea surface temperatures used to spin-up the atmosphere model appear to be too warm in the Hudson Bay region, and that this leads to deficient sea ice cover. If realistic ice cover could be achieved within the stand-alone atmosphere model, it is possible that the initial adjustment within the coupled model would not occur. The cooling in the North Atlantic, and hence in the ocean, could therefore be averted.

It should be noted, however, that the cooling trend is much smaller than that exhibited by the majority of coupled general circulation models (*Bell et al.*, 2000; *Lambert and Boer*, 2001). Table 5.2 shows the rate of drift in global-mean surface air temperature, as exhibited by 15 models which participated in the Coupled Model Intercomparison Project (*Lambert and Boer*, 2001, Table 7). The drift exhibited by Mk3L is less, typically by between one and two orders of magnitude, than that exhibited by all seven of the non-flux adjusted models, and by all but one of the eight models which employed flux adjustments.

Only the CSIRO Mk2 coupled model exhibits a lower rate of drift; the stability of the control climate of this model has been noted in other studies (e.g. *Hirst et al.*, 2000; *Bi et al.*, 2001; *Bi*, 2002; *Hunt*, 2004). The drift exhibited by the CSIRO Mk3 coupled model, which does not employ flux adjustments, is much larger, however, with *Gordon et al.* (2002) finding that the global-mean sea surface temperature declines $\sim 0.5^\circ\text{C}$ over the course of an 80-year control simulation.

While the drift exhibited by non-flux adjusted models can be attributed to deficiencies in the model physics, Table 5.2 indicates that even models that employ flux adjustments can exhibit considerable drift. *Power* (1995) hypothesises that this is a result of the asymmetric response of ocean models to perturbations about a mean surface flux (see the discussion in Section 1.3).

Model	Trend in global-mean SAT ($^{\circ}\text{C}/\text{century}$)
<i>Flux adjusted</i>	
CCCma	+0.240
CCSR	+0.735
CSIRO	-0.009
GFDL	+0.197
MPI_E3/L	+0.188
MPI_E4/O	-0.124
MRI	+1.057
UKMO	+0.030
<i>Non-flux adjusted</i>	
CERFACS	+0.553
COLA	+0.352
GISS_MILL	+0.929
GISS_RUSS	+0.702
LMD	+4.206
NCAR_CSM	-0.211
NCAR_WM	+0.892

Table 5.2: The rate of drift in global-mean surface air temperature (SAT) for 15 coupled general circulation models which participated in the Coupled Model Inter-comparison Project (*Lambert and Boer, 2001*). Both flux adjusted and non-flux adjusted models are shown.

An apparent freshwater conservation error has also been identified within the Mk3L coupled model, which requires further investigation.

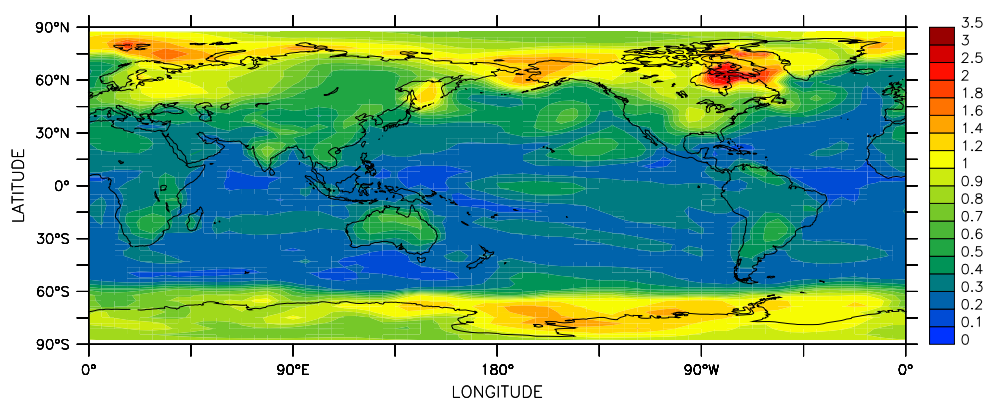
5.3 Climate variability

5.3.1 Interannual variability

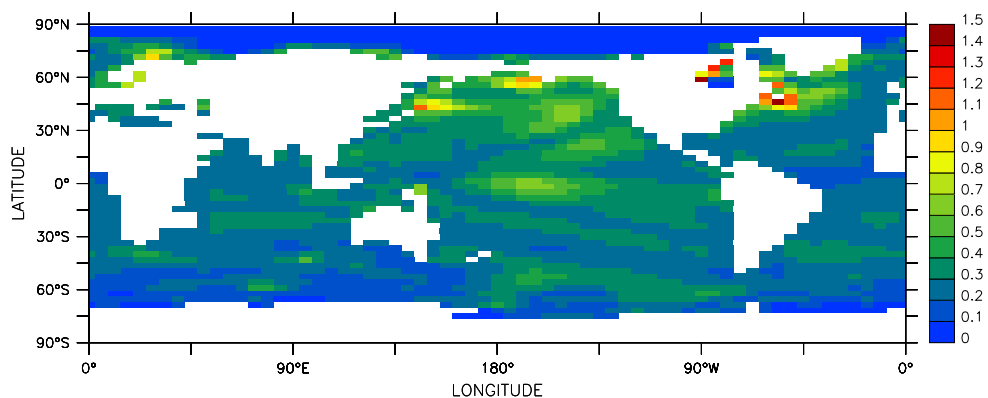
Figure 5.20 shows the standard deviations in the annual-mean surface air temperature (SAT), sea surface temperature (SST) and sea surface salinity (SSS), for years 101–1400 of run CON-DEF. Note that the first 100 years of the run have been excluded, in order to allow for any initial adjustment, and that the data has been de-trended through the application of a high-pass filter. This filter was used to remove variability on timescales longer than 100 years, and hence to remove the effects of any drift in the model climate.

Variability in the annual-mean SAT is greatest over the high-latitude oceans, reflecting interannual variability in the sea ice cover. At mid-latitudes, the variability is greater over land than over the ocean, reflecting the differing surface heat capacities, while, in the tropics, the interannual variability is greatest over the central Pacific Ocean.

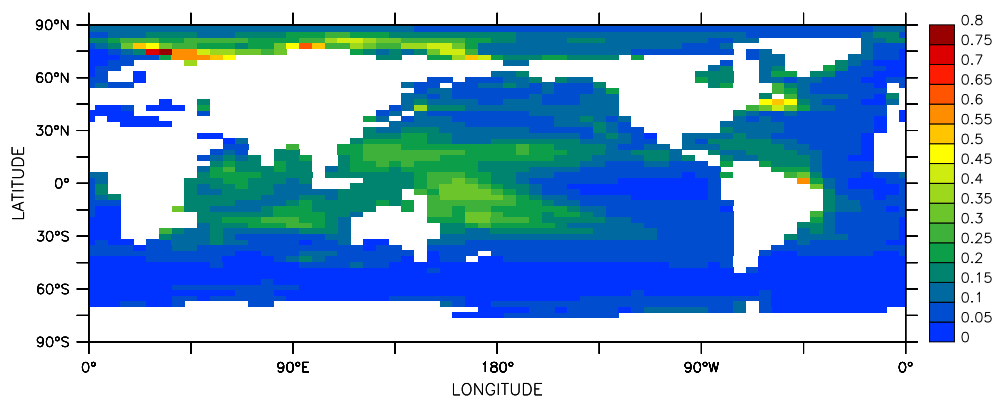
The annual-mean SST exhibits the greatest variability at a few isolated locations



(a) Surface air temperature



(b) Sea surface temperature



(c) Sea surface salinity

Figure 5.20: Standard deviations in annual-mean surface fields for years 101–1400 of coupled model run CON-DEF: (a) surface air temperature ($^{\circ}\text{C}$), (b) sea surface temperature ($^{\circ}\text{C}$), and (c) sea surface salinity (psu). The data has been high-pass filtered to remove variability on timescales longer than 100 years.

along the edge of the Northern Hemisphere sea ice zone, again reflecting interannual variability in the sea ice cover. However, as a result of the insulating effects of sea ice, variability in the annual-mean SST is otherwise small at high latitudes. The Pacific Ocean exhibits the greatest variability at low latitudes, with the largest standard deviation of 0.66°C occurring in the central Pacific; this indicates the presence of a simulated El Niño-Southern Oscillation (see below). Overall, the annual-mean SST exhibits less variability than the annual-mean SAT, with the area-weighted global-mean standard deviations being 0.30°C and 0.45°C respectively.

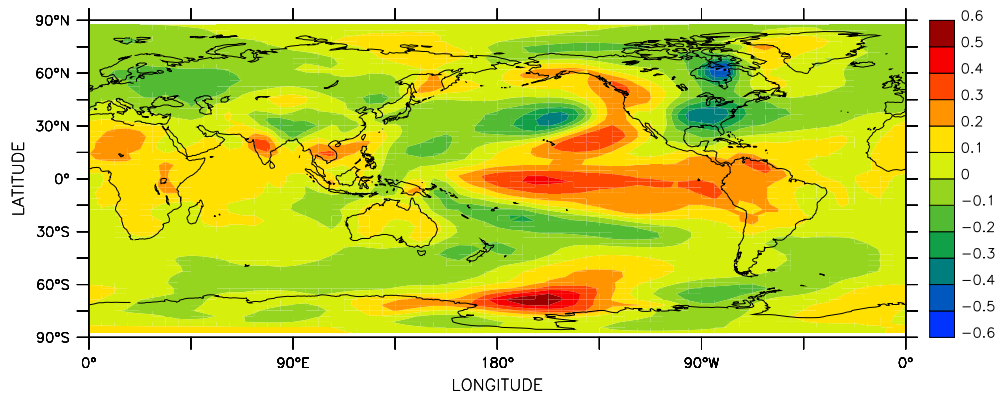
Variability in the annual-mean SSS (Figure 5.20c) is dominated by two processes. The largest variability occurs over the Arctic Ocean and along the Atlantic coast of Canada, reflecting interannual variability in the sea ice cover. At lower latitudes, however, the greatest variability occurs in the monsoonal regions, reflecting interannual variability in the strength and position of the monsoons.

Figure 5.21 shows the leading principal components (*Wilks, 1995*) of the annual-mean surface air temperature, sea surface temperature and sea surface salinity for years 101–1400 of run CON-DEF. As with the standard deviations, the first 100 years of the run have been excluded from the analysis and, prior to calculating the principal components, a high-pass filter was applied in order to remove variability on timescales longer than 100 years. The fractions of the total variance to be described by the leading principal components are 10.6%, 22.3% and 18.1%, for the SAT, SST and SSS respectively. In contrast, the second principal components describe 5.5%, 6.0% and 8.1% respectively.

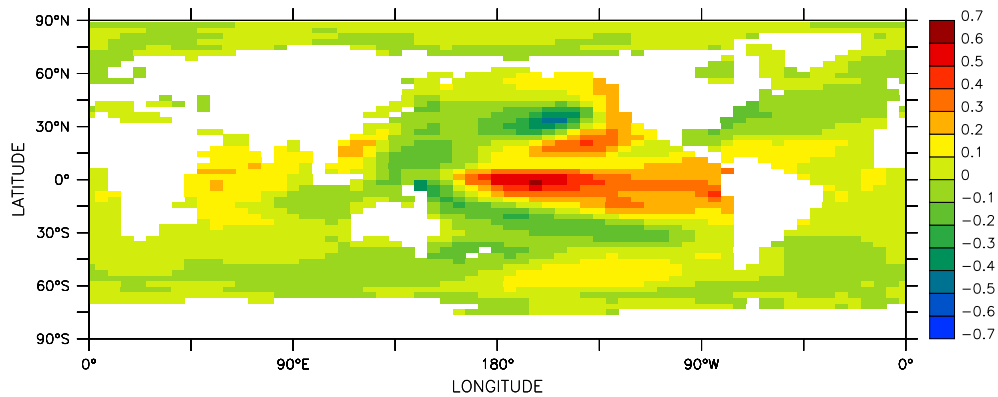
In the case of the SST, the leading mode of variability is therefore dominant to an extent not encountered in the case of either the SAT or SSS. The spatial pattern shown in Figure 5.21b is associated with a time-dependent amplitude, which indicates both the strength and the phase of the mode. The positive phase consists of positive anomalies in the eastern tropical Pacific Ocean, with the largest anomalies occurring over the equator near 160°W . These are accompanied by negative anomalies to the west and at higher latitudes, with the largest anomalies occurring in the central northern Pacific Ocean, at $\sim 160^{\circ}\text{W}$, $\sim 35^{\circ}\text{N}$. In the negative phase of this mode, the signs of the anomalies are reversed.

The leading mode of variability in the annual-mean surface air temperature, while representing a smaller fraction of the total variance, clearly represents the same physical mode. Positive and negative temperature anomalies over the Pacific Ocean exhibit the same spatial structure as for the SST. However, there is also associated variability at higher latitudes, with temperature anomalies over the Ross Sea, Hudson Bay, and the eastern United States, which exceed in magnitude those over the Pacific Ocean.

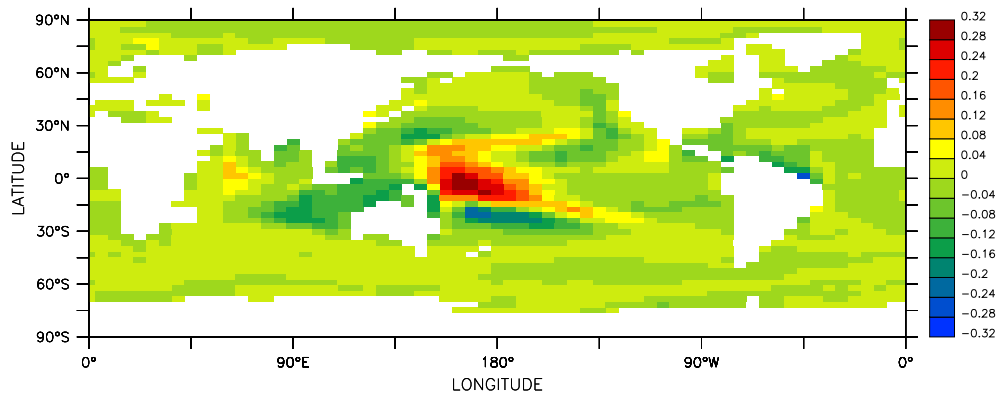
In contrast, the spatial structure of the leading mode of variability in the annual-mean sea surface salinity (Figure 5.21c) exhibits the largest anomalies in the monsoonal regions. This indicates that interannual variability in the strength and position of the monsoons is the largest single influence on variability in the annual-mean SSS.



(a) Surface air temperature



(b) Sea surface temperature



(c) Sea surface salinity

Figure 5.21: The leading principal components of annual-mean surface fields for years 101–1400 of coupled model run CON-DEF: (a) surface air temperature ($^{\circ}\text{C}$), (b) sea surface temperature ($^{\circ}\text{C}$), and (c) sea surface salinity (psu). The data has been high-pass filtered prior to calculating the principal components to remove variability on timescales longer than 100 years.

5.3.2 El Niño-Southern Oscillation

The leading mode of variability in the annual-mean sea surface temperature exhibits the same spatial structure in the Pacific Ocean as the temperature anomalies which occur during El Niño events. The El Niño-Southern Oscillation (ENSO) phenomenon (e.g. *Philander*, 1990) represents the dominant mode of internal variability within the coupled atmosphere-ocean system, and is one of the largest sources of interannual climate variability.

An El Niño event occurs when mean sea level pressure (MSLP) decreases over the central and eastern tropical Pacific Ocean. As a result, the easterly trade winds weaken, and the warmer waters of the western tropical Pacific Ocean migrate eastwards. An El Niño event is therefore characterised by positive (negative) SST (MSLP) anomalies in the eastern tropical Pacific Ocean, and negative (positive) SST (MSLP) anomalies in the western tropical Pacific Ocean. A La Niña event represents the opposite phase, with negative (positive) SST (MSLP) anomalies in the east, and positive (negative) SST (MSLP) anomalies in the west.

Trenberth (1997) defines an El Niño event as one where the five-month running mean of the SST anomalies in the Niño 3.4 region (170°–120°W, 5°S–5°N) exceeds 0.4°C for at least six consecutive months. The Niño 3.4 SST anomalies are derived from years 101–1400 of run CON-DEF, through the application of a high-pass filter which removes variability on timescales longer than 100 years. The standard deviation of the five-month running mean of the simulated anomalies is 0.49°C, as compared to the observed value for the period 1950–1979 of 0.71°C (*Trenberth*, 1997).

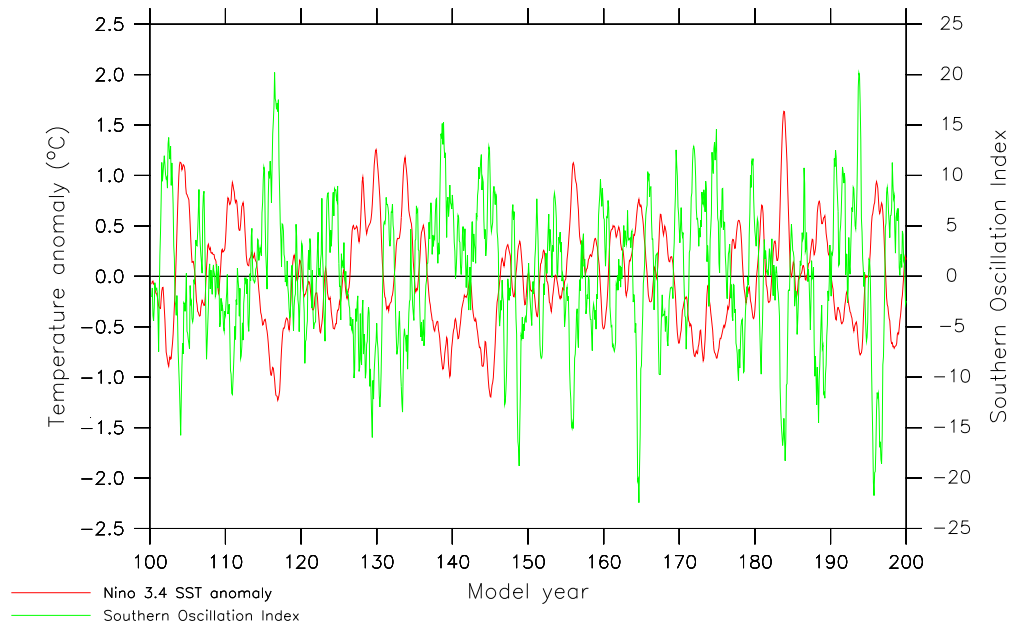
While the Niño 3.4 SST anomaly is a measure of the oceanic changes associated with ENSO, the Southern Oscillation Index (SOI, e.g. *Ropelewski and Jones*, 1987) is a measure of the atmospheric changes. The SOI represents the standardised anomaly of the MSLP difference between Tahiti (149.6°W, 17.5°S) and Darwin (130.9°E, 12.5°S). Let P_i be the MSLP difference (Tahiti minus Darwin) for calendar month i , let \bar{P}_i be the long-term mean of P_i , and let σ_i be the long-term standard deviation of P_i . The SOI is therefore given by

$$\text{SOI} = 10 \left(\frac{P_i - \bar{P}_i}{\sigma_i} \right) \quad (5.7)$$

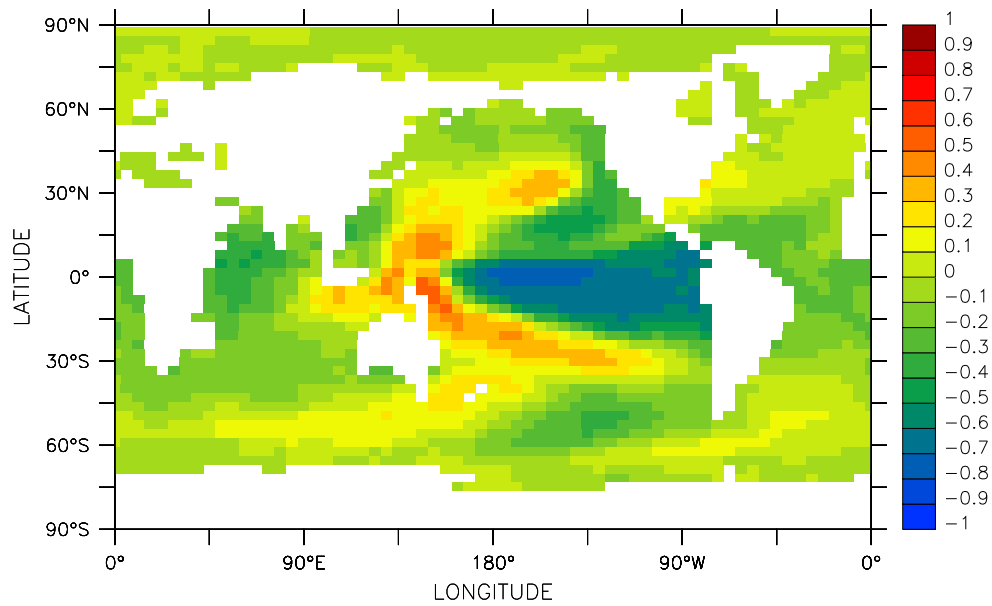
The factor of 10 is included by convention. Negative values of the SOI represent positive MSLP anomalies in the western tropical Pacific Ocean, and negative MSLP anomalies in the eastern tropical Pacific Ocean, as occur during an El Niño event. Values of the SOI are diagnosed from years 101–1400 of run CON-DEF, with the MSLP anomalies $P_i - \bar{P}_i$ being calculated through the application of a high-pass filter which removes variability on timescales longer than 100 years.

The Niño 3.4 SST anomaly and Southern Oscillation Index are strongly anti-correlated, with a correlation coefficient of -0.78. This is illustrated by Figure 5.22, which shows the values of the two indices for years 101–200 of run CON-DEF.

Figure 5.22b also shows the correlation between the simulated SST anomalies at each gridpoint, and the Southern Oscillation Index. There is excellent agreement with the observed correlations (*Trenberth and Hoar*, 1996), with strong negative correlations throughout the eastern Pacific Ocean, and strong positive correlations



(a) Nino 3.4 SST anomaly and SOI



(b) Correlation between SST and SOI

Figure 5.22: The El Niño-Southern Oscillation phenomenon in coupled model run CON-DEF: (a) the Niño 3.4 sea surface temperature (SST) anomaly, and the Southern Oscillation Index (SOI), for years 101–200, and (b) the correlation between SST and the SOI for years 101–1400. The values shown for the Niño 3.4 SST anomaly and the SOI are five-month running means.

throughout the western Pacific Ocean. The maximum anti-correlation of -0.77 occurs at 163°W , 2°N , within the Niño 3.4 region. The spatial structure of the correlations strongly resembles that of the leading principal component of the annual-mean SST (Figure 5.21b).

Applying the definition of *Trenberth* (1997), there are 166 simulated El Niño events during years 101–1400 of run CON-DEF, with an average return period of 7.8 ± 0.5 years (note that the errors quoted in this section represent one standard deviation in the mean). The average duration of the events is 17.4 ± 0.8 months, and the average magnitude of the events, defined here as the maximum size of the Niño 3.4 SST anomaly, is $0.88 \pm 0.02^\circ\text{C}$. Using observed sea surface temperatures for the period January 1950–March 1997, *Trenberth* (1997) identifies 15 El Niño events, giving an observed return period of ~ 3.2 years. The average duration of these events is 11.8 months, and the average magnitude is $\sim 1.3^\circ\text{C}$. Thus, relative to observations, the simulated frequency is too low, and the simulated El Niño events are too long and too weak.

Figure 5.23 shows the power spectra of the simulated Niño 3.4 SST anomaly and Southern Oscillation Index, and of the amplitude of the leading principal component of the annual-mean SST; note that variability on timescales longer than 100 years was removed from the original data through the application of a high-pass filter. Note also that the spectra have been smoothed through the application of a Hann window (*Press et al.*, 1992) of width 25, which corresponds to a width of ~ 0.019 years $^{-1}$ in frequency units. A Hann window is defined by the function

$$w_j = \frac{1}{2} \left[1 - \cos \left(\frac{2\pi j}{N} \right) \right] \quad (5.8)$$

If no smoothing is applied, the standard deviation in each value is $\pm 100\%$; however, the application of a smoother of width N reduces the standard deviation by a factor of \sqrt{N} (*Wilks*, 1995). A Hann window of width N has an *effective* width of $\sim \frac{1}{2}N$ (*Press et al.*, 1992), and so the standard deviation in each value in Figure 5.23 is $\sim \pm 28\%$.

Apparent from Figure 5.23 is the strong correlation between the power spectra for the Niño 3.4 SST anomaly and the leading principal component of annual-mean SST. Interdecadal variability can be seen to dominate, with peaks at ~ 0.028 years $^{-1}$ and ~ 0.048 years $^{-1}$, corresponding to periods of ~ 35 years and ~ 21 years respectively. Thus there is strong interdecadal modulation of the simulated El Niño–Southern Oscillation, consistent with the ENSO-like interdecadal variability observed in the Pacific Ocean (*Zhang et al.*, 1997; *Lohmann and Latif*, 2005). Such interdecadal variability is also exhibited by the CSIRO Mk2 coupled model (*Walland et al.*, 2000; *Vimont et al.*, 2002).

The power spectra of observed ENSO indices show a broad peak at periods of ~ 3 – 6 years (e.g. *Trenberth*, 1997; *AchutaRao and Sperber*, 2002). Within Mk3L, the simulated ENSO is therefore too weak, not only relative to observations, but also relative to the simulated interdecadal variability in the Pacific Ocean.

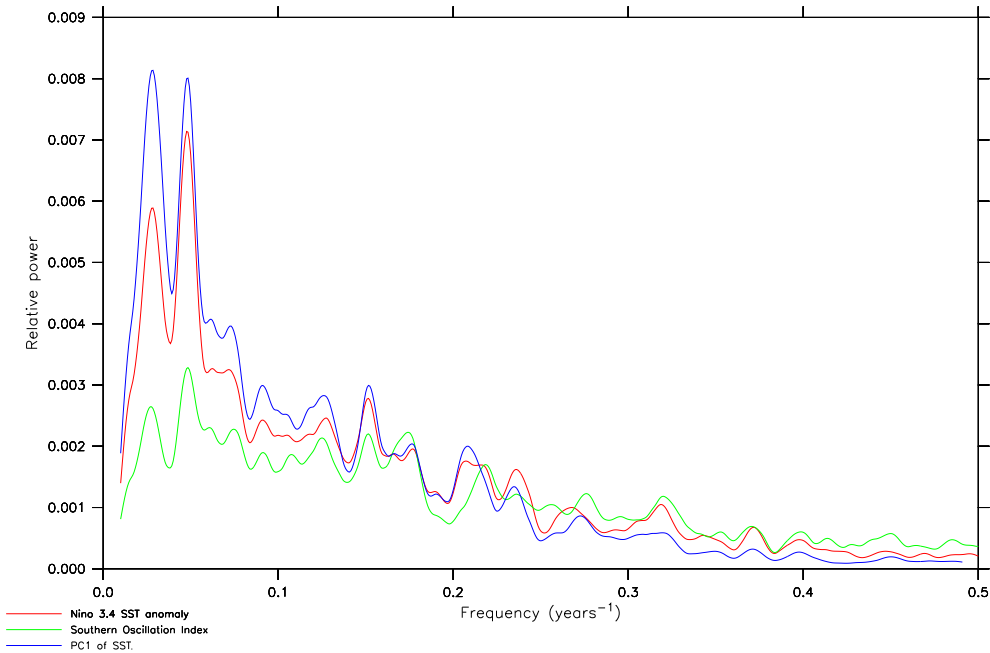


Figure 5.23: The normalised power spectra of the Niño 3.4 sea surface temperature anomaly (red), the Southern Oscillation Index (green), and the amplitude of the leading principal component of annual-mean sea surface temperature (dark blue), for years 101–1400 of coupled model run CON-DEF. Each spectrum has been normalised so that the total power is equal to 1, and then smoothed through the application of a Hann window of width 25.

5.3.3 Summary

The dominant mode of internal variability has been shown to exhibit the same spatial structure and correlations as the observed El Niño-Southern Oscillation phenomenon. The frequency is too low, however, and the simulated El Niño events are too long and too weak. There is also excessive modulation on interdecadal timescales.

The strength of the simulated ENSO, as defined by the standard deviation of the Niño 3.4 SST anomalies, is typical of low-resolution coupled models, such as those which participated in the Coupled Model Intercomparison Project (*AchutaRao and Sperber, 2002*); many of these models also failed to correctly simulate the observed frequency. However, higher-resolution coupled models, such as those which contributed to the IPCC Fourth Assessment Report, have a much more realistic ENSO (*Guilyardi, 2006*).

The simulated El Niño-Southern Oscillation within Mk3L is significantly stronger than that simulated by the CSIRO Mk2 coupled model (*AchutaRao and Sperber, 2002; Vimont et al., 2002; Hunt and Elliott, 2003*). As Mk2 and Mk3L employ the same ocean model, this can be attributed to the enhancements to the atmosphere model in Mk3L (Section 2.2.1); indeed, *Guilyardi et al. (2004)* find that the atmospheric component of coupled models is dominant in determining the characteristics

		CON-DEF	CON-SHF	CON-EFF
Change in global-mean SAT ($^{\circ}\text{C}$)		-0.21	-0.31	-0.45
RMS change in annual-mean SAT ($^{\circ}\text{C}$)		0.52	0.68	0.82
Sea ice extent (10^{12} m^2)	NH	12.0	12.5	13.2
	SH	13.3	14.1	15.6
Sea ice volume (10^{12} m^3)	NH	12.5	14.7	16.4
	SH	5.5	6.1	6.4

Table 5.3: Some statistics for years 1001–1100 of coupled model runs CON-DEF, CON-SHF and CON-EFF: the change in global-mean surface air temperature (SAT), relative to the atmosphere model spin-up runs; the root-mean-square (RMS) change in the SAT; and the sea ice extents and volumes for each hemisphere.

of the simulated El Niño. However, the CSIRO Mk3 coupled model, which employs a much higher spatial resolution than Mk3L, is successful at capturing both the magnitude and frequency of the observed ENSO phenomenon (*Gordon et al.*, 2002; *Cai et al.*, 2003; *Guilyardi*, 2006).

5.4 The impact of the spin-up procedure

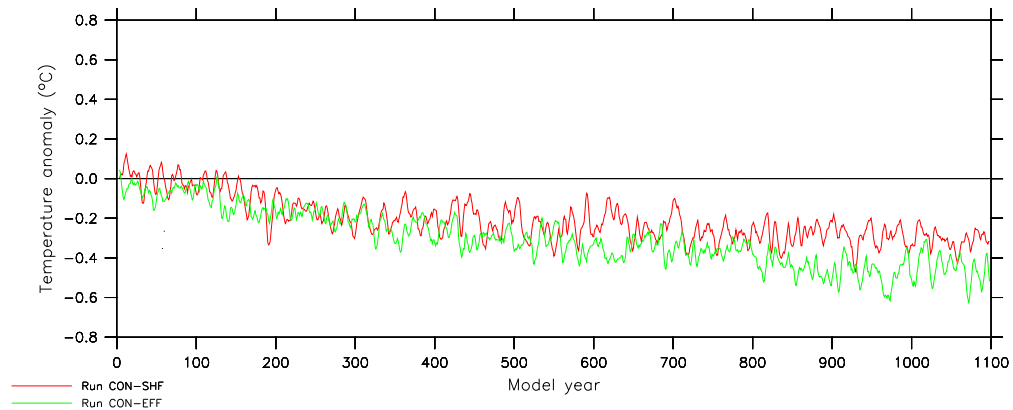
5.4.1 Climate drift: atmosphere

Some statistics on the drift in the climate of the atmosphere model during coupled model control runs CON-SHF and CON-EFF are shown in Table 5.3; statistics are also provided for the equivalent period of run CON-DEF. The nature of the drift is discussed in the following section.

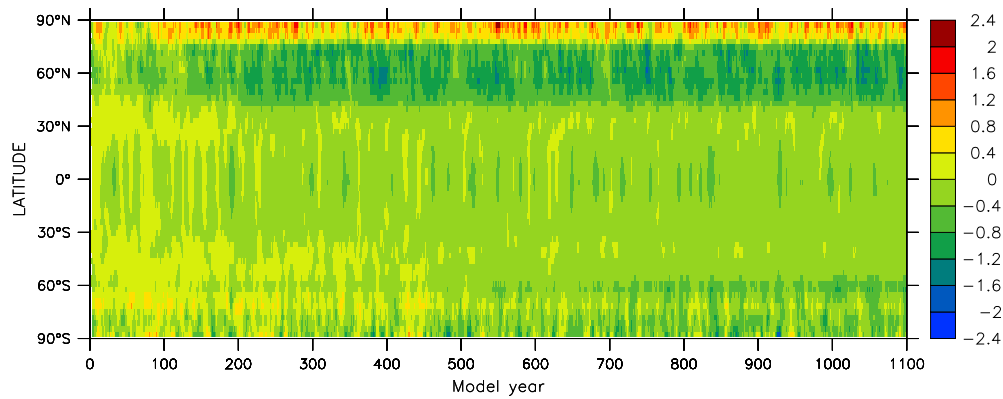
Surface air temperature

The evolution of the simulated global-mean and zonal-mean surface air temperature (SAT) during runs CON-SHF and CON-EFF is shown in Figure 5.24. While the global-mean SAT exhibits only a slight downward trend for both runs, the rate of cooling is greater than for run CON-DEF. The evolution of the zonal-mean SAT is similar to run CON-DEF for both runs, with an initial cooling at $\sim 60^{\circ}\text{N}$, an initial warming at $\sim 80^{\circ}\text{N}$, and an ongoing cooling trend at $\sim 60^{\circ}\text{S}$. However, while the cooling at $\sim 60^{\circ}\text{N}$ stabilises during the initial centuries of run CON-SHF, it appears to represent an ongoing trend in run CON-EFF. The cooling trend at $\sim 60^{\circ}\text{S}$ in run CON-EFF is also stronger than in either of runs CON-DEF or CON-SHF.

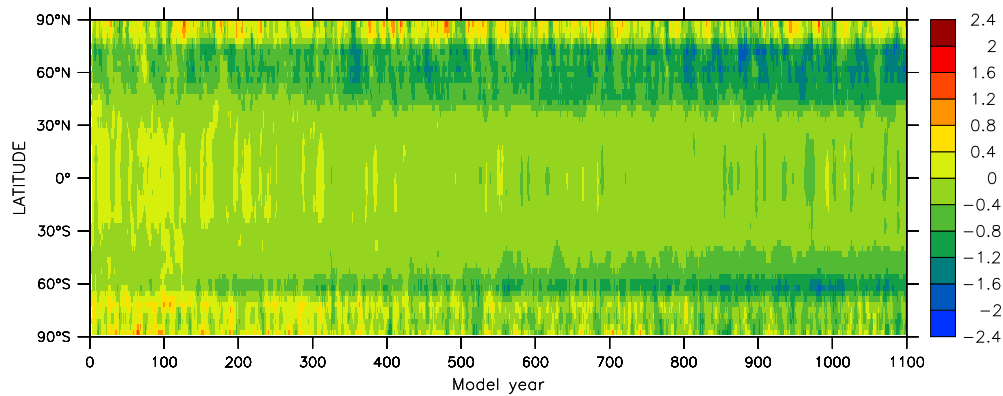
The nature of the drift is similar to run CON-DEF, with a strong reduction in winter temperatures in the Barents Sea, the Sea of Okhotsk and Hudson Bay, and a warming in the Greenland Sea (not shown). Both runs also experience strong cooling over the Caspian Sea, while run CON-EFF experiences a strong reduction in winter temperatures in the Southern Ocean.



(a) Global mean



(b) Run CON-SHF



(c) Run CON-EFF

Figure 5.24: The drift in annual-mean surface air temperature ($^{\circ}\text{C}$) during coupled model runs CON-SHF and CON-EFF: (a) the global mean, for runs CON-SHF (red) and CON-EFF (green), (b) the zonal mean for run CON-SHF, and (c) the zonal mean for run CON-EFF. The values shown are five-year running means, and are expressed as anomalies relative to the average surface air temperature for the final 40 years of the atmosphere model spin-up runs.

Sea ice

Figure 5.25 shows the evolution of the sea ice extent and volume in each hemisphere, for runs CON-SHF and CON-EFF. Both runs experience an increase in Northern Hemisphere sea ice extent during the initial centuries; the extent stabilises thereafter in run CON-SHF, but exhibits a slight upward trend in run CON-EFF. Consistent with the cooling trends over the Southern Ocean, both runs experience an upward trend in sea ice extent in the Southern Hemisphere, although the trend is only slight in the case of run CON-SHF.

The sea ice volume in each hemisphere varies in a similar manner to the sea ice extent. After some initial adjustment, the Northern Hemisphere ice volume is stable in run CON-SHF, but exhibits a slight upward trend in run CON-EFF. The Southern Hemisphere ice volume exhibits a slight upward trend in both runs.

The changes in sea ice extent are similar to those within run CON-DEF, with the ice cover expanding into Hudson Bay, the Labrador Sea and the Caspian Sea, an increase in ice cover in the Barents Sea and the Sea of Okhotsk, and a decrease in cover in the Greenland Sea (not shown). In run CON-SHF, ice persists throughout the summer in the Gulf of St Lawrence (on the Atlantic coast of Canada), while in run CON-EFF, the sea ice concentrations in Hudson Bay are higher than for run CON-DEF.

Relative to run CON-DEF, there is little difference in the ice thicknesses exhibited by runs CON-SHF and CON-EFF (not shown). However, the model's upper limit of 6 m is reached by both runs over the Caspian Sea, indicating the degree to which this basin has cooled.

5.4.2 Climate drift: ocean

Some statistics on the drift in the climate of the ocean model during coupled model control runs CON-SHF and CON-EFF are shown in Table 5.4; statistics are also provided for the equivalent period of run CON-DEF. The nature of the drift is discussed in the following section.

Sea surface temperature and salinity

Figures 5.26 and 5.27 show the evolution of the simulated global-mean and zonal-mean sea surface temperature (SST) and sea surface salinity (SSS), respectively, for runs CON-SHF and CON-EFF.

The global-mean SST exhibits a slight cooling trend for both runs, with the rate of cooling being greater than for run CON-DEF. The evolution of the zonal-mean SST resembles that of run CON-DEF, with an initial cooling at $\sim 60^\circ\text{N}$, and an initial warming in the Southern Ocean, which is followed by a cooling trend. However, while the cooling at $\sim 60^\circ\text{N}$ appears to stabilise in the case of run CON-SHF, there is an ongoing cooling trend in run CON-EFF. The nature of the drift is similar to run CON-DEF, with strong cooling occurring along the Atlantic coast of Canada, and in Hudson Bay, the Sea of Okhotsk and the Barents Sea (not shown). However, strong cooling also occurs over the Caspian Sea and in the Southern Ocean, particularly in the case of run CON-EFF.

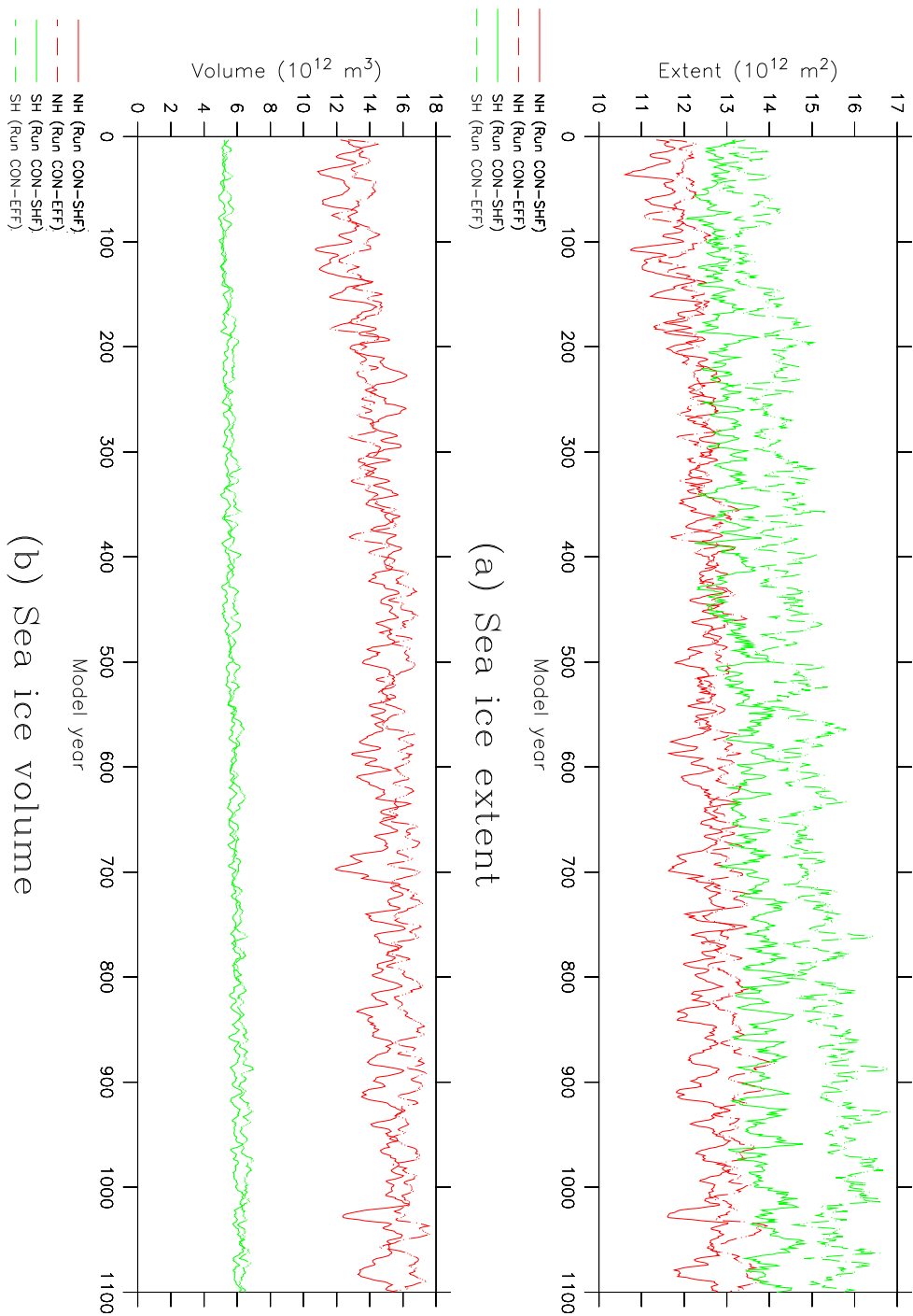
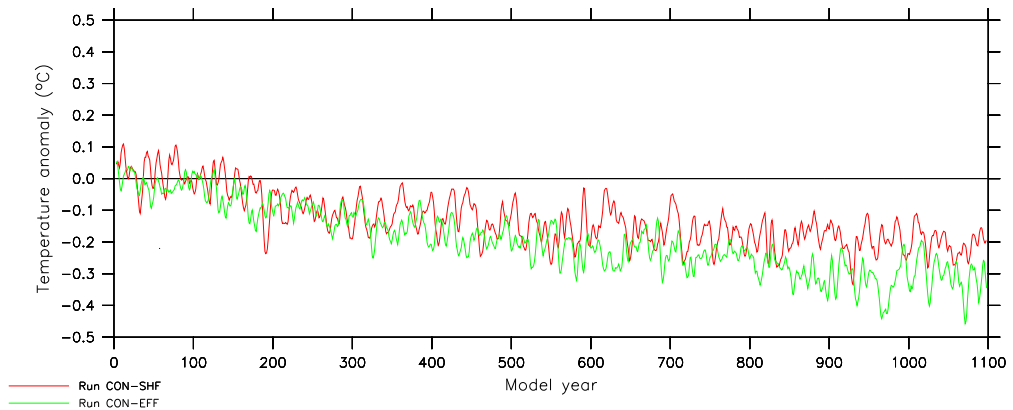
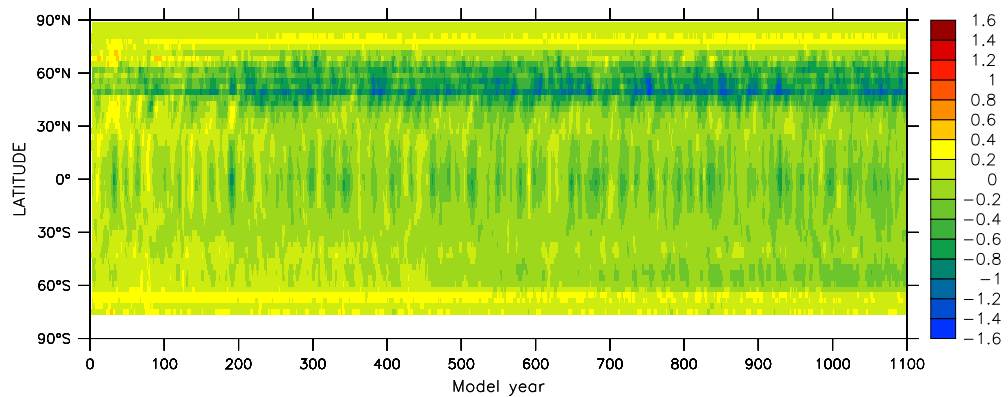


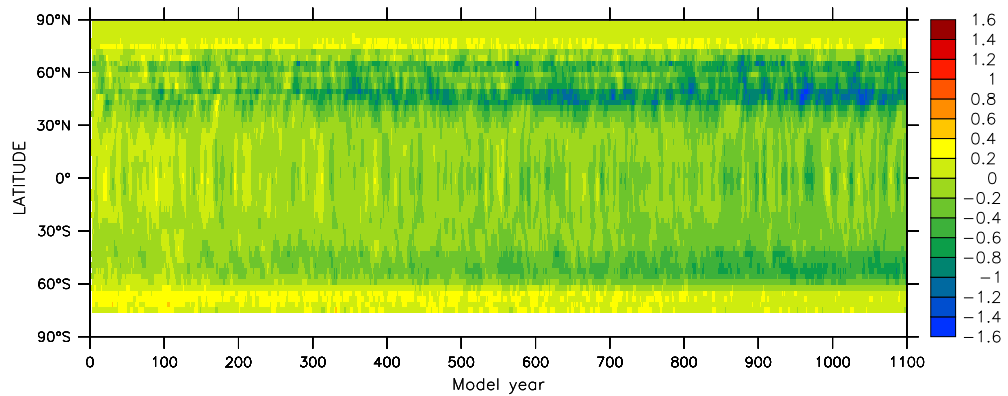
Figure 5.25: The annual-mean sea ice extent and volume for coupled model runs CON-SHF (solid lines) and CON-EFF (dashed lines), for the Northern Hemisphere (red) and Southern Hemisphere (green): (a) sea ice extent, and (b) sea ice volume. The values shown are five-year running means.



(a) Global mean

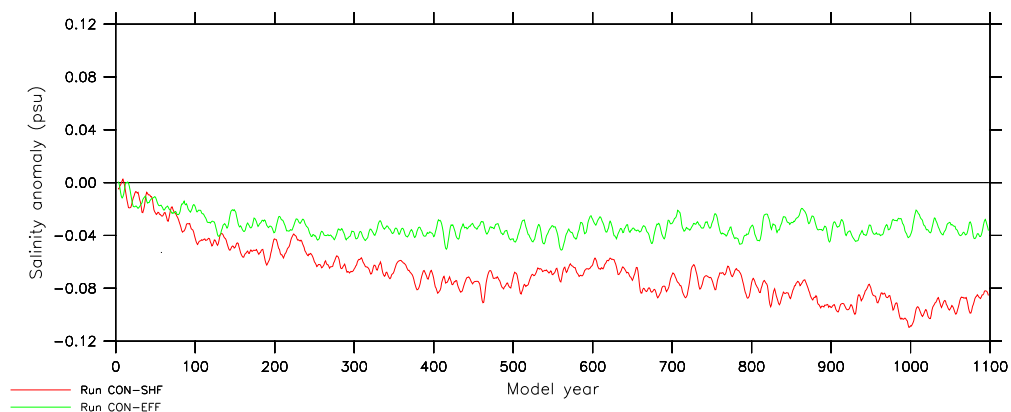


(b) Run CON-SHF

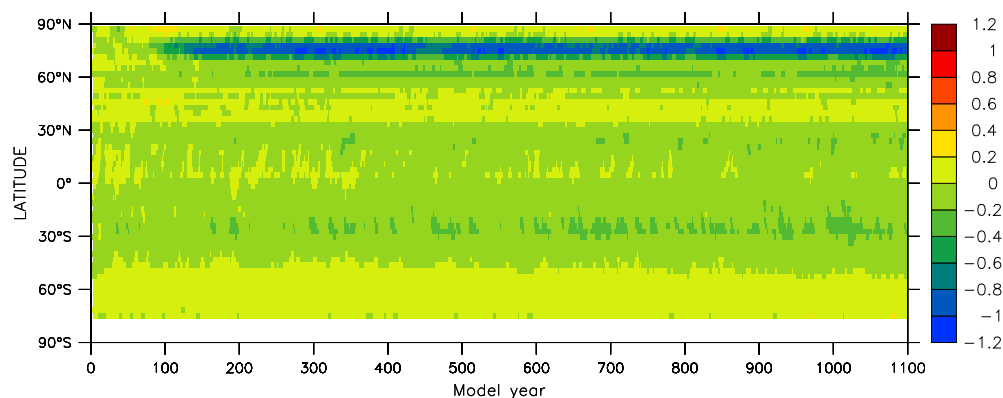


(c) Run CON-EFF

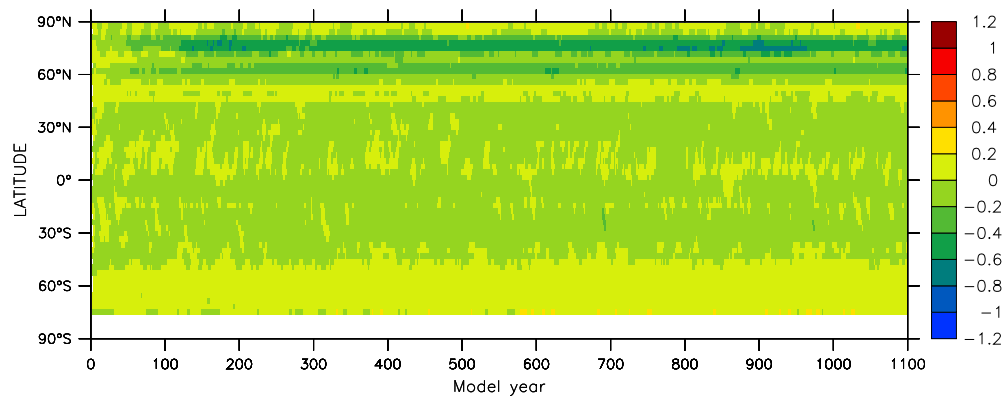
Figure 5.26: The drift in annual-mean sea surface temperature (°C) during coupled model runs CON-SHF and CON-EFF: (a) the global mean, for runs CON-SHF (red) and CON-EFF (green), (b) the zonal mean for run CON-SHF, and (c) the zonal mean for run CON-EFF. The values shown are five-year running means, and are expressed as anomalies relative to the average sea surface temperature for the final 100 years of the ocean model spin-up runs.



(a) Global mean



(b) Run CON-SHF



(c) Run CON-EFF

Figure 5.27: The drift in annual-mean sea surface salinity (psu) during coupled model runs CON-SHF and CON-EFF: (a) the global mean, for runs CON-SHF (red) and CON-EFF (green), (b) the zonal mean for run CON-SHF, and (c) the zonal mean for run CON-EFF. The values shown are five-year running means, and are expressed as anomalies relative to the average sea surface salinity for the final 100 years of the ocean model spin-up runs.

	CON-DEF	CON-SHF	CON-EFF
Change in global-mean SST (°C)	-0.14	-0.20	-0.31
Change in global-mean SSS (psu)	-0.053	-0.093	-0.034
RMS change in annual-mean SST (°C)	0.31	0.38	0.47
RMS change in annual-mean SSS (psu)	0.33	0.31	0.23
Change in mean potential temperature (°C)	-0.18	-0.30	-0.39
Change in mean salinity (psu)	+0.006	+0.009	+0.015
Change in mean σ_θ (kgm^{-3})	+0.025	+0.040	+0.052
Rate of NADW formation (Sv)	14.0	14.2	17.6
Rate of AABW formation (Sv)	11.7	12.6	10.4
Strength of ACC (Sv)	148.8	150.6	136.7
Change in mean sea level (cm)	-11.6	-18.5	-24.7

Table 5.4: Some statistics for years 1001–1100 of coupled model runs CON-DEF, CON-SHF and CON-EFF: the changes in global-mean sea surface temperature (SST) and sea surface salinity (SSS), relative to the ocean model spin-up runs; the root-mean-square (RMS) changes in the SST and SSS; the changes in the mean potential temperature, salinity and σ_θ of the ocean; the rates of North Atlantic Deep Water (NADW) and Antarctic Bottom Water (AABW) formation; the strength of the Antarctic Circumpolar Current; and the change in mean sea level by year 1100.

The global-mean SSS exhibits a slight freshening trend in both runs. The zonal-mean SSS exhibits a freshening at $\sim 75^\circ\text{N}$, as with run CON-DEF, and is otherwise stable for both runs. The nature of the drift is similar to run CON-DEF, with freshening over the Barents Sea, and slight salinity increases along the Atlantic coast of Canada (not shown). While both runs exhibit less drift in the salinity of the Caspian Sea than run CON-DEF, there is increased drift in other locations, including a freshening of Hudson Bay. Overall, the sea surface salinity in run CON-EFF exhibits a smaller root-mean-square change than in either of runs CON-DEF or CON-SHF.

Water properties

The evolution of the simulated global-mean potential temperature, salinity and potential density of the world ocean, and of the simulated global-mean vertical profiles, during runs CON-SHF and CON-EFF are shown in Figures 5.28, 5.29 and 5.30 respectively.

The world ocean cools more rapidly than in run CON-DEF, as a result of the stronger surface cooling. The nature of the cooling is similar to run CON-DEF, being dominated by a decrease in the temperature of North Atlantic Deep Water

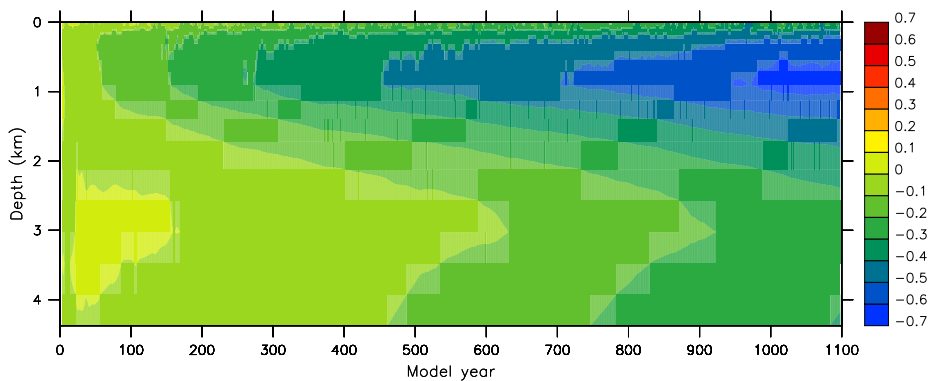
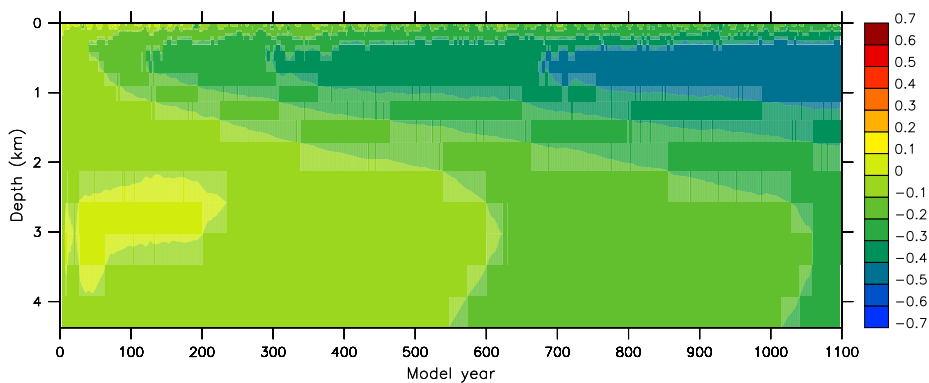
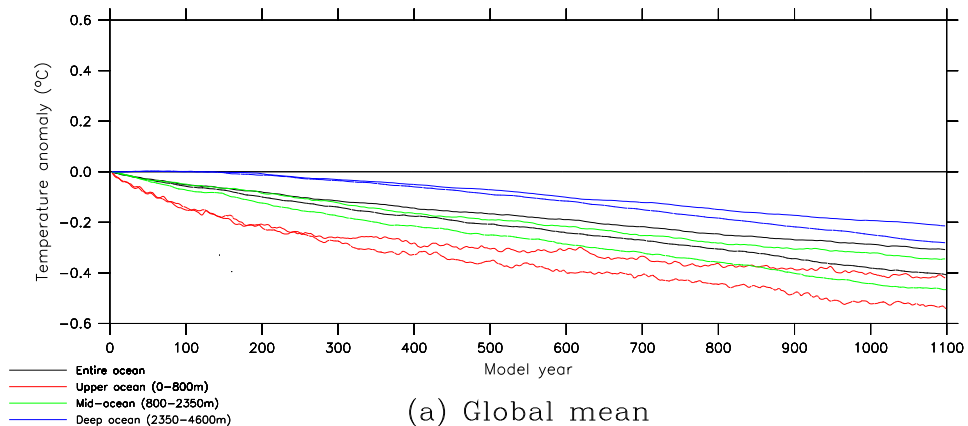
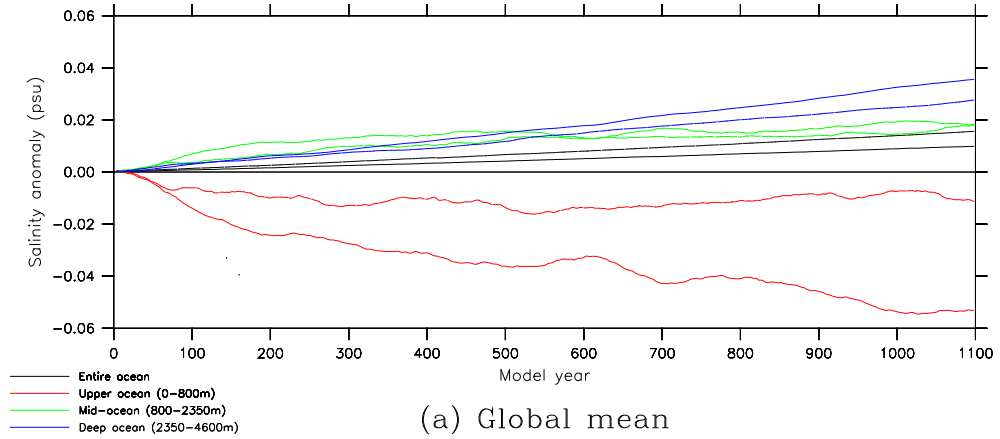
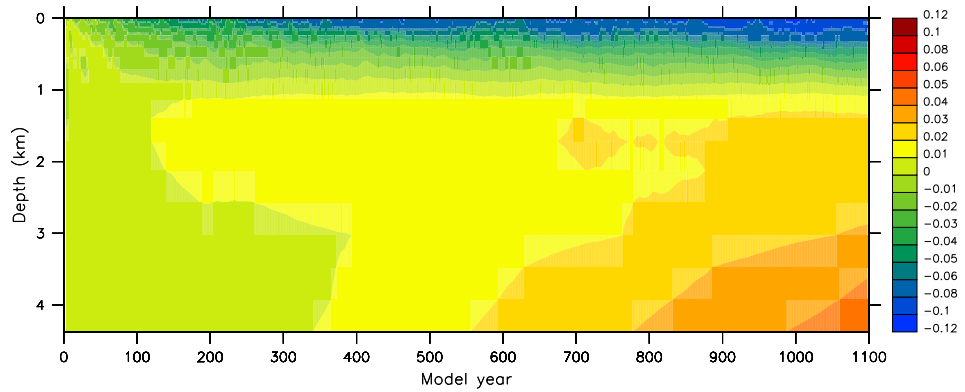


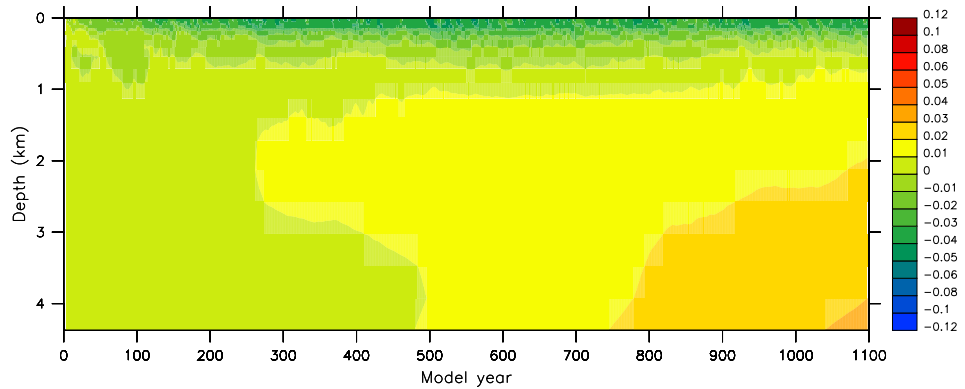
Figure 5.28: The drift in annual-mean potential temperature (°C) during coupled model runs CON-SHF (solid lines) and CON-EFF (dashed lines): (a) the global means for the entire ocean (black), upper ocean (red, 0–800 m), mid-ocean (green, 800–2350 m) and deep ocean (dark blue, 2350–4600 m), (b) the global-mean vertical profile for run CON-SHF, and (c) the global-mean vertical profile for run CON-EFF. The values shown are five-year running means, and are expressed as anomalies relative to the annual-mean potential temperature for the final 100 years of the ocean model spin-up runs.



(a) Global mean



(b) Run CON-SHF



(c) Run CON-EFF

Figure 5.29: The drift in annual-mean salinity (psu) during coupled model runs CON-SHF (solid lines) and CON-EFF (dashed lines): (a) the global means for the entire ocean (black), upper ocean (red, 0–800 m), mid-ocean (green, 800–2350 m) and deep ocean (dark blue, 2350–4600 m), (b) the global-mean vertical profile for run CON-SHF, and (c) the global-mean vertical profile for run CON-EFF. The values shown are five-year running means, and are expressed as anomalies relative to the annual-mean salinity for the final 100 years of the ocean model spin-up runs.

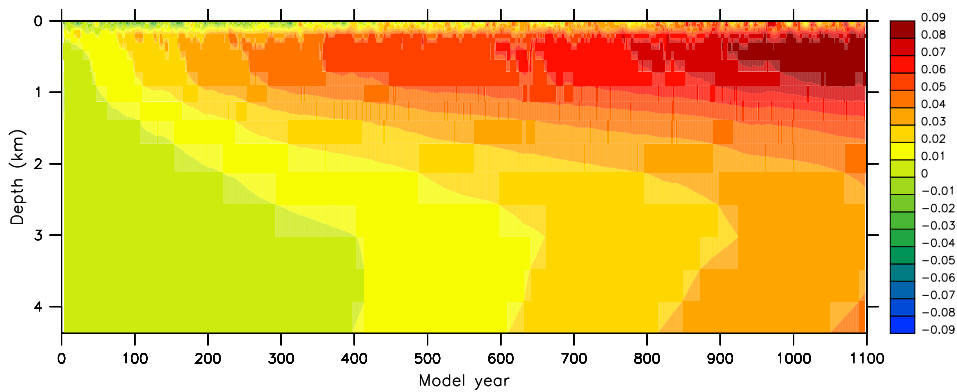
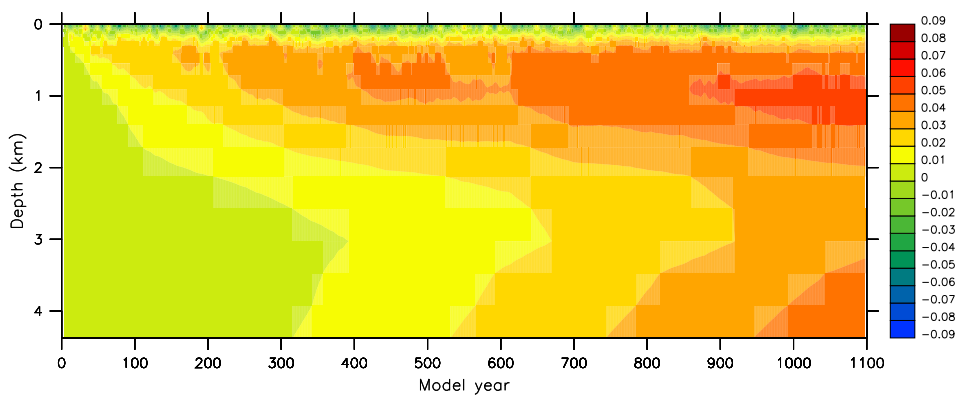
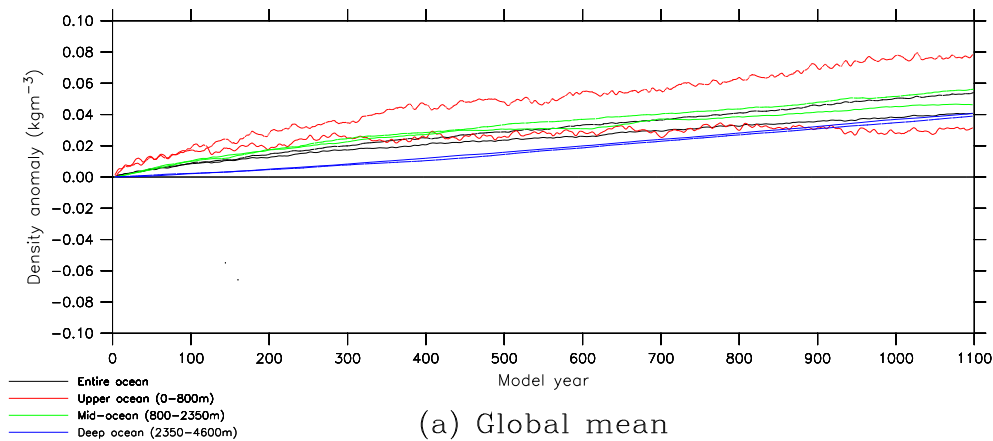


Figure 5.30: The drift in annual-mean σ_θ (kgm^{-3}) during coupled model runs CON-SHF (solid lines) and CON-EFF (dashed lines): (a) the global means for the entire ocean (black), upper ocean (red, 0–800 m), mid-ocean (green, 800–2350 m) and deep ocean (dark blue, 2350–4600 m), (b) the global-mean vertical profile for run CON-SHF, and (c) the global-mean vertical profile for run CON-EFF. The values shown are five-year running means, and are expressed as anomalies relative to the annual-mean σ_θ for the final 100 years of the ocean model spin-up runs.

(not shown). However, both runs also experience a decrease in the temperature of Antarctic Intermediate Water; this is particularly pronounced in the case of run CON-EFF, and can be attributed to the surface cooling in the Southern Ocean.

The drift in the mean salinity of the ocean is small, as with run CON-DEF. A vertical redistribution of salt is again encountered, with freshening of the surface layers and an increase in the salinity of the deep ocean. Changes in the potential density of the ocean are also small for both runs. The surface layers become slightly more buoyant, as a result of the freshening of the upper ocean; otherwise, there is a small increase in density throughout the water column.

Circulation

Figure 5.31 shows the evolution in the rates of North Atlantic Deep Water (NADW) formation and Antarctic Bottom Water (AABW) formation, and in the rate of volume transport through Drake Passage, during runs CON-SHF and CON-EFF. After some initial adjustment, the rates of deep water formation are stable for both runs. As with run CON-DEF, both runs exhibit a slight upward trend in the strength of the Antarctic Circumpolar Current.

Mean sea level

Figure 5.32 shows the changes in mean sea level inferred from runs CON-SHF and CON-EFF. As a result of the greater cooling of the world ocean, the declines in the mean sea level are greater than for run CON-DEF.

5.4.3 Climate variability

Interannual variability

Figure 5.33 shows the standard deviations in the annual-mean surface air temperature (SAT) and sea surface temperature (SST), for years 101–1100 of coupled model runs CON-SHF and CON-EFF. As with run CON-DEF, the first 100 years of each run have been excluded, in order to allow for any initial adjustment, and a high-pass filter has been applied to remove variability on timescales longer than 100 years. For both runs, the interannual variability in SAT and SST is very similar to run CON-DEF, with the only large-scale difference being that run CON-EFF exhibits greater variability over the Southern Ocean; this is the region where the largest changes were made to the amplitude of the annual cycle in the prescribed sea surface temperatures (Section 4.4).

The area-weighted global-mean standard deviations in the annual-mean SAT are 0.45°C and 0.47°C for runs CON-SHF and CON-EFF respectively, compared with a value of 0.45°C for run CON-DEF. Likewise, the global-mean standard deviations in the annual-mean SST are 0.30°C and 0.32°C respectively, compared with a value of 0.30°C for run CON-DEF.

The leading principal components of the annual-mean surface air temperature and sea surface temperature, for years 101–1100 of runs CON-SHF and CON-EFF, are shown in Figure 5.34. The fractions of the total variance described by the leading principal components of the annual-mean SST are 23.6% and 20.9%, for

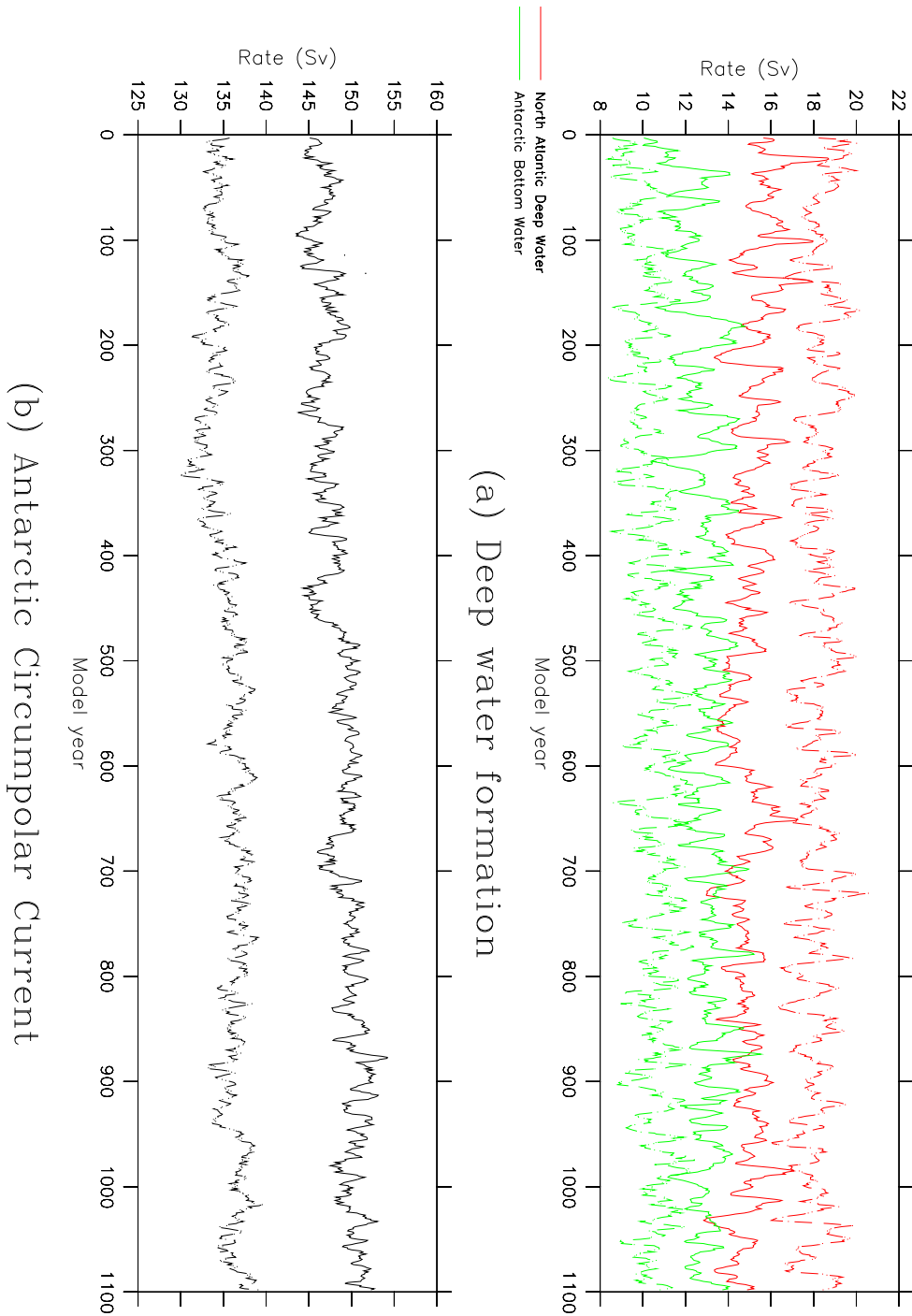


Figure 5.31: The rates of deep water formation, and the strength of the Antarctic Circumpolar Current, for coupled model runs CON-SHF (solid lines) and CON-EFF (dashed lines): (a) the rates of formation of North Atlantic Deep Water (red) and Antarctic Bottom Water (green), and (b) the rate of volume transport through Drake Passage. The values shown are five-year running means.

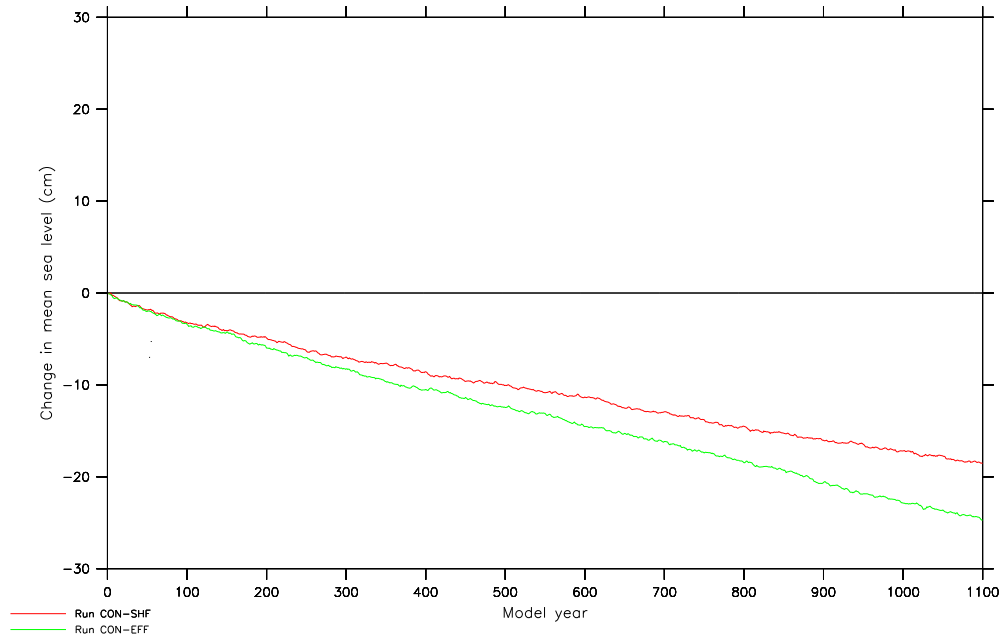


Figure 5.32: The steric changes in mean sea level diagnosed from coupled model runs CON-SHF and CON-EFF.

runs CON-SHF and CON-EFF respectively, and 10.9% and 10.0%, respectively, for the leading principal components of the annual-mean SAT. These figures are very similar to those of 22.3% and 10.6% for run CON-DEF. For both the SST and the SAT, the magnitudes and spatial structures of the principal components are also very similar to those for run CON-DEF, further indicating the similarity between the interannual variability within the three runs.

El Niño-Southern Oscillation

Figure 5.35 shows the correlation between the simulated SST anomalies at each gridpoint and the SOI, for runs CON-SHF and CON-EFF. The correlations are very similar to those for run CON-DEF; the only significant difference is that the increased interannual variability in the Southern Ocean sea surface temperatures within run CON-EFF tends to weaken the correlations with the SOI.

Statistics for the simulated El Niño-Southern Oscillation are shown in Table 5.5. The greater internal variability within run CON-EFF gives rise to greater SST variability in the Niño 3.4 region, but there are no statistically significant differences between the El Niño statistics for the three runs.

Figure 5.36 shows the power spectra of the Niño 3.4 SST anomaly for runs CON-DEF, CON-SHF and CON-EFF. Note that a Hann window of width 25, equivalent to 0.025 years^{-1} in frequency units, has been applied to the spectra, reducing the standard deviation in each value to $\sim \pm 28\%$ (Section 5.3.2). The power spectrum for run CON-SHF resembles that for run CON-DEF, with interdecadal variability dominating. Maximum power occurs at $\sim 0.037 \text{ years}^{-1}$, with a secondary peak

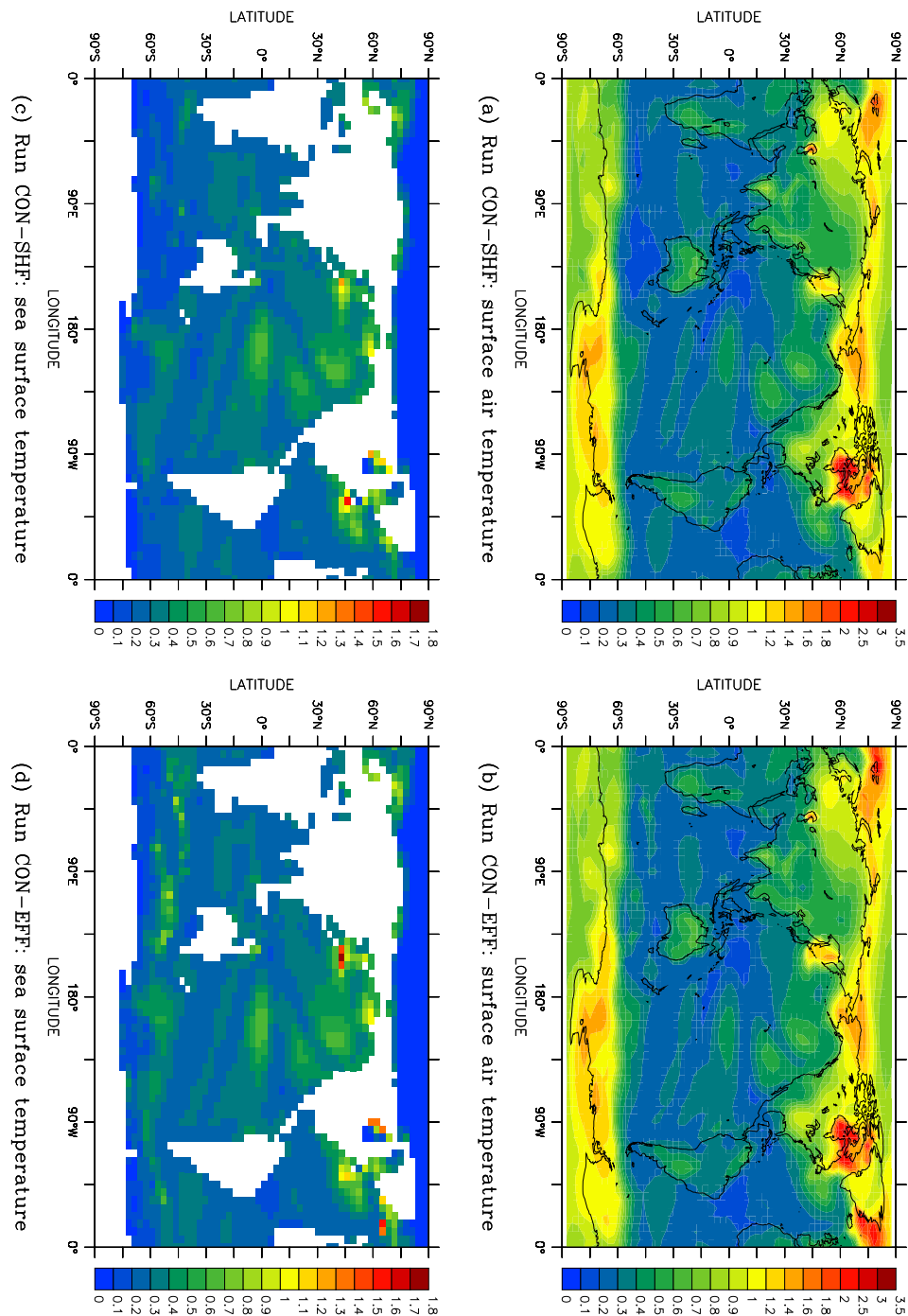


Figure 5.33: Standard deviations in annual-mean surface fields for years 101–1100 of coupled model runs CON-SHF and CON-EFF: (a), (b) surface air temperature ($^{\circ}\text{C}$), runs CON-SHF and CON-EFF respectively, and (c), (d) sea surface temperature ($^{\circ}\text{C}$), runs CON-SHF and CON-EFF respectively. The data has been high-pass filtered to remove variability on timescales longer than 100 years.

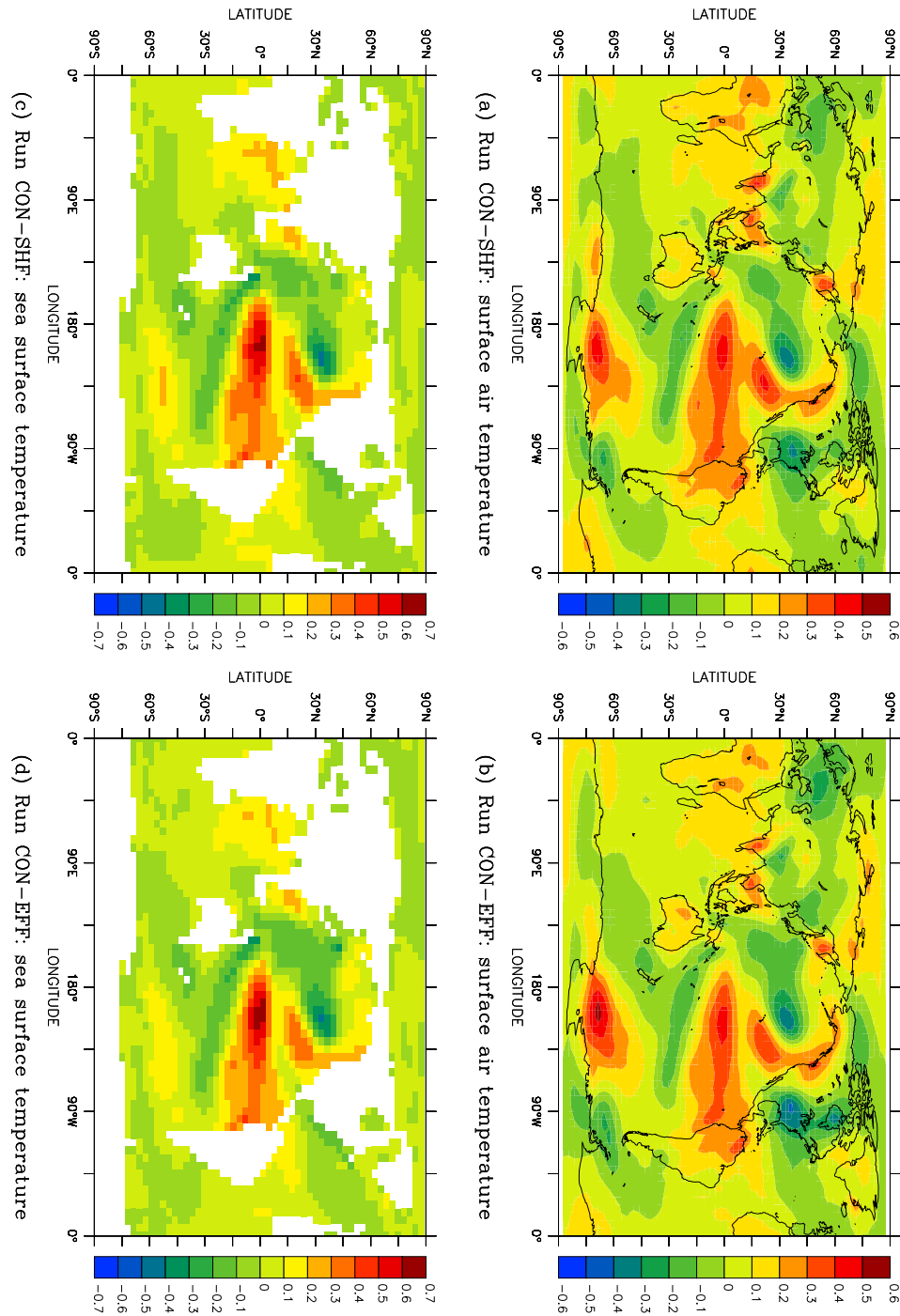
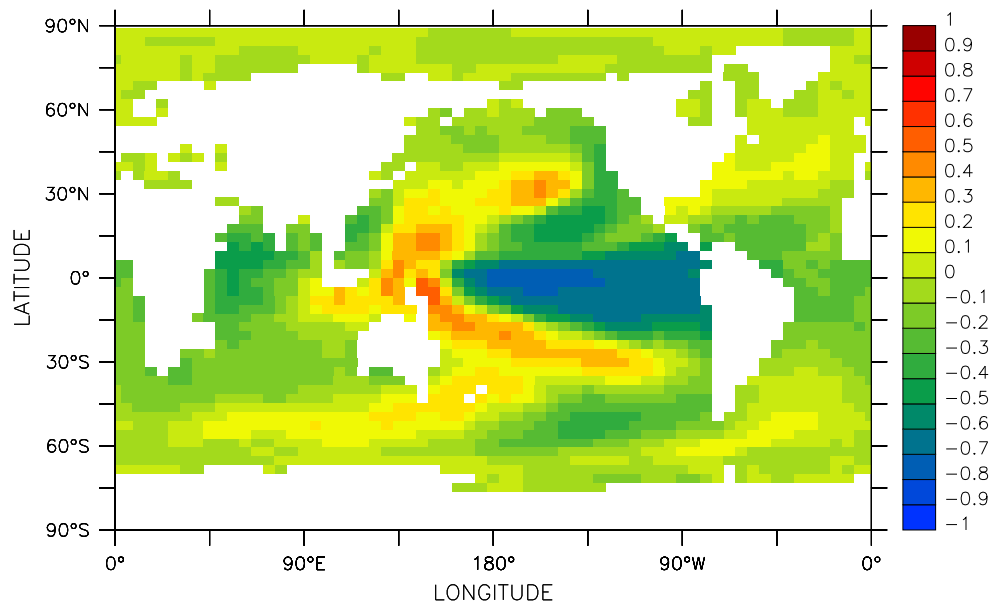
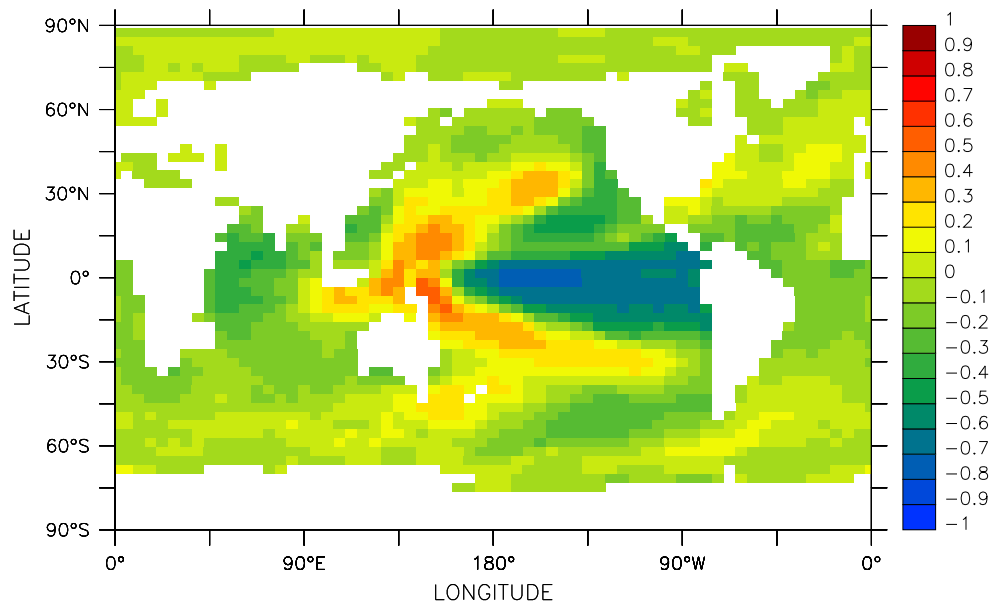


Figure 5.34: The leading principal components of annual-mean surface fields for years 101–1100 of coupled model runs CON-SHF and CON-EFF: (a), (b) surface air temperature ($^{\circ}\text{C}$), runs CON-SHF and CON-EFF respectively, and (c), (d) sea surface temperature ($^{\circ}\text{C}$), runs CON-SHF and CON-EFF respectively. The data has been high-pass filtered prior to calculating the principal components to remove variability on timescales longer than 100 years.



(a) Run CON-SHF



(b) Run CON-EFF

Figure 5.35: The correlation between sea surface temperature and the Southern Oscillation Index for years 101–1100 of coupled model runs CON-SHF and CON-EFF: (a) run CON-SHF, and (b) run CON-EFF.

	CON-DEF	CON-SHF	CON-EFF
Correlation between Niño 3.4 SST anomaly and SOI	-0.78	-0.79	-0.77
Standard deviation of Niño 3.4 SST anomaly (°C)	0.49	0.50	0.54
Average return period of El Niño events (years)	7.8±0.5	7.4±0.5	7.2±0.5
Average duration of El Niño events (months)	17.5±0.9	17.2±1.0	18.3±1.0
Average magnitude of El Niño events (°C)	0.88±0.02	0.89±0.02	0.94±0.03

Table 5.5: Some El Niño statistics for years 101–1100 of coupled model runs CON-DEF, CON-SHF and CON-EFF: the correlation between the Niño 3.4 sea surface temperature (SST) anomaly and the Southern Oscillation Index (SOI); the standard deviation of the five-month running mean of the Niño 3.4 SST anomaly; the average return period of El Niño events; the average duration of El Niño events; and the average magnitude of El Niño events.

at $\sim 0.15 \text{ years}^{-1}$; these frequencies correspond to periods of ~ 27 and ~ 6.7 years respectively. Thus, as with run CON-DEF, the simulated ENSO is too weak relative to the simulated interdecadal variability in the Pacific Ocean.

The power spectrum for run CON-EFF differs, however, with more power on interannual timescales, and less on interdecadal timescales. While maximum power occurs at $\sim 0.025 \text{ years}^{-1}$ (~ 40 years), a strong secondary peak is also apparent at $\sim 0.12 \text{ years}^{-1}$ (~ 8.1 years). Although the simulated ENSO therefore remains too weak, the bias toward interdecadal variability is sharply reduced.

5.4.4 Summary

Runs CON-SHF and CON-EFF both exhibit a high degree of stability, although the global-mean surface air temperature declines slightly more rapidly than in run CON-DEF. There is an apparent correlation between the rate of drift and the magnitude of the flux adjustments: the heat flux adjustments employed within both runs are smaller than those employed within run CON-DEF and, in both cases, the sea surface temperature exhibits greater drift. The salinity tendency adjustments employed within run CON-SHF are also smaller than those employed within run CON-DEF, and the sea surface salinities exhibit greater drift; however, the salinity tendency adjustments employed within run CON-EFF are *larger* than those employed within run CON-DEF, and the sea surface salinities exhibit *less* drift. This correlation is worthy of further investigation.

The use of phase-shifted surface tracers to spin up the ocean model, and the corresponding reduction in the magnitude of the flux adjustments applied within the coupled model, appears to have negligible effect upon the nature of the internal variability. The use of effective surface tracers to spin up the ocean model, however, does give rise to a small increase in the magnitude of internal variability. There

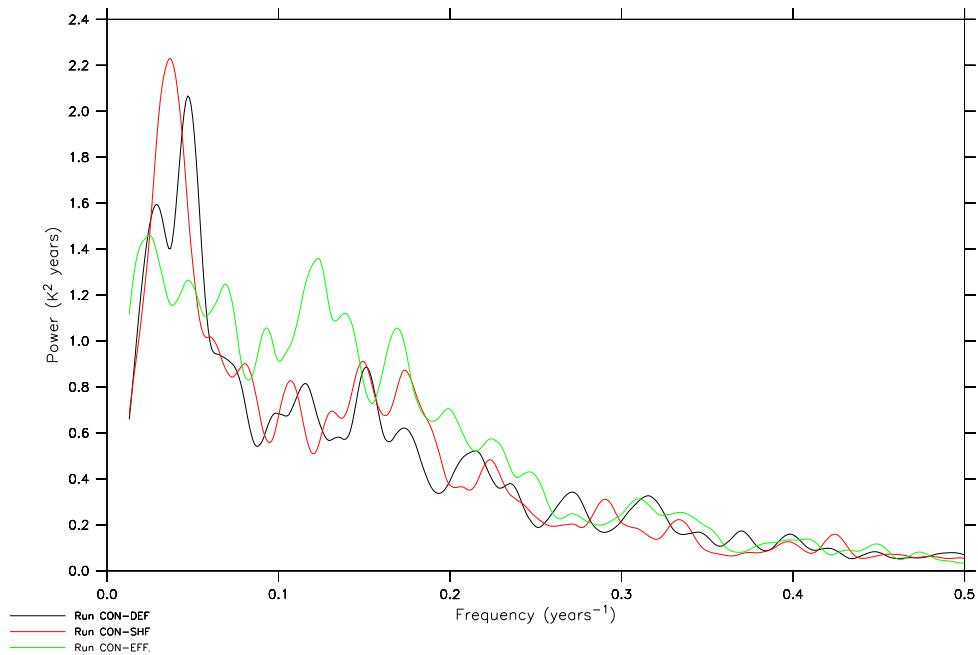


Figure 5.36: The normalised power spectra of the Niño 3.4 sea surface temperature anomaly for years 101–1100 of coupled model runs CON-DEF (black), CON-SHF (red) and CON-EFF (green). Each spectrum has been smoothed through the application of a Hann window of width 25.

is a slight increase in the interannual variability in both the SAT and SST, with a particular increase in variability over the Southern Ocean, and a strengthening of the simulated El Niño-Southern Oscillation. The nature of the simulated ENSO is also more realistic, with a sharply reduced bias towards variability on interdecadal timescales.

Chapter 6

The climate of the mid-Holocene

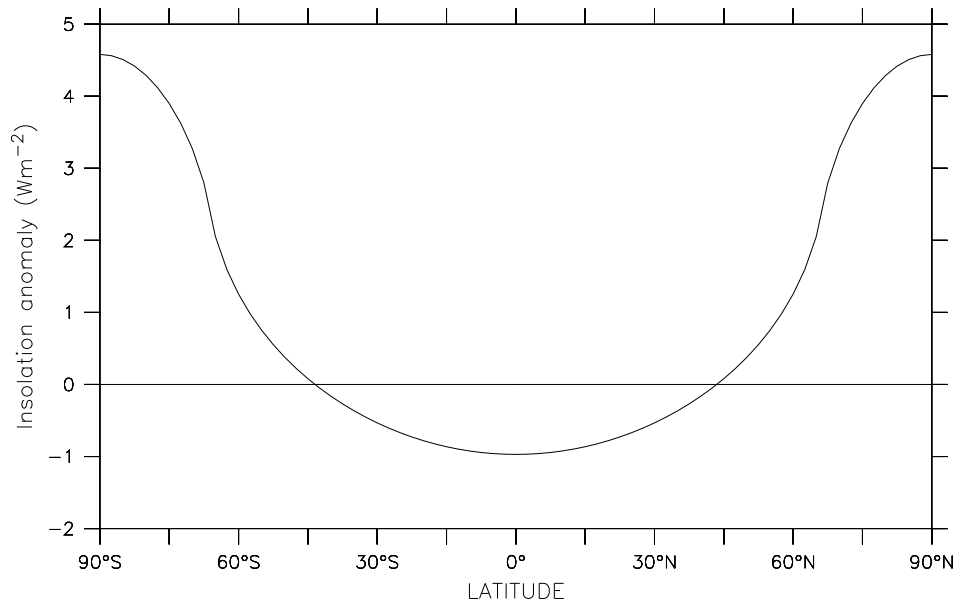
6.1 Introduction

The climate of the mid-Holocene (6,000 years BP) has frequently been used to evaluate the ability of climate models to simulate climatic change. This epoch represents the relatively recent past, and extensive and high-quality reconstructions of the mid-Holocene climate are therefore available against which to evaluate the performance of the models (e.g. *Yu and Harrison, 1996; Cheddadi et al., 1997; Hoelzmann et al., 1998; Jolly et al., 1998a,b; Prentice and Webb, 1998; Kohfeld and Harrison, 2000; Prentice et al., 2000*). The external forcing, which is mainly due to insolation changes arising from changes in the Earth's orbital parameters, is also well-known, and can be precisely defined (e.g. *Joussaume et al., 1999*).

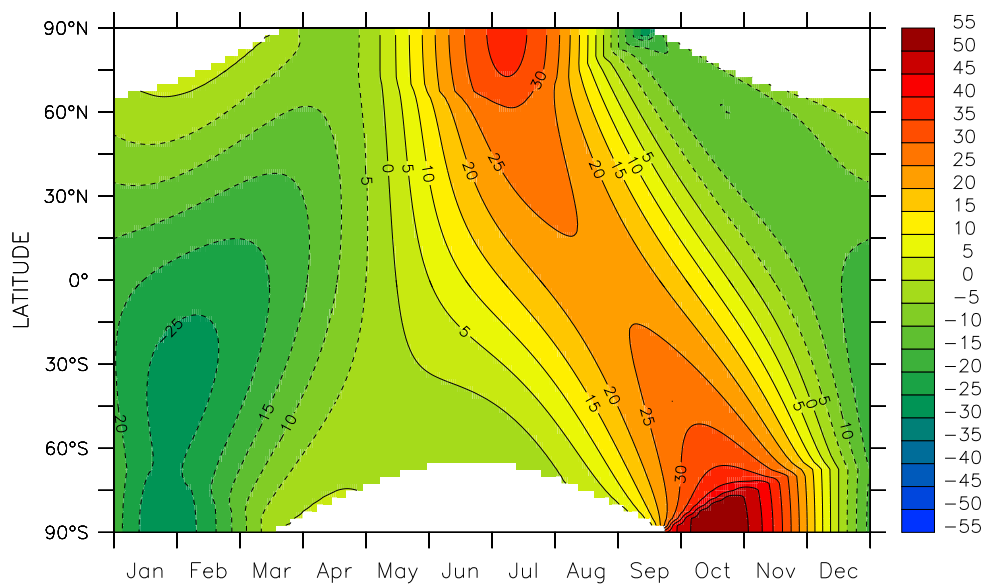
During the mid-Holocene, the Earth's axial tilt was only slightly greater than it is today (24.105° at 6,000 years BP, as opposed to the present-day value of 23.446°). The annual-mean insolation was therefore similar (Figure 6.1a), with a reduction of $\sim 1 \text{ Wm}^{-2}$ in the tropics, and an increase of $\sim 4.5 \text{ Wm}^{-2}$ at the poles. However, as a result of the precession of the equinoxes, there were significant differences in the seasonal cycle (Figure 6.1b). Insolation was considerably greater than today during the Northern Hemisphere summer and Southern Hemisphere spring, and considerably reduced during the Southern Hemisphere summer.

The differences between the climate of the mid-Holocene, and that of the present day, are therefore predominantly seasonal in nature, rather than being expressed in the annual-mean climate. Over Europe, for example, summers were warmer in the northwest, while winters were warmer in the northeast and colder in the southwest (*Cheddadi et al., 1997*). The most significant feature of the mid-Holocene climate, however, was the strengthening and northward migration of the Northern Hemisphere monsoons, particularly over Africa. Geomorphological and biostratigraphic data indicates that northern Africa was considerably wetter than it is today, while biome reconstructions generated from pollen and plant macrofossils indicate that it was extensively vegetated (*Jolly et al., 1998a,b; Joussaume et al., 1999*).

Many studies have used climate models to simulate the climate of the mid-Holocene, often motivated by a desire to evaluate the performance of the mod-



(a) Annual-mean insolation



(b) Daily insolation

Figure 6.1: The insolation (Wm^{-2}) at 6,000 years BP, expressed as an anomaly relative to the present day: (a) the annual mean, and (b) daily values.

els. Early studies used stand-alone atmospheric general circulation models, forced by present-day sea surface temperatures (e.g. *Kutzbach and Street-Perrott, 1985; Kutzbach and Guetter, 1986; Prell and Kutzbach, 1987; COHMAP members, 1988; de Noblet et al., 1996; Dong et al., 1996; Hewitt and Mitchell, 1996; Kutzbach et al., 1996; Lorenz et al., 1996; Coe and Bonan, 1997; Hall and Valdes, 1997; Masson and Joussaume, 1997; Broström et al., 1998; Masson et al., 1998; Texier et al., 2000; Vettoretti et al., 2000*). Phase I of the Paleoclimate Modelling Intercomparison Project, which sought to systematically compare the performance of different models, adopted this approach (e.g. *Harrison et al., 1998; Joussaume et al., 1999; Masson et al., 1999; Braconnot et al., 2000a; Bonfils et al., 2004; Hoar et al., 2004*). PMIP1 revealed that stand-alone atmosphere models are successful at capturing both the intensification and the northward migration of the African monsoon; however, it also revealed that they are unable to capture the magnitude of the northward shift (*Joussaume et al., 1999; Braconnot et al., 2000a*).

Other studies have employed atmospheric general circulation models coupled to a mixed-layer ocean (e.g. *Foley et al., 1994; Liao et al., 1994; TEMPO, 1996; Kutzbach et al., 1998; Vettoretti et al., 1998*), and coupled atmosphere-ocean general circulation models (e.g. *Hewitt and Mitchell, 1998; Bush, 1999; Otto-Bliesner, 1999; Braconnot et al., 2000b; Liu et al., 2000; Voss and Mikolajewicz, 2001; Kitoh and Murakami, 2002; Liu et al., 2003a,b; Mikolajewicz et al., 2003; Otto-Bliesner et al., 2006*). The latter approach has been adopted by Phase II of the Paleoclimate Modelling Intercomparison Project (*Harrison et al., 2002; Crucifix et al., 2005; Paleoclimate Modelling Intercomparison Project, 2005*). While the inclusion of oceanic feedbacks leads to an improved simulation of the mid-Holocene climate, the precipitation over northern Africa remains deficient (e.g. *Hewitt and Mitchell, 1998; Braconnot et al., 2000b; Otto-Bliesner et al., 2006*).

The failure to adequately capture the changes in the African monsoon can be attributed, at least in part, to the static nature of the vegetation within these simulations. The vegetation is therefore unable to respond to the changed atmospheric conditions, and vegetation feedbacks are neglected. The importance of these feedbacks becomes apparent, however, when atmospheric general circulation models are forced with land surface conditions based on biome reconstructions (e.g. *Kutzbach et al., 1996; Broström et al., 1998; Texier et al., 2000*). The vegetation changes are found to enhance the effects of the orbital forcing, leading to a greater northward shift of the African monsoon.

In order to fully represent the effects of vegetation feedbacks, many studies have therefore sought to employ dynamic vegetation models. These have been coupled to atmospheric general circulation models (e.g. *Claussen and Gayler, 1997; Texier et al., 1997; de Noblet-Ducoudré et al., 2000*), atmosphere-slab ocean models (e.g. *Pollard et al., 1998; Doherty et al., 2000*) and atmosphere-ocean general circulation models (e.g. *Braconnot et al., 1999; Levis et al., 2004*). These studies confirm the role of both oceanic and vegetation feedbacks in giving rise to the wetter conditions that prevailed over northern Africa during the mid-Holocene.

While the coupled atmosphere-ocean-vegetation models are the most successful at simulating the intensification and northward migration of the African monsoon, even these fail to adequately simulate the increase in precipitation over northern

Africa. This is attributed to deficiencies in the model physics (*Braconnot et al.*, 1999), and a failure to adequately represent the effects of soil feedbacks (*Levis et al.*, 2004). Thus the mid-Holocene African monsoon remains a daunting test of the ability of models to simulate climatic change.

In addition to changes in the mean state of the climate, changes in the nature of climate variability during the mid-Holocene have also received some attention. Proxy records indicate a strengthening of interannual variability in the tropical Pacific Ocean during the Holocene. For example, analysis of corals from Papua New Guinea reveals that ENSO activity at $\sim 6,500$ years BP was much weaker than at present (*Tudhope et al.*, 2001). A 15,000-year sedimentation record from an alpine lake in Ecuador indicates a lack of variability on El Niño timescales prior to 7,000 years BP, with ENSO-type variability beginning at $\sim 7,000$ years BP and reaching its modern strength at $\sim 5,000$ years BP (*Rodbell et al.*, 1999). A further analysis of a 12,000-year sedimentation record from the same lake confirms the initiation of ENSO at $\sim 7,000$ years BP, with strong variability on millennial timescales thereafter (*Moy et al.*, 2002). Pollen evidence from northern Australia also indicates a strengthening of ENSO during the Holocene, with the onset of an ENSO-dominated climate at $\sim 4,000$ years BP (*Shulmeister and Lees*, 1998).

Using a simple coupled ocean-atmosphere model, *Clement et al.* (2000) find a steady increase in both the frequency and magnitude of El Niño events during the Holocene. They hypothesise that the behaviour of ENSO is determined by the seasonal cycle of insolation in the tropics, and particularly by the amount of insolation during the northern summer. According to their hypothesis, the enhanced summer heating during the mid-Holocene, combined with the zonally-asymmetric response of the atmosphere, resulted in enhanced convection over the western Pacific Ocean. The easterly trade winds were therefore stronger than at present, increasing the zonal gradient in the sea surface temperature, and hence suppressing the development of El Niño events.

Only a few studies have used coupled atmosphere-ocean general circulation models to investigate the nature of the El Niño-Southern Oscillation during the mid-Holocene. *Otto-Bliesner* (1999) finds that the simulated ENSO at 6,000 years BP is similar in both magnitude and frequency to that of the present day. Both *Liu et al.* (2000) and *Otto-Bliesner et al.* (2006), however, find a $\sim 20\%$ reduction in the strength of the simulated ENSO. Consistent with the hypothesis of *Clement et al.* (2000), *Liu et al.* (2000) also find enhanced atmospheric convection over the western Pacific Ocean during the northern summer, resulting in a strengthening of the trade winds and an increase in the zonal temperature gradient. None of the models, however, simulate a reduction in the strength of ENSO as large as that indicated by the proxy records (e.g. *Rodbell et al.*, 1999; *Tudhope et al.*, 2001); *Liu et al.* (2000) suggest that this is a result of deficiencies in the model physics, noting the inability of their model to correctly simulate the characteristics of the present-day ENSO.

The ability of the Mk3L coupled model to simulate the climate of the mid-Holocene is evaluated in this chapter, and the impact of the ocean model spin-up procedure upon the response of the model is assessed. Three simulations of the mid-Holocene climate are presented; these are designated 6ka-DEF, 6ka-SHF and 6ka-EFF. They are initialised from the states of the control runs CON-DEF, CON-

SHF and CON-EFF, respectively, at the end of year 100, and are each integrated to year 900. The mid-Holocene simulations differ from the equivalent control runs only in that the Earth's orbital parameters for the epoch 6,000 years BP are employed, and that the atmospheric carbon dioxide concentration is reduced from 280 ppm to 277 ppm. The experimental design follows that of PMIP2 (*Paleoclimate Modelling Intercomparison Project*, 2005), and is outlined in detail in Appendix A.

Section 6.2 considers the changes in the mean climate, as simulated by run 6ka-DEF, while the changes in the nature of the internal variability are analysed in Section 6.3. Runs 6ka-SHF and 6ka-EFF are assessed in Section 6.4.

6.2 Mean climate

Figure 6.2 shows the average surface air temperature (SAT) for years 201–900 of run 6ka-DEF, expressed as an anomaly relative to the control run. It should be noted that the first 100 years of each mid-Holocene simulation are excluded from analysis, in order to allow the model to respond to the changes in external forcing.

The seasonal nature of the differences in the mid-Holocene climate is apparent. Consistent with the changes in the annual-mean insolation, the differences in the annual-mean SAT (Figure 6.2a) are small, with only a slight cooling at low latitudes, and a slight warming at high latitudes. However, there is strong warming over the Northern Hemisphere landmasses in August (Figure 6.2c), and cooling at low latitudes, and throughout the Southern Hemisphere, in February (Figure 6.2d).

The differences in the zonal-mean SAT for each month of the year are shown in Figure 6.2b; a clear correlation between the SAT differences and the insolation differences is apparent, albeit with a time lag of approximately one month. This reflects the fact that surface temperatures represent a time-integrated response to the surface heat flux, and not an instantaneous response. The zonal-mean SAT changes are very similar to those simulated by *Hewitt and Mitchell* (1998), who use a low-resolution coupled model similar in nature to Mk3L.

To enable the simulated temperature changes to be compared with data syntheses, and with the models that participated in PMIP1, two bioclimatic variables are derived. These are the mean SAT for the coldest month of the year, and the GDD5. The GDD5, or growing-degree days above 5°C, is a measure of both the temperature and duration of the growing season. If $T(j)$ is the mean SAT, in degrees Celsius, for day j , then the GDD5 is given by (*Masson et al.*, 1999):

$$\text{GDD5} = \sum_{j=1}^{365} \begin{cases} T(j) - 5 & T(j) \geq 5 \\ 0 & \text{otherwise} \end{cases} \quad (6.1)$$

Values of $T(j)$ are estimated by linearly interpolating between the mean SAT for each month.

Reconstructions of these two bioclimatic variables from pollen data (*Cheddadi et al.*, 1997) indicate that, during the mid-Holocene, the temperature of the coldest month was higher than at present over northeastern Europe and Scandinavia, and lower over southwestern Europe. They also indicate that the GDD5 was higher than at present over northwestern Europe and the Alps, but lower across the southern half of Europe.

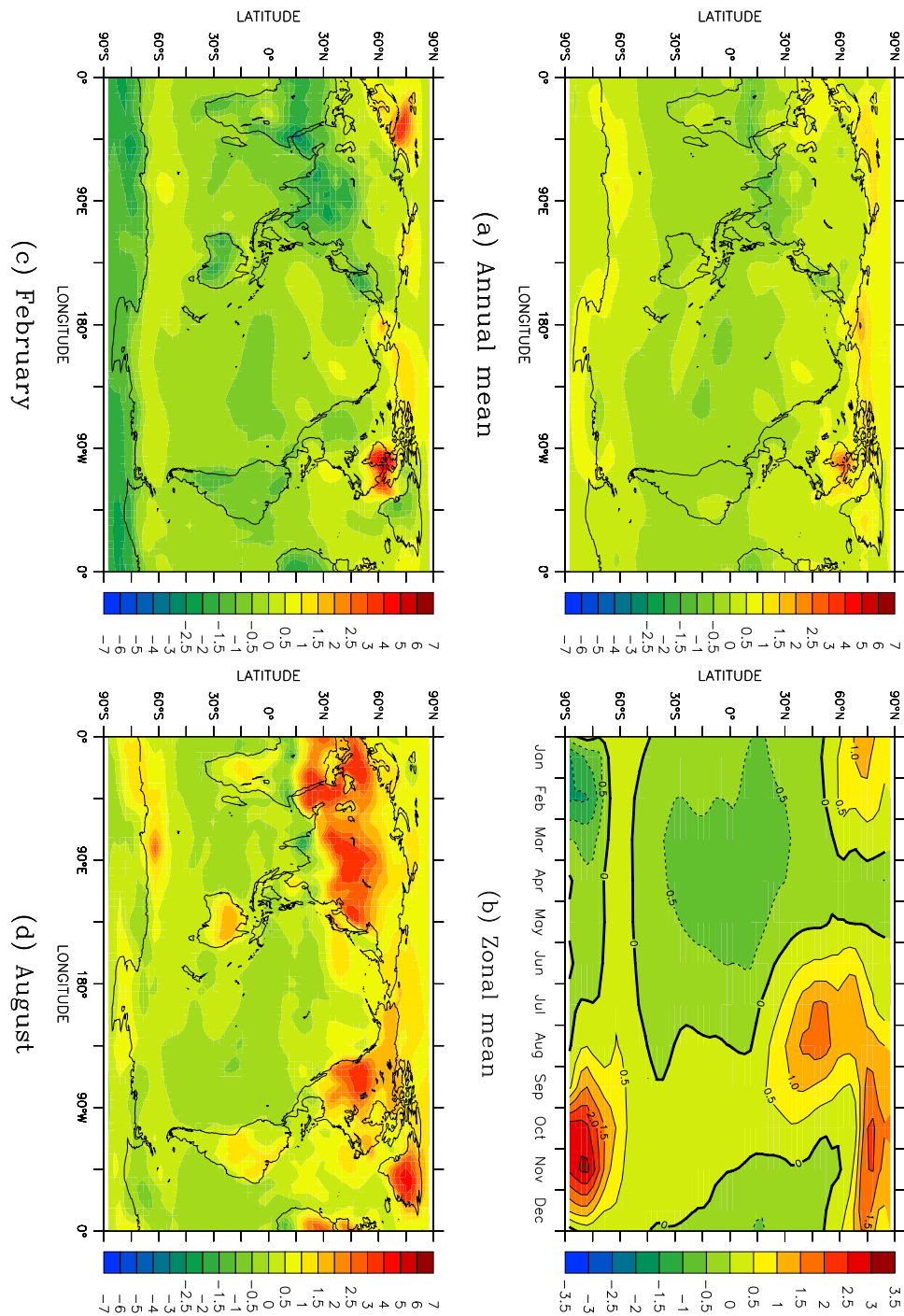
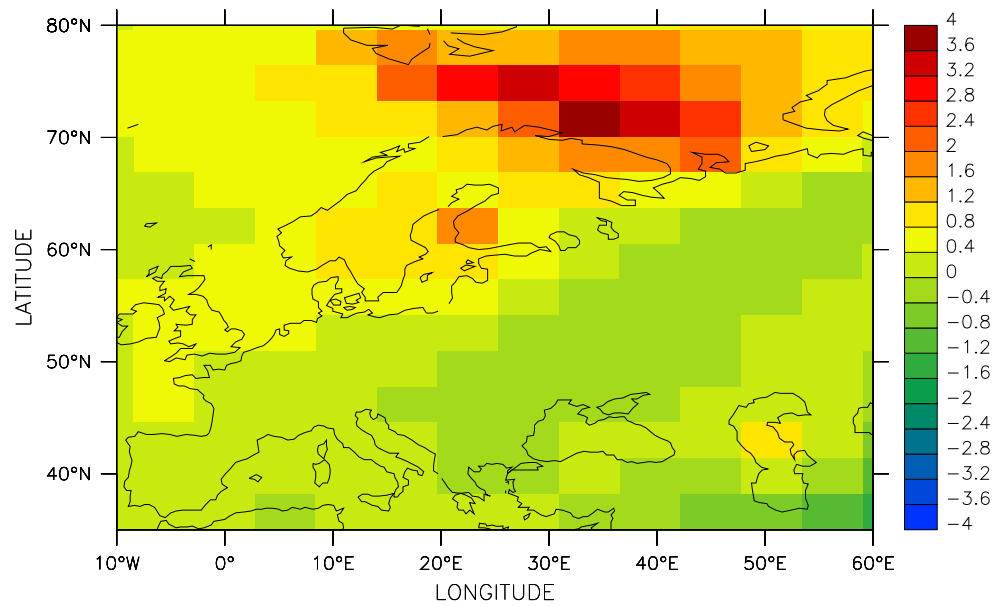
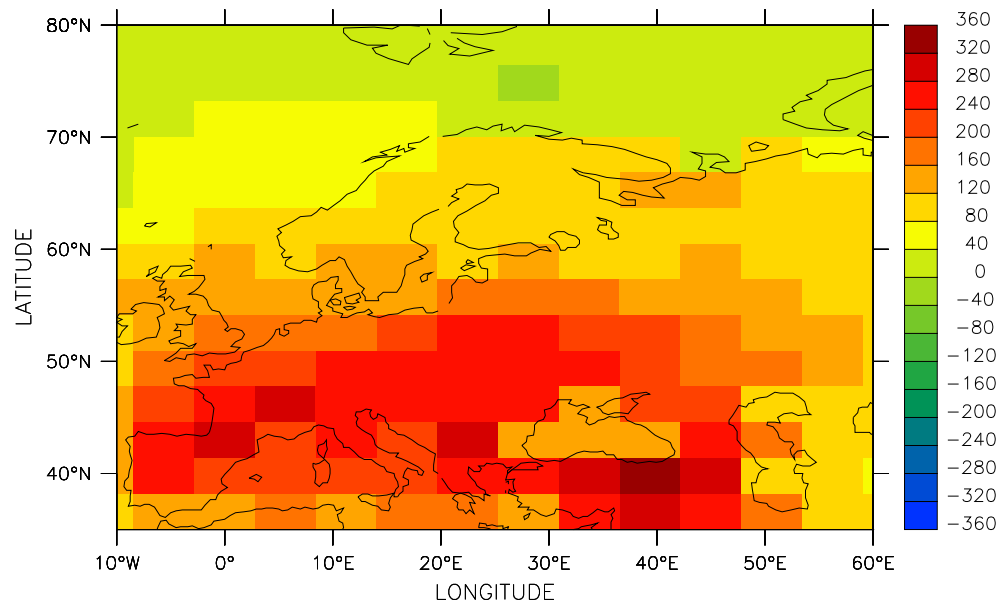


Figure 6.2: The average surface air temperature ($^{\circ}\text{C}$) for years 201–900 of run 6ka-DEF, expressed as an anomaly relative to the average surface air temperature for years 201–900 of control run CON-DEF: (a) the annual mean, (b) the zonal mean, (c) February, and (d) August.



(a) Temperature of coldest month



(b) GDD5

Figure 6.3: Bioclimatic variables for years 201–900 of run 6ka-DEF, expressed as anomalies relative to those for years 201–900 of control run CON-DEF: (a) the mean surface air temperature for the coldest month of the year ($^{\circ}\text{C}$), and (b) the GDD5 ($^{\circ}\text{C}\cdot\text{days}$).

Figure 6.3 shows the simulated changes in each of the two variables. Mk3L is successful at capturing the higher winter temperatures over Scandinavia; however, it fails to simulate any other large-scale temperature changes over land, capturing neither the warming over northeastern Europe, nor the cooling over southwestern Europe. The model is also successful at capturing the increase in the GDD5 over northwestern Europe and the Alps, but fails to simulate the decrease over southern Europe.

While the performance of Mk3L is disappointing, the models that participated in PMIP1 were also unsuccessful at simulating the changes in these bioclimatic variables. Of 16 models assessed by *Masson et al.* (1999), only three simulated a significant warming over northeastern Europe in winter, and none simulated a significant cooling over southwestern Europe. Similarly, while most of the models simulated a general increase in the GDD5 over northern Europe, none of them simulated a decrease over the southern part.

Masson et al. (1999) are unable to account for these discrepancies, although they note that the PMIP1 simulations do not allow for the effects of either oceanic or vegetation feedbacks. The Mk3L coupled model includes a dynamic ocean, and yet is also unable to reproduce the reconstructed temperature changes over Europe. This failure therefore appears to arise, at least in part, from the fact that it does not allow for the effects of vegetation feedbacks.

Figures 6.4a and 6.4b show the annual-mean precipitation for years 201–900 of runs CON-DEF and 6ka-DEF, respectively, while Figure 6.4c shows the difference between the two runs. Despite the seasonal nature of the differences in the mid-Holocene climate, the intensification and northward migration of the African-Asian monsoon is reflected in the annual-mean precipitation, with increased precipitation over northern Africa and southeast Asia.

The changes in the African monsoon are apparent from Figure 6.4d, which shows the change in the zonal-mean precipitation over North Africa. Also shown are the minimum and maximum estimates of the increase in precipitation, relative to the present day, that would be required in order to support grassland at each latitude (*Joussaume et al.*, 1999). Biome reconstructions indicate that grasslands were present at least as far north as 23°N during the mid-Holocene (*Jolly et al.*, 1998b; *Joussaume et al.*, 1999); the simulated precipitation anomaly should therefore exceed these estimated amounts at latitudes less than 23°N.

While an intensification and northward migration of the African monsoon is apparent, with a decrease of 50 mm in the annual precipitation at ~5°N, and an increase of 115 mm at ~14°N, the simulated precipitation is deficient at latitudes greater than ~17°N. The magnitude of the precipitation anomalies is consistent with the models that participated in PMIP1 (e.g. *Joussaume et al.*, 1999), as is the failure to simulate sufficient precipitation over northern Africa. As numerous studies have shown that dynamic vegetation is required in order for models to be able to simulate the changes in the African monsoon (see the discussion in Section 6.1), this failure can be attributed, at least in part, to the fact that Mk3L does not allow for the effects of vegetation feedbacks.

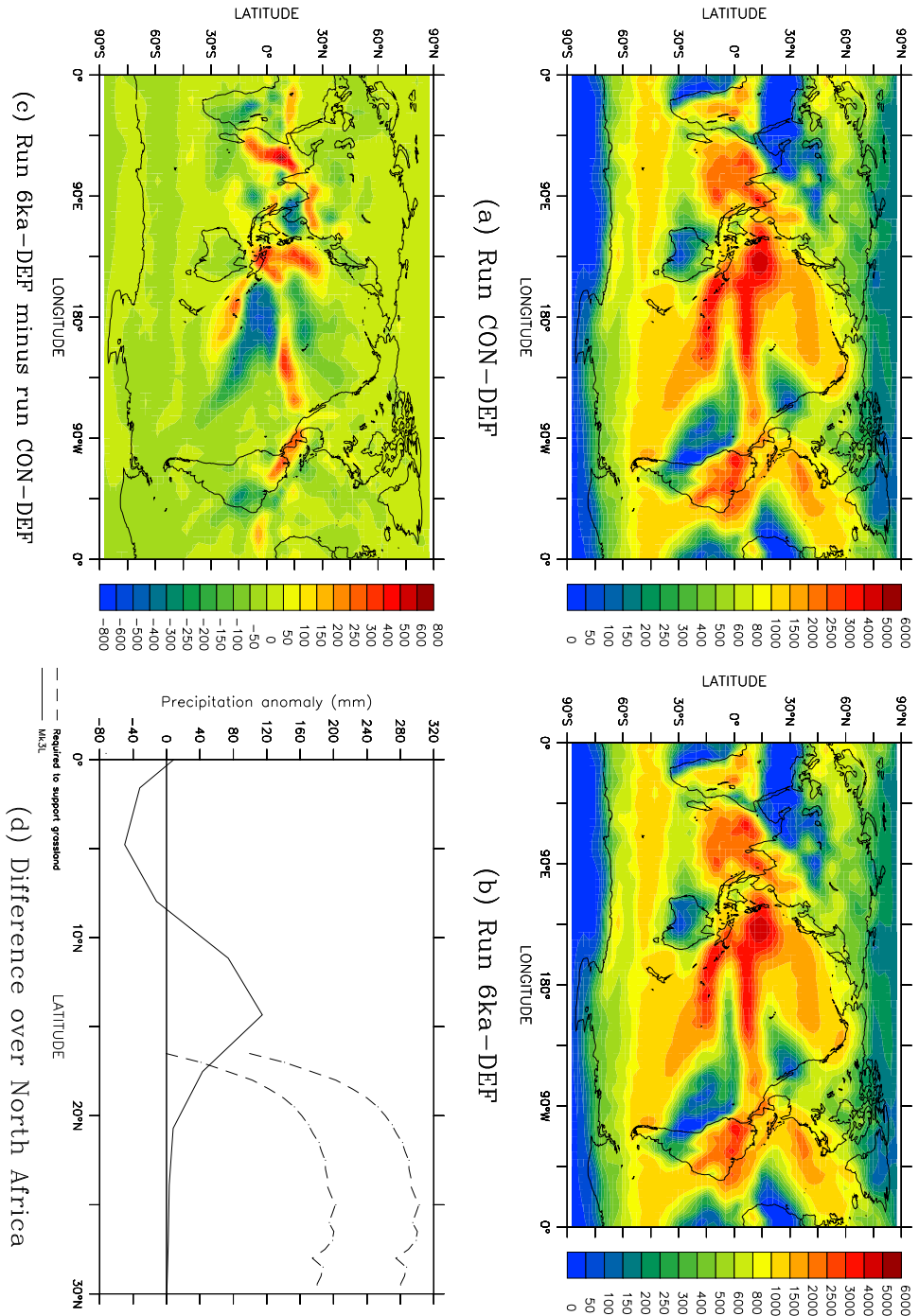


Figure 6.4: The annual precipitation (mm) for years 201–900 of runs CON-DEF and 6ka-DEF: (a) run CON-DEF, (b) run 6ka-DEF, (c) run 6ka-DEF minus run CON-DEF, and (d) the zonal-mean difference over North Africa (20°W–30°E). In (d), minimum and maximum estimates of the precipitation increase required to support grassland at each latitude are also shown (*Joussaume et al., 1999*).

6.2.1 Summary

The Mk3L coupled model is capable of simulating the global-scale differences between the climate of the mid-Holocene and that of the present day, with warmer summers at northern mid-latitudes, and slight cooling in the tropics. However, it is less successful when assessed at a regional scale, being unable to capture the cooling over southern Europe, or the increased precipitation over northern Africa. These failures appear to be due, at least in part, to the static nature of the vegetation within Mk3L.

6.3 Climate variability

6.3.1 Interannual variability

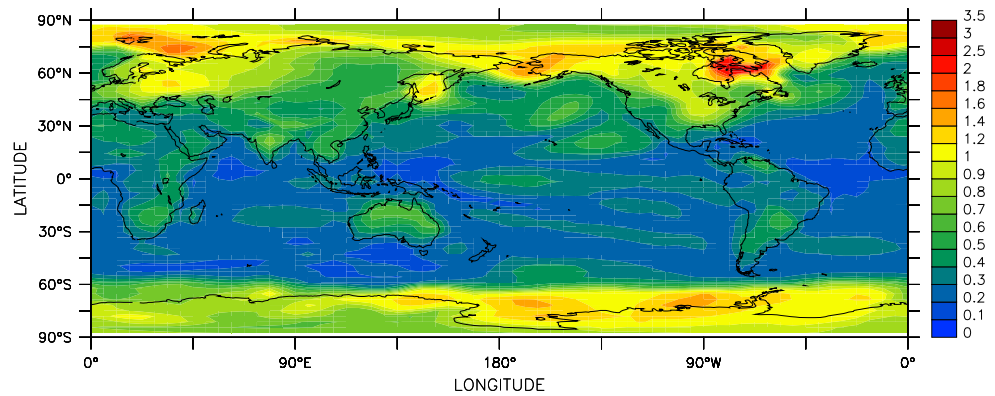
Figure 6.5 shows the standard deviations in the annual-mean surface air temperature (SAT), sea surface temperature (SST) and sea surface salinity (SSS), for years 201–900 of run 6ka-DEF; comparison with Figure 5.20 indicates that the interannual variability is very similar, in both magnitude and spatial structure, to that exhibited by the control run CON-DEF.

However, on a regional scale, there are some significant differences in the magnitude of the interannual variability; these become apparent when the standard deviations for run 6ka-DEF are plotted as a fraction of those for run CON-DEF (Figure 6.6). At low latitudes, there is increased temperature variability over the western tropical Pacific Ocean, the tropical Indian Ocean and central Africa. There is also a decrease in variability over the central Pacific, particularly in the case of the sea surface salinity; this can be attributed to the decrease in precipitation in this region (Figure 6.4).

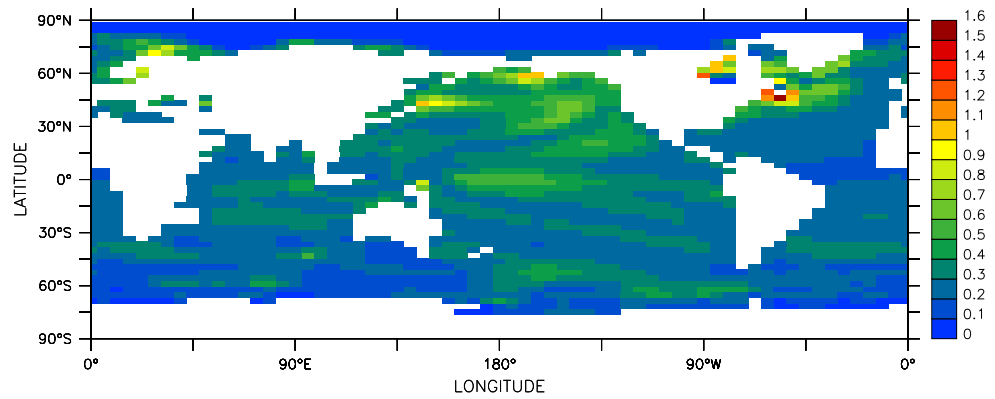
At high latitudes, the increased surface air temperatures (Figure 6.2), and the associated reduction in sea ice cover (not shown), result in some changes in the temperature variability. The removal of the ice cover, with its insulating effects, leads to decreased variability in the SAT, as atmospheric temperatures are now moderated by the temperature of the underlying ocean. There is an associated increase in variability in the SST, however, as the ocean is now exposed to much greater surface heat fluxes. Such changes in surface temperature variability are particularly apparent off the coast of East Antarctica, and in the vicinity of Hudson Bay.

The leading principal components of the annual-mean SAT, SST and SSS are shown in Figure 6.7. Comparison with Figure 5.21 reveals that these are similar in magnitude and spatial structure to the leading principal components derived from run CON-DEF; the leading modes of variability in the annual-mean SAT and SST therefore correspond to the simulated El Niño-Southern Oscillation, while the leading mode of variability in the annual-mean SSS represents variability in the strength and position of the monsoons.

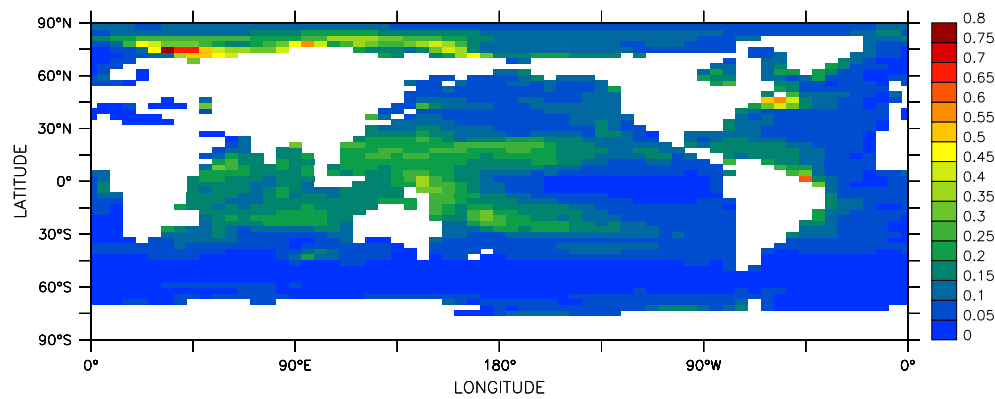
As a result of the increased variability in the western Pacific, however, and the decreased variability in the central Pacific, the principal components are shifted slightly to the west. In the case of the sea surface temperature, for example, the leading principal component has its maximum value at 163°W in the case of run



(a) Surface air temperature

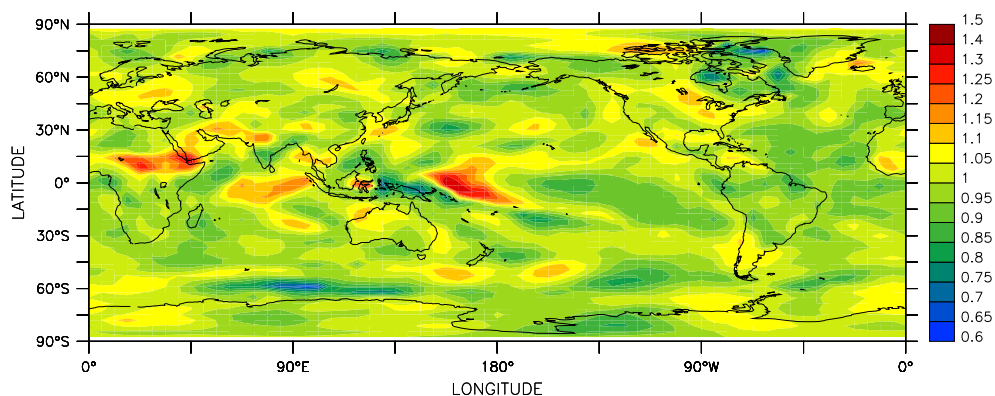


(b) Sea surface temperature

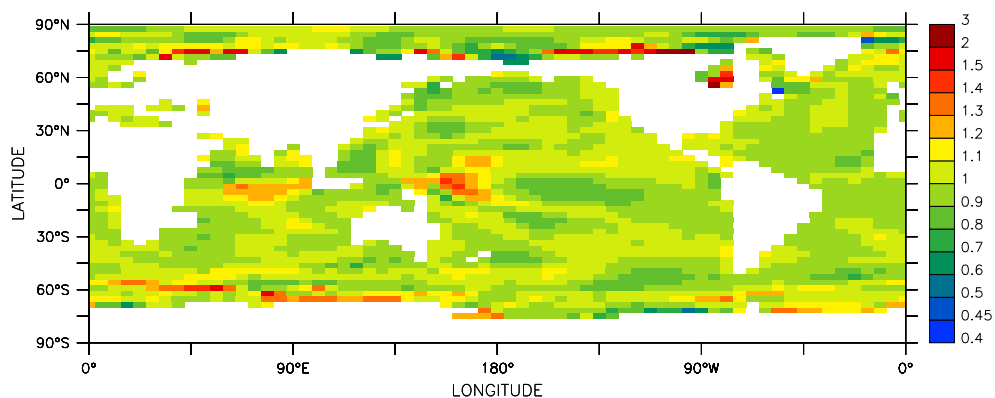


(c) Sea surface salinity

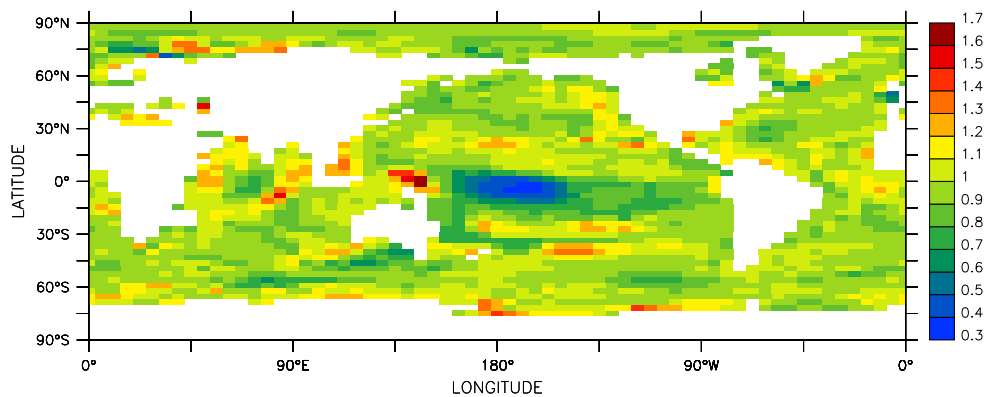
Figure 6.5: Standard deviations in annual-mean surface fields for years 201–900 of coupled model run 6ka-DEF: (a) surface air temperature ($^{\circ}\text{C}$), (b) sea surface temperature ($^{\circ}\text{C}$), and (c) sea surface salinity (psu). The data has been high-pass filtered to remove variability on timescales longer than 100 years.



(a) Surface air temperature

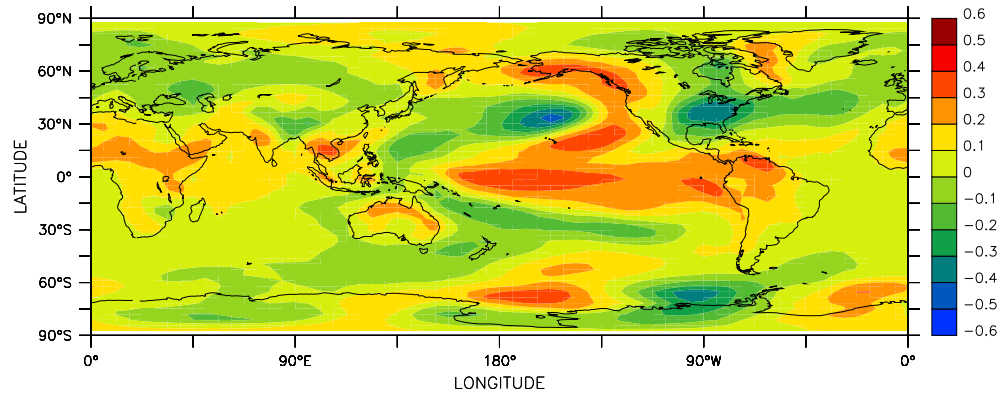


(b) Sea surface temperature

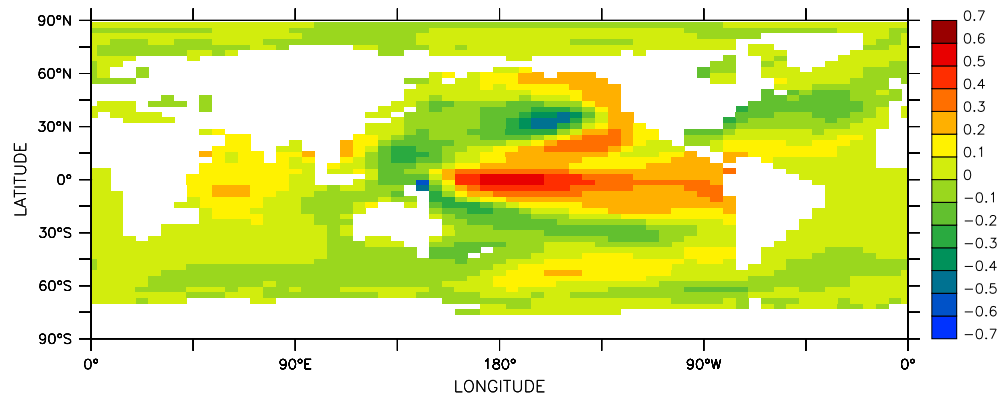


(c) Sea surface salinity

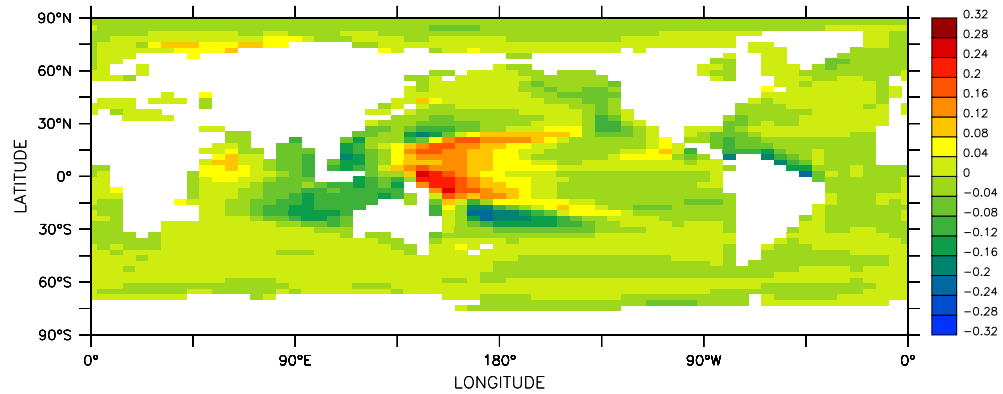
Figure 6.6: Standard deviations in annual-mean surface fields for years 201–900 of coupled model run 6ka-DEF, expressed as a ratio relative to the standard deviations for years 201–900 of run CON-DEF: (a) surface air temperature, (b) sea surface temperature, and (c) sea surface salinity. The data has been high-pass filtered to remove variability on timescales longer than 100 years.



(a) Surface air temperature



(b) Sea surface temperature



(c) Sea surface salinity

Figure 6.7: The leading principal components of annual-mean surface fields for years 201–900 of coupled model run 6ka-DEF: (a) surface air temperature ($^{\circ}\text{C}$), (b) sea surface temperature ($^{\circ}\text{C}$), and (c) sea surface salinity (psu). The data has been high-pass filtered prior to calculating the principal components to remove variability on timescales longer than 100 years.

	CON-DEF	6ka-DEF
Standard deviation of Niño 3.4 SST anomaly ($^{\circ}\text{C}$)	0.49	0.43
Average return period of El Niño events (years)	7.6 ± 0.6	8.6 ± 0.9
Average duration of El Niño events (months)	17.2 ± 1.0	16.3 ± 1.1
Average magnitude of El Niño events ($^{\circ}\text{C}$)	0.87 ± 0.03	0.76 ± 0.03

Table 6.1: Some El Niño statistics for years 201–900 of coupled model runs CON-DEF and 6ka-DEF: the standard deviation of the five-month running mean of the Niño 3.4 sea surface temperature (SST) anomaly; the average return period of El Niño events; the average duration of El Niño events; and the average magnitude of El Niño events.

CON-DEF, but at 180°E in the case of run 6ka-DEF. This shift causes the principal component to more closely resemble the observed present-day interdecadal variability in the Pacific Ocean (*Zhang et al.*, 1997; *Lohmann and Latif*, 2005).

6.3.2 El Niño-Southern Oscillation

Table 6.1 shows some El Niño statistics for runs CON-DEF and 6ka-DEF. The El Niño-Southern Oscillation is weaker in run 6ka-DEF, with a $\sim 13\%$ decrease in the standard deviation of the Niño 3.4 sea surface temperature anomaly. There is also a decrease in the magnitude of El Niño events, and an increase in the return period, although the latter is not statistically significant. The simulated reduction in the strength of ENSO is smaller in magnitude than that implied by the palaeoclimate record (e.g. *Rodbell et al.*, 1999; *Tudhope et al.*, 2001); however, it is consistent with other modelling studies, which simulate decreases in the strength of ENSO that range from zero (*Otto-Bliesner*, 1999) to $\sim 20\%$ (*Liu et al.*, 2000; *Otto-Bliesner et al.*, 2006).

Figure 6.8 shows the simulated changes in the zonal wind stress and sea surface temperature over the equatorial Pacific Ocean. Consistent with the hypothesis of *Clement et al.* (2000), the increased insolation during the northern summer leads to an increase in the strength of the easterly trade winds during the northern summer and autumn (Figure 6.8a). This gives rise to an increase in the zonal temperature gradient (Figure 6.8d), and acts to suppress the development of El Niño events. The magnitudes of the zonal wind stress and SST changes are similar to those simulated by *Liu et al.* (2000).

The power spectra of the simulated Niño 3.4 SST anomalies for runs CON-DEF and 6ka-DEF are shown in Figure 6.9. Note that a Hann window of width 25, equivalent to $\sim 0.036 \text{ years}^{-1}$ in frequency units, has been applied to the spectra, reducing the standard deviation in each value to $\sim \pm 28\%$ (Section 5.3.2). Consistent with the reduced variability in the Niño 3.4 region, run 6ka-DEF exhibits less power at almost all frequencies. There is an increase in variability on interdecadal timescales,

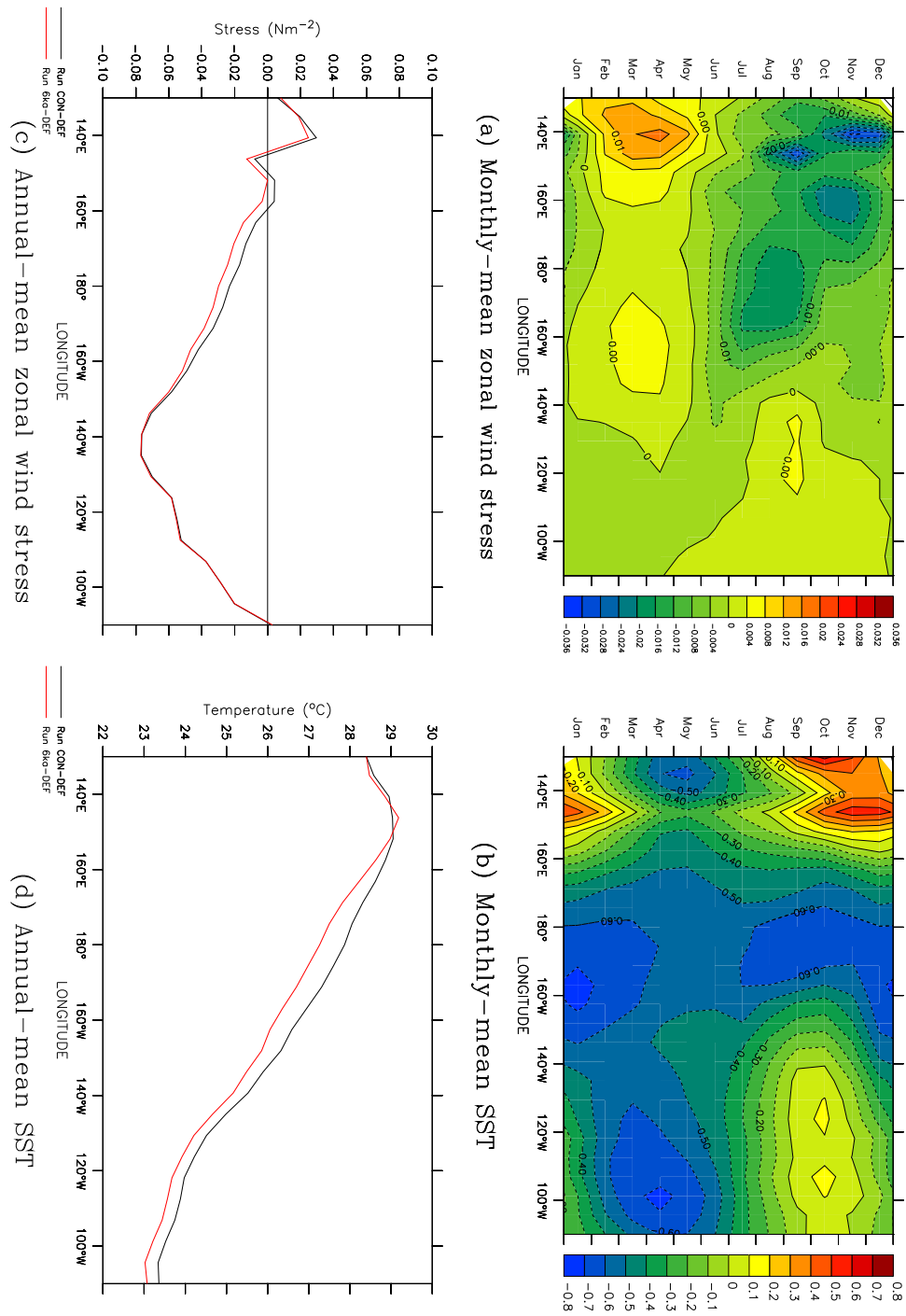


Figure 6.8: The equatorial zonal wind stress (Nm^{-2}) and sea surface temperature (SST, $^{\circ}\text{C}$) for years 201–900 of coupled model run 6ka-DEF, expressed as anomalies relative to years 201–900 of control run CON-DEF: (a) monthly-mean zonal wind stress, (b) monthly-mean sea surface temperature, (c) annual-mean zonal wind stress, and (d) annual-mean sea surface temperature. The values shown are averages over the region 5°S – 5°N .

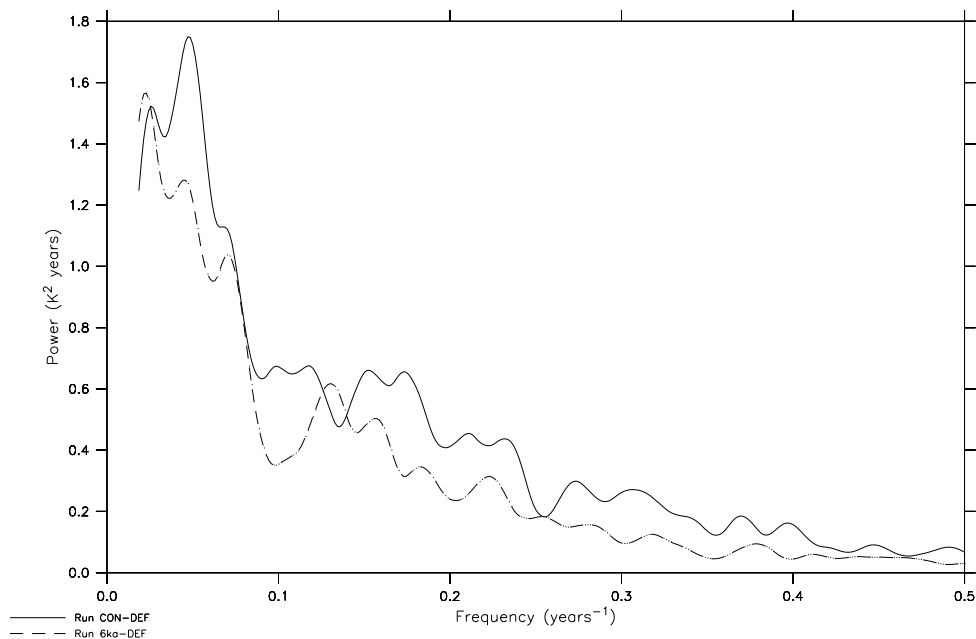


Figure 6.9: The power spectra of the Niño 3.4 sea surface temperature anomaly, for years 201–900 of coupled model runs CON-DEF (solid line) and 6ka-DEF (dashed line) respectively. Each spectrum has been smoothed through the application of a Hann window of width 25.

however, with the power spectrum exhibiting maximum power at $\sim 0.023 \text{ years}^{-1}$ (~ 44 years).

6.3.3 Summary

The simulated climate variability during the mid-Holocene exhibits a similar magnitude and spatial structure to that simulated for the present day. There are regional differences, however, with increased variability in the western Pacific, and decreased variability in the central Pacific. This westward shift leads to reduced variability within the Niño 3.4 region, and hence a reduction in the strength of the El Niño-Southern Oscillation. There is, however, an increase in ENSO variability on interdecadal timescales.

The simulated reduction in the strength of ENSO is smaller in magnitude than that implied by the palaeoclimate record. It should be noted, however, that the simulated present-day ENSO is too weak relative to observations, and does not exhibit the correct frequency characteristics (Section 5.3.2). This indicates deficiencies in the model physics, which may therefore account for the deficiencies in the model response.

6.4 The impact of the spin-up procedure

6.4.1 Mean climate

Figure 6.10 shows the zonal-mean SAT response of runs 6ka-SHF and 6ka-EFF; the statistically-significant *differences* between the response of each run, and that of run 6ka-DEF, are also shown. Both runs simulate a very similar pattern of warming and cooling to run 6ka-DEF. The temperature changes exhibited by run 6ka-SHF are particularly similar; apart from some warm anomalies at $\sim 45^\circ\text{N}$, the only statistically-significant differences in the response are small in magnitude. The response of run 6ka-EFF, while showing the same warm anomalies at $\sim 45^\circ\text{N}$, is cooler throughout the Southern Hemisphere, with particularly large differences in the response over the Southern Ocean in winter.

The simulated changes in the August SAT for runs 6ka-SHF and 6ka-EFF are shown in Figure 6.11, along with the statistically-significant differences between the response of each run, and that of run 6ka-DEF. Again, both runs exhibit a very similar response to run 6ka-DEF, with warming over the Northern Hemisphere land-masses, and localised cooling in the tropics. However, run 6ka-EFF also simulates cooling over the Southern Ocean, which run 6ka-SHF does not.

Relative to run 6ka-DEF, there are large differences in the temperature changes over the Caspian Sea. These differences account for the anomalies at $\sim 45^\circ\text{N}$ in the zonal-mean SAT response, and can be attributed to the cooling trend exhibited by the control runs over the Caspian Sea (Section 5.4). Otherwise, the response of run 6ka-SHF is very similar to that of run 6ka-DEF, while the cooler response of run 6ka-EFF across the Southern Ocean is apparent.

Figures 6.12 and 6.13 show the simulated anomalies in the mean SAT for the coldest month of the year, and in the GDD5, respectively. The statistically-significant differences between the response of each run, and that of run 6ka-DEF, are also shown. Large differences are apparent in the response over the Caspian Sea, and can be attributed to the cooling trend within the control runs; otherwise, the responses of the runs are similar to that of run 6ka-DEF. Both runs capture the higher winter temperatures over Scandinavia, but fail to simulate either the warming over northeastern Europe, or the cooling over southwestern Europe. Likewise, runs 6ka-SHF and 6ka-EFF both capture the increase in the GDD5 over northwestern Europe and the Alps, but fail to simulate the decrease over the southern half of Europe.

The annual precipitation anomalies for runs 6ka-SHF and 6ka-EFF, as well as any statistically-significant differences between the response of each run and that of run 6ka-DEF, are shown in Figure 6.14. The precipitation changes simulated by both runs are very similar to those simulated by run 6ka-DEF, with no large-scale discrepancies in the response. The robustness of the simulated precipitation changes are further indicated by Figure 6.15, which shows the changes in the annual precipitation over North Africa, relative to the control runs, for each of runs 6ka-DEF, 6ka-SHF and 6ka-EFF. The simulated decreases in precipitation at $\sim 5^\circ\text{N}$ are very similar, as are the increases at $\sim 14^\circ\text{N}$.

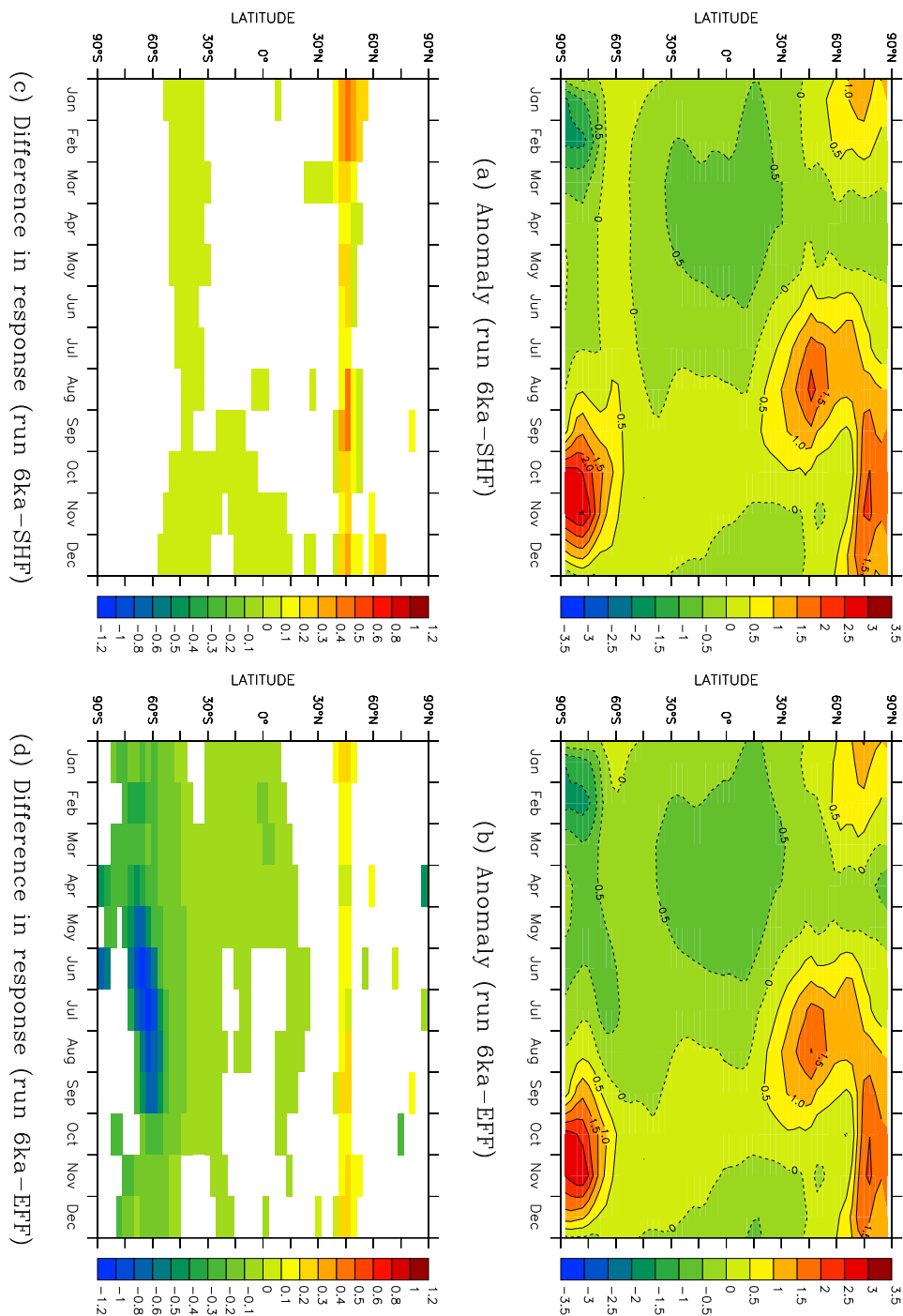


Figure 6.10: The zonal-mean surface air temperature ($^{\circ}\text{C}$) for years 201–900 of runs 6ka-SHF and 6ka-EFF, expressed as anomalies relative to the control runs: (a), (b) the temperature anomalies, runs 6ka-SHF and 6ka-EFF respectively, and (c), (d) the response of each run, relative to that of run 6ka-DEF, runs 6ka-SHF and 6ka-EFF respectively. In (c) and (d), only those values which are significant at the 99% confidence level are shown.

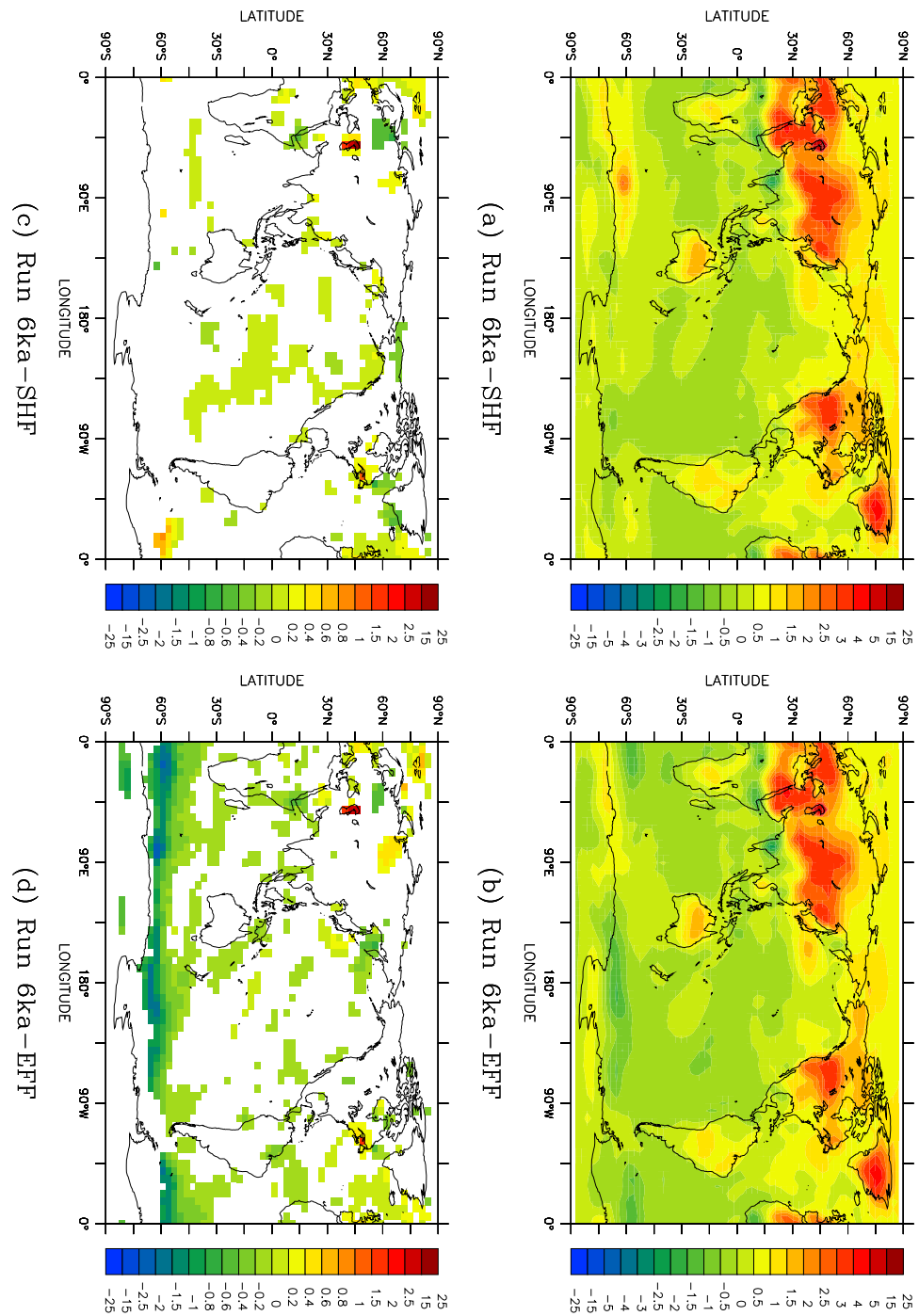


Figure 6.11: The August surface air temperature ($^{\circ}\text{C}$) for years 201–900 of runs 6ka-SHF and 6ka-EFF, expressed as anomalies relative to the control runs: (a), (b) the temperature anomalies, runs 6ka-SHF and 6ka-EFF respectively, and (c), (d) the response of each run, relative to that of run 6ka-DEF, runs 6ka-SHF and 6ka-EFF respectively. In (c) and (d), only those values which are significant at the 99% confidence level are shown.

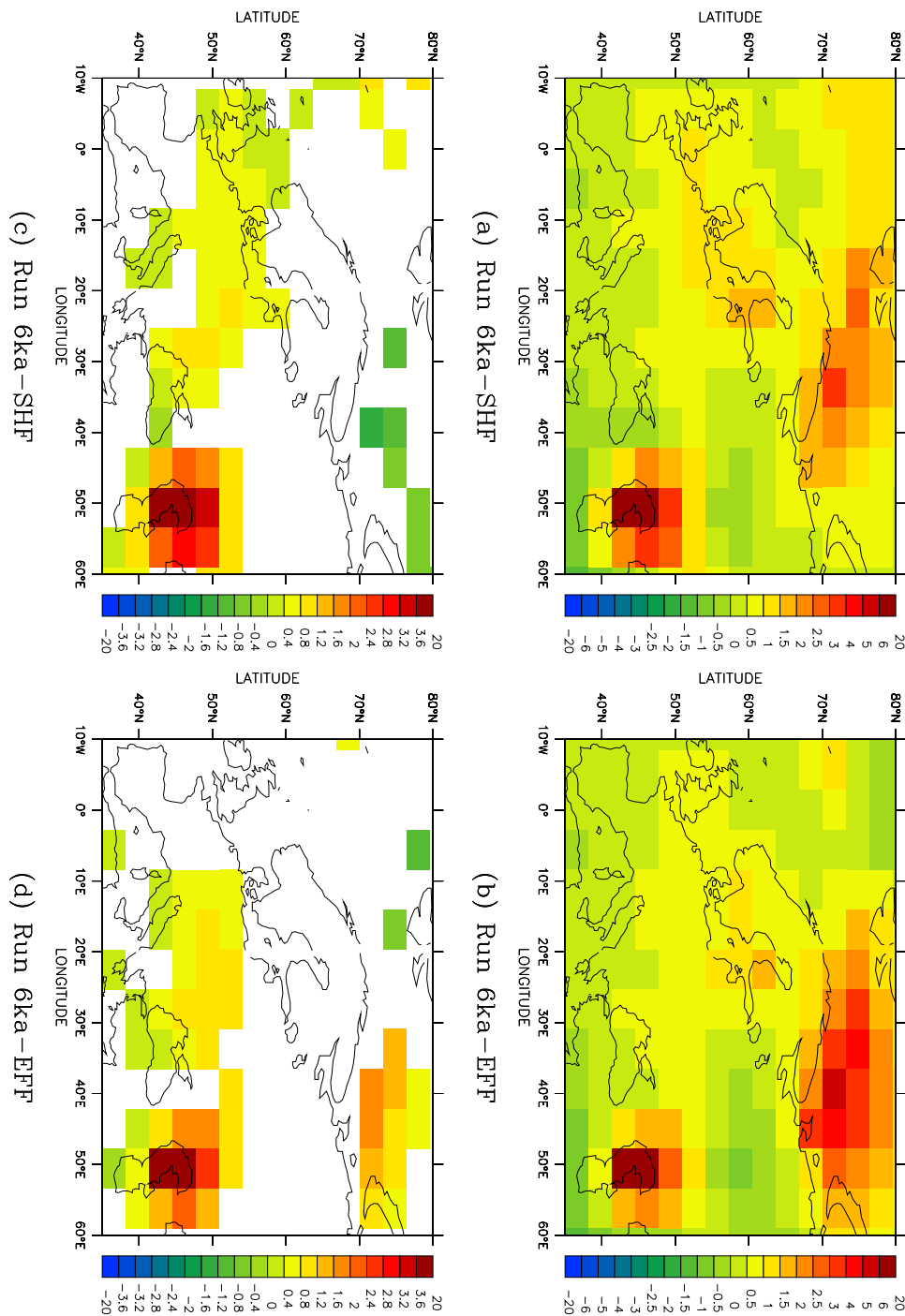


Figure 6.12: The mean surface air temperature of the coldest month of the year ($^{\circ}\text{C}$) for years 201–900 of runs 6ka-SHF and 6ka-EFF, expressed as anomalies relative to the control runs: (a), (b) the temperature anomalies, runs 6ka-SHF and 6ka-EFF respectively, and (c), (d) the response of each run, relative to that of run 6ka-DEF, runs 6ka-SHF and 6ka-EFF respectively. In (c) and (d), only those values which are significant at the 99% confidence level are shown.

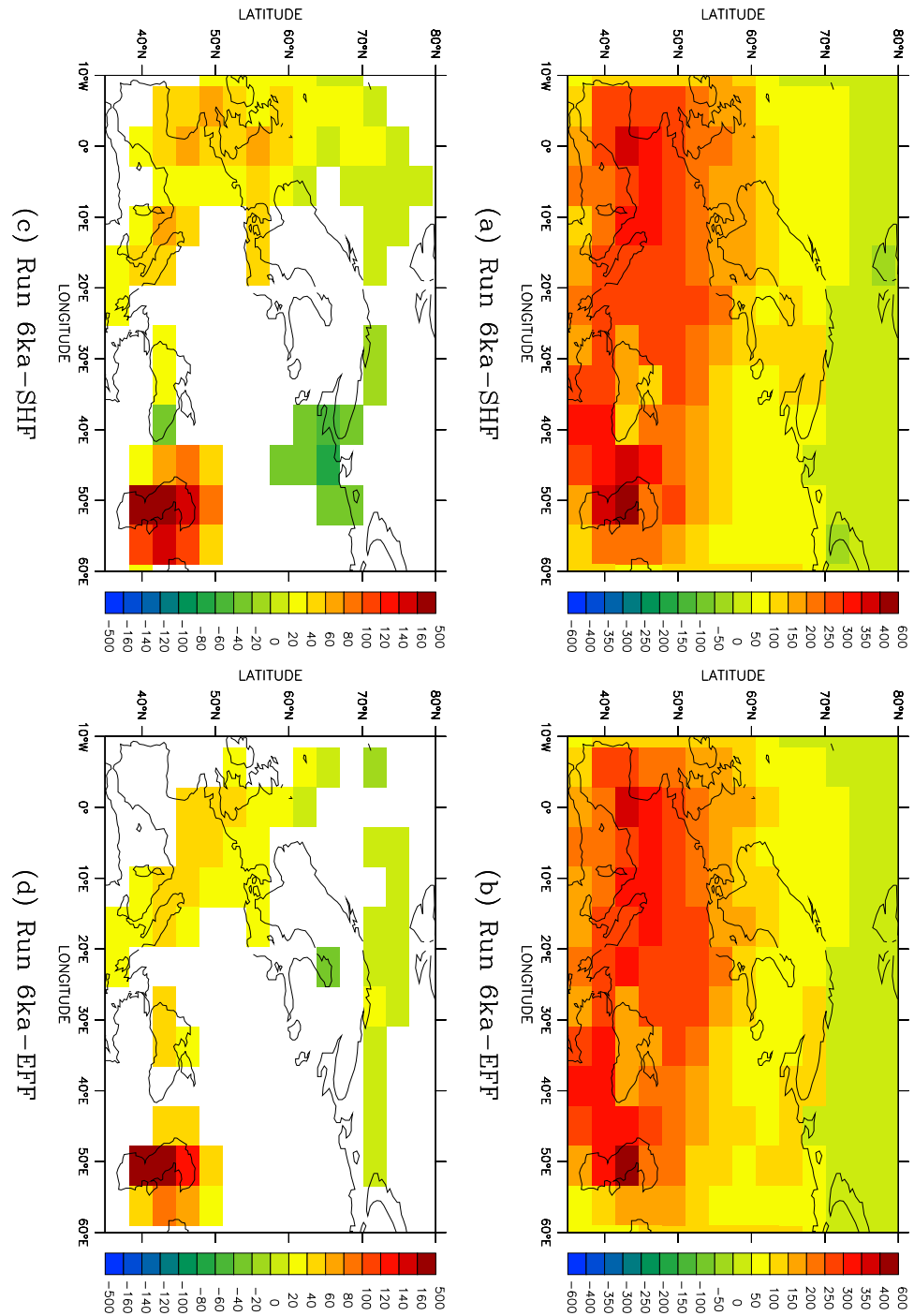


Figure 6.13: The GDD5 ($^{\circ}\text{C}\cdot\text{days}$) for years 201–900 of runs 6ka-SHF and 6ka-EFF, expressed as anomalies relative to the control runs: (a), (b) the anomalies, runs 6ka-SHF and 6ka-EFF respectively, and (c), (d) the response of each run, relative to that of run 6ka-DEF, runs 6ka-SHF and 6ka-EFF respectively. In (c) and (d), only those values which are significant at the 99% confidence level are shown.

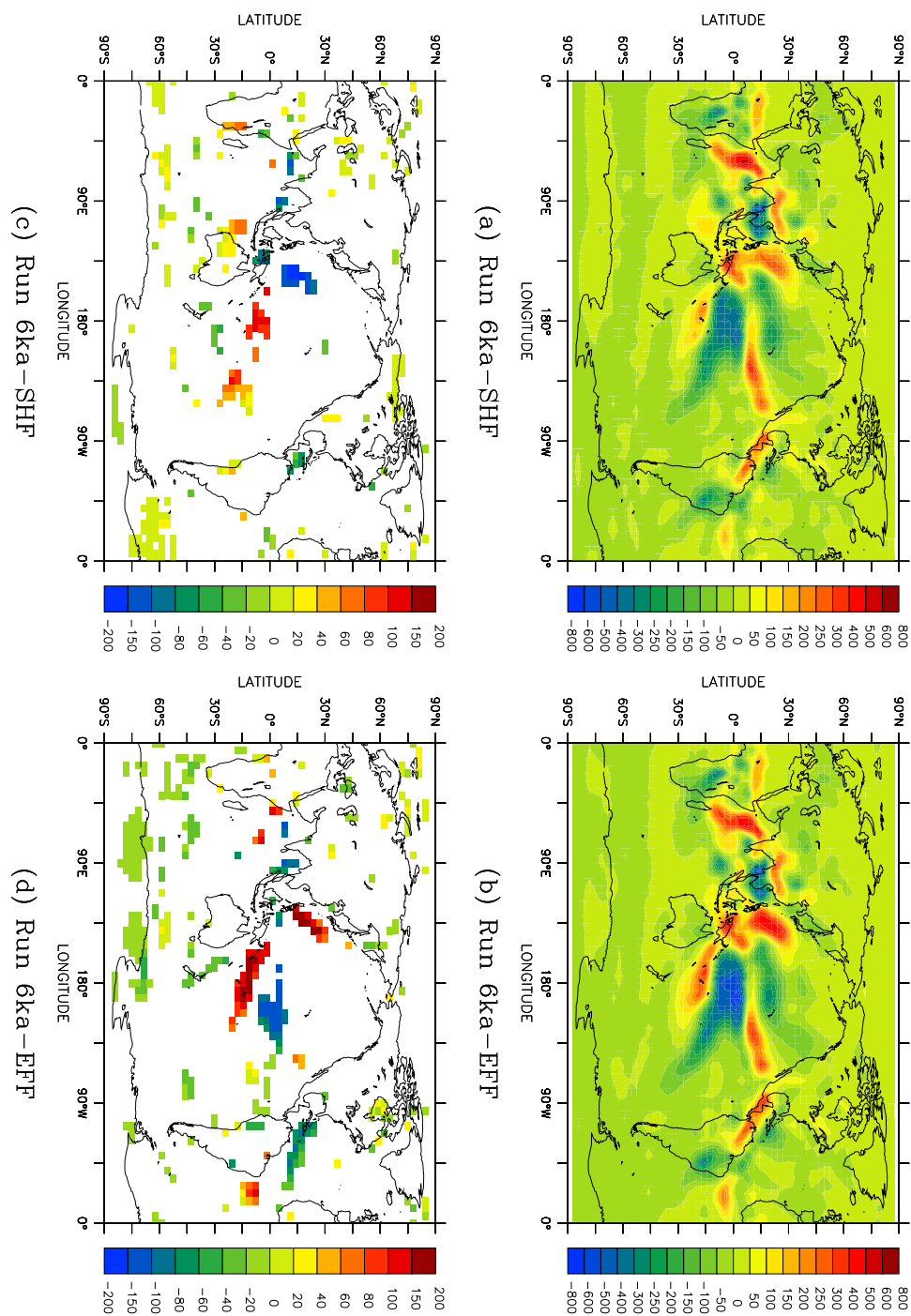


Figure 6.14: The annual precipitation (mm) for years 201–900 of runs 6ka-SHF and 6ka-EFF, expressed as anomalies relative to the control runs: (a), (b) the precipitation anomalies, runs 6ka-SHF and 6ka-EFF respectively, and (c), (d) the response of the runs, relative to the response of run 6ka-DEF, runs 6ka-SHF and 6ka-EFF respectively. In (c) and (d), only those values which are significant at the 99% confidence level are shown.

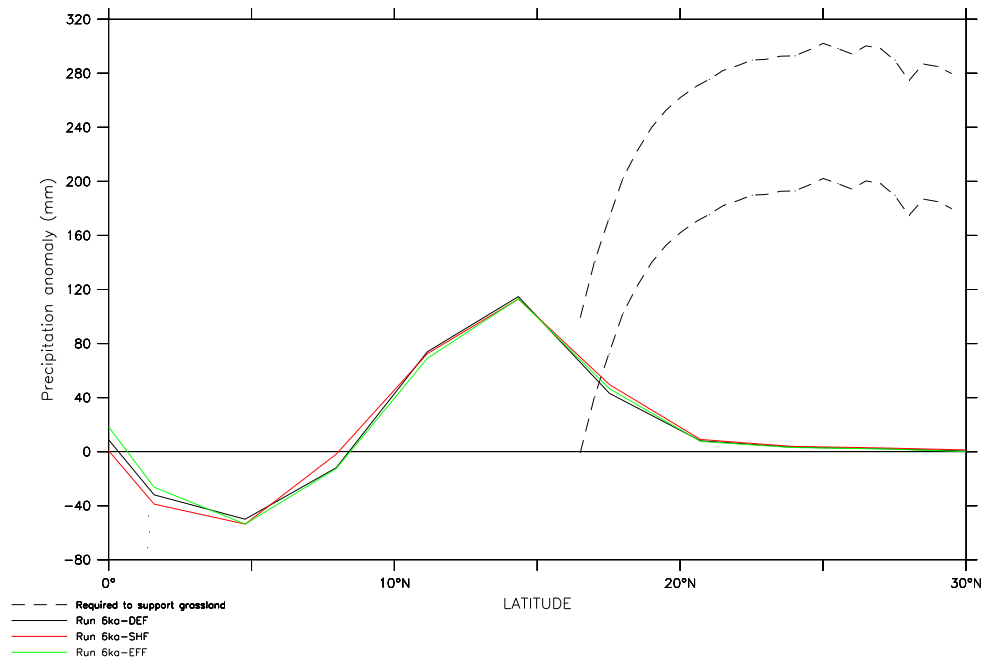


Figure 6.15: The zonal-mean annual precipitation (mm) over North Africa for years 201–900 of runs 6ka-DEF, 6ka-SHF and 6ka-EFF, expressed as anomalies relative to the control runs. Minimum and maximum estimates of the precipitation increase required to support grassland at each latitude are also shown (*Joussaume et al.*, 1999).

6.4.2 Climate variability

Interannual variability

Figure 6.16 shows the standard deviations in the annual-mean surface air temperature (SAT) and sea surface temperature (SST) for years 201–900 of runs 6ka-SHF and 6ka-EFF, expressed as a fraction of those for the control runs. As in the case of run 6ka-DEF, regional differences in the magnitude of the interannual variability are apparent. At low latitudes, the increases in temperature variability over the western tropical Pacific Ocean, the tropical Indian Ocean, and sub-Saharan Africa are again apparent, although the increase in variability over the Indian Ocean is only slight in the case of run 6ka-SHF.

One noticeable difference in behaviour is that run 6ka-EFF exhibits increases in SAT variability across much of the Southern Ocean, whereas run 6ka-DEF experiences localised decreases. This can be attributed to the differential response of the model; run 6ka-EFF does not experience any warming over the Southern Ocean, and hence does not experience any decrease in sea ice cover (not shown). It is the removal of the ice cover, with its insulating effects, that gives rise to the reduced SAT variability in run 6ka-DEF.

Figure 6.17 shows the leading principal components of the annual-mean SAT and SST for runs 6ka-SHF and 6ka-EFF. As in the case of run 6ka-DEF, they are similar

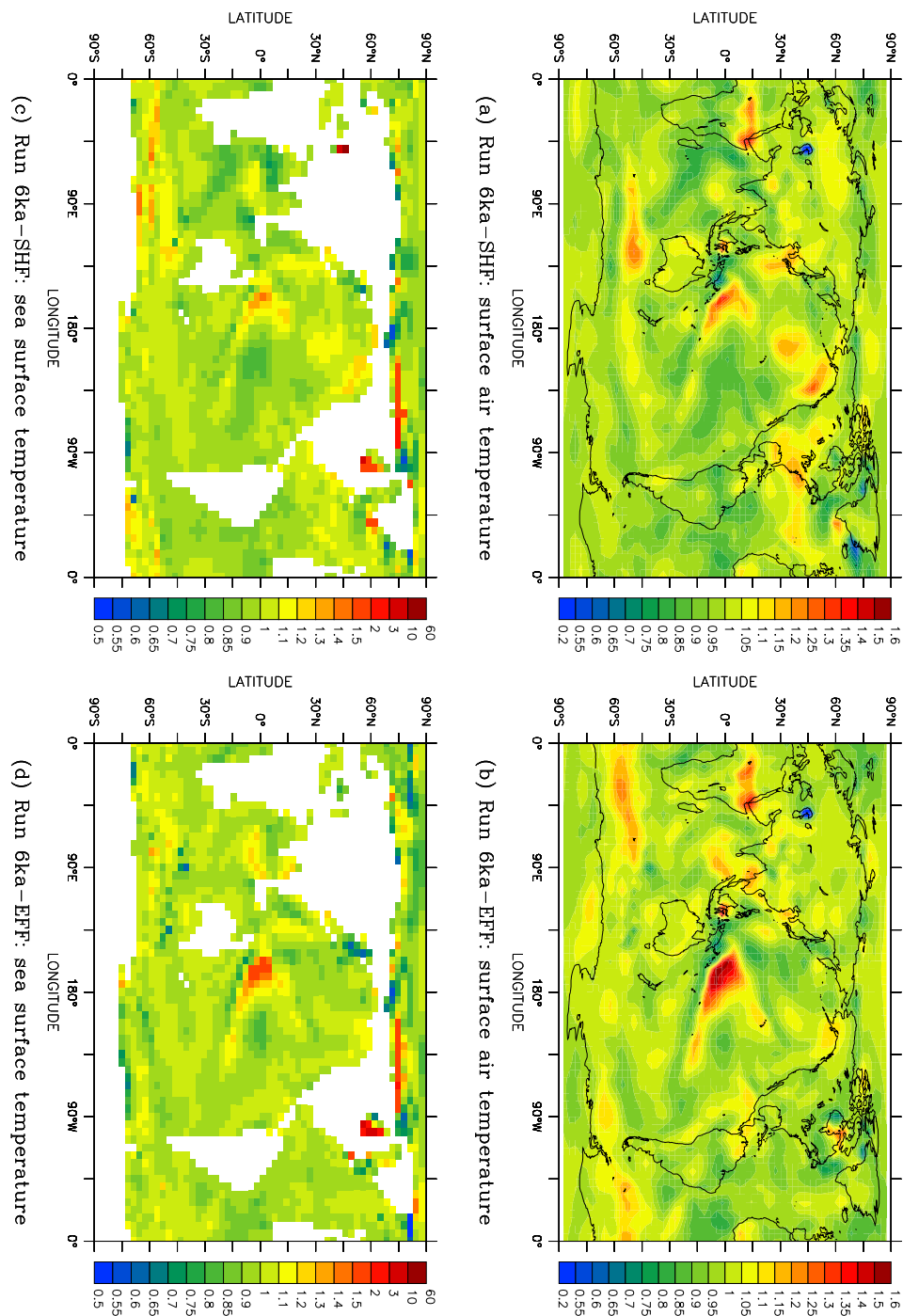


Figure 6.16: Standard deviations in annual-mean surface fields for years 201–900 of coupled model runs 6ka-SHF and 6ka-EFF, expressed relative to the standard deviations for years 201–900 of the control runs: (a), (b) surface air temperature, runs 6ka-SHF and 6ka-EFF respectively, and (c), (d) sea surface temperature, runs 6ka-SHF and 6ka-EFF respectively. The data has been high-pass filtered to remove variability on timescales longer than 100 years.

	CON-SHF	CON-EFF	6ka-SHF	6ka-EFF
Standard deviation of Niño 3.4 SST anom. ($^{\circ}\text{C}$)	0.50	0.51	0.43	0.45
Average return period of El Niño events (years)	7.9 ± 0.7	7.2 ± 0.5	7.8 ± 0.7	8.9 ± 0.9
Average duration of El Niño events (months)	18.0 ± 1.2	17.5 ± 1.0	16.1 ± 1.2	19.0 ± 1.2
Average magnitude of El Niño events ($^{\circ}\text{C}$)	0.92 ± 0.03	0.92 ± 0.03	0.75 ± 0.02	0.83 ± 0.02

Table 6.2: Some El Niño statistics for years 201–900 of coupled model runs CON-SHF, CON-EFF, 6ka-SHF and 6ka-EFF: the standard deviation of the five-month running mean of the Niño 3.4 sea surface temperature (SST) anomaly; the average return period of El Niño events; the average duration of El Niño events; and the average magnitude of El Niño events.

in structure and magnitude to those derived from the control runs (Figure 5.34), but with the same westward shift in the tropical Pacific Ocean. The leading principal components of the sea surface temperature, for example, have their maximum values located at 180°E in runs 6ka-SHF and 6ka-EFF, whereas they are located at 163°E in the control runs.

El Niño-Southern Oscillation

Table 6.2 shows some El Niño statistics for runs CON-SHF, CON-EFF, 6ka-SHF and 6ka-EFF. As in the case of run 6ka-DEF, the El Niño-Southern Oscillation is weaker in both mid-Holocene simulations. The standard deviation of the Niño 3.4 sea surface temperature anomaly decreases by $\sim 15\%$ and $\sim 12\%$ in the case of runs 6ka-SHF and 6ka-EFF respectively; these decreases are similar to the $\sim 13\%$ decrease simulated by run 6ka-DEF.

The simulated changes in the zonal wind stress and sea surface temperature over the equatorial Pacific Ocean are shown in Figure 6.18. Both runs exhibit a similar response to run 6ka-DEF, with enhanced trade winds over the western Pacific during the northern summer and autumn. These result in lower sea surface temperatures in the central and eastern Pacific, enhancing the zonal temperature gradient. Run 6ka-EFF exhibits a stronger SST response than run 6ka-DEF, with a greater decrease in sea surface temperatures over the central and eastern Pacific.

Figure 6.19 shows the power spectra of the simulated Niño 3.4 sea surface temperature anomalies for runs 6ka-SHF and 6ka-EFF, comparing them with run 6ka-DEF, and with the corresponding control runs. Note that a Hann window of width 25, equivalent to $\sim 0.036 \text{ years}^{-1}$ in frequency units, has been applied to the spectra, reducing the standard deviation in each value to $\sim \pm 28\%$ (Section 5.3.2).

Run 6ka-SHF exhibits similar behaviour to run 6ka-DEF, with a decrease in power at almost all frequencies; this is particularly apparent at frequencies of $\sim 0.14\text{--}0.2 \text{ years}^{-1}$, corresponding to periods of $\sim 5\text{--}7$ years. The sharp decline in power at

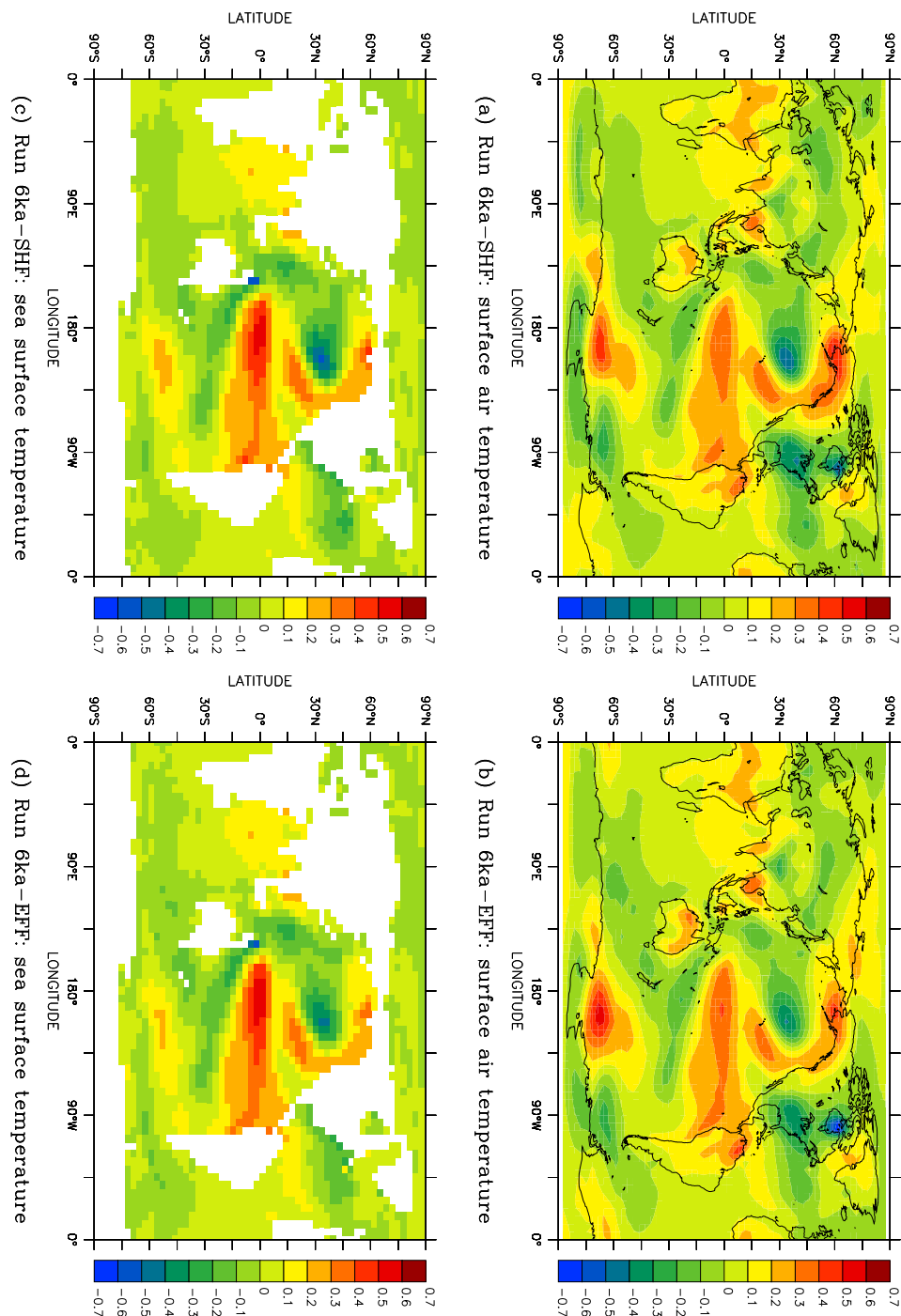


Figure 6.17: The leading principal components of annual-mean surface fields for years 201–900 of coupled model runs 6ka-SHF and 6ka-EFF: (a), (b) surface air temperature ($^{\circ}\text{C}$), runs 6ka-SHF and 6ka-EFF respectively, and (c), (d) sea surface temperature ($^{\circ}\text{C}$), runs 6ka-SHF and 6ka-EFF respectively. The data has been high-pass filtered prior to calculating the principal components to remove variability on timescales longer than 100 years.

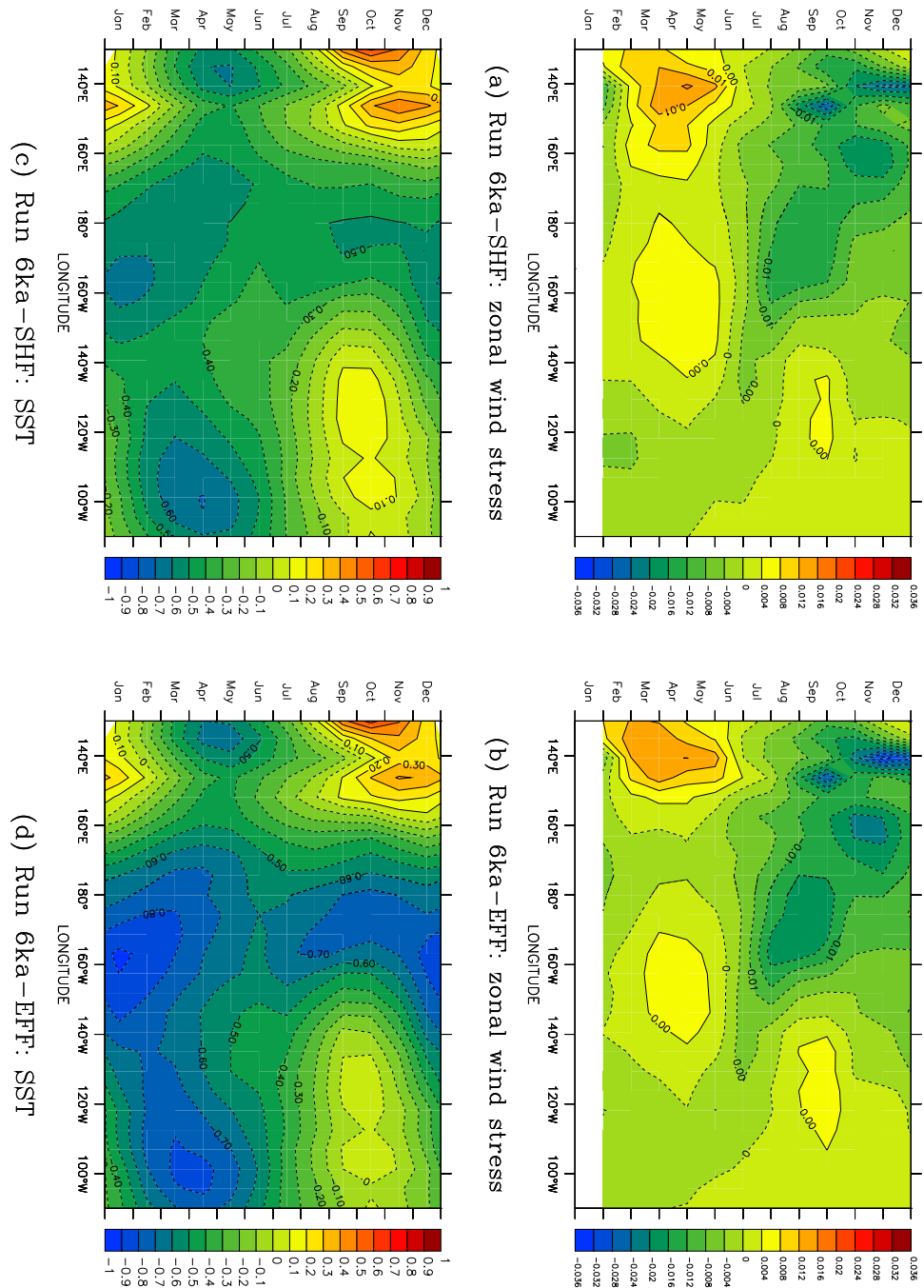


Figure 6.18: The equatorial zonal wind stress (Nm^{-2}) and sea surface temperature (SST, $^{\circ}\text{C}$) for years 201–900 of coupled model runs 6ka-SHF and 6ka-EFF, expressed as anomalies relative to the control runs: (a), (b) monthly-mean zonal wind stress, runs 6ka-SHF and 6ka-EFF respectively, and (c), (d) monthly-mean sea surface temperature, runs 6ka-SHF and 6ka-EFF respectively. The values shown are averages over the region 5°S–5°N.

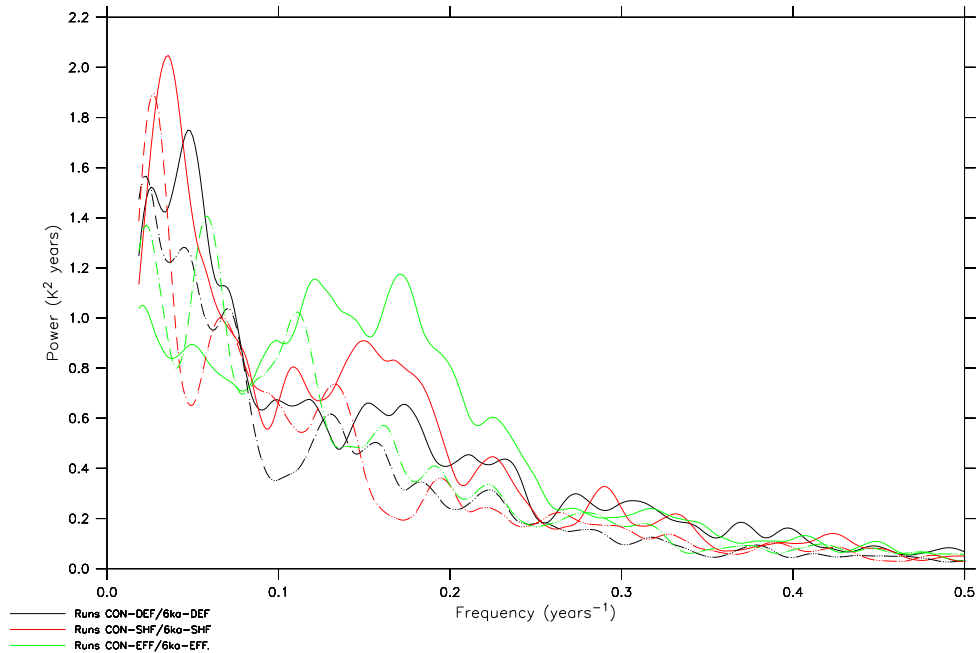


Figure 6.19: The power spectra of the Niño 3.4 sea surface temperature anomaly, for years 201–900 of coupled model runs CON-DEF (solid black line), CON-SHF (solid red line), CON-EFF (solid green line), 6ka-DEF (dashed black line), 6ka-SHF (dashed red line) and 6ka-EFF (dashed green line) respectively. Each spectrum has been smoothed through the application of a Hann window of width 25.

these periods indicates the extent to which El Niño-type variability is diminished. As with run 6ka-DEF, however, there is also an increase in variability on interdecadal timescales. Maximum power now occurs at a frequency of $\sim 0.027 \text{ years}^{-1}$, corresponding to a period of ~ 37 years.

The shift towards variability on interdecadal timescales is even more pronounced in the case of run 6ka-EFF. There is a sharp decline in power at frequencies greater than $\sim 0.11 \text{ years}^{-1}$, corresponding to periods shorter than ~ 9 years. However, there is an increase in power on interdecadal timescales, with maxima at ~ 0.023 and $\sim 0.059 \text{ years}^{-1}$, corresponding to periods of ~ 44 and ~ 17 years respectively.

6.4.3 Summary

On a global scale, the response of run 6ka-SHF is consistent with that of run 6ka-DEF. It does simulate a large temperature increase over the Caspian Sea, however, as a result of drift within the control run. While there is therefore no evidence that flux adjustments *directly* affect the response of the model to insolation changes, there is evidence that they *indirectly* affect the response of the model, through their effect on the rate of drift within the control run.

The changes simulated by run 6ka-EFF are also generally consistent with those simulated by run 6ka-DEF. There are differences in the temperature response, however; as with run 6ka-SHF, drift within the control run causes it to simulate a large

temperature increase over the Caspian Sea. Run 6ka-EFF is also cooler over the Southern Ocean, causing the model to exhibit greater interannual variability in the surface air temperature. There is evidence, therefore, that the control climate of the ocean model can influence the regional response of the coupled model to insolation changes.

Chapter 7

$3\times\text{CO}_2$ stabilisation experiments

7.1 Introduction

The ability of the Mk3L coupled model to simulate the climate of the mid-Holocene was evaluated in Chapter 6. In this chapter, the transient response of the model to an increase in the atmospheric carbon dioxide concentration is investigated. A scenario is employed in which the CO_2 concentration is stabilised at three times the pre-industrial level.

Three transient climate change simulations are presented. These are designated 3CO2-DEF, 3CO2-SHF and 3CO2-EFF; they are initialised from the states of the control runs CON-DEF, CON-SHF and CON-EFF, respectively, at the end of year 100, and are integrated to years 1400, 1100 and 1100. The transient simulations differ from the equivalent control runs only in that the atmospheric carbon dioxide concentration is increased at 1% per year. A concentration of 560 ppm (twice the pre-industrial value of 280 ppm) is reached in year 170, and a concentration of 840 ppm (three times the pre-industrial value) is reached in year 211. The CO_2 concentration is held constant at 840 ppm thereafter. Further details regarding the experimental design are provided in Appendix A.

The scenario employed here differs from that of *Bi et al.* (2001, 2002) and *Bi* (2002), who study the response of the CSIRO Mk2 coupled model to an increase in the atmospheric carbon dioxide concentration. While they also stabilise the CO_2 concentration at three times the pre-industrial value, it is increased in accordance with the IS92a emission scenario (*Houghton et al.*, 1994); a trebling of the CO_2 concentration is therefore only achieved after 202 years. The scenario employed herein imposes a 1% per year increase, however, as it allows a direct comparison with the models which participated in the Coupled Model Intercomparison Project (e.g. *Covey et al.*, 2003).

Run 3CO2-DEF is analysed in Section 7.2, indicating the response of the default configuration of the Mk3L coupled model to an increase in the atmospheric carbon dioxide concentration. Section 7.3 contrasts runs 3CO2-SHF and 3CO2-EFF with run 3CO2-DEF, assessing the impact of the ocean model spin-up procedure upon the model response.

7.2 The default model response

7.2.1 Atmosphere

Surface air temperature

The evolution of the simulated global-mean and zonal-mean surface air temperature (SAT) during run 3CO2-DEF are shown in Figure 7.1. Dashed vertical lines indicate year 100, being the year after which the atmospheric CO_2 concentration begins to increase, and year 211, being the year in which the concentration reaches 840 ppm. The global-mean SAT increases rapidly as the CO_2 concentration increases, with warming of 1.6°C upon a doubling of the CO_2 concentration, and 2.7°C upon a trebling. [These figures represent the average SAT changes for years 155–184 and 196–225 respectively, being the 30-year periods centred on the points at which the CO_2 concentration reaches two and three times the pre-industrial concentration.]

The global-mean SAT continues increasing once the CO_2 concentration has stabilised, although at a reduced rate. By the final century of the run (i.e. years 1301–1400), the global-mean SAT has increased by 5.3°C relative to the control run, and is continuing to increase at a rate of $\sim 0.08^\circ\text{C}/\text{century}$. The mean SAT changes are greater over land than over the ocean, with increases of 6.2°C and 4.8°C , respectively, by the final century.

Figure 7.2 shows the changes in SAT by years 1301–1400. The strongest warming occurs over the high-latitude oceans, with increases in annual-mean SAT as large as 19.4°C in the Northern Hemisphere, and 15.6°C in the Southern Hemisphere. Figures 7.2b and 7.2c show that the warming at high latitudes occurs primarily in winter, with relatively little change in the summer temperatures. This is explained by the lack of insolation at high latitudes in winter, as a result of which the surface temperature is governed by the re-radiation of longwave radiation, and by the surface heat capacity. The increase in the atmospheric CO_2 concentration leads to a reduction in the outgoing longwave radiation, while a reduction in the sea ice cover - which has a strong insulating effect - increases the effective surface heat capacity. Both these changes result in higher winter surface air temperatures over the high-latitude oceans.

The climate sensitivity of the Mk3L coupled model, as indicated by the increase of 1.6°C in the global-mean SAT upon a doubling of the CO_2 concentration, is consistent with those models which participated in the Coupled Model Intercomparison Project (CMIP, e.g. *Raper et al.*, 2002; *Covey et al.*, 2003). However, the long-term response of the model to a trebling of the CO_2 concentration is $\sim 20\%$ weaker than that of the CSIRO Mk2 coupled model (*Hirst*, 1999; *Bi*, 2002).

Sea ice

Figure 7.3 shows the evolution of the sea ice extent and volume in each hemisphere during runs CON-DEF and 3CO2-DEF. There is a rapid decline in sea ice cover as the atmospheric CO_2 concentration increases. Upon a doubling of the atmospheric CO_2 concentration, the annual-mean sea ice extents have decreased by $2.5\times 10^{12}\text{ m}^2$ in each of the Northern and Southern Hemispheres; as with the change in global-mean SAT, these changes are consistent with those models which participated in

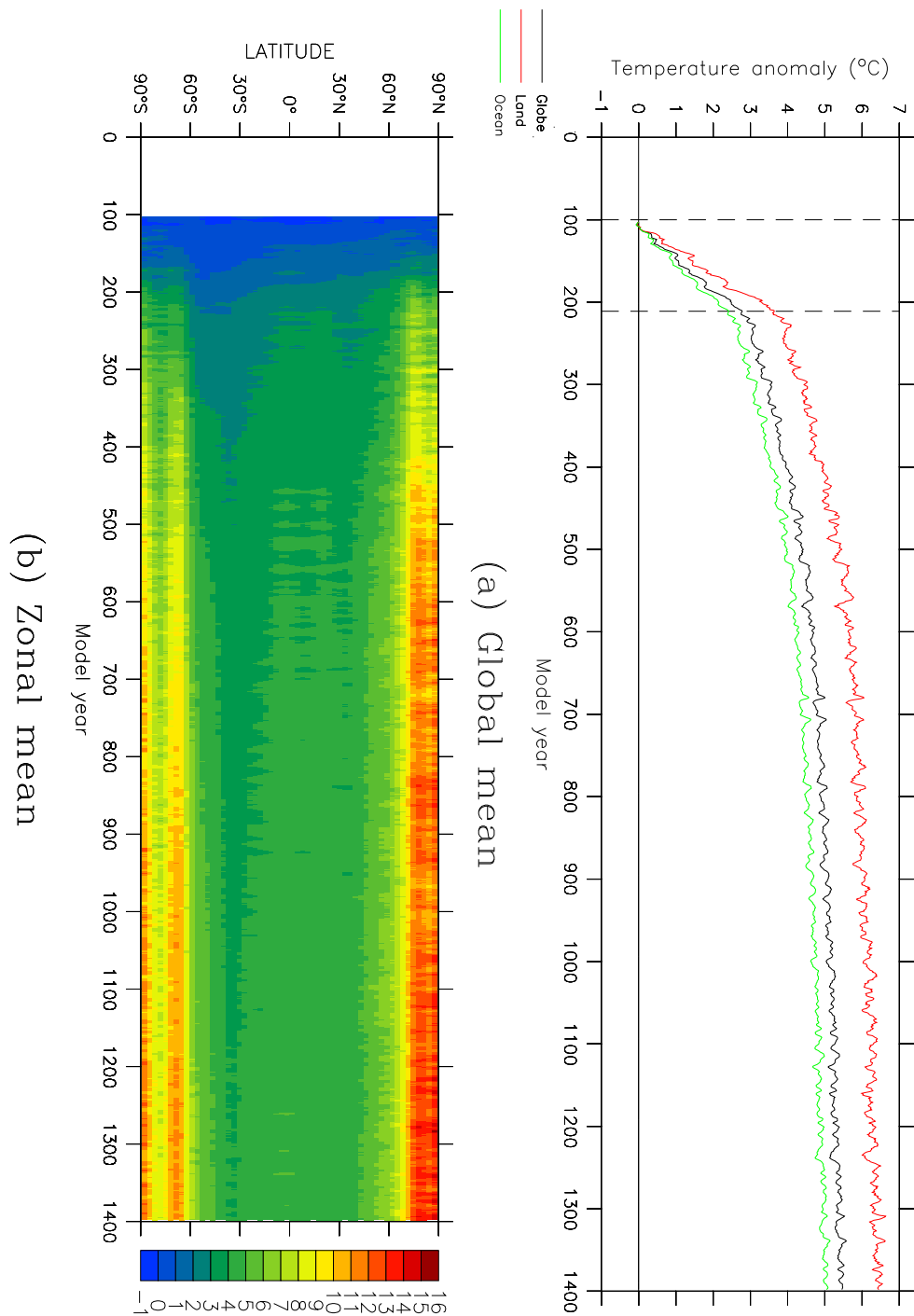
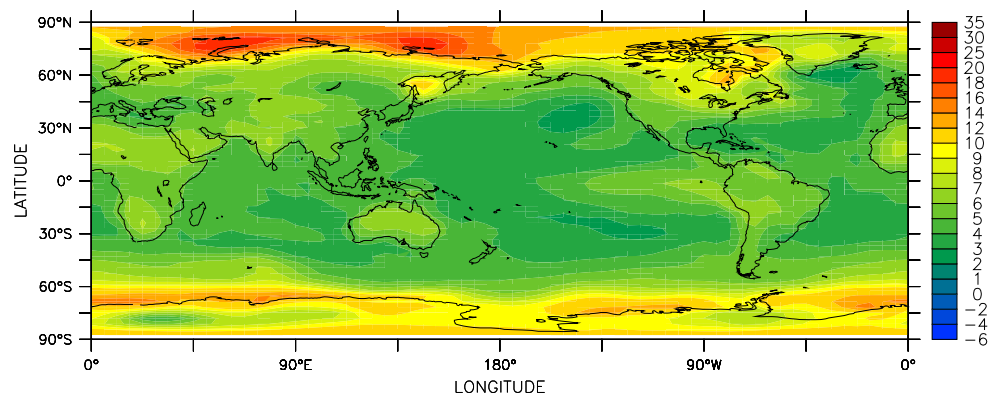
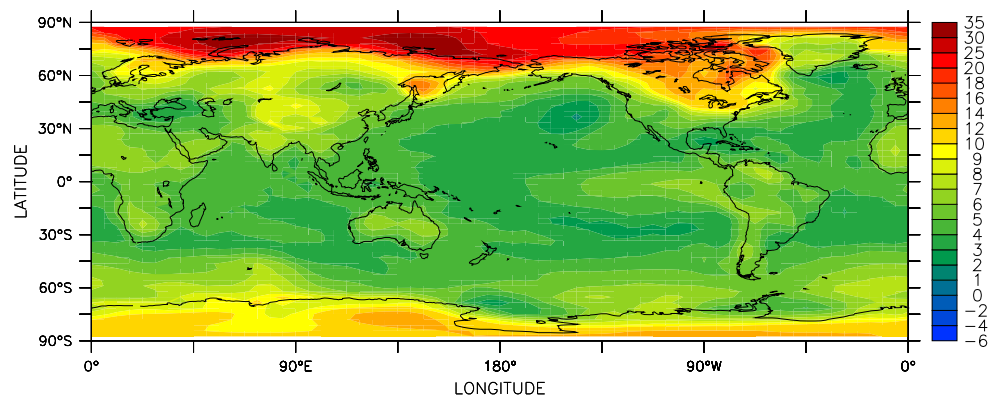


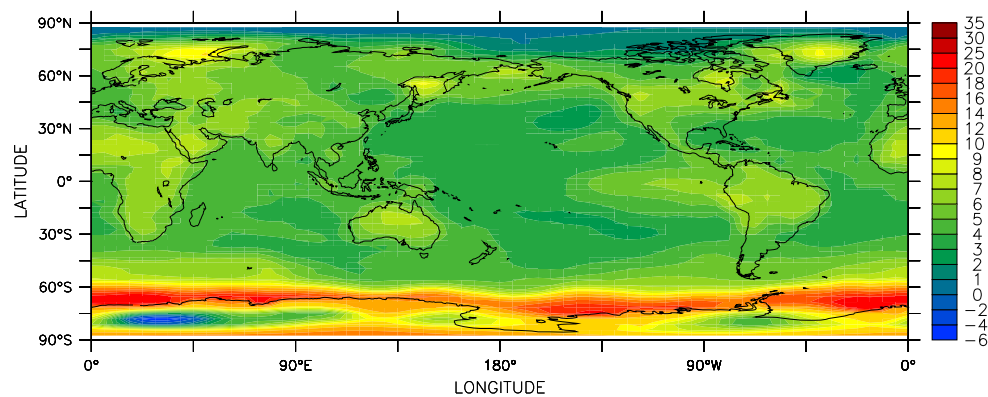
Figure 7.1: The change in annual-mean surface air temperature ($^{\circ}\text{C}$) during run 3CO2-DEF: (a) the global mean (black), and the means over land (red) and the ocean (green), and (b) the zonal mean. The values shown are five-year running means, and are expressed as anomalies relative to control run CON-DEF. Vertical lines indicate years 100 and 211.



(a) Annual mean



(b) DJF average



(c) JJA average

Figure 7.2: The average surface air temperature ($^{\circ}\text{C}$) for years 1301–1400 of run 3CO₂-DEF, expressed as an anomaly relative to the average surface air temperature for years 1301–1400 of control run CON-DEF: (a) the annual mean, (b) the December-January-February (DJF) average, and (c) the June-July-August (JJA) average.

CMIP (*Flato and Participating CMIP Modelling Groups, 2004*).

The decline in sea ice cover continues once the CO₂ concentration is stabilised. By the final century of run 3CO2-DEF, sea ice has almost disappeared in the Southern Hemisphere; the average sea ice extent and volume are reduced by 90% and 92%, respectively, relative to the control run. There is also a sharp reduction in the sea ice cover in the Northern Hemisphere, with the average sea ice extent and volume reduced by 64% and 83%, respectively. *Bi (2002)*, using the CSIRO Mk2 coupled model, finds larger changes during a similar 1400-year simulation, with the sea ice disappearing completely in the Northern Hemisphere; this behaviour is consistent with the greater warming exhibited by this model.

Figures 7.4 and 7.5 show the average sea ice concentrations and thicknesses, respectively, for the final century of the run; Figures 5.4 and 5.5 show equivalent values for run CON-DEF. The extent to which the sea ice has disappeared in each hemisphere is apparent, with summer ice cover confined to the western Ross Sea in the Southern Hemisphere, and to the central Arctic Ocean in the Northern Hemisphere. That sea ice which does form is thinner than in the control run, typically by ~50% in the Northern Hemisphere, and by ~20% in the Southern Hemisphere; this accounts for the fact that the sea ice volumes in each hemisphere exhibit a larger fractional decline than the extents.

7.2.2 Ocean

Sea surface temperature and salinity

The evolution of the simulated global-mean and zonal-mean sea surface temperature (SST) and sea surface salinity (SSS) during run 3CO2-DEF are shown in Figures 7.6 and 7.7 respectively. As with the surface air temperature, the global-mean SST increases rapidly as the atmospheric CO₂ concentration increases, with warming of 1.0°C upon a doubling of the CO₂ concentration, and 1.9°C upon a trebling. The global-mean SST continues to increase, albeit at a decreasing rate, once the CO₂ concentration is stabilised. By the final century of the run, the global-mean SST has increased by 4.1°C relative to the control run, and is continuing to increase at a rate of ~0.07°C/century. The zonal-mean SST exhibits the strongest warming at ~60°S and ~60°N, but there is also strong warming over the tropics.

In contrast to the surface air temperature and sea surface temperature, the global-mean SSS exhibits relatively little change as the atmospheric CO₂ concentration increases. However, it exhibits a steady downward trend over the following centuries, before gradually beginning to stabilise. By the final century of the run, the global-mean SSS has decreased by 0.42 psu relative to the control run. The zonal-mean SSS exhibits a slight freshening at most latitudes; however, there is strong freshening at the North Pole, and an increase in the zonal-mean SSS at ~75°N.

Figures 7.8 shows the changes in SST by the final century of the run, relative to the control run. In those limited regions of the Southern Ocean and Arctic Ocean where sea ice cover persists, the SST remains essentially unchanged. However, there are strong increases in those regions where the sea ice cover has disappeared. Due to the relatively large heat capacity of the ocean, as compared to that of the atmosphere, and to the consequently smaller magnitude of the annual cycle in sea

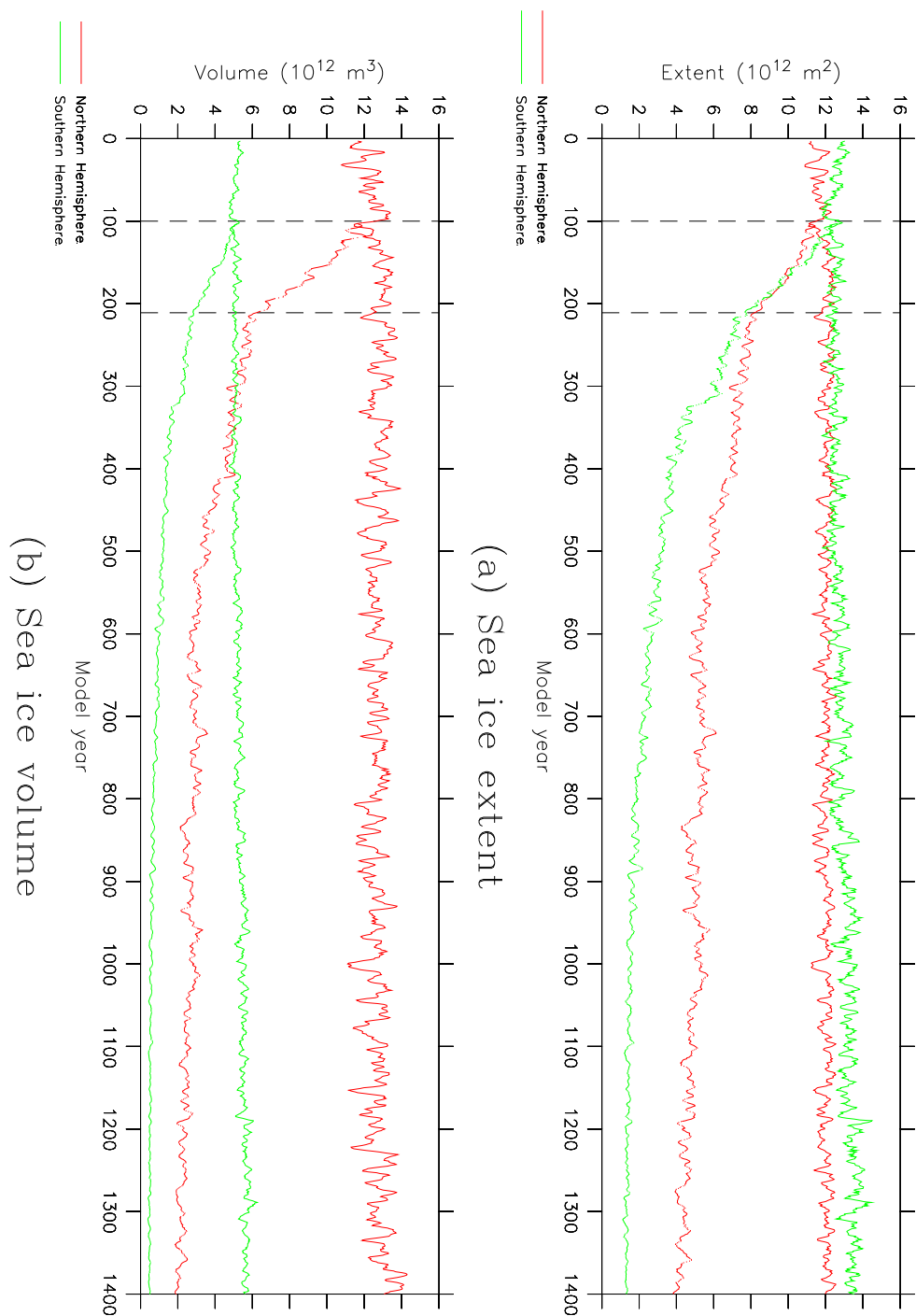


Figure 7.3: The annual-mean sea ice extent and volume for runs CON-DEF (solid lines) and 3CO_2 -DEF (dashed lines), for the Northern Hemisphere (red) and the Southern Hemisphere (green): (a) sea ice extent, and (b) sea ice volume. The values shown are five-year running means. Vertical lines indicate years 100 and 211.

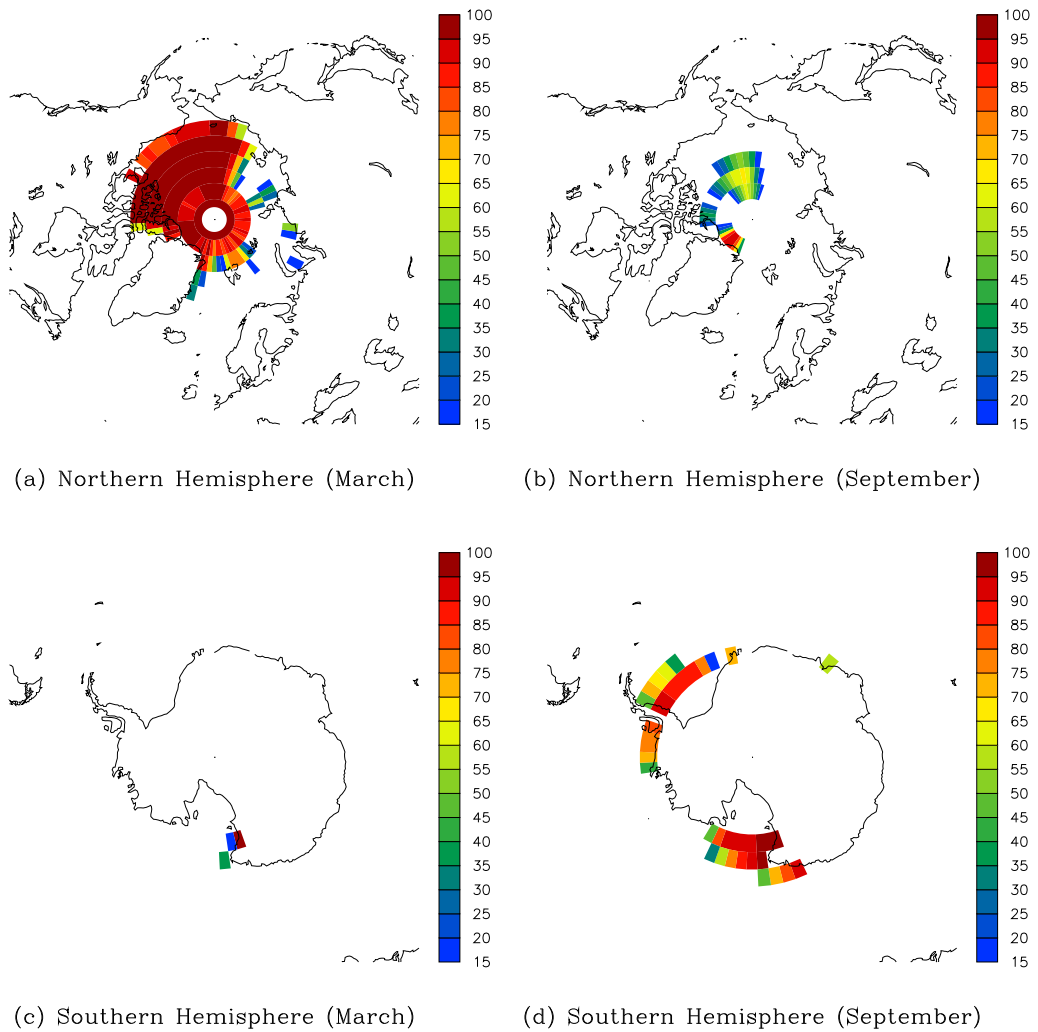


Figure 7.4: The average sea ice concentration (percent) for years 1301–1400 of run 3CO2-DEF: (a), (b) Northern Hemisphere, March and September respectively, and (c), (d) Southern Hemisphere, March and September respectively. Values are only shown where the concentration is greater than or equal to 15%.

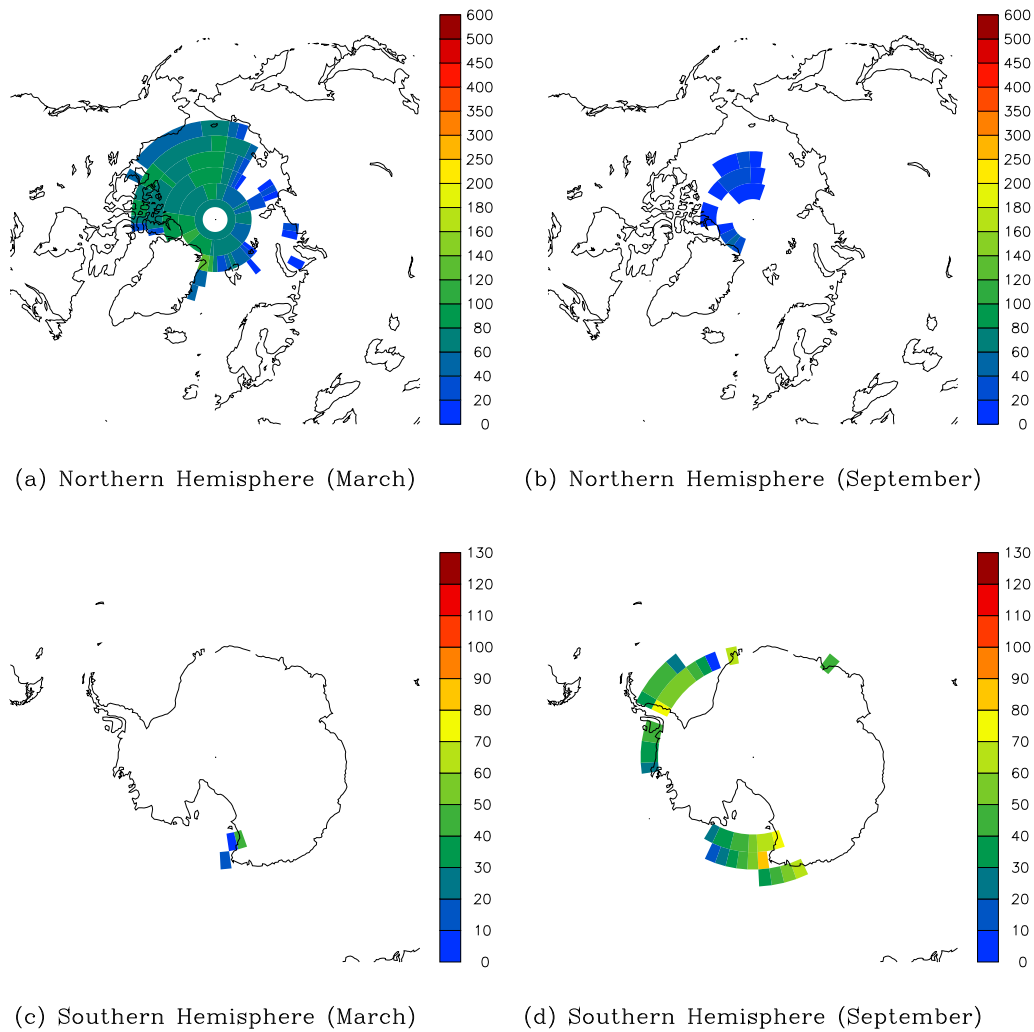


Figure 7.5: The average sea ice thickness (cm) for years 1301–1400 of run 3CO2-DEF: (a), (b) Northern Hemisphere, March and September respectively, and (c), (d) Southern Hemisphere, March and September respectively. Values are only shown where the concentration is greater than or equal to 15%.

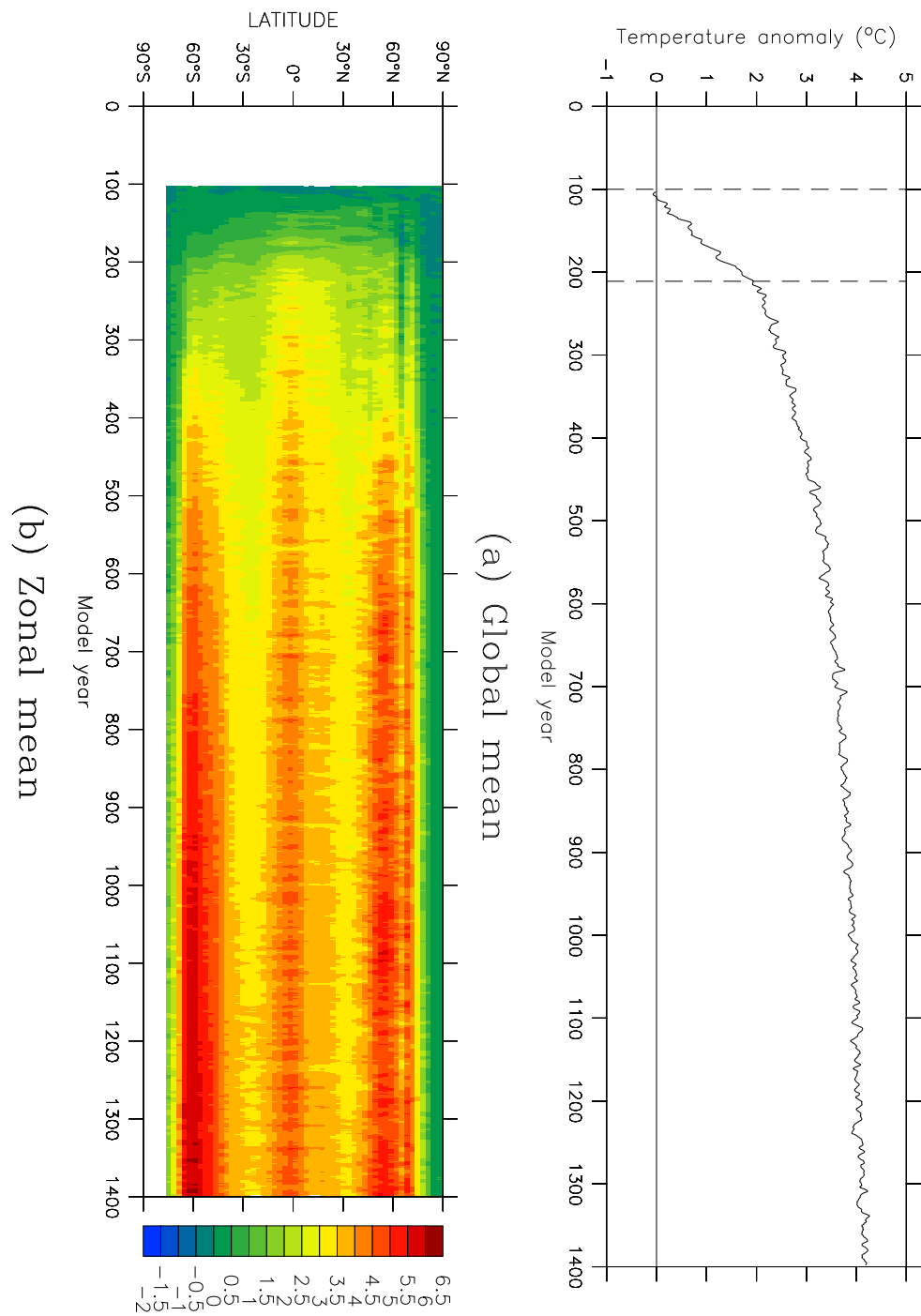


Figure 7.6: The change in annual-mean sea surface temperature (°C) during run 3CO2-DEF: (a) the global mean, and (b) the zonal mean. The values shown are five-year running means, and are expressed as anomalies relative to control run CON-DEF. Vertical lines indicate years 100 and 211.

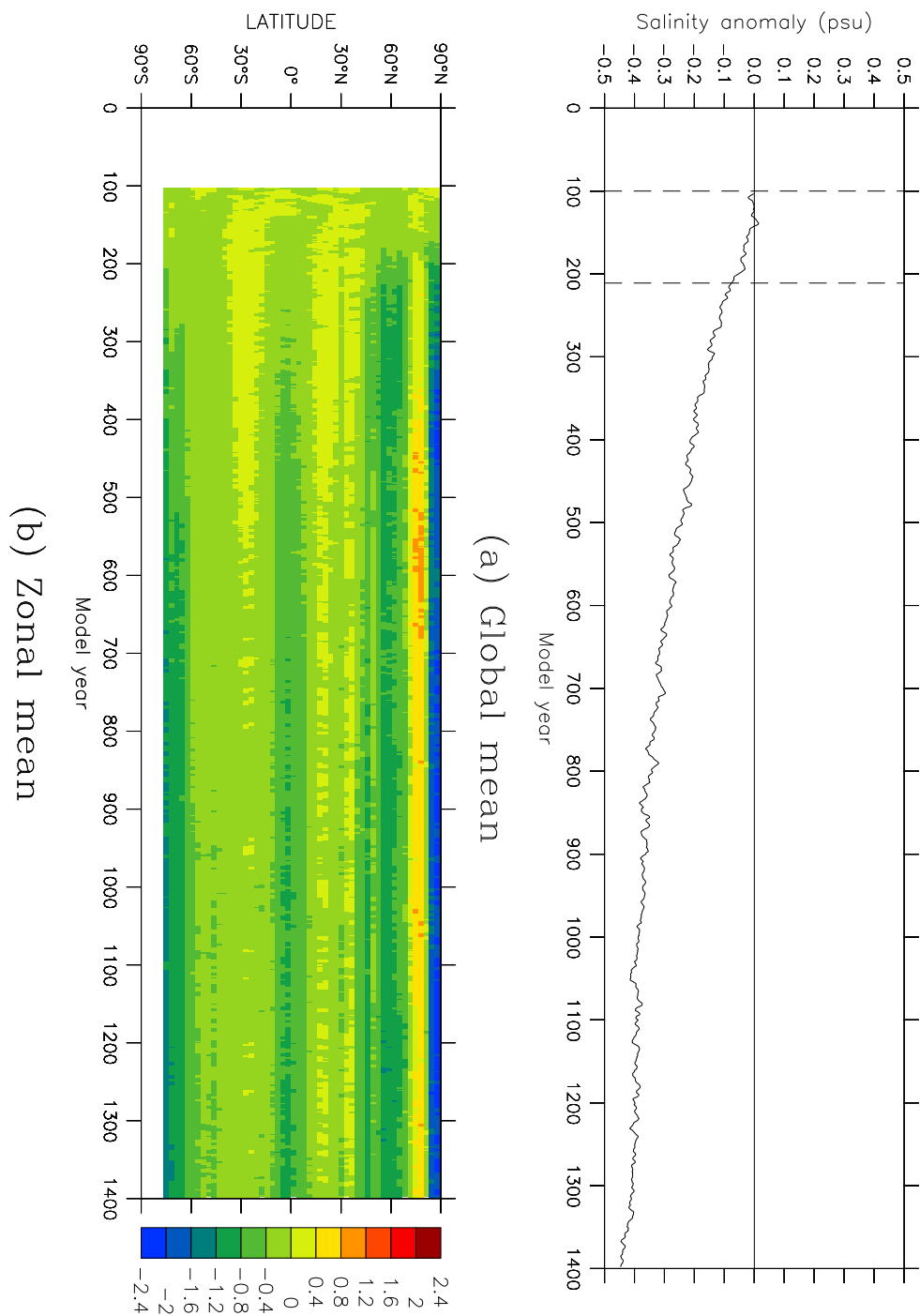


Figure 7.7: The change in annual-mean sea surface salinity (psu) during run 3CO2-DEF: (a) the global mean, and (b) the zonal mean. The values shown are five-year running means, and are expressed as anomalies relative to control run CON-DEF. Vertical lines indicate years 100 and 211.

surface temperatures, the SST increases are relatively uniform throughout the year. This is in contrast to the surface air temperature, where there is a much larger temperature increase in winter than during summer.

Figure 7.9 shows the change in the annual-mean SSS by the final century of the run. The isolation of the Caspian Sea from the world ocean is revealed by a decrease of 20.4 psu in the mean SSS relative to the control run. This arises from an increase of 6.7 psu in the mean SSS during run CON-DEF, and a decrease of 13.7 psu during run 3CO2-DEF. Of the remainder of the inland seas, there is a considerable increase in the salinity of the Mediterranean Sea. The Arafura Sea, between Australia and Indonesia, also experiences an increase of 6.7 psu in the mean SSS. While not an inland sea, it represents an embayment on the Mk3L ocean model grid, and is too small to contain any horizontal velocity gridpoints. The model can therefore only represent the diffusive component of the exchange of water properties with the world ocean, with the advective component being neglected.

At high latitudes, the SSS increases over the eastern Arctic Ocean, in the region where the sea ice cover has disappeared, but there is a freshening in those regions where sea ice cover persists. Over the remainder of the ocean, there is a slight salinity increase across much of the Atlantic Ocean, and a slight freshening across much of the Pacific Ocean.

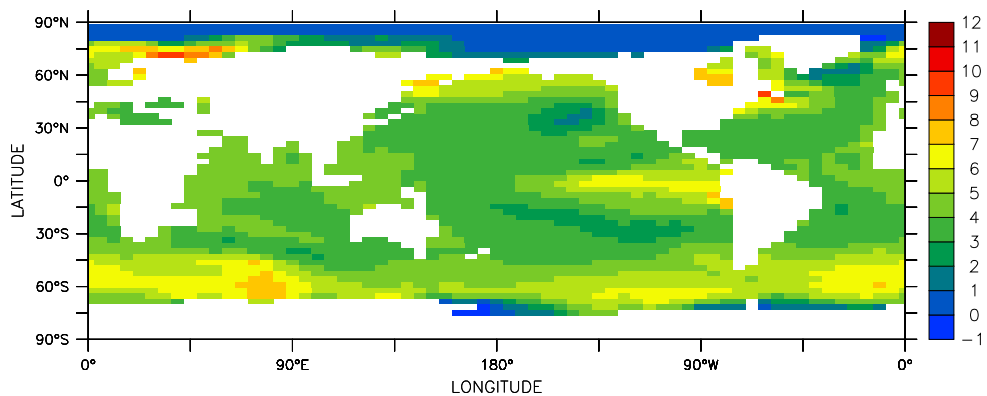
Water properties

The evolution of the simulated global-mean potential temperature, salinity and potential density of the world ocean, and of the simulated global-mean vertical profiles, during run 3CO2-DEF are shown in Figures 7.10, 7.11 and 7.12 respectively.

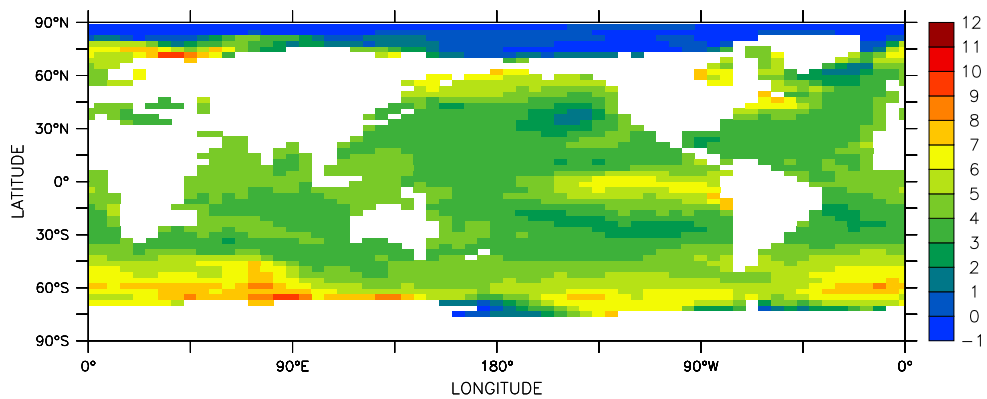
The temperature of the ocean increases steadily throughout the run, warming 3.43°C, relative to the control run, by year 1400. Consistent with the changes in surface air temperature, the upper ocean warms rapidly as the atmospheric CO₂ concentration increases. It continues to warm, but at a decreasing rate, once the CO₂ concentration is stabilised; by year 1400, the temperature of the upper ocean has increased by 4.52°C, and it is continuing to warm at a rate of ~0.07°C/century. While the upper ocean exhibits the greatest warming, the temperatures of the mid- and deep oceans are still increasing rapidly by the end of the run, increasing at rates of ~0.18°C/century and ~0.22°C/century respectively. Thus, while the largest global-mean temperature increase of 4.85°C occurs at a depth of 710 m, it can be expected that the warming of the world ocean will ultimately become more uniform.

The evolution of the zonal-mean potential temperature during run 3CO2-DEF is shown in Figure 7.13. Average values are shown for years 186–235, representing the 50-year period centred on the point at which the atmospheric CO₂ concentration is stabilised, for years 586–635 and 986–1035, and for the final 50 years of the run. The largest temperature increases occur in the upper ocean, at ~60°S and ~40°N. These warmings propagate horizontally throughout the ocean, and can be attributed to increases in the temperatures of Antarctic Intermediate Water and North Atlantic Deep Water, arising from the surface warming.

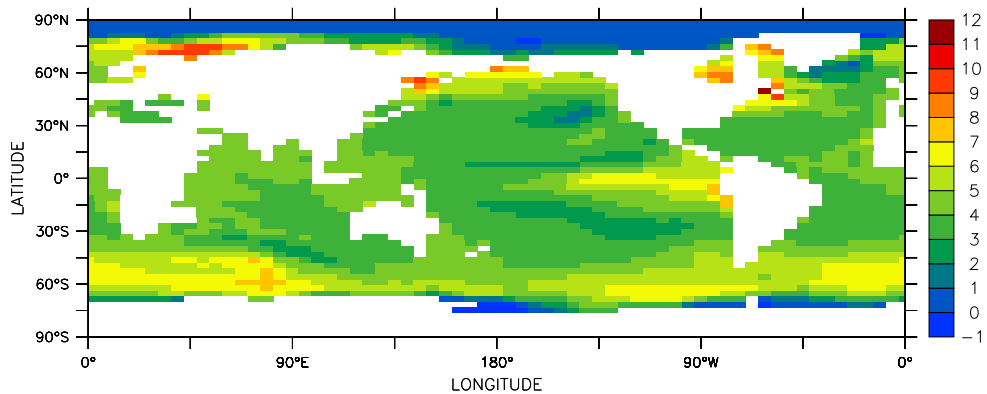
North of 30°S, the contours are horizontal throughout the mid-ocean, indicating the lack of any deep convection in this region. Although Antarctic Bottom Water formation ceases during the run, convection in the Southern Ocean causes the sur-



(a) Annual mean



(b) DJF average



(c) JJA average

Figure 7.8: The average sea surface temperature ($^{\circ}\text{C}$) for years 1301–1400 of run 3CO2-DEF, expressed as an anomaly relative to the average sea surface temperature for years 1301–1400 of control run CON-DEF: (a) the annual mean, (b) the December-January-February (DJF) average, and (c) the June-July-August (JJA) average.

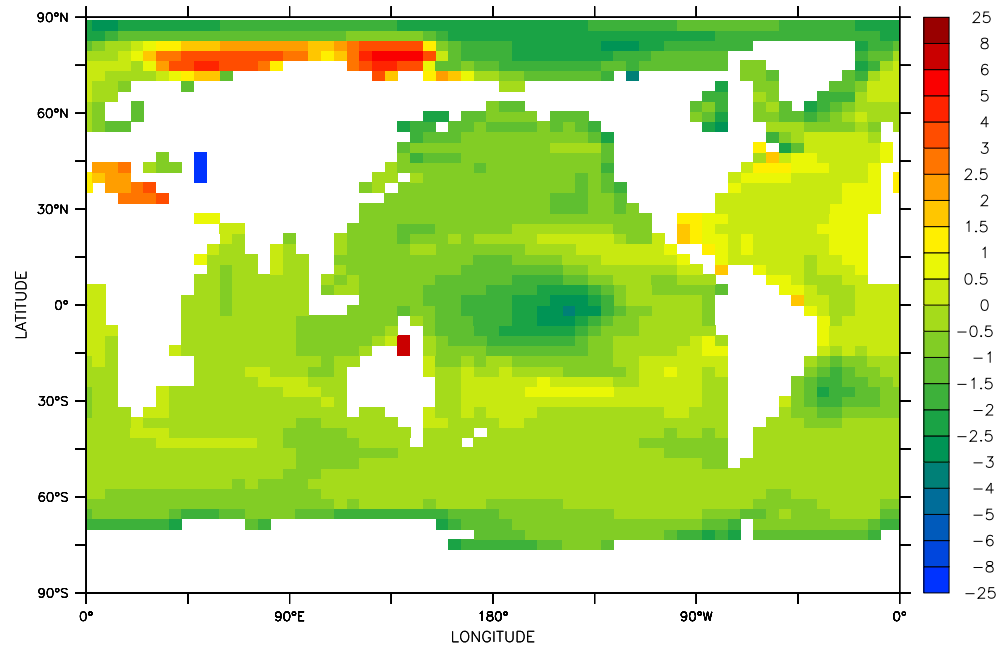


Figure 7.9: The annual-mean sea surface salinity (psu) for years 1301–1400 of run 3CO2-DEF, expressed as an anomaly relative to the annual-mean sea surface salinity for years 1301–1400 of control run CON-DEF.

face warming to penetrate slowly to depth (see below). This convection represents the only ventilation of the abyssal ocean, with the most rapid warming therefore occurring in the deep Southern Ocean. In contrast to the remainder of the world ocean, the deep Arctic Ocean cools during the first thousand years of the run; however, this trend appears to reverse thereafter.

The mean salinity of the ocean decreases by just 0.004 psu, relative to the control run, during the 1300 years of run 3CO2-DEF. This is in contrast to the freshening of ~ 0.1 psu encountered by *Bi* (2002) during a similar simulation, and indicates that the modifications to the coupling between the atmosphere and ocean models in Mk3L (*Phipps*, 2006) are successful at ensuring the conservation of freshwater. The surface freshening identified above, with the global-mean SSS decreasing by 0.42 psu by the end of the run, therefore represents a vertical redistribution of salt, with the surface freshening balanced by a slight increase in the salinity of the mid- and deep ocean. The evolution of the zonal-mean salinity during run 3CO2-DEF is shown in Figure 7.14. Apart from a freshening of the surface layers and of the Arctic Ocean, the zonal-mean SSS is generally stable throughout the run.

Reflecting the warming of the ocean, the mean potential density declines by 0.43 kgm^{-3} , relative to the control run, during run 3CO2-DEF. The change in density is greatest in the surface layers, reflecting both the greater temperature increase and the considerable freshening. The stratification of the ocean therefore increases; this is apparent from Figure 7.15, which shows the evolution of the zonal-mean potential density.

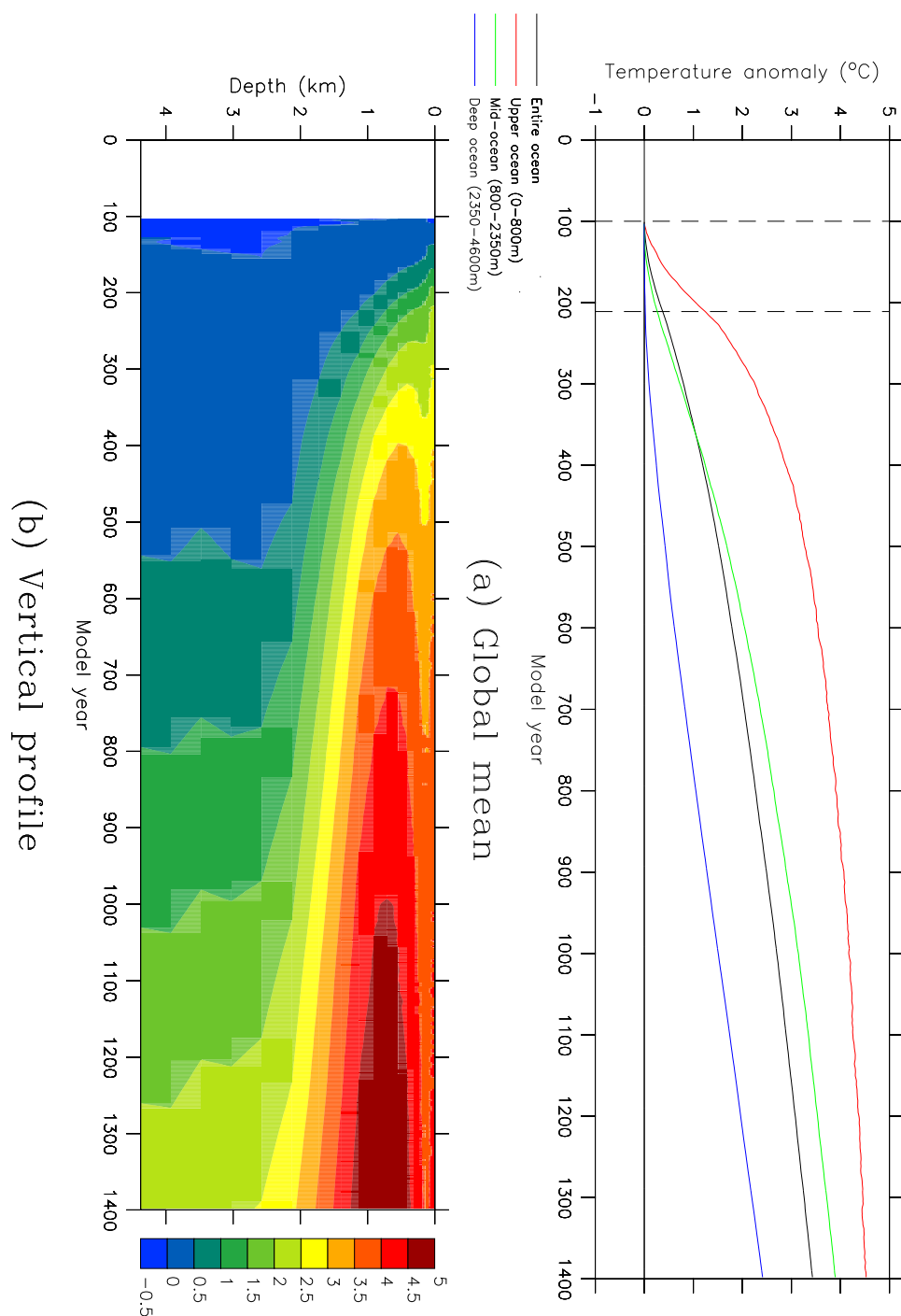


Figure 7.10: The change in annual-mean potential temperature (°C) during run 3CO2-DEF: (a) the global means for the entire ocean (black), upper ocean (red, 0–800 m), mid-ocean (green, 800–2350 m) and deep ocean (dark blue, 2350–4600 m), and (b) the global-mean vertical profile. The values shown are five-year running means, and are expressed as anomalies relative to control run CON-DEF. Vertical lines indicate years 100 and 211.

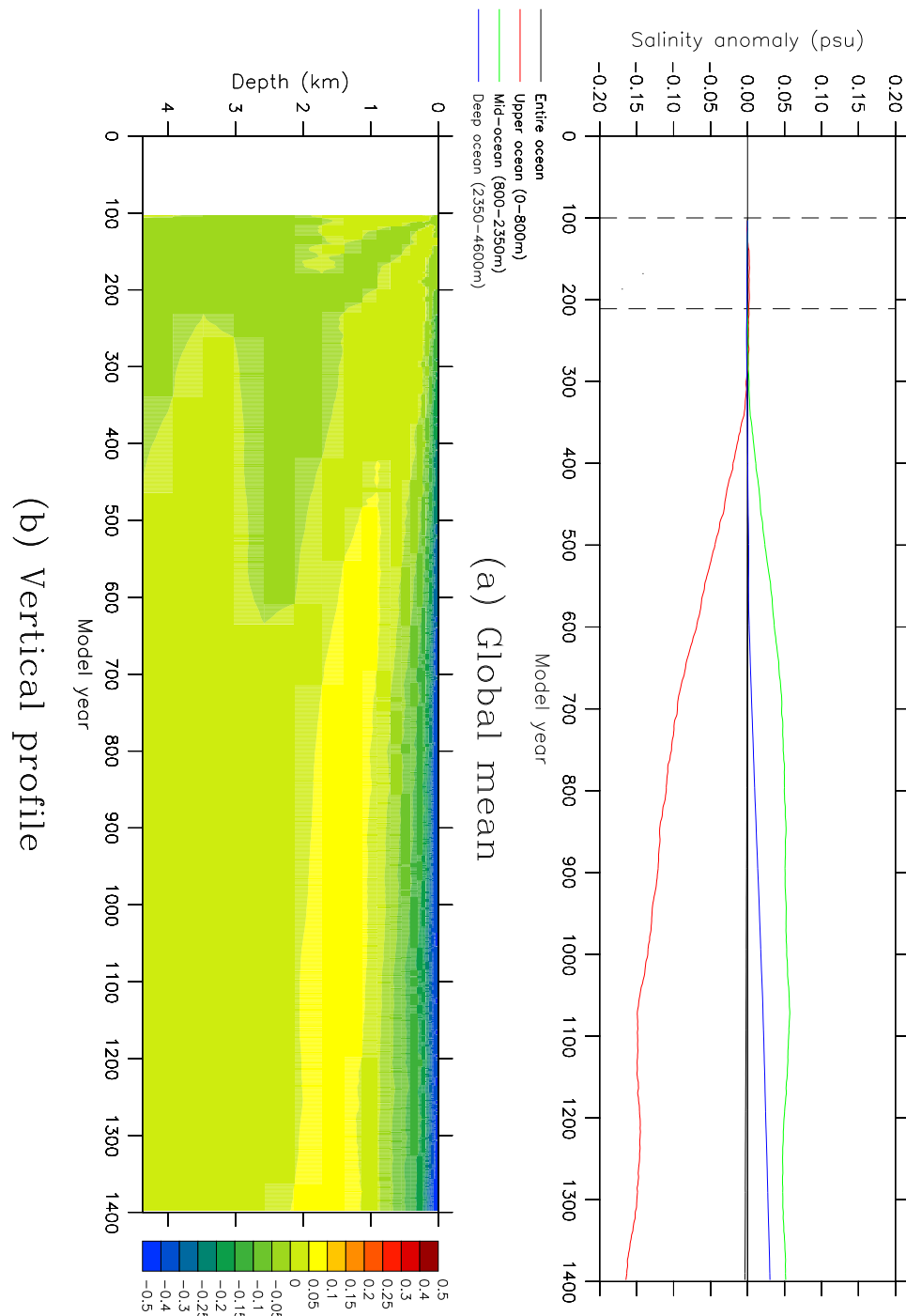


Figure 7.11: The change in annual-mean salinity (psu) during run 3CO2-DEF: (a) the global means for the entire ocean (black), upper ocean (red, 0–800 m), mid-ocean (green, 800–2350 m) and deep ocean (dark blue, 2350–4600 m), and (b) the global-mean vertical profile. The values shown are five-year running means, and are expressed as anomalies relative to control run CON-DEF. Vertical lines indicate years 100 and 211.

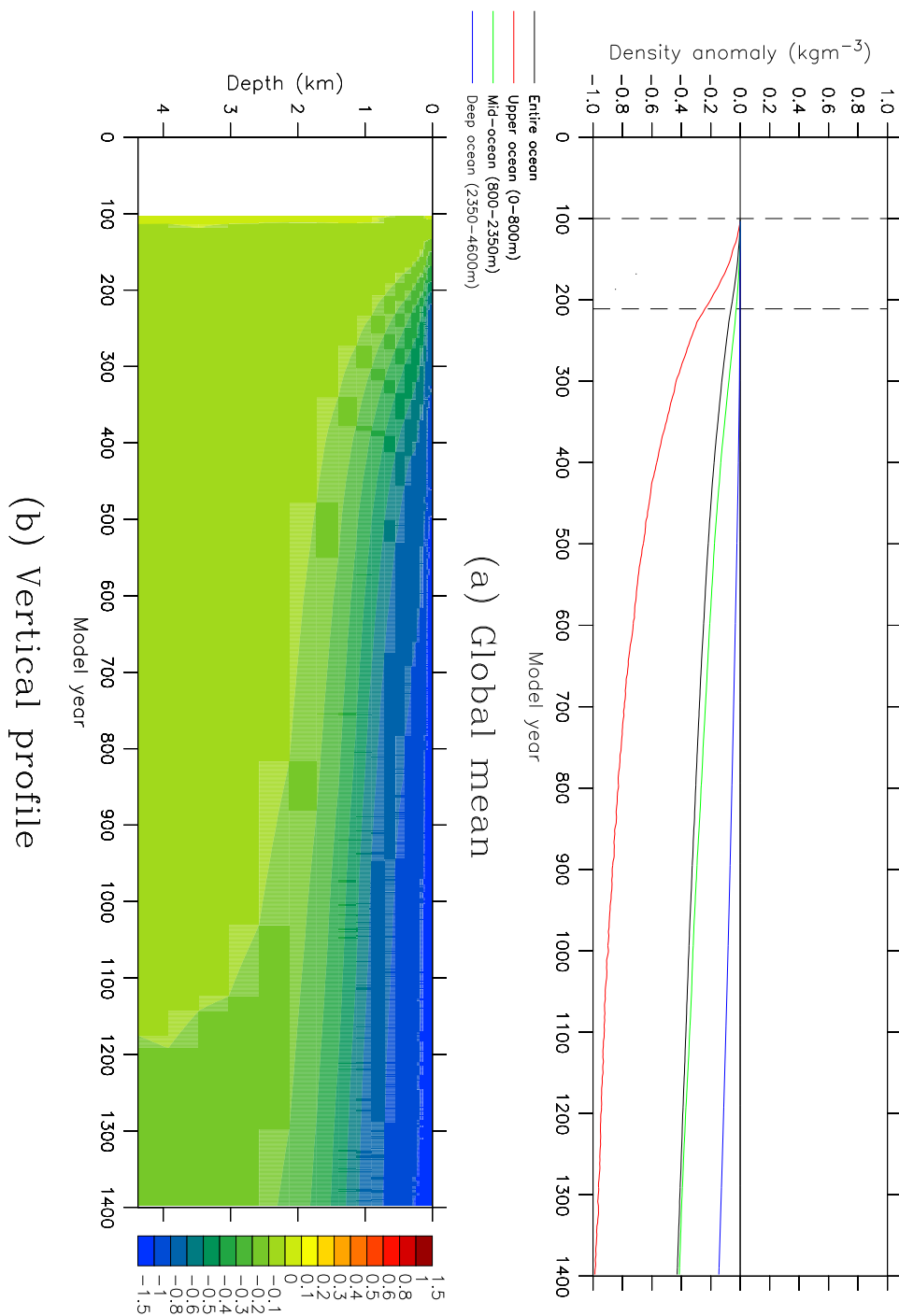


Figure 7.12: The change in annual-mean σ_θ (kgm^{-3}) during run 3CO2-DEF: (a) the global means for the entire ocean (black), upper ocean (red, 0–800 m), mid-ocean (green, 800–2350 m) and deep ocean (dark blue, 2350–4600 m), and (b) the global-mean vertical profile. The values shown are five-year running means, and are expressed as anomalies relative to control run CON-DEF. Vertical lines indicate years 100 and 211.

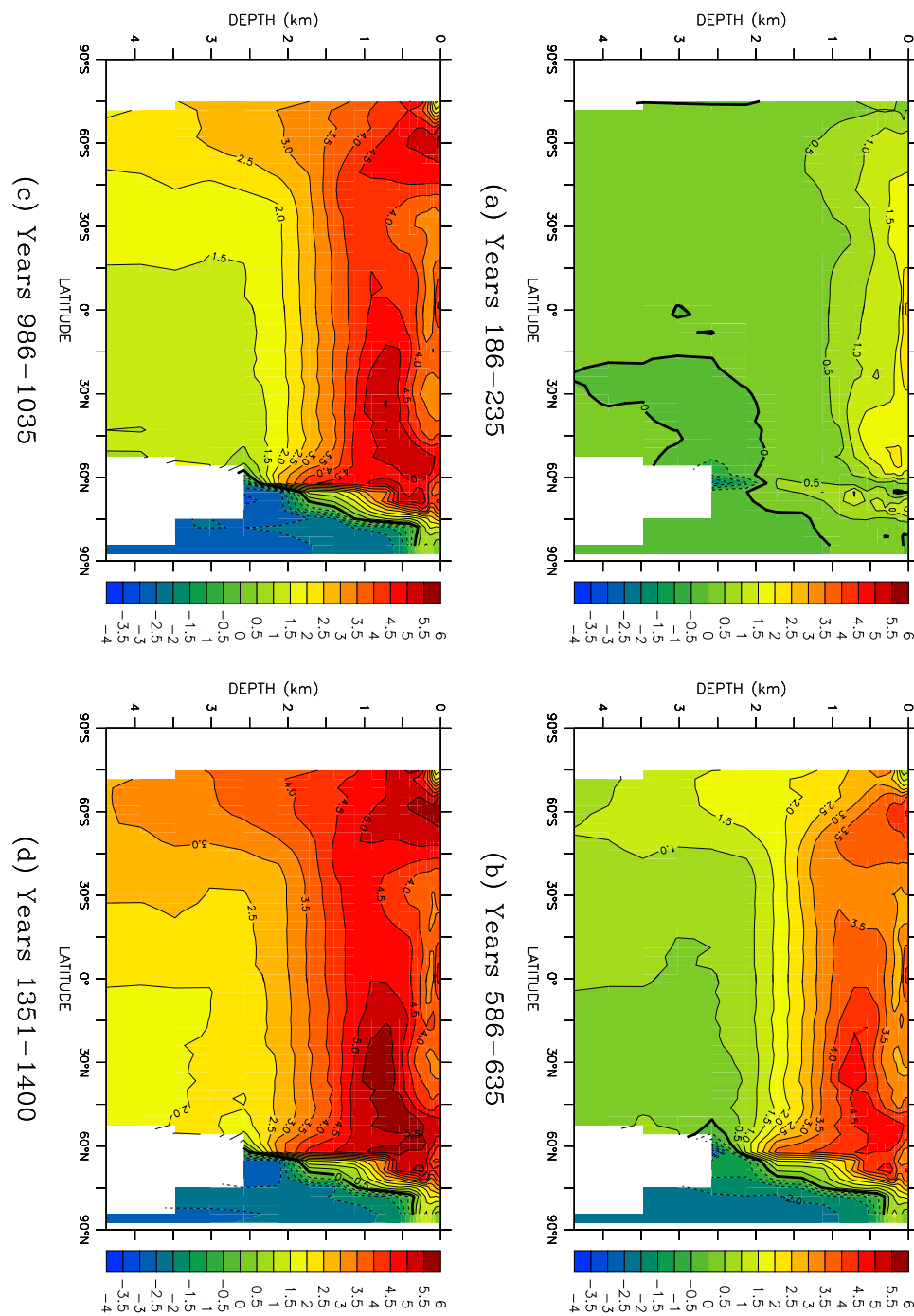


Figure 7.13: The evolution of the zonal-mean potential temperature ($^{\circ}\text{C}$) during run 3CO2-DEF, expressed as an anomaly relative to control run CON-DEF: (a) years 186–235, (b) years 586–635, (c) years 986–1035, and (d) years 1351–1400. The inland seas are excluded when calculating the zonal means.

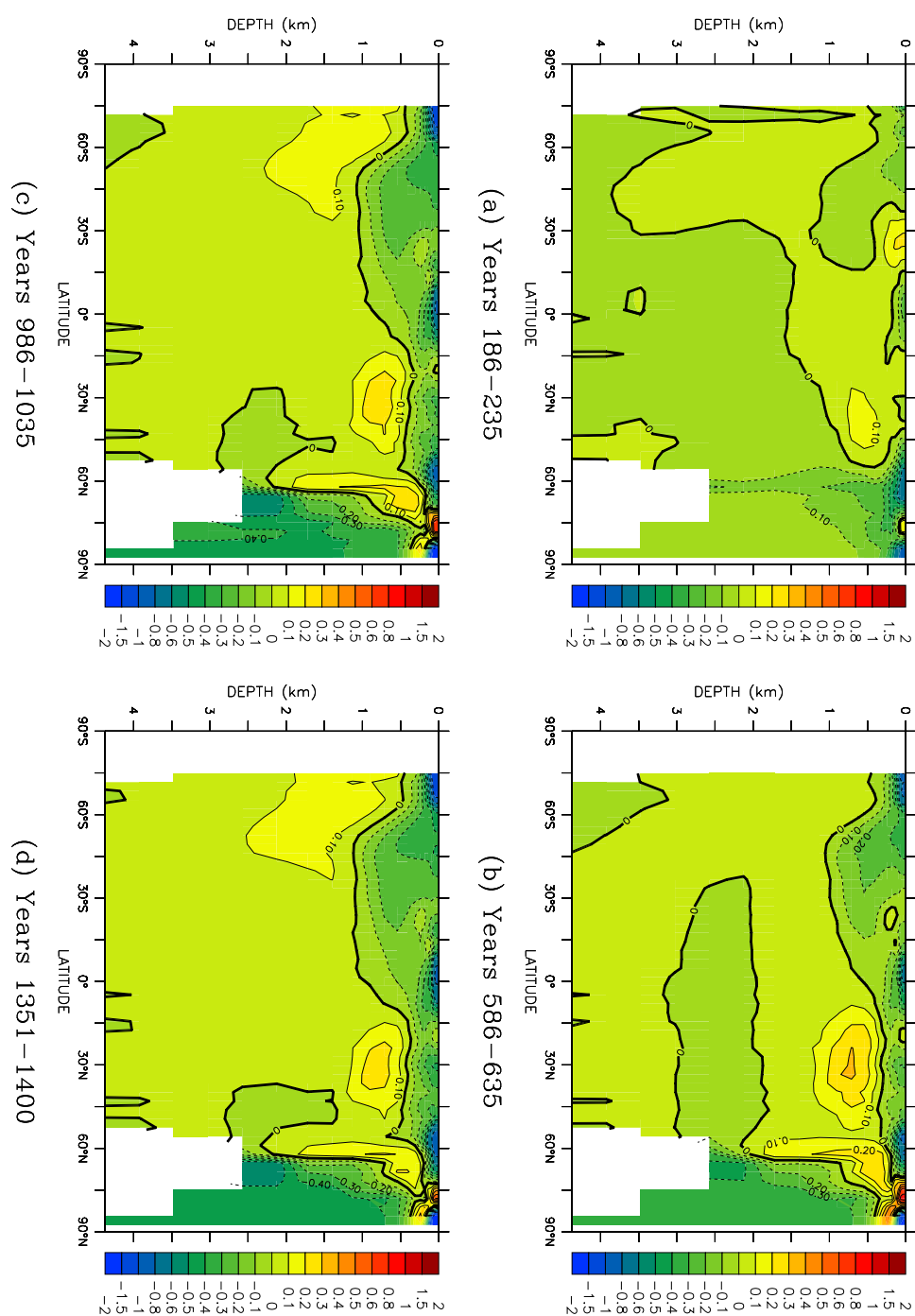


Figure 7.14: The evolution of the zonal-mean salinity (psu) during run 3CO2-DEF, expressed as an anomaly relative to control run CON-DEF: (a) years 186–235, (b) years 586–635, (c) years 986–1035, and (d) years 1351–1400. The inland seas are excluded when calculating the zonal means.

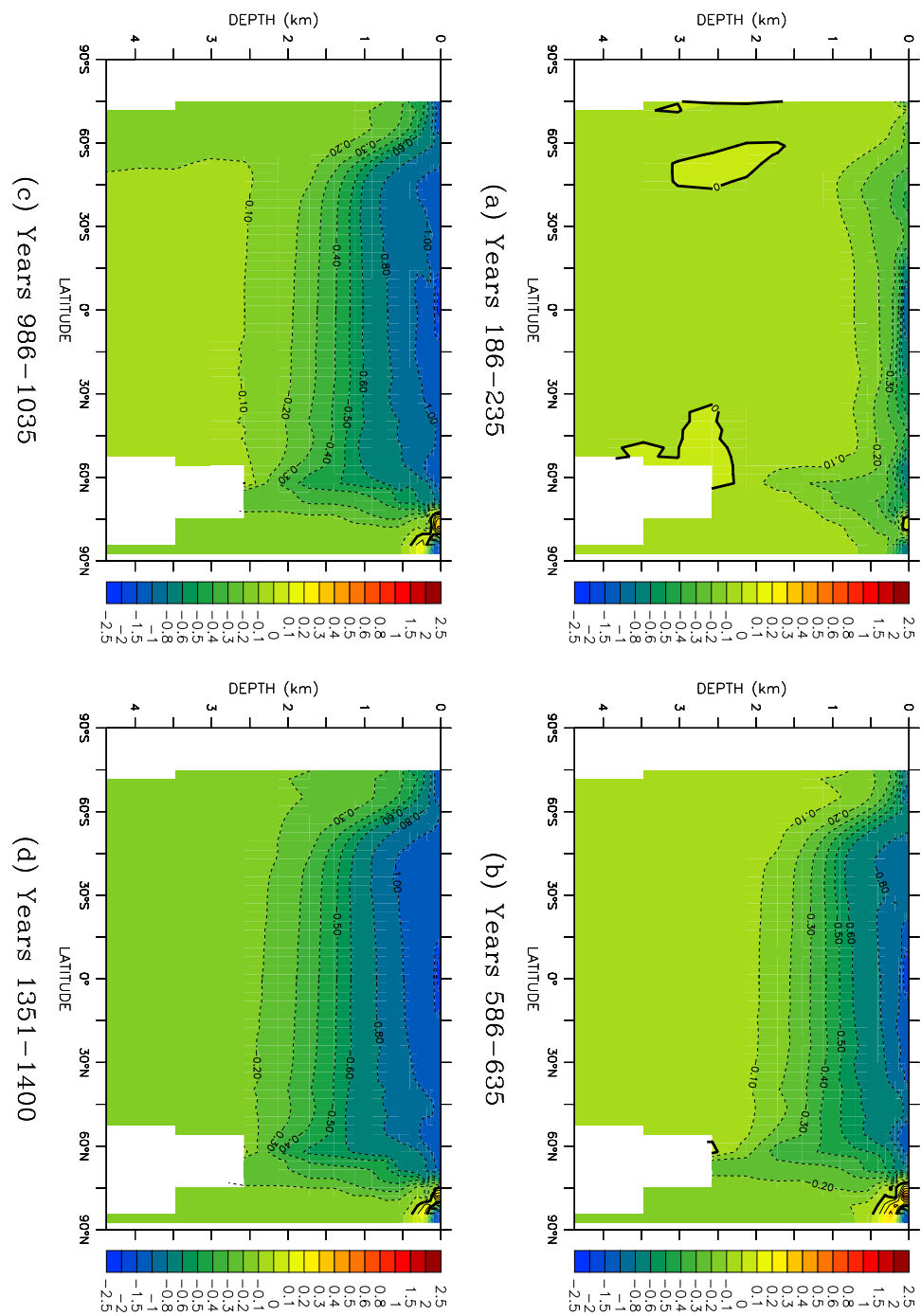


Figure 7.15: The evolution of the zonal-mean σ_θ (kgm^{-3}) during run 3CO2-DEF, expressed as an anomaly relative to control run CON-DEF: (a) years 186–235, (b) years 586–635, (c) years 986–1035, and (d) years 1351–1400. The inland seas are excluded when calculating the zonal means.

Circulation

Figure 7.16 shows the evolution in the rates of North Atlantic Deep Water (NADW) and Antarctic Bottom Water (AABW) formation, and in the rate of volume transport through Drake Passage, during runs CON-DEF and 3CO₂-DEF. The rate of NADW formation weakens significantly as the atmospheric CO₂ concentration increases, with the average rate for years 211–260 being 7.5 Sv; this is 49% weaker than the average rate of NADW formation for the equivalent period of the control run.

The weakening of the thermohaline circulation in response to an increase in the atmospheric CO₂ concentration is a common feature of coupled models, and has been widely studied (e.g. *Manabe and Stouffer, 1994; Stouffer and Manabe, 2003; Wood et al., 2003; Hu et al., 2004; Gregory et al., 2005*). The decrease in the rate of NADW formation exhibited by Mk3L is larger than that exhibited by most of the models studied by *Gregory et al. (2005)*. They study the response of 11 models to a 1% per year increase in the CO₂ concentration, and find a 10–50% decrease in the rate of NADW formation upon a *quadrupling* of the CO₂ concentration.

Once the atmospheric CO₂ concentration has been stabilised, the rate of NADW formation gradually recovers, and has almost returned to its original strength by the end of the run. For years 1301–1400, the average rate of NADW formation for run 3CO₂-DEF is 13.0 Sv, as opposed to a rate of 14.1 Sv for run CON-DEF. This recovery in the thermohaline circulation is very similar to that encountered by *Stouffer and Manabe (2003)* upon a stabilisation of the CO₂ concentration at *twice* the pre-industrial value. In response to a stabilisation at four times the pre-industrial value, however, they find that the thermohaline circulation shuts down almost completely, only beginning to recover ~ 1000 years after the CO₂ concentration is stabilised. The rate of NADW formation also recovers in the CSIRO Mk2 coupled model when the CO₂ concentration is stabilised at three times the pre-industrial value, although the recovery is somewhat slower than in Mk3L, and the thermohaline circulation does not return to its original strength (*Hirst, 1999; Bi et al., 2001; Bi, 2002*).

The rate of AABW formation also weakens significantly as the atmospheric CO₂ concentration increases. However, it continues to decline once the CO₂ concentration is stabilised, and does not exhibit any recovery; the mean rate for the final century of run 3CO₂-DEF is just 1.8 Sv. This shutdown of Antarctic Bottom Water formation can be attributed to the large reduction in Antarctic sea ice cover, and to the corresponding reduction in brine rejection. As a result, the surface water masses no longer have sufficient density to reach the abyssal ocean. A similar shutdown of AABW formation is also exhibited by the CSIRO Mk2 coupled model (*Hirst, 1999; Bi et al., 2001, 2002; Bi, 2002*).

The changes in the nature of deep water formation are illustrated by Figure 7.17, which shows the annual-maximum depths of convection for the final centuries of runs CON-DEF and 3CO₂-DEF. While deep water formation in the North Atlantic persists in run 3CO₂-DEF, the formation of bottom water in the Weddell Sea has completely ceased. Convection in the Southern Ocean, and particularly in the Indian Ocean sector, continues however, accounting for the penetration of the surface warming to depth at high southern latitudes.

Figure 7.16b indicates that the Antarctic Circumpolar Current (ACC) strength-

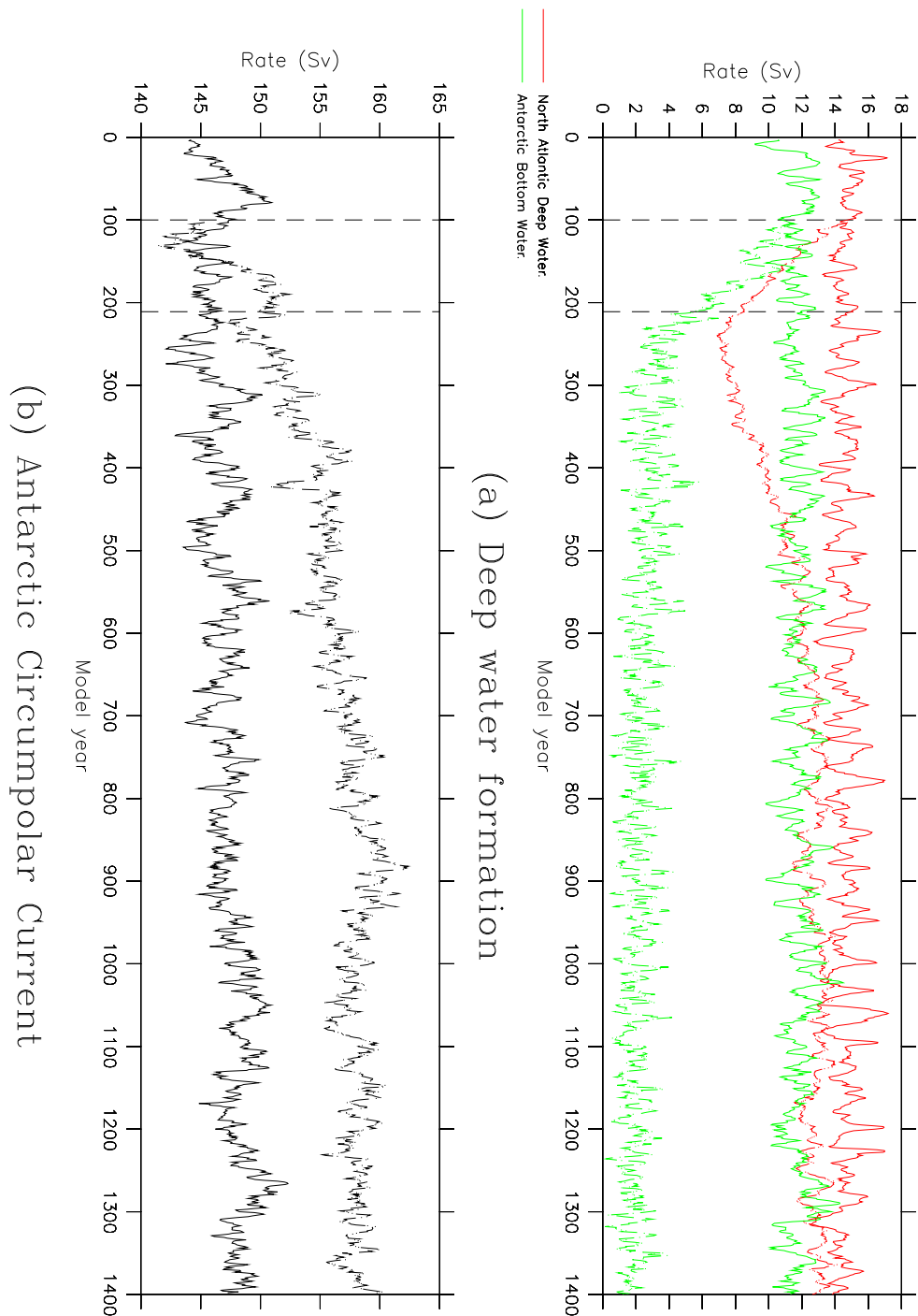
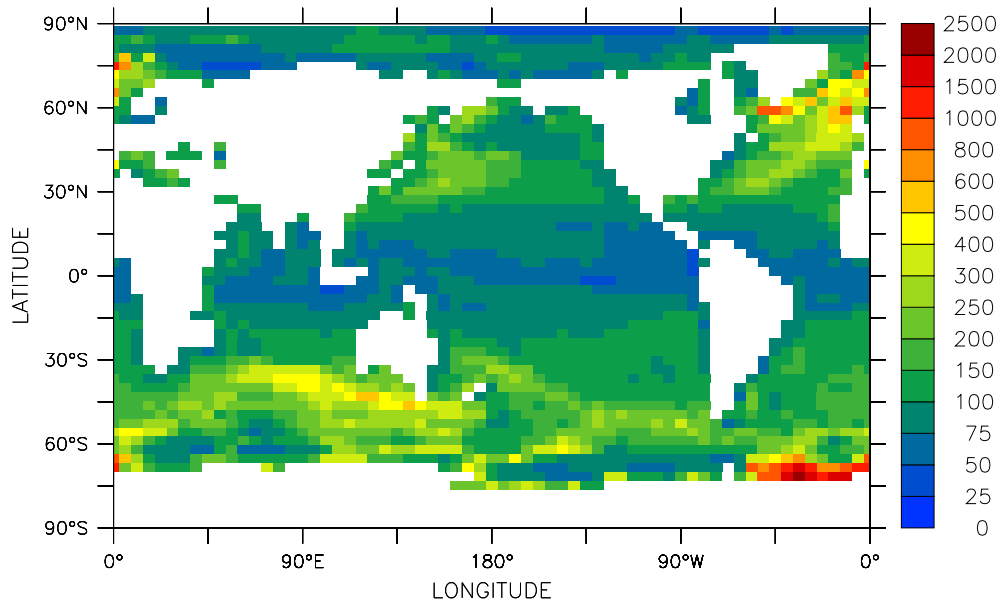
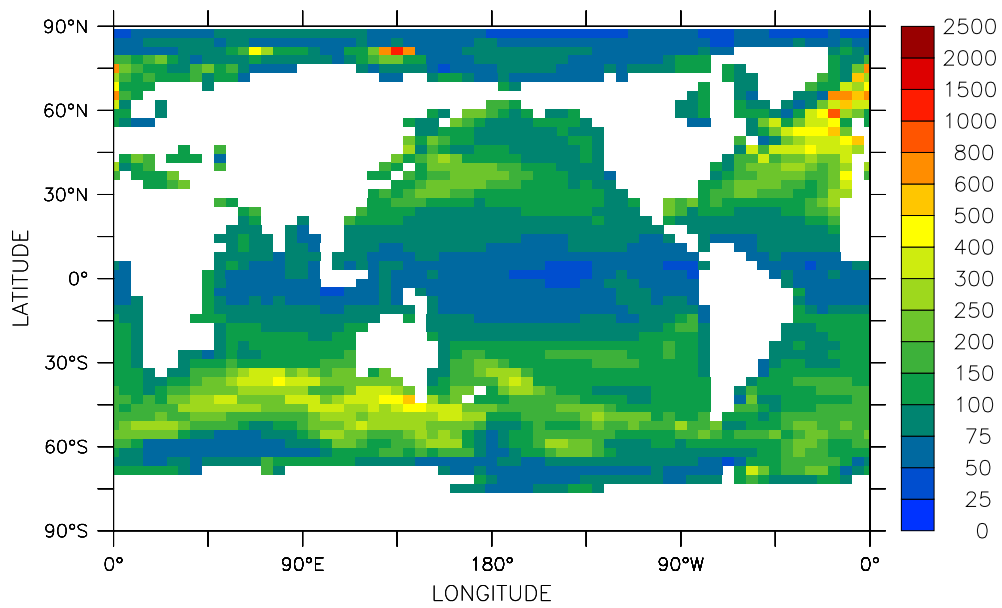


Figure 7.16: The rates of deep water formation, and the strength of the Antarctic Circumpolar Current, for runs CON-DEF (solid lines) and 3CO2-DEF (dashed lines): (a) the rates of formation of North Atlantic Deep Water (red) and Antarctic Bottom Water (green), and (b) the rate of volume transport through Drake Passage. The values shown are five-year running means. Vertical lines indicate years 100 and 211.



(a) Run CON-DEF



(b) Run 3CO2-DEF

Figure 7.17: The average annual-maximum depths of convection (m) for years 1301–1400 of runs CON-DEF and 3CO2-DEF: (a) run CON-DEF, and (b) run 3CO2-DEF.

ens slightly as the atmospheric CO₂ concentration increases; it continues to strengthen during the following centuries, although it appears to have stabilised by the end of the run. The average strength for the final century is 157.9 Sv, which is 9.8 Sv stronger than in the control run. This change in the ACC is consistent with the response of the CSIRO Mk2 coupled model (*Bi et al.*, 2002; *Bi*, 2002).

The evolution of the meridional overturning streamfunctions, for the world ocean and the Atlantic Ocean respectively, during run 3CO2-DEF are shown in Figures 7.18 and 7.19; Figure 5.18 shows the meridional overturning streamfunctions for the final century of run CON-DEF. The cessation of AABW formation is apparent, as is the weakening, and subsequent recovery, of NADW formation. By the final century of run 3CO2-DEF, the overturning cell in the North Atlantic has recovered to a state that it is almost identical to that for the equivalent period of run CON-DEF.

Mean sea level

Figure 7.20 shows the changes in mean sea level, relative to the control run, inferred from run 3CO2-DEF; these represent the changes in the *steric* sea level only, being those arising from changes in the density of the ocean. The increase in the temperature of the ocean causes it to expand, with the ongoing warming, particularly at depth, causing an ongoing increase in the mean sea level. By year 1400, the sea level has risen by 198 cm, relative to the control run, and is still rising at a rate of ~ 10 cm/century.

The increase in the mean sea level is $\sim 12\%$ less than that experienced by year 1400 of a similar simulation conducted using the CSIRO Mk2 coupled model (*Bi*, 2002). The smaller sea level rise is consistent with the difference in the surface air temperature increases simulated by the two models.

7.2.3 Summary

The Mk3L coupled model exhibits significant, and ongoing, warming in response to a trebling of the atmospheric carbon dioxide concentration. For a scenario in which the CO₂ concentration is increased at 1% per year, the global-mean surface air temperature (SAT) increases by 1.6°C upon a doubling of CO₂, and by 2.7°C upon a trebling. By the end of a 1400-year simulation, 1189 years after the CO₂ concentration is stabilised at three times the pre-industrial value, the global-mean SAT increase is 5.3°C. The sea ice extent and volume also exhibit rapid, and ongoing, declines in both hemispheres. By the end of the simulation, 64% of the sea ice cover has disappeared in the Northern Hemisphere, and 90% in the Southern Hemisphere.

The thermohaline circulation weakens as the atmospheric CO₂ concentration increases, with the rate of North Atlantic Deep Water (NADW) formation declining by 49% upon a trebling of CO₂. Once the CO₂ concentration has been stabilised, however, the rate of NADW formation begins to recover, and it has almost returned to its original strength by the end of the simulation. The rate of Antarctic Bottom Water (AABW) formation also begins to weaken as the atmospheric CO₂ concentration increases, and ceases completely during the centuries following stabilisation

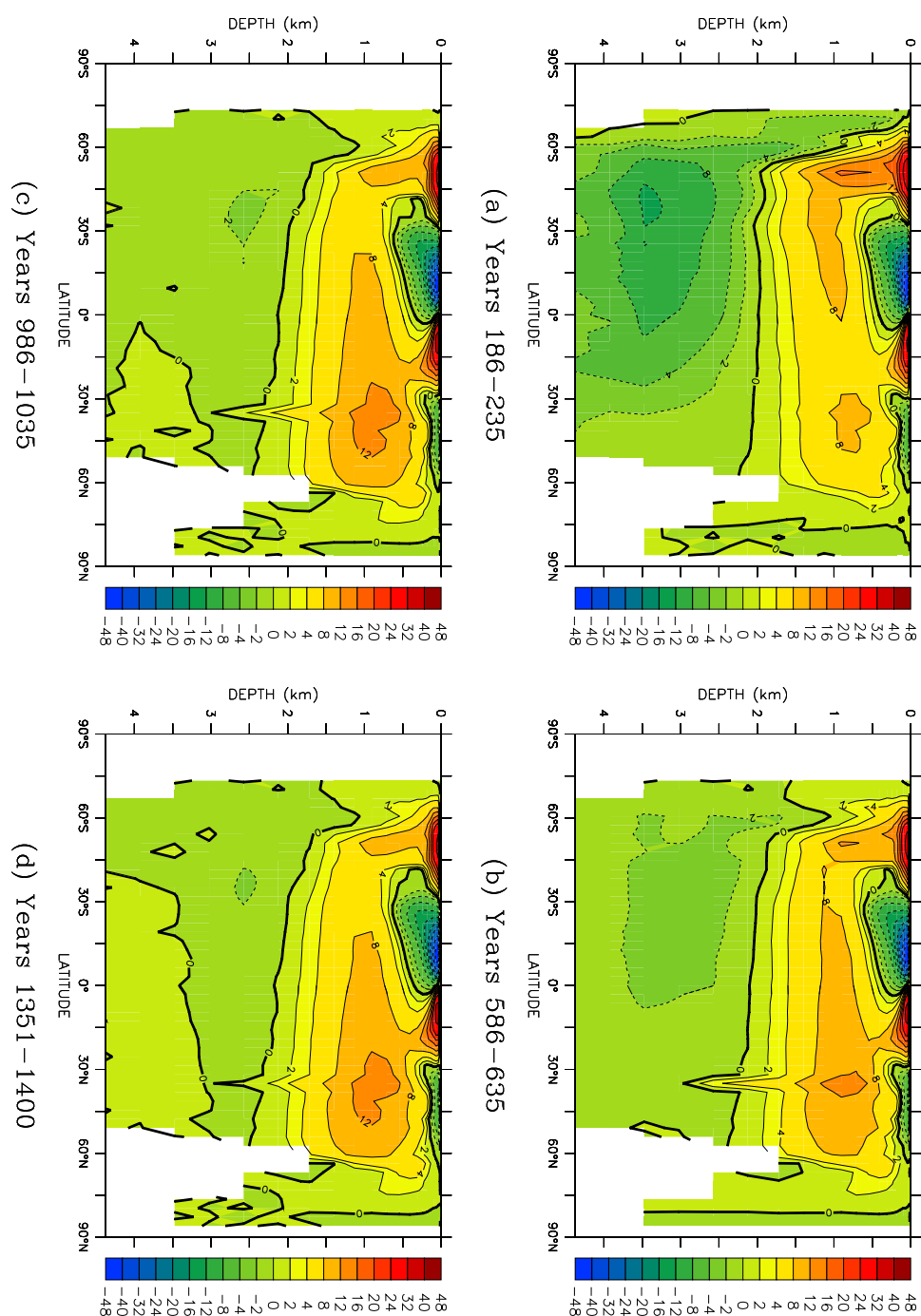


Figure 7.18: The evolution of the global meridional overturning streamfunction (Sv) during run 3CO2-DEF: (a) years 186–235, (b) years 586–635, (c) years 986–1035, and (d) years 1351–1400.

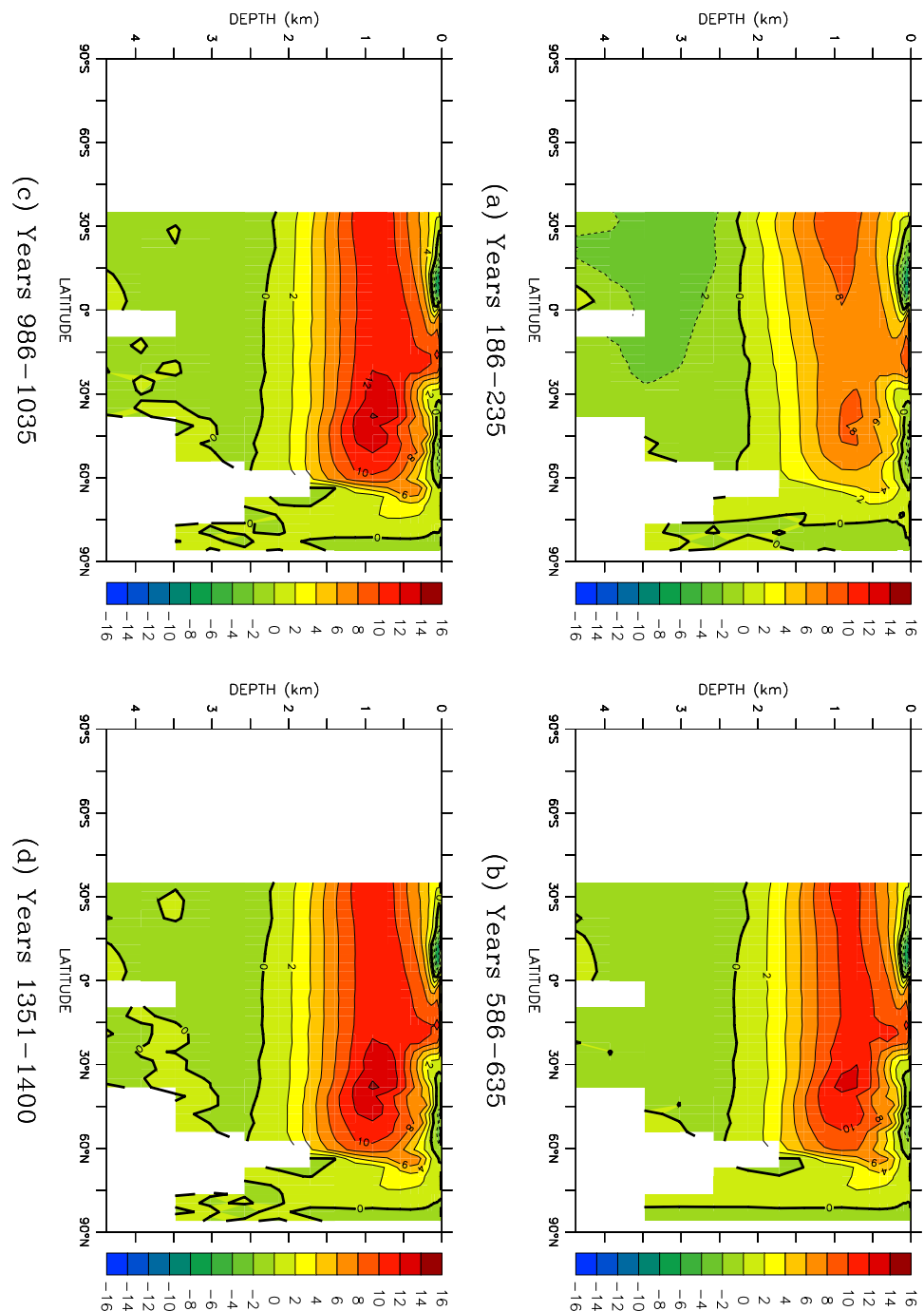


Figure 7.19: The evolution of the Atlantic Ocean meridional overturning streamfunction (Sv) during run 3CO2-DEF: (a) years 186–235, (b) years 586–635, (c) years 986–1035, and (d) years 1351–1400.

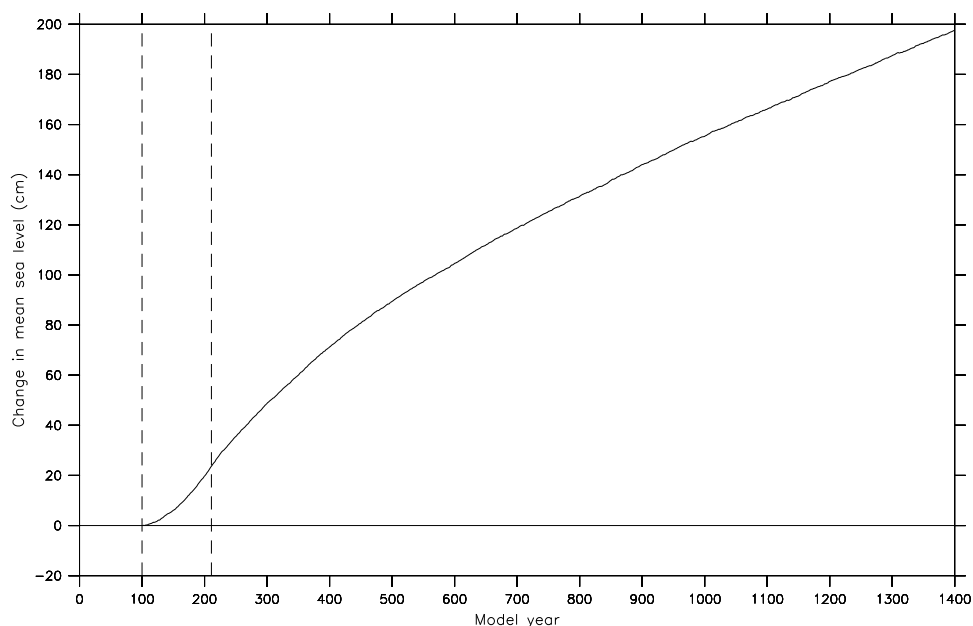


Figure 7.20: The steric change in mean sea level diagnosed from run 3CO2-DEF, expressed as an anomaly relative to the steric change in mean sea level diagnosed from control run CON-DEF. Vertical lines indicate years 100 and 211.

at three times the pre-industrial value. There is also a slight strengthening of the Antarctic Circumpolar Current.

With the cessation of AABW formation, ventilation of the abyssal ocean becomes restricted to convection in the Southern Ocean, and hence the penetration of the surface warming to depth is slow. By the end of the simulation, the deep ocean has only warmed by 2.4°C , as opposed to a surface warming of 4.1°C , and is still warming at a rate of $\sim 0.22^\circ\text{C}/\text{century}$. As a result of this differential warming with respect to depth, and also because of a slight freshening of the surface layers, there is an increase in the stratification of the ocean, with the density of the upper ocean decreasing by 0.99 kgm^{-3} by the end of the simulation.

The warming of the ocean causes it to expand, with a steric mean sea level increase of 198 cm by year 1400. As a result of the ongoing warming at depth, the sea level is still rising at a rate of $\sim 10\text{ cm}/\text{century}$.

7.3 The impact of the spin-up procedure

7.3.1 Atmosphere

Statistics on the changes in the climate of the atmosphere model during runs 3CO2-SHF and 3CO2-EFF are shown in Table 7.1; statistics are also provided for the equivalent period of run 3CO2-DEF. The nature of the changes is discussed in the following section.

Quantity	Years/ Hemisphere	3CO2-DEF	3CO2-SHF	3CO2-EFF
Change in global-mean SAT (°C)	155–184	+1.55	+1.55	+1.69
	196–225	+2.70	+2.71	+2.79
	1001–1100	+5.21	+5.26	+5.44
Sea ice extent (10 ¹² m ²)	NH	5.0	5.1	5.8
	SH	1.5	1.6	2.1
Sea ice volume (10 ¹² m ³)	NH	2.6	2.7	3.2
	SH	0.5	0.6	0.8

Table 7.1: Statistics for runs 3CO2-DEF, 3CO2-SHF and 3CO2-EFF: the changes in global-mean surface air temperature (SAT), relative to the control runs; and the average sea ice extents and volumes for each hemisphere, for years 1001–1100.

Surface air temperature

The evolution of the simulated global-mean and zonal-mean surface air temperature (SAT) during runs 3CO2-SHF and 3CO2-EFF are shown in Figure 7.21. While the changes exhibited by both runs are very similar to those exhibited by run 3CO2-DEF, there are slightly greater increases in the global-mean SAT in run 3CO2-EFF.

Tests can be made as to statistical significance of these differences. Let $T_{\langle run \rangle}$ be the surface air temperature for run $\langle run \rangle$. The changes in the surface air temperature for runs 3CO2-DEF and 3CO2-EFF, relative to the control runs, are therefore given by

$$\Delta T_{DEF} = T_{3CO2-DEF} - T_{CON-DEF} \quad (7.1)$$

$$\Delta T_{EFF} = T_{3CO2-EFF} - T_{CON-EFF} \quad (7.2)$$

The difference in the response of run 3CO2-EFF, relative to run 3CO2-DEF, is then given by

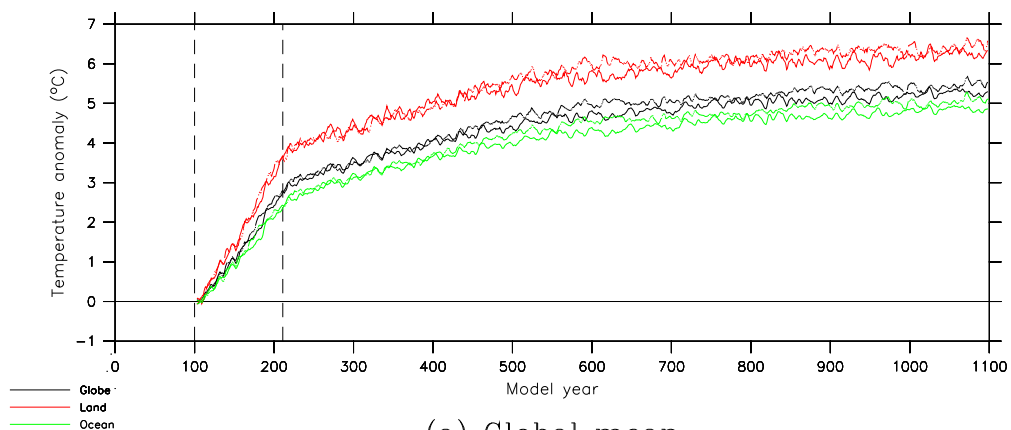
$$\Delta\Delta T_{EFF} = \Delta T_{EFF} - \Delta T_{DEF} \quad (7.3)$$

$$= (T_{3CO2-EFF} - T_{CON-EFF}) - (T_{3CO2-DEF} - T_{CON-DEF}) \quad (7.4)$$

By calculating the mean and standard deviation of $\Delta\Delta T_{EFF}$ over any given period, a t test (*Wilks*, 1995) can then be performed in order to test for statistical significance. Letting T equal the global-mean SAT, the mean value of $\Delta\Delta T_{EFF}$ for years 155–184 is $+0.135 \pm 0.030^\circ\text{C}$. The error quoted here represents the standard error in the mean; if T_i is the value of statistic T for year i , and \bar{T} is the average value of T for years 1 to N , then the standard error in the mean is given by

$$\sigma = \left[\frac{1}{N(N-1)} \sum_{i=1}^N (T_i - \bar{T})^2 \right]^{1/2} \quad (7.5)$$

For the null hypothesis that there is no difference between the global-mean SAT changes exhibited by runs 3CO2-DEF and 3CO2-EFF, the value of the t statistic



(a) Global mean

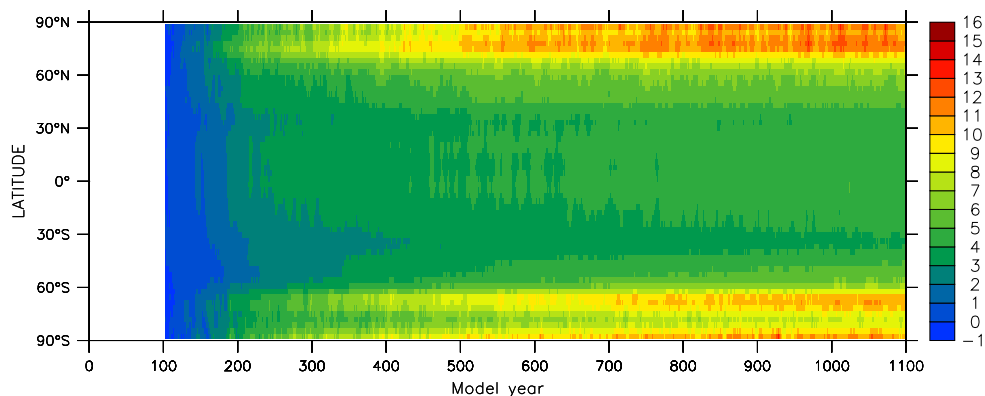
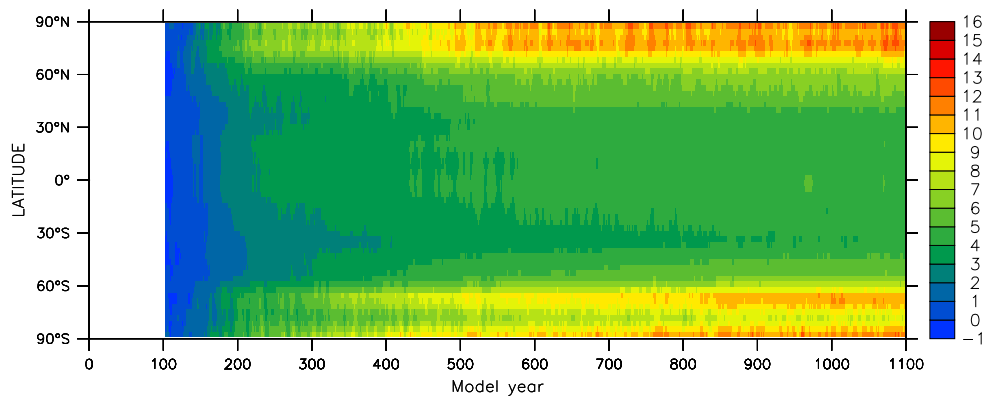
(b) Run 3CO₂-SHF(c) Run 3CO₂-EFF

Figure 7.21: The change in annual-mean surface air temperature ($^{\circ}\text{C}$) during runs 3CO₂-SHF and 3CO₂-EFF: (a) the global mean (black), and the means over land (red) and the ocean (green), for runs 3CO₂-SHF (solid lines) and 3CO₂-EFF (dashed lines); (b) the zonal mean for run 3CO₂-SHF; and (c) the zonal mean for run 3CO₂-EFF. The values shown are five-year running means, and are expressed as anomalies relative to the control runs. Vertical lines indicate years 100 and 211.

is $+4.55$. There is therefore evidence at the 99% confidence level to reject the null hypothesis, and it can be stated that the difference is statistically significant.

For years 196–225 and 1001–1100, the mean values of $\Delta\Delta T_{EFF}$ are $+0.083\pm 0.023^\circ\text{C}$ and $+0.224\pm 0.015^\circ\text{C}$ respectively. In both cases, the differences in the global-mean SAT changes are statistically significant at the 99% confidence level.

Comparing the global-mean SAT changes exhibited by runs 3CO2-DEF and 3CO2-SHF, the mean differences between the responses of the two runs, for years 155–184, 196–225 and 1001–1100, are $+0.002\pm 0.022^\circ\text{C}$, $+0.008\pm 0.022^\circ\text{C}$ and $+0.045\pm 0.013^\circ\text{C}$ respectively. The first two of these differences are not statistically significant; however, while the difference in the global-mean SAT changes for year 1001–1100 is very small, it *is* statistically significant at the 99% confidence level.

Figures 7.22a and 7.22b shows the changes in the annual-mean SAT, by the final centuries of runs 3CO2-SHF and 3CO2-EFF respectively. For both runs, the changes are very similar to those exhibited by run 3CO2-DEF. Figures 7.22c and 7.22d show the *differences* in the response of each run, relative to run 3CO2-DEF; only differences which are significant at the 99% confidence level are shown. Run 3CO2-EFF exhibits greater warming over much of the surface of the ocean, but particularly over the Southern Ocean and the North Atlantic. However, it also exhibits significantly reduced warming over the Weddell Sea and the eastern Arctic Ocean.

As with the mid-Holocene simulations (Section 6.4), runs 3CO2-SHF and 3CO2-EFF both exhibit greater warming over the Caspian Sea. This can again be attributed to the cooling trend within the control runs.

Sea ice

Figure 7.23 shows the evolution of the sea ice extent and volume in each hemisphere, for runs CON-SHF, CON-EFF, 3CO2-SHF and 3CO2-EFF. The responses of runs 3CO2-SHF and 3CO2-EFF are very similar to that of run 3CO2-DEF, with the sea ice cover in the Southern Hemisphere disappearing almost completely, and with a large reduction in the sea ice cover in the Northern Hemisphere.

7.3.2 Ocean

Statistics on the changes in the climate of the ocean model during runs 3CO2-SHF and 3CO2-EFF are shown in Table 7.2; statistics are also provided for the equivalent period of run 3CO2-DEF. The nature of the changes is discussed in the following section.

Sea surface temperature and salinity

Figures 7.24 and 7.25 show the evolution of the simulated global-mean and zonal-mean sea surface temperature (SST) and sea surface salinity (psu), respectively, during runs 3CO2-SHF and 3CO2-EFF. The changes are very similar to those exhibited by run 3CO2-DEF, with a rapid increase in global-mean SST as the atmospheric CO_2 concentration increases, and an ongoing warming trend thereafter. Run

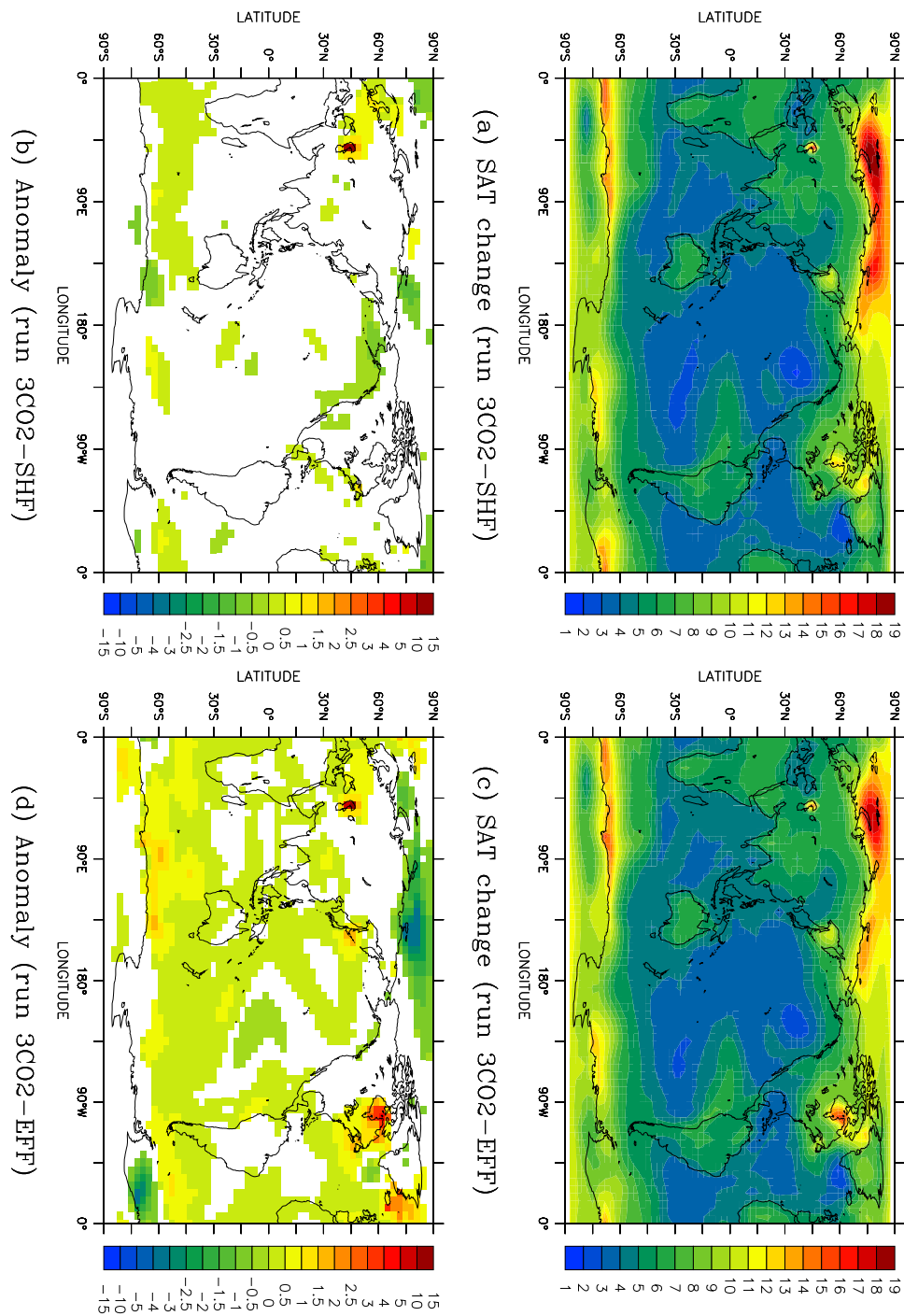


Figure 7.22: The annual-mean surface air temperature (SAT, °C) for years 1001–1100 of runs 3CO2-SHF and 3CO2-EFF, expressed as anomalies relative to the annual-mean SAT for years 1001–1100 of the control runs: (a), (b) runs 3CO2-SHF and 3CO2-EFF respectively, and (c), (d) the annual-mean SAT changes, expressed as anomalies relative to run 3CO2-DEF, with only those values which are significant at the 99% confidence level shown.

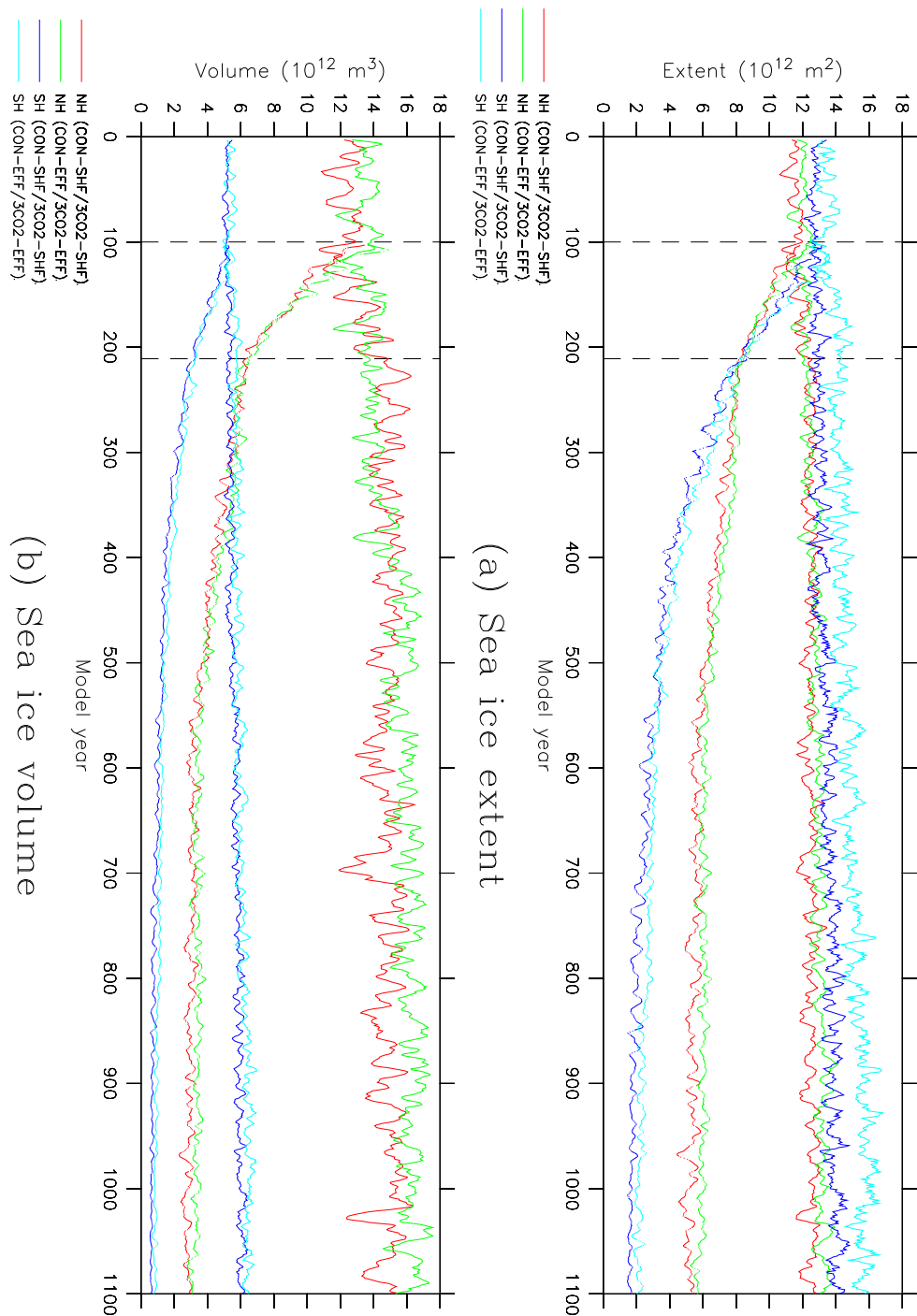


Figure 7.23: The annual-mean sea ice extent and volume for runs CON-SHF (solid lines, red and dark blue), CON-EFF (solid lines, green and light blue), 3CO2-SHF (dashed lines, red and dark blue) and 3CO2-EFF (dashed lines, green and light blue), for the Northern Hemisphere (NH) and the Southern Hemisphere (SH): (a) sea ice extent, and (b) sea ice volume. The values shown are five-year running means. Vertical lines indicate years 100 and 211.

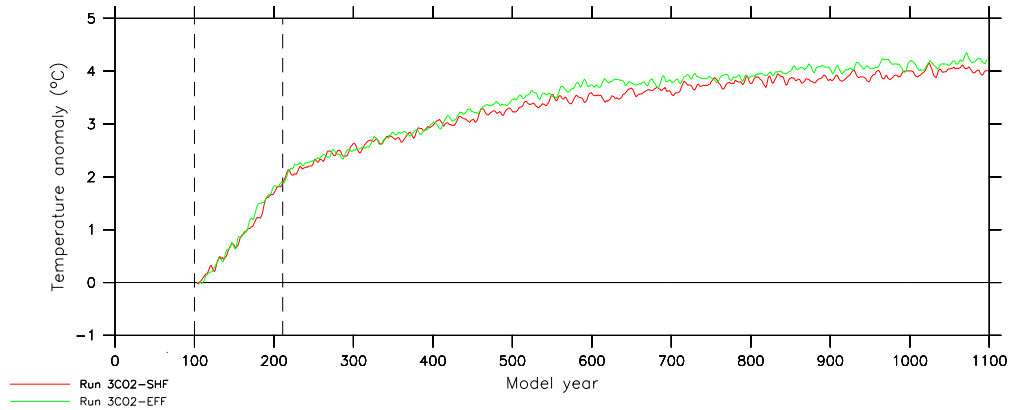
Change	Year(s)/ Depths	3CO2-DEF	3CO2-SHF	3CO2-EFF
Global-mean SST ($^{\circ}\text{C}$)	155–184	+1.04	+1.04	+1.15
	196–225	+1.87	+1.90	+1.93
	1001–1100	+3.98	+4.01	+4.15
Global-mean SSS (psu)	155–184	-0.032	-0.027	-0.022
	196–225	-0.073	-0.075	-0.068
	1001–1100	-0.394	-0.356	-0.392
Mean sea level (cm)	170	+10.7	+10.7	+10.7
	211	+23.7	+23.4	+23.6
	1100	+166.1	+168.3	+159.4
Potential temperature ($^{\circ}\text{C}$)	Entire ocean	+2.80	+2.85	+2.75
	0–800 m	+4.23	+4.29	+4.25
	800–2350 m	+3.25	+3.29	+3.14
	2350–4600 m	+1.63	+1.67	+1.58
Salinity (psu)	Entire ocean	-0.002	-0.003	-0.004
	0–800 m	-0.144	-0.114	-0.159
	800–2350 m	+0.055	+0.048	+0.066
	2350–4600 m	+0.020	+0.009	+0.013
σ_{θ} (kgm^{-3})	Entire ocean	-0.359	-0.362	-0.342
	0–800 m	-0.914	-0.899	-0.896
	800–2350 m	-0.331	-0.337	-0.289
	2350–4600 m	-0.090	-0.101	-0.098

Table 7.2: Statistics for runs 3CO2-DEF, 3CO2-SHF and 3CO2-EFF: the changes in global-mean sea surface temperature (SST) and sea surface salinity (SSS); the steric changes in mean sea level; and the changes in the mean potential temperature, salinity and σ_{θ} of the ocean for years 1001–1100.

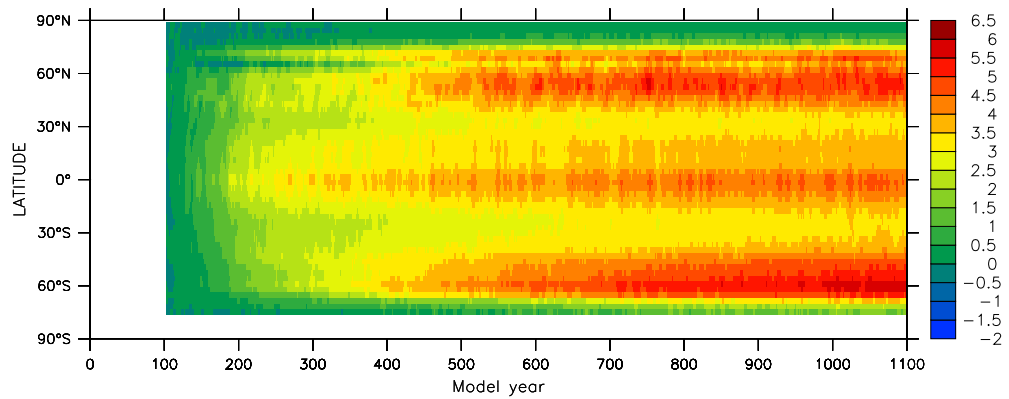
3CO2-EFF exhibits a slightly greater increase than run 3CO2-SHF. The strongest warming in both runs occurs at $\sim 60^{\circ}\text{S}$ and $\sim 60^{\circ}\text{N}$, with strong warming also occurring in the tropics. The changes in the sea surface salinity are also very similar to those exhibited by run 3CO2-DEF, with an ongoing freshening trend in the global-mean SSS, which begins to stabilise by the end of the runs. The zonal-mean SSS exhibits a slight freshening at most latitudes, with stronger freshening at the North Pole, and an increase in salinity at $\sim 75^{\circ}\text{N}$.

As with the surface air temperature, tests can be made as to statistical significance of any differences in the responses of the runs, relative to the response of run 3CO2-DEF. Letting T represent the global-mean SST, then the mean values of ΔT_{EFF} for years 155–184, 196–225 and 1001–1100 are $+0.115\pm 0.024^{\circ}\text{C}$, $+0.062\pm 0.018^{\circ}\text{C}$ and $+0.176\pm 0.011^{\circ}\text{C}$ respectively. Each of these differences is statistically significant at the 99% confidence level, indicating that the global-mean SST changes exhibited by run 3CO2-EFF are significantly larger than those exhibited by run 3CO2-DEF.

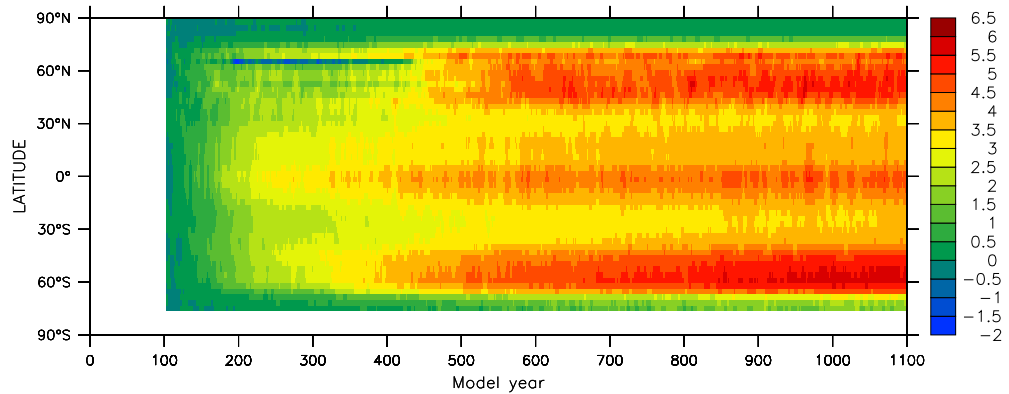
Comparing the global-mean SST response of run 3CO2-SHF with that of run



(a) Global mean

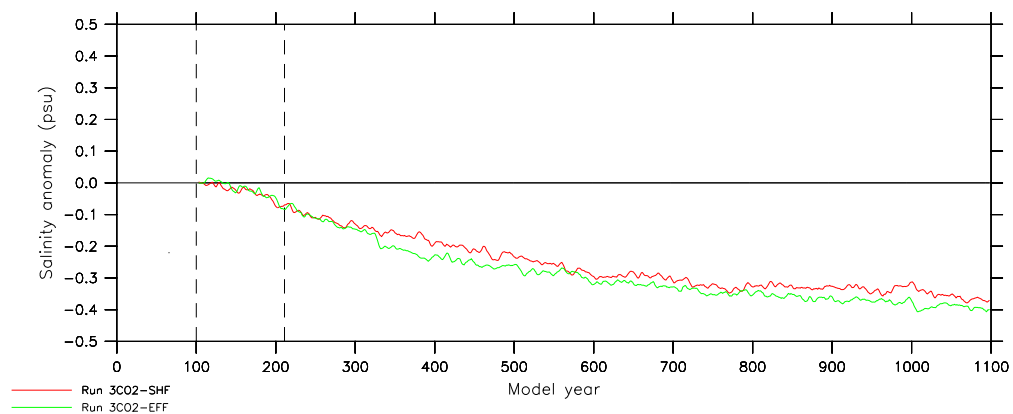


(b) Run 3CO2-SHF



(c) Run 3CO2-EFF

Figure 7.24: The change in annual-mean sea surface temperature ($^{\circ}\text{C}$) during runs 3CO2-SHF and 3CO2-EFF: (a) the global mean, for runs 3CO2-SHF (red) and 3CO2-EFF (green), (b) the zonal mean for run 3CO2-SHF, and (c) the zonal mean for run 3CO2-EFF. The values shown are five-year running means, and are expressed as anomalies relative to the control runs. Vertical lines indicate years 100 and 211.



(a) Global mean

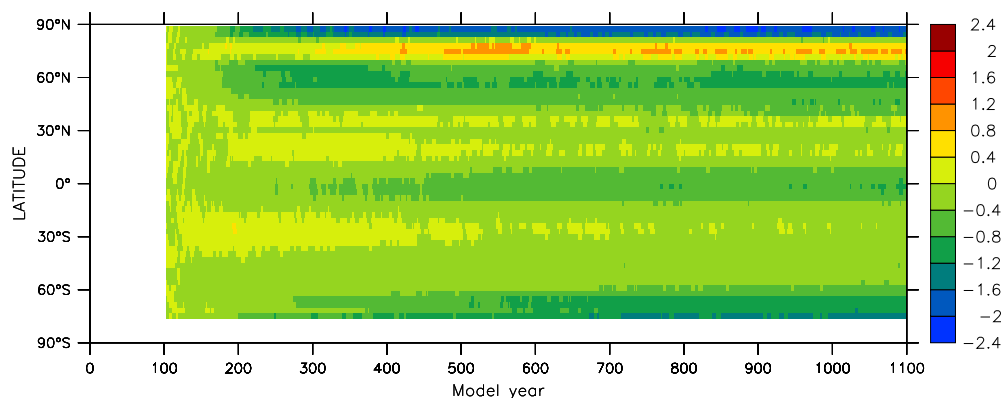
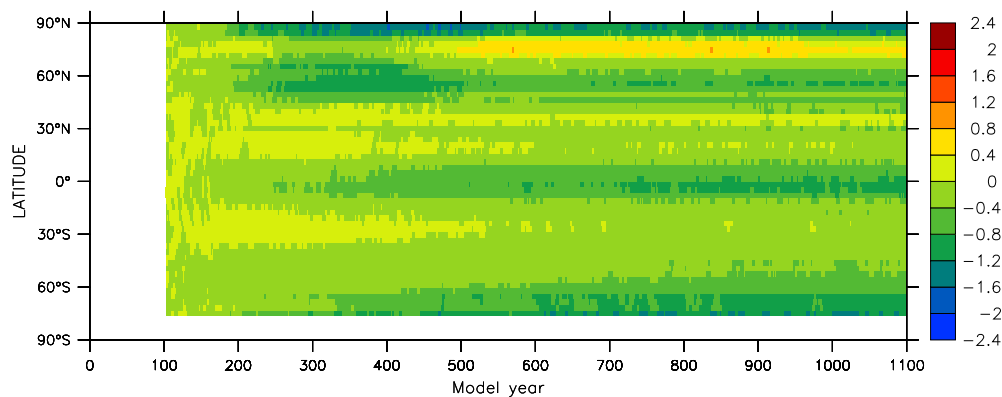
(b) Run 3CO₂-SHF(c) Run 3CO₂-EFF

Figure 7.25: The change in annual-mean sea surface salinity (psu) during runs 3CO₂-SHF and 3CO₂-EFF: (a) the global mean, for runs 3CO₂-SHF (red) and 3CO₂-EFF (green), (b) the zonal mean for run 3CO₂-SHF, and (c) the zonal mean for run 3CO₂-EFF. The values shown are five-year running means, and are expressed as anomalies relative to the control runs. Vertical lines indicate years 100 and 211.

3CO2-DEF, the differences in the average response for years 155–184, 196–225 and 1001–1100 are $-0.001 \pm 0.016^\circ\text{C}$, $+0.0241 \pm 0.017^\circ\text{C}$ and $+0.030 \pm 0.010^\circ\text{C}$ respectively. Only the differences for years 1001–1100 represent a statistically-significant difference in the response of the model.

Figure 7.26 shows the changes in the annual-mean SST, relative to the control runs, by the final century of runs 3CO2-SHF and 3CO2-EFF; the statistically-significant *differences* between the response of each run, and that of run 3CO2-DEF, are also shown. As with the surface air temperature, the response of run 3CO2-SHF is very similar to that of run 3CO2-DEF, with the differences generally being small and statistically insignificant. In contrast, run 3CO2-EFF exhibits statistically-significant differences over most of the surface of the ocean, with greater warming across the Southern Ocean, and in the North Atlantic and North Pacific. There is also reduced warming in those regions where sea ice cover persists, particularly in the Weddell Sea and eastern Arctic Ocean, and in the central Pacific. Runs 3CO2-SHF and 3CO2-EFF both experience greater warming over the Caspian Sea, again as a result of the cooling trend within the control runs.

Figure 7.27 shows the changes in the the annual-mean SSS, and the statistically-significant differences between the response of each run, and that of run 3CO2-DEF. While there are significant differences in the response across much of the surface of the ocean, particularly for run 3CO2-EFF, the differences are generally small in magnitude. Run 3CO2-EFF does however, exhibit significantly greater freshening across much of the Pacific Ocean, and also the eastern Arctic Ocean. Both runs exhibit statistically-significant differences in the SSS changes over the Caspian Sea; these can be attributed to the freshening trend within the control runs (Section 5.4).

Water properties

The evolution of the simulated global-mean potential temperature, salinity and potential density of the world ocean, and of the simulated global-mean vertical profiles, during runs 3CO2-SHF and 3CO2-EFF, are shown in Figures 7.28, 7.29 and 7.30 respectively. The responses of both runs are very similar to that of run 3CO2-DEF, although run 3CO2-SHF experiences slightly greater warming at all levels, while both the mid- and deep-ocean are slightly cooler in run 3CO2-EFF. The vertical redistribution of salt is also slightly more pronounced in run 3CO2-EFF, with a greater decrease in the salinity of the upper ocean, and a greater increase in the salinity of the mid-ocean. Overall, run 3CO2-EFF experiences a smaller increase in the stratification of the ocean than the other runs, with smaller decreases in the density of the upper and mid-ocean.

Figures 7.31 and 7.32 show the evolution of the zonal-mean potential temperature, during runs 3CO2-SHF and 3CO2-EFF respectively. While the responses of both runs are very similar to that of run 3CO2-DEF, the warming in the Southern Ocean penetrates slightly more slowly to depth in run 3CO2-EFF, while that at mid-latitudes in the Northern Hemisphere penetrates to depth slightly more rapidly. This can be attributed to weaker convection in the Southern Ocean in run 3CO2-EFF, relative to run 3CO2-SHF, as is apparent from Figure 7.33.

The weaker convection in run 3CO2-EFF can be attributed, in turn, to the use of effective surface tracers to spin up the ocean model (Section 4.4). This leads

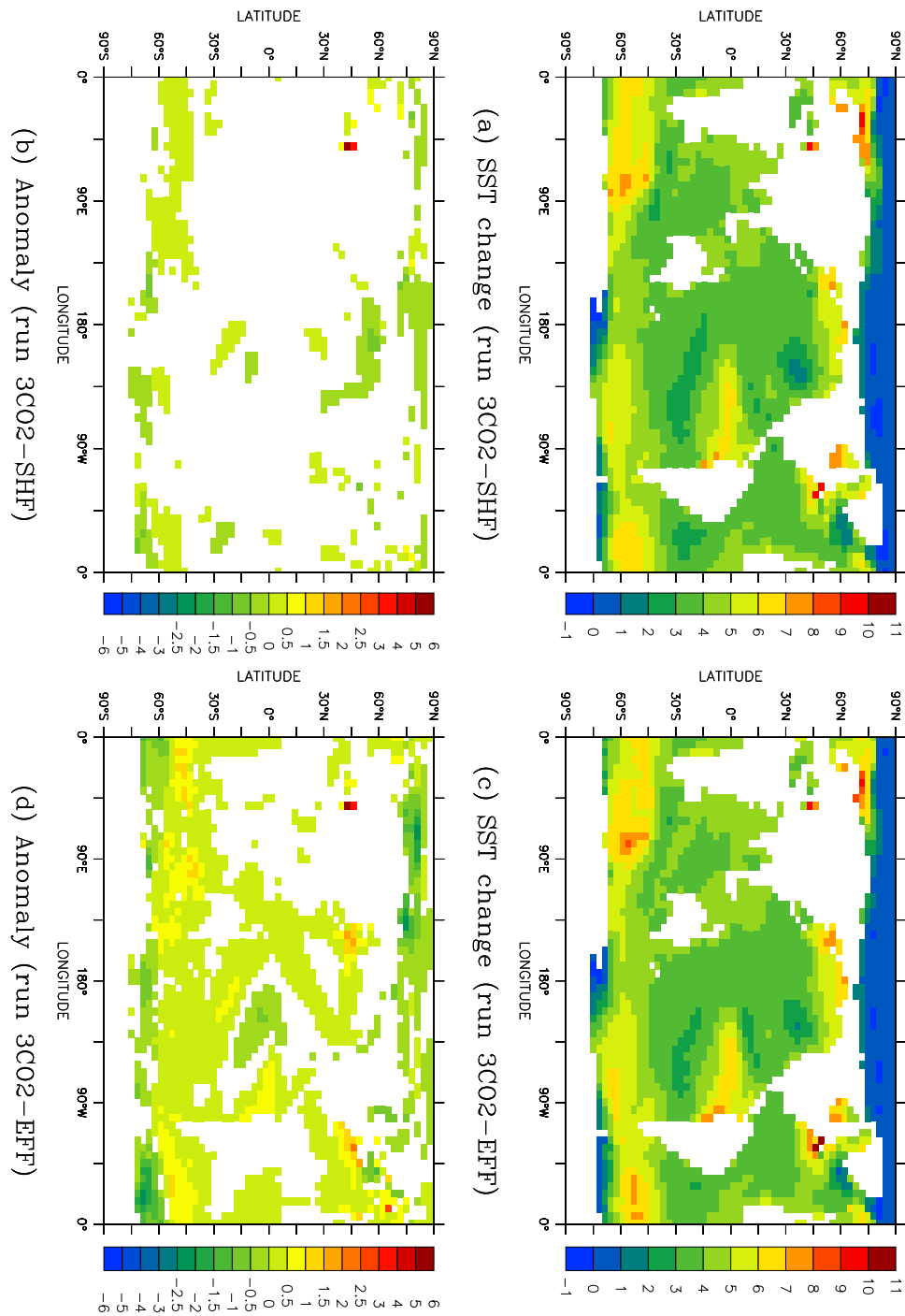


Figure 7.26: The annual-mean sea surface temperature (SST, °C) for years 1001–1100 of runs 3CO2-SHF and 3CO2-EFF, expressed as anomalies relative to the annual-mean SST for years 1001–1100 of the control runs: (a), (b) runs 3CO2-SHF and 3CO2-EFF respectively, and (c), (d) the annual-mean SST changes, expressed as anomalies relative to run 3CO2-DEF, with only those values which are significant at the 99% confidence level shown.

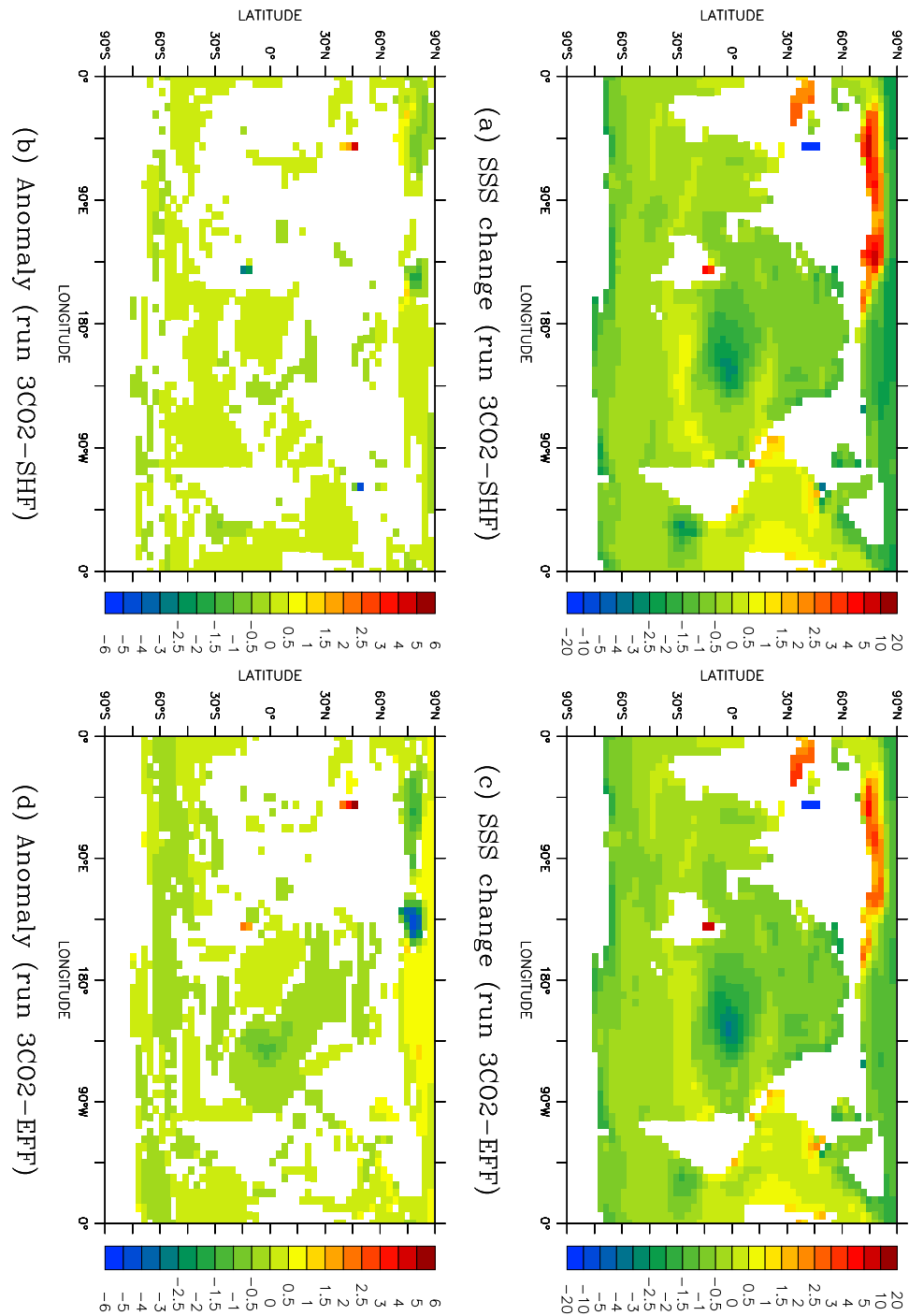


Figure 7.27: The annual-mean sea surface salinity (SSS, psu) for years 1001–1100 of runs 3CO2-SHF and 3CO2-EFF, expressed as anomalies relative to the annual-mean SSS for years 1001–1100 of the control runs: (a), (b) runs 3CO2-SHF and 3CO2-EFF respectively, and (c), (d) the annual-mean SSS changes, expressed as anomalies relative to run 3CO2-DEF, with only those values which are significant at the 99% confidence level shown.

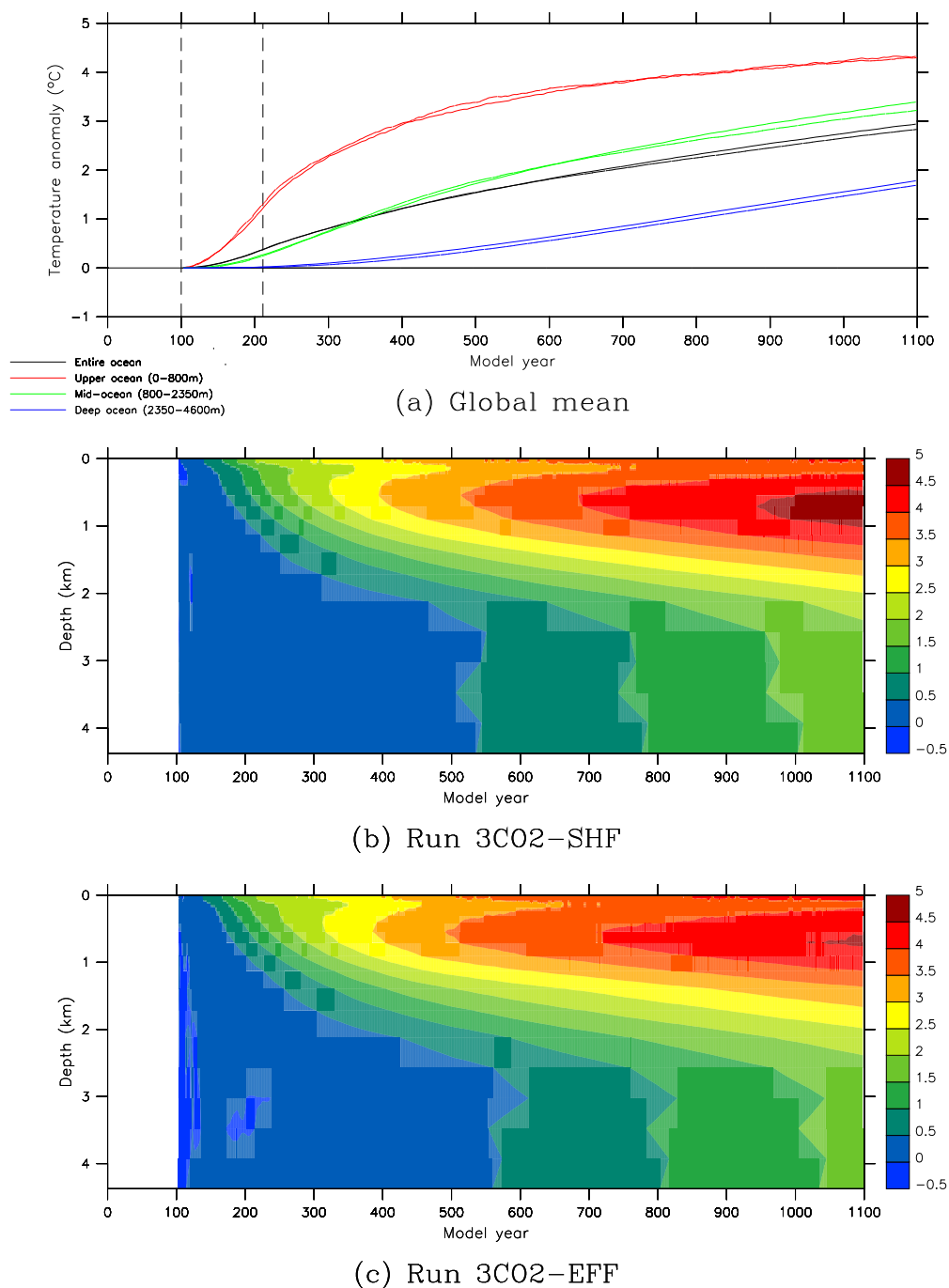


Figure 7.28: The change in annual-mean potential temperature ($^{\circ}\text{C}$) during runs 3CO₂-SHF (solid lines) and 3CO₂-EFF (dashed lines): (a) the global means for the entire ocean (black), upper ocean (red, 0–800 m), mid-ocean (green, 800–2350 m) and deep ocean (dark blue, 2350–4600 m), (b) the global-mean vertical profile for run 3CO₂-SHF, and (c) the global-mean vertical profile for run 3CO₂-EFF. The values shown are five-year running means, and are expressed as anomalies relative to the control runs. Vertical lines indicate years 100 and 211.

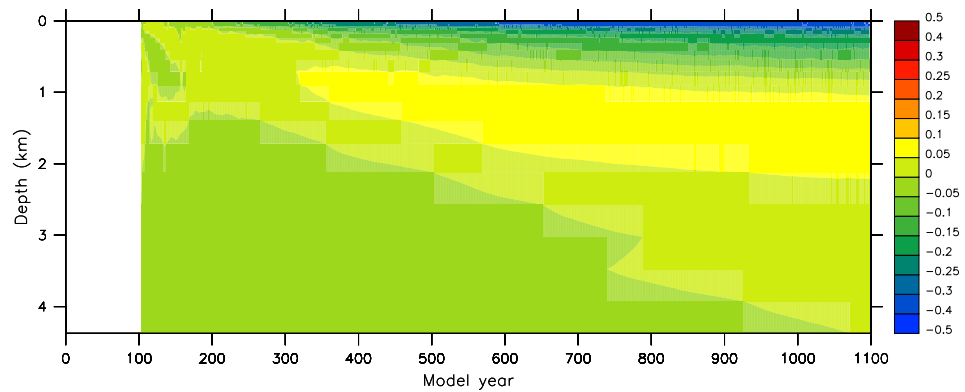
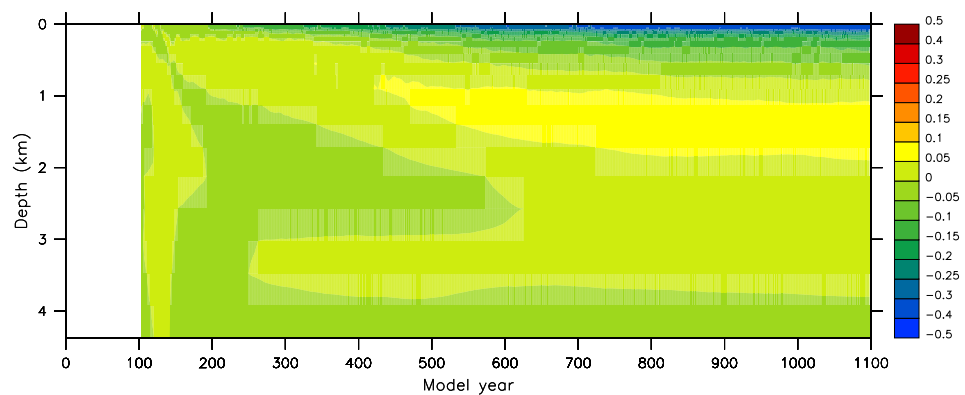
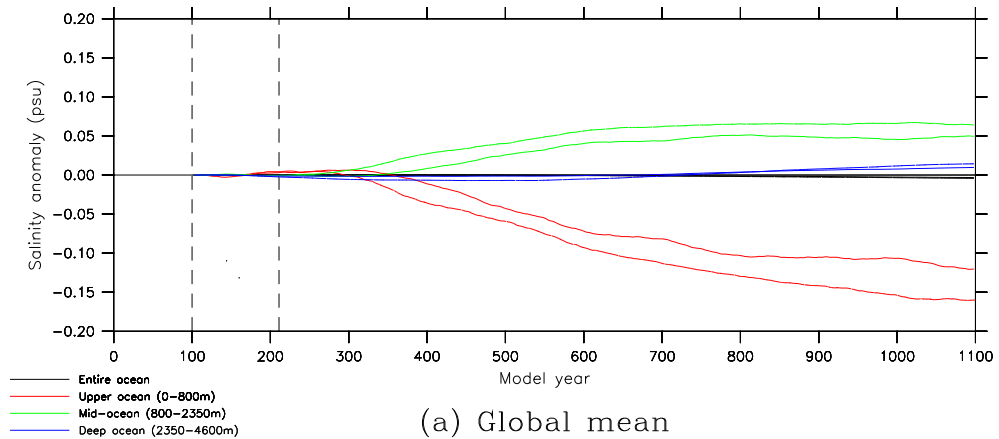


Figure 7.29: The change in annual-mean salinity (psu) during runs 3CO2-SHF (solid lines) and 3CO2-EFF (dashed lines): (a) the global means for the entire ocean (black), upper ocean (red, 0–800 m), mid-ocean (green, 800–2350 m) and deep ocean (dark blue, 2350–4600 m), (b) the global-mean vertical profile for run 3CO2-SHF, and (c) the global-mean vertical profile for run 3CO2-EFF. The values shown are five-year running means, and are expressed as anomalies relative to the control runs. Vertical lines indicate years 100 and 211.

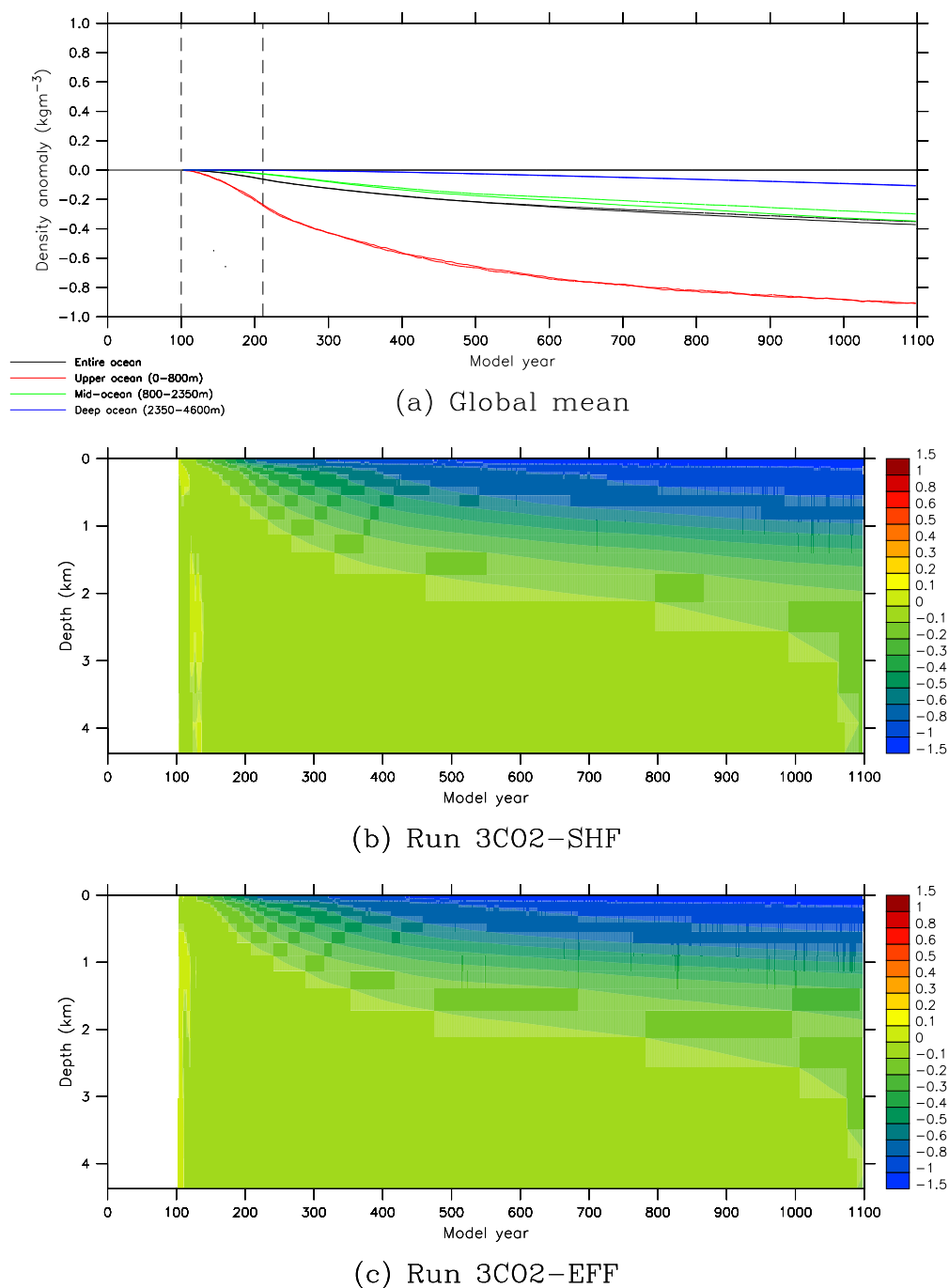
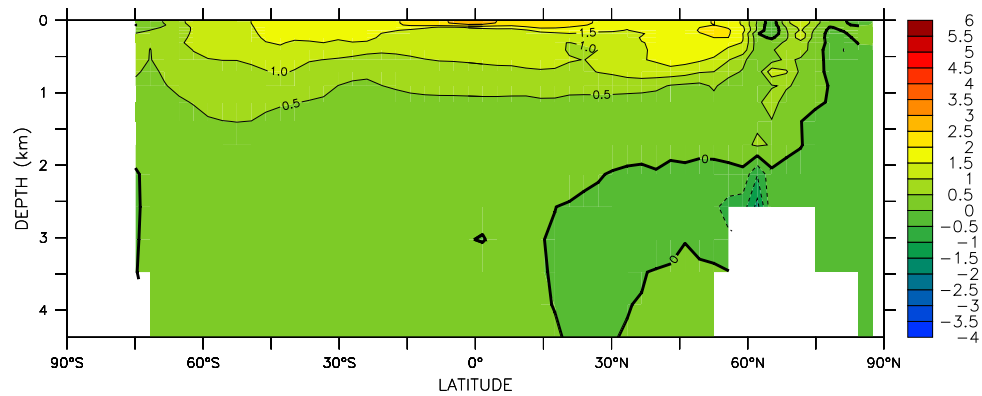
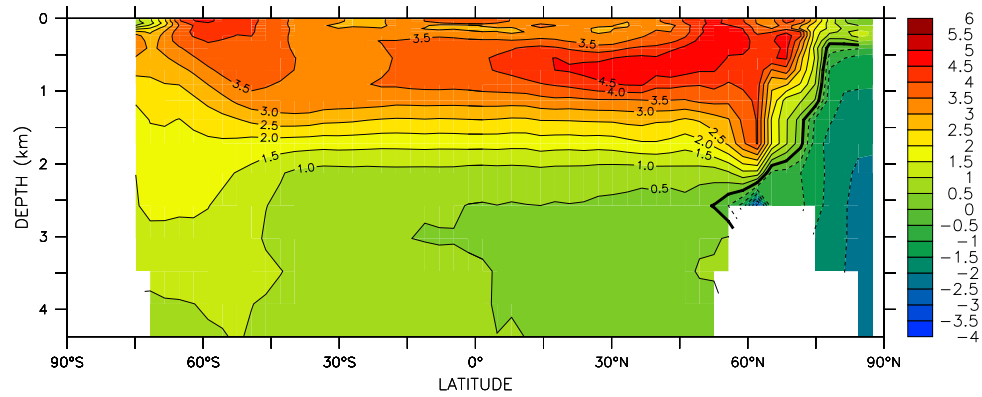


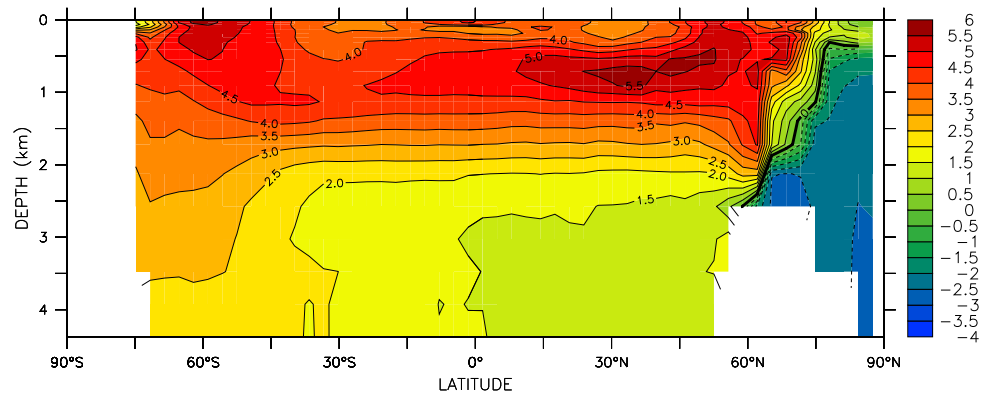
Figure 7.30: The change in annual-mean σ_θ (kgm^{-3}) during runs 3CO2-SHF (solid lines) and 3CO2-EFF (dashed lines): (a) the global means for the entire ocean (black), upper ocean (red, 0–800 m), mid-ocean (green, 800–2350 m) and deep ocean (dark blue, 2350–4600 m), (b) the global-mean vertical profile for run 3CO2-SHF, and (c) the global-mean vertical profile for run 3CO2-EFF. The values shown are five-year running means, and are expressed as anomalies relative to the control runs. Vertical lines indicate years 100 and 211.



(a) Years 186–235

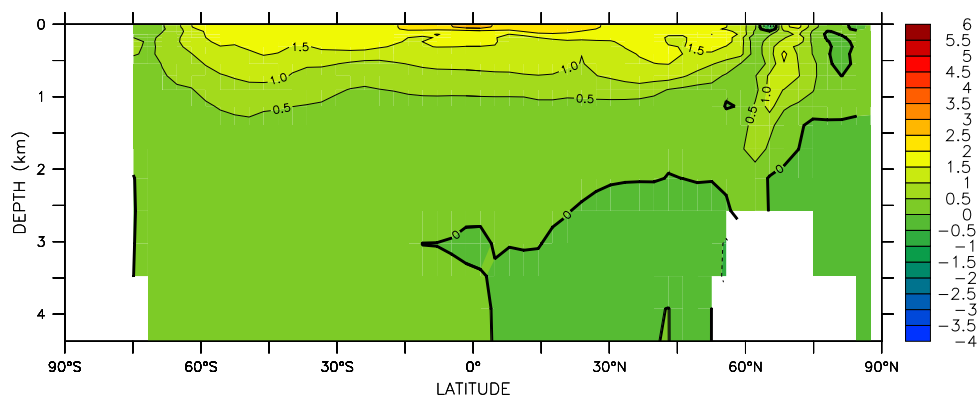


(b) Years 586–635

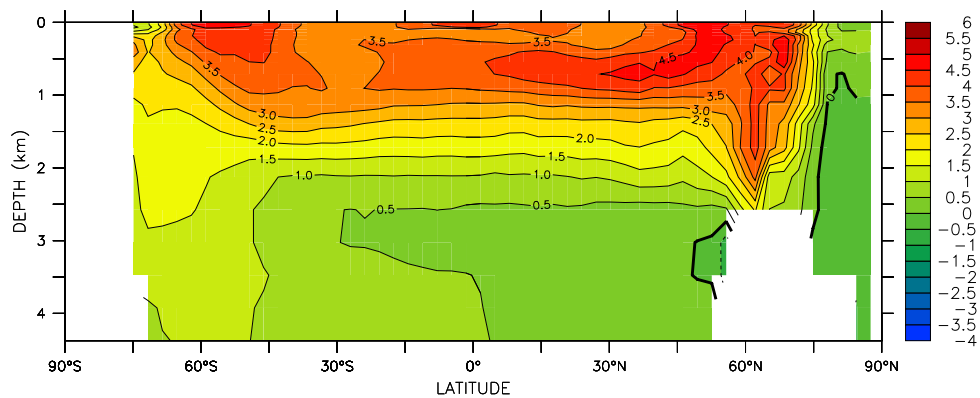


(c) Years 1051–1100

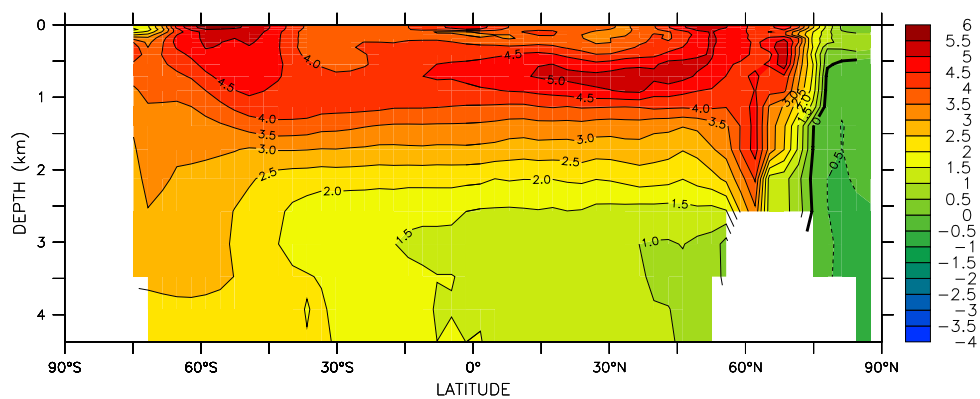
Figure 7.31: The evolution of the zonal-mean potential temperature ($^{\circ}\text{C}$) during run 3CO₂-SHF, expressed as an anomaly relative to control run CON-SHF: (a) years 186–235, (b) years 586–635, and (d) years 1051–1100. The inland seas are excluded when calculating the zonal means.



(a) Years 186–235



(b) Years 586–635



(c) Years 1051–1100

Figure 7.32: The evolution of the zonal-mean potential temperature ($^{\circ}\text{C}$) during run 3CO2-EFF, expressed as an anomaly relative to control run CON-EFF: (a) years 186–235, (b) years 586–635, and (d) years 1051–1100. The inland seas are excluded when calculating the zonal means.

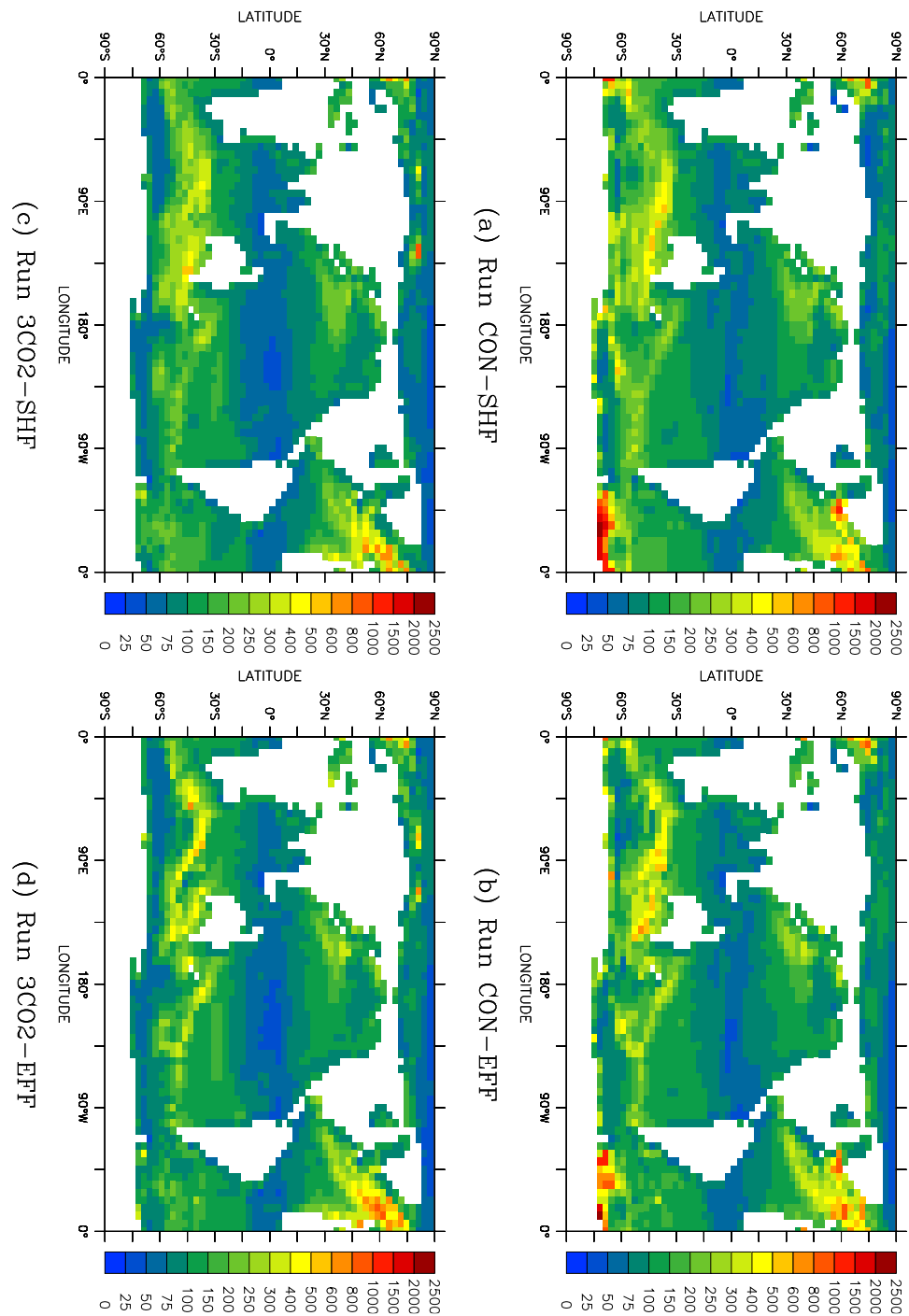


Figure 7.33: The average annual-maximum depths of convection (m) for years 1001–1100 of runs CON-SHF, CON-EFF, 3CO2-SHF and 3CO2-EFF: (a) run CON-SHF, (b) CON-EFF, (c) run 3CO2-SHF, and (d) run 3CO2-EFF.

to a more realistic vertical density profile, with the greater stratification of the water column leading to a reduction in the extent of convection over the Southern Ocean within the coupled model. This is apparent within both the control run (run CON-EFF, Figure 7.33b), and within the simulated response to an increase in the atmospheric CO_2 concentration (run 3CO2-EFF, Figure 7.33d).

Circulation

Figure 7.34 shows the evolution in the rates of North Atlantic Deep Water (NADW) and Antarctic Bottom Water (AABW) formation, and in the rate of volume transport through Drake Passage, during runs CON-SHF, CON-EFF, 3CO2-EFF and 3CO2-SHF. The responses of runs 3CO2-SHF and 3CO2-EFF are very similar to that of run 3CO2-DEF, with a rapid decline in the rate of NADW formation as the atmospheric CO_2 concentration increases. A minimum rate is achieved during the decades following the stabilisation of the CO_2 concentration, with a gradual recovery thereafter. The average rates of NADW formation for years 211–260 of runs 3CO2-SHF and 3CO2-EFF are 7.5 Sv and 10.5 Sv respectively; these figures are 7.8 Sv (51%) and 8.2 Sv (44%) weaker than the average rates of NADW formation for the equivalent periods of the control runs.

As with run 3CO2-DEF, both runs experience a collapse in the rate of AABW formation, while the Antarctic Circumpolar Current strengthens. The average rates of volume transport through Drake Passage for the final centuries of runs 3CO2-SHF and 3CO2-EFF are 158.4 Sv and 146.7 Sv respectively; these figures represent increases of 7.8 Sv and 10.0 Sv, respectively, on the strengths for the equivalent periods of the control runs.

Figure 7.35 shows the average meridional overturning streamfunctions for the final centuries of runs 3CO2-SHF and 3CO2-EFF. The cessation of Antarctic Bottom Water formation in both runs is apparent, as is the recovery of the overturning cell in the North Atlantic.

Mean sea level

Figure 7.36 shows the steric changes in the mean sea level, relative to the control runs, during runs 3CO2-SHF and 3CO2-EFF. The reduced penetration of the warming to depth in 3CO2-EFF leads to a reduced expansion of the ocean, and hence a smaller increase in the mean sea level.

7.3.3 Summary

The impact of the spin-up procedure upon the response of the model to an increase in the atmospheric carbon dioxide concentration has been studied. Differences in global-mean statistics have been shown to be small, with larger changes in the model response only occurring on a regional scale.

For run 3CO2-SHF, the increases in the global-mean surface air temperature (SAT), and in the mean sea level, by the end of a 1100-year simulation are only $\sim 1\%$ larger than the changes exhibited by the default configuration of the model. On a regional scale, the differences in the response of the model are generally small

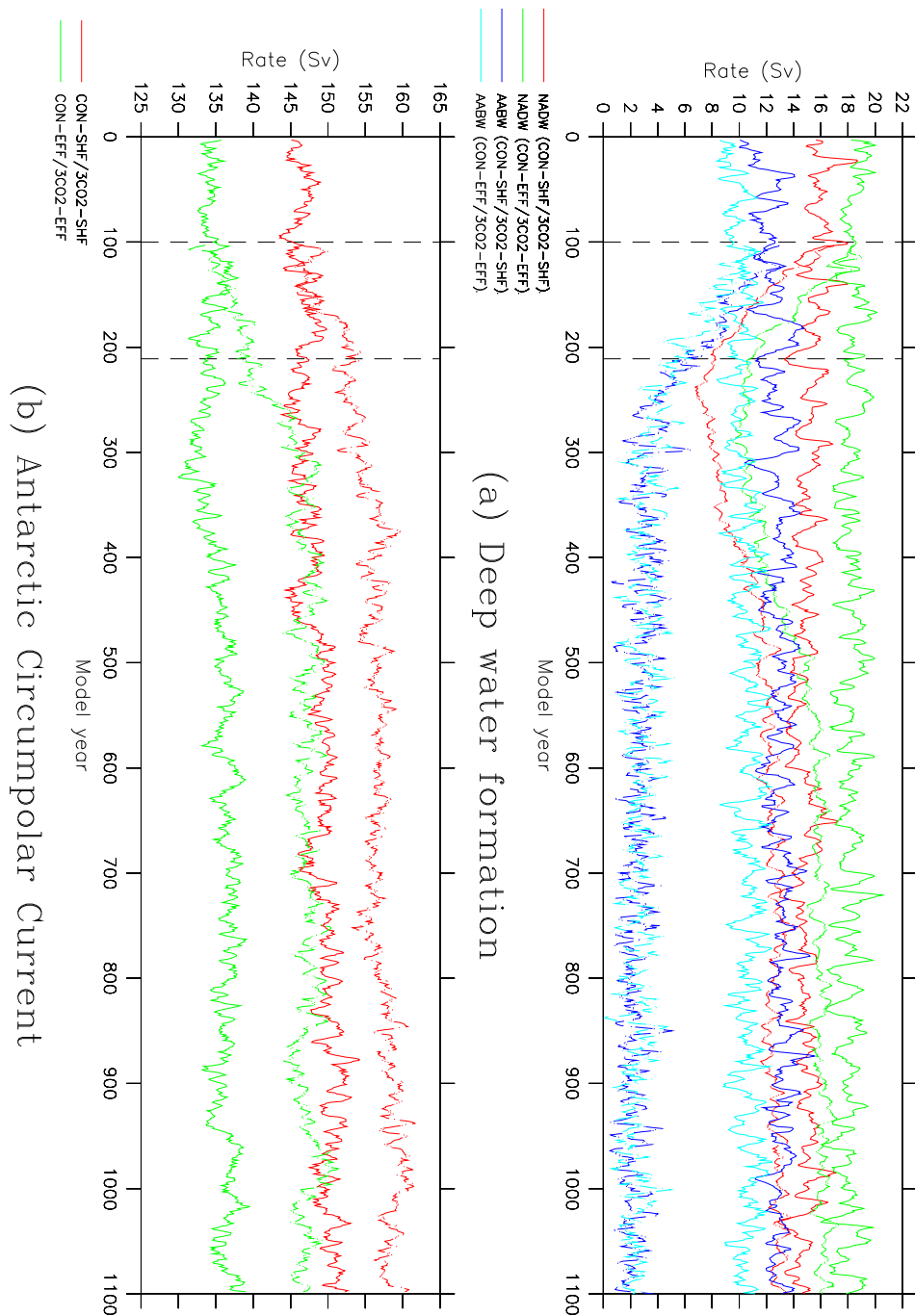


Figure 7.34: The rates of deep water formation, and the strength of the Antarctic Circumpolar Current, for runs CON-SHF (solid lines, red and dark blue), CON-EFF (solid lines, green and light blue), 3CO2-SHF (dashed lines, red and dark blue) and 3CO2-EFF (dashed lines, green and light blue): (a) the rates of formation of North Atlantic Deep Water (NADW) and Antarctic Bottom Water (AABW), and (b) the rate of volume transport through Drake Passage. The values shown are five-year running means. Vertical lines indicate years 100 and 211.

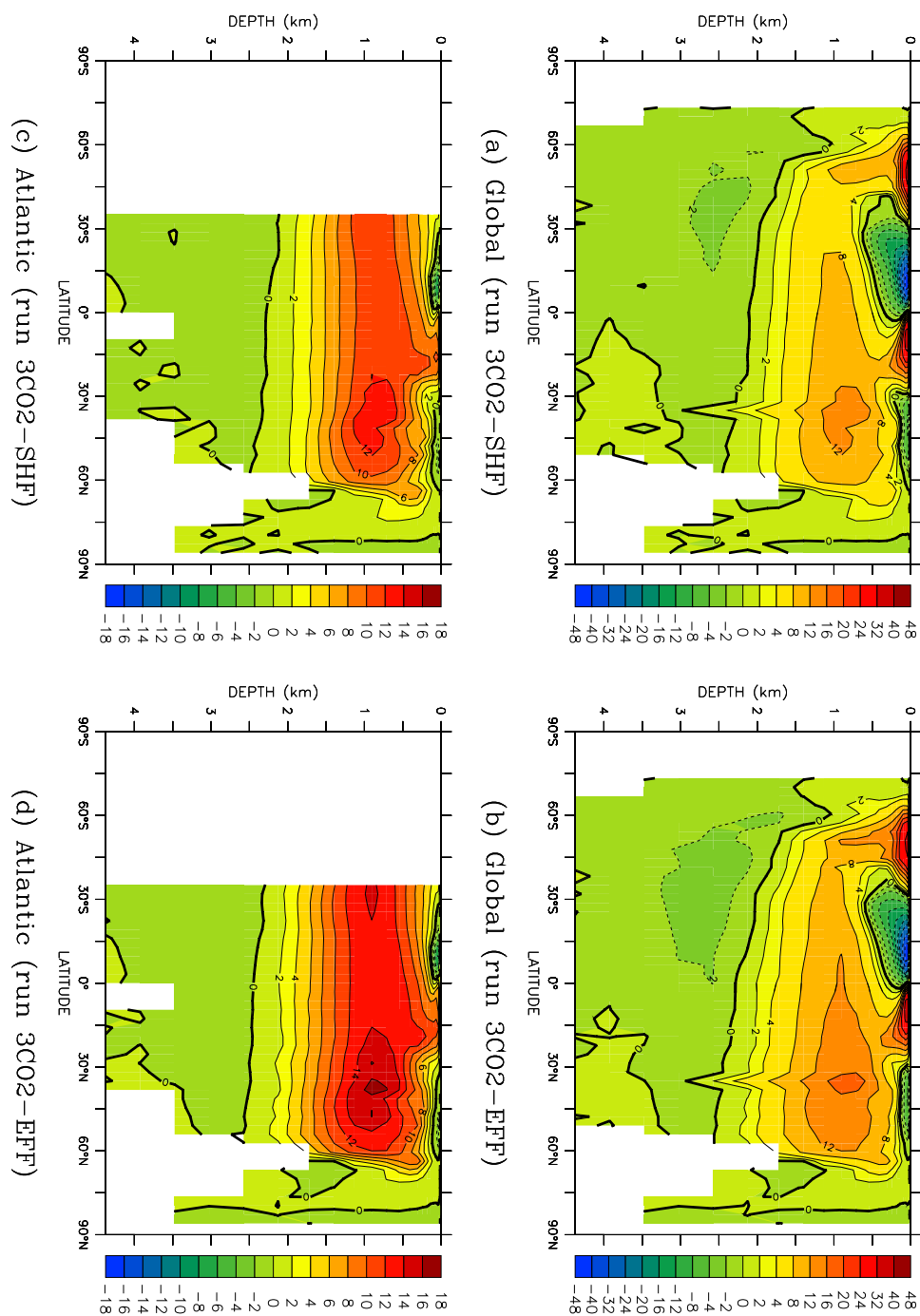


Figure 7.35: The average meridional overturning streamfunctions (S_v) for years 1001-1100 of runs 3CO₂-SHF and 3CO₂-EFF: (a), (b) the global meridional overturning streamfunction, runs 3CO₂-SHF and 3CO₂-EFF respectively, and (c), (d) the Atlantic meridional overturning streamfunction, runs 3CO₂-SHF and 3CO₂-EFF respectively.

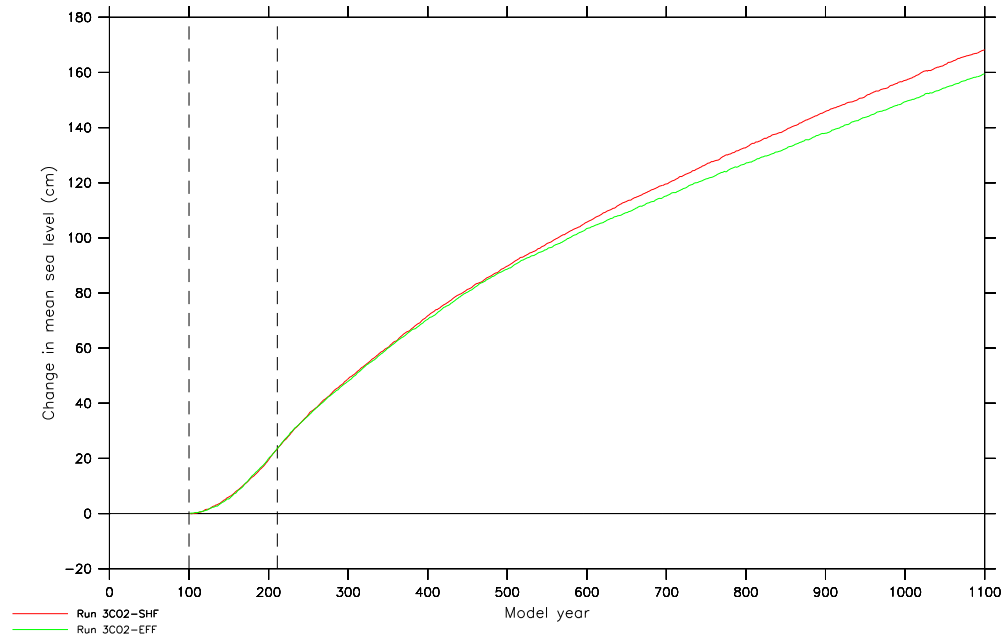


Figure 7.36: The steric changes in mean sea level diagnosed from runs 3CO2-SHF and 3CO2-EFF, expressed as anomalies relative to the steric changes in mean sea level diagnosed from the control runs. Vertical lines indicate years 100 and 211.

and statistically insignificant. There is therefore little evidence to reject the null hypothesis that flux adjustments have no *direct* impact upon the sensitivity of the model to external forcing. However, drift within the control run results in statistically-significant differences in the response over the Caspian Sea. There is therefore evidence that flux adjustments can *indirectly* affect the sensitivity of the model.

In the case of run 3CO2-EFF, the increases in the global-mean SAT, and in the mean sea level, by the end of a 1100-year simulation are 4% greater and 4% less, respectively, than the changes exhibited by the default configuration of the model. On a regional scale, there are statistically-significant differences in the model response across much of the surface of the ocean. Relative to the default configuration of the model, the surface warming in run 3CO2-EFF penetrates more slowly to depth in the Southern Ocean, and the deep ocean therefore warms at a slower rate. This results in a smaller increase in the mean sea level and, as a consequence of the reduced deep ocean heat uptake, a greater surface temperature response.

These differences in the model response arise from the greater stratification of the water column, relative to the default configuration of the model, and from the resulting reduction in convection throughout the Southern Ocean. It has therefore been demonstrated that the control climate of the ocean model can influence the response of the coupled model to increased atmospheric CO₂.

Chapter 8

Concluding remarks

8.1 Conclusions

The aims of this project were to use a coupled atmosphere-ocean general circulation model to address the following questions:

1. How does the spin-up procedure for the ocean model influence the degree of realism of the control climate, and the magnitude of the flux adjustments which are diagnosed for use within the coupled model?
2. Do the flux adjustments influence the nature of the internal variability within the model, and the response to external forcing?
3. Does the control climate of the ocean model influence the nature of the internal variability within the model, and the response to external forcing?

The success of the project in meeting each of these aims is considered in this section.

8.1.1 A coupled atmosphere-ocean general circulation model

The CSIRO Mk3L climate system model was used to address the above questions. This model consists of a low-resolution version of the atmosphere-sea ice component of the CSIRO Mk3 coupled model, coupled to the oceanic component of the CSIRO Mk2 coupled model. A horizontal spectral resolution of R21 is employed, giving zonal and meridional resolutions of 5.625° and $\sim 3.18^\circ$ respectively. There are 18 vertical levels in the atmosphere, and 21 vertical levels in the ocean.

The atmospheric and oceanic components of Mk3L were spun up for pre-industrial conditions, consistent with PMIP2 experimental design. The control climate of the atmosphere model was found to be realistic, with the simulated surface air temperature, sea ice, cloud cover and precipitation exhibiting broad agreement with observations. However, the model fails to form sea ice in Hudson Bay, resulting in surface air temperatures which are too warm in this region in winter; this discrepancy can be attributed to a warm bias in the sea surface temperatures which were prescribed as the bottom boundary condition. Other discrepancies in the simulated climate include Arctic sea ice which is generally too thin, excessive cloud

cover over the tropical oceans, poor representation of marine stratocumulus, and limited success in reproducing the positions of the monsoons. These discrepancies can be attributed to deficiencies in the model physics.

The control climate of the ocean model is only moderately realistic. The rate of North Atlantic Deep Water formation is too weak, the rate of Antarctic Bottom Water formation is too strong, and the deep ocean is too fresh, too cold and too buoyant. While the simulated strength of the Antarctic Circumpolar Current agrees well with observations, the western boundary currents are too weak and diffuse. The poor representation of the boundary currents is a consequence of the coarse horizontal resolution, but the other deficiencies in the ocean model climate can be attributed, at least in part, to the relaxation boundary condition on the temperature and salinity of the upper layer of the model. The use of such a boundary condition ensures that the peak winter density and salinity of the high-latitude surface waters do not attain the maximum observed values.

Flux adjustments were diagnosed from the differences between the surface fluxes derived from the atmosphere and ocean model spin-up runs. The oceanic meridional transports of heat and salt, as simulated by the ocean model and as implied by the atmosphere model, are in good agreement, and hence the flux adjustments exhibit relatively little variability in the meridional direction. However, there is high spatial variability in the zonal direction, arising largely from the failure of the atmosphere model to adequately represent marine stratocumulus, and from the failure of the ocean model to adequately represent the western boundary currents. The flux adjustments also exhibit a large seasonal cycle, with the result that the adjustments applied at individual gridpoints and in individual months can exceed in magnitude the fluxes which occur naturally within the climate system.

The coupled model was integrated for 1400 years, with the atmospheric and oceanic components being initialised from the final states of the spin-up runs, and with flux adjustments being applied. The control climate was found to be highly stable, with the global-mean surface air temperature declining just 0.23°C over the course of the simulation. This drift arises from changes in the Northern Hemisphere sea ice cover during the first century, with the resulting decline in the temperature of North Atlantic Deep Water leading to a slight, but ongoing, cooling trend within the ocean. Otherwise, there is little change in either global or regional statistics, with the thermohaline circulation exhibiting a high degree of stability, and with negligible drift in the surface air temperature over most of the Earth's surface. The Caspian Sea, which has no connection with the world ocean within Mk3L, exhibits an upward drift in salinity, which can be attributed to changes in the simulated precipitation and evaporation. The salinity of the remainder of the world ocean increases by just 0.004 psu; however, this increase cannot be accounted for by changes in the sea ice volume or in the surface freshwater fluxes, and it therefore appears to represent a conservation error within the model.

The simulated internal variability within the model was examined, and was found to exhibit the same spatial structure and correlations as the observed El Niño-Southern Oscillation (ENSO) phenomenon. The simulated return period of ~ 8 years for El Niño events is longer than the observed period of $\sim 3\text{--}6$ years, and the simulated events are too long and too weak. The simulated ENSO also exhibits

excessive modulation on interdecadal timescales.

The ability of Mk3L to simulate the climate of the mid-Holocene was evaluated. The model is capable of simulating the global-scale changes in the climate, with warmer summers at northern mid-latitudes, and slight cooling in the tropics. However, it is less successful when assessed at a regional scale, being unable to capture the cooling over southern Europe, or the increased precipitation over northern Africa. These failures can be attributed, at least in part, to the static nature of the vegetation within Mk3L. While the model also simulates a $\sim 13\%$ reduction in the strength of ENSO, this is a much smaller reduction than that implied by the palaeoclimate record. This discrepancy may be a consequence of deficiencies in the model physics, as indicated by its inability to correctly simulate the characteristics of the present-day ENSO.

The response of the model to a trebling of the atmospheric carbon dioxide concentration was also assessed. The CO_2 concentration was increased at 1% per year, until it reached three times the pre-industrial level; it was held constant thereafter. The global-mean surface air temperature increases by 1.6°C upon a doubling of the CO_2 concentration, and by 2.7°C upon a trebling. There is also a 49% reduction in the rate of North Atlantic Deep Water (NADW) formation.

Upon stabilisation of the atmospheric CO_2 concentration at three times the pre-industrial level, the global-mean surface air temperature continues to increase, with a warming of 5.3°C by the end of a 1400-year simulation. The rate of NADW formation recovers, however. The sea ice cover exhibits an ongoing decline, with 90% of the sea ice in the Southern Hemisphere, and 64% in the Northern Hemisphere, disappearing by the end of the simulation. The loss of sea ice cover in the Southern Hemisphere, and the associated reduction in brine rejection, results in the cessation of Antarctic Bottom Water (AABW) formation. Ventilation of the abyssal ocean therefore becomes restricted to convection in the Southern Ocean, and the surface warming penetrates only slowly to depth. By the end of the simulation, the deep ocean is still warming at a rate of $\sim 0.22^\circ\text{C}/\text{century}$, indicating that it is far from equilibrium. Thermal expansion of the ocean results in a steric sea level increase of 198 cm, with the continuing warming of the deep ocean giving rise to an ongoing increase of ~ 10 cm/century.

8.1.2 The ocean model spin-up procedure

The default ocean model spin-up run was found to exhibit three distinct errors in the simulated sea surface temperatures (SSTs) and sea surface salinities (SSSs): an error in the annual mean, an error in the amplitude of the annual cycle, and a phase lag between the simulated and observed fields. These errors can be attributed, at least in part, to the relaxation surface boundary condition, and account for the failure to simulate the peak winter density and salinity of the high-latitude surface waters.

A number of modifications to the ocean model spin-up procedure were evaluated, with the aim of obtaining high-latitude surface waters which have a realistic peak winter density and salinity, and hence with the aim of improving the realism of the ocean model climate. A simple theoretical model was used to study the response of an ocean model under the relaxation boundary condition, and was found to

reproduce many of the features of the response of the Mk3L ocean model. The response of the theoretical model was found to be strongest when the observed annual cycle in the SST or SSS was sinusoidal, and to weaken as the annual cycle became increasingly dominated by higher frequencies. A reduction in the relaxation timescale improved the model response, but with an undesirable increase in the magnitude of the surface fluxes.

A series of spin-up runs was conducted using the Mk3L ocean model, in which the relaxation timescale was varied from 5 to 80 days. The response was found to vary in the same manner as that of the theoretical model, with a reduction in the relaxation timescale reducing the errors in the simulated SSTs and SSSs, and increasing the magnitude of the surface fluxes. A reduction in the timescale resulted in more realistic peak surface water densities, and a corresponding improvement in the properties of the deep ocean, but a cold and fresh bias remained.

Further attempts to modify the ocean model spin-up procedure concentrated upon the prescribed surface tracers. An attempt was made to modify the prescribed SSTs and SSSs at high latitudes to allow for the presence of sea ice and, in particular, to allow for the effects of brine rejection. It was possible to obtain realistic peak surface water densities and salinities, and hence to obtain realistic vertical profiles of density and salinity within the ocean, but the cold bias of the deep ocean was increased. This was found to result from increased errors in the simulated thermohaline circulation, with an increase in the rate of AABW formation, and a decrease in the rate of NADW formation.

To address the time lag between observations and the model response, the effect of shifting the observed SSTs and SSSs forward in time by one month was assessed. This was found to have negligible impact upon the annual-mean climate of the ocean model, or upon the simulated seasonal cycle, but reduced the global-mean time lags in the simulated SSTs and SSSs to close to zero. By also reducing the phase difference between the surface fluxes simulated by the ocean model, and those simulated by the atmosphere model, the amplitudes of the annual cycles in the flux adjustments were reduced. Thus a new configuration of the coupled model (designated SHF herein) was obtained, in which the annual-mean climate and the seasonal cycles were negligibly different from the default configuration of coupled model, but within which the magnitude of the flux adjustments was reduced.

A novel spin-up technique was also developed, whereby the response of the ocean model is used to derive *effective* surface tracers. The annual means of the prescribed SSTs and SSSs, and the amplitudes of the annual cycles, are modified in an iterative fashion, with the aim of minimising the errors in the model response. A uniform phase shift of one month is also applied, in order to reduce the phase lags in the simulated SSTs and SSSs. This technique was found to be highly successful, with the iterative process converging towards a solution after just 14 iterations. There was a large improvement in the ocean model climate, with realistic vertical profiles of salinity and density, and with a reduction in the cold bias of the deep ocean. The rates of NADW and AABW formation were also consistent with observations. Furthermore, there was a slight reduction in the magnitude of the flux adjustments. A third configuration of the coupled model (designated EFF herein) was therefore obtained, within which the ocean model climate was much more realistic.

8.1.3 The effect of flux adjustments

SHF was integrated for 1100 years. The rate of drift in the control climate was found to be slightly greater than for the default configuration of the model, but it is still very small. The reduction in the flux adjustments was found to have no significant effect upon the nature of the simulated internal variability. There is therefore no evidence to reject the null hypothesis that flux adjustments have no influence upon the simulated internal variability.

The response to the insolation conditions which applied at the time of the mid-Holocene, and to an increase in the atmospheric carbon dioxide concentration, was studied. While there are some statistically-significant differences between the response of SHF and that of the default configuration of the model, these are generally small in magnitude. The exception is the response over the Caspian Sea, where the differences in the response of the model were found to arise from a cooling and freshening trend within the control run.

While there is therefore little evidence to reject the null hypothesis that flux adjustments have no *direct* influence upon the response of the model to external forcing, there is evidence that flux adjustments can *indirectly* affect the response.

8.1.4 The effect of the control climate

EFF was integrated for 1100 years. The rate of drift in the control climate was found to be slightly greater than for the default configuration of the model, but it is still very small. The simulated internal variability was also found to be slightly stronger, with a $\sim 10\%$ increase in the strength of the simulated El Niño-Southern Oscillation.

The response to mid-Holocene insolation was found to exhibit some significant differences relative to the default configuration of the model, most notably lower temperatures in the Southern Ocean. The response to an increase in the atmospheric carbon dioxide concentration was also studied. Relative to the default configuration, the surface warming is enhanced by $\sim 4\%$, and there is reduced penetration of this warming to depth. These differences were found to arise from the enhanced realism of the control climate, with an increased vertical density profile within the ocean. This results in reduced convection within the Southern Ocean, and hence to reduced ventilation of the abyssal ocean.

It has therefore been demonstrated that the control climate of the ocean model can influence both the nature of the internal variability within a coupled model, and the response of a coupled model to external forcing.

8.1.5 Summary

The project has been successful in achieving its aims. A number of modifications to the ocean model spin-up procedure have been assessed. Two of these have been found to result in an overall improvement in the climate of the ocean model, without increasing the magnitude of the flux adjustments. Two new configurations of the Mk3L coupled model have therefore been obtained.

These configurations have been used to assess the impact of flux adjustments, and of the control climate of the model, upon the simulated internal variability, and

upon the response to external forcing. The flux adjustments have been found to have no effect upon the internal variability, and to have only an indirect effect upon the response of the model. An increase in the realism of the ocean climate has been found to lead to a slight increase in the magnitude of the internal variability, and also to influence the response to external forcing.

8.2 Future work

All of the coupled model simulations presented herein are still being integrated at the time of writing. Unless the simulations begin to exhibit significant drift, it is intended to integrate them for as long as resources permit; it should therefore be possible to extend them for many millennia. For the control simulations, this will enable the stability of the control climate of Mk3L on millennial timescales to be assessed, and will allow millennial-scale variability within the model to be investigated. The origin of the drift should be studied further, with the intention of ensuring that the control climate is stable on timescales of $O(10^4)$ years and longer. Conservation of physical quantities within the model should also be studied, as a slight salinity drift within the control simulations appears to represent a conservation error within the model.

An extension of the mid-Holocene simulations will also enable natural climate variability during this epoch to be studied. For the scenario in which the atmospheric carbon dioxide has been stabilised at three times the pre-industrial value, it will be possible to integrate the simulations towards equilibrium. This will enable the impact of the ongoing warming of the deep ocean to be evaluated, particularly with regard to the possibility that the resulting decrease in the stratification of the water column will enable the re-establishment of deep overturning in the Southern Ocean (e.g. *Bi et al.*, 2001).

Further simulations should focus upon alternative scenarios, for both the past and future. As simulations have already been conducted for two of the three standard PMIP2 experiments - the pre-industrial era and the mid-Holocene - simulations should also be conducted for the third experiment (the Last Glacial Maximum, 21,000 years BP). Simulations could also be conducted for the additional “water-hosing” experiment, in which an external source of freshwater is applied to the surface of the North Atlantic.

The computational efficiency of Mk3L makes transient palaeoclimate simulations possible. Using the equilibrium simulations for the mid-Holocene as the starting point, the Earth’s orbital parameters could be varied dynamically, enabling a transient simulation from 6,000 years BP to the present day to be conducted. This would enable changes in the mean climate state, and in the natural climate variability, through the Holocene to be studied. Such simulations should address the role of vegetation feedbacks, either through the specification of appropriate vegetation types, as derived from biome reconstructions, or through the incorporation of a dynamic vegetation model. Comparison could also be made with similar simulations conducted using models of intermediate complexity (e.g. *Weber*, 2001; *Brovkin et al.*, 2002; *Crucifix et al.*, 2002; *Weber et al.*, 2004; *Renssen et al.*, 2005), and a study which employed a coupled atmosphere-ocean general circulation model, but

which accelerated the rate of change in the Earth's orbital parameters (*Lorenz and Lohmann, 2004*).

Scenarios which consider future climate change should focus upon stabilising the atmospheric carbon dioxide concentration at different levels, enabling the relative long-term response of the climate system to be studied. Such scenarios should include stabilisation of the CO₂ concentration at two and four times the pre-industrial level, enabling comparison with other studies (e.g. *Stouffer and Manabe, 2003*).

The role of flux adjustments within Mk3L should also be investigated further. Having established that a reduction in the amplitude of the flux adjustments has no significant effect upon the internal variability, and only an indirect effect upon the response to external forcing, other methods of reducing the flux adjustments should be assessed. These should include the “minimum” flux adjustment of *Weaver and Hughes (1996)*, in which the flux adjustments are zonally averaged across each ocean basin prior to being applied within the coupled model. Such adjustments are designed only to correct for the differences in the oceanic meridional transports of heat and salt, between those simulated by the ocean model and those implied by the atmosphere model, and would therefore be small in magnitude in the case of Mk3L. Alternative methods for reducing the magnitude of the flux adjustments would be to apply annual-mean adjustments only, and to derive “regional” flux adjustments through spatial averaging.

Appendix A

Experimental design

A.1 Introduction

The experimental design employed throughout this project followed that specified by PMIP2 (*Paleoclimate Modelling Intercomparison Project*, 2005), enabling a direct comparison between Mk3L and other models. PMIP2 experimental design is summarised in Section A.2, while Sections A.3 and A.4 provide further details regarding spin-up procedures and the coupled model experiments respectively.

The procedures followed to generate the restart and auxiliary files required by Mk3L are described in detail by *Phipps* (2006).

A.2 PMIP2 experimental design

PMIP2 experimental design is summarised in Table A.1. For coupled model experiments, it is specified that a control run be conducted for pre-industrial conditions, which are taken as being those which existed around the year AD 1750. Pre-industrial values are specified for the atmospheric concentrations of the “greenhouse gases” carbon dioxide (CO₂), methane (CH₄) and nitrous oxide (N₂O); it is also specified that the atmospheric concentration of chlorofluorocarbons be set to zero. The specified epoch is 0 years Before Present, and the values for the Earth’s orbital parameters therefore correspond to the year AD 1950. Otherwise, “modern” boundary conditions are specified, which can be interpreted as meaning that present-day values should be used.

While no specific spin-up procedure is prescribed for the coupled model, it is specified that the ocean model should be initialised using the World Ocean Atlas 1998 dataset (*National Oceanographic Data Center*, 2002, commonly referred to as the “Levitus 1998” dataset).

The boundary conditions for the mid-Holocene experiment differ only in the atmospheric methane concentration and the values of the Earth’s orbital parameters. While the ocean model can again be initialised using the World Ocean Atlas 1998 dataset, it can also be initialised from year 100 of a control run.

Boundary condition	Control run (~AD 1750)	Mid-Holocene (6ka BP)
Vegetation	Fixed	As for control run
Ice sheets	Modern	As for control run
Topography/coastlines	Modern	As for control run
CO ₂ concentration [ppm]	280	280
CH ₄ concentration [ppb]	760	650
N ₂ O concentration [ppb]	270	270
Chlorofluorocarbons	None	None
O ₃ concentration	Modern	As for control run
Solar constant [Wm ⁻²]	1365	1365
Epoch [years BP]	0	6,000
Eccentricity of Earth's orbit	0.016724	0.018682
Obliquity of Earth's axis [°]	23.446	24.105
Longitude of perihelion [°]	102.04	0.87
Initial ocean state	World Ocean Atlas 1998	World Ocean Atlas 1998 <i>or</i> year 100 of control run

Table A.1: PMIP2 experimental design for coupled model experiments: the pre-industrial control run, and the mid-Holocene experiment.

A.3 Spin-up procedures

The spin-up procedures for the atmosphere and ocean models are outlined in Sections 2.3.1 and 2.3.2 respectively. This section provides further information regarding the experimental design.

A.3.1 Ocean model

Configuration

The default configuration of the ocean model was employed, as described by *Phipps* (2006). Following PMIP2 experimental design, the bathymetry and coastlines were configured for the present day.

Initial state

The initial state of the ocean model was one in which the ocean is at rest. Following PMIP2 experimental design, the initial temperatures and salinities were set equal to the annual-mean World Ocean Atlas 1998 values.

Boundary conditions

The default surface boundary conditions on the stand-alone ocean model were derived from the World Ocean Atlas 1998, and from the NCEP-DOE Reanalysis 2 (*Kanamitsu et al.*, 2002).

As the upper layer of the Mk3L ocean model has a thickness of 25 m, the temperature and salinity of this layer simulate the average temperature and salinity of the upper 25 m of the water column, and not the sea surface temperature (SST) and sea surface salinity (SSS) *per se*. The temperature and salinity of this layer should be relaxed towards an equivalent observational quantity; the surface boundary conditions on the ocean model were *not* therefore the observed SST and SSS, but were instead the averages of the World Ocean Atlas 1998 temperatures and salinities over the upper 25 m of the water column.

The surface wind stresses were taken from the NCEP-DOE Reanalysis 2, and consisted of the climatological wind stresses for the period 1979–2003.

A.3.2 Atmosphere model

Configuration

The default configuration of the atmosphere model was employed, as described by *Phipps* (2006). Following PMIP2 experimental design, the topography, coastlines, ice sheets and vegetation were configured for the present day. The solar constant was set to 1365 Wm^{-2} , and AD 1950 values were used for the Earth's orbital parameters. The atmospheric carbon dioxide concentration was set to 280 ppm, and ozone concentrations were taken from the AMIP II recommended dataset (*Wang et al.*, 1995).

PMIP2 experimental design also specifies the atmospheric concentrations of methane, nitrous oxide and chlorofluorocarbons; however, the Mk3L atmosphere model does not allow for the radiative effects of these gases.

Initial state

The atmosphere model was initialised using the original restart file, as supplied with the model source code.

Boundary conditions

For consistency with the ocean model, the surface boundary conditions on the stand-alone atmosphere model consisted of the averages of the World Ocean Atlas 1998 temperature and salinity over the upper 25 m of the water column.

The currents required by the sea ice model were diagnosed from the final 100 years of ocean model spin-up runs, avoiding any need to apply “flux” adjustments to the currents within the coupled model.

A.4 Coupled model

A.4.1 Control runs

Configuration

For coupled model control runs, the atmosphere and ocean models were configured exactly as for the respective spin-up runs. Flux adjustments were derived using the

surface fluxes, sea surface temperatures and sea surface salinities diagnosed from the spin-up runs, as described in Section 2.6.

Initial state

The atmospheric and oceanic components of the coupled model were initialised from the state of each model at the end of the appropriate spin-up run.

A.4.2 Mid-Holocene experiments

Configuration

For the mid-Holocene experiments, only two changes were made to the configuration of the coupled model, relative to the control runs. Following PMIP2 experimental design, the epoch was changed from 0 to 6,000 years BP. The atmospheric carbon dioxide concentration was also reduced to 277 ppm, in order to represent the radiative forcing arising from the specified reduction in the methane concentration (Table A.1).

This *effective* carbon dioxide concentration was calculated using the following expressions, which give the radiative forcings arising from changes in the atmospheric concentrations of carbon dioxide and methane (*Ramaswamy et al.*, 2001, Table 6.2):

$$\text{CO}_2 : \quad \Delta F = 5.35 \ln \left(\frac{C}{C_0} \right) \quad (\text{A.1})$$

$$\text{CH}_4 : \quad \Delta F = 0.036(\sqrt{M} - \sqrt{M_0}) - (f(M, N_0) - f(M_0, N_0)) \quad (\text{A.2})$$

In these expressions, ΔF is the radiative forcing (Wm^{-2}), C_0 and C are the original and perturbed carbon dioxide concentrations respectively (ppm), M_0 and M are the original and perturbed methane concentrations respectively (ppb), N_0 is the nitrous oxide concentration (ppb), and $f(M, N)$ is given by

$$F(M, N) = 0.47 \ln \left[1 + 2.01 \times 10^{-5} (MN)^{0.75} + 5.31 \times 10^{-15} M (MN)^{1.52} \right] \quad (\text{A.3})$$

Using $M_0 = 760$ ppb, $M = 650$ ppb and $N_0 = 270$ ppb, Equations A.2 and A.3 give a value of -0.066 Wm^{-2} for the radiative forcing arising from the reduction in the atmospheric methane concentration.

By re-arranging Equation A.1, the following expression is obtained, enabling an *effective* carbon dioxide concentration C to be derived, which gives rise to a radiative forcing ΔF (Wm^{-2}) relative to the *actual* concentration C_0 :

$$C = C_0 e^{\Delta F/5.35} \quad (\text{A.4})$$

Using $C_0 = 280$ ppm and $\Delta F = -0.066 \text{ Wm}^{-2}$, this expression gives a value for the effective carbon dioxide concentration of 277 ppm.

Initial state

Following PMIP2 experimental design, the coupled model was initialised from the end of year 100 of the appropriate control run.

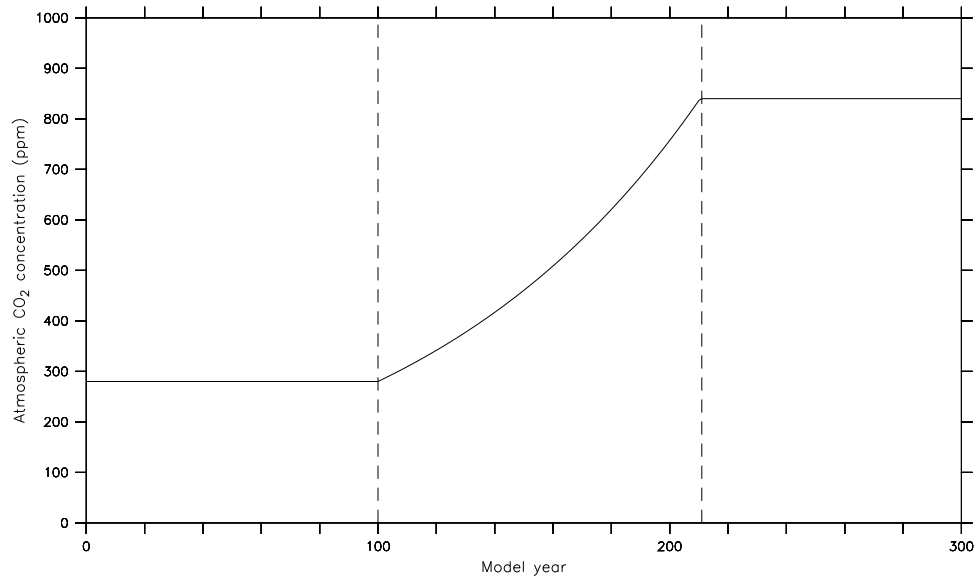


Figure A.1: The atmospheric carbon dioxide concentration for the $3\times\text{CO}_2$ stabilisation experiments. After being held constant at the pre-industrial concentration of 280 ppm for the first 100 years, the carbon dioxide concentration was increased at 1% per year, until it reached 840 ppm (three times the pre-industrial concentration) in year 211. It was held constant thereafter.

A.4.3 $3\times\text{CO}_2$ stabilisation experiments

Configuration

For the $3\times\text{CO}_2$ stabilisation experiments, the only change to the configuration of the coupled model, relative to the control runs, was an increase in the atmospheric carbon dioxide concentration. The experiments began in year 101, with the carbon dioxide concentration being increased at 1% per year. It reached 840 ppm, three times the pre-industrial level, in year 211, and was held constant thereafter. The resulting carbon dioxide concentrations are shown in Figure A.1.

Initial state

As for the mid-Holocene experiments, the coupled model was initialised from the end of year 100 of the appropriate control run.

Appendix B

Details of simulations

The simulations presented herein were conducted primarily at the Australian Partnership for Advanced Computing National Facility (*Australian Partnership for Advanced Computing*, 2005) in Canberra. Two different machines were used:

AlphaServer SC 126 Compaq AlphaServer SC nodes, each containing:
- $4 \times$ 1GHz EV68 (Alpha 21264C) CPUs
- between 4 and 16GB of RAM
Tru64 UNIX operating system

Linux Cluster 152 Dell Precision 350 nodes, each containing:
- $1 \times$ 2.66GHz Intel Pentium 4 CPU
- 1GB RAM
Linux operating system

Some of the simulations conducted on the AlphaServer SC were completed on an equivalent facility located at the Interactive Virtual Environments Centre in Perth, Western Australia.

Statistics are provided in Tables B.1, B.2 and B.3, for the atmosphere model, ocean model and coupled model simulations respectively.

Simulation	Facility	Original name	Duration (years)
A-DEF	APAC AlphaServer SC	c15	50
A-EFF	APAC AlphaServer SC	c17	50
A-SHF	APAC AlphaServer SC	c16	50

Table B.1: Atmosphere model simulations: the name used herein, the facility on which it was conducted, the name used on that facility, and the duration.

Simulation	Facility	Original name	Duration (years)
O-5d	APAC Linux Cluster	h73	4500
O-7.5d	APAC Linux Cluster	h74	3500
O-10d	APAC Linux Cluster	h69	3500
O-15d	APAC Linux Cluster	h70	4500
O-30d	APAC Linux Cluster	h71	5500
O-40d	APAC Linux Cluster	h72	5500
O-60d	APAC Linux Cluster	h75	5500
O-80d	APAC Linux Cluster	h76	6500
O-0.25psu	APAC Linux Cluster	h57	4500
O-0.5psu	APAC Linux Cluster	h56	4500
O-1psu	APAC Linux Cluster	h55	4500
O-DEF	APAC Linux Cluster	h53	4500
O-EFF	APAC Linux Cluster	h65	8600
O-SHF	APAC Linux Cluster	h61	500

Table B.2: Ocean model simulations: the name used herein, the facility on which it was conducted, the name used on that facility, and the duration.

Simulation	Facility	Original name	Model years
<i>Control runs</i>			
CON-DEF	APAC AlphaServer SC iVEC AlphaServer SC	d73	1–176 177–1400*
CON-EFF	APAC AlphaServer SC iVEC AlphaServer SC	d70	1–623 624–1100*
CON-SHF	APAC AlphaServer SC iVEC AlphaServer SC	d68	1–630 631–1100*
<i>mid-Holocene experiments</i>			
6ka-DEF	APAC Linux Cluster	d95	101–900*
6ka-EFF	APAC Linux Cluster	d94	101–900*
6ka-SHF	APAC Linux Cluster	d92	101–900*
<i>3×CO₂ stabilisation experiments</i>			
3CO2-DEF	APAC AlphaServer SC iVEC AlphaServer SC	d86	101–185 186–1400*
3CO2-EFF	APAC AlphaServer SC iVEC AlphaServer SC	d85	101–638 639–1100*
3CO2-SHF	APAC AlphaServer SC iVEC AlphaServer SC	d83	101–637 638–1100*

Table B.3: Coupled model simulations: the name used herein, the facility on which it was conducted, the name used on that facility, and the model years which were conducted on that facility. The mid-Holocene and 3×CO₂ stabilisation experiments began at model year 101. *The simulation is still underway at the time of writing.

Bibliography

- AchutaRao, K., and K. R. Sperber (2002), Simulation of the El Niño Southern Oscillation: Results from the Coupled Model Intercomparison Project, *Climate Dynamics*, 19, 191–209.
- Alexander, M., J. Yin, G. Branstator, A. Capotondi, C. Cassou, R. Cullather, Y.-O. Kwon, J. Norris, J. Scott, and I. Wainer (2006), Extratropical atmosphere-ocean variability in CCSM3, *Journal of Climate*, 19(11), 2496–2525.
- Arakawa, A., and V. R. Lamb (1977), Computational design of the basic dynamical processes of the UCLA general circulation model, in *General Circulation Models of the Atmosphere, Methods in Computational Physics*, vol. 17, edited by J. Chang, pp. 173–265, Academic Press.
- Australian Partnership for Advanced Computing (2005), APAC National Facility Home Page, URL <http://nf.apac.edu.au/>, viewed 23 April 2005.
- Bard, E. (2002), Climate shock: Abrupt changes over millennial time scales, *Physics Today*, pp. 32–38.
- Bell, J., P. Duffy, C. Covey, L. Sloan, and the CMIP investigators (2000), Comparison of temperature variability in observations and sixteen climate model simulations, *Geophysical Research Letters*, 27(2), 261–264.
- Berger, A., and M. F. Loutre (2004), Astronomical theory of climate change, *Journal de Physique IV France*, 121, 1–35.
- Bi, D. (2002), Transient and long-term behaviour of the world ocean under global warming, Ph.D. thesis, University of Tasmania.
- Bi, D., W. F. Budd, A. C. Hirst, and X. Wu (2001), Collapse and reorganisation of the Southern Ocean overturning under global warming in a coupled model, *Geophysical Research Letters*, 28(20), 3927–3930.
- Bi, D., W. F. Budd, A. C. Hirst, and X. Wu (2002), Response of the Antarctic Circumpolar Current transport to global warming in a coupled model, *Geophysical Research Letters*, 29(24), 2173, doi:10.1029/2002GL015919.
- Bigg, G. R., and M. R. Wadley (2001), Millennial-scale variability in the oceans: an ocean modelling view, *Journal of Quaternary Science*, 16(5), 309–319.

- Boer, G. J., G. Flato, M. C. Reader, and D. Ramsden (2000), A transient climate change simulation with greenhouse gas and aerosol forcing: experimental design and comparison with the instrumental record for the twentieth century, *Climate Dynamics*, *16*, 405–425.
- Bonfils, C., N. de Noblet-Ducoudré, J. Guiot, and P. Bartlein (2004), Some mechanisms of mid-Holocene climate change in Europe, inferred from comparing PMIP models to data, *Climate Dynamics*, *23*, 79–98.
- Boville, B. A., and P. R. Gent (1998), The NCAR Climate System Model, version one, *Journal of Climate*, *11*, 1115–1130.
- Braconnot, P., S. Joussaume, O. Marti, and N. de Noblet (1999), Synergistic feedbacks from ocean and vegetation on the African monsoon response to mid-Holocene insolation, *Geophysical Research Letters*, *26*(16), 2481–2484.
- Braconnot, P., S. Joussaume, N. de Noblet, and G. Ramstein (2000a), Mid-Holocene and Last Glacial Maximum African monsoon changes as simulated within the Paleoclimate Modelling Intercomparison Project, *Global and Planetary Change*, *26*, 51–66.
- Braconnot, P., O. Marti, S. Joussaume, and Y. Leclainche (2000b), Ocean feedback in response to 6 kyr BP insolation, *Journal of Climate*, *13*, 1537–1553.
- Bretherton, C. S., T. Uttal, C. W. Fairall, S. E. Yuter, R. A. Weller, D. Baumgardner, K. Comstock, R. Wood, and G. B. Raga (2004), The EPIC 2001 stratocumulus study, *Bulletin of the American Meteorological Society*, *85*(7), 967–977.
- Broccoli, A. J., K. W. Dixon, T. L. Delworth, T. R. Knutson, and R. J. Stouffer (2003), Twentieth-century temperature and precipitation trends in ensemble climate simulations including natural and anthropogenic forcing, *Journal of Geophysical Research*, *108*(D24), 4798, doi:10.1029/2003JD003812.
- Broecker, W. S. (1986), Oxygen isotope constraints on surface ocean temperatures, *Quaternary Research*, *26*, 121–134.
- Broström, A., M. Coe, S. P. Harrison, R. Gallimore, J. E. Kutzbach, J. Foley, I. C. Prentice, and P. Behling (1998), Land surface feedbacks and palaeomonsoons in northern Africa, *Geophysical Research Letters*, *25*(19), 3615–3618.
- Brovkin, V., J. Bendtsen, M. Claussen, A. Ganopolski, C. Kubatzki, V. Petoukhov, and A. Andreev (2002), Carbon cycle, vegetation, and climate dynamics in the Holocene: Experiments with the CLIMBER-2 model, *Global Biogeochemical Cycles*, *16*(4), 1139, doi:10.1029/2001GB001662.
- Bryan, F. (1986), High-latitude salinity effects and interhemispheric thermohaline circulations, *Nature*, *323*, 301–304.
- Bryan, F. O., G. Danabasoglu, N. Nakashiki, Y. Yoshida, D.-H. Kim, J. Tsutsui, and S. C. Doney (2006), Response of the North Atlantic thermohaline circulation and ventilation to increasing carbon dioxide in CCSM3, *Journal of Climate*, *19*(11), 2382–2397.

- Bryan, K. (1969), A numerical method for the study of the circulation of the world ocean, *Journal of Computational Physics*, *4*, 347–376.
- Bryan, K., S. Manabe, and R. C. Pacanowski (1975), A global ocean-atmosphere climate model. Part II. The oceanic circulation, *Journal of Physical Oceanography*, *5*, 30–46.
- Bryden, H. L. (1973), New polynomials for thermal expansion, adiabatic temperature gradient and potential temperature of sea water, *Deep-Sea Research*, *20*, 401–408.
- Bush, A. B. G. (1999), Assessing the impact of Mid-Holocene insolation on the atmosphere-ocean system, *Geophysical Research Letters*, *26*(1), 99–102.
- Cai, W. (1995), Interdecadal variability driven by mismatch between surface flux forcing and oceanic freshwater/heat transport, *Journal of Physical Oceanography*, *25*, 2643–2666.
- Cai, W., M. A. Collier, H. B. Gordon, and L. J. Waterman (2003), Strong ENSO variability and a super-ENSO pair in the CSIRO coupled climate model, *Monthly Weather Review*, *131*, 1189–1210.
- Carmack, E. C. (1977), Water characteristics of the Southern Ocean south of the Polar Front, *Deep-Sea Research*, *24*(Supplement), 15–41.
- Cess, R. D., and G. L. Potter (1987), Exploratory studies of cloud radiative forcing with a general circulation model, *Tellus*, *39A*, 460–473.
- Cheddadi, R., G. Yu, J. Guiot, S. P. Harrison, and I. C. Prentice (1997), The climate of Europe 6000 years ago, *Climate Dynamics*, *13*, 1–9.
- Chouinard, C., M. B eland, and N. McFarlane (1986), A simple gravity wave drag parameterization for use in medium-range weather forecast models, *Atmosphere-Ocean*, *24*(2), 91–110.
- Chu, P. C., Y. Chen, and S. Lu (1998), On Haney-type surface thermal boundary conditions for ocean circulation models, *Journal of Physical Oceanography*, *28*, 890–901.
- Claussen, M., and V. Gayler (1997), The greening of the Sahara during the mid-Holocene: results of an interactive atmosphere-biome model, *Global Ecology and Biogeography Letters*, *6*, 369–377.
- Claussen, M., L. A. Mysak, A. J. Weaver, M. Crucifix, T. Fichet, M.-F. Loutre, S. L. Weber, J. Alcamo, V. A. Alexeev, A. Berger, R. Calov, A. Ganopoloski, H. Goosse, G. Lohmann, F. Lunkeit, I. I. Mokhov, V. Petoukhov, P. Stone, and Z. Wang (2002), Earth system models of intermediate complexity: closing the gap in the spectrum of climate system models, *Climate Dynamics*, *18*, 579–586.
- Clement, A. C., R. Seager, and M. A. Cane (2000), Suppression of El Ni o during the mid-Holocene by changes in the Earth’s orbit, *Paleoceanography*, *15*(6), 731–737.

- Coe, M. T., and G. B. Bonan (1997), Feedbacks between climate and surface water in northern Africa during the middle Holocene, *Journal of Geophysical Research*, *102*(D10), 11,087–11,101.
- COHMAP members (1988), Climatic changes of the last 18,000 years: Observations and model simulations, *Science*, *241*, 1043–1052.
- Collins, W. D., C. M. Bitz, M. L. Blackmon, G. B. Bonan, C. S. Bretherton, J. A. Carton, P. Chang, S. C. Doney, J. J. Hack, T. B. Henderson, J. T. Kiehl, W. G. Large, D. S. McKenna, B. D. Santer, and R. D. Smith (2006), The Community Climate System Model version 3 (CCSM3), *Journal of Climate*, *19*(11), 2122–2143.
- Covey, C., K. N. AchutaRao, U. Cubasch, P. Jones, S. J. Lambert, M. E. Mann, T. J. Phillips, and K. E. Taylor (2003), An overview of results from the Coupled Model Intercomparison Project, *Global and Planetary Change*, *37*, 103–133.
- Cox, M. D. (1984), A primitive equation, 3-dimensional model of the ocean, *Technical Report 1*, Geophysical Fluid Dynamics Laboratory Ocean Group.
- Cox, M. D. (1987), Isopycnal diffusion in a z -coordinate ocean model, *Ocean Modelling*, *74*, 1–5.
- Crucifix, M., M.-F. Loutre, P. Tulkens, T. Fichefet, and A. Berger (2002), Climate evolution during the Holocene: a study with an Earth system model of intermediate complexity, *Climate Dynamics*, *19*, 43–60.
- Crucifix, M., P. Braconnot, S. P. Harrison, and B. Otto-Bliesner (2005), Second phase of Paleoclimate Modelling Intercomparison Project, *EOS, Transactions, American Geophysical Union*, *86*(28), 264.
- Cubasch, U., K. Hasselmann, H. Höck, E. Maier-Reimer, U. Mikolajewicz, B. D. Santer, and R. Sausen (1992), Time-dependent greenhouse warming computation with a coupled atmosphere-ocean model, *Climate Dynamics*, *8*, 55–69.
- Cubasch, U., G. A. Meehl, G. J. Boer, R. J. Stouffer, M. Dix, A. Noda, C. A. Senior, S. Raper, and K. S. Yap (2001), Projections of future climate change, in *Climate Change 2001: The Scientific Basis*, edited by J. T. Houghton, Y. Ding, D. J. Griggs, M. Noguer, P. J. van der Linden, X. Dai, K. Maskell, and C. A. Johnson, chap. 9, pp. 525–582, Cambridge University Press.
- Cunningham, S. A., S. G. Alderson, B. A. King, and M. A. Brandon (2003), Transport and variability of the Antarctic Circumpolar Current in Drake Passage, *Journal of Geophysical Research*, *108*(C5), 8084, doi:10.1029/2001JC001147.
- Delworth, T. L., A. J. Broccoli, A. Rosati, R. J. Stouffer, V. Balaji, J. A. Beesley, W. F. Cooke, K. W. Dixon, J. Dunne, K. A. Dunne, J. W. Durachta, K. L. Findell, P. Ginoux, A. Gnanadesikan, C. T. Gordon, S. M. Griffies, R. Gudgel, M. J. Harrison, I. M. Held, R. S. Hemler, L. W. Horowitz, S. A. Klein, T. R. Knutson, P. J. Kushner, A. R. Langenhorst, H.-C. Lee, S.-J. Lin, J. Lu, S. L. Malyshev, P. C. D.

- Milly, V. Ramaswamy, J. Russell, M. D. Schwarzkopf, E. Shevliakova, J. J. Sirutis, M. J. Spelman, W. F. Stern, M. Winton, A. T. Wittenberg, B. Wyman, F. Zeng, and R. Zhang (2006), GFDL's CM2 global coupled climate models. Part I: Formulation and simulation characteristics, *Journal of Climate*, *19*, 643–674.
- de Noblet, N., P. Braconnot, S. Joussaume, and V. Masson (1996), Sensitivity of simulated Asian and African summer monsoons to orbitally induced variations in insolation 126, 115 and 6 kBP, *Climate Dynamics*, *12*, 589–603.
- de Noblet-Ducoudré, N., M. Claussen, and C. Prentice (2000), Mid-Holocene greening of the Sahara: first results of the GAIM 6000 year BP experiment with two asynchronously coupled atmosphere/biome models, *Climate Dynamics*, *16*, 643–659.
- Deser, C., A. Capotondi, R. Saravanan, and A. S. Phillips (2006), Tropical Pacific and Atlantic climate variability in CCSM3, *Journal of Climate*, *19*(11), 2451–2481.
- Dixon, K. W., T. L. Delworth, T. R. Knutson, M. J. Spelman, and R. J. Stouffer (2003), A comparison of climate change simulations produced by two GFDL coupled climate models, *Global and Planetary Change*, *37*, 81–102.
- Doherty, R., J. Kutzbach, J. Foley, and D. Pollard (2000), Fully coupled climate/dynamical vegetation model simulations over Northern Africa during the mid-Holocene, *Climate Dynamics*, *16*, 561–573.
- Dong, B., P. J. Valdes, and N. M. J. Hall (1996), The changes of monsoonal climates due to Earth's orbital perturbations and ice age boundary conditions, *Palaeoclimates*, *1*, 203–240.
- Duffy, P. B., and K. Caldeira (1997), Sensitivity of simulated salinity in a three-dimensional ocean model to upper ocean transport of salt from sea-ice formation, *Geophysical Research Letters*, *24*(11), 1323–1326.
- Duffy, P. B., J. Bell, C. Covey, L. Sloan, and the CMIP investigators (2000), Effects of flux adjustments on temperature variability in climate models, *Geophysical Research Letters*, *27*(6), 763–766.
- England, M. H. (1993), Representing the global-scale water masses in ocean general circulation models, *Journal of Physical Oceanography*, *23*, 1523–1552.
- England, M. H., and A. C. Hirst (1997), Chlorofluorocarbon uptake in a world ocean model: 2. Sensitivity to surface thermohaline forcing and subsurface mixing parameterisations, *Journal of Geophysical Research*, *102*(C7), 15,709–15,731.
- Fanning, A. F., and A. J. Weaver (1997), On the role of flux adjustments in an idealized coupled climate model, *Climate Dynamics*, *13*, 691–701.
- Fels, S. B., and M. D. Schwarzkopf (1975), The simplified exchange approximation: A new method for radiative transfer calculations, *Journal of the Atmospheric Sciences*, *32*, 1475–1488.

- Fels, S. B., and M. D. Schwarzkopf (1981), An efficient, accurate algorithm for calculating CO₂ 15 μ m band cooling rates, *Journal of Geophysical Research*, *86*(C2), 1205–1232.
- Flato, G. M., and W. D. Hibler III (1990), On a simple sea-ice dynamics model for climate studies, *Annals of Glaciology*, *14*, 72–77.
- Flato, G. M., and W. D. Hibler III (1992), Modeling pack ice as a cavitating fluid, *Journal of Physical Oceanography*, *22*, 626–651.
- Flato, G. M., and Participating CMIP Modelling Groups (2004), Sea-ice and its response to CO₂ forcing as simulated by global climate models, *Climate Dynamics*, *23*, 229–241.
- Fofonoff, N. P. (1985), Physical properties of seawater: A new salinity scale and equation of state for seawater, *Journal of Geophysical Research*, *90*(C2), 3332–3342.
- Foley, J. A., J. E. Kutzbach, M. T. Coe, and S. Levis (1994), Feedbacks between climate and boreal forests during the Holocene epoch, *Nature*, *371*, 52–54.
- Folland, C. K., T. R. Karl, J. R. Christy, R. A. Clarke, G. V. Gruza, J. Jouzel, M. E. Mann, J. Oerlemans, M. J. Salinger, and S.-W. Wang (2001), Observed climate variability and change, in *Climate Change 2001: The Scientific Basis*, edited by J. T. Houghton, Y. Ding, D. J. Griggs, M. Noguer, P. J. van der Linden, X. Dai, K. Maskell, and C. A. Johnson, chap. 2, pp. 99–181, Cambridge University Press.
- Gargett, A. E. (1984), Vertical eddy diffusivity in the ocean interior, *Journal of Marine Research*, *42*(2), 359–393.
- Gates, W. L., and A. B. Nelson (1975a), A new (revised) tabulation of the Scripps topography on a 1 degree global grid: Part I, Terrain heights, *Technical Report R-1276-1-ARPA*, The Rand Corporation.
- Gates, W. L., and A. B. Nelson (1975b), A new (revised) tabulation of the Scripps topography on a 1 degree global grid: Part II, Ocean depths, *Technical Report R-1277-1-ARPA*, The Rand Corporation.
- Gent, P. R., and J. C. McWilliams (1990), Isopycnal mixing in ocean circulation models, *Journal of Physical Oceanography*, *20*, 150–155.
- Gent, P. R., J. Willebrand, T. J. McDougall, and J. C. McWilliams (1995), Parameterizing eddy-induced tracer transports in ocean circulation models, *Journal of Physical Oceanography*, *25*, 463–474.
- Gill, A. E. (1973), Circulation and bottom water formation in the Weddell Sea, *Deep-Sea Research*, *20*, 111–140.
- Gleckler, P. J., D. A. Randall, G. Boer, R. Colman, M. Dix, V. Galin, M. Helfand, J. Kiehl, A. Kitoh, W. Lau, X.-Y. Lang, V. Lykossov, B. McAvaney, K. Miyakoda, S. Planton, and W. Stern (1995), Cloud-radiative effects on implied oceanic energy

transports as simulated by atmospheric general circulation models, *Geophysical Research Letters*, *22*, 791–794.

Gnanadesikan, A., K. W. Dixon, S. M. Griffies, V. Balaji, M. Barreiro, J. A. Beesley, W. F. Cooke, T. L. Delworth, R. Gerdes, M. J. Harrison, I. M. Held, W. J. Hurlin, H.-C. Lee, Z. Liang, G. Nong, R. C. Pacanowski, A. Rosati, J. Russell, B. L. Samuels, Q. Song, M. J. Spelman, R. J. Stouffer, C. O. Sweeney, G. Vecchi, M. Winton, A. T. Wittenberg, F. Zeng, R. Zhang, and J. P. Dunne (2006), GFDL's CM2 global coupled climate models. Part II: The baseline ocean simulation, *Journal of Climate*, *19*, 675–697.

Goosse, H., F. M. Selten, R. J. Haarsma, and J. D. Opsteegh (2003), Large sea-ice volume anomalies simulated in a coupled climate model, *Climate Dynamics*, *20*, 523–536.

Gordon, A. L. (1986), Inter-ocean exchange of thermocline water, *Journal of Geophysical Research*, *91*(C4), 5037–5046.

Gordon, C., C. Cooper, C. A. Senior, H. Banks, J. M. Gregory, T. C. Johns, J. F. B. Mitchell, and R. A. Wood (2000), The simulation of SST, sea ice extents and ocean heat transports in a version of the Hadley Centre coupled model without flux adjustments, *Climate Dynamics*, *16*, 147–168.

Gordon, H. B. (1981), A flux formulation of the spectral atmospheric equations suitable for use in long-term climate modeling, *Monthly Weather Review*, *109*, 56–64.

Gordon, H. B., and S. P. O'Farrell (1997), Transient climate change in the CSIRO coupled model with dynamic sea ice, *Monthly Weather Review*, *125*(5), 875–907.

Gordon, H. B., L. D. Rotstayn, J. L. McGregor, M. R. Dix, E. A. Kowalczyk, S. P. O'Farrell, L. J. Waterman, A. C. Hirst, S. G. Wilson, M. A. Collier, I. G. Watterson, and T. I. Elliott (2002), The CSIRO Mk3 climate system model, *Technical Report 60*, CSIRO Atmospheric Research.

Gregory, D., and P. R. Rowntree (1990), A mass flux convection scheme with representation of cloud ensemble characteristics and stability-dependent closure, *Monthly Weather Review*, *118*, 1483–1506.

Gregory, J. M., and J. F. B. Mitchell (1997), The climate response to CO₂ of the Hadley Centre coupled AOGCM with and without flux adjustment, *Geophysical Research Letters*, *24*(15), 1943–1946.

Gregory, J. M., K. W. Dixon, R. J. Stouffer, A. J. Weaver, E. Driesschaert, M. Eby, T. Fichfet, H. Hasumi, A. Hu, J. H. Jungclaus, I. V. Kamenkovich, A. Levermann, M. Montoya, S. Murakami, S. Nawrath, A. Oka, A. P. Solokov, and R. B. Thorpe (2005), A model intercomparison of changes in the Atlantic thermohaline circulation in response to increasing atmospheric CO₂ concentration, *Geophysical Research Letters*, *32*, L12703, doi:10.1029/2005GL023209.

- Guilyardi, E. (2006), El Niño-mean state-seasonal cycle interactions in a multi-model ensemble, *Climate Dynamics*, *26*, 329–348.
- Guilyardi, E., S. Gualdi, J. Slingo, A. Navarra, P. Delecluse, J. Cole, G. Madec, M. Roberts, M. Latif, and L. Terray (2004), Representing El Niño in coupled ocean-atmosphere GCMs: The dominant role of the atmospheric component, *Journal of Climate*, *17*, 4623–4629.
- Hahn, C. J., S. G. Warren, and J. London (1995), The effect of moonlight on observation of cloud cover at night, and application to cloud climatology, *Journal of Climate*, *8*(5), 1429–1446.
- Hall, N. M. J., and P. J. Valdes (1997), A GCM simulation of the climate 6000 years ago, *Journal of Climate*, *10*, 3–17.
- Han, Y.-J. (1984), A numerical world ocean general circulation model. Part II. A baroclinic experiment, *Dynamics of Atmospheres and Oceans*, *8*, 141–172.
- Haney, R. L. (1971), Surface thermal boundary conditions for ocean circulation models, *Journal of Physical Oceanography*, *1*, 241–248.
- Harrison, S. P., D. Jolly, F. Laarif, A. Abe-Ouchi, B. Dong, K. Herterich, C. Hewitt, S. Joussaume, J. E. Kutzbach, J. Mitchell, N. de Noblet, and P. Valdes (1998), Intercomparison of simulated global vegetation distributions in response to 6 kyr BP orbital forcing, *Journal of Climate*, *11*, 2721–2742.
- Harrison, S. P., P. Braconnot, S. Joussaume, C. Hewitt, and R. J. Stouffer (2002), Comparison of palaeoclimate simulations enhances confidence in models, *EOS, Transactions, American Geophysical Union*, *83*(40), 447.
- Haywood, J. M., R. J. Stouffer, R. T. Wetherald, S. Manabe, and V. Ramaswamy (1997), Transient response of a coupled model to estimated changes in greenhouse gas and sulfate concentrations, *Geophysical Research Letters*, *24*(11), 1335–1338.
- Heil, P. (pers. comm.), Australian Antarctic Division.
- Hewitt, C. D., and J. F. B. Mitchell (1996), GCM simulations of the climate of 6 kyr BP: Mean changes and interdecadal variability, *Journal of Climate*, *9*, 3505–3529.
- Hewitt, C. D., and J. F. B. Mitchell (1998), A fully coupled GCM simulation of the climate of the mid-Holocene, *Geophysical Research Letters*, *25*(3), 361–364.
- Hirst, A. C. (1999), The Southern Ocean response to global warming in the CSIRO coupled ocean-atmosphere model, *Environmental Modelling & Software*, *14*, 227–241.
- Hirst, A. C., and W. Cai (1994), Sensitivity of a world ocean GCM to changes in subsurface mixing parameterization, *Journal of Physical Oceanography*, *24*, 1256–1279.
- Hirst, A. C., and J. S. Godfrey (1993), The role of Indonesian throughflow in a global ocean GCM, *Journal of Physical Oceanography*, *23*, 1057–1086.

- Hirst, A. C., and T. J. McDougall (1996), Deep-water properties and surface buoyancy flux as simulated by a z -coordinate model including eddy-induced advection, *Journal of Physical Oceanography*, *26*, 1320–1343.
- Hirst, A. C., and T. J. McDougall (1998), Meridional overturning and diapycnal transport in a z -coordinate model including eddy-induced advection, *Journal of Physical Oceanography*, *28*, 1205–1223.
- Hirst, A. C., H. B. Gordon, and S. O’Farrell (1996), Global warming in a coupled climate model including oceanic eddy-induced advection, *Geophysical Research Letters*, *23*(23), 3361–3364.
- Hirst, A. C., S. P. O’Farrell, and H. B. Gordon (2000), Comparison of a coupled ocean-atmosphere model with and without oceanic eddy-induced advection. Part I: Ocean spinup and control integration, *Journal of Climate*, *13*, 139–163.
- Hoar, M. R., J. P. Palutikof, and M. C. Thorne (2004), Model intercomparison for the present day, the mid-Holocene, and the Last Glacial Maximum over western Europe, *Journal of Geophysical Research*, *109*, D08104, doi:10.1029/2003JD004161.
- Hoelzmann, P., D. Jolly, S. P. Harrison, F. Laarif, R. Bonnefille, and H.-J. Pachur (1998), Mid-Holocene land-surface conditions in northern Africa and the Arabian peninsula: A data set for the analysis of biogeophysical feedbacks in the climate system, *Global Biogeochemical Cycles*, *12*(1), 35–51.
- Houghton, J. T., L. G. Meira Filho, J. Bruce, H. Lee, B. A. Callander, E. F. Haites, N. Harris, and K. Maskell (Eds.) (1994), *Climate Change 1994: Radiative Forcing of Climate Change and an Evaluation of the IPCC IS92 Emission Scenarios*, Cambridge University Press.
- Hu, A., G. A. Meehl, W. M. Washington, and A. Dai (2004), Response of the Atlantic thermohaline circulation to increased atmospheric CO₂ in a coupled model, *Journal of Climate*, *17*, 4267–4279.
- Hunt, B. G. (2004), The stationarity of global mean climate, *International Journal of Climatology*, *24*, 795–806.
- Hunt, B. G., and T. I. Elliott (2003), Secular variability of ENSO events in a 1000-year climatic simulation, *Climate Dynamics*, *20*, 689–703.
- Johns, T. C., C. F. Durman, H. T. Banks, M. J. Roberts, A. J. McLaren, J. K. Ridley, C. A. Senior, K. D. Williams, A. Jones, G. J. Rickard, S. Cusack, W. J. Ingram, M. Crucifix, D. M. H. Sexton, M. M. Joshi, B.-W. Dong, H. Spencer, R. S. R. Hill, J. M. Gregory, A. B. Keen, A. K. Pardaens, J. A. Lowe, A. Bodas-Salcedo, S. Stark, and Y. Searl (2006), The new Hadley Centre Climate Model (HadGEM1): Evaluation of coupled simulations, *Journal of Climate*, *19*, 1327–1353.

- Jolly, D., S. P. Harrison, B. Damnati, and R. Bonnefille (1998a), Simulated climate and biomes of Africa during the late Quaternary: Comparison with pollen and lake status data, *Quaternary Science Reviews*, *17*, 629–657.
- Jolly, D., I. C. Prentice, R. Bonnefille, A. Ballouche, M. Bengo, P. Brenac, G. Buchet, D. Burney, J.-P. Cazet, R. Cheddadi, T. Ector, H. Elenga, S. El-moutaki, J. Guiot, F. Laarif, H. Lamb, A.-M. Lezine, J. Maley, M. Mbenza, O. Peyron, M. Reille, I. Reynaud-Farrera, G. Riollet, J. C. Ritchie, E. Roche, L. Scott, I. Ssemmanda, H. Straka, M. Umer, E. V. Campo, S. Vilimumbalo, A. Vincens, and M. Waller (1998b), Biome reconstruction from pollen and plant macrofossil data for Africa and the Arabian peninsula at 0 and 6000 years, *Journal of Biogeography*, *25*, 1007–1027.
- Jones, P. D., and M. E. Mann (2004), Climate over past millennia, *Reviews of Geophysics*, *42*, RG2002, doi:10.1029/2003RG000143.
- Joussaume, S., K. E. Taylor, P. Braconnot, J. F. B. Mitchell, J. E. Kutzbach, S. P. Harrison, I. C. Prentice, A. J. Broccoli, A. Abe-Ouchi, P. J. Bartlein, C. Bonfils, B. Dong, J. Guiot, K. Herterich, C. D. Hewitt, D. Jolly, J. W. Kim, A. Kislov, A. Kitoh, M. F. Loutre, V. Masson, B. McAvaney, N. McFarlane, N. de Noblet, W. R. Peltier, J. Y. Peterschmitt, D. Pollard, D. Rind, J. F. Royer, M. E. Schlesinger, J. Sytkus, S. Thompson, P. Valdes, G. Vettoretti, R. S. Webb, and U. Wypotta (1999), Monsoon changes for 6000 years ago: Results of 18 simulations from the Paleoclimate Modeling Intercomparison Project (PMIP), *Geophysical Research Letters*, *26*(7), 859–862.
- Kanamitsu, M., W. Ebisuzaki, J. Woollen, S.-K. Yang, J. J. Hnilo, M. Fiorino, and G. L. Potter (2002), NCEP-DOE AMIP-II Reanalysis (R-2), *Bulletin of the American Meteorological Society*, *83*(11), 1631–1643.
- Kiehl, J. T., C. A. Shields, J. J. Hack, and W. D. Collins (2006), The climate sensitivity of the Community Climate System Model version 3 (CCSM3), *Journal of Climate*, *19*(11), 2584–2596.
- Killworth, P. D., D. A. Smeed, and A. J. G. Nurser (2000), The effects on ocean models of relaxation toward observations at the surface, *Journal of Physical Oceanography*, *30*, 160–174.
- Kitoh, A., and S. Murakami (2002), Tropical Pacific climate at the mid-Holocene and the Last Glacial Maximum simulated by a coupled ocean-atmosphere general circulation model, *Paleoceanography*, *17*(3), 1047, doi:10.1029/2001PA000724.
- Kohfeld, K. E., and S. P. Harrison (2000), How well can we simulate past climates? Evaluating the models using global palaeoenvironmental datasets, *Quaternary Science Reviews*, *19*, 321–346.
- Kowalczyk, E. A., J. R. Garratt, and P. B. Krummel (1991), A soil-canopy scheme for use in a numerical model of the atmosphere - 1D stand-alone model, *Technical Report 23*, CSIRO Division of Atmospheric Research.

- Kowalczyk, E. A., J. R. Garratt, and P. B. Krummel (1994), Implementation of a soil-canopy scheme into the CSIRO GCM - regional aspects of the model response, *Technical Report 32*, CSIRO Division of Atmospheric Research.
- Kutzbach, J., G. Bonan, J. Foley, and S. P. Harrison (1996), Vegetation and soil feedbacks on the response of the African monsoon to orbital forcing in the early to middle Holocene, *Nature*, *384*, 623–626.
- Kutzbach, J., R. Gallimore, S. Harrison, P. Behling, R. Selin, and F. Laarif (1998), Climate and biome simulations for the past 21,000 years, *Quaternary Science Reviews*, *17*, 473–506.
- Kutzbach, J. E., and P. J. Guetter (1986), The influence of changing orbital parameters and surface boundary conditions on climate simulations for the past 18 000 years, *Journal of the Atmospheric Sciences*, *43*(16), 1726–1759.
- Kutzbach, J. E., and F. A. Street-Perrott (1985), Milankovitch forcing of fluctuations in the level of tropical lakes from 18 to 0 kyr BP, *Nature*, *317*, 130–134.
- Lacis, A. A., and J. E. Hansen (1974), A parameterization for the absorption of solar radiation in the earth's atmosphere, *Journal of the Atmospheric Sciences*, *31*, 118–133.
- Lambert, S. J., and G. J. Boer (2001), CMIP1 evaluation and intercomparison of coupled climate models, *Climate Dynamics*, *17*, 83–106.
- Large, W. G., and S. Pond (1981), Open ocean momentum measurements in moderate to strong winds, *Journal of Physical Oceanography*, *11*, 324–336.
- Large, W. G., and S. Pond (1982), Sensible and latent heat flux measurements over the sea, *Journal of Physical Oceanography*, *12*, 464–482.
- Large, W. G., G. Danabasoglu, S. C. Doney, and J. C. McWilliams (1997), Sensitivity to surface forcing and boundary layer mixing in a global ocean model: Annual-mean climatology, *Journal of Physical Oceanography*, *27*, 2418–2447.
- Legates, D. R., and C. J. Willmott (1990), Mean seasonal and spatial variability in gauge-corrected, global precipitation, *International Journal of Climatology*, *10*, 111–127.
- Levis, S., G. B. Bonan, and C. Bonfils (2004), Soil feedback drives the mid-Holocene North African monsoon northward in fully coupled CCSM2 simulations with a dynamic vegetation model, *Climate Dynamics*, *23*, 791–802.
- Levitus, S. (1982), Climatological atlas of the World Ocean, *Professional Paper 13*, National Oceanographic and Atmospheric Administration.
- Liao, X., A. Street-Perrott, and J. F. B. Mitchell (1994), GCM experiments with different cloud parameterization: Comparisons with palaeoclimatic reconstructions for 6000 years B.P., *Palaeoclimates*, *1*, 99–123.

- Liu, Z., J. Kutzbach, and L. Wu (2000), Modeling climate shift of El Niño variability in the Holocene, *Geophysical Research Letters*, *27*(15), 2265–2268.
- Liu, Z., E. Brady, and J. Lynch-Stieglitz (2003a), Global ocean response to orbital forcing in the Holocene, *Paleoceanography*, *18*(2), 1041, doi:10.1029/2002PA000819.
- Liu, Z., B. Otto-Bliesner, J. Kutzbach, L. Li, and C. Shields (2003b), Coupled climate simulation of the evolution of global monsoons in the Holocene, *Journal of Climate*, *16*, 2472–2490.
- Lohmann, K., and M. Latif (2005), Tropical Pacific decadal variability and the subtropical-tropical cells, *Journal of Climate*, *18*, 5163–5178.
- Lorenz, S., B. Grieger, Ph. Helbig, and K. Herterich (1996), Investigating the sensitivity of the atmospheric general circulation model ECHAM 3 to paleoclimatic boundary conditions, *Geologische Rundschau*, *85*, 513–524.
- Lorenz, S. J., and G. Lohmann (2004), Acceleration technique for Milankovitch type forcing in a coupled atmosphere-ocean circulation model: method and application for the Holocene, *Climate Dynamics*, *23*, 727–743.
- Manabe, S., and R. J. Stouffer (1994), Multiple-century response of a coupled ocean-atmosphere model to an increase of atmospheric carbon dioxide, *Journal of Climate*, *7*, 5–23.
- Mann, M. E., and P. D. Jones (2003), Global surface temperatures over the past two millennia, *Geophysical Research Letters*, *30*(15), 1820, doi:10.1029/2003GL017814.
- Massom, R. (pers. comm.), Australian Antarctic Division.
- Masson, V., and S. Joussaume (1997), Energetics of the 6000-yr BP atmospheric circulation in boreal summer, from large-scale to monsoon areas: A study with two versions of the LMD AGCM, *Journal of Climate*, *10*, 2888–2903.
- Masson, V., S. Joussaume, S. Pinot, and G. Ramstein (1998), Impact of parameterizations on simulated winter mid-Holocene and Last Glacial Maximum climatic changes in the northern hemisphere, *Journal of Geophysical Research*, *103*(D8), 8935–8946.
- Masson, V., R. Cheddadi, P. Braconnot, S. Joussaume, D. Texier, and PMIP participants (1999), Mid-Holocene climate in Europe: what can we infer from PMIP model-data comparisons?, *Climate Dynamics*, *15*, 163–182.
- McAvaney, B. J., C. Covey, S. Joussaume, V. Kattsov, A. Kitoh, W. Ogana, A. J. Pitman, A. J. Weaver, R. A. Wood, and Z.-C. Zhao (2001), Model evaluation, in *Climate Change 2001: The Scientific Basis*, edited by J. T. Houghton, Y. Ding, D. J. Griggs, M. Noguer, P. J. van der Linden, X. Dai, K. Maskell, and C. A. Johnson, chap. 8, pp. 471–523, Cambridge University Press.

- McGregor, J. L. (1993), Economical determination of departure points for semi-Lagrangian models, *Monthly Weather Review*, *121*, 221–230.
- McGuffie, K., and A. Henderson-Sellers (1997), *A Climate Modelling Primer*, second ed., John Wiley and Sons.
- McGuffie, K., and A. Henderson-Sellers (2001), Forty years of numerical climate modelling, *International Journal of Climatology*, *21*, 1067–1109.
- Meehl, G. A., W. M. Washington, J. M. Arblaster, T. W. Bettge, and W. G. Strand, Jr. (2000), Anthropogenic forcing and decadal climate variability in sensitivity experiments of twentieth and twenty-first-century climate, *Journal of Climate*, *13*(21), 3728–3744.
- Meehl, G. A., C. Covey, B. McAvaney, M. Latif, and R. J. Stouffer (2005), Overview of the Coupled Model Intercomparison Project, *Bulletin of the American Meteorological Society*, *86*(1), 89–93.
- Meehl, G. A., W. M. Washington, B. D. Santer, W. D. Collins, J. M. Arblaster, A. Hu, D. M. Lawrence, H. Teng, L. E. Buja, and W. G. Strand (2006), Climate change projections for the twenty-first century and climate change commitment in the CCSM3, *Journal of Climate*, *19*(11), 2597–2616.
- Mikolajewicz, U., M. Scholze, and R. Voss (2003), Simulating near-equilibrium climate and vegetation for 6000 cal. years BP, *The Holocene*, *13*(3), 319–326.
- Mitchell, J. F. B., T. C. Johns, J. M. Gregory, and S. F. B. Tett (1995), Climate response to increasing levels of greenhouse gases and sulphate aerosols, *Nature*, *376*, 501–504.
- Mitchell, J. F. B., D. J. Karoly, G. C. Hegerl, F. W. Zwiers, M. R. Allen, and J. Marengo (2001), Detection of climate change and attribution of causes, in *Climate Change 2001: The Scientific Basis*, edited by J. T. Houghton, Y. Ding, D. J. Griggs, M. Noguer, P. J. van der Linden, X. Dai, K. Maskell, and C. A. Johnson, chap. 12, pp. 695–738, Cambridge University Press.
- Montoya, M., A. Griesel, A. Levermann, J. Mignot, M. Hofmann, A. Ganopolski, and S. Rahmstorf (2005), The earth system model of intermediate complexity CLIMBER-3 α . Part I: description and performance for present-day conditions, *Climate Dynamics*, *25*, 237–263.
- Moore, A. M., and H. B. Gordon (1994), An investigation of climate drift in a coupled atmosphere-ocean-sea ice model, *Climate Dynamics*, *10*, 81–95.
- Moore, A. M., and C. J. C. Reason (1993), The response of a global ocean general circulation model to climatological surface boundary conditions for temperature and salinity, *Journal of Physical Oceanography*, *23*, 300–328.
- Moy, C. M., G. O. Seltzer, D. T. Rodbell, and D. M. Anderson (2002), Variability of El Niño/Southern Oscillation activity at millennial timescales during the Holocene epoch, *Nature*, *420*, 162–165.

- National Oceanographic Data Center (2002), World Ocean Atlas 1998, URL http://www.nodc.noaa.gov/OC5/pr_woa.html, viewed 13 September 2005.
- Oberhuber, J. M. (1993), Simulation of the Atlantic circulation with a coupled sea ice-mixed layer-isopycnal general circulation model. Part I: Model description, *Journal of Physical Oceanography*, *23*, 808–829.
- O’Farrell, S. P. (1998), Investigation of the dynamic sea ice component of a coupled atmosphere-sea ice general circulation model, *Journal of Geophysical Research*, *103*(C8), 15,751–15,782.
- Olbers, D., D. Borowski, C. Völker, and J.-O. Wölf (2004), The dynamical balance, transport and circulation of the Antarctic Circumpolar Current, *Antarctic Science*, *16*(4), 439–470.
- Oreskes, N., K. Shrader-Frechette, and K. Belitz (1994), Verification, validation, and confirmation of numerical models in the earth sciences, *Science*, *263*, 641–646.
- Orsi, A. H., G. C. Johnson, and J. L. Bullister (1999), Circulation, mixing, and production of Antarctic Bottom Water, *Progress in Oceanography*, *43*, 55–109.
- Orsi, A. H., S. S. Jacobs, A. L. Gordon, and M. Visbeck (2001), Cooling and ventilating the abyssal ocean, *Geophysical Research Letters*, *28*(15), 2923–2926.
- Otto-Bliesner, B. L. (1999), El Niño/La Niña and Sahel precipitation during the middle Holocene, *Geophysical Research Letters*, *26*(1), 87–90.
- Otto-Bliesner, B. L., E. C. Brady, G. Clauzet, R. Tomas, S. Levis, and Z. Kothavala (2006), Last Glacial Maximum and Holocene climate in CCSM3, *Journal of Climate*, *19*(11), 2526–2544.
- Paleoclimate Modelling Intercomparison Project (2005), Paleoclimate Modelling Intercomparison Project Phase II, URL <http://www-lsce.cea.fr/pmip2/>, viewed 19 September 2005.
- Parkinson, C. L., D. L. Cavalieri, P. Gloersen, H. J. Zwally, and J. C. Comiso (1999), Arctic sea ice extents, areas, and trends, 1978–1996, *Journal of Geophysical Research*, *104*(C9), 20,837–20,856.
- Pavlov, A. A., O. B. Toon, A. K. Pavlov, J. Bally, and D. Pollard (2005), Passing through a giant molecular cloud: “Snowball” glaciations produced by interstellar dust, *Geophysical Research Letters*, *32*, L03705, doi:10.1029/2004GL021890.
- Philander, S. G. (1990), *El Niño, La Niña, and the Southern Oscillation*, Academic Press.
- Phipps, S. J. (2006), The CSIRO Mk3L climate system model, *Technical Report 3*, Antarctic Climate and Ecosystems Cooperative Research Centre, Hobart, Tasmania, Australia.
- Pierce, D. R. (1996), Reducing phase and amplitude errors in restoring boundary conditions, *Journal of Physical Oceanography*, *26*, 1552–1560.

- Pollard, D., J. C. Bergengren, L. M. Stillwell-Soller, B. Felzer, and S. L. Thompson (1998), Climate simulations for 10000 and 6000 years BP using the GENESIS global climate model, *Paleoclimates*, 2(2-3), 183–218.
- Power, S. B. (1995), Climate drift in a global ocean general circulation model, *Journal of Physical Oceanography*, 25, 1025–1036.
- Power, S. B., and R. Kleeman (1993), Multiple equilibria in a global ocean general circulation model, *Journal of Physical Oceanography*, 23, 1670–1681.
- Prell, W. L., and J. E. Kutzbach (1987), Monsoon variability over the past 150,000 years, *Journal of Geophysical Research*, 92(D7), 8411–8425.
- Prentice, I. C., and T. Webb, III (1998), BIOME 6000: reconstructing global mid-Holocene vegetation patterns from palaeoecological records, *Journal of Biogeography*, 25, 997–1005.
- Prentice, I. C., D. Jolly, and BIOME 6000 participants (2000), Mid-Holocene and glacial-maximum vegetation and geography of the northern continents and Africa, *Journal of Biogeography*, 27, 507–519.
- Press, W. H., S. A. Teukolsky, W. T. Vetterling, and B. P. Flannery (1992), *Numerical Recipes in C: The Art of Scientific Computing*, second ed., Cambridge University Press.
- Ramaswamy, V., O. Boucher, J. Haigh, D. Hauglustaine, J. Haywood, G. Myhre, T. Nakajima, G. Y. Shi, and S. Solomon (2001), Radiative forcing of climate change, in *Climate Change 2001: The Scientific Basis*, edited by J. T. Houghton, Y. Ding, D. J. Griggs, M. Noguer, P. J. van der Linden, X. Dai, K. Maskell, and C. A. Johnson, chap. 6, pp. 349–416, Cambridge University Press.
- Raper, S. C. B., J. M. Gregory, and R. J. Stouffer (2002), The role of climate sensitivity and ocean heat uptake on AOGCM transient temperature response, *Journal of Climate*, 15, 124–130.
- Renssen, H., H. Goosse, T. Fichefet, V. Masson-Delmotte, and N. Koç (2005), Holocene climate evolution in the high-latitude Southern Hemisphere simulated by a coupled atmosphere-sea ice-ocean-vegetation model, *The Holocene*, 15(7), 951–964.
- Reynolds, R. W., N. A. Rayner, T. M. Smith, D. C. Stokes, and W. Wang (2002), An improved in situ and satellite SST analysis for climate, *Journal of Climate*, 15, 1609–1625.
- Robert, A. J. (1966), The integration of a low order spectral form of the primitive meteorological equations, *Journal of the Meteorological Society of Japan*, 44(5), 237–244.
- Robertson, A., J. Overpeck, D. Rind, E. Mosley-Thompson, G. Zielinski, J. Lean, D. Koch, J. Penner, I. Tegen, and R. Healy (2001), Hypothesised climate forcing time series for the last 500 years, *Journal of Geophysical Research*, 106(D14), 14,783–14,803.

- Rodbell, D. T., G. O. Seltzer, D. M. Anderson, M. B. Abbott, D. B. Enfield, and J. H. Newman (1999), An ~15,000-year record of El Niño-driven alluviation in southwestern Ecuador, *Science*, *283*, 516–520.
- Ropelewski, C. F., and P. D. Jones (1987), An extension of the Tahiti-Darwin Southern Oscillation Index, *Monthly Weather Review*, *115*, 2161–2165.
- Rotstayn, L. D. (1997), A physically based scheme for the treatment of stratiform clouds and precipitation in large-scale models. I: Description and evaluation of the microphysical processes, *Quarterly Journal of the Royal Meteorological Society*, *123*, 1227–1282.
- Rotstayn, L. D. (1998), A physically based scheme for the treatment of stratiform clouds and precipitation in large-scale models. II: Comparison of modelled and observed climatological fields, *Quarterly Journal of the Royal Meteorological Society*, *124*, 389–415.
- Rotstayn, L. D. (2000), On the “tuning” of autoconversion parameterizations in climate models, *Journal of Geophysical Research*, *105*(D12), 15,495–15,507.
- Ruddiman, W. F. (2003), The anthropogenic greenhouse era began thousands of years ago, *Climatic Change*, *61*, 261–293.
- Sausen, R., K. Barthel, and K. Hasselmann (1988), Coupled ocean-atmosphere models with flux correction, *Climate Dynamics*, *2*, 145–163.
- Schott, F. A., T. N. Lee, and R. Zantopp (1988), Variability of structure and transport of the Florida Current in the period range of days to seasonal, *Journal of Physical Oceanography*, *18*, 1209–1230.
- Schwarzkopf, M. D., and S. B. Fels (1985), Improvements to the algorithm for computing CO₂ transmissivities and cooling rates, *Journal of Geophysical Research*, *90*(D6), 10,541–10,550.
- Schwarzkopf, M. D., and S. B. Fels (1991), The simplified exchange method revisited: An accurate, rapid method for computation of infrared cooling rates and fluxes, *Journal of Geophysical Research*, *96*(D5), 9075–9096.
- Semtner, A. J., Jr. (1976), A model for the thermodynamic growth of sea ice in numerical investigations of climate, *Journal of Physical Oceanography*, *6*, 379–389.
- Shulmeister, J., and B. G. Lees (1998), Pollen evidence from tropical Australia for the onset of an ENSO-dominated climate at c. 4000 BP, *Holocene*, *5*(1), 10–18.
- Sloan, L. C. (2006), A framework for regional modeling of past climates, *Theoretical and Applied Climatology*, *86*, 271–279, doi:10.1007/s00704-005-0207-3.
- Smethie, W. M., Jr., and R. A. Fine (2001), Rates of North Atlantic Deep Water formation calculated from chlorofluorocarbon inventories, *Deep-Sea Research Part I: Oceanographic Research Papers*, *48*, 189–215.

- Stainforth, D. A., T. Aina, C. Christensen, M. Collins, N. Faull, D. J. Frame, J. A. Kettleborough, S. Knight, A. Martin, J. M. Murphy, C. Piani, D. Sexton, L. A. Smith, R. A. Spicer, A. J. Thorpe, and M. R. Allen (2005), Uncertainty in predictions of the climate response to rising levels of greenhouse gases, *Nature*, *433*(7024), 403–406.
- Stammer, D., C. Wunsch, R. Giering, C. Eckert, P. Heimbach, J. Marotzke, A. Adcroft, C. N. Hill, and J. Marshall (2003), Volume, heat, and freshwater transports of the global ocean circulation 1993–2000, estimated from a general circulation model constrained by World Ocean Circulation Experiment (WOCE) data, *Journal of Geophysical Research*, *108*(C1), 3007, doi:10.1029/2001JC001115.
- Stouffer, R. J., and S. Manabe (2003), Equilibrium response of thermohaline circulation to large changes in atmospheric CO₂ concentration, *Climate Dynamics*, *20*, 759–773.
- Stouffer, R. J., A. J. Broccoli, T. L. Delworth, K. W. Dixon, R. Gudgel, I. Held, R. Hemler, T. Knutson, H.-C. Lee, M. D. Schwarzkopf, B. Soden, M. J. Spelman, M. Winton, and F. Zeng (2006), GFDL’s CM2 global coupled climate models. Part IV: Idealised climate response, *Journal of Climate*, *19*, 723–740.
- TEMPO (1996), Potential role of vegetation feedback in the climate sensitivity of high-latitude regions: A case study at 6000 years B.P., *Global Biogeochemical Cycles*, *10*(4), 727–736.
- Terray, L. (1998), Sensitivity of climate drift to atmospheric physical parameterizations in a coupled ocean-atmosphere general circulation model, *Journal of Climate*, *11*, 1633–1658.
- Texier, D., N. de Noblet, S. P. Harrison, A. Haxeltine, D. Jolly, S. Joussaume, F. Laarif, I. C. Prentice, and P. Tarasov (1997), Quantifying the role of biosphere-atmosphere feedbacks in climate change: coupled model simulations for 6000 years BP and comparison with palaeodata for northern Eurasia and northern Africa, *Climate Dynamics*, *13*, 865–882.
- Texier, D., N. de Noblet, and P. Braconnot (2000), Sensitivity of the African and Asian monsoons to mid-Holocene insolation and data-inferred surface changes, *Journal of Climate*, *13*, 164–181.
- Toggweiler, J. R., and B. Samuels (1995), Effect of sea ice on the salinity of Antarctic bottom waters, *Journal of Physical Oceanography*, *25*, 1980–1997.
- Trenberth, K. E. (1997), The definition of El Niño, *Bulletin of the American Meteorological Society*, *78*(12), 2771–2777.
- Trenberth, K. E., and T. J. Hoar (1996), The 1990–1995 El Niño–Southern Oscillation event: Longest on record, *Geophysical Research Letters*, *23*(1), 57–60.
- Tudhope, A. W., C. P. Chilcott, M. J. McCulloch, E. R. Cook, J. Chappell, R. M. Ellam, D. W. Lea, J. M. Lough, and G. B. Shimmield (2001), Variability in the

- El Niño-Southern Oscillation through a glacial-interglacial cycle, *Science*, *291*, 1511–1517.
- Tziperman, E., J. R. Toggweiler, Y. Feliks, and K. Bryan (1994), Instability of the thermohaline circulation with respect to mixed boundary conditions: Is it really a problem for realistic models?, *Journal of Physical Oceanography*, *24*, 217–232.
- UNESCO (1981), Background papers and supporting data on the International Equation of State of Seawater 1980, *Technical Papers in Marine Science* *38*, UNESCO.
- Vettoretti, G., W. R. Peltier, and N. A. McFarlane (1998), Simulations of mid-Holocene climate using an atmospheric general circulation model, *Journal of Climate*, *11*, 2607–2627.
- Vettoretti, G., W. R. Peltier, N. A. McFarlane, and PMIP participating groups (2000), The simulated response of the climate system to changes in soil moisture parameterization under paleoclimatic boundary conditions at 6000 years before present, *Canadian Journal of Earth Sciences*, *37*(5), 635–660.
- Vimont, D. J., D. S. Battisti, and A. C. Hirst (2002), Pacific interannual and interdecadal equatorial variability in a 1000-yr simulation of the CSIRO coupled general circulation model, *Journal of Climate*, *15*, 160–178.
- Voss, R., and U. Mikolajewicz (2001), The climate of 6000 years BP in near-equilibrium with a coupled AOGCM, *Geophysical Research Letters*, *28*(11), 2213–2216.
- Wadhams, P. (2000), *Ice in the Ocean*, Gordon and Breach Science Publishers.
- Walland, D. J., S. B. Power, and A. C. Hirst (2000), Decadal climate variability simulated in a coupled general circulation model, *Climate Dynamics*, *16*, 201–211.
- Wang, W.-C., X.-Z. Liang, M. P. Dudek, D. Pollard, and S. L. Thompson (1995), Atmospheric ozone as a climate gas, *Atmospheric Research*, *37*, 247–256.
- Wang, Y., L. A. Mysak, Z. Wang, and V. Brovkin (2005), The greening of the McGill Paleoclimate Model. Part I: Improved land surface scheme with vegetation dynamics, *Climate Dynamics*, *24*, 469–480.
- Warren, S. G., C. J. Hahn, J. London, R. M. Chervin, and R. L. Jenne (1986), Global distribution of total cloud cover and cloud type amounts over land, *Technical Note NCAR/TN-273+STR*, NCAR.
- Warren, S. G., C. J. Hahn, J. London, R. M. Chervin, and R. L. Jenne (1988), Global distribution of total cloud cover and cloud type amounts over the ocean, *Technical Note NCAR/TN-317+STR*, NCAR.
- Washington, W. M., and C. L. Parkinson (1986), *An Introduction to Three-Dimensional Climate Modeling*, Oxford University Press.

- Weaver, A. J., and T. M. C. Hughes (1996), On the incompatibility of ocean and atmosphere models and the need for flux adjustments, *Climate Dynamics*, *12*, 141–170.
- Weaver, A. J., and E. S. Sarachik (1991a), Evidence for decadal variability in an ocean general circulation model: An advective mechanism, *Atmosphere-Ocean*, *29*(2), 197–231.
- Weaver, A. J., and E. S. Sarachik (1991b), The role of mixed boundary conditions in numerical models of the ocean's climate, *Journal of Physical Oceanography*, *21*(9), 1470–1493.
- Weaver, A. J., J. Marotzke, P. F. Cummins, and E. S. Sarachik (1993), Stability and variability of the thermohaline circulation, *Journal of Physical Oceanography*, *23*, 39–60.
- Weaver, A. J., M. Eby, E. C. Wiebe, C. M. Bitz, P. B. Duffy, T. L. Ewen, A. F. Fanning, M. M. Holland, A. MacFadyen, H. D. Matthews, K. J. Meissner, O. Saenko, A. Schmittner, H. Wang, and M. Yoshimori (2001), The UVic Earth System Climate Model: Model description, climatology, and applications to past, present and future climates, *Atmosphere-Ocean*, *39*(4), 361–428.
- Weber, S. L. (2001), The impact of orbital forcing on the climate of an intermediate-complexity coupled model, *Global and Planetary Change*, *30*, 7–12.
- Weber, S. L., T. J. Crowley, and G. van der Schrier (2004), Solar irradiance forcing of centennial climate variability during the Holocene, *Climate Dynamics*, *22*, 539–553.
- Wigley, T. M. L., and S. C. B. Raper (1987), Thermal expansion of sea water associated with global warming, *Nature*, *330*, 127–131.
- Wilks, D. S. (1995), *Statistical Methods in the Atmospheric Sciences*, Academic Press.
- Wittenberg, A. T., A. Rosati, N.-C. Lau, and J. A. Ploshay (2006), GFDL's CM2 global coupled climate models. Part III: Tropical Pacific climate and ENSO, *Journal of Climate*, *19*, 698–722.
- Wood, R. A., M. Vellinga, and R. Thorpe (2003), Global warming and thermohaline circulation stability, *Philosophical Transactions of the Royal Society of London A*, *361*, 1961–1975.
- Yu, G., and S. P. Harrison (1996), An evaluation of the simulated water balance of Eurasia and northern Africa at 6000 y BP using lake status data, *Climate Dynamics*, *12*, 723–735.
- Zhang, S., R. J. Greatbatch, and C. A. Lin (1993), A reexamination of the polar halocline catastrophe and implications for coupled ocean-atmosphere modeling, *Journal of Physical Oceanography*, *23*, 287–299.

Zhang, Y., J. M. Wallace, and D. S. Battisti (1997), ENSO-like interdecadal variability: 1900-1993, *Journal of Climate*, *10*, 1004–1020.